August 198

JAN 7

SSD 80-0108-2

NAS8-32475
DPD567
DR MA-04

Satellite Power Systems (SPS)
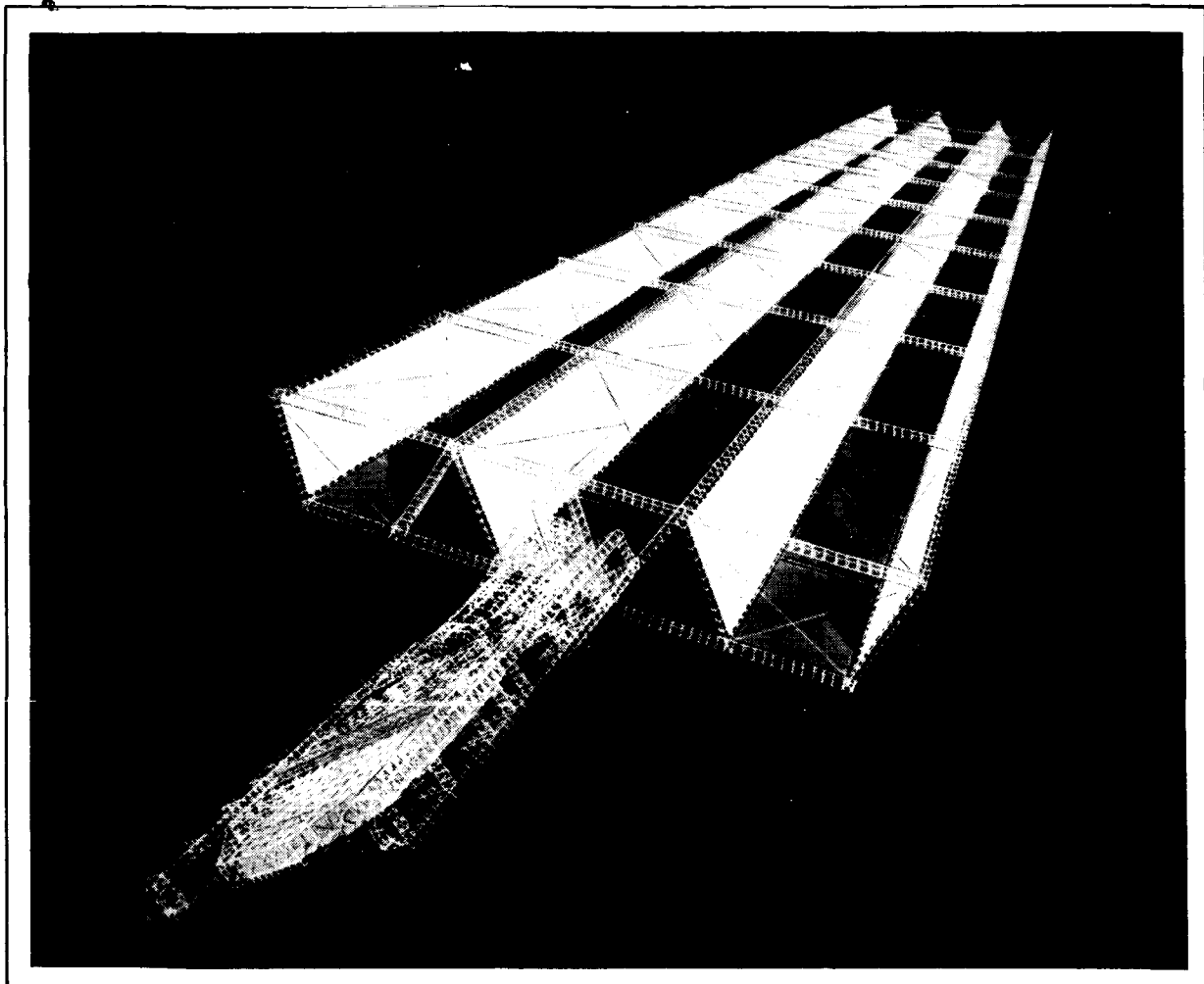
Concept Definition Study

FINAL REPORT (EXHIBIT D)

VOLUME II

SYSTEMS/SUBSYSTEMS ANALYSES

Rockwell International

Space Operations and
Satellite Systems Division

SSD 80-0108-2

Satellite Power Systems (SPS) Concept Definition Study

FINAL REPORT (EXHIBIT D)
VOLUME II

SYSTEMS/SUBSYSTEMS ANALYSES

Submitted by

G. HANLEY
Program Manager

Approved

C.H. GUTTMAN
SPS Study Team Manager, NASA/MSFC

FOREWORD

Volume II, Systems/Subsystems Analysis, encompasses SPS system and subsystem analyses performed to establish the impact of technological advancements on the reference concept and to develop and select new solid-state SPS concepts where economic viability is potentially enhanced. Volume II of the SPS concept definition study final report is submitted by Rockwell International through the Space Operations and Satellite Systems Division. All work was completed in response to NASA/MSFC contract NAS8-32475, Exhibit D, dated June 1979.

The SPS final report will provide the NASA with additional information on the selection of a viable SPS concept, and will furnish a basis for subsequent technology exploratory development activities. A more comprehensive matrix of solid-state concepts have been devised and evaluated to select approaches for more detailed definition. The current reference concept with klystron dc/RF converters has been updated, primarily to determine impacts of advanced multi-bandgap solar cells. Appropriate tradeoff data is presented to substantiate design details. Other volumes of the final report are listed as follows:

Volume	Title
I	Executive Summary
III	Transportation Analyses
IV	Operations Analyses
V	Systems Engineering/Integration Analyses
VI	Cost and Programmatics
VII	Systems/Subsystems Requirements Data Book

The SPS Program Manager, G. M. Hanley, may be contracted on any of the technical or management aspects of this report. He can be reached at 213/594-3911, Seal Beach, California.

INTRODUCTION

This volume presents results of studies to determine desirable modifi-
cations to the reference concept and to identify new solid-state concepts
and define the best approaches. Results are presented which show the impact
of the high-efficiency multi-bandgap solar array on the reference concept
design. System trade studies are described for several solid-state concepts,
including the sandwich concept and a separate antenna/solar array concept.
Results are presented to shown an evaluation of several approaches for each
overall concept. Two solid-state concepts were selected and a design defin-
ition presented for each. A special study was conducted to evaluate
magnetrons as an alternative to the reference klystrons for dc/RF conversion.
System definitions are presented for the preferred klystron and solid state
concepts. Supporting subsystem-level analyses is included with major
analyses in the microwave, structures, and power distribution areas. Micro-
wave studies include different antenna configurations, antenna power density
variations, assessment of unique phase control approaches to solid-state
systems, power-module combining, antenna module design, and GaAs MESFET
device modeling and power conversion simulation. Because of blockage of
either the microwave beam or incoming solar energy with primary and/or
secondary structure, the space frame structure is not appropriate for the
sandwich concepts. Structures studies were performed to evaluate alternative
approaches and assess the viability of the compression frame/tension web con-
cept. Power distribution studies considered several approaches to providing
power to the solid-state devices for the separate solar array/antenna con-
cepts. Results from ancillary studies for thermal control and attitude
control and stationkeeping are included. Details of a multi-bandgap solar cell
study are included.

Finally, the results of a study considering the meteorological effects of
a laser beam power transmission concept have been provided. In addition, a
few thoughts regarding advanced laser concepts have been included.

CONTENTS

Section   Page

ILLUSTRATIONS

TABLES

GLOSSARY

A	Ampere
$\overset{o}{A}$	Angstrom
ac	Alternating current
ACSS	Attitude control and stationkeeping system
AMO	Air mass zero
ARDS	Attitude reference determination system
$\overline{B}$	Billions of dollars
$B_e O$	Beryllium oxide (Berlox)
BCD	Binary coded decimal
BCU	Bus control units
BOL	Beginning of life
BT	Battery tie contactor
°C	Degree centigrade
C_e	Cesium
cm	Centimeter
CMD	Command
COTV	Cargo orbital transfer vehicle
CPU	Central processing unit
CR	Concentration ratio
CR_E	Effective concentration ratio
CVD	Controlled vapor deposit
D/A	Digital to analog
dB	Decibel
dc	Direct current
DOE	Department of Energy
DVM	Digital voltmeter

EBS	Electron beam semiconductor
E_g	Bandgap energy
EMI	Electromagnetic interference
EOL	End of life
EOTV	Electric orbital transfer vehicle
EVA	Extra-vehicular activity
f	Frequency
°F	Degree Fahrenheit
FEP	Adhesive material
FET	Field-effect transistor
FOC	Final operational capability
f_p	Pilot frequency
f_r	Reference signal frequency
f_T	Transmitted frequency
G	Giga- (10^9)
G	Gear, switch
GaAlAs	Gallium aluminum arsenide
GaAs	Gallium arsenide
GEO	Geosynchronous, equatorial orbit
GHz	Gigahertz
GPS	Global Positioning System
GRS	Ground receiving station
GW	Gigawatt
HLLV	Heavy-lift launch vehicle
HPWB	Half-power-point beamwidth
HV	High voltage
Hz	Hertz
IB	Interface bus
IBM	International Business Machines Corp.
IMCS	Information management and control system
IMS	Information management system (see IMCS)

IOC	Initial operations capability
IOP	In-orbit plane
IOTV	Inter-orbit transfer vehicle
IUS	Inter-orbit utility stage

k	Kilo (10^3)
K	Potassium
°K	Degree Kelvin
km	Kilometer (1000 meters)
kN	Kilonewton
KSC	Kennedy Space Flight Center
kV	Kilovolts

LED	Light-emitting diode
LEO	Low earth orbit
LH_2	Liquid hydrogen
LOX	Liquid oxygen
LPE	Liquid phase **epitaxal**
LRB	Liquid rocket booster
LRU	Line replaceable unit
LSST	Large space structures technology

m	Meter
M	Mega- (10^6)
MBG	Multi-bandgap
MC-ABES	Multi-cycle airbreathing engine system
MeV	Millions of electron volts
µp	Microprocessor
MPCA	Master phase reference control amplifier
MPTS	Microwave power transmission system
MSFC	Marshall Space Flight Center
MTBF	Mean time between failure
MTTF	Mean time to failure
MW	Megawatt
MW	Microwave

MW_e	Megawatt—electrical
MWM	Manned work modules
MW_T	Megawatt—thermal
M_X	Disturbance torque along X-axis

N	Newton
NaK	Sodium-potassium
NASA	National Aeronautics and Space Administration
N-S	North-South

O&M	Operations and maintenance
OTV	Orbit transfer vehicle

PDS	Power distribution system
PLV	Personnel launch vehicle
PM	Personnel module
POP	Perpendicular to orbit plane
POTV	Personnel orbital transfer vehicle
psi	Pounds per square inch

RAC	Remote acquisition and control
R&D	Research and development
R&T	Research and technology
RCA	Radio Corporation of America
RCI	Replacement cost investment
RCR	Resonant cavity radiator
RCS	Reaction control system
RF	Radio frequency
RFI	Radio frequency interference
RTE	Real-time evaluation

S/A	Solar array
SCB	Space construction base
SG	Switch gear
Si	Silicon

SIT	Static induction transistor
SM	Sub-multiplexer
SOC	Space Operations Center
SPS	Satellite Power Systems
SRB	Solid rocket booster
STS	Space Transportation System
T	Temperature
TBD	To be determined
T&E	Test and evaluation
TFU	Theoretical first unit
TT&C	Telemetry, tracking, and communications
TWT	Traveling wave tubes
UI	Utility interface
V	Volt
VHF	Very high frequency
VSWR	Voltage standing wave ratio
VTO	Vertical take-off
W	Watt
Wh	Watt-hour
X,Y,Z	Coordinate axes of satellite

Symbols

ε	Error signals
λ	Wavelength of frequency f (Hertz)
μ	Micro-
η	Efficiency
ϕ	Phase
ϕ	Coordinate axis angle—Phi
θ	Coordinate axis (angle)—Theta

1.0 SPS CONCEPTS

Included in this section are descriptions of the various candidate concepts studied with associated conclusions and recommendations. Two overall approaches were considered for solid-state microwave transmission concepts: solar array mounted (sandwich) and antenna mounted. The solar array mounted sandwich concept is a totally new satellite concept developed to exploit fully the potential advantages of solid-state technology. This concept was first introduced during the final quarter of the Exhibit C study as a result of a joint MSFC-Rockwell effort. The end-mounted solid-state antenna approach is basically the reference concept reconfigured to accommodate the solid-state amplifiers. Each of these concepts was varied and parametric data developed to illustrate the mass and economic sensitivities. The most promising concepts are further defined.

The Rockwell reference klystron concept is based on using thin film GaAs solar cells with the guidelined ionospheric power density limit of 23 mW/cm^2. Reference concept changes are recommended in an updated version of this concept. Advanced multi-bandgap solar cells with increased cell efficiency were evaluated since these solar cells are on the verge of being available. These cells result in a smaller overall satellite size, lower satellite mass, and reduced satellite cost. Configurational changes to the reference satellite design through the use of high efficiency multi-bandgap solar cells are illustrated.

An efficiency of 90 percent (dc to RF conversion) for the magnetron is projected, based on a reported value of 85 percent already measured on an existing magnetron tube. Using 90 percent efficiency a magnetron system concept is described and evaluated against the reference klystron concept.

1.1 SOLID-STATE CONCEPTS

The baseline satellite concept utilizes high voltage (HV) klystron dc-RF converters to amplify the 2.45-GHz microwave reference signal. The power for the RF converters is transferred from the solar array at 40 kV dc (nominal) across the antenna slip rings, converted to five selected high voltage dc voltages and utilized by the klystrons. The use of solid-state devices may result in system concepts that vary greatly from the approach considered for vacuum tube based microwave power amplifiers. The klystron device has very high power output per device (50-70 kW), whereas output of the individual solid-state driven dipoles is only 4-50 W. This results in a large number of solid-state power amplifiers individually phase controlled. The klystron is a more complex device and it is expected that the cost/unit power of the solid-state amplifiers will be lower because of the ability to mass-produce them. Individual integration of the klystrons is necessary because of their complexity. A major area of concern for the solid-state system is development of a phase control and power feed system which allows for mass production and simple orbital integration.

A major study goal of Exhibit D has been to devise satellite approaches using low voltage solid state devices. The desire to replace klystrons with solid state devices is driven primarily by their potential for higher improved satellite reliability; klystrons probably will have to be replaced at least two and perhaps three times during the 30-year operational period.

Solid state microwave design drivers identified are: their maximum breakdown voltage limits (10 to 70 V dc), function temperature constraints (<200 C), output power limits (100 watts), and circuit efficiencies (78 percent to 90 percent). During the final quarter of the Exhibit C study, a joint MSFC-Rockwell effort produced new solid state satellite concepts which contrast sharply with configurations studied previously. Figure 1.1-1 illustrates one of the concepts which uses the sandwich panel approach composed of a solid-state amplifier panel "sandwiched" between the solar cell and radiating antenna panels (described in Section 1.1.1). For comparison purpose, a second approach for solid state dc-RF converters has been evaluated with the reference concept reconfigured and employing two antennas, one at each end of the solar array (described in Section 1.1.2).

DIRECT/REFLECTED SUNLIGHT

SOLAR CELL
BLANKET PANEL

SOLID-STATE
AMPLIFIER
PANEL

TRANSMITTING
ANTENNA PANEL

RF ENERGY TO EARTH

*Primary
Reflector*

*Secondary
Reflector*
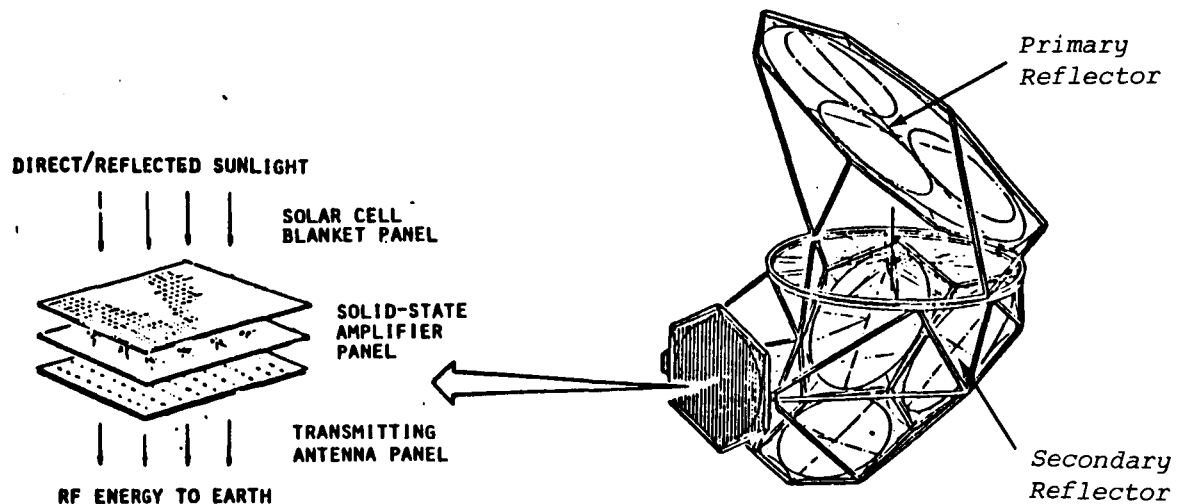
Figure 1.1-1. Sandwich Panel SPS Concept

1.1.1 SANDWICH CONCEPTS

One of the major problems related to the use of solid state devices for dc/RF conversion on the satellite is the need to provide power to numerous power amplifiers which operate at low power levels (e.g., 5 W) and low voltages (e.g., 10 V). This leads to a much more complex and massive power distribution system when the reference concept approach of a separate microwave antenna and solar array are employed.

An alternate solid state concept was developed which results in an integrated solar array and microwave transmission system. This concept utilizes a sandwich with the solar cells on one side and the microwave antenna on the other side. Since the antenna must stare at a point on the earth, it is necessary to use a set of two reflectors to direct sunlight on the solar cells

continuously. One of the reflectors remains fixed relative to the array
(secondary reflector) while the other remains pointed toward the sun (primary
reflector) to reflect solar energy onto the solar array. The solar cells
provide electrical energy to solid-state power amplifiers directly behind
them which, in turn, feed the antenna elements. In order to provide any sig-
nificant power at the utility interface on the ground from this type of concept,
it is necessary to increase the available power density to the antenna from the
solar array by concentrating solar energy on the sandwich. For this reason,
such a concept requires GaAs solar cells or other solar cells that can operate
efficiently at the high temperatures resulting from high concentration ratios.
Silicon solar cells are not acceptable in this application. This section
describes the evaluation of the sandwich design and the resulting point design
concept.

Initial studies of the sandwich concept were parametric in nature. The
main thrust of these studies was to identify the concept driving characteristics
and to determine the best overall approach for a subsequent point design analy-
sis.

Candidate Concepts

Figure 1.1-2 illustrates the matrix of sandwich concepts that have been
considered. The conventional approach to reflecting sunlight onto the sand-
wich when the antenna stares directly at the ground site is shown by Concepts
1 and 2. Concept 1 has a large, flat primary reflector that reflects sunlight
into a multi-faceted secondary reflector system that concentrates the solar
energy on the solar array side of the sandwich. Concept 2 has multi-faceted
primary reflectors that reflect onto a flat secondary reflector for concentra-
tion onto the sandwich. Concept 2 has a smaller reflector area than Concept 1.

Concepts 3 and 4 have single, multi-faceted reflectors that concentrate
sunlight directly onto the sandwich. Concept 3 has an antenna which is
oriented at an angle relative to the ground receiving station. The major
problem of this concept is the variation in the angle relative to the receiv-
ing site of the antenna during the year. This results in a varying peak power
density and power distribution over the antenna. Additionally, the antenna
area is increased by at least 40 percent compared to a concept which has the
antenna normal to the line of sight.

Concept 4 appears to have improved characteristics compared to Concept 3.
In this case, the RF reflector reflects the beam to the rectenna. Surface
irregularities in the reflector are compensated for by the phase control
system, since the pilot beam is also reflected from the RF reflector to reach
the satellite antenna. Multi-path reflections from the RF reflector may be a
serious problem that needs to be studied.

The final concept is one that combines multiple antennas on a single
satellite. In this particular arrangement, the reflector areas are excessive.
Better arrangements, with smaller area reflectors, can be realized with
multiple antennas using the general arrangements of Concepts 1 or 2.

Space Operations and
Satellite Systems Division
Space Systems Group

Rockwell International

(1) FLAT PRIMARY/FACETED SECONDARY

(2) FLAT SECONDARY/ FACETED PRIMARY

(3) INCLINED ANTENNA/ SINGLE FACETED REFLECTOR

(4) RF REFLECTOR/SINGLE MULTI-FACETED REFLECTOR

(5) MULTI-ANTENNA CONCEPT
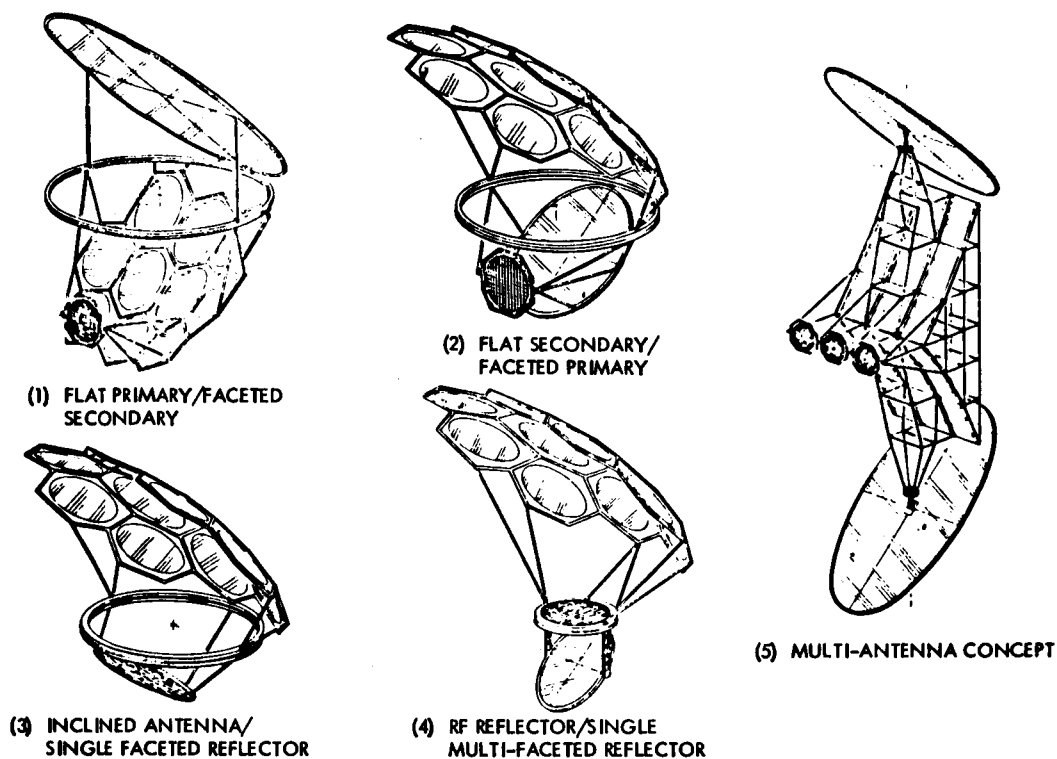
Figure 1.1-2. Alternative Solid State Sandwich Concepts

As a result of these preliminary studies, it was decided that further effort should be concentrated on Concept 2 for parametric evaluation. This concept is preferred over Concept 1 on the basis of a reduced reflector area. Concept 4 is still considered to be a viable concept that may significantly reduce mass; however, a very detailed analysis is needed to fully evaluate the feasibility of use of an RF reflector. Concept 3 was not considered to be viable.

Major Support Tradeoffs

Initial studies of the sandwich concept were parametric in nature to determine some of the more important drivers. These are summarized in Figure 1.1-3. Figure 1.1-3(A) shows installation cost ($/kW)$_{UI}$ effects of effective concentration ratio (CR$_E$) and the ability of the solar array to reject waste heat through the rear of the array. Two thermal conditions are illustrated: (1) no radiation through the rear from the solar array, and (2) a 2/3 view factor from the cells through the rear. It is assumed that the cells have a view factor of 1 from the front of the array. In both cases, the installation cost parameter ($/kW)$_{UI}$ becomes flat in the region of CR$_E$ = 6. If the solar cells are limited to a temperature of 200°C, CR$_E$ is limited to CR$_E$ = 6 for a 2/3 rear view factor, and to CR$_E$ = 4 for no rear radiation (view factor = 0). As shown, this results in an increase in installation parameter cost of 22 percent.

1-4

(A) SOLAR ARRAY THERMAL IMPACTS

CELL TEMP T_c (°C)

NO RADIATION THROUGH REAR

RELATIVE INSTALLATION COST

1.0
0.8
0.6
0.4
0.2
0

167
122   203
151   233   259   302   339
- 176   197
234   265

0.67 REAR VIEW FACTOR

0   1   2   3   4   5   6   7   8   9   10

EFFECTIVE CONCENTRATION RATIO (CR$_E$)

(B) GAAS VS MBG ARRAY

P_{UI} (GW)   0.81

P_{UI} (GW)   0.98   1.08   GaAs SOLAR ARRAY

1.26   1.40   1.52

1.34   MULTI-BANDGAP SOLAR ARRAY

1.59   1.79   1.96

RELATIVE INSTALLATION COST

1.0
0.8
0.6
0.4
0.2
0

0   1   2   3   4   5   6   7   8   9   10

EFFECTIVE CONCENTRATION RATIO (CR$_E$)

(C) SPECIFIC MASS

$\left(\frac{kg}{kW}\right)$

14
12
10
8
6
4
2
0

GaAs ARRAY

MULTI-BANDGAP ARRAY

0   1   2   3   4   5   6   7   8   9   10

EFFECTIVE CONCENTRATION RATIO (CR$_E$)

(D) IONOSPHERE POWER DENSITY IMPACT

P_{UI} (GW) = 0.83

P_{UI} (GW) = 1.05

RELATIVE INSTALLATION COST

1.0
0.8
0.6
0.4
0.2
0

1.18
1.44   GaAs ARRAY
1.67   1.86
1.48
1.82   MULTI-BANDGAP ARRAY
2.10   2.34

CURRENT BASELINE

2X CURRENT BASELINE

0   10   20   30   40   50

POWER DENSITY (mW/cm^2)
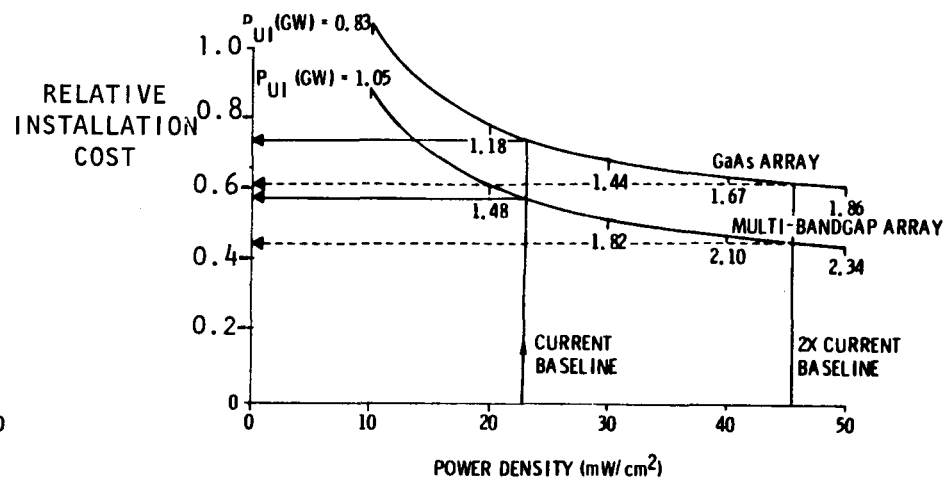
Figure 1.1-3.   System Tradeoffs

Figure 1.1-3(B) shows the effects of CR_E and the type of solar array (GaAs or multi-bandgap) on the installation cost parameter and power at the utility interface. The effects on the installation cost parameter of CR_E are about the same for both arrays, and installation cost flattens out beyond CR_E = 6. (The array temperatures are about 200°C at CR_E = 6). The effect of using a multi-bandgap (MBG) solar array results in an installation cost parameter reduction of 22% compared to the GaAs array.

Figure 1.1-3(C) shows the effect on satellite specific mass (kg/kW) of the effective concentration ratio (CR_E) for GaAs and MBG arrays. At the low values of CR_E, specific mass increases rapidly. Beyond CR_E = 6, little change occurs in specific mass. Because of the much smaller antenna/array diameter, the MBG concept has a much lower specific mass than the GaAs concept.

The current level permitted for microwave beam power density in the ionosphere is 23 mW/cm^2. This limit is based on very little data, and steps are being taken to determine the value that should be used for design of the SPS. Figure 1.1-3(D) shows the effect that power density in the ionosphere has on installation cost. As shown, decreases to values below the current design limit of 23 mW/cm^2 would seriously impact SPS economics. Conversely, increases in this limit could lead to significant installation cost reductions (e.g., a 14 percent reduction for GaAs array concepts and 18 percent reduction for MBG array concepts at 40 mW/cm^2).

These early studies led to a concerted effort to maximize the effective concentration ratio by allowing as much heat as practical to radiate from the solar cells (in both directions). It also showed that benefits from the MBG solar arrays may be large.

Because of the desire to reduce sidelobe radiation levels and improve transmission efficiency, power tapers of 10 dB have been used for the klystron reference design. A study was conducted to evaluate the 0 dB taper (uniform illumination). Table 1.1-1 summarizes the data comparing 0 dB and 10 dB antenna power tapers for the solid state sandwich concept. Two approaches might be used to achieve a 10 dB taper: (1) a redistribution of power could be obtained to obtain greater power in the center of the antenna by conducting some of the power from the periphery of the antenna toward the center (the antenna would be of smaller diameter than the solar array) or (2) a 10 dB power taper could be obtained on the solar array by decreasing the solar energy (CR_E) from the center to the edge of the solar array. The first approach would lead to extreme complexity and would destroy the primary desirable feature of the sandwich panel concept—simple power distribution within each sandwich panel. This approach has been rejected. The second approach can be implemented by cutting small circular holes in the secondary reflector. The reflector density can then be made to decrease from center to edge in the proper pattern to obtain the 10 dB power taper.

The data are shown in Table 1.1-1 for the 10-dB taper, assuming the second approach. The important comparison is the relative installation cost parameter ($/kW)$_{UI}$, which is 1.0 for the 10 dB and 0.654 for a 0 dB taper. The 0 dB taper is the obvious choice despite higher sidelobe levels.

Table 1.1-1. Comparison of 0 dB and 10 dB Antenna Power Taper

	0 dB	10 dB
Type of solar array	MBG	MBG
Maximum effective concentration ratio	6.0	6.0
Amplifier efficiency	0.8	0.8
Maximum antenna power density (W/m)	1235	1235
Antenna diameter (km)	1.578	2.049
Total transmitted power (GW)	2.418	1.588
Power at utility interface (GW)	1.591	1.127
Rectenna boresight diameter (km)	5.600	4.929
Total satellite mass (10 kg)	10.13	13.30
Relative installation cost ($/kW)$_{UI}$	0.654	1.0

As a result of the trade studies, the following design requirements were derived for the solid state sandwich concept:

- 23 mW/cm^2 maximum intensity at the center of the receiving antenna (same as for reference concept)

- 0.1 mW/cm^2 maximum microwave intensity at receiving station control boundary (same as for reference concept)

- 0-dB antenna power taper (reference concept has 10 dB power taper)

- Maximum solar array temperature of 200°C (maximum temperature derived from analysis of GaAs solar array)

- Maximum temperature at power amplifier base of 125°C (considered highest allowable using improved technology and about 5 watts amplifier output)

- Relative minimum installation costs ($/kW) at the utility interface within above constraints

Sizing Model

A sizing model of the sandwich concept was developed to assess additional parameters and establish sizing sensitivities. The definition of the model terms are given in Table 1.1-2. The model of Figure 1.1-4 shows all conducted and radiated, electrical and thermal power as well as the incident solar power (PI). The analysis assumed that the only significant PI is the power concentrated and reflected onto the solar array. At times, the RF antenna could absorb solar power at a concentration ratio of 1 and the system would have to radiate that heat energy.

Table 1.1-2. Definition of Model Terms

```
CR    =   SOLAR CONCENTRATION RATIO
TR    =   ANTENNA TEMPERATURE
TS    =   SOLAR CELL TEMPERATURE
NR    =   RF SUBSYSTEM EFFICIENCY
NS    =   SOLAR CELL EFFICIENCY
PI    =   INCIDENT SOLAR POWER
PS    =   SOLAR CELL ELECTRICAL POWER
PR    =   RF POWER OUT
P'S   =   CELL RADIATED HEAT
P'R   =   ANTENNA RADIATED HEAT
PH    =   HEAT THROUGH BARRIER
εS    =   CELL EMITTANCE
εR    =   ANTENNA EMITTANCE
FJ    =   OPTICS • DEGRADATION FACTORS
FK    =   CELL ABSORBTION • FILTER
σ     =   5.67×10⁻⁸ W/m² °K⁴
ε     =   EMITTANCE OF SURFACE
T IS IN °C, P IS IN W/m²
```

$$(1) \quad TS = \left[\frac{PI(FK-NS)-PH}{\sigma \epsilon_S} \right]^{1/4} - 273$$

$$(2) \quad TR = \left[\frac{PS(1-NR)+PH}{\sigma \epsilon_R} \right]^{1/4} - 273$$

$$(3) \quad NS = 0.2095 - 0.00038 TS$$

$$(4) \quad PI = CR \cdot 1353 \cdot FJ$$

$$(5) \quad PS = PI \cdot NS \qquad PR = PS \cdot NR = PI \cdot NS \cdot NR$$

$$(6) \quad P'S = TS^4 \cdot \sigma \cdot \epsilon S \qquad P'R = TR^4 \cdot \sigma \cdot \epsilon R$$
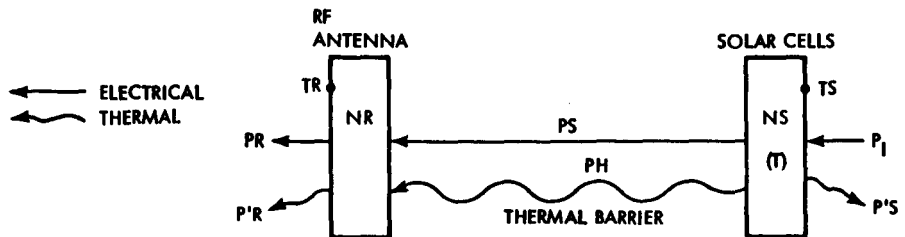
Figure 1.1-4. Sandwich Concept Sizing Analysis
Thermal and Power Relationship

The efficiency of the solar cell is based on the total solar power (PI) into the cell; therefore, the power (PI•NS) will be conducted away from the cell as electricity. The amount of power into the cell is based on the cells ability to absorb the solar power. This absorbtion could be modified by a filter (FK). The filter FK must not effect the solar power over the spectrum that the cell converts solar power to electricity. Any filtering over this spectrum would be taken care of by the parameter FJ. The analysis includes the amount of heat that would be leaked through the thermal barrier (PH) to

maintain the temperatures required. The thermal conductivity of the material required for a thermal barrier can be calculated using the value of PH.

The amount of power into the RF antenna is PS+PH. The power out of the antenna is the radiated RF power (PR) which is PS NR. The difference between the power in and the power out must be radiated as heat (P'R) determining the temperature of the antenna.

Because of the interrelationship between equations (2) and (3), identified in Figure 1.1-4, the value of TS must be iterated if TS is an unknown.

The reference system in Table 1.1-3 is a design for comparison purposes in order to see the effects on the system due to parameter changes. This concept is not an optimum design. All parameters were selected within a realistic range of values that could be obtained. The dc to RF converter efficiency of 71.5% with a gain of 10 gives a RF system efficiency of 65% (goal of the Rockwell SPS solid state technology task)[1].

Table 1.1-3. Sandwich Concept Sizing Analysis Results

A REFERENCE SYSTEM FOR COMPARISON IS DEFINED AS FOLLOWS:

| FK = 0.6607 | ϵS = 0.82 | TS = 200°C | N = 0.715 |
| FJ = 0.76 | ϵR = 0.75 | TR = 125°C | G = 10 |

NS(TS) = 0.2095 - 0.00038·TS WHERE NS = 20% @ 25°C

RESULTS OF PARAMETER VARIATIONS

PARAMETER CHANGED	TS	TR	CR	NS	PS	PH	PR	Δ(PR) / Δ(PARAMETER)*
REFERENCE SYSTEM	200	125	5.8	0.134	796	788	518	
TS = 300°C	300	125	9.9	0.096	972	727	632	+11.3
TR = 135°C	200	135	5.9	0.134	810	895	526	+ 8.9
FK = 0.5945	200	125	6.5	0.134	892	745	580	- 8.9
NR = 0.81	200	125	6.0	0.134	824	911	667	+ 7.3
NS = 34.6% @ 25°C	200	125	6.9	0.280	1983	373	1289	+38.8+64.1
CR = 5.8 PH = 0	241	3	5.8	0.118	704	0	458	
CR = 4.3 PH = 0	200	-9	4.3	0.134	590	0	384	

*PARTIALS WHERE Δ(PARAMETER) IS +10°C OR 1%, WHICHEVER IS APPLICABLE.

This reference system was analyzed and results are shown in Table 1.1-3. The rest of the analysis left all parameters the same as the reference concept except with a change in the parameter shown. The partials show the change in output power with a 10°C change in TS or TR or a ±1% change in any other parameter. Where NS was allowed to change from 20% to 21% the change in output power was 38.8 W/m². When NS changed from 34.6% to 35.6% the change in output power was 64.1 W/m².

[1]*Study Plan for a Satellite Power Systems (SPS) Concept Definition Study (Exhibit D—Task 6)*, Rockwell International, SSD 79-0131, June 27, 1979

The last two analysis shown in Table 1.1-3, where PH=0, was performed to demonstrate the need for allowing PH>0. The first analysis used the same CR as the reference case. It shows that with PH=0 the cell temperature is too high and the antenna temperature is too low with a resulting reduction in output power. The next analysis held the temperature at 200°C at the cell and adjusted the concentration ratio accordingly. The results were even lower output power.

The most significant parameter was determined to be antenna power density. It is possible to increase power density for this concept by using higher efficiency solar cells (multi-bandgap cells), raising the allowable surface temperatures (solar cell and RF elements and/or use of optical filters) and improved dc-RF converter efficiency. Figure 1.1-5 illustrates the impact on the sandwich concept antenna power density from increased solar cell efficiency at an RF system efficiency of 76%. The thermal barrier between solar cells and RF elements must be controlled to permit balanced surface temperatures; otherwise, the allowable solar cell temperature (200°C) would be reached before reaching the RF element allowable surface temperature (125°C) resulting in a significant penalty in RF power density. The power distribution is an integral part of the concept and wiring mass is not a major consideration.

$$CR_{eff} = \frac{T^4 \sigma (\epsilon_F + \epsilon_B)}{S(a - \eta)}$$

$\epsilon_F = 0.82$

$\epsilon_B = 0.45$

$a = 0.61$

$T = 200C$

$PR = CR_{eff} \cdot S(NS') NR$

$NS' = NS (0.89) (0.96)$

$\frac{\Delta NS}{\Delta T} = 0.0287\%/°C$

$NR = 0.76$

PK @ CENTER = 23 mw/cm^2

RECTENNA EDGE = 0.1 mw/cm^2
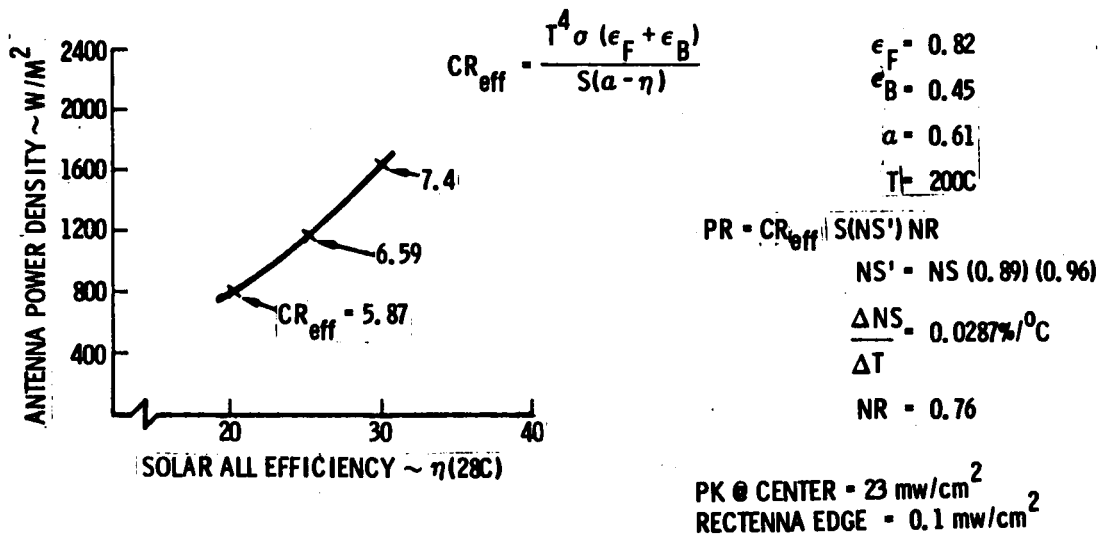
Figure 1.1-5. Sandwich Concept Power Density
(Influence of Solar Cell Efficiency)

Sandwich Design Concepts

Several options were considered for the design of the sandwich panel. The major options are listed in Table 1.1-4, and the selected concept and the rationale for selection are also shown. Three types of antennas were considered, including a resonant cavity (Figure 1.1-6), a patch resonator (Figure 1.1-7), and a dipole antenna (Figure 1.1-8). The structural and thermal characteristics of these three antennas are compared in Table 1.1-5. The data shows that the dipole antenna is superior in both structural and thermal characteristics. The dipole concept was selected.

Table 1.1-4. Sandwich Concept Options

OPTION AND SELECTION	RATIONALE
ANTENNA TYPE • RESONANT CAVITY • PATCH RESONATOR • DIPOLE✓	LOWEST MASS, HIGHEST POWER DENSITY
AMPLIFIER LOCATION • DIPOLE MOUNTED✓ • GROUND-PLANE MOUNTED	GREATEST POWER DENSITY
RF FEED SYSTEM TYPE • STRIPLINE CORPORATE FEED✓ • COAXIAL CORPORATE FEED	LOWEST MASS AND CONSTRUCTION EASE
DIPOLE SUPPORT STRUCTURE • TRUSS GRID✓ • BEAM GRID	LOWEST MASS
SOLAR ARRAY SUPPORT STRUCTURE • HONEYCOMB SANDWICH✓ • FOAM SANDWICH	GREATEST POWER DENSITY
✓ = SELECTED CONCEPT	

THICKNESS ~ 1.1 cm, WEIGHT ~ 3.73 kg/m^2
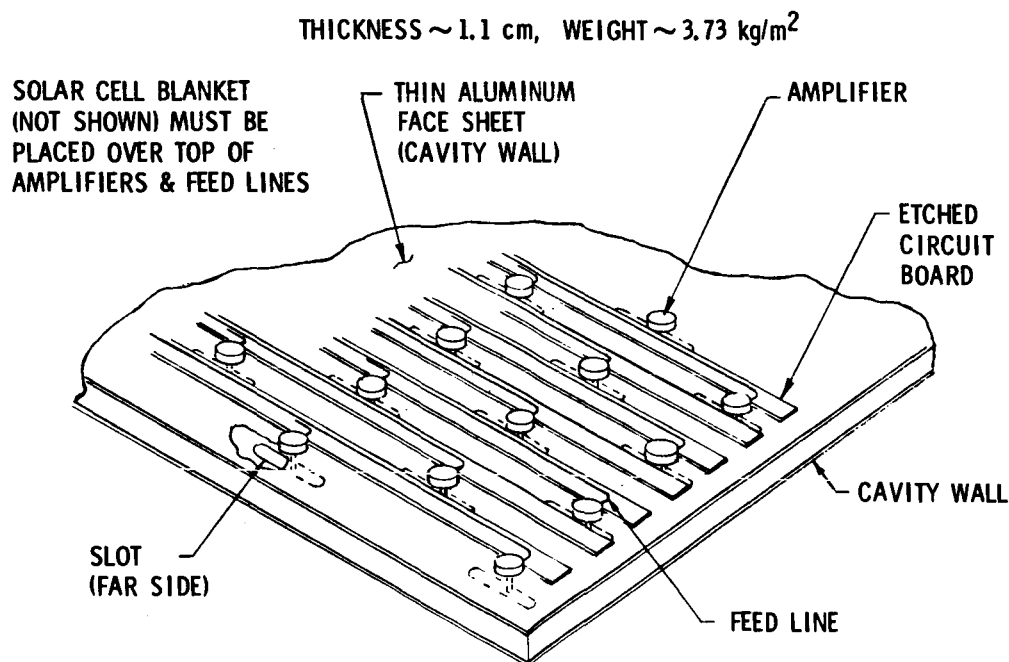
Figure 1.1-6. Resonant Cavity Radiator Sandwich Antenna

For the dipole antenna concept, the next variation to be considered was in the location of the solid state power amplifier; dipole-mounted or ground plane mounted. A thermal trade study showed that the ground-plane mounted amplifier resulted in blockage of heat transfer from the solar array through the antenna side, which lowers power density. Since the dipole-mounted concept was thermally more acceptable, it was selected (the dipole-mounted concept allowed effective concentration ratios up to 7.3 compared to 4.6 for the ground-plane mounted concept).

THICKNESS ~ 0.6 cm, WEIGHT ~ 2.79 kg/m^2

KAPTON PC GROUND PLANE

METALLIZED PATCH RESONATOR

AMPLIFIER

10 cm

10 cm

ETCHED CIRCUIT LINES

EGG CRATE SUPPORT STRUCTURE

SOLAR CELLS
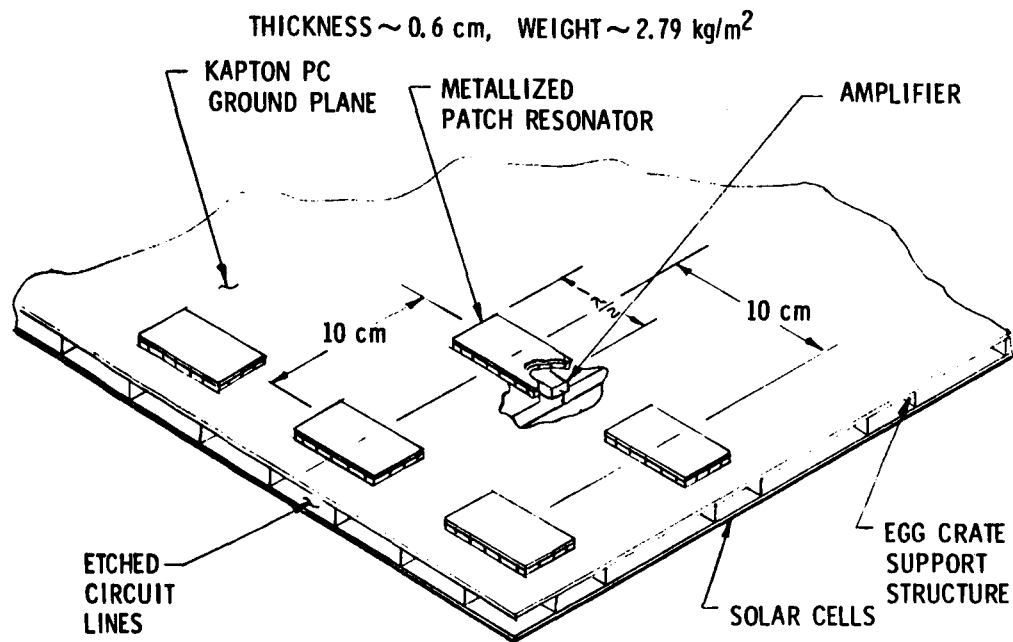
Figure 1.1-7. Microstrip Patch Resonator Sandwich Antenna

THICKNESS ~ 3.8 CM, WEIGHT ~ 1.44 KG/M^2

USE .05 x .05: IN BAR (SILICA FIBERS) FOR ALL MEMBERS

METALLIZED KAPTON PC BOARD

3 CM

SOLAR CELL

MICROSTRIP RF & ETCHED DC LINES

10 CM

10 CM

NOTE: BAR JOINING TO BE ULTRASONIC BY MACHINE THAT AUTOMATICALLY FABRICATES TRUSSES
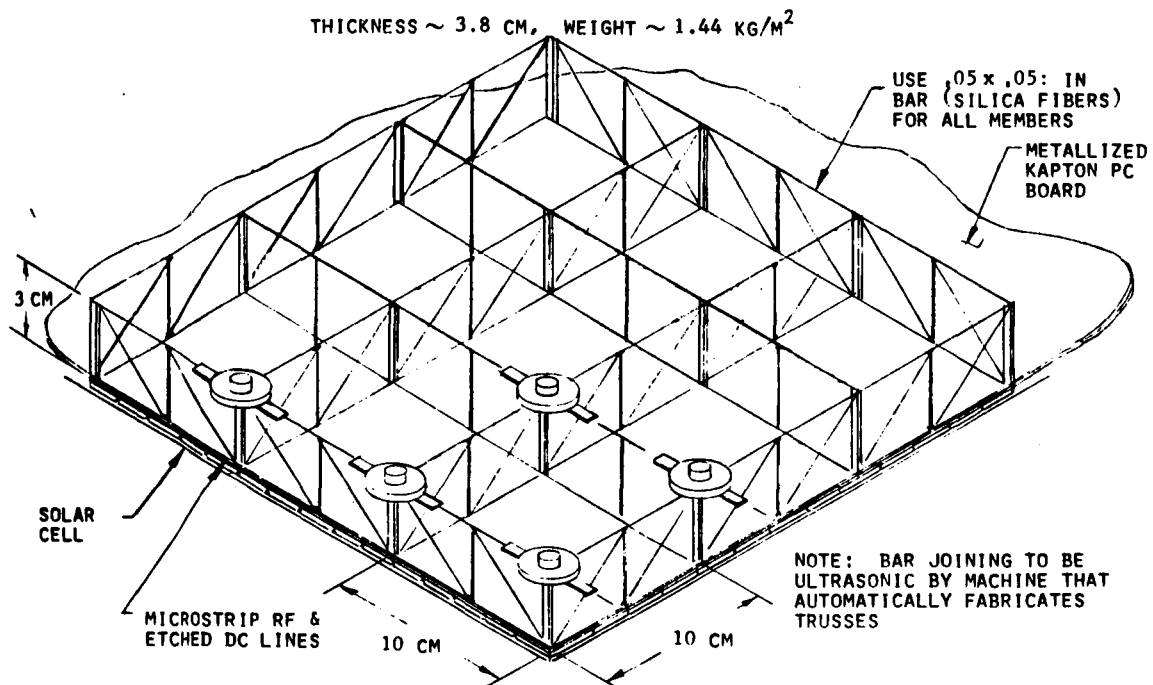
Figure 1.1-8. Dipole Sandwich Antenna

Two approaches to the feed system for the RF drive signal were evaluated: one using a stripline corporate feed system and the other using a coaxial cable corporate feed system. The stripline concept was preferred because of low mass

Table 1.1-5. Comparison of Antenna Concepts

CONFIGURATION	STRUCTURAL CHARACTERISTICS	THERMAL CHARACTERISTICS
DIPOLE	MIN. WEIGHT (1.4 kg/m²) MAX. THICKNESS (3.8 cm)	125°C BASE TEMP. 730 W/m² RADIATED (+) (6 cm BeO DISC. DIA.)
MICROSTRIP	MED. WEIGHT (2.8 kg/m²) MIN. THICKNESS (0.6 cm)	140°C Base Temp. <730 W/m² RADIATED (+)
RCR	MAX. WEIGHT (3.7 kg/m²) MED. THICKNESS (1.1 cm)	178°C BASE TEMP. <730 W/m² RADIATED

and potential for mass production. Initially, it was believed that cross-overs of the feed system would occur, making a stripline system infeasible. However, a method of feeding the signal was identified that did not lead to cross-overs.

Both truss and beam grid structures were considered for the dipole antenna support structure. The truss structure was the lowest in mass and also appeared to lend itself to mass production. The solar array support structure also had two approaches initially, a low-mass foam sandwich and an open-core honeycomb sandwich. The foam sandwich blocked heat from passing through the antenna side of the sandwich from the solar array, thus decreasing the allowable solar concentration on the array and therefore the power density. For this reason, the open-core honeycomb was selected.

The detailed design characteristics of the sandwich will be discussed in the section on solid state concept point design definition (Section 2.3.2).

1.1.2 END MOUNTED ANTENNA SOLID STATE CONCEPT

The Rockwell end-mounted antenna concept utilizes solid state elements for conversion from dc to RF. Based on tradeoff study results the point design was accomplished for a **series-parallel arrangement of power amplifiers with a 640 V dc** input requirement. High voltage is generated on the solar array (40 kV) and transferred across the rotary point with subsequent dc-dc conversion on the antenna. The concept initially studied by Rockwell assumed that 50-kW solid state power modules would replace 50-kW klystrons in an antenna configuration basically the same as that used for the klystrons. Considerations of power density limits based on thermal constraints suggested a distributed solid state approach. The low voltage required by the solid state modules results in a significant power conditioning penalty. To minimize this penalty it is necessary to project significant improvements in dc-dc converter efficiency and specific mass. One approach to achieve these improvements is to take advantage of scaling relationships and design around use of large converter ratings, e.g., transformer mass varies to the 0.75 power of the rating if all parameters such as current density, flux density, etc., are kept constant[1]. The following paragraphs describe the major considerations that were studied leading to the resultant details of a point design for this concept.

---

[1]Westinghouse Electric Corporation, Report LY20686, prepared for Rockwell International, Satellite Power Systems Study, December 1977

Power Density and Beam Distribution

As with the sandwich concept, antenna power density is an important sizing parameter. Since heat rejection for this configuration is accomplished from both sides of the antenna higher power density is achieved. Figure 1.1-9 shows a plot of power density as a function of phase control/amplifier efficiency. The design point (η_R^1 = .792) includes an allowance for circuit losses associated with gain and device efficiency and results in an allowable power density of 6638 W/m^2. (Note: The klystron reference design is 21,000 W/m^2.)

POWER @ BEAM CENTER = 23 mw/cm^2 (PK)
TR = 125C
a = 0.2
ϵ = 0.8

DESIGN POINT ~ 6638 w/m^2

PHASE CONTROL AND SOLID STATE
AMPLIFIER EFFICIENCY ~ η_R
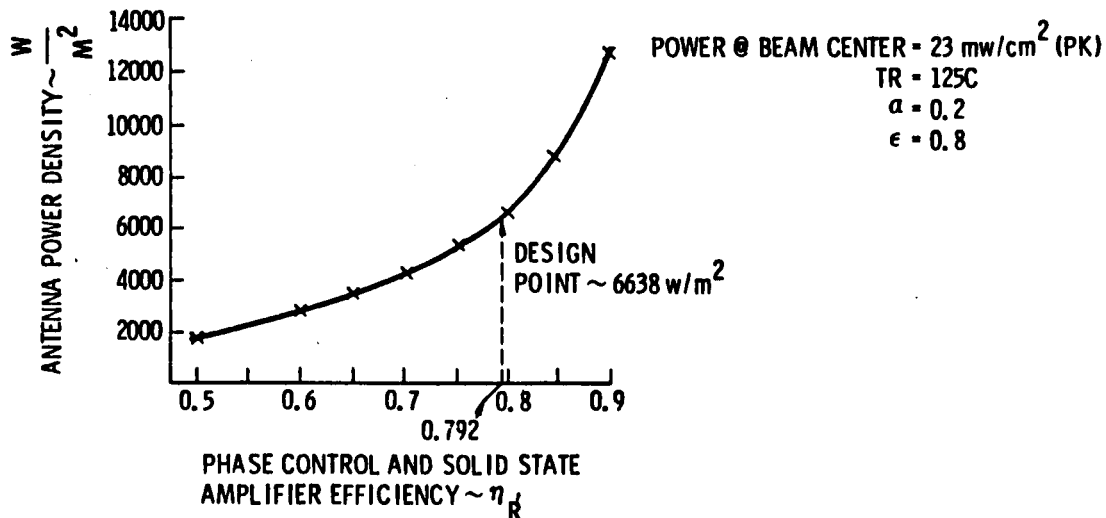
Figure 1.1-9. Effect of Amplifier Efficiency
on Antenna Power Density

A 10 dB Gaussian antenna illumination was selected for this concept as the best RF beam distribution. Trade data comparisons are given in Table 1.1-6. The Gaussian beam resulted in higher overall efficiency but less power at the utility interface (i.e., within the 23 mW/cm^2 ionospheric limit). The major reason for selecting 10-dB Gaussian is the fact that this results in reduced side lobes at the rectenna.

Power densities (at the center of the beam) are plotted in Figure 1.1-10 as a function of antenna diameter for a uniform 0-dB beam and a Gaussian 10-dB beam. The antenna power density is treated as a parameter. At an antenna peak power density of 6638 W/m^2 the 10-dB Gaussian results in a larger antenna diameter, 1.35 km versus 1.03 km for the 0-dB uniform beam. The plot indicates a significantly larger antenna diameter penalty for the 10 dB Gaussian beam as its power density is reduced, i.e., below 1000 W/m^2 as in the sandwich concept.

Major Support Tradeoffs

A computer program was used to conduct a parametric analysis of the solid state end-mounted antenna concept. This program allowed for variations in amplifier efficiency, effective radiation temperature for heat rejection from the power amplifiers, and the use of 0-dB and 10-dB antenna power tapers on the antenna.

Table 1.1-6. Antenna Illumination Comparison

10 dB Gaussian antenna illumination best		
	Gaussian	Uniform
• Overall efficiency	6.24%	5.79%
• Power per satellite	2.61 $GW_{(UTIL)}$	3.69 $GW_{(UTIL)}$
• Power distribution weight	1.72 kg/kW_{UTIL}	2.16 kg/kW_{UTIL}
• Antenna area	1.422×10^6 m^2	0.844×10^6 m^2
• Rectenna radii	6.8 km (0.1 MW/cm^2)	8.8 km (0.1 MW^3/cm^2)
	3.8 km (1.0 MW/cm)	4.3 km (1.0 MW^3/cm^2)
• Relative cost ($/kW$_{UTIL}$)	1.0	0.98
• Sidelobe power density	*Reduced levels*	-
• Total satellite mass	7.7 kg/kW$_{UTIL}$	8.0 kg/kW$_{UTIL}$
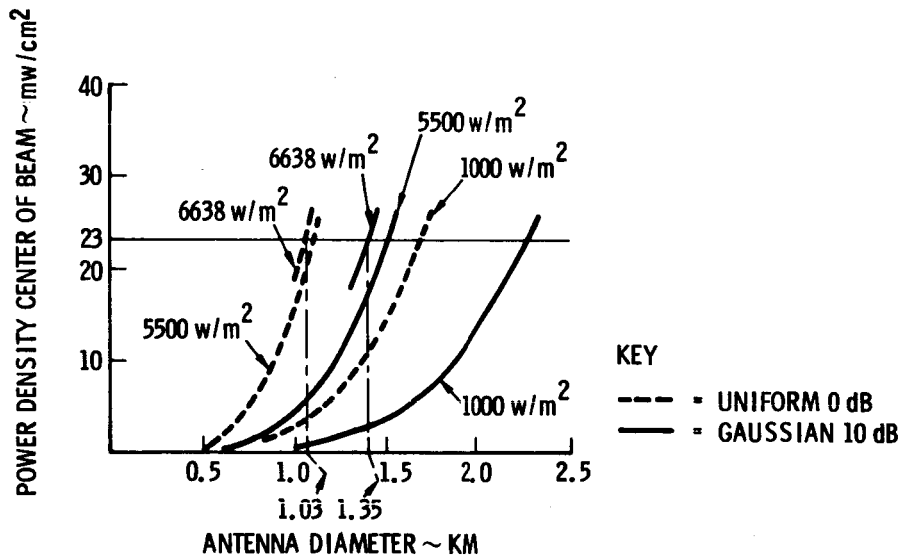
Figure 1.1-10. Rectenna Center Power Density versus Transmitting Antenna Diameter

The program sizes the antenna area, based on thermal requirements to reject waste heat from the solid state power amplifiers. The constraint of 23 mW/cm^2 at the center of the beam and at the earth's surface is imposed as an additional requirement. This allows a determination of antenna power output, antenna power input and rectenna diameter. Dual dc/dc converters are assumed to determine the mass of the power distribution and control system. Solar array mass is ratioed from the "reference" concept data, based on area. The program calculates total mass and cost and installation cost per kW at the utility interface (installation cost).

Several parametric variations were studied to determine the best approach. Antenna radiation temperature effects on relative installation costs ($/kw utility) are shown in Figure 1.1-11. The cost drops slowly beyond 50°C and there appears to be little cost incentive to go to temperatures higher than the currently design point of 125°C
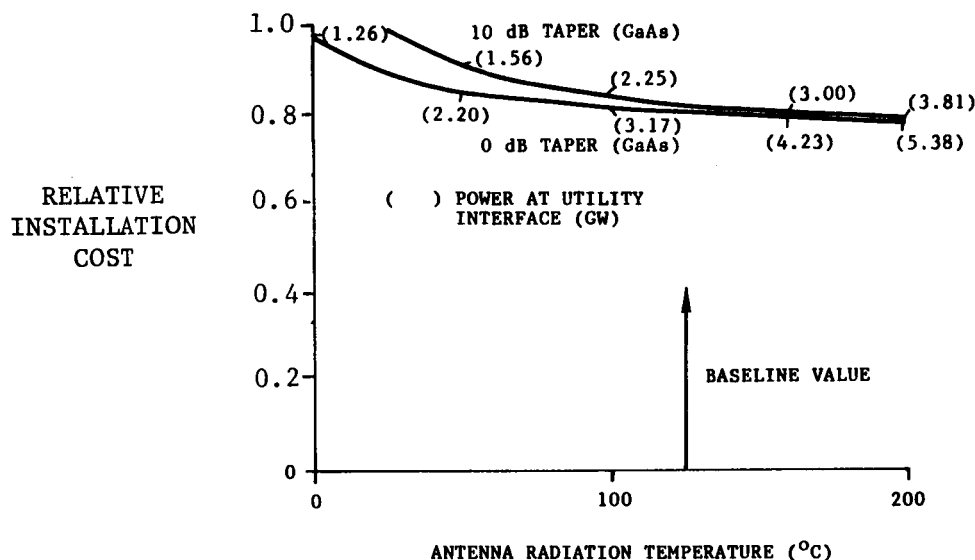
Figure 1.1-11. Reference Solid State Concept Effect of
Antenna Radiation Temperature on Installation Cost

Effects of amplifier efficiency, antenna power taper (0 dB and 10 dB), and solar array concept on the relative installation cost are shown in Figure 1.1-12. The baseline GaAs solar cells at a nominal 20% efficiency are compared to multibandgap (MBG) solar cells at a nominal 30% efficiency. The results shown in Figure 1.1-12 indicate that, for the end-mounted solid-state concept, amplifier efficiency has a very important impact on cost. Based on current technology results, an amplifier efficiency of about 80% appears achievable. Antenna power taper ratio does not have a significant impact on relative cost (refer back to Table 1.1-6). The impact of a multi-bandgap solar array on cost is about 7%.

The current level of microwave beam power density in the ionosphere is 23 mW/cm^2. Figure 1.1-13 shows the effect that power density in the ionosphere has on installation cost ($/kW)$_{UI}$. Increases in this limit could lead to significant installation cost reductions (e.g., 13% reduction at 40 mW/cm^2).

Power Distribution Efficiency Options

A number of power distribution options for this concept were evaluated including elimination of dc converters by allowing greater power distribution losses and relatively high solid state amplifier input voltages. A parametric study was done to assess the impact from a range of power distribution efficiencies (50% to 83%), antenna module voltage levels (100 V to 45,000 V), dc converter efficiencies (50% to 95%), and dc specific masses (0.27 kg/kW to 1.8 kg/kW).

RELATIVE
INSTALLATION
COST

AMPLIFIER EFFICIENCY (η_{AMP})
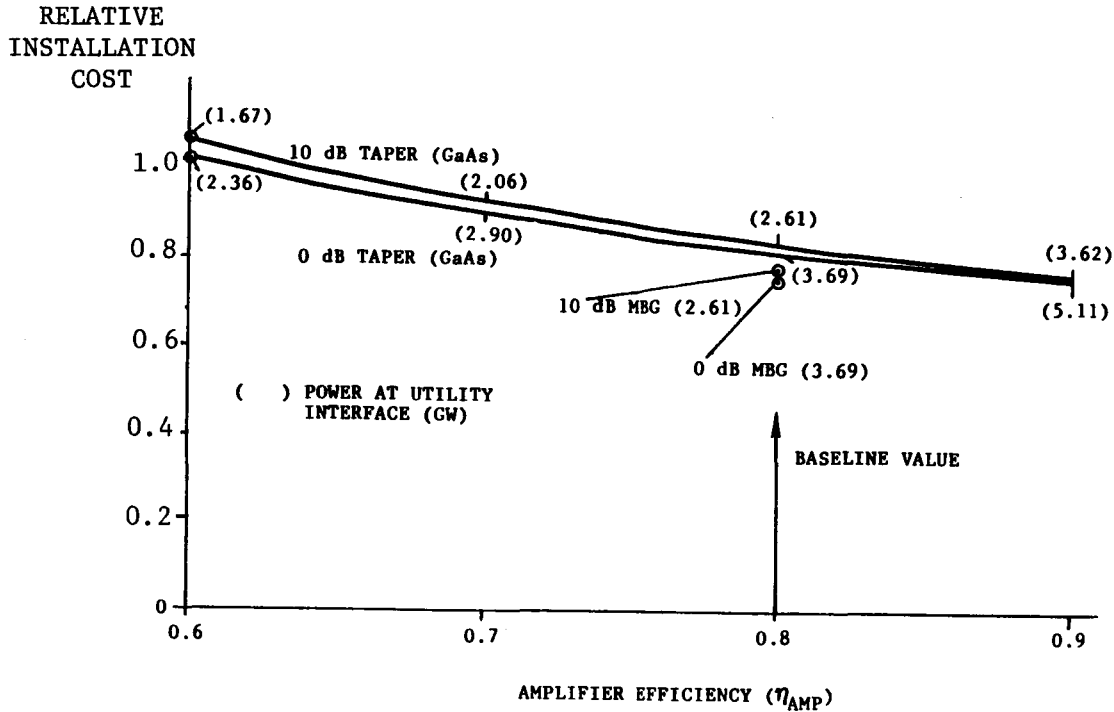
Figure 1.1-12. Reference Solid State Concept Effect of
Amplifier Efficiency on Installation Cost

RELATIVE
INSTALLATION
COST

POWER DENSITY (mW/cm^2)
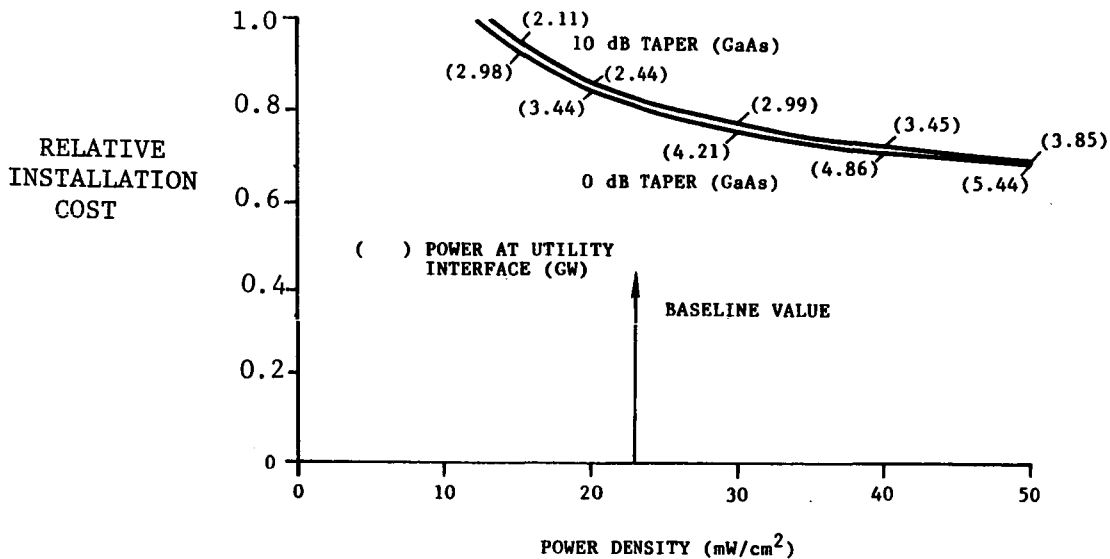
Figure 1.1-13. Reference Solid State Concept Effect of
Ionospheric Power Density on Installation Cost

The baseline klystron concept utilizing high voltage transmission and dc
converters at the klystrons results in a power distribution (PD) efficiency of
83.1%. A direct analogy to this concept but substituting solid state power
amplifiers for the klystrons results in a PD efficiency of 79% as illustrated
in Figure 1.1-14.
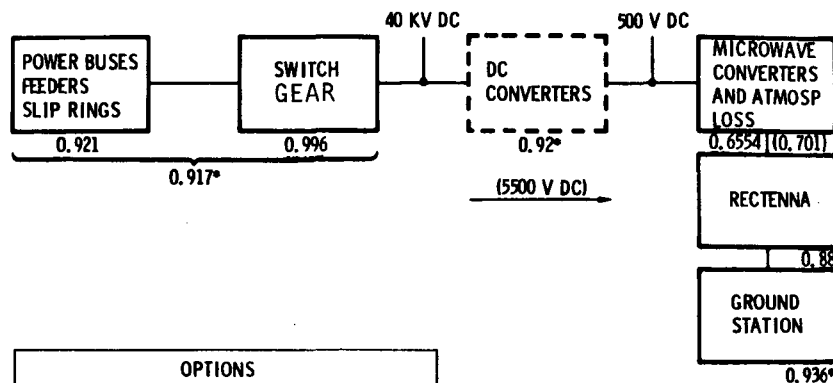
OPTIONS		
DC-RF	P.D. EFFICIENCY	COMMENT
KLYSTRON	0.831	BASELINE
SOLID STATE*	0.79	WITH DC CONVERTERS
SOLID STATE	0.7 - 0.5	WITHOUT DC CONVERTERS

*These values apply only to the
solid-state configurations
indicated in chart.

Figure 1.1-14. Power Distribution Efficiency Options

Concepts which eliminate the dc converter by use of low loss series paralleling of amplifiers were evaluated at a nominal 5500 V dc and over a range of 5000 V to 8000 V. For these concepts a power distribution efficiency ranging from 50% to 70% was assumed.

The SPS efficiency and specific weight goals are shown in Table 1.1-7 and compared to an initial technology assessment. It may not be possible to achieve both high efficiency and low specific weight. Weight sensitivities were derived for efficiency changes from the baseline 92% down to 50%, and for specific weight changes from the baseline 0.25 kg/kW up to 1.8 kg/kW as shown in Table 1.1-8. Solar array and power distribution wiring mass are affected most by a change in PD efficiency. In Table 1.1-8 the reference satellite mass penalty has been determined, in brackets, for η = 0.92, 0.65, and 0.5 with a fixed converter specific mass; however, only converter mass is shown for the three converter specific mass variations (i.e., 0.27, 1.4, and 1.8). The issue of dc converters is one requiring considerable added effort.

Table 1.1-7. DC Converter Technology Assessment
(Reference Solid State Concept)

PARAMETER	SPS GOAL	INITIAL TECHNOLOGY ASSESSMENT*	
η	92%	92 - 95%	50% - 65%
SP MASS $\frac{kg}{kW}$	0.27	1.4 - 1.8	0.27

*WESTINGHOUSE TELECOM 8-28-79

Table 1.1-8. Initial Trade Results
(Converter Specific Mass, Efficiency, and Mass Penalty)

CONVERTER SP MASS kg/KW	η	MASS PENALTY $\Delta kg/kW_{UTIL}$
0.27	0.92	(3.19)
0.27	0.65	1.9
0.27	0.5	4.41
0.27	0.92	(0.54)
1.4	0.92	2.81
1.8	0.92	3.62

( ) = REFERENCE MASS

Table 1.1-9 summarizes power distribution subsystem mass comparisons. The reference klystron end mounted antenna with a Gaussian power beam distribution junction is compared to solid state end mounted antenna with either a uniform power beam distribution or a Gaussian. Power distribution weights for the solid-state concepts range from 1.72 kg/kW$_{UT}$ to 2.72 kg/kW$_{UT}$ compared to the

Table 1.1-9. Power Distribution Comparison Reference
Klystron and End-Mounted Solid-State Concept, 10^6 kg

ITEM	KLYSTRON	SOLID STATE			
SOLAR ARRAY POWER (GW)	9.94	8.727 ———→		5.735 ———→	
POWER DELIVERED AT UTIL (GW)	5.07	3.685 ———→		2.61 ———→	
POWER AMPLIFIER VOLTAGE (V)	5 VOLTAGES	200	100	200	100
SOLAR CELL EFFICIENCY (%)	18.16	18.16	18.16	18.16	18.16
DISTRIBUTION	GAUSSIAN	UNIFORM (0 dB) ———→		GAUSSIAN ———→	
WEIGHTS 10⁶ KG					
MAIN FEEDERS	2.02	1.912			
SECONDARY FEEDERS	0.048	0.045			
SUMMING BUS	1.234	1.167		1.468	1.468
TIE BAR	0.144	0.136			
INSULATION	0.051	0.025			
SWITCH GEAR	0.186	0.163	3.862	0.107	0.107
REG AND CONVERTERS	0.009	0.009		0.009	0.009
ROTARY JOINT	0.043	0.043		0.043	0.043
AC THRUSTER CABL'G	0.0053	0.0053		0.0053	0.0053
BATTERY	0.006	0.006		0.006	0.006
SUPPORT STRUCTURE	0.374	0.351		0.164	0.164
SUB NON-ROTATING	4.120	3.862	3.862	1.802	1.802
RISERS	0.567	0.536	0.536	0.240	0.240
SUMMING BUS/ANT. FEEDERS	0.621	0.176	0.176	0.191	0.191
ANTENNA MODULE CABLES	0.125	0.631	2.524	0.414	1.656
SWITCH GEAR	0.343	0.329	0.329	0.216	0.216
ROTARY JOINT	0.017	0.017	0.017	0.017	0.017
DC CONVERTERS	1.48	1.952[1]	1.952[1]	1.313[1]	1.313[1]
INSULATION	0.086	0.081	0.081	0.053	0.053
SUPPORT STRUCTURE	0.324	0.372	0.562	0.244	0.369
SUB ROTATING	3.563	4.094	6.177	2.688	4.055
TOTAL PDS	7.683	7.956	10.039	4.490	5.857
Kg/KW$_{UT}$	1.515	2.159	2.724	1.720	2.244

[1] 38% INCREASE IN DC CONVERTER SPECIFIC WEIGHT DERIVED FOR TWO STAGE DEVICE

reference at 1.52 kg/kW$_{UT}$. Antenna module cable weight is shown to be significant at the low voltage of 100 to 200 V. Analysis showed this weight to become negligible when using an antenna module voltage of about 500 V dc.

A trade analysis was done to compare weight and cost for configurations without dc converters. Solid state antenna module voltages of 5000, 8000 and 11,000 volts were compared for power distribution efficiencies of 50% and 70%. The reference klystron power distribution efficiency is 83.1% and a comparable solid state power distribution efficiency using dc converters is 79%. Solar array reflector, and power distribution specific mass comparisons are given in Table 1.1-10. Power distribution efficiency is a parameter and dc converter specific masses are shown to establish voltage cross-overs, i.e., the transmission voltage level required (without dc converters) to compete on a weight basis with the solid state approach using 45 kV transmission and dc converters. The data indicates a heavy mass penalty for voltages below 10,000 volts and cross-over voltages at very high levels (Table 1.1-11), assuming lightweight converters.

Table 1.1-10. Solid-State Module Voltage Trade Data
(Antenna End-Mounted Configuration)

IDENTIFICATION	DISTR. VOLTAGE (kV)	SP. WEIGHT, KG/kW$_{UTIL}$			POWER DISTR. EFFICIENCY	DC CONV. SP. WT. (kg/kW)
		SOLAR ARRAY/ REFLECTOR	POWER DISTR.	SUBTOTAL		
REFERENCE KLYSTRON	45	1.61	1.51	3.12	0.831	0.196
	45	1.61	2.01	3.62	0.831	0.5
SOLID STATE*	45	1.80	1.54	3.35	0.79	0.27
	45	1.80	2.01	3.81	0.79	0.5
	45	1.80	3.03	4.84	0.79	1.0
SOLID STATE	11	2.41	1.59	4.01	0.7	N/A
	8	2.41	2.79	5.20	0.7	N/A
	5	2.41	6.55	8.96	0.7	N/A
SOLID STATE	11	3.02	1.15	4.17	0.5	N/A
	8	3.02	1.57	4.59	0.5	N/A
	5	3.02	4.41	7.42	0.5	N/A

*50 V DC ANTENNA MODULE WIRING WEIGHT NEGLIGIBLE.

Table 1.1-11. Antenna Module Voltage Cross-Over
(Without dc Converters)

DC CONVERTER SPECIFIC MASS kg/kW	CROSS-OVER VOLTAGE ~V dc (WITHOUT dc CONVERTERS)	
	$\eta = 0.5$	$\eta = 0.7$
2.0	5,200	6,000
1.0	7,800	8,400
0.5	13,500	13,000
0.27	30,000	21,000
η = POWER DISTRIBUTION EFFICIENCY		

Cost data are summarized in Table 1.1-12 for a comparative analysis of 5000 V and 40,000 V and power distribution efficiencies of 50%, 70%, and 79% (with and without dc converters). The cost comparison shows that lower cost results from utilizing dc converters with high transmission voltages. The baseline dc converter mass of 0.27 kg/kW at high transmission (40 kV) results in the lowest cost ($/kW$_{UT}$); however, at a dc converter specific weight of 0.5 kg/kW, the total cost approaches the 5000-V case which assumes a 70% power distribution efficiency. At 8000 V dc transmission, the total cost is reduced from that shown for 5000 V dc ($1273.1/kW$_{UT}$ reduces to $908.8 kW$_{UT}$). Cost factors used in the comparison are identified in the table.

Table 1.1-12. Cost Penalty Assessment

TRANSMISSION VOLTAGE	POWER DISTRU EFFICIENCY	SOLAR ARRAY ANA M²/KW$_{UTIL}$	S.A. + PD SP MASS KG/KW$_{UTIL}$	COST $/KW$_{UTIL}$				
				S.A./ REFL	WIRING	S.G./ CON-VERTERS	TRANSP	TOTAL
40 kV*	0.79	6.11	3.35	440	19	206	124	791*
5000 V**	0.7	8.18	8.96	589	65	177	336	1168**
5000 V	0.5	10.23	7.42	736	37	222	278	1273

*BASELINE DC CONVERTER SP MASS = 0.27 kg/kW
USING 0.5 kg/kW RESULTS IN A TOTAL COST =
$1033/kW$_{UT}$

**8000 VDC RESULTS IN A TOTAL COST = $908/kW$_{UTIL}$

COST FACTORS (1977 DOLLARS)
SG/CONVERTERS = $252/KG
CONDUCTORS = 3.93/KG
SOLAR BLANKETS = $67/M²
REFLECTORS = $2.5/M²
TRANSPORTATION = $37.5 TO GEO

DC Converter Technology Assessment

Major conclusions of a study conducted by Westinghouse Electric Corporation under contract to Rockwell International to update dc converter technology assessments are listed in Table 1.1-13. (Details of the study are given in Section 3.2.) Westinghouse concluded that the 1990 goals for normalized weight per kVA of output and efficiency can be met if semiconductor device technology improves in what is considered to be a reasonable manner. Improvements in magnetic material properties as well as in capacitor materials will further ensure that the goals can be met.

Table 1.1-13. DC Converter Technology (Update)*

	INPUT VOLTAGES	OUTPUT VOLTAGES	SOA TECHNOLOGY (15 MVA)		1990 TECHNOLOGY EXTRAPOLATION (15 MVA)	
			KG/KW	η	KG/KW	η
KLYSTRON BASELINE	40 kV	8 kV, 16 kV, 24 kV, 32 kV, 40 kV	0.70	>99%	0.11	>99%
SOLID STATE	20 kV	200 V	0.47	>94%	0.34	>96%

- SPECIFIC WEIGHT GOAL OF 0.197 KG/KW FOR 1990 TECHNOLOGY APPEARS TO BE REASONABLE.
- 1990 EFFECIENCY GOAL OF 96% APPEARS TO BE REASONABLE.
- IMPROVEMENTS IN TRANSISTOR OR MOSFET DEVICE TECHNOLOGY, CURRENT, AND SWITCHING TIME WILL BE NEEDED TO MEET 1990 GOALS.
- IMPROVEMENTS IN MAGNETIC MATERIAL PROPERTIES AND CAPACITOR MATERIALS WILL IMPROVE SYSTEM PERFORMANCE, BUT ARE NOT A PRECONDITION TO MEETING 1990 GOALS.

*EMERSON, RAY, WESTINGHOUSE ELECTRIC CORPORATION, ADVANCED ENERGY SYSTEMS DIVISION, PITTSBURGH, PA. JANUARY 31, 1980

1.1.3 OTHER SOLID-STATE CONCEPTS

A number of alternative satellite concepts were generated during the first phase of the study. A brief summary of the design features of each of these follows, and perspective drawings are presented. The orientation of these drawings is earth-midnight with the uppermost (primary) reflector pointed at the sun. The concepts referred to as "decoupled" are those where the solar cell blankets are separated from the microwave transmitter (as in the NASA/DOE reference satellite concept). When termed "integrated," the concepts employ the sandwich panel configuration referred to earlier.

Decoupled Concepts

Decoupled Concept 1 uses a large flat reflector that is pivot-mounted to the outside ring of a mechanical rotary joint, shown in Figure 1.1-15. This mirror rotates around the rest of the satellite once a day and, by tilting the mirror through a $\pm 11.75°$ cycle once a year, the annual variation in solar inclination

$CR_E = 2.8$

Flat Primary Reflector

Solar Cell Field Secondary Reflectors on Solar Array

Mechanical Rotary Joint

MW Solid-State Panel Antenna Back-to-Back with Solar Cell Field
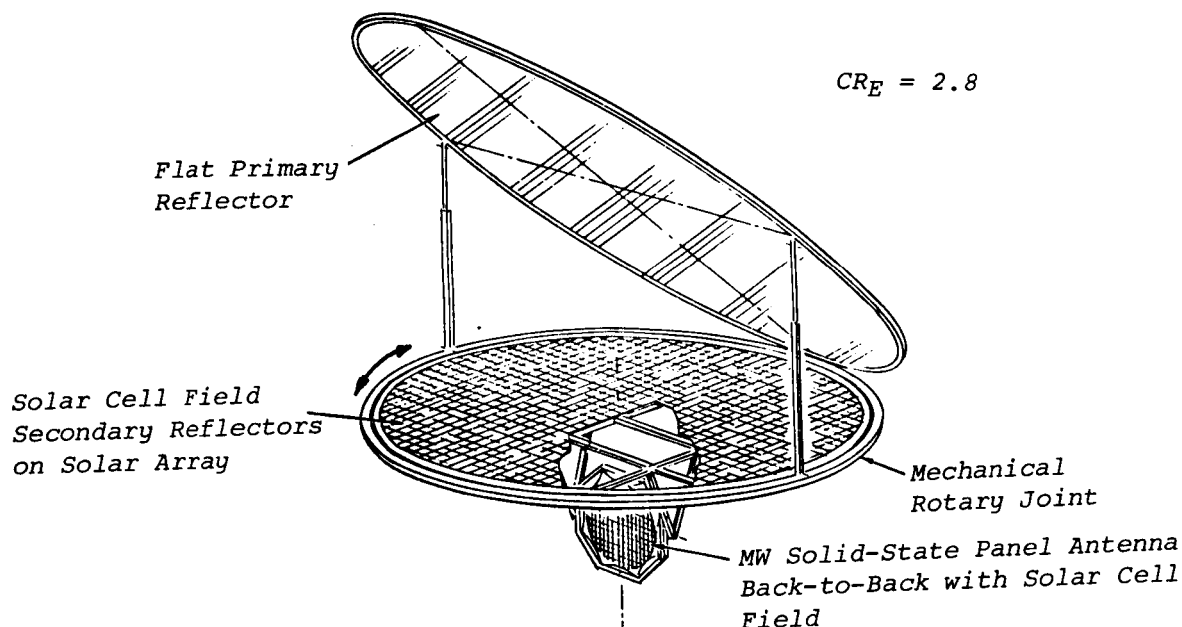
Figure 1.1-15. Decoupled Concept No. 1
(Perspective)

is accommodated without suffering insolation "cosine" losses. The solar field is comprised of a grid of small truncated pentahedral reflectors which are designed to yield a geometric concentration ratio (CR_G) of 4. Using an end-of-life reflectivity of 0.83 for the reflectors, the actual effective concentration ratio (CR_E) is calculated to be 2.8. The microwave (MW) antenna is mounted beneath the solar field as depicted. The major attributes of this concept are three-fold: (1) power transfer across a rotary joint is not required; (2) since the MW antenna is effectively located at the center of the solar cell array, the power distribution and control (PD&C) wiring mass is greatly reduced over concepts like the "reference" configuration; and (3) a significant reduction in solar cells is achieved by employing a higher CR_E.

Replacement of a large flat concentrator with a number of faceted, flat
reflectors as depicted in the perspective (Figure 1.1-16) of Decoupled Concept
No. 2, offers some obvious physical advantages; e.g., smaller-diameter mechan-
ical rotary joint, a decrease in the required solar array area resulting from
a higher CR_E, and further savings in PD&C wiring masses. However, these gains
are achieved at the expense of operational and/or technological requirements. To
maintain the full level of solar insulation requires tilting the entire satel-
lite through a ±23.5° cycle. Whenever the satellite is in an orientation other
than earth equatorial, then the boresight axis of the MW antenna will experi-
ence a daily cycle that must be overcome either by mechanical action or elec-
tronic steering (or a combination of both). Based on the comparative cost
model, and with the assumption that these issues can be resolved, there is
approximately an 8% decrease in capital investment ($/kW) over the Rockwell
"reference" concept.

$CR_E = 7.2$

10-Mirror
Primary
Reflector

Solar Cell Field

Actuator

Mechanical
Rotary
Joint

MW Solid-State
Panel Antennas
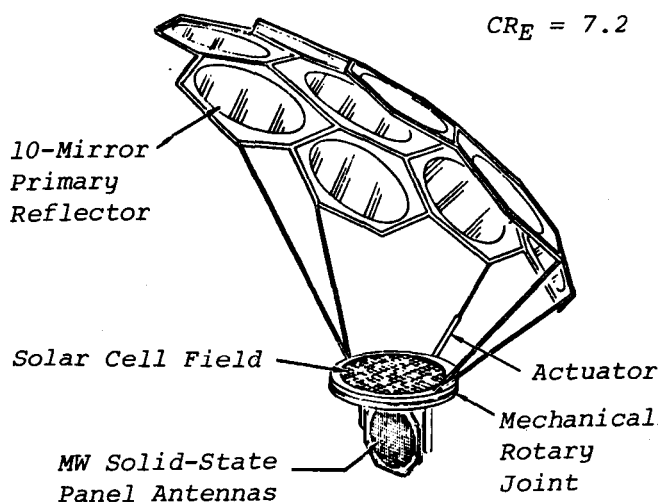
Figure 1.1-16. Decoupled Concept No. 2
(Perspective)

At this early stage of investigation into solid-state concepts, the deci-
sion was made to select the end-mounted decoupled configuration, basically
because a great amount of subsystems data had already been developed for that
concept, and the alternative configurations introduced new operational and/or
technological challenges without offering the potential of adequate percentage
cost advantages.

Integrated Concepts

In all of the alternative integrated (i.e., sandwich panel) concepts pre-
sented, it should be noted that increases in MW power densities will result in
smaller antenna diameters. Increases may be achieved through either designing
for higher concentration ratios, and/or increasing concentrator reflectivities,
and/or incorporating solar cells of higher efficiencies (e.g., multi-bandgap
cells). As the transmitting antenna is reduced in area, there is a correspond-
ing increase in the size and cost of the ground-based rectenna. It has been
found that the practical upper limit of these satellite "efficiency" increases

is set by thermal considerations of the sandwich panel; however, up that limit, there are highly significant reductions achieved in $/kW capital costs since the increased power levels of the sytem more than offset the overall system cost increases.

Integrated Concept No. 1 (Figure 1.1-17) is identical to that described as the sandwich panel concept in Exhibit C, except for being configured for a CR_E of 6.0. This double-reflector concept was used as a basis for conducting the economic sensitivity analyses presented elsewhere in this report. Operationally, only the large flat "primary" reflector is moved (i.e., rotated and tilted) to accommodate the relative change of sun angle, as described for Decoupled Concept No. 1. Each reflecting "facet" in the "secondary" is an elipse whose minor axis is ≈ MW antenna diameter and whose major axis is sized for their relative position angles.
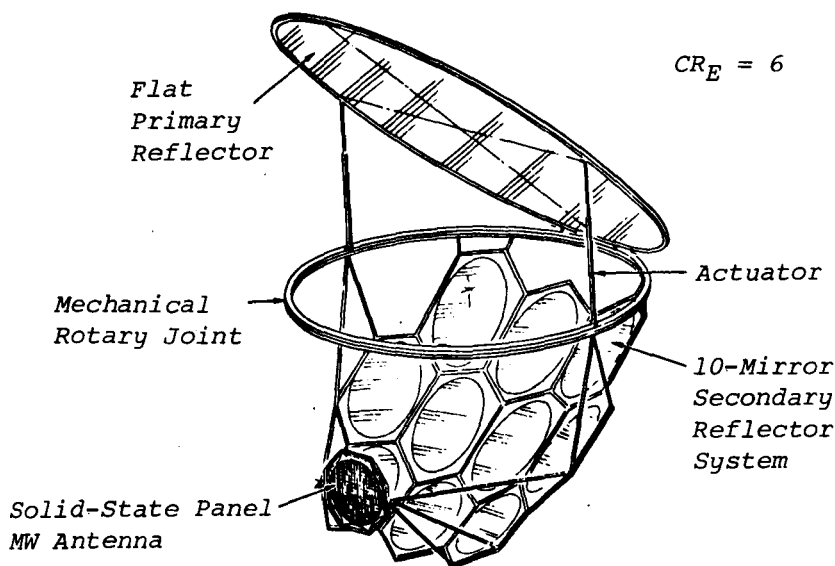
Figure 1.1-17. Integrated Concept No. 1
(Perspective)

Figure 1.1-18 illustrates Integrated Concept No. 2. A variation of this concept was selected for detailed definition and costing. Each of the alternative single-antenna integrated concepts was found to present significant attitude control/stationkeeping problems resulting in comparatively severe mass penalties for propellant requirements. Ultimately, the most cost-effective design approach was determined to be one which incorporates the dual-antenna concept previously described in this volume. Of all the alternative integrated concepts analyzed, Concepts No. 1 and No. 2 posed the fewest technological problems. This was deemed a significant criterion for developing the first detailed definition of a completely new satellite concept. The dominant reason for selecting Concept No. 2 over No. 1 was that the faceted primary approach appeared to require less structure and reflector area for the same CR_E.

In the attempt to minimize satellite mass per unit of transmitted power, one of the most direct approaches is to eliminate the need for a double

$CR_E = 6$

10-Mirror
Primary
System

Mechanical
Rotary
Joint

Solid-State Panel
MW Antenna

Flat Secondary
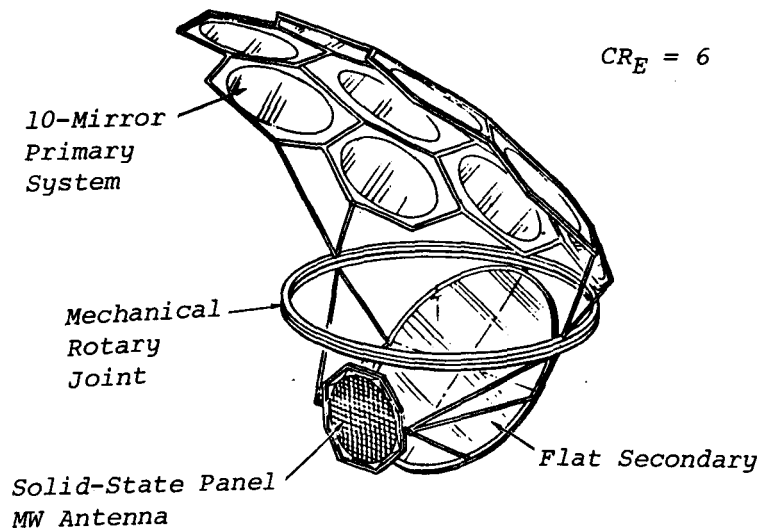
Figure 1.1-18. Integrated Concept No. 2
(Perspective)

reflection of the intercepted sunlight. Integrated Concept No. 3 (shown in
Figure 1.1-19) illustrates a configuration based on this approach; however,
the performance increase is partially offset by sizing the primary reflector
for a cosine loss that must be accepted for the angled sandwich panel. Fur-
thermore, added burdens are placed on the phase control technology for this
concept.

$CR_E = 5$

10-Mirror
Primary
Reflector

Mechanical
Rotary
Joint

Solid-State Panel
MW Antenna Electronic Scan
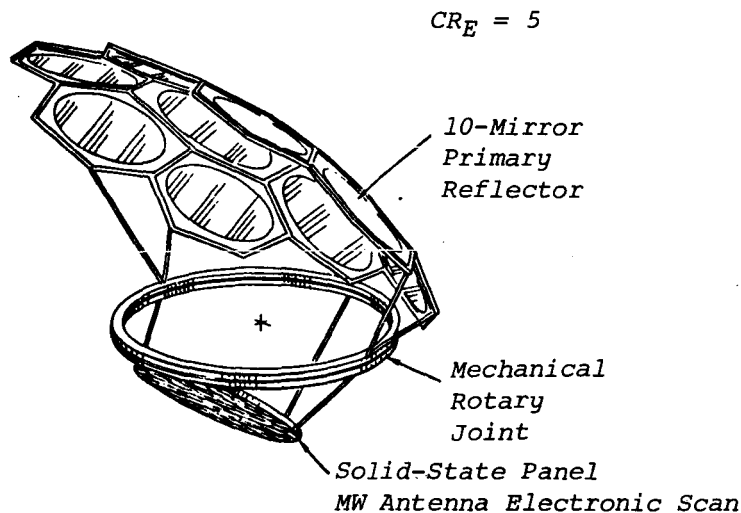
Figure 1.1-19. Integrated Concept No. 3
(Perspective)

The concept of employing an RF reflector on the satellite was first intro-
duced by Rockwell for a klystron amplifier system using the reference configur-
ation in Exhibit B of the current SPS series studies. The "show stopper"

encountered was in maintaining phase control along waveguides leading to a horn-type transmitter at one end of the satellite. Since the sandwich panel transmits power directly from its face, it is not confronted with the same technological problem. Integrated Concept No. 4 takes advantage of the RF reflector approach, as shown in Figure 1.1-20. The single-faceted primary yields a higher CR_E with a smaller mechanical rotary joint than any of the other alternatives; however, control of the signal being reflected off a flat "screen" adds yet another dimension to the phase control technology which has yet to be entirely resolved. This concept should represent the lowest in mass per unit power of all the alternatives investigated; but further definition must await complete resolution of the basic SPS phase control problem.

CR$_E$ • 7.2

10 MIRROR PRIMARY SYSTEM

SOLAR CELL FIELD

FLAT SCREEN RF REFLECTOR
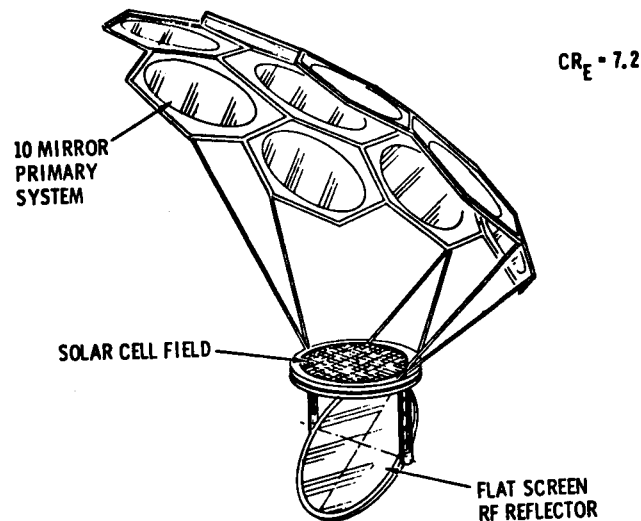
Figure 1.1-20.   Integrated Concept No. 4
(Perspective)

Of the integrated concepts shown, all are constrained by the ionospheric power density limit of 23 mW/cm^2 to a transmitted power level of about two gigawatts. One of the key issue concerns for SPS is available orbiting "stations" in the post-2000 time frame; and, of course, more stations would be required for the lower power satellites. One approach to increasing the power level for sandwich panel concepts is depicted in Figure 1.1-21 as Integrated Concept No. 5. Although originally conceived as a potential solution to the orbital spacing problem, further investigation of the single antenna concepts pointed out the advantages of this approach to overcoming the propellant mass penalties associated with attitude control and stationkeeping. This specific concept was developed early in the study and did serve to illustrate as an example of the multi-antenna configuration. Its major drawback was in using in-line secondary reflectors which limited the effective CR to a value of 3.4. Subsequent redesign of Integrated Concept No. 2 resulted in a concept quite similar to this configuration.

Integrated Concept No. 2 was chosen for detailed definition in the latter half of this study. The concept selected was the one which did not present
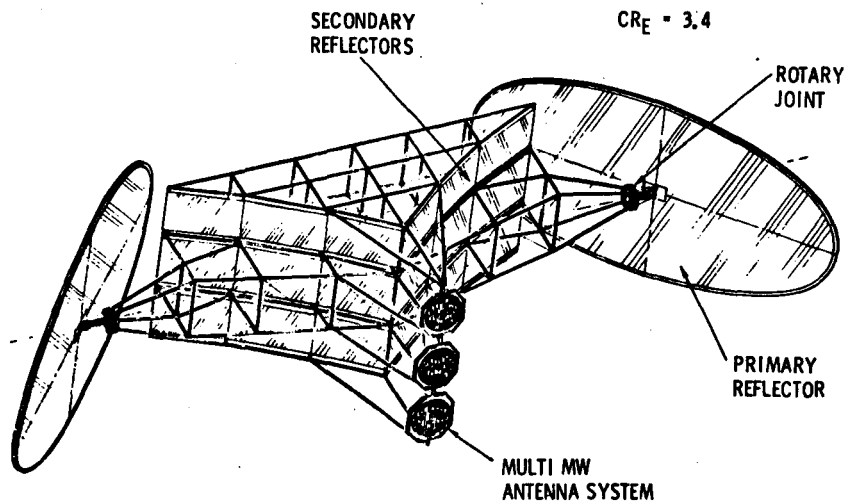
Figure 1.1-21. Integrated Concept No. 5
(Perspective)

additional technological burdens over and above those already posed by develop-
ment of solid-state systems. Assuming resolution of technology problems for
the solid-state concepts selected, future studies may be directed toward
developing other, potentially more cost-effective configurations such as
Integrated Concept No. 4.

1.2 REFERENCE CONCEPT UPDATE

A major task in the contract Exhibit D study was to continue the upgrading of the reference (GaAs solar cell/klystron power amplifier) satellite concept as prior analysis were refined or as new analysis provided additional requirements. This section considers the configuration as it was at the end of Exhibit C and as it appears at the present time.

The reference concept at the end of Exhibit C was presented in two versions. Both approaches required the same solar array planview but in one case the antenna was located at one end of the solar array while in the second version the solar array was split and the antenna was located on a strongback frame at the middle of the satellite. The two versions are illustrated in Figure 1.2-1. Both of these concepts were designed to provide 4.61 GW at the utility interface with the efficiency chain defined at that time (Figure 1.2-2).
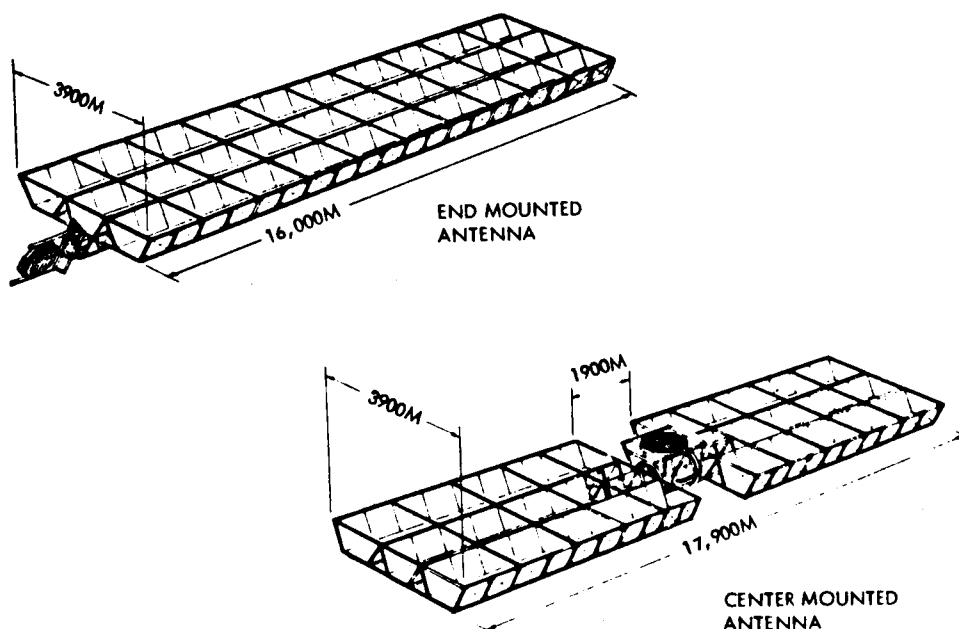
Figure 1.2-1. Three Trough Coplanar Configurations

The reference concept consisted of 27×10^6 m^2 of GaAs solar array consisting of 24 strips 25 m wide by 750 m long in 60 groups or bays. The bays were arranged in three troughs with solar concentrators mounted at a 60° slant angle to the solar arrays, located on each side of the bay along the long axis of the solar panel. The solar cells were of GaAs with an efficiency rating of 18.2% AMO at 113°C. Overall dimensions of the end mounted version solar array were as follows:

        Length   16 km
        Width   3.9 km
        Depth   0.564 km

The antenna added an additional 1.9 km to the overall satellite length.

(9.52 GW)

SWITCH GEAR — SWITCH GEAR — SLIP RING/ BRUSH — (8.92 GW)

0.952   0.999   0.988   0.999

0.9381
POWER DIST

(7.07 GW)   (8.319 GW)

RCR — KLYSTRON — SWITCH GEAR — SWITCH GEAR — SWITCH GEAR — (FEEDERS) — SWITCH GEAR — DC/DC CONV — RISER — SWITCH GEAR

(6.79 GW)

0.96   0.85   0.999   0.999   0.999   0.99   0.999   0.96   0.99   0.999

0.7608
MW ANT

5.53   (4.924 GW)

BEAM EFF & ATMOS — RECTENNA ARRAY — MOTOR SWITCH — SWITCH GEAR — (BUS) — SWITCH GEAR — DC/AC CONVERT STATION — SWITCH GEAR — (BUS) — SWITCH GEAR — (4.61 GW) CUSTOMER

0.815   0.89   0.999   0.999   0.99   0.999   0.96   0.999   0.99   0.999

(0.6791)
GROUND

= POWER GEN. X POWER DIST. X MW ANT. X GROUND

(13.35%)   (93.81%)   (76.08%)   (67.91%)

6.47%

Figure 1.2-2.   System Efficiency Chain—Photovoltaic (CR-2)

The satellite design assumed that the primary construction site would be located at GEO. The antenna design was based on a rigid space frame concept (Figure 1.2-3) similar to that described in the NASA/JSC documentation. Over-all system efficiency was estimated at 6.47%.
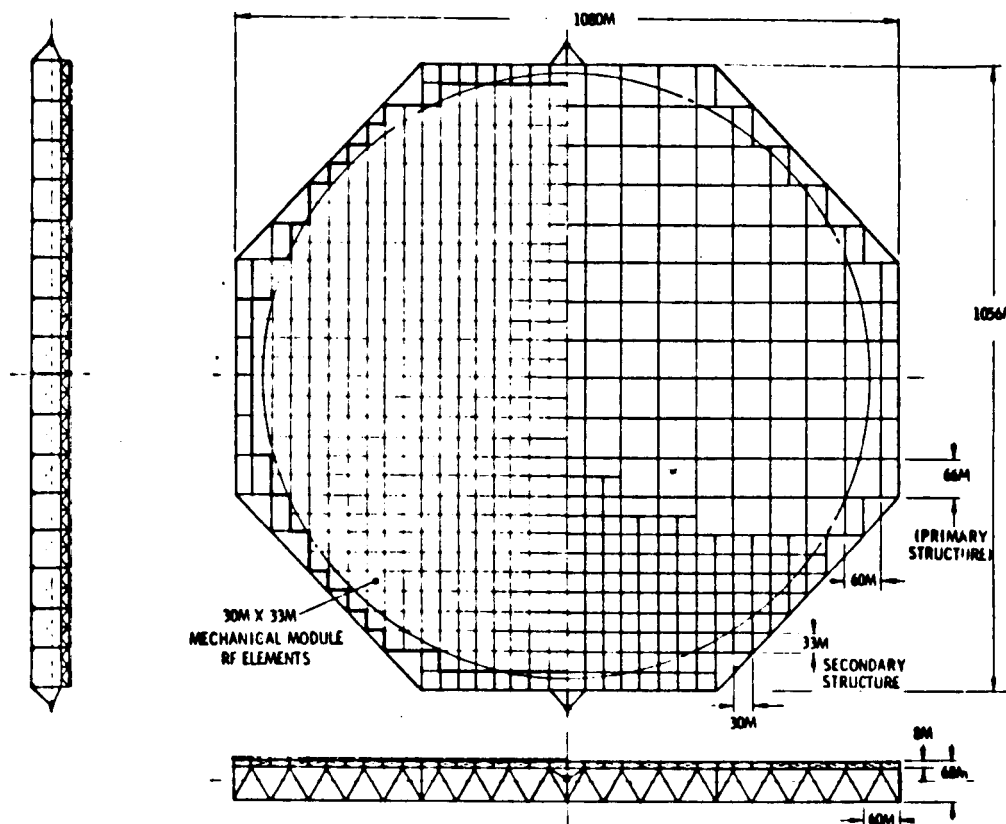
Figure 1.2-3. Space Frame Antenna Configuration

The present configuration is similar to the configuration defined in March 1979 with several major revisions. The most significant revision is the increase in power available at the utility interface (power utility network or grid) from 4.61 GW in March 1979 to 5.07 GW at the present time. The increase in available power was accomplished by an improvement in the system efficiency chain (Figure 1.2-4) and by increasing the transmitted power to 7.14 GW. The increase in transmission power was made possible by: 1) increasing the number of klystrons on the antenna to 142,902 units (was 135,864) and 2) by increasing the solar panel area to 28.47×10^6 m^2 (was 27.0×10^6 m^2). Table 1.2-1 summarizes the power levels at the end of each study phase.

Other changes resulting from the increased power level was the increase in required solar panel width to 650 m (26-25 m strips). This in turn required an increase in satellite width to 4200 m (was 3900 m).

Other system modifications that have been implemented are the use of a tension web/compression frame concept for the antenna main structure (Figure 1.2-5) and the use of an end mounted antenna configuration, at this time, and a modification in the PD&C subsystem.

ARRAY ORIENT.	REFLECTOR DEGRAD.	CELL EFFICIENCY	PACK. FACTOR	ARRAY DESIGN	UV DEGRAD.	SWITCH GEAR	POWER BUSES & FEEDERS	SWITCH GEAR	TIE BARS	SLIP RING/ BRUSH
0.968	CRE = 1.83 0.915	0.1816 AT 113°C 0.2756 AT 113°C MBG	0.95	0.94	0.96	0.997	0.952	0.999	0.988	0.999

9.94 GW   9.33 GW

45.7 KV

◄———————— POWER SOURCE (0.1375) ————————►◄———— POWER DISTRIBUTION (0.9387) ————►

BEAM EFF & ATMOS	ANTENNA	KLYSTRON & DRIVER	SWITCH GEAR	SWITCH GEAR	SWITCH GEAR	FEEDERS	SWITCH GEAR	DC-DC CONV.	RISERS	SWITCH GEAR
0.862*	0.96	0.842	0.999	0.999	0.999	0.99	0.999	0.97	0.99	0.999

7.14 GW   7.44 GW   8.96 GW   2.46 GW   9.23 GW

40 KV

◄—————————— MICROWAVE ANTENNA & POWER DISTRIBUTION (0.6592) ——————————►

5.35 GW

6.15 GW

RECTENNA	MOTOR SWITCH 0.999	SWITCH GEAR	(BUS)	SWITCH GEAR	DC-AC CONV. STATION	SWITCH GEAR	POWER DISTR	SWITCH GEAR
0.88		0.999	0.99	0.999	0.96	0.999	0.99	0.999

5.07 GW

40 KV

*BEAM EFF   – 0.95
PHASE ERROR   – 0.945
OUTAGE   – 0.98
ATMOSPHERE   – 0.98
PRODUCT   = 0.862

◄———— POWER COLLECTION (0.8695) ————►◄———— GRID INTERFACE (0.9476) ————►

η_T = POWER SOURCE X POWER DIST. X MW ANT X POWER COLLECTION X GRID INTERFACE

13.75%   93.87%   65.92%   86.95%   94.76%

= 7.00%

Figure 1.2-4.   System Efficiency Chain—Reference Concept
(April 1980)

Table 1.2-1. Satellite Power History

CONTRACT EXHIB.	SOLAR ARRAY OUTPUT	KLYSTRON		TRANSMITTED	UTILITY INTERFACE	SYSTEM EFFICIENCY
		NO.	POWER			
A/B	9.76 GW	135,864	54.3 kW	7.09 GW	5.0	6.08%
C	9.52 GW	135,864	52 kW	6.79 GW	4.61	6.47%
D	9.94 GW	142,902	51.8 kW	7.14 GW	5.07	7.00%
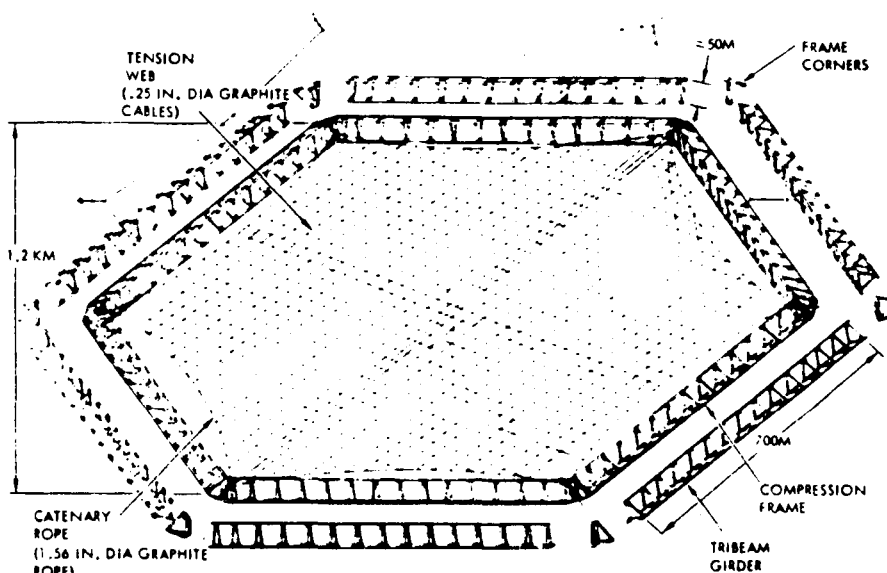
Figure 1.2-5. Microwave Antenna Structure
Selected Design Concept

The decision to utilize the tension web/compression frame structure con-
cept, first proposed during the Exhibit A/B study phase rather than to utilize
the space frame concept suggested for the NASA/reference concept was based
upon a detailed analysis performed during the Exhibit D activity that showed
significant mass savings and reduced thermal impact. The full analysis is
discussed in Volume II.

The use of an end mounted antenna configuration rather than the previously
suggested center mounted configuration is based upon the possible simplifica-
tion in design (smaller rings, although 30 ring pairs are required) and
in the improved thermal characteristics that can be realized since the waste
heat from the antenna is not radiated onto the rings. Thus despite the fact
that system mass will increase (approximately 2×10^6 kg) because of higher
average main bus length, the overall effect is system improvement.

The third major change, in the power distribution and conversion subsystem, is the elimination of the solar array summing buses, used with the large center-mounted rotary joint, resulting in a significant reduction in overall solar array wire mass despite the increase in average wire length and an increase in current carrying capability.

A relatively minor change, a reduction in the thermal insulation on the antenna subarray was also made to permit the waste heat to be radiated from both surfaces (Figure 1.2-6). This permits the maximum power density to increase to 25 kW/m^2 without exceeding thermal limitations of the antenna sub-array materials.
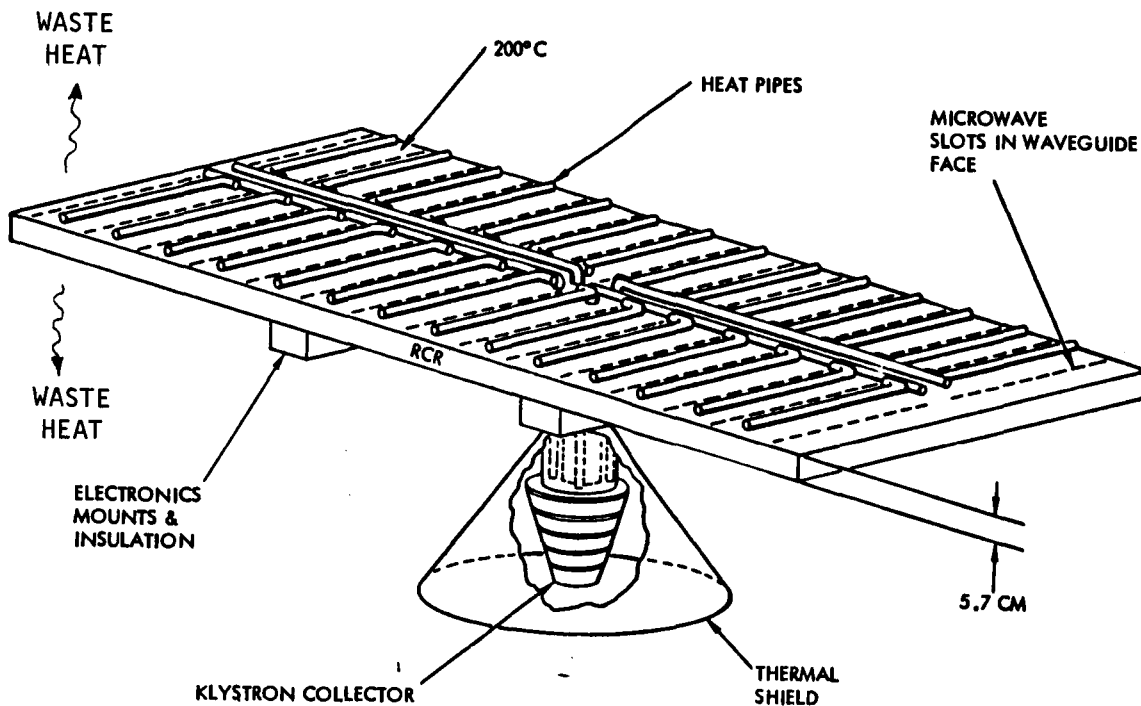
Figure 1.2-6. Radiating Face of Power Module

The Exhibit D (July 1980) configuration is shown in Figure 1.2-7.

A continuing aspect of the present SPS study contract was the maintenance of an up-to-date version of the reference concept mass estimate. It became very evident that, due to changes in assigned personnel, the various approaches to developing the mass estimates were varied although all were logical. Accordingly, a more consistent approach was developed and utilized for all seven concepts that were eventually defined and are described in Volume VII of the Final Report for Exhibit D of Contract NAS8-32475.

At the same time the various mass elements were redistributed in a format that conforms to the work breakdown structure (WBS) presently in force. This redistribution included the regrouping of certain elements of mass into a new group identified as the interface group which included everything mounted on the antenna yoke section. An added result of the redistribution was the high-lighting of the relative impact of certain system factors. This in turn forced

1-33
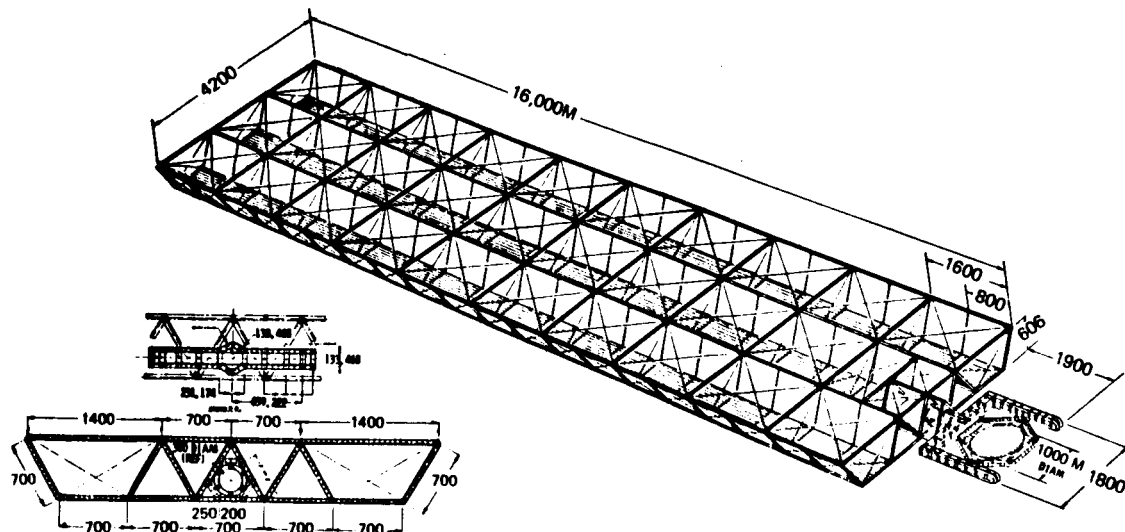
Figure 1.2-7. Solar Power Satellite—Reference Configuration
Single End-Mounted Tension Web Antenna—Klystron

a review of the selected design factors. One example of this impact was the
decision to return to using a tension web-compression web form of antenna.
The subsequent subsystem analysis showed the validity of this concept (dis-
cussed in Volume II) and resulted in a mass reduction of approximately
200,000 kg.

Other factors which impacted the overall satellite system mass were the
reduction of thermal insulation on the antenna subarray and the addition of
maintenance and gantry structure that were not included in prior mass properties
listings.

Overall mass of the June 1980 reference satellite is estimated at 31.632×10^6 kg,
a 4.2% reduction from the estimate of 33.02×10^6 kg for the Exhibit C reference
satellite. A summary of both the March 1979 and the June 1980 estimates are
tabulated in Table 1.2-2.

Table 1.2-2. Mass Properties—Reference Concept Comparison
$(\times 10^{-6}$ kg$)$

	JUNE 1980	MAR 1979
	GaAs	GaAs
1.1.1 ENERGY CONVERSION (SOLAR ARRAY)		
STRUCTURE	1.514	1.060
PRIMARY	(0.928)	(0.702)
SECONDARY	(0.586)	(0.358)
MECHANISMS	0.070	0.200
CONCENTRATOR	1.030	1.037
SOLAR PANEL	7.174	6.818
POWER DISTRIBUTION AND CONTROL	2.757	2.603
POWER COND. EQUIPMENT AND BATT.	(0.319)	(0.193)
POWER DISTRIBUTION	(2.438)	(2.410)
THERMAL	NONE	NONE
MAINTENANCE	0.092	—
*1.1.3 INFORMATION MANAGEMENT AND CONTROL	0.050	0.050
DATA PROCESSING	(0.021)	(0.021)
INSTRUMENTATION	(0.029)	(0.029)
*1.1.4 ATTITUDE CONTROL	0.116	0.116
TOTAL	12.803	11.884
1.1.2 POWER TRANSMISSION (ANTENNA)		
STRUCTURE	0.838	0.786
PRIMARY	(0.023)	(0.120)
SECONDARY	(0.815)	(0.666)
MECHANISM	0.002	0.191
SUBARRAY	7.050	6.870
POWER DISTRIBUTION AND CONTROL	2.453	4.505
POWER COND. EQUIPMENT AND BATT.	(1.680)	(1.901)
POWER DISTRIBUTION	(0.773)	(2.604)
THERMAL	0.720	1.408
ANTENNA CONTROL ELECTRONICS	0.170	0.142
MAINTENANCE	0.107	—
*1.1.3 INFORMATION MANAGEMENT AND CONTROL	0.640	0.630
DATA PROCESSING	(0.380)	(0.380)
INSTRUMENTATION	(0.260)	(0.250)
*1.1.4 ATTITUDE CONTROL	NEGL.	NEGL.
TOTAL	11.980	14.532
1.1.6 INTERFACE		
STRUCTURE	0.170	↑
PRIMARY	(0.136)	
SECONDARY	(0.034)	INCLUDED
MECHANISMS	0.033	IN 1.1.2
POWER DISTRIBUTION AND CONTROL	0.288	ABOVE
POWER DISTRIBUTION	(0.271)	
SLIP RING BRUSHES	(0.017)	↓
THERMAL	NONE)	
MAINTENANCE	0.032	—
COMMUNICATION	TBD	TBD
TOTAL	0.523	—
SPS TOTAL (DRY)	25.306	26.416
GROWTH (25%)	6.326	6.604
TOTAL SPS (DRY) WITH GROWTH	31.632	33.020
SATELLITE POWER @ UTILITY I/F (GW)	5.07	4.61
SATELLITE DENSITY, KG/KW$_{UI}$	6.24	7.16
*PARTIAL		

1.3 MULTI-BANDGAP SOLAR ARRAY CONFIGURATION

The Rockwell SPS reference design used (for cost purposes) is based on a GaAs technology having a cell performance of 20% efficiency at AMO and 28°C. Although this cell is believed to offer the highest AMO conversion efficiency of all the single-crystal photovoltaic cells developed to present, it is essential for a long-term project of the magnitude and importance of the SPS to be planned so that future technology developments having a significant positive impact on its performance and cost can be incorporated with minimum delay and technological complication. The cell conversion efficiency under orbital operating conditions is a critical performance parameter that in turn affects essentially all other design aspects of the SPS. The prospect of a dramatic increase in cell operating efficiency, even with respect to the present high value of 20%, is offered by the concept of the tandem, multiple band-gap solar cell.

Rockwell SPS design goals and a technology assessment made by Research Triangle Institute[1], a comparison of the cell efficiency, temperature coefficient, equivalent radiation degradation, mass and cost is shown in Table 1.3-1. A design goal of 30 percent conversion efficiency was set by Rockwell with an assumption that the temperature coefficient would be comparable to that used for GaAs in the reference design concept. Equivalent radiation degradation was also assumed with 5% mass and 10-20% cost penalties.

Table 1.3-1. Multi-Bandgap Solar Cell Technology Assessment

PARAMETER	SPS DESIGN (GOALS)	TECHNOLOGY ASSESSMENT[1]
AMO EFFICIENCY (%)	30 (28°C) 25.1 (200°C)	32 (28°C) 19 (200°C)
TEMPERATURE COEFFICIENT	COMPARABLE TO GaAs (-0.0287%/°C)	-0.085%/°C FOR GaAlAs/GaInAs CELL
EQUIVALENT RADIATION DEGRADATION	4% (30 YEARS)	UNDER STUDY
MASS (KG/M^2)	0.265 (5% HIGHER THAN GaAs BASELINE CELL)	SAME
COST ($/M^2)	73.7 – 80.4 (10-20% HIGHER THAN GaAs BASE-LINE CELL)[2]	$200 (FACTOR 3 TIMES DUE TO LOW YIELD)

[1]RTI TECHNOLOGY ASSESSMENT BASED ON A TWO-JUNCTION GaAlAs/GaInAs MULTI-BANDGAP SOLAR CELL.

[2]MAJOR COST INCREASE IS IN THE FABRICATION PROCESSES.

1.3.1 EFFICIENCY CHAIN COMPARISON

The reference concept using klystrons on the antenna was compared to the three basic solid state antenna satellite approaches and Table 1.3-2 shows the relative efficiencies for each item in the satellite efficiency chain. Overall efficiencies range from a low of 4.2% for the sandwich concept with standard

---

[1]*Multi-Bandgap Solar Cell Study*, Contract No. M9L8GDS-897406D performed for Rockwell International, June 1, 1980

Table 1.3-2. Efficiency Chain Comparison—Satellite Concepts

	REF.—KLYSTRON		REF.—ARRAY/ S-S ANTENNA		SANDWICH (SINGLE)		SANDWICH (DUAL)	
	STD	MBG	STD	MBG	STD	MBG	STD	MBG
POWER SOURCE								
CELL EFFICIENCY	0.1816	0.2756	0.1816	0.2756	0.151	0.239	0.151	0.239
EFFECTIVE REFLECTOR EFFICIENCY	0.915	0.915	0.915	0.915	0.83	0.83	0.689	0.689
POINTING/SEASONAL FACTOR	0.968	0.968	0.968	0.968	0.98	0.98	0.98	0.98
DESIGN FACTOR	0.893	0.893	0.893	0.893	0.893	0.893	0.893	0.893
UV DEGRADATION	0.96	0.96	0.96	0.96	0.96	0.96	0.96	0.96
SWITCH GEAR	0.997	0.997	0.997	0.999	-	-	-	-
TOTAL	(0.1375)	(0.2086)	(0.1377)	(0.2091)	(0.1053)	(0.1667)	(0.0874)	(0.1383)
POWER DISTRIBUTION								
BUSES	0.9405	0.9405	0.9405	0.9405	-	-	-	-
SWITCH GEAR	0.999	0.999	0.999	0.999	-	-	-	-
SLIP RING BRUSHES	0.999	0.999	0.999	0.999	-	-	-	-
TOTAL	(0.9387)	(0.9387)	(0.9387)	(0.9387)	(-)	(-)	(-)	(-)
MICROWAVE ANTENNA								
BUSES	0.9801	0.9801	0.9801	0.9801	1.0	1.0	1.0	1.0
SWITCH GEAR	0.995	0.995	0.997	0.997	-	-	-	-
DC-DC CONVERSION	0.97	0.97	0.92	0.92	-	-	-	-
REGULATION	-	-	-	-	0.96	0.96	0.96	0.96
KLYSTRONS & DRIVERS	0.842	0.842	-	-	-	-	-	-
S-S AMP. & DRIVERS	-	-	0.792	0.792	0.792	0.792	0.792	0.792
ANTENNA	0.96	0.96	0.96	0.96	0.96	0.96	0.96	0.96
BEAM EFFICIENCY & ATMOSPHERICS	0.862	0.862	0.799	0.799	0.799	0.799	0.799	0.799
TOTAL	(0.6591)	(0.6591)	(0.5461)	(0.5461)	(0.5832)	(0.5832)	(0.5832)	(0.5832)
GROUND SYSTEM	(0.8237)	(0.8237)	(0.8237)	(0.8237)	(0.8327)	(0.8237)	(0.8237)	(0.8237)
OVERALL TOTAL	0.700	0.106	0.058	0.088	0.051	0.0801	0.0420	0.0665
POWER AT UTILITY INTERFACE (GW)	5.07		2.61		1.21	1.53	2.42	3.06

(STD) GaAs reference solar cells to 10% for the reference klystron concept
with multi-bandgap (MBG) solar cells. Overall power delivered to the utility
interface varies from 5.07 GW (Reference—klystron concept) to 1.263 GW (GaAs
standard solar cell—sandwich concept). The sandwich concept was compared for
single (SINGLE) reflector and double (DOUBLE) reflector concepts. A dual
antenna version of the reference array/solid state antenna concept could
provide 5.22 GW at the utility interface utilizing a 10-dB Gaussian antenna
illumination pattern.

1.3.2 MULTI-BANDGAP SOLAR ARRAY DESIGN

     The solar cell voltage characteristics are one of the main factors that
drive the array design. Solar cell voltage outputs are listed in Table 1.3-3.
As shown, the multi-junction cells result in significantly higher voltage out-
puts per cell (~ factor of 2 to 3 higher). The reference GaAs single junction
cell utilized two panels in series each 730 m in length to build up a voltage
of 45.7 kV on the array. These two solar panels make up one structural bay on
the satellite. With the multi-junction cells the length of solar panels would
be directly related to the cell voltage and impact the arrangement and dimen-
sions of the structural bay layouts illustrated for the dual mounted antenna
solid state concept in Table 1.3-4. System voltage requirements for this con-
cept is to deliver 40 kV at the input to the dc converters on the antenna. To
meet this and the efficiency chain shown in Figure 1.3-1 requires an array out-
put voltage of 43.3 kV. The resultant panel dimensions are 650 m (width) and
465 m (length) with one panel providing an output voltage of 43.3 kV.

Table 1.3-3. Solar Cell Voltage Characteristics

CELL MATERIAL		OPS TEMP (°C)	INITIAL[1] CELL VOLTAGE (VOLTS)	EOL CELL VOLTAGE (VOLTS)	VOLTAGE[2] PER METER (VOLTS)
SINGLE JUNCTION	GaAs	113	0.69 (0.85)	0.657	31.48
		200	0.575 (0.85)	0.547	26.26
DUAL JUNCTION	GaAlAs/GaInAs	113	1.45 (1.6)	1.382	66.34
		200	1.32 (1.6)	1.254	41.38
	GaAlAs/GaAs	113	2.05 (2.2)	1.952	93.7
		200	1.92 (2.2)	1.82	40.04

[1]CELL TEMPERATURE COEFFICIENT = -0.00175 V/°C, ( ) = 28°C VALUE

[2]48 CELLS IN SERIES, EACH 2.04 CM LENGTH X 3.59 CM WIDTH FOR SINGLE JUNCTION CELL.

33 CELLS IN SERIES, EACH 2.5 CM LENGTH X 3.33 CM WIDTH FOR GaAlAs/GaInAs CELL AT 200°C

22 CELLS IN SERIES, EACH 2.5 CM LENGTH X 4.44 CM WIDTH FOR GaAlAs/GaAs CELL AT 200°C

48 CELLS IN SERIES, EACH 2.0 CM LENGTH X 4.0 CM WIDTH FOR GaAlAs/GaAs, GaAlAs/GaInAs CELLS AT 113°C

Table 1.3-4. Dual Mounted Antenna
(Solid State Concept)

CHARACTERISTIC	GaAs SINGLE JUNCTION	GaAlAs/GaAs DUAL JUNCTION
CELL EFFICIENCY AMO, 28C 113C	20% 18.15%	30% 27.56%
CELL VOLTAGE 113C, EOL	0.657 V/CELL (31.48V/METER)	1.952 V/CELL (93.7 VOLTS/METER)
PANEL DIMENSIONS 45.7 KV REQMT	650M (WIDTH) 690M (LENGTH) 2 PANELS IN SERIES	650M (WIDTH) 465M (LENGTH) 1 PANEL
SOLAR ARRAY AREA	32.29 X 10^6 M^2	19.95 X 10^6 M^2
SATELLITE DIMENSIONS	4200M X 18000M	4200M X 12000M

- CR_{eff} = 1.83
- PUTIL = 7.36 GW
- PSA = 11.46 GW

The higher solar cell efficiency results in significantly reduced overall satellite dimensions, i.e., 12,000 m versus 18,000 m.

1.3.3 SATELLITE MASS

Mass characteristics of three of the point design concepts utilizing a GaAlAs/GaAs multi-junction (MBG) solar cell are shown in Table 1.3-5. The total satellite mass density to delivered power at the utility interface (kg/kW_{UI}) is 5.12, 6.81, and 5.35 for the reference klystron, dual end-mounted solid state and sandwich solid state concepts. Note: The reference klystron single junction GaAs solar cell concept is 6.24 kg/kW_{UI}. A summary of the major characteristics of the three satellite configurations utilizing both GaAs and GaAlAs/GaAs (MBG) solar cells is shown in Table 1.3-6.
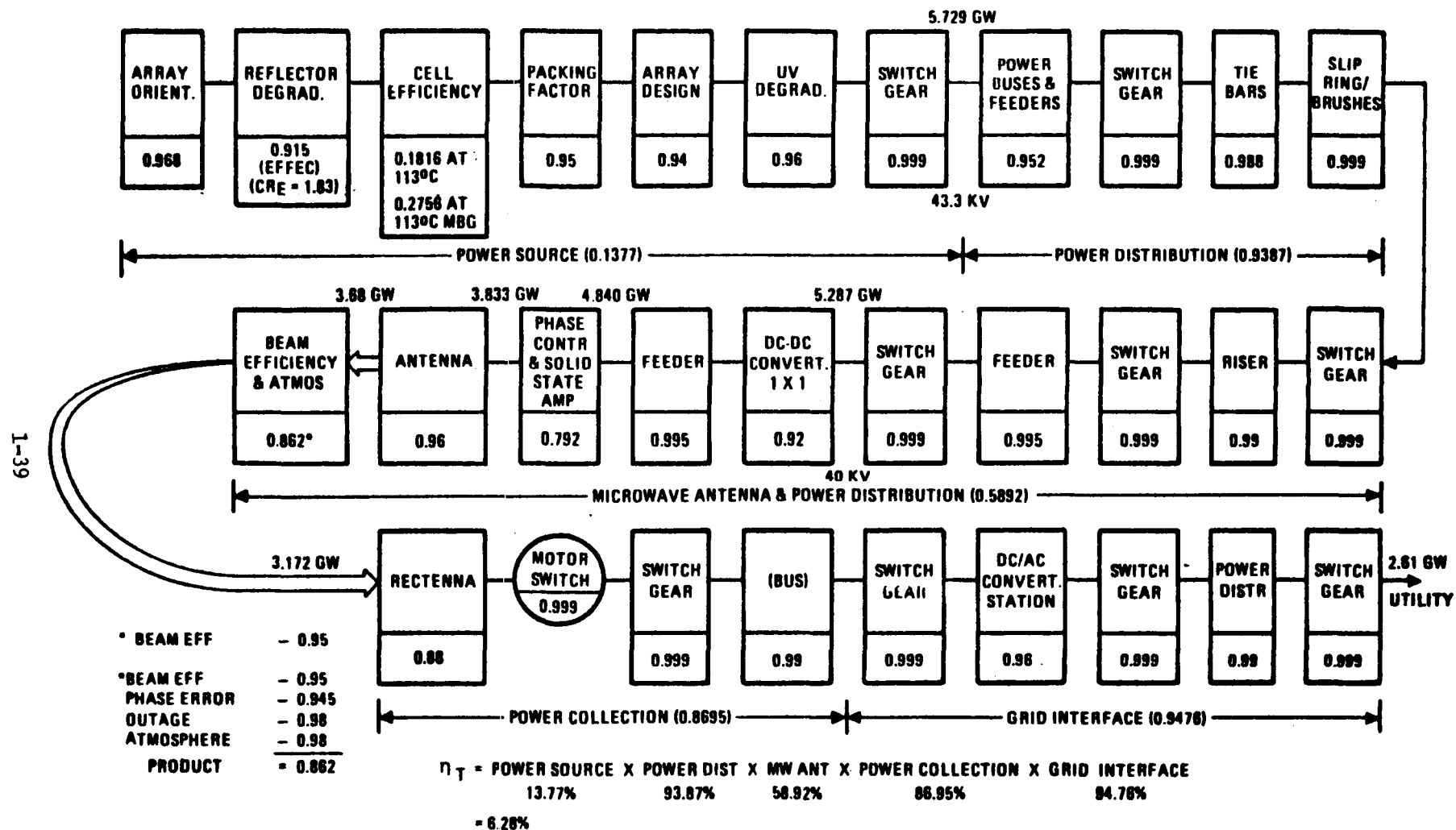
Figure 1.3-1. System Efficiency Chain Dual End-Mounted Concept (Solid State Antenna) April 1980

Row 1:

5.729 GW

ARRAY ORIENT.	REFLECTOR DEGRAD.	CELL EFFICIENCY	PACKING FACTOR	ARRAY DESIGN	UV DEGRAD.	SWITCH GEAR	POWER BUSES & FEEDERS	SWITCH GEAR	TIE BARS	SLIP RING/ BRUSHES
0.968	0.915 (EFFEC) (CRE = 1.83)	0.1816 AT 113°C 0.2756 AT 113°C MBG	0.95	0.94	0.96	0.999	0.952	0.999	0.988	0.999

43.3 KV

◄───── POWER SOURCE (0.1377) ─────►◄─── POWER DISTRIBUTION (0.9387) ───►

Row 2:

3.68 GW   3.833 GW   4.840 GW   5.287 GW

BEAM EFFICIENCY & ATMOS	ANTENNA	PHASE CONTR & SOLID STATE AMP	FEEDER	DC-DC CONVERT. 1 X 1	SWITCH GEAR	FEEDER	SWITCH GEAR	RISER	SWITCH GEAR
0.862*	0.96	0.792	0.995	0.92	0.999	0.995	0.999	0.99	0.999

40 KV

◄───────── MICROWAVE ANTENNA & POWER DISTRIBUTION (0.5892) ─────────►

Row 3:

3.172 GW

RECTENNA	MOTOR SWITCH	SWITCH GEAR	(BUS)	SWITCH GEAR	DC/AC CONVERT. STATION	SWITCH GEAR	POWER DISTR	SWITCH GEAR
0.88	0.999	0.999	0.99	0.999	0.96	0.999	0.99	0.999

2.61 GW UTILITY

◄─── POWER COLLECTION (0.8695) ───►◄──── GRID INTERFACE (0.9476) ────►

* BEAM EFF   – 0.95
*BEAM EFF   – 0.95
 PHASE ERROR   – 0.945
 OUTAGE   – 0.98
 ATMOSPHERE   – 0.98
 PRODUCT   = 0.862

η_T = POWER SOURCE X POWER DIST X MW ANT X POWER COLLECTION X GRID INTERFACE
           13.77%   93.87%   58.92%   86.95%   94.76%

= 6.28%

1-39

Space Operations and Satellite Systems Division Space Systems Group

Rockwell International

Table 1.3-5. Mass Properties Summary (MBG)
Exhibit D (April 1980) ($\times 10^{-6}$ kg)

	KLYSTRON CONCEPT	SOLID-STATE CONCEPTS	
		DUAL END-MOUNTED	DUAL SANDWICH
1.1.1 ENERGY CONVERSION (SOLAR ARRAY)			
STRUCTURE	(1.133)	(1.233)	(2.411)
PRIMARY	0.804	0.902	2.138
SECONDARY	0.429	0.331	0.273
MECHANISMS	(0.070)	(0.078)	(0.019)
CONCENTRATOR	(0.648)	(0.766)	(1.646)
SOLAR PANEL	(4.804)	(5.607)	(0.076)*
POWER DISTRIBUTION & CONTROL	(1.388)	(0.846)	(0.015)
POWER COND. EQUIP. & BATT.	0.206	0.222	0.013
POWER DISTRIBUTION	1.182	0.624	0.002
THERMAL	(NONE)	(NONE)	(NONE)
MAINTENANCE	(0.063)	(0.056)	(0.100)
1.1.3 INFORMATION MANAGEMENT & CONTROL (PARTIAL)	(0.050)	(0.057)	(0.033)**
DATA PROCESSING	0.021	0.025	0.014
INSTRUMENTATION	0.029	0.032	0.019
1.1.4 ATTITUDE CONTROL (PARTIAL)	(0.116)	(0.116)	(0.103)
TOTAL	8.272	8.759	4.403

*AUXILIARY POWER ONLY
**TWO-THIRDS MASS OF REFERENCE CONCEPT

	KLYSTRON CONCEPT	DUAL END-MOUNTED	DUAL SANDWICH
1.1.2 POWER TRANSMISSION (ANTENNA)			
STRUCTURE	(0.828)	(1.409)	(0.649)
PRIMARY	0.023	0.094	0.143
SECONDARY	0.815	1.315	0.506
MECHANISM	(0.002)	(0.004)	(NONE)
SUBARRAY	(7.050)	(10.561)	(7.053)
POWER DISTRIBUTION & CONTROL	(2.453)	(4.405)	(INCLUDED)
POWER CONDITIONING & BATT.	1.680	2.164	NONE
POWER DISTRIBUTION	0.773	2.241	INCLUDED
THERMAL	(0.720)	(NONE)	(NONE)
ANTENNA CONTROL ELECTRONICS	(0.170)	(0.340)	(0.340)
MAINTENANCE	(0.107)	(0.448)	(0.408)
1.1.3 INFORMATION MANAGEMENT & CONTROL (PARTIAL)	(0.640)	(1.622)	(0.256)*
DATA PROCESSING	0.380	1.385	0.152
INSTRUMENTATION	0.260	0.237	0.104
1.1.4 ATTITUDE CONTROL (PARTIAL)	(NEGL.)	(NEGL.)	(NEGL.)
TOTAL	11.970	18.789	8.706

*20% REF. MASS PER ANTENNA

	KLYSTRON CONCEPT	DUAL END-MOUNTED	DUAL SANDWICH
1.1.6 INTERFACE			
STRUCTURE	(0.170)	(0.236)	(N/A)
PRIMARY	0.136	0.168	
SECONDARY	0.034	0.068	
MECHANISMS	(0.033)	(0.072)	(N/A)
POWER DISTRIBUTION & CONTROL	(0.288)	(0.538)	(N/A)
POWER DISTRIBUTION	0.271	0.487	
SLIP RING BRUSHES	0.017	0.051	
THERMAL	(NONE)	(NONE)	(N/A)
MAINTENANCE	(0.032)	(0.064)	(—)
COMMUNICATION	(TBD)	(TBD)	(TBD)
TOTAL	0.523	0.910	—
SPS TOTAL (DRY)	20.765	28.458	13.109
GROWTH (25%)	5.191	7.114	3.277
TOTAL SPS (DRY) WITH GROWTH	25.956	35.572	16.386
SATELLITE PWR @ UTILITY I/F (GW)	5.07	5.22	3.06
SATELLITE DENSITY KG/KW$_{UI}$	5.12	6.81	5.35

Table 1.3-6. Satellite System Summary
(Exhibit D) Alternate Concepts

	GaAs SOLAR CELL			GaAlAs/GaAs SOLAR CELL		
	REFERENCE	DUAL END-MOUNTED	DUAL SANDWICH	REFERENCE	DUAL END-MOUNTED	DUAL SANDWICH
SATELLITE						
TYPE	PLANAR	PLANAR	COMPOUND	PLANAR	PLANAR	COMPOUND
CR_E	1.83	1.83	5.2	1.83	1.83	5.2
DIMENSION (METERS)	42×16,000	42×18,000	6600×28,500	4200×11,000	4200×12,000	TBD
MASS (×10^6 KG)	31.63	39.97	20.53	25.96	35.57	16.39
SOLAR ARRAY/ANTENNA	DECOUPLED	DECOUPLED	SANDWICH	DECOUPLED	DECOUPLED	SANDWICH
NUMBER OF BAYS	30	36	—	30	36	—
SOLAR ARRAY						
NUMBER OF PANELS	60	72	—	58	70	—
PANEL DIMENSION (METERS)	650W×730L	650W×690L	1.83D (×2)	650W×490L	650W×465L	1.63D (×2)
AREA (×10^6 M^2)	28.47	32.29	5.26	18.47	21.16	4.17
GEN. POWER (GW)	9.94	11.46	4.82	9.94	11.46	6.11
ANTENNA						
TYPE	KLYSTRON	SOLID STATE	SOLID STATE	KLYSTRON	SOLID STATE	SOLID STATE
POWER OUTPUT (GW)	7.14	7.36	3.66	7.14	7.36	4.64
ILLUMINATION	10 dB GAUS.	10 dB GAUS.	UNIFORM	10 dB GAUS.	10 dB GAUS.	UNIFORM
APERTURE (KM)	~1.0	1.35	1.83 (×2)	~1.0	1.35	1.63 (×2)
UTILITY INTERFACE POWER (GW)	5.07	5.22	2.42	5.07	5.22	3.06
NUMBER OF SATELLITES ($P_T \geq 300$ GW)	60	58	125	60	58	98
MASS DENSITY (KG/KW_{UI})	6.24	7.66	8.48	5.12	6.81	5.35

1.4 MAGNETRON SYSTEM CONCEPT

The magnetron system as defined by Rockwell International consists of a solar collection array similar in concept to the reference concept, but with the antenna design based upon the use of a magnetron cavity resonator rather than the klystron as a power amplifier. In general appearance, the satellite is similar to the configuration depicted in Section 2.3.1.

The basic system generates and transmits microwave power at a level sufficient to provide 5.6 GW at the utility interface. The overal dimensions for the magnetron based satellite are: (1) length, 15.0 km; (2) width, 4.2 km; and (3) depth, 0.564 km. The mass is estimated to be 26.7×10^6 kg and includes a 25% growth factor. The configuration utilizing the MBG solar cell is 10 km in length and contains a mass of 21.5×10^6 kg. The other dimensions are the same as for the standard cell concept.

Figure 1.4-1 presents the efficiency of the SPS system utilizing the magnetron power amplifier. Overall efficiency of the standard cell configuration is shown to be approximately 7.9%.

A detailed satellite mass property summary for the magnetron based system is shown in Table 1.4-1.

The magnetron satellite concept is comprised of seven major subsystems (same as for the reference klystron). Power generation, distribution, and transmission remain the dominant mission function, while the need for thermal control is virtually eliminated. Coordination of satellite functions and operations remains the province of the information and control subsystem (IMCS).

Row 1:

ARRAY ORIENT.	REFLECTOR DEGRAD.	CELL EFFICIENCY	PACK. FACTOR	ARRAY DESIGN	UV DEGRAD.	SWITCH GEAR	POWER BUSES & FEEDERS	SWITCH GEAR	TIE BARS	SLIP RING/ BRUSH
0.968	CRE = 1.83 0.915	0.1816 AT 113°C / 0.2756 AT 113°C MBG	0.95	0.94	0.96	0.997	0.952	0.999	0.988	0.999

9.8 GW 9.21 GW

21.85 KV

POWER SOURCE (0.1375) — POWER DISTRIBUTION (0.9387)

Row 2:

8.0 GW   8.08 GW   8.98 GW

BEAM EFF & ATMOS	ANTENNA	MAGNETRON & DRIVER	SWITCH GEAR	SWITCH GEAR	SWITCH GEAR	FEEDERS	SWITCH GEAR	RISERS	SWITCH GEAR
0.850 *	0.99	0.9	0.999	0.999	0.999	0.99	0.999	0.99	0.999

20 KV   20.06 KV   20.28 KV

MICROWAVE ANTENNA & POWER DISTRIBUTION (0.7386)

Row 3:

6.15 GW   5.35 GW   5.6 GW

RECTENNA	MOTOR SWITCH	SWITCH GEAR	(BUS)	SWITCH GEAR	DC-AC CONV. STATION	SWITCH GEAR	POWER DISTR	SWITCH GEAR
0.88	0.999	0.999	0.99	0.999	0.96	0.999	0.99	0.999

40 KV

POWER COLLECTION (0.8695) — GRID INTERFACE (0.9476)

*BEAM EFF   − 0.937
PHASE ERROR − 0.945
OUTAGE   − 0.98
ATMOSPHERE   − 0.98
PRODUCT   = 0.850

η_T = POWER SOURCE X POWER DIST. X MW ANT X POWER COLLECTION X GRID INTERFACE

13.75%   93.87%   73.86%   86.95%   94.76%

= 7.85%

Figure 1.4-1. System Efficiency Chain—Magnetron Concept
((June 1980)

Table 1.4-1. Mass Properties—Magnetron Antenna
(April 1980)

	STD CELL GaAs	MBG CELL GaAlAs/GaAs
	**	**
1.1.1 ENERGY CONVERSION (SOLAR ARRAY)		
STRUCTURE	1.601	1.245
PRIMARY	(0.904)	(0.565)
SECONDARY	(0.697)	(0.680)
MECHANISMS	0.070	0.070
CONCENTRATOR	0.988	0.663
SOLAR PANEL	6.880	4.619
POWER DISTRIBUTION & CONTROL	4.146	2.874
POWER COND. EQUIP. & BATT.	(0.319)	(0.319)
POWER DISTRIBUTION	(3.827)	(2.555)
THERMAL	NONE	NONE
MAINTENANCE -	0.092	0.092
1.1.3* INFORMATION MANAGEMENT & CONTROL	0.050	0.050
DATA PROCESSING	(0.021)	(0.021)
INSTRUMENTATION	(0.029)	(0.029)
1.1.4* ATTITUDE CONTROL	0.116	0.116
SUBTOTAL	13.943	9.729
1.1.2 POWER TRANSMISSION (ANTENNA)		
STRUCTURE	0.547	0.547
PRIMARY	(0.023)	(0.023)
SECONDARY	(0.524)	(0.524)
MECHANISM	0.002	0.002
SUBARRAY	3.320	3.320
POWER DISTRIBUTION & CONTROL	1.515	1.515
POWER CONDITIONING & BATT.	(0.346)	(0.346)
POWER DISTRIBUTION	(1.169)	(1.169)
THERMAL	NONE	NONE
ANTENNA CONTROL ELECTRONICS	0.170	0.170
MAINTENANCE	0.107	0.107
1.1.3* INFORMATION MANAGEMENT AND CONTROL	0.320	0.320
DATA PROCESSING	(0.190)	(0.190)
INSTRUMENTATION	(0.130)	(0.130)
1.1.4* ATTITUDE CONTROL	NEGLIG.	NEGLIG.
SUBTOTAL	5.981	5.981
1.1.6 INTERFACE		
STRUCTURE	0.257	0.257
PRIMARY	(0.136)	(0.136)
SECONDARY	(0.121)	(0.121)
MECHANISMS	0.033	0.033
POWER DISTRIBUTION & CONTROL	1.194	1.194
POWER DISTRIBUTION	(1.177)	(1.177)
SLIP RING BRUSHES	(0.017)	(0.017)
THERMAL	NONE	NONE
MAINTENANCE	0.032	0.032
COMMUNICATION	TBD	TBD
SUBTOTAL	1.516	1.516
SPS TOTAL (DRY)	21.44	17.226
GROWTH (25%)	5.36	4.307
TOTAL SPS (DRY) WITH GROWTH	26.8	21.533
SAT. PWR @ UTILITY INTERFACE (GW)	5.6	5.6
SATELLITE DENSITY, KG/KW$_{UI}$	4.79	3.85

*PARTIAL   **10^6 kg

The solar array supplies 9.8 GW at 21.85 kV over 30 independent (two panels in parallel) main feeders (Figure 1.4-2).

The microwave power transmission subsystem consists of a microwave phase reference generator, an RF distribution network, and approximately 2.35×10^6 magnetrons used as power amplifiers to drive a resonant cavity radiator antenna. The layout of a typical segment of the antenna is shown in Figure 1.4-3. A summary of the satellite reference design is presented in Table 1.4-2.
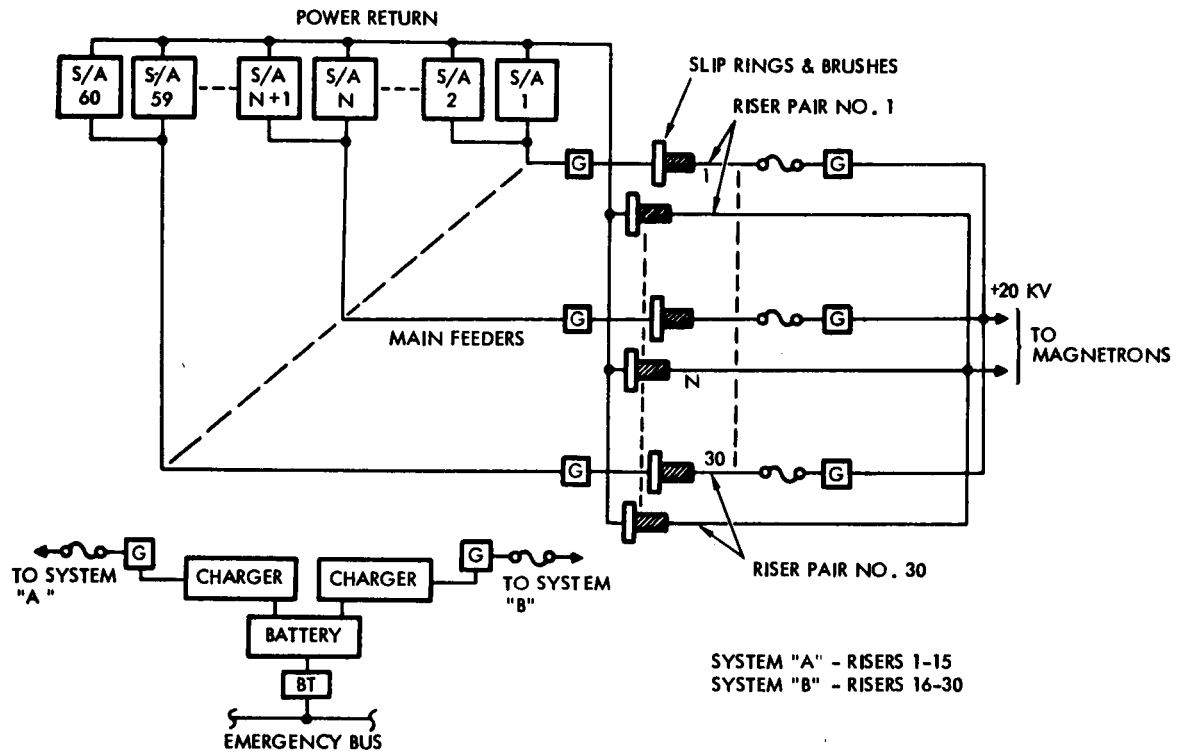
Figure 1.4-2. Magnetron Satellite Power Distribution
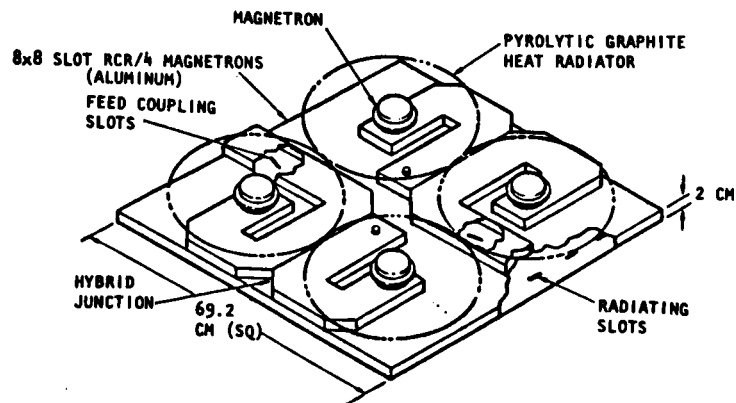
Figure 1.4-3. Typical Segment of Antenna

Table 1.4-2. Magnetron Satellite Design Summary

Basic

Frequency	2.45 GHz
Power density at rectenna	23 mW/cm^2 (center) 1 mW/cm^2 (edge)
Location	GEO
Transmission technique	Microwave
Power generation	Photovoltaic GaAs or GaAlAs/GaAs CR_E = 1.83

System	GaAs	GaAlAs/GaAs
Power at utility interface	5.6 GW	5.6 GW
Solar array configuration	Planar	Planar
Number of troughs	3	3
Antenna location	End	End
Planform Area	4200 m (W) × 15,000 m (L) (63 km^2)	4200 m (W)×10,000 m (L) (42 km^2)
Solar panel area	27.3 km^2	18.3 km^2
Reflector area	54.6 km^2	56.6 km^2
Microwave antenna type	Magnetron tube	Magnetron tube
Number of tubes	2.3×10^6	2.3×10^6
Transmitted power	8 GW	8 GW
Overall efficiency	7.9%	11.9%
Overall satellite mass (with 25% growth)	26.8×10^6 kg	21.5×10^6 kg

2.0 PREFERRED CONCEPTS

Configuration analyses gave sufficient insight to recommend selection of solid-state concepts for further point design definition. This section describes these recommendations and provides concept definitions for comparison with the NASA/DOE reference concepts.

2.1 RECOMMENDED CONCEPT ALTERNATIVES

The Rockwell configuration (reference concept), as of October 1979, recommended for a coplanar satellite with an end-mounted antenna is shown in Figure 2.1-1. The satellite has three troughs, each with ten bays, and is 4200 m wide at the longeron points and 16,000 m long (plus antenna); 26 solar blanket strips, measuring 25 m by 730 m, are installed in each bay along the bottom of the trough. The reflectors are attached to the inner diagonal sides of the troughs as indicated. The space frame end-mounted antenna with slip rings, support

$\eta(T) = 18.16\% \ (T = 113°C)$
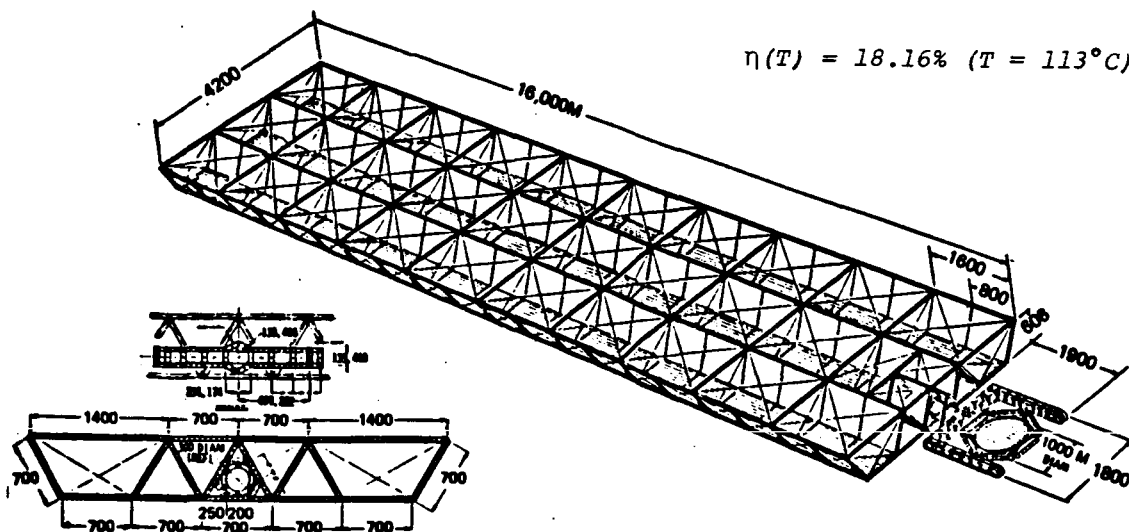
Figure 2.1-1. GaAs SPS Reference Configuration

structure, and trunnion arms extend 1900 m from the basic satellite. The general arrangement of the solid-state sandwich concept recommended for point design is shown in Figure 2.1-2. This concept has a single primary reflector and multiple secondary reflectors and formed the initial baseline. The recommended reference solid-state end-mounted concept is shown in Figure 2.1-3. An antenna power taper ratio of 10 dB was selected because there is little cost difference between 0 dB and 10 dB, and 10 dB results in lower side lobes. Because of the relatively low power level per antenna, two antennas (located on each end of the solar array) were recommended. The point designs are accomplished for concepts with a GaAs single-junction cell solar array.

2-1

$CR_E = 6$

10 Mirror
Primary
System

Rotary
Joint

Solid-State Panel
MW Antenna

Flat Secondary
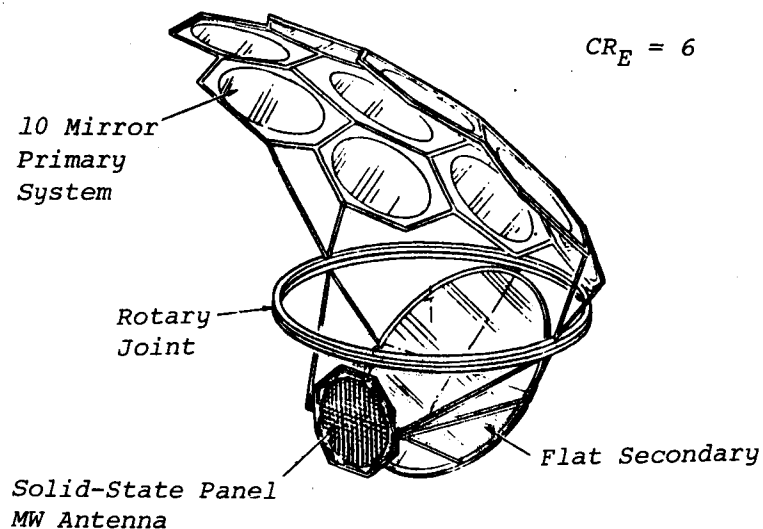
Figure 2.1-2. Concept Selected by Preliminary Studies

CR = 2

2500 M

4200 M

19200 M

1600 M

800

AVG DIAM 1500 M

4200 M

1400 M

650

700 M

700 M

1000 M
DIAM

2160 M

1600 M

2500 M
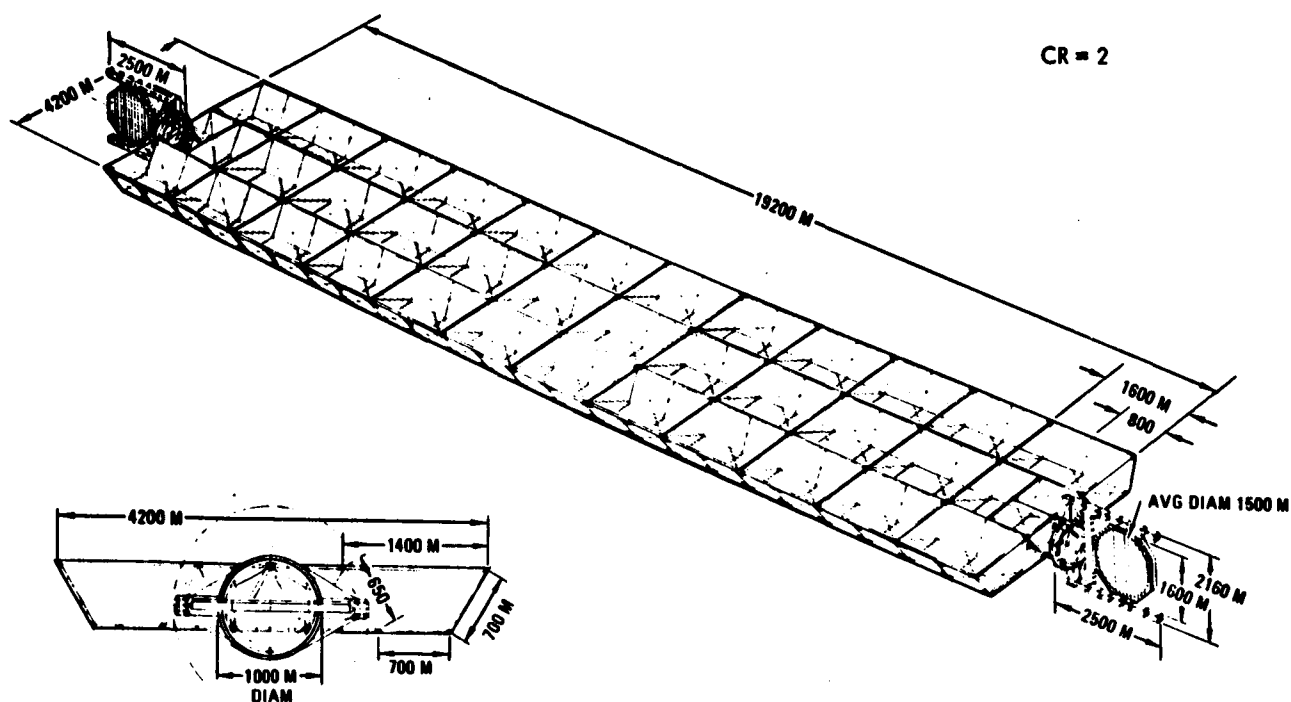
Figure 2.1-3. Reference Solid-State Concept
Recommended for Point Design

2.2 BASIC CONTROLLING CHARACTERISTICS

The GaAs reference concept characteristics are compared in Table 2.2-1 as of March 1979 (end of Exhibit C study) with updated characteristics at the time of concept recommendations (October 1979). The major change is in the power level delivered at the utility interface (5.07 GW compared to 4.61 GW). This change is due primarily to the redistribution of klystrons in the antenna layout to achieve the required 10-dB taper within the 23 mW/cm^2 ionospheric limitation at the center of the beam. This redistribution resulted in an increase in power requirement from the solar array which leads to a change in overall solar array dimensions (4.2 km × 16.0 km, compared to 3.9 km × 16.0 km).

Table 2.2-1. Updated Reference Concept Satellite Characteristics

	March 1979	October 1980
Power at utility interface (GW)	4.61	5.07
Overall solar array planform dimensions (km)	3.9×16.0	4.2×16.0
Satellite mass (×10^6 kg)	33.0	34.1
Structural material	Composites	Composites
Construction location	GEO	GEO
Number of antennas	1	1
DC-RF converter	Klystron	Klystron
Antenna aperture (km)	1.0	1.0
Frequency (GHz)	2.45	2.45
Rectenna dimensions (km)	10×13	10×13
Rectenna power density (mW/cm^2)		
• Center	23	23
• Edge	1	1

The characteristics shown in Table 2.2-2 describe the initial characteristics of the sandwich concept. Because of the more advanced state of technology, the single-junction GaAs array was recommended for the sandwich point

Table 2.2-2. Preliminary Concept Characteristics—Sandwich

Solar array type	GaAs
Effective CR	6
Solar array temperature (°C)	200
Amplifier base temperature (°C)	125
Amplifier efficiency	0.8
Antenna taper ratio (dB)	0
Antenna diameter (km)	1.77
Power at utility interface (GW)	1.26
Rectenna boresight diameter (km)	6.10

design. Data from this study can be used to further define a GaAs multijunction array concept. Table 2.2-3 lists the characteristics of the recommended end-mounted solid-state concept.

Table 2.2-3. Recommended Reference End-Mounted
Solid-State Concept Characteristics

- GaAs solar array
- Geometric CR = 2.0
- Dual end-mounted microwave antennas
- Amplifier base temperature, 125°C
- Amplifier efficiency, 0.8
- Antenna power taper, 10 dB
- Antenna diameter, 1.35 km
- Power at utility interface, 2.61 GW per antenna (5.22 GW total)
- Rectenna boresight diameter, 7.51 km per rectenna

2.3 CURRENT OVERALL SYSTEM DESCRIPTION

The concepts recommended and described in the previous section formed the basis for a series of point design definition studies conducted during the later part of the contract. This effort is described in this section.

2.3.1 REFERENCE CONCEPT

The reference concept was re-examined to provide an updated concept incorporating changes to the design where improvements (either technical or cost savings) could be accomplished. The updated reference (klystron) concept is described below.

System Description

The basic features of the Rockwell reference satellite is the use of gallium arsenide solar cells at a concentration ratio of 2 (CR = 2) (nominal) to convert solar energy into its electrical equivalent, and 50-kW (nominal) klystron power amplifiers as the means of developing the high-power microwave beam necessary to the efficient transfer of energy from GEO.

The satellite may be considered to be made up of a solar pointing section (associated with the conversion of solar energy to electrical energy) and an earth pointing section (concerned with the conversion of electrical energy into its RF equivalent and the transmission of the RF to the associated ground receiver).

The reference (GaAs) photovoltaic concept was shown in Figure 2.1-1 (Section 2.1); it has been designed to supply 5 GW (nominal) of electrical power to the utility grid on the ground. The SPS is a three-trough configuration having reflective membranes at a 60° slant angle. It has a single microwave antenna, located at the end of the configuration. The overall dimensions of the SPS troughs using standard GaAs solar cells are approximately: (1) length, 16.0 km; (2) width, 4.2 km; and (3) depth 0.606 km. The mass is estimated to be 31.6×10^6 kg, and includes a 25% growth factor. The length and mass of the MBG solar cell version are 11.0 km and 26.0×10^6 kg, respectively.

In geosynchronous orbit, the longitudinal axis of the SPS is oriented perpendicular to the orbit plane. The reference design is based on construction in GEO.

Figure 2.3-1 presents the basic efficiency of the overall reference SPS concept and indicates the relative efficiencies of each of the major subelements of the system. Overall efficiency of the reference system is shown to be approximately 7.00 percent.
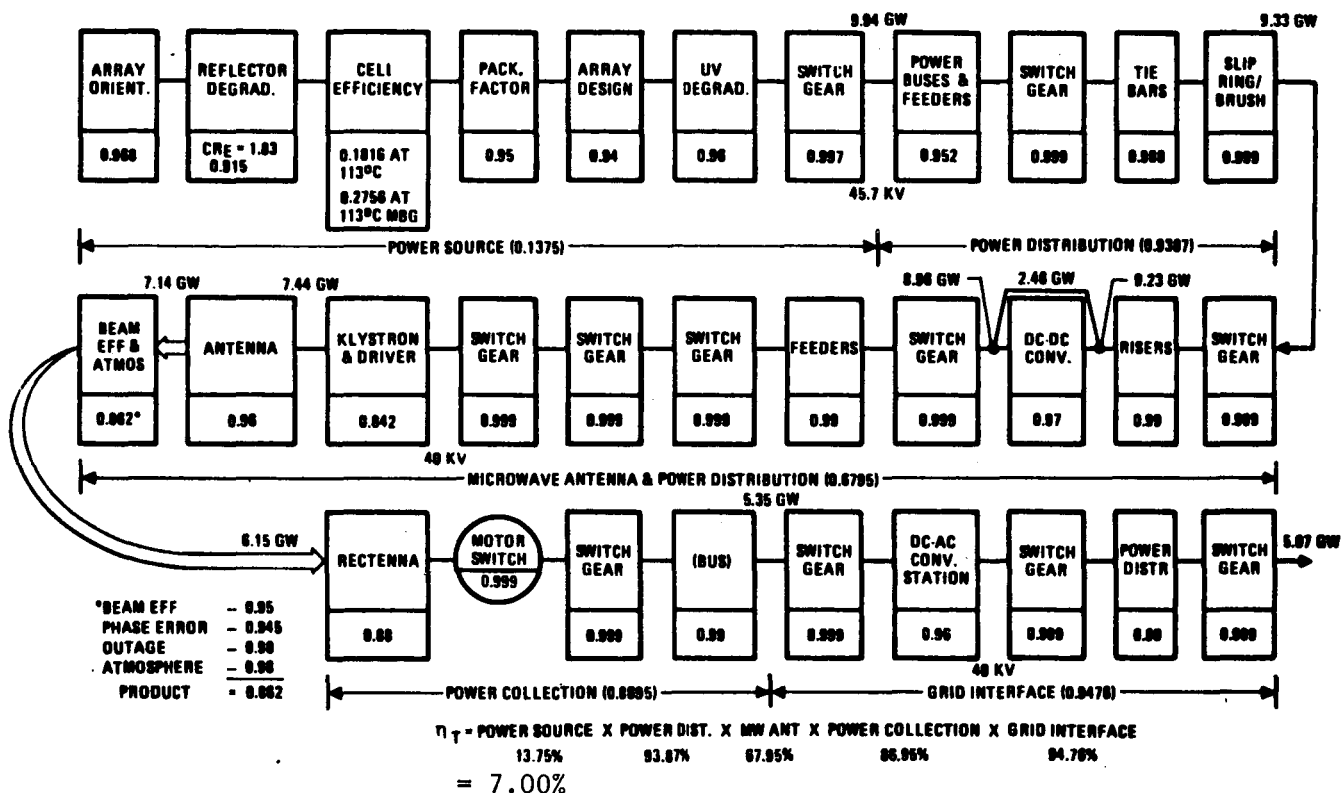
Figure 2.3-1. System Efficiency Chain—Reference Concept
(October 1980)

A detailed satellite mass property summary for the reference configuration using both standard and MBG solar cells is presented in Table 2.3-1.

Reference Satellite Subsystems

The reference satellite is comprised of seven major subsystems, as shown in Figure 2.3-2. Attitude control directly affects power generation efficiency and includes satellite-rectenna pointing. Power generation, distribution, and transmission are dominant functions, while thermal control is essential to dissipation of the large amounts of waste heat. Coordination of satellite functions and operations is performed by the information management and control subsystem (IMCS) as illustrated in Figure 2.3-3.

Table 2.3-1. Mass Properties Summary,
Exhibit D—April 1980 ($\times 10^{-6}$ kg)

		STANDARD CELL GaAs	MBG CELL GaAlAs/GaAs
1.1.1	ENERGY CONVERSION (SOLAR ARRAY)		
	STRUCTURE	1.514	1.133
	PRIMARY	(0.928)	(0.804)
	SECONDARY	(0.586)	(0.329)
	MECHANISMS	0.070	0.070
	CONCENTRATOR	1.030	0.648
	SOLAR PANEL	7.174	4.804
	POWER DISTRIBUTION & CONTROL	2.757	1.388
	PWR COND. EQUIP. & BATT.	(0.319)	(0.206)
	POWER DISTRIBUTION	(2.438)	(1.182)
	THERMAL	NONE	NONE
	MAINTENANCE	0.092	0.063
1.1.3 (PARTIAL)	INFORMATION MANAGEMENT & CONTROL	0.050	0.050
	DATA PROCESSING	(0.021)	(0.021)
	INSTRUMENTATION	(0.029)	(0.029)
1.1.4 (PARTIAL)	ATTITUDE CONTROL	0.116	0.116
	SUBTOTAL	**12.803**	**8.272**
1.1.2	POWER TRANSMISSION (ANTENNA)		
	STRUCTURE	0.838	0.838
	PRIMARY	(0.023)	(0.023)
	SECONDARY	(0.815)	(0.815)
	MECHANISM	0.002	0.002
	SUBARRAY	7.050	7.050
	POWER DISTRIBUTION & CONTROL	2.453	2.453
	POWER COND. & BATT.	(1.680)	(1.680)
	POWER DISTRIBUTION	(0.773)	(0.773)
	THERMAL	0.720	0.720
	ANTENNA CONTROL ELECTRONICS	0.170	0.170
	MAINTENANCE	0.107	0.107
1.1.3 (PARTIAL)	INFORMATION MANAGEMENT & CONTROL	0.640	0.640
	DATA PROCESSING	(0.380)	(0.380)
	INSTRUMENTATION	(0.260)	(0.260)
1.1.4 (PARTIAL)	ATTITUDE CONTROL	NEGLIGIBLE	NEGLIGIBLE
	SUBTOTAL	**11.980**	**11.980**
1.1.6	INTERFACE		
	STRUCTURE	0.170	0.170
	PRIMARY	(0.136)	(0.136)
	SECONDARY	(0.034)	(0.034)
	MECHANISMS	0.033	0.033
	POWER DISTRIBUTION & CONTROL	0.288	0.288
	POWER DISTRIBUTION	(0.271)	(0.271)
	SLIP RING BRUSHES	(0.017)	(0.017)
	THERMAL	NONE	NONE
	MAINTENANCE	0.032	0.032
	COMMUNICATION	TBD	TBD
	SUBTOTAL	**0.523**	**0.523**
	SPS TOTAL (DRY)	**25.306**	**20.775**
	GROWTH (25%)	**6.326**	**5.194**
	TOTAL SPS (DRY) WITH GROWTH	**31.632**	**25.969**
	SATELLITE POWER @ UTILITY INTERFACE (GW)	5.07	5.07
	SATELLITE DENSITY, KG/KW$_{UI}$	6.24	5.12
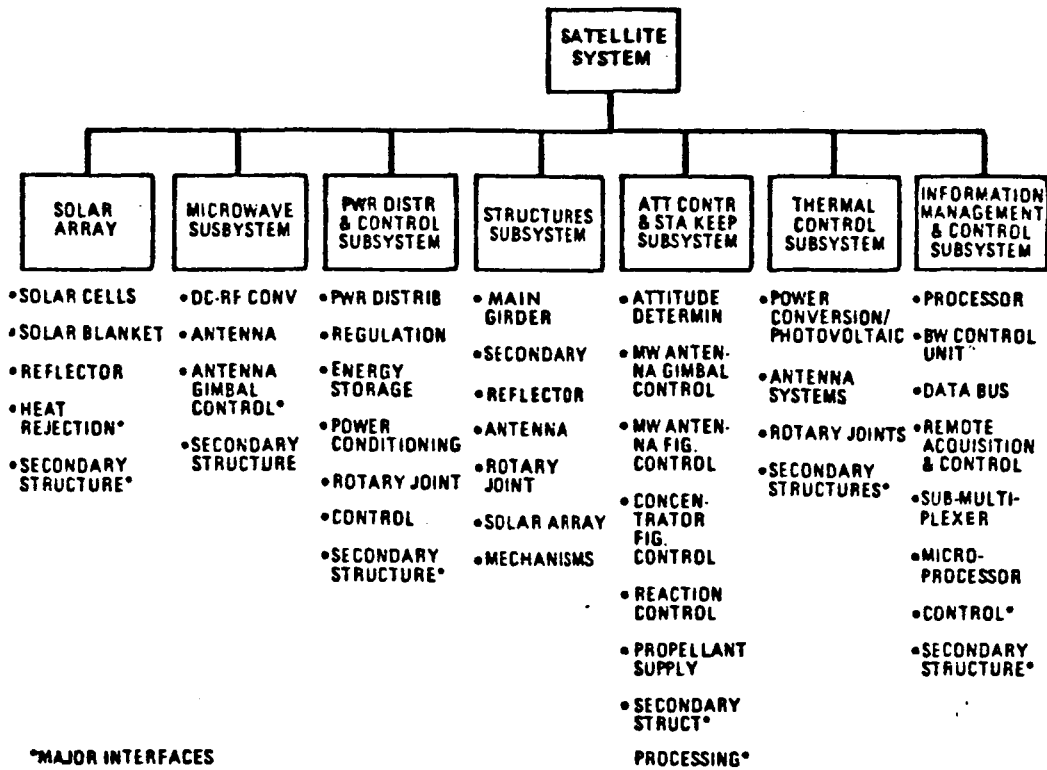
Figure 2.3-2.   Satellite Subsystems
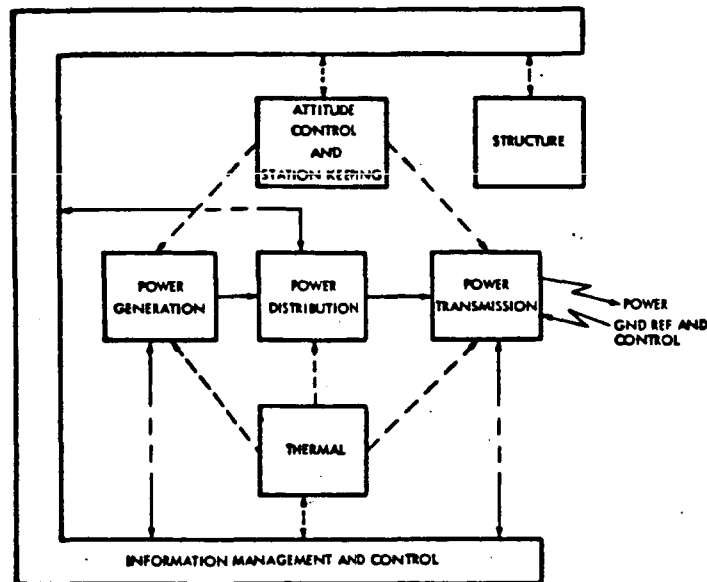
Figure 2.3-3.   Subsystem IMCS Relationships

All subsystems support the mission functions of power generation, distri-
bution, and transmission. Electrical power output from the solar panels is
fed via switch gears into feeder buses and then into main distribution buses
to the antenna (Figures 2.3-4 and 2.3-5). Power is also distributed from batter-
ies so that critical functions, such as information management and control (IMCS),
can be provided through solar eclipses.
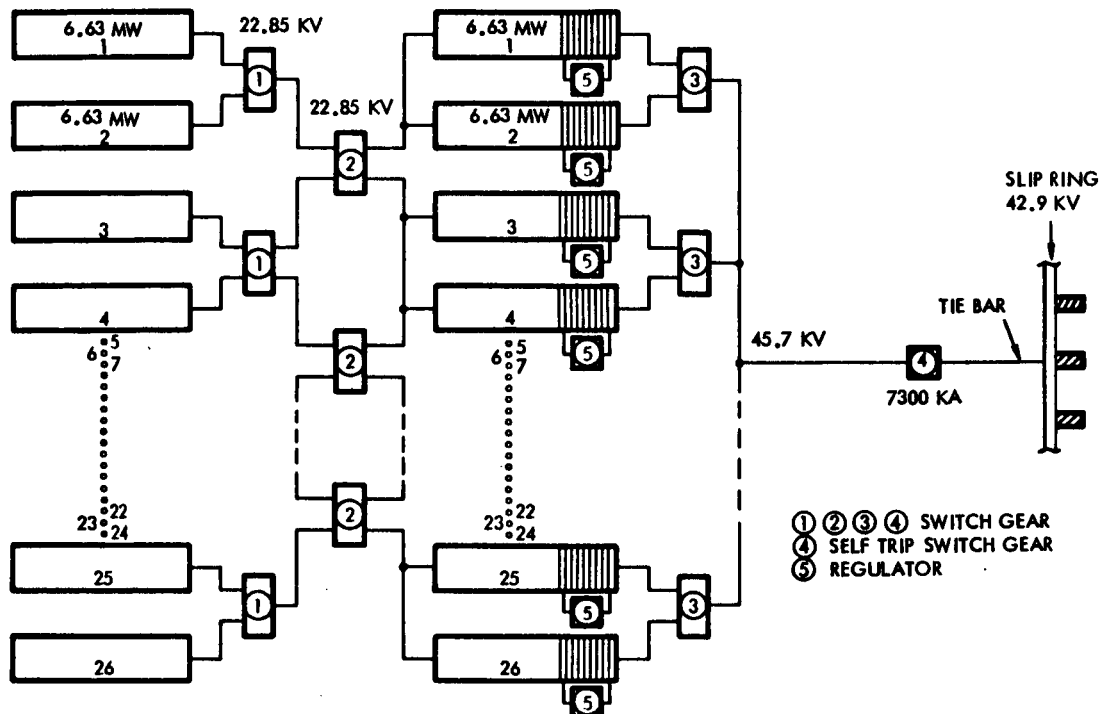
Figure 2.3-4. Power Generation Subsystem

The microwave power transmission subsystem (MPTS), Figure 2.3-6, consists
of a reference system and high-power amplifier devices which feed an array
antenna. Phasing control is maintained by use of a pilot beam originating at
the rectenna and received at the satellite antenna.

A reasonable way to view the satellite system is to consider the entire
satellite as being made up of two major on-orbit assemblies with a connecting
interface assembly operating in concert at GEO. These on-orbit assemblies are
the sun pointing solar arrays and the earth pointing power antenna.

The solar array consists of the GaAs solar cells and the supporting sub-
systems required to operate the satellite in a sun-oriented mode. Included in
this sub-element are information management and control subsystem assemblies
required to monitor and control the power generation devices; and the power
distribution network, as well as all remaining subsystem functions. The solar
panels are grouped in 60 independent panels. The power supplied totals 9.94 GW
at 45.7 kV over 30 independent (two panels in series) main feeders (Figure 2.3-5).

The antenna consists of the antenna primary and secondary structures, the
microwave conversion and transmission assemblies, and the elements of the various
supporting subsystems required to operate the microwave transmission system.

2-8

POWER RETURN

SLIP RING & BRUSHES

S/A 30 — S/A 20 — S/A 19 — — S/A 2 — S/A 1

G

(+)

(−)

RISER PAIR NO. 1

RP NO. 2

RP NO. 19

MAIN FEEDERS

RP NO. 20

S/A - SOLAR ARRAY
G   - SWITCH GEAR
BT - BATTERY TIE
      CONTACTOR

A SYSTEM RISER 1-15
B SYSTEM RISER 16-30

RP NO. 32

POWER MODULE

40 KV 32 KV 24 KV 16 KV 8 KV RTN

G

HV
DC-DC
CONV

TYPICAL 32 PATHS
16 ON EACH YOKE ARM

TO SYSTEM "A"   TO SYSTEM "B"

G   G

CHARGER   CHARGER

BATTERY

BT

EMERGENCY BUS
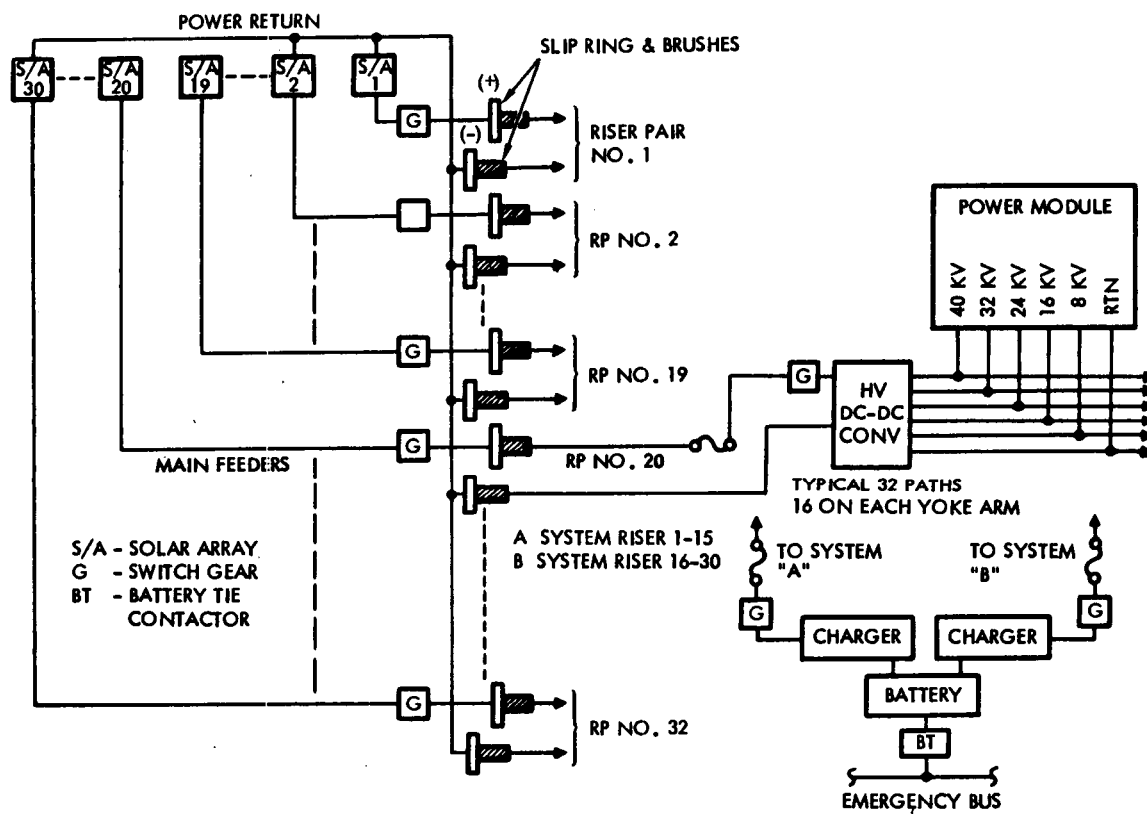
Figure 2.3-5. Power Distribution Subsystem

MECHANICAL POINTING REQUIREMENTS: ±0.05°
ELECTRONIC POINTING REQUIREMENTS: ±3 ARC SEC

COMMUNICATION
TO REST OF
SPS SYSTEM

CENTRAL
COMPUTER

REFERENCE
PHASE
GENERATOR

N-WAY
POWER
DIVIDER

DATA
BUS

REFERENCE
DISTRIBUTION
SERVO

RETRO
ELECTRONICS

MICROPROCESSOR
AND
MEMORY

PILOT
RECEIVER

SUBARRAY
POWER
MODULES

MODULE
CONTROL

SENSOR
INPUTS

PERFORMANCE
DATA

PILOT SIGNAL

RADIATION

MECHANICAL
CONTROL
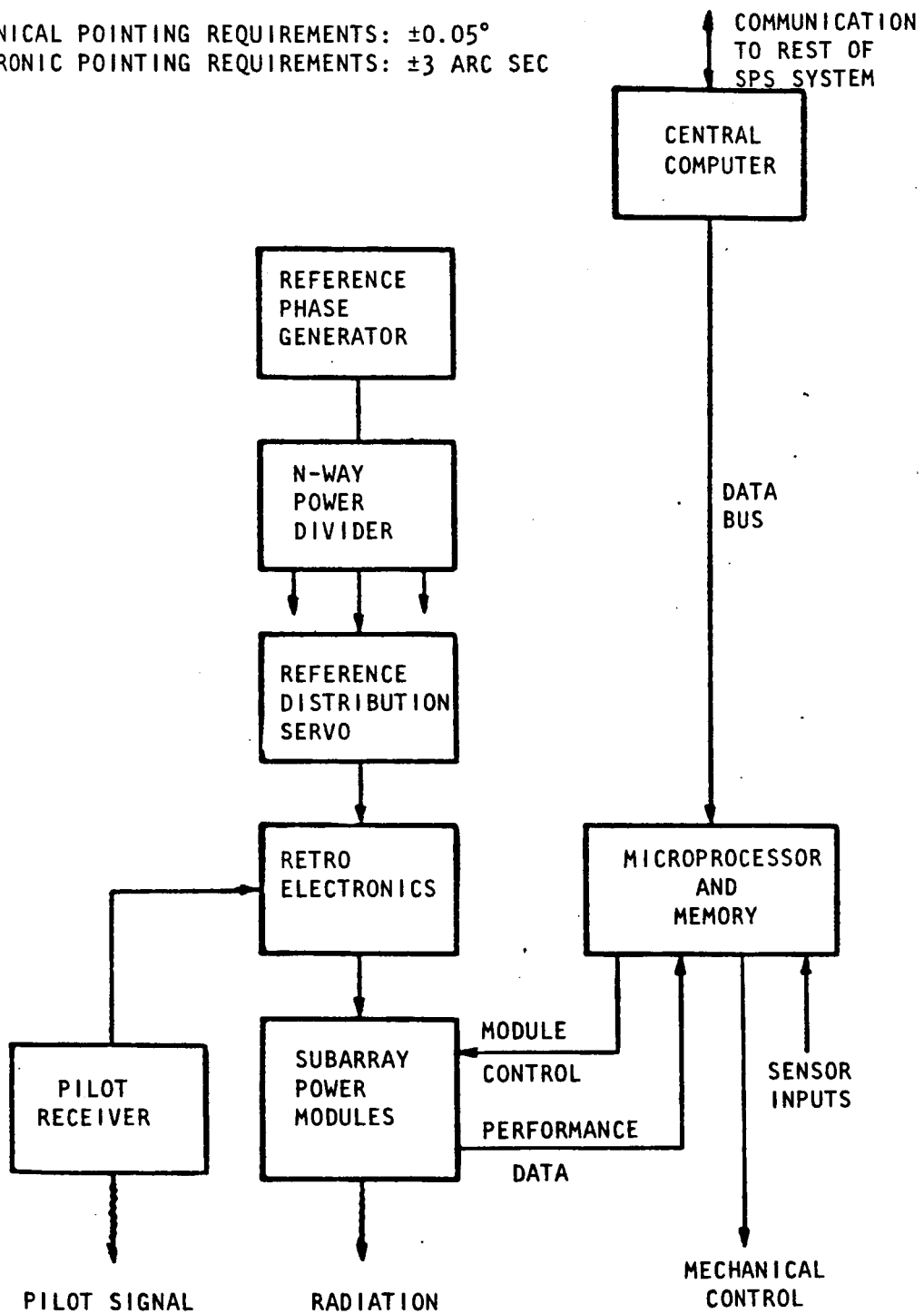
Figure 2.3-6. Microwave Transmission System

A summary of the satellite reference design is provided in Table 2.3-2.

Table 2.3-2.   Satellite Reference Design Summary

Basic

Frequency	2.45 GHz
Power density of rectenna	
Center	23 mW/cm^2
Edge	1 mW/cm^2
Location	GEO
Transmission technique	10 dB Gaussian/microwave
Power generation	Photovoltaic
	GaAs or GaAlAs/GaAs
	$CR_E = 1.83$

System	GaAs	GaAlAs/GaAs
Power at utility interface	5 GW	5 GW
Solar array configuration	Planar	Planar
Number of troughs	3	3
Antenna location	End	End
Planform	4200 m (W)×16,000 m (L)	4200 m (W)×11,000 m (L)
Area	(67.2 km^2)	(46.2 km^2)
Solar panel area	28.47×10^6 m^2	18.13×10^6 m^2
Reflector array area	56.94×10^6 m^2	36.26×10^6 m^2
MW dc-RF converter type	Klystron	Klystron
Number of tubes	142,902	142,902
Transmitted power	7.14 GW	7.14 GW
Overall efficiency	7.2%	16.0%
Overall satellite mass (with 25% growth)	31.6×10^6 kg	25.96×10^6 kg

More detailed subsystem descriptions can be found in Volume VII, System/ Subsystem Requirements Data Book.

2.3.2   SOLID-STATE CONCEPTS

As described in Sections 2.1 and 2.2, there were two basic solid-state concepts recommended for additional point design definition; these two concepts are detailed below.

Sandwich Solid-State Concept

The previously defined concept was studied in more detail to obtain a better definition of its characteristics and try to optimize the design. These studies included overall design, structural design, reflector design, attitude control requirements, phase control approach, and sandwich design. The design improvements resulting from the use of multi-bandgap solar arrays were also determined.

Point Design Concept

As a result of these more detailed studies, the satellite concept shown in Figure 2.3-7, having the characteristics listed in Table 2.3-3, was defined. Several improvements were made when compared to the initial concept previously shown in Figure 1.1-1.

1.8 KM
(APERTURE)

28.5 KM
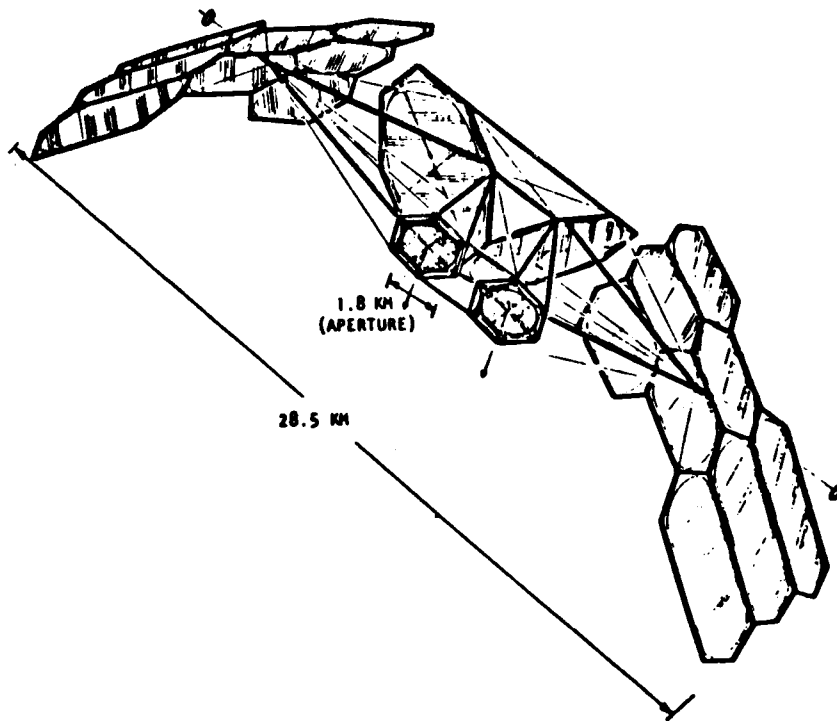
Figure 2.3-7. Solid-State Sandwich Satellite
Point Design Concept

Table 2.3-3. Solid-State Sandwich
Point Design Characteristics

• SOLAR ARRAY TYPE	GALLIUM ARSENIDE
• EFFECTIVE CONCENTRATION RATIO	5.2 (EOL)
• MAXIMUM SOLAR ARRAY TEMP. (°C)	200
• MAXIMUM POWER AMP. BASE TEMP. (°C)	125
• AMPLIFIER EFFICIENCY	0.792
• REFLECTOR EOL EFFICIENCY	0.83
• ANTENNA TAPER RATIO (dB)	0
• ANTENNA APERTURE (km)	1.83
• TRANSMITTED POWER DENSITY (W/m²)	696
• MAXIMUM POWER DENSITY AT RECTENNA (mW/cm²)	23
• RECTENNA BORESIGHT DIAMETER (km)	4.8
• RECEIVING SITE DIMENSIONS (km)	10 x 13 (34° N. LATITUDE)
• POWER AT UTILITY INTERFACE (GW)	2.42 (1.21 PER SITE)
• SATELLITE SPECIFIC MASS (kg/kW)	8.48

2-12

This concept is symmetrical, with two microwave antennas rather than one. This change was made for two reasons: (1) it reduced significantly the propellant required for combined attitude control and stationkeeping by reducing the solar pressure torques, and (2) it allowed twice as much power to be transmitted by a single satellite.

"Maypole" supports are used for the multiple secondary reflectors. The large ring was eliminated when it was determined that very small forces and moments needed to be reacted from the secondary reflectors.

Each of the antennas provide 1.21 GW of power at the utility interface on the ground. The rectennas are smaller than the 5-GW rectennas for the reference system (4.8 km diameter along the boresight). However, a site 10×13 km in dimensions is needed to reduce the intensity level to less than 0.1 mW/cm^2 (because of the use of a 0-dB taper on the antenna rather than the 10-dB taper used on the reference satellite antenna).

With an end-of-life reflector efficiency of 0.83, a concentration ratio of 5.2 can be obtained with this concept. Power loss versus pointing error for this concept is given in Table 2.3-4.

The total mass of the satellite is 20.5 million kilograms. Most of this mass is in the sandwich panels, but a substantial fraction is in the reflectors and the reflector support structure. The specific mass is 8.5 kg/kW compared to 6.2 for the reference concept. Cost estimates and comparisons are presented in Volume VI of this final report; construction of this satellite is described in Volume IV.

Table 2.3-4. Sandwich Satellite Point Design Mass Properties

OPTICS BEAM TRACE
OF REFLECTOR #6 OR #8

POINTING ERROR (DEGREE)	POWER LOSS (%)		
	$+0.1^0$	$+0.5^0$	$+1^0$
MIRROR #1 OR #3	1.1%	5.52%	11%
MIRROR #2	1.06%	5.34%	10.7%
MIRROR #4 OR #5	1.56%	7.8%	15.6%
MIRROR #7	1.54%	7.6%	15.4%
SECONDARY MIRROR	0.13	0.6%	1.3%
TOTAL (AVG.)	1.4%	7.1%	14.4%
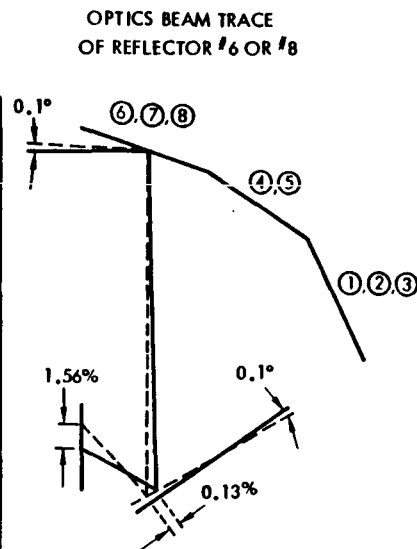
Structural Design

Because of the need for an unobstructed view on both the front and rear of the sandwich panels to receive concentrated solar energy and to transmit microwave energy, a compression-frame, tension-web type of structure is required. For this reason, a comprehensive structural analysis, reported separately in this volume (Section 3.3), was conducted to determine the feasibility and characteristics of this concept at large diameters. In order to avoid excessive antenna element angle variations relative to the boresight, it is necessary to restrict the maximum deflection of the antenna center to about 18 cm. This results in an antenna frame mass of only 95,000 kg. An analysis also determined that interactions of the structural frequencies and other control frequencies should not occur.

Reflector System Characteristics

A structural analysis of the reflectors was also conducted. An analysis similar to that conducted for the antenna was employed, since a compression frame structure also is used for the reflectors. The resulting reflector characteristics are as follows:
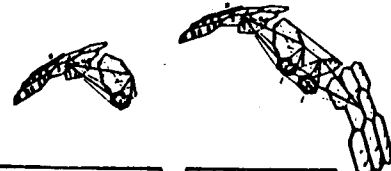
- 1/2-mil aluminized kapton reflective material

- Reflectivity: 0.87 BOL, and 0.83 EOL

- Primary reflector maximum deflection: 24 cm

- Secondary reflector maximum deflection: 24 cm

- Structural mass (composite)
  - Primary reflector 2.38×10^6 kg
  - Secondary reflector 0.85×10^6 kg

- Reflector mass
  - Primary reflector 1.21×10^6 kg
  - Secondary reflector 0.87×10^6 kg

Attitude Control and Stationkeeping Requirements

The sandwich concept is considerably different from the reference concept. For this reason, an analysis was conducted to determine the requirements for attitude control and stationkeeping; the results are summarized in Figure 2.3-8. Initially, a satellite with a single antenna was considered. Because of the large attitude control requirements (solar and gravity-gradient torques) caused by the asymmetric geometry, a dual antenna concept was studied. As a result, the 30-year propellant mass was reduced from 41% of satellite mass to 28%. The 28% propellant mass is considerably higher than a 7% requirement for the reference concept. The difference is caused by solar pressure on the very large area reflectors. A detailed description of this analysis is presented separately in this volume (refer to Section 3.5).

Overall Phase Control Concept

Figure 2.3-9 illustrates the overall phase control concept. A phase reference signal is generated by a transmitter located in the center of the two

DRY MASS (THOUSAND KG)	SINGLE SATELLITE	DUAL SATELLITE
• ATTITUDE DETERMINATION	0.2	0.2
• THRUSTERS & SUPPORT STRUCT	12.0	17.5
• TANKS, LINES, & REFRIG	20.2	25.5
TOTAL DRY MASS	32.4	43.2
30-YEAR PROPELLANT MASS (% S/C MASS)	41	28
POWER REQUIREMENT (MW)	45	59

Figure 2.3-8. Attitude Control and Stationkeeping Requirements
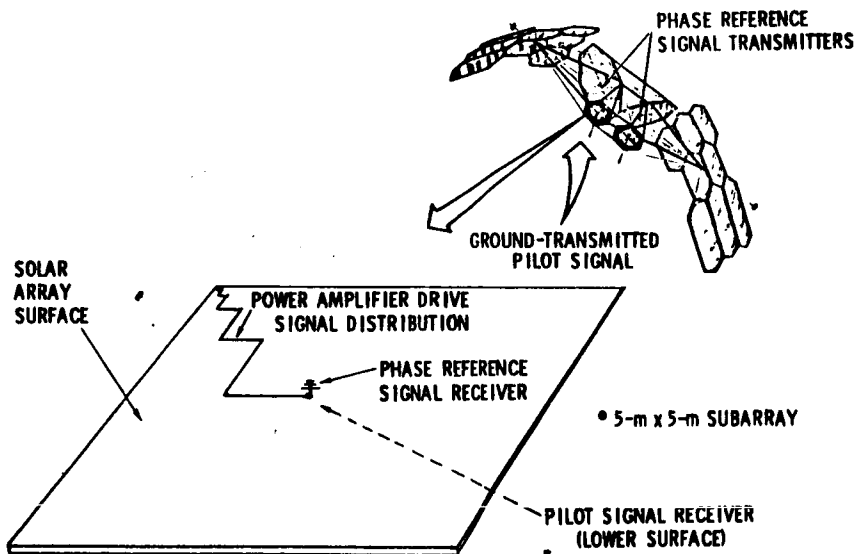
Figure 2.3-9. Phase Distribution Concept

secondary reflectors. This signal is received by an antenna located on the solar cell side of the sandwich for each 5-m×5-m subarray. The pilot signal transmitted from the ground is received by antennas on the transmitter side of the sandwich. These signals are processed to develop the phase control drive for the power amplifiers and the drive signal is distributed in a corp-orate stripline system which is an integral part of the sandwich panels. This concept is presented in greater detail separately in this volume (Section 3.6).

Sandwich Design

Figure 2.3-10 shows the building blocks that comprise the antenna solar array. A mechanical module which is space-assembled and placed into the tension web matrix is 30 m on a side. This mechanical module is made up from 5-m-on-a-side subarrays that are assembled on the ground and transported to orbit. Each subarray is completely independent and has no interfaces with other subarrays. The only interface with the subarray is via RF with the ground pilot transmitter and the on-board phase reference signal transmitter.

MECHANICAL MODULE
(SPACE ASSEMBLED)

SUBARRAY
(GROUND ASSEMBLED)
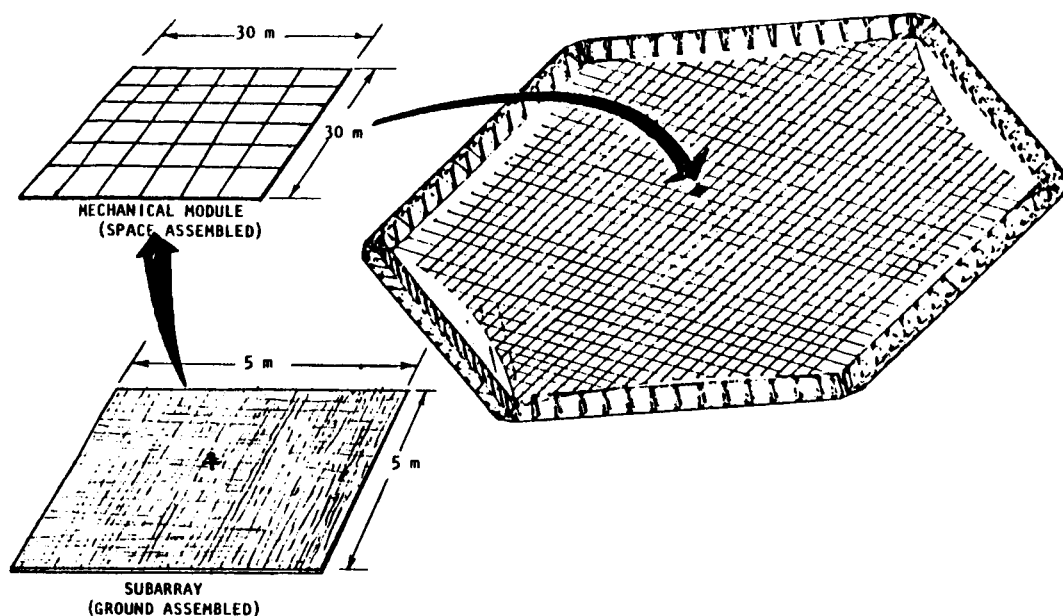
Figure 2.3-10. Antenna/Solar Array Buildup

The details of the solid-state sandwich modules are shown in Figure 2.3-11. The dipole antenna is fed by a power amplifier, located at the dipole center, and mounted to a beryllium-oxide disc heat sink/radiator. Power output for each power amplifier is 4.4 W. A silica fiber truss structure supports the antenna and provides sufficient capability for the launch environment. A honeycomb sandwich containing the RF drive distribution system is bonded to the antenna truss structure. The bottom of the honeycomb structure has a bonded aluminized kapton ground plane and the top has the bonded GaAs solar array. The dc power and RF drive signal are brought to the power amplifier through conductors in the silica fiber amplifier support post. Most of the solar array waste heat is radiated from the front of the array. Approximately one-fourth of the heat is transported through to the antenna side of the sandwich.

A detailed mass estimate for the sandwich module is presented in Table 2.3-5 in terms of kg/m^2. The honeycomb and truss structure contribute about one half of the mass. The amplifier modules are a very small portion of the mass. A detailed mass properties statement for this concept is presented in Table 2.3-6.

VIEW FROM SUN ──────→

GaAs SOLAR CELLS
(0.252 KG/M2)
[0.26 KG/M^2, MBG]
(5 M X 5 M = 4,096 DIPOLES)

DIPOLE
SOLID-STATE AMP
BERLOX RADIATOR
RISER STEM

7.61 CM   7.61 CM

MASS DENSITY
1.68 KG/M2 *

FIBERGLASS
TRUSS

*1.69 KG/M^2 FOR MBG
SOLAR CELLS

VIEW FROM EARTH

1.0 CM
HONEYCOMB
SANDWICH

SOLAR
CELLS

TOP OF AMPLIFIER
GROUND PLANE
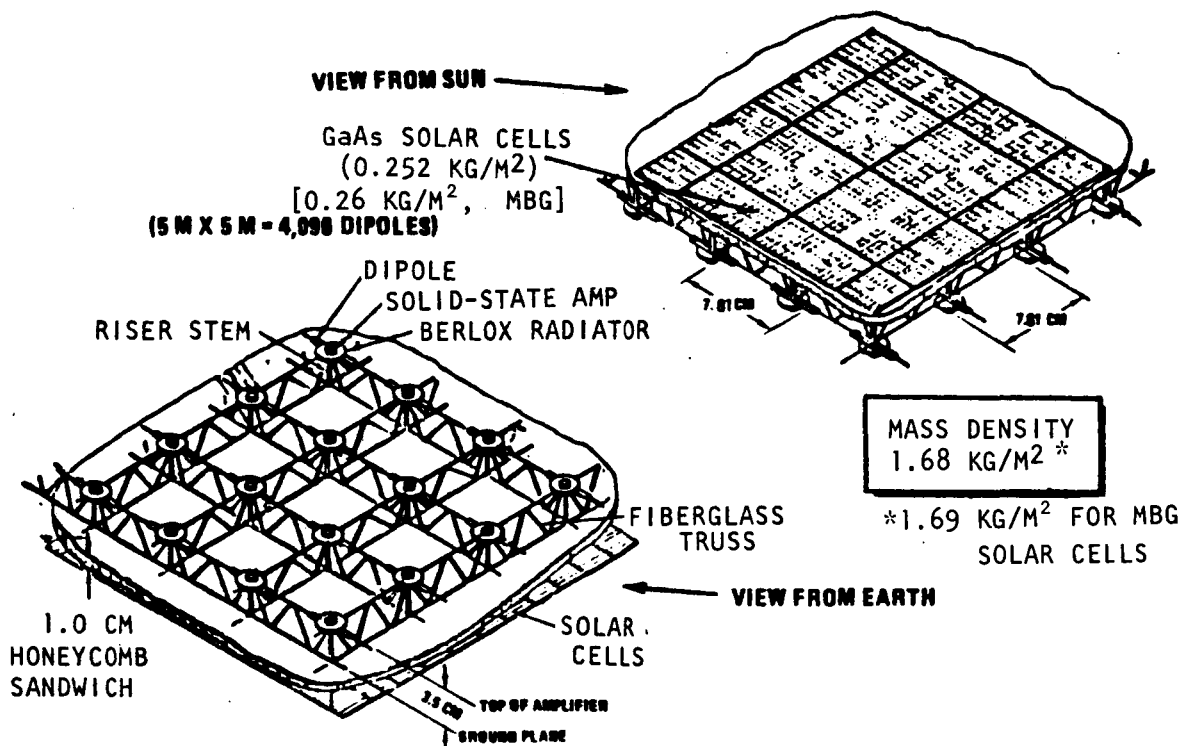
Figure 2.3-11. Solid-State Sandwich Design

Table 2.3-5. Sandwich Module Mass Properties

Element	Mass (kg/m^2)
Structure	.
Honeycomb	0.40
Truss	0.44
Dipole Assembly	
Amplifier module	0.81
Dipoles	Negl.
B$_e$O$_2$	0.20
Ground Plane	0.15
RF Distribution	0.07
Solar Cells—GaAs	0.25
—GaAlAs/GaAs	0.26
DC Distribution	0.09
Total	1.68
	(1.69) MBG

Table 2.3-6. Mass Properties Summary,
Exhibit D—April 1980 ($\times 10^{-6}$ kg)

		STD CELL GaAs	MBG CELL GaAlAs/GaAs
1.1.1	ENERGY CONVERSION (SOLAR ARRAY)		
	STRUCTURE	3.412	2.411
	PRIMARY	(3.026)	(2.138)
	SECONDARY	(0.386)	(0.273)
	MECHANISMS	0.027	0.019
	CONCENTRATOR	2.075	1.646
	SOLAR PANEL	0.076*	0.076*
	POWER DISTRIBUTION AND CONTROL	0.015	0.015
	POWER COND. EQUIP. & BATT.	(0.013)	(0.013)
	POWER DISTRIBUTION	(0.002)	(0.002)
	THERMAL	NONE	NONE
	MAINTENANCE	0.100	0.100
1.1.3 (PARTIAL)	INFORMATION MANAGEMENT AND CONTROL	0.033**	0.033**
	DATA PROCESSING	(0.014)	(0.014)
	INSTRUMENTATION	(0.019)	(0.019)
1.1.4 (PARTIAL)	ATTITUDE CONTROL	0.103	0.103
	SUBTOTAL	**5.841**	**4.403**
1.1.2	POWER TRANSMISSION (ANTENNA)		
	STRUCTURE	0.729	0.649
	PRIMARY	(0.161)	(0.143)
	SECONDARY	(0.568)	(0.506)
	MECHANISM	NONE	NONE
	SUBARRAY	8.821	7.053
	POWER DISTRIBUTION AND CONTROL	INCLUDED	INCLUDED
	THERMAL	NONE	NONE
	ANTENNA CONTROL ELECTRONICS	0.340	0.340
	MAINTENANCE	0.436	0.408
1.1.3 (PARTIAL)	INFORMATION MANAGEMENT & CONTROL	0.256***	0.256***
	DATA PROCESSING	(0.152)	(0.152)
	INSTRUMENTATION	(0.104)	(0.104)
1.1.4 (PARTIAL)	ATTITUDE CONTROL	NEGLIG.	NEGLIG.
	SUBTOTAL	**10.582**	**8.706**
1.1.6	INTERFACE		
	STRUCTURE	N/A	N/A
	PRIMARY		
	SECONDARY		
	MECHANISMS	N/A	N/A
	POWER DISTRIBUTION AND CONTROL	N/A	N/A
	POWER DISTRIBUTION		
	SLIP RING BRUSHES		
	THERMAL	N/A	N/A
	MAINTENANCE	-	-
	COMMUNICATION	TBD	TBD
	SUBTOTAL	**-**	**-**
	SPS TOTAL (DRY)	16.423	13.109
	GROWTH (25%)	4.106	3.277
	TOTAL SPS (DRY) WITH GROWTH	20.529	16.386
	SAT. PWR @ UTILITY INTERFACE (GW)	2.41	3.06
	SAT. DENSITY, KG/KW$_{UI}$	8.52	5.35

*AUXILIARY POWER ONLY
**TWO-THIRDS MASS OF REFERENCE CONCEPT
***20% REF. MASS PER ANTENNA

Figure 2.3-12 illustrates the stripline corporate feed system used in the sandwich concept. Originally, it was believed that it would be necessary to use a coaxial cable system because of cross-over among feed elements. However, a system was devised that had no cross-overs (shown here), and it was feasible to use a stripline system that could be more easily manufactured.
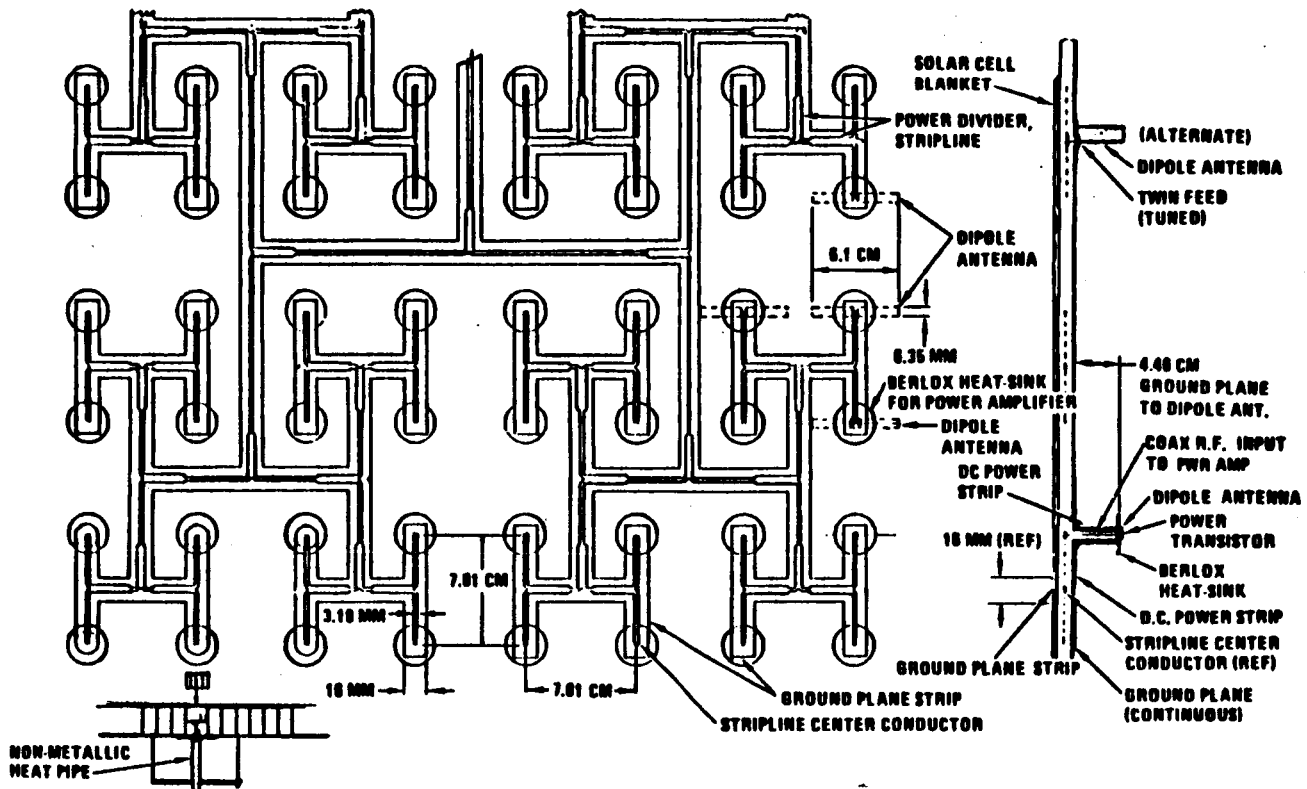
Figure 2.3-12. Stripline Corporate Feed System

A thermal analysis was conducted on the design concept shown in Figure 2.3-7 to determine the maximum concentration ratio for a maximum solar array temperature of 200°C and the base of the power amplifier held to a maximum 125°C. Within these two temperature constraints, it was estimated that an effective concentration ratio of 5.7 could be achieved rather than the point design value of 5.2. An additional primary reflector could be added to achieve this capability.

Effect of Multi-Bandgap Solar Array

An analysis was conducted to estimate the effect on the design and capability of the solid-state sandwich concept using a multi-bandgap solar array. The results of this analysis are shown in Table 2.3-7, which compares the two solar array concepts. At 200°C, the GaAs solar cell has an efficiency of 15.7%; whereas, the multi-bandgap (MBG) array has an efficiency of 25.1%. The antenna aperture is smaller for the MBG array (1.63 km versus 1.83 km), and the antenna power density is higher (1112 W/m^2 versus 696 W/m^2). Because of the higher power density, it is necessary to feed each dipole pair with two power amplifiers rather than one. The BeO_2 dish becomes larger in area as

a result of the increased waste heat. The power at the utility interface per antenna increases significantly from 1.21 GW to 1.53 GW. Most significantly, the satellite specific mass decreases from 8.5 kg/kW to 5.4 kg/kW.

Table 2.3-7. Comparison of GaAs and GaAs/GaAlAs (MBG) Sandwich Concepts

	GaAs	GaAs/GaAlAs (MBG)
• Concentration ratio (EOL)	5.2	5.2
• Solar array temperature (°C)	200	200
• Cell efficiency at 200°C (BOL)	0.157	0.251
• Amplifier efficiency	0.792	0.792
• Antenna aperture (km)	1.83	1.63
• Antenna power density (W/m^2)	696	1112
• Rectenna boresight diameter (km)	4.76	5.40
• Receiving site dimension (km)	10.0×13.0	11.1×14.4
• Power at utility interface (GW/antenna)	1.21	1.53
• Satellite specific mass (kg/kW)	8.48	5.35

Solid-State End-Mounted Antenna Point Design

A solid-state configuration for an end-mounted satellite that evolved from the Rockwell study is shown in Figure 2.3-13. Characteristics of the satellite are identified in Table 2.3-8. Gallium arsenide solar cells are
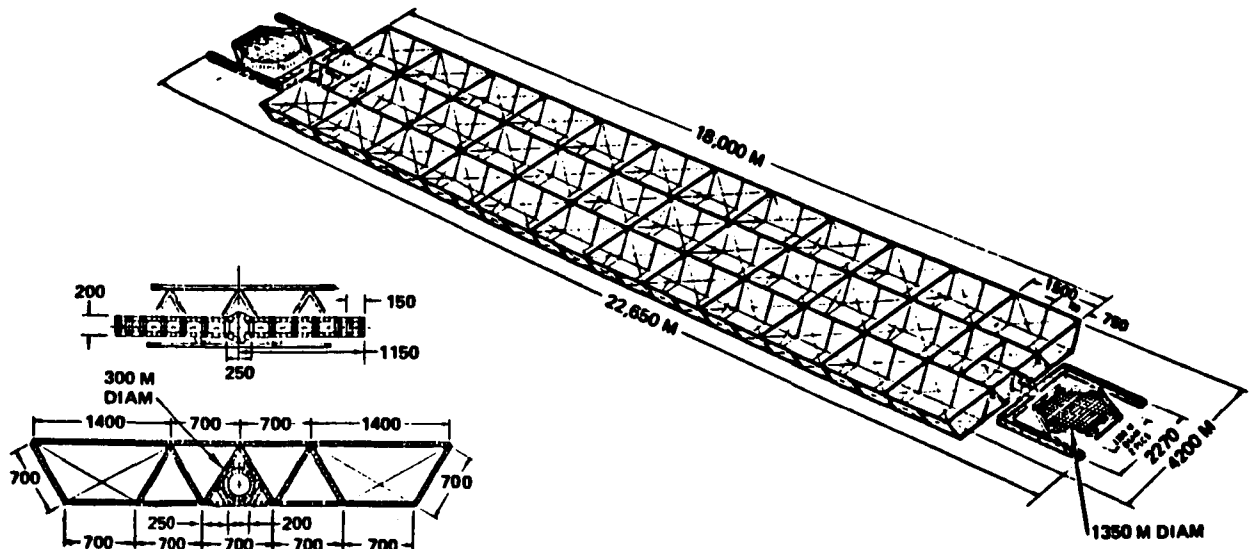
Figure 2.3-13. Solid-State End-Mounted Antenna Satellite Design

Table 2.3-8. Solid-State End Mounted
Antenna System Characteristics

- GaAs SOLAR ARRAY *(or GaAlAs/GaAs)*
- EFFECTIVE CR_E = 1.83
- 640 V SERIES PARALLEL STRINGS (2600 W MAXIMUM) WITH DUAL DC/DC CONVERSION FROM 40,000 V
- DUAL END-MOUNTED MICROWAVE ANTENNAS
- AMPLIFIER BASE TEMPERATURE = 125°C
- AMPLIFIER EFFICIENCY = 0.8
- ANTENNA POWER TAPER = 10 dB
- ANTENNA DIAMETER = 1.35 km
- POWER AT UTILITY INTERFACE = 2.61 GW PER ANTENNA (5.22 GW TOTAL)
- RECTENNA BORESIGHT DIAMETER = 7.51 km PER RECTENNA
- SPECIFIC MASS = 7.66 kg/kW *(6.81 MBG)*

utilized at a geometric concentration ratio (CR) of 2 (CR_{eff} = 1.83 end of life). High-voltage dc is generated on the solar array with the array made up of 36 bays (each bay consisting of two solar panels 650 m wide by 690 m long to generate 40 kV dc power). Power is transferred from the 36 bays across the rotary joints (one-half the power to each antenna). On the antenna the power is converted to 640 V dc to supply the solid-state voltage requirements. The antenna mechanical module layout is given in Figure 2.3-14. Dipole-amplifiers are series-paralleled in the manner shown, with each dipole requiring 10 V dc and up to nine power amplifiers paralleled per dipole. A total of 64 dipoles are series-connected for a 640-V input requirement. These series-connected dipoles are made up into subarrays of 5 m by 5 m installed into mechanical modules 30 m by 30 m. Each mechanical module has four dc converters to provide the 640 V to the series-connected dipoles.

The efficiency chain configuration for this concept is illustrated in Figure 2.3-15. The solar array is sized for a summer solstice (1311.5 W/m^2) solar constant (lowest value during the year) using an array factor of 0.137 for end-of-life considerations. This factor includes a reflector degradation allowance for 30 years, cell operating temperature-efficiency effects, array design, UV/radiation degradation (non-annealable allowance), switch gear, and misorientation effects. The array specific power output is 359.4 W/m^2 with an array power output requirement of 5.735 GW per antenna. There is 5.383 GW transferred across each rotary point which is sufficient to supply 5.287 GW to each antenna's dc converters. The overall antenna efficiency is 58.92%. The system is sized for a voltage drop allowance on the array of approximately 6 percent. Rectenna and ground station efficiency is 82.37%, and the overall system efficiency is 6.24%. The power delivered to the utility interface is 2.61 GW per antenna. Input voltage to the dc converters is 40 kV. The antenna feeder layout is shown in Figure 2.3-16. There are 1588 mechanical modules on each antenna. One-fourth of the antenna section is shown (i.e., 397 mechanical modules).
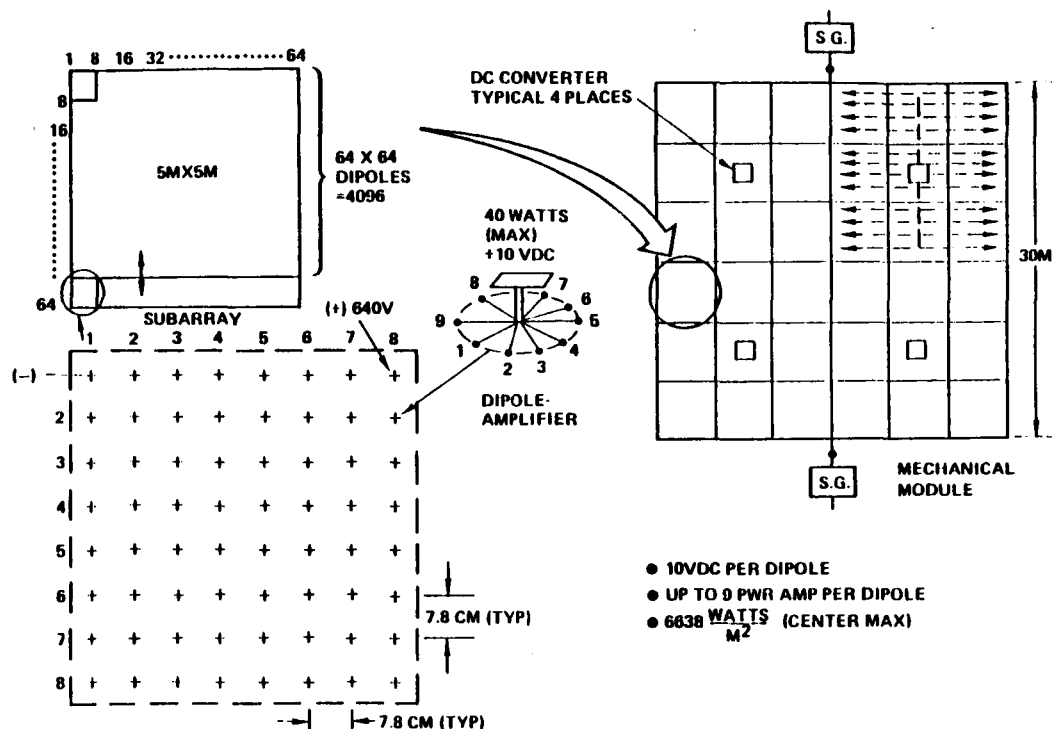
Figure 2.3-14.   Mechanical Module Layout (Solid-State End-Mounted)

$M_{OA} = 6.24\%$
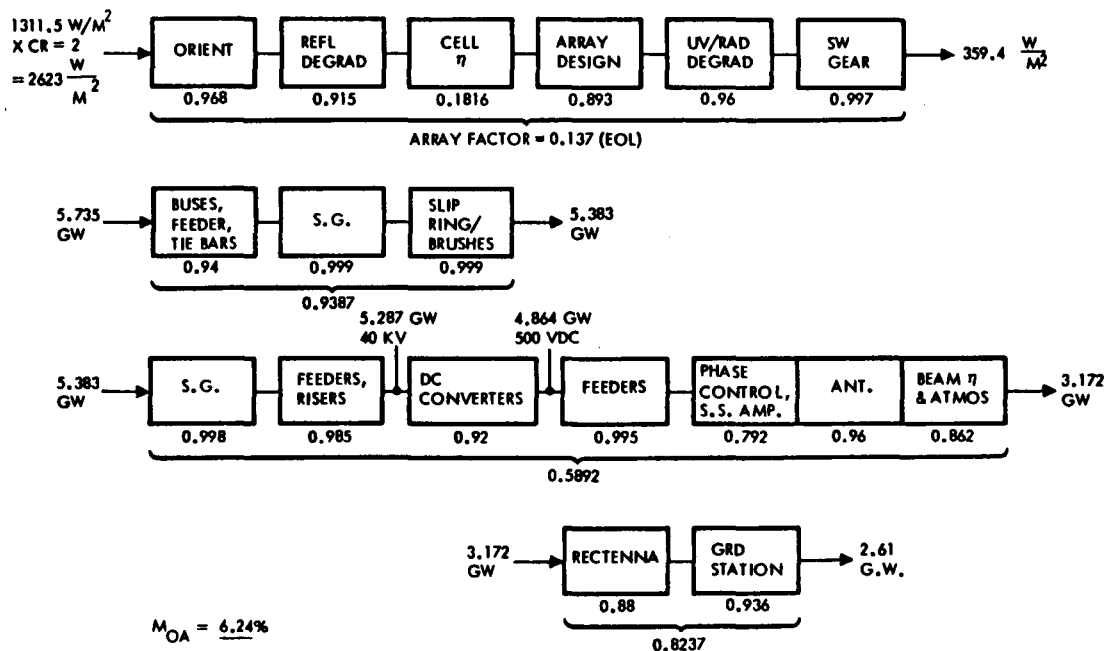
Figure 2.3-15.   System Efficiency Chain Reference Array
(Solid-State Antenna)

NOTE: THERE ARE 1588 MECHANICAL MODULES
30 M X 30 M EACH. FEEDERS OVERSIZED
BY FACTOR 1.07 FOR FAULT OVERLOAD
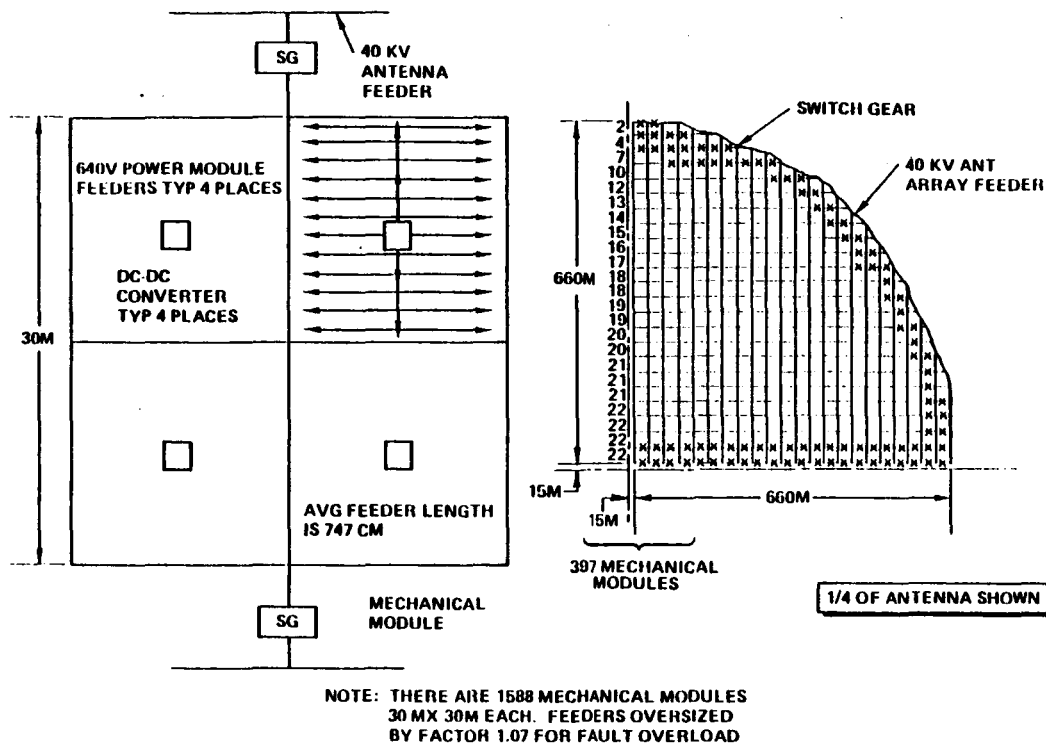
Figure 2.3-16.   Antenna Feeder Diagram
(Solid-State End-Mounted)

Configuration details of the dipole amplifier are shown in Figures 2.3-17 and 2.3-18. Each dipole is spaced 7.81 cm on center as shown (Figure 2.3-18). Power output per dipole is 40.5 W (maximum) to satisfy a Gaussian 10-dB taper illumination beam.

Table 2.3-9 gives a detailed mass breakdown for the solid-state antenna section. End-mounted solid-state specific mass, 3.32 kg/m^2, is compared to sandwich solid-state (1.68 kg/m^2). A detailed mass properties statement for this concept is shown in Table 2.3-10.

Trade study results showed that for the solid-state end-mounted antenna concept, high-voltage transmission is required. Future consideration might be given to reducing the reference 40 kV, down into a range of 10 kV to 15 kV. In any case, high-efficiency and lightweight dc converters are critical to the design concept. A 10-dB Gaussian power beam was selected for the solid-state end-mounted antenna to reduce side lobes. For the solid-state end-mounted antenna, a power amplifier module voltage of 640 V dc was selected to reduce module wiring mass. Additional study is required of the losses associated with series-paralleling solid-state amplifiers to meet this voltage requirement.
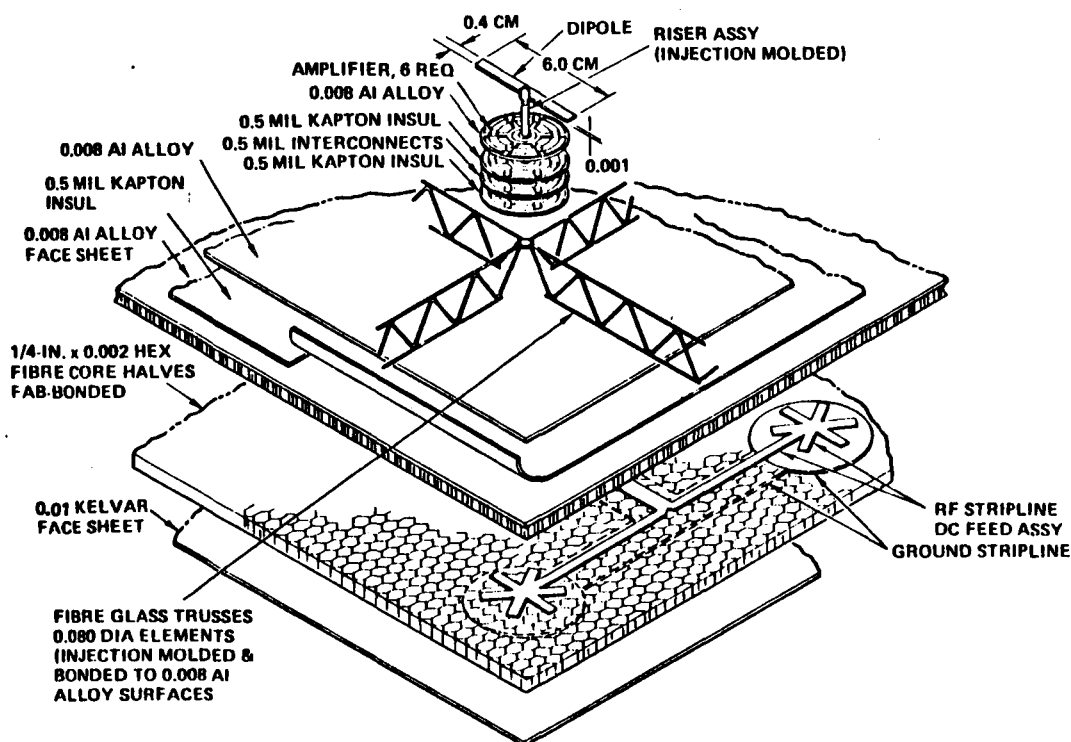
Figure 2.3-17.   Dipole Amplifier Assembly—Exploded View,
Solid-State End-Mounted (Preliminary)

Table 2.3-9.   Antenna Mass Statement

	End-Mounted Solid-State (kg/m^2)
Structure	
Honeycomb	0.85
Truss	0.44
Dipole Assembly	
Amplifier modules	0.49
Dipoles	Negl.
B_eO_2	–
Ground Plane	1.08
RF Distribution	0.07
Solar Cells	–
DC Distribution	0.03
Kapton Backing	0.036 (10 mils)
Total	3.32

STRIPLINE FEED
(SUPERIMPOSED IN
PHANTOM FOR CLARITY)

0.010 KAPTON, FACE SHEET,
(PERFORATED FOR COOLING)

1/4 IN. x 0.002 HEX FIBRE CELL

0.008 Al ALLOY, FACE SHEET

0.0005 KAPTON, INSUL DIELECTRIC

0.008 Al ALLOY,
GROUND PLANE

7.81 CM

7.81 CM

VIEW LOOKING OPPOSITE SIDE

SP. MASS
3.68 KG/M^2

7.81 CM

7.81 CM

3.06 CM

1.0 CM
HONEYCOMB
SANDWICH

VIEW LOOKING FROM EARTH
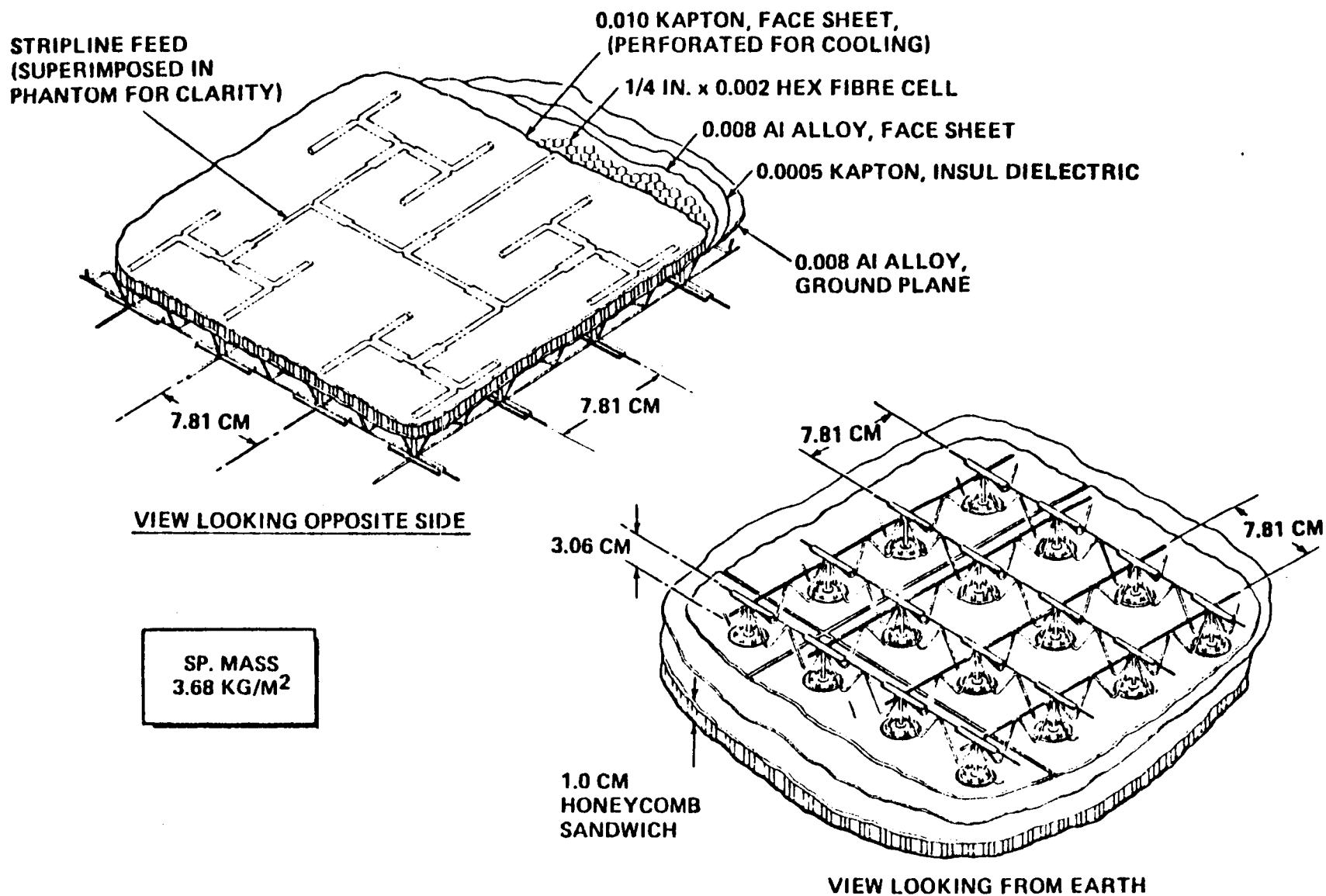
Figure 2.3-18.   Dipole Amplifier Panel Configuration, Solid-State End-Mounted (Preliminary)

Space Operations and
Satellite Systems Division
Space Systems Group

Rockwell
International

Table 2.3-10. Mass Properties Summary,
Exhibit D—April 1980 ($\times 10^{-6}$ kg)

		STD CELL GaAs	MBG CELL GaAlAs/GaAs
1.1.1	ENERGY CONVERSION (SOLAR ARRAY)		
	STRUCTURE	1.496	1.233
	PRIMARY	(1.077)	(0.902)
	SECONDARY	(0.419)	(0.331)
	MECHANISMS	0.087	0.078
	CONCENTRATOR	1.169	0.766
	SOLAR PANEL	8.138	5.607
	POWER DISTRIBUTION AND CONTROL	1.112	0.846
	POWER COND. EQUIP. & BATT.	(0.102)	(0.222)
	POWER DISTRIBUTION	(1.010)	(0.624)
	THERMAL	NONE	NONE
	MAINTENANCE	0.104	0.056
1.1.3 (PARTIAL)	INFORMATION MANAGEMENT AND CONTROL	0.057	0.057
	DATA PROCESSING	(0.024)	(0.024)
	INSTRUMENTATION	(0.033)	(0.033)
1.1.4 (PARTIAL)	ATTITUDE CONTROL	0.116	0.116
	SUBTOTAL	12.279	8.759
1.1.2	POWER TRANSMISSION (ANTENNA)		
	STRUCTURE	1.409	1.409
	PRIMARY	(0.094)	(0.094)
	SECONDARY	(1.315)	(1.315)
	MECHANISM	0.004	0.004
	SUBARRAY	10.561	10.561
	POWER DISTRIBUTION AND CONTROL	4.405	4.405
	POWER CONDITIONING & BATT.	(2.164)	(2.164)
	POWER DISTRIBUTION	(2.241)	(2.241)
	THERMAL	NONE	NONE
	ANTENNA CONTROL ELECTRONICS	0.340	0.340
	MAINTENANCE	0.448	0.448
1.1.3 (PARTIAL)	INFORMATION MANAGEMENT AND CONTROL	1.622	1.662
	DATA PROCESSING	(1.385)	(1.385)
	INSTRUMENTATION	(0.237)	(0.237)
1.1.4 (PARTIAL)	ATTITUDE CONTROL	NEGLIG.	NEGLIG.
	SUBTOTAL	18.789	18.789
1.1.6	INTERFACE		
	STRUCTURE	0.236	0.236
	PRIMARY	(0.168	(0.168)
	SECONDARY	(0.068)	(0.068)
	MECHANISMS	0.072	0.072
	POWER DISTRIBUTION AND CONTROL	0.538	0.538
	POWER DISTRIBUTION	(0.487)	(0.487)
	SLIP RING BRUSHES	(0.051)	(0.051)
	THERMAL	NONE	NONE
	MAINTENANCE	0.064	0.064
	COMMUNICATION	TBD	TBD
	SUBTOTAL	0.910	0.910
	SPS TOTAL (DRY)	31.978	28.458
	GROWTH (25%)	7.995	7.114
	TOTAL SPS (DRY) WITH GROWTH	39.973	35.572
	SATELLITE POWER @ UTILITY INTERFACE (GW)	5.22	5.22
	SATELLITE DENSITY, KG/KW_{UI}	7.66	6.81

3.0 TRADE SUMMARY

The subsystem analysis effort consisted of tradeoffs and studies to derive necessary supporting data to define reference concept variations and develop new solid-state concepts. The major subsystems investigated were the solar array, power distribution, structure, thermal control, attitude control, stationkeeping, and microwave.

3.1 SOLAR ARRAY

The major study effort that was accomplished for the solar array was to evaluate a multiple-bandgap (MBG) solar cell with significantly higher operating efficiency than the reference GaAs solar cell. The cell conversion efficiency is a critical performance parameter, and the MBG concept can now be seriously considered—primarily because of the remarkable progress made in thin-film photovoltaic material technologies in the past several years. Preliminary experimental research and development is being carried out at Rockwell's Electronic Research Laboratory as part of an Air Force/Aero Propulsion Laboratory contract (Reference 1). The objective of this program is the development of a technology to fabricate solar cell assemblies with greater than 25-percent conversion efficiency at 28°C under one sun intensity in space sunlight (AMO, 135 mW/cm^2).

Research Triangle Institute (R. D. Alberts) supported the Rockwell SPS effort under a separate subcontract and provided supporting technical data. Research Triangle Institute's current activities include investigations of materials, requirements, and development of high-efficiency MBG cells for delivery to the Air Force.

Solar cell operating temperature limitations, use of optical filters, and reflector pointing requirements were evaluated for the sandwich concept in an effort to improve its competitive position by increasing antenna radiative power densities.

3.1.1 SOLAR CELL EFFICIENCY (GaAs SINGLE JUNCTION)

An update of the GaAs solar cell efficiency is listed in Table 3.1-1. Based on today's technology, at air-mass-zero (AMO) condition and 28°C, 22% cell efficiency is expected to be achieved around the year 1990. The best laboratory GaAs solar cell from Hughes Research Laboratory (HRL), with a 0.5-μm junction depth, has an 18.1% efficiency at 28°C. Shallower junctions will produce higher efficiency and possibly radiation-hardened cells. High-efficiency solar cells are well underway to reach the SPS efficiency goal of 20 percent (nominal).

Table 3.1-1. Review of GaAs Solar Cell Performance

PARAMETER	ROCKWELL ERC ESTIMATE	HUGHES		
		HRL ESTIMATE	REALISTIC MAXIMUM ESTIMATE*	BEST TODAY $(X_j = 0.5\mu)$**
SHORT-CIRCUIT CURRENT	34 mA/cm^2	32 mA/cm^2	35 mA/cm^2	32 mA/cm^2
OPEN-CIRCUIT VOLTAGE	1.0 V	1.01 V	1.05 V	1.015 V
FILL FACTOR	0.88	0.85	0.88	0.752
EFFICIENCY	22.1%	20.3%	24%	18.1%

* NOTE: ALL DATA ARE BASED ON CR = 1; AMO, 28°C; THEORETICAL MAXIMUM
EFFICIENCY OF GaAs SOLAR CELL IS ABOUT 26%.

**JUNCTION DEPTH

3.1.2 MULTI-BANDGAP CELL CONCEPT

The most efficient response of p-n junction cells is to photons of energy
just exceeding the bandgap energy. If two or more solar cells of differing
bandgap energy (and thus of different composition) could be arranged appropri-
ately to "share" the solar spectrum, each operating on that portion of the
spectrum to which it is most responsive, a combination converter with an overall
power efficiency exceeding that of the individual cells used separately could
quite possibly be realized. This concept is not new, having first been pro-
posed by Jackson (Reference 2) in 1955, and examined by various workers at
intervals since that time.

There are two principal embodiments of this concept. One involves inter-
posing dichroic mirrors or filters (i.e., "beam splitters") in the incident
beam of solar radiation so that selected radiation of a portion of the spec-
trum is diverted to a solar cell whose properties [mainly bandgap energy
(E_{g1})] allow it to make relatively efficient use of that selected band of
radiation, while allowing the remainder of the spectrum to pass on to a sec-
ond filter/mirror which again selects a portion of the spectrum to direct onto
a second cell of bandgap energy (E_{g2}) while transmitting the remainder to a
third cell (or a third filter/mirror), and so on.

The beam-splitting, filter/mirror concept was not evaluated for SPS since
it was felt that this concept would be more costly and complex; however, future
efforts should include an assessment of such a concept since this might lead
to even higher efficiencies. The other approach that was evaluated involves
two or more solar cells of differing composition (and thus differing bandgap
energies) used optically in series, in a tandem or stacked arrangement. The
cell of largest bandgap energy E_{g1} and transmitting the radiation of energy

$<E_{g1}$ onto the second cell of bandgap E_{g2}, which utilizes the narrowed band of energies to generate photovoltage and photocurrent consistent with its photovoltaic properties and transmits the remaining radiation of energy $<E_{g2}$ onto a third cell, if used, and so on. This configuration of the tandem or stacked multiple-bandgap solar cell is shown schematically in Figure 3.1-1.

$E_{g1} > E_{g2} > E_{g3}$
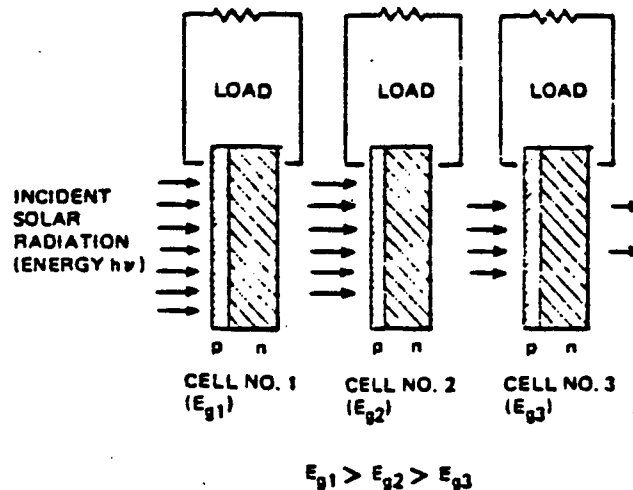
Figure 3.1-1. Schematic Representation of
Stacked Multiple-Bandgap Solar Cell

Although simple in concept, the stacked multiple-bandgap (MBG) solar cell involves difficult material problems and design and fabrication complexities. A major problem to be solved is the question of the design of the interface between the back side of the first component and the front side (incident light) of the cell next in line in the stack. Should the electrical contact be made simply a series connection, with the current leaving the first cell entering the second cell directly (conceptually the simplest structure, and shown in Figure 3.1-2), or should the photon-generated current of each cell be extracted separately? In the series connection first instance, it becomes necessary to match photocurrents of the two adjoining cells at their operating points (not the short-circuit currents), and this requirement alone is accompanied by major difficulties in both material selection and interface design. However, this arrangement is by far the more attractive, since it makes maximum use of the compactness and fabrication advantages of monolithic thin-film semiconductor technologies.

Over-simplified theoretical models of stacked MBG configurations can give rise to a variety of possible cell combinations (or, more correctly, possible combinations of bandgap energies) that appear to offer very attractive combined conversion efficiencies—some approaching the probable theoretical upper limit of 40 to 50 percent for solar conversion efficiency of a semiconductor-based converter system having no loss of the excess photon energy (Reference 3).

More accurate models of such configurations, however, result in relatively few combinations of either two- or three-cell systems that meet design requirements and yet represent material composites that are compatible and fabricable by presently known technologies. The complexity of systems involving

four (or more) component cells goes up rapidly, as does the difficulty of successfully fabricating the system even on an experimental laboratory basis.
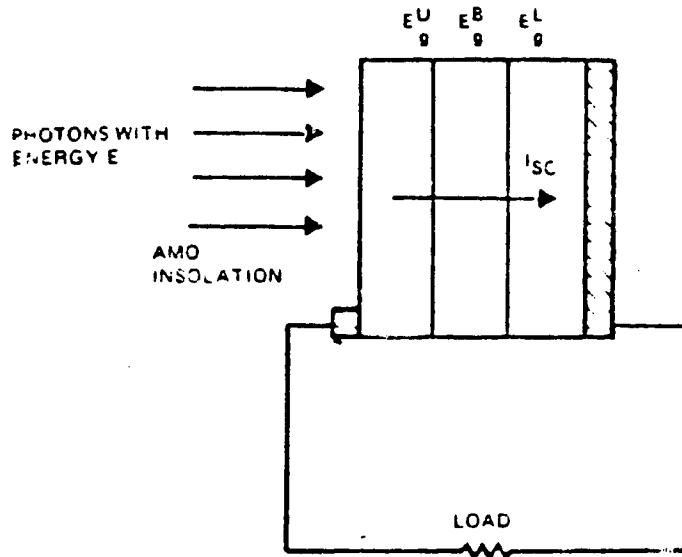
Figure 3.1-2. Schematic Representation of MBG Configuration
Involving Both Electrical/Optical Series Arrangement

   Preliminary modeling of MBG solar cell assemblies of the type shown in Figure 3.1-2 has recently been carried out at Rockwell, and Table 3.1-2 presents a summary of the results of the preliminary modeling using the basic principles that must be applied to the MBG solar cell concept. The various materials considered and photovoltaic device design factors that must be applied are quite complex, but the net result is indicated on the table. Individual cells that compose the two-, three-, or four-cell stacks are identified by the bandgap energy of the active cell material. The 1.42-eV cell involved in each of the combinations listed is the GaAs cell.

Table 3.1-2. Calculated Ideal and Expected AMO Efficiencies
for MBG Solar Cell Combinations

BANDGAP ENERGY	EFFICIENCY (%)					
	TWO CELLS		THREE CELLS		FOUR CELLS	
	IDEAL η	EXPECTED η	IDEAL η	EXPECTED η	IDEAL η	EXPECTED η
2.0 eV			20.0	14.9	20.0	14.9
1.42 eV (GaAs)	26.4	19.8	13.0	9.7	13.0	9.7
1.0 eV			7.7	5.6	7.8	5.6
0.8 eV	7.5	4.9			3.5	2.3
COMBINED η TOTAL	33.9	24.7	33.0	24.6	40.8	30.2

3-4

The table gives both theoretical conversion efficiencies for the various combinations, based on idealized junction characteristics and no current collection losses, and realistic projections of efficiencies that could be expected in practical assemblies after adequate development of the particular structures involved, based on empirical data obtained with experimental high-efficiency thin-film GaAs solar cells. The possibility of achieving efficiencies of over 25 percent—possibly greater than 30 percent—is evident from these data, provided the required materials and device technology problems can be adequately solved. Figure 3.1-3 shows parametric data useful in selecting the proper bandgap materials to ascertain a similar lattice constant. A good match of lattice constant greatly reduces materials interface states to maintain high short-circuited current output.

0.7 eV

Ge
GaSb

1.1 eV

Si
$In_xGa_{1-x}As$
$GaAs_{1-x}Sb_x$
$Ga_yIn_{1-y}As_{1-x}P_x$
$Al_yGa_{1-y}As_{1-x}Sb_x$

1.7 eV

$Al_xGa_{1-x}As$
$GaAs_{1-x}P_x$
$Al_yGa_{1-y}As_{1-x}Sb_x$
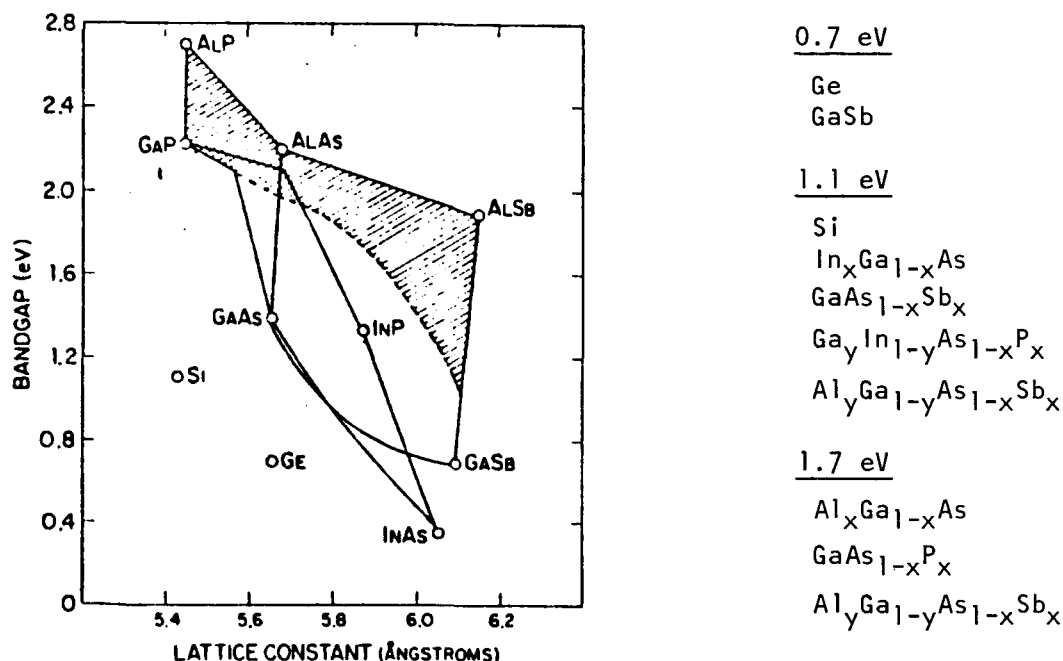
Note: The shaded portion represents indirect bandgap alloys.

Figure 3.1-3. Bandgap Vs. Lattice Constant for
Potential Multi-Bandgap Solar Cells

Short-circuit current contribution of each material of representative combinations are shown in Figure 3.1-4. Since these materials are electrically in series, the lowest current value is used as the cell current output (same current in the device). Efficiency values calculated for the cell combinations listed in Figure 3.1-4 are given in Table 3.1-3. Efficiency values are shown for practical and also in brackets (ideal); e.g., the dual-junction GaAs/Ge cell should have a practical achievable efficiency of 25.5% compared to an ideal efficiency of 33%. Table 3.1-3 is based on achieving a current at maximum power point of 95% short-circuited current.

E, eV

Figure 3.1-4. Short-Circuit Current of Multi-Bandgap Solar Cell
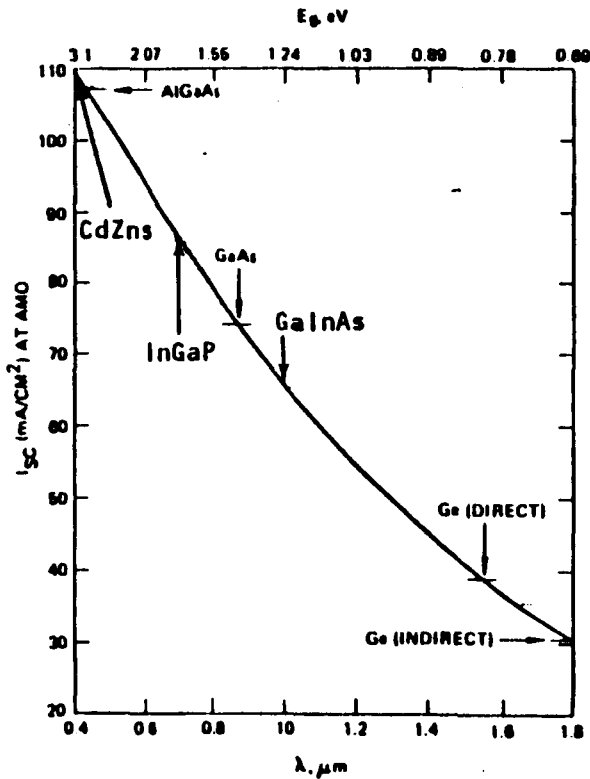
AVAILABLE SOLAR CELL SHORT-CIRCUIT CURRENTS

DUAL JUNCTION	I_{SC} (AMO)
AlGaAs / GaAs	32.6 mA/cm^2
GaAs / Ge	35 mA/cm^2

THREE JUNCTION	
CdZns / InGaP	23.4
InGaP / GaInAs	21.9
GaInAs / Ge	23.4

FOUR JUNCTION	
CdZnS / GaPAs	21.6
GaPAs / GaAs	21.0
GaAs / InAsP	20.3
InAsP / Ge	20.7

Table 3.1-3. Multi-Bandgap Solar Cell Efficiency

MATERIAL	V_{MP} (VOLTS)	I_{MP} (mA/cm^2) ($I_{MP} = 0.95 \times I_{SC}$)	$\eta = \dfrac{V_{MP} \cdot I_{MP}}{135.3}$ (%) (AMO, 28°C)
DUAL JUNCTION			
GaAs	0.9	31.0	
Ge	0.2	33.2	
TOTAL	1.1	31.0	25.2 (33.0)
THREE-JUNCTION			
InGaP	1.28	22.3	
GaInAs	0.77	20.8	
Ge	0.20	22.3	
TOTAL	2.25	20.8	34.6 (40.8)
FOUR-JUNCTION			
GaPAs	1.3	20.5	
GaAs	0.8	20.0	
InAsP	0.42	19.3	
Ge	0.18	19.7	
TOTAL	2.7	19.3	38.5 (44.8)

(IDEAL EFFICIENCY)

3.1.3 MASS AND COST ESTIMATES

Mass breakdown of various multi-bandgap solar cells are shown in Table 3.1-4 and compared with the single-function GaAs/Al$_2$O$_3$ cell. As shown, both silicon and germanium materials contribute significant mass penalties since these are indirect bandgap semiconductors and require at least 50-μm thickness in order to convert the usable solar spectrum. GaAlAs/GaInAs cell (RTI approach) and GaAlAs/GaAs cell (ERC approach) would show almost no change in mass, compared to the single-junction GaAs/Al$_2$O$_3$ cell. For this reason, the preliminary selection is the GaAsAs/GaInAs and GaAlAs/GaAs dual-junction as the SPS multi-bandgap cell options. It was felt that since a high-efficiency two-junction cell has not yet been demonstrated experimentally, three- (or more) junction cells should not be selected for this study.

Table 3.1-4. Mass Estimate Model of Multi-Bandgap Solar Cell

ITEM	SINGLE JUNCTION GaAs/Al$_2$O$_3$	TWO JUNCTION GaAs/Ge	TWO JUNCTION GaAs/Si	THREE JUNCTION Cd/ZnS/InGaP/ GaInAs/Ge
20 μM Al$_2$O$_3$	7.96			
INTERCONNECTS/TOP GRIDS	3.4			
.3-.5 GaAlAs	.03			
5 μM GaAs	2.66	25.25	25.25	22.55
.5-1 μM OHMIC CONTACT	4.0			
13 μM FEP	2.7			
25 μM KAPTON	3.6			
6 μM POLYMER	.9			
50 μM Ge		26.6		
50 μM Si			11.6	
5 μM CdZnS				2.4
5 μM InGaP				2.4
5 μM GaInAs				2.75
50 μM Ge				26.6
TOTAL	25.25 (.252 KG/M^2)	51.85	37.85	56.7

In reality, the GaAlAs/GaAs cell is only a special case of GaAlAs/GaInAs cell version (when the contamination of In approaches zero in GaInAs material. Both cell structures are the same, as shown in Figure 3.1-5, with an estimated panel mass of 0.265 kg/m^2. The multi-bandgap cell cost estimate of GaAlAs/ GaInAs and its comparison to GaAs/Si cell is shown in Table 3.1-5. Based on the total solar array area of 61.2 km^2, the cost estimate of the GaAlAs/GaAs array is about \$76.2/m^2.* Most of the cost increase over the GaAs single-junction cell is due to the tunnel diode fabrication requirement. The cell structure parameters such as junction depth, layers' thickness, and doping concentration need to be optimized for the cell operating temperature. Rockwell's SPS designs have calculated two solar cell operating temperatures: (1) operating temperature of 113°C for CR = 2 design, and (2) operating temperature of 200°C for effective CR = 5 design. The projected cell performance data obtained from the computer modeling simulation is presented in Figures 3.1-6 through 3.1-9 for GaAlAs/GaInAs (CR = 2, CR = 5), GaAlAs/GaAs (CR = 2, CR = 5)

*1977 dollars

ITEM	WEIGHT (MG/CM^2)
20 μM AL$_2$O$_3$	7.96
INTERCONNECTS AND TO GRID CONTACTS	3.4
0.1 μM GaAlAs (WINDOW)	0.03
2-3 μM GaAlAs	0.69
4-6 μM GaAs	2.24
0.5-1.0 μM OHMIC CENTACT	2.0
13 μM FEP	2.7
25 μM KAPTON (BLANKET)	3.6
6 μM POLYMER THERMAL COATING	0.9
CONTINGENCY	3.0
	26.5
	(0.265 KG/M^2)

*WEIGHT IS THE SAME FOR GaAlAs/GaAs
AND GaAlAs/GaInAs SOLAR CELL
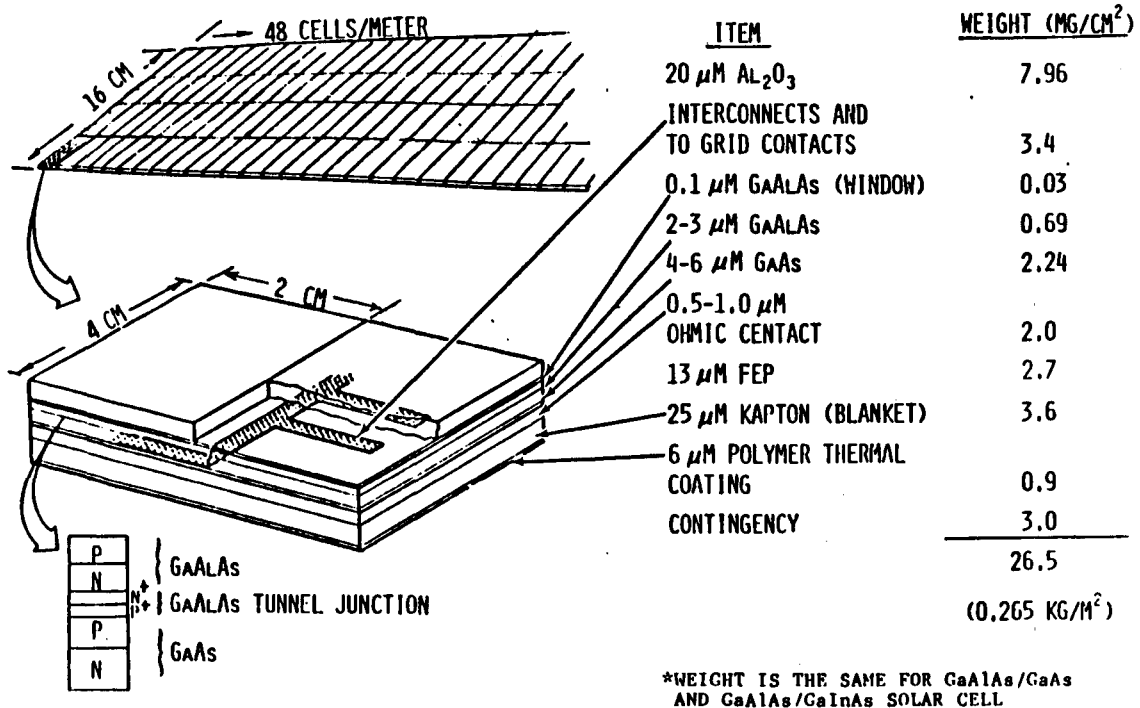
Figure 3.1-5. Dual-Junction Multi-Bandgap Solar Cell Blanket Cross Section

Table 3.1-5. Cost Estimate Model of Multi-Bandgap Solar Cell

			TOTAL COST OF MATERIAL ($M)	
			(A)	(B)
MATERIAL	AMOUNT REQUIRED (MT)	UNIT COST OF MATERIAL	GaAlAs/GaInAs	GaAs/Si
GALLIUM	780	$200/KG	156	156
ARSENIC	840	$100.09/KG ($45.4/LB)(99.999%)	84.1	84.1
SELENIUM	27 KG	$192/KG (99.999%)		
INDIUM	26	$96.5/KG ($3/TROY OZ.)	2.5	
SILVER	310	$159.39/KG ($72.30/LB)	49.4	49.4
SILICA				
SILICON (MG)	59,311	$1/KG (REF. 1)		59.3
SILICON (SEG)	13,162	$10/KG		13.2
ZINC	9 KG	$1170/KG (99.999%)		
ALUMINUM	100 (FOR A),10 (FOR B)	$138/KG (99.999%)	14.	1.4
GOLD FILM + BASE METAL		$1.82/M^2 (REF. 2)	115.67	115.67
TIN	880	$12.21/KG ($5.54/LB)	10.8	10.8
Al$_2$O$_3$ (SAPPHIRE)	4872	$325/KG	1,583.	1,583.
COPPER	860	$1.17/KG ($0.53/LB)	1.0	1.0
TEFLON	1650	$0.08/KG ($0.0344/LB)	0.1	0.1
KAPTON	2200	$66.14/KG ($30/LB) (25 μm FILM)	146.	146.
			2,162.57	2,219.97
			($35.3/M^2)	($36.27/M^2)

TOTAL ARRAY $/M^2 = MATERIALS + PROCESSING (DOE GOAL)

GaAlAs/GaInAs ARRAY $/M^2 = $35.3/M^2 + ($34/M^2 x 1.2) = 76.2/M^2 (1977 dollars)

REFERENCES:
(1) EVALUATION OF SOLAR CELLS & ARRAYS FOR POTENTIAL SOLAR POWER SATELLITE APPLICATION, ADL, MARCH 31, 1978 (NAS9-15294).

(2) HIGH EFFICIENCY THIN FILM GaAs SOLAR CELLS, R. J. STIRN, JPL, APRIL, 1976 (NSF/RA 760/28).

Operated at various temperatures from 300°K to 600°K, 2 suns,
AMO, and surface recombination velocity 10⁶ cm/sec.
(GaAlAs/GaInAs, 1.84-1.24 eV)
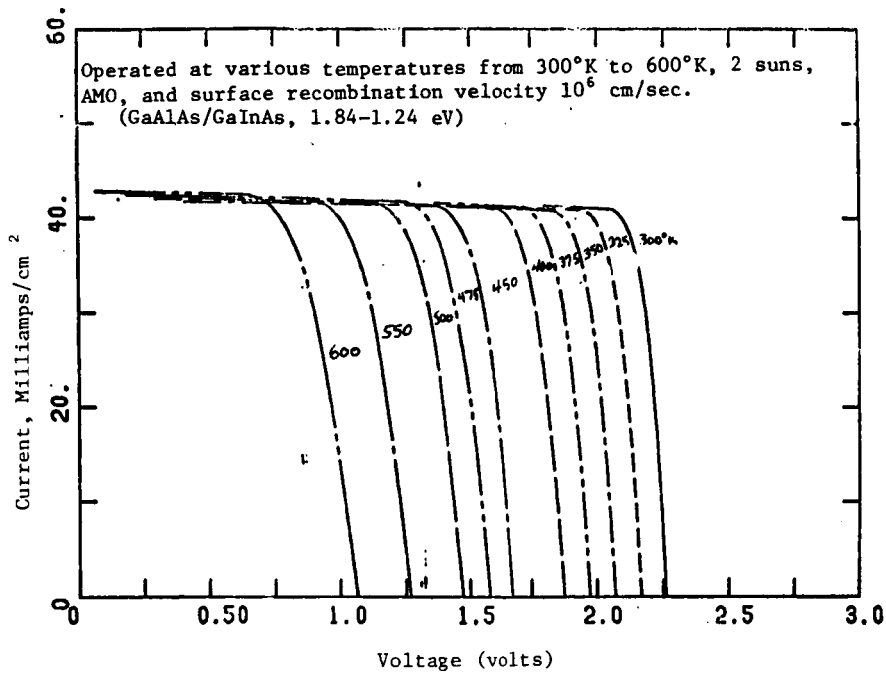
Figure 3.1-6.   Current Vs. Voltage for a Cascade Cell Optimized for
475°K, Two Suns

Operated at various temperatures from 300°K to 600°K, 5 suns,
AMO, and surface recombination velocity 10⁶ cm/sec.
(GaAlAs/GaInAs, 1.84-1.24 eV)
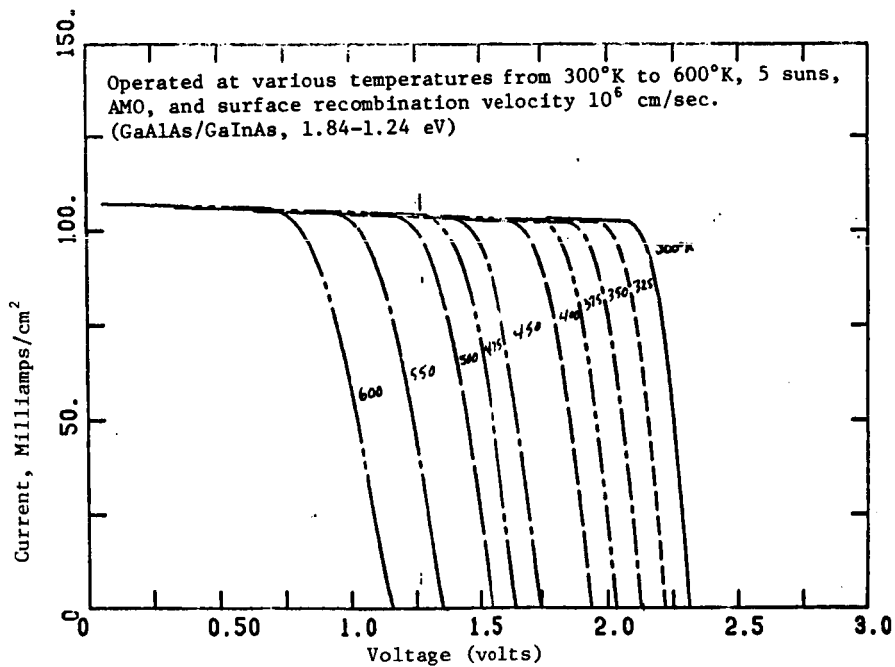
Figure 3.1-7.   Current Vs. Voltage for a Cascade Cell Optimized for
475°K, Five Suns
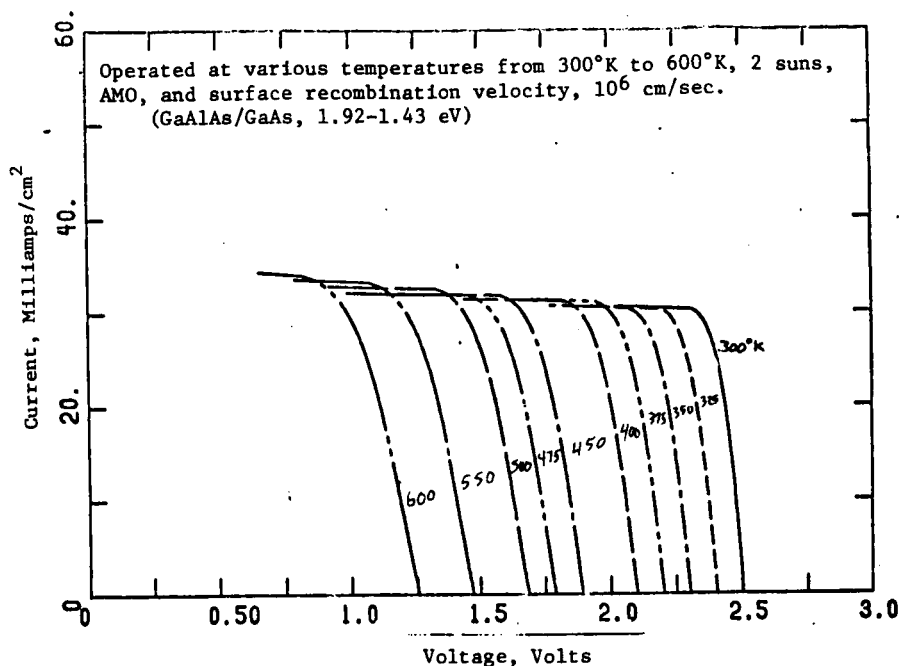
Figure 3.1-8. Current Vs. Voltage for a Cascade Cell Optimized for
475°K, Two Suns
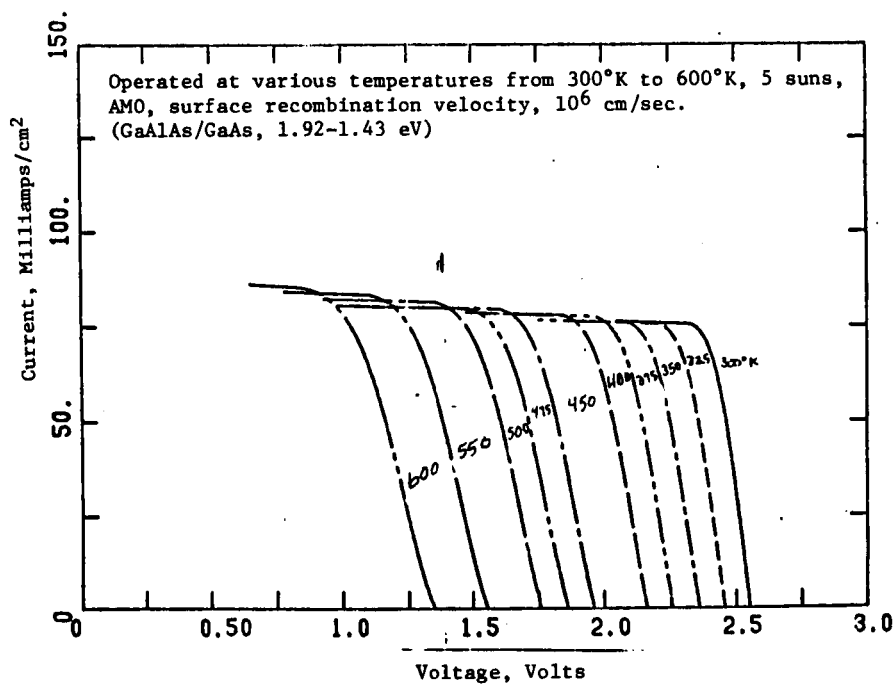
Figure 3.1-9. Current Vs. Voltage for a Cascade Cell Optimized for
475°K, Five Suns

3-10

multi-bandgap solar cells, respectively. As expected, the current increases linearly and voltage logarithmically as solar illumination (or CR) increases. The baseline dual-junction solar cells should have similar cell efficiency temperature coefficients as for single-junction GaAs (about 0.0287%/°C)—which is twice better than that of Si cells—because of the larger bandgap that allows higher temperature operation of the junction. Also, these multi-bandgap solar cells utilizing III-IV compound semiconductor typically have low minority carrier lifetimes, diffusion lengths, and steep optical absorption edge; therefore, they are less susceptible to radiation damage and potentially capable of low-temperature self-annealing characteristics.

3.1.4 GALICON SOLAR CELL

A galicon solar cell has been proposed by Dr. Dick Stern at JPL. The cell structure and specific mass are shown in Figure 3.1-10. There is a great deal of similarity between the galicon cell and the SPS GaAs/Al_2O_3 cell. The galicon cell potentially has higher efficiency; the GaAs/Al_2O_3 cell has integrated form (cell with cover) and less specific mass.

ITEM	THICKNESS (M)	MASS (MG/CM^2)
KAPTON-H	25	3.6
SI WAFER	50	11.7
SI/Ge GRADED LAYER	5	2.0
GaAs	5	2.7
METALLIZATION (Ag) (6% GRID)	3	3.3
INTERCONNECT MOLY	12	0.8
Ag	5	0.3
ADHESIVE (DC 93-500)	50	5.4
FEP COVER	50	10.6
TOTAL		40.4

NOTE: DR. RICHARD STIRN (JPL) HAS PROPOSED A GALICON SOLAR CELL. THE CELL STRUCTURE HAS GaAs ON SI POTENTIALLY A MULTI-BANDGAP CONCEPT. CELL EFFICIENCY ESTIMATES VARIES FROM 22% TO 30% (AMI). CELL COST ESTIMATE IS $79.4/M^2 (1980 DOLLARS) $46.5/M^2 (1975 DOLLARS)

Figure 3.1-10. Galicon Solar Cell

3.1.5 TEMPERATURE LIMITATIONS ON GaAs SOLAR CELL

The effects of temperature on GaAs solar cells in the area of cell material and device parameters are similar to all of the solar cells (such as silicon, CdS). At high temperature, the V_{oc} decreases, the I_{sc} slightly increases, and fill factor decreases due to the softness knee of the I-V curve.

The array elements failure mechanisms were investigated and are summarized in Table 3.1-6. The results indicate that the present solar array will stand up in the high temperature range of 250°C to 350°C. Long-term (30 years) metallurgical effects in space are not known.

Table 3.1-6. Temperature Limitation on GaAs Solar Cell Array Elements

CHARACTERISTICS	FAILURE TEMPERATURE RANGE
DEBONDING OF SOLDERED LEADS	300°C - 460°C
DELAMINATION OF CELL FROM SUBSTRATE	180°C - 400°C (MELTING, BUBBLING, AND DARKENING)
DEGRADATION OF COVER ADHESIVE	300°C - 520°C
DEGRADATION OF CELL ELECTRICAL PARAMETER	250°C - 350°C*
DEGRADATION OF CELL COVER	>430°C

*BASED ON THREE-LAYER STRUCTURE, GaAlAs/GaAs (BOTTOM LAYER = 200-350 μm N-TYPE GaAs, MIDDLE LAYER = 1 μm, ZINC-DOPED P-TYPE GaAs, AND TOP LAYER = <1-μm-THICK ZINC-DOPED, P-TYPE GaAlAs)→POTENTIAL DEGRADATION MECHANISMS: (1) ZINC DIFFUSION FOR THE ZN-DOPED P-LAYER INTO N GaAs; (2) ALUMINUM DIFFUSION FROM LPE GROWN TOP LAYER INTO SUBSTRATE; AND (3) ARSENIC EVAPORATION.

REFERENCE: NASA-CR-158491, Long-Term Temperature Effects on GaAs Solar Cells, April 1979.

3.1.6 OPTICAL FILTERS (α FACTORS)

Lower values of α can cause cells to run cooler in space, with subsequent increases in cell output. By a combination of UV filter and back surface reflectors (BSR), it is estimated that α's ≤ 0.61 can be achieved with an ultimate value of 0.56 (Reference 4).

Parametric data were generated to show relative sensitivities for the sandwich solid-state concept to α values ranging from $\alpha = 0.546$ to $\alpha = 0.85$. A block diagram of the model used in generating the parametric data is shown in Figure 3.1-11. This figure also shows values of the power density (PR) of the antenna, power onto the solar cells (P_{IN}), effective concentration ratio (CR_E), antenna area ratio to power delivered at the utility (AT/P_{UT}), and the power delivered (P_{UT}). Solar cell temperature is fixed at 200°C, and the maximum antenna radiating surface temperature is 125°C.

Mass comparison for selected absorptivity values showed that increasing α from 0.546 to 0.85 adds 7.1 kg/kW$_{UI}$. The following mass factors (kg/m^2) were used: structure, 0.0087; reflector, 0.0192; antenna panels, 3.293;

α	0.61	0.56	0.546	0.78	0.85
P_R (W/m^2)	669.2	741.3	761.8	504.5	453
P_{IN} (W/m^2)	6684	7404	7609	5039	4524
CR_E	4.94	5.47	5.62	3.72	3.34
A_T/P_{UT} (m^2/kW)	2.437	2.20	2.142	3.234	3.603
P_{UT} (GW)	1.091	1.157	1.162	0.933	0.872
A_{REFL} (km^2)	82.75	87.7	88.1	70.7	66.1

SOLAR CELLS

P_R — P_{IN}

$CR_E = P_{IN}/S$

DC/RF ELEMENTS

SANDWICH

P_T — ANTENNA ARRAY — DC/RF — FEEDERS — • — UV DEGR. — ARRAY DESIGN — PKG. FACT. — $\eta(T)$ — P_{IN} — CONC. DEGR. — ARRAY DESIGN

0.75   1.0   1.0   .1335

P_T — BEAM EFF. & ATMOS — RECTENNA ARRAY — DISTRIBUTION/ CONDITIONING — P_{UT}

0.744   0.88   0.936

0.613

$T_S = 200$ C
$T_R = 125$ C

Figure 3.1-11.   Optical Filters Parametric Data (Sandwich)

secondary structure, 0.128; and solar cells, 0.252. The attitude control, information management system, and mechanisms were held constant. The major mass factor impacting the comparison is atennna panel mass of 3.293 kg/m^2. It should be mentioned that the reference klystron baseline (Exhibit C) mass is 6.65 kg/kW$_{UI}$ for the total satellite. With an α = 0.61 and using antenna panels = 1.0 kg/m^2, total solid-state satellite mass = 8.12 kg/kW$_{UI}$.

Cost comparison for selected absorptivity values showed that increasing α from 0.546 to 0.85 adds $1587/kW. The cost model for the comparison is as follows: structure = $27.92/kg, reflector = $1.244/m^2, antenna panels = $624.1/m^2, IMS (antenna) = $70.9/m^2, mechanical/secondary structure = $103.2/kg, solar cells = $57.66/m^2, and transportation = $61.6/kg (GEO). The attitude control and IMS (on the solar array) were held constant. The major cost factor impacting the comparison is the antenna panel cost of $624.1/m^2. The comparable baseline klystron satellite cost (Exhibit C) = 1176/kW$_{UI}$. With an α = 0.61 and using an antenna panel = $200/m^2, the satellite cost = $1045/kW$_{UI}$. Based on this analysis, the use of reduced solar cell absorptivity values is very cost effective and should be incorporated into the satellite design. To be competitive with klystrons, it appears that the solid-state sandwich concept must be developed with an antenna specific mass of ~1.0 kg/m^2 at a cost of ~$200/m^2.

3.1.7 REFLECTOR POINTING REQUIREMENTS (SANDWICH CONCEPT)

Rockwell is currently using ±0.5 degree pointing error for both primary reflector and secondary reflector. There are eight primary mirror facets in the Rockwell sandwich design (Figure 3.1-12). The sun-angle misorientation has greater effect on Reflectors 6, 7, and 8 than on Reflectors 1, 2, and 3 due to the local focal length difference. Full concentration by mirrors will occur within the disk of the mirror with the shortest local focal length; the least concentration is within the disk of the longest local focal length. Unlike the V-trough reference concept, the displacement power loss due to the pointing error cannot be compensated simply by oversizing the reflectors.
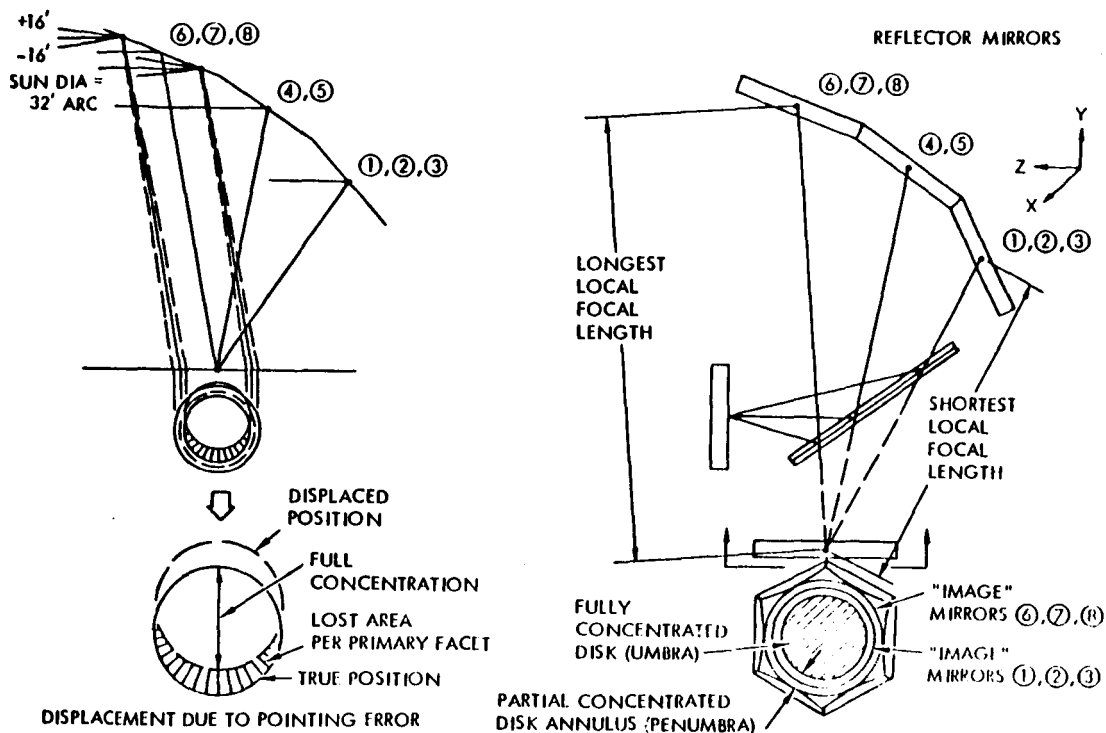
Figure 3.1-12. Pointing Error of Sandwich Concept

The optical system is derived from a Newtonian telescope. The Newtonian paraboloidal primary has been replaced by eight flat mirror facets tangent to a paraboloid of desired focal length. The Newtonian flat secondary is retained. A solar cell blanket replaces the Newtonian eyepiece at the primary focal point. The properties (aberrations, focal length, etc.) of the optical system shown are similar to those of a classical Newtonian telescope, especially for rays that are incident to the primary at the facet tangent points.

A ray trace program has been developed for the Hewlett-Packard 9845 desktop computer to analyze the optics. The program is a modified geometrical ray trace analysis that is published in MIL-HDBK-141, *Military Standardized Handbook, Optical Design*. The program permits a ten-facet primary, with or without a secondary, and an "image" surface to be randomly located. The image surface and secondary mirror are assumed fixed after preliminary location is

defined. The relative earth-scan/sun-track motions are followed by Euler EY, EX angles noted. The EY Euler angle reproduces daily orbit motion around the earth (EY parallel to earth N/S polar axis) and earth motion around the sun. The auxiliary EX Euler angle provides declination motion to follow the sun ±23.5 degrees relative to the equatorial plane.

The program stores, on cassette tape, optical configuration data; prints optical configuration, ray trace, and projection of image (solar cell field outline) on mirrors data; and plots configuration and ray trace diagrams. Figures 3.1-13 and 3.1-14 illustrate computer or printouts for ray traces of the configuration for a view direction of 0 degrees and 45 degrees.
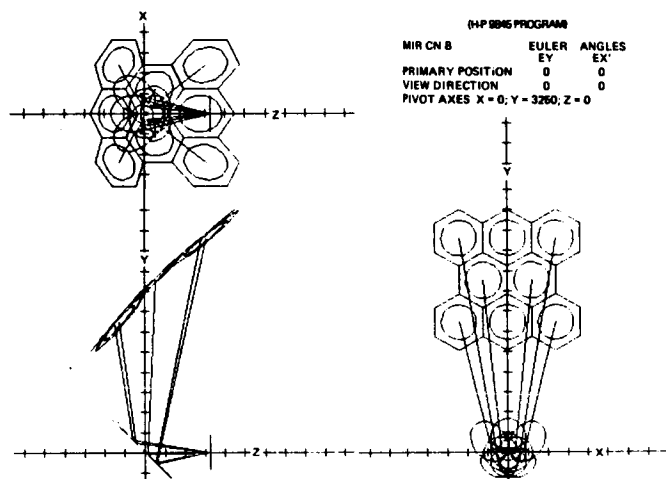
Figure 3.1-13. SPS Ray Trace Diagrams—View Direction, 0°
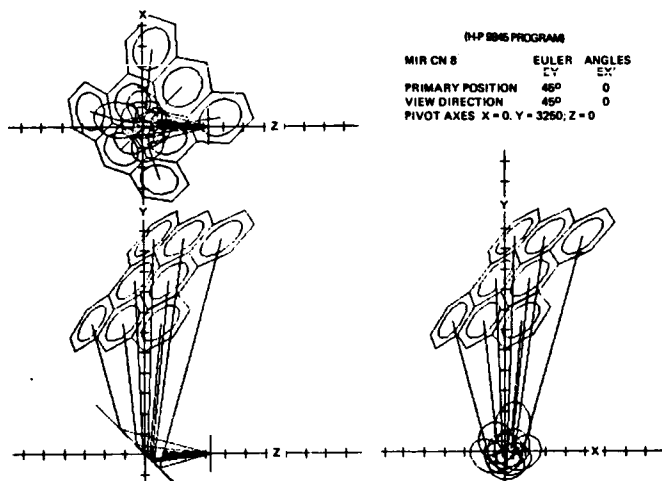
Figure 3.1-14. SPS Ray Trace Diagrams—View Direction, 45°

The concentration ratio impact on solar array orientation requirements is shown in Figure 3.1-15. Sun pointing error is a critical design parameter of the solar concentrator system; the pointing error sensitivity is dependent on the CR and optics alignment. For CR = 2 (V-trough), the power loss can be compensated by increasing the reflector size. For the eight primary mirror facets, CR = 7.8 (solid-state dual sandwich concept), an average 50% oversizing of the eight primary reflector facets is required to compensate for the comatic aberration of a large view angle relative to the axis of the primary mirror parabolic shape (even when faceted).

CR	POINTING ERROR (DEG)	POWER LOSS (%)
1	4.0	0.2
2	1.0 (MIN REFLECTOR)	1.6
2	1.0 (8% INCREASE IN REFLECTOR SIZE)	0
7.8	0.1	1.4
7.8	0.5	7.1
7.8	1.0	14.4

• CR = 1, NO ATTITUDE OR FIGURE CONTROL PROBLEMS

• CR = 2, 8% INCREASE IN REFLECTOR SIZE RESULTS IN 100% COLLECTOR EFFICIENCY WITHOUT ACTIVE FIGURE CONTROL

• CR = 7.8, 50% OVERSIZE IN REFLECTOR IS BUILT TO COMPENSATE THE 23.5° SEASONAL SUN ANGLE VARIATION
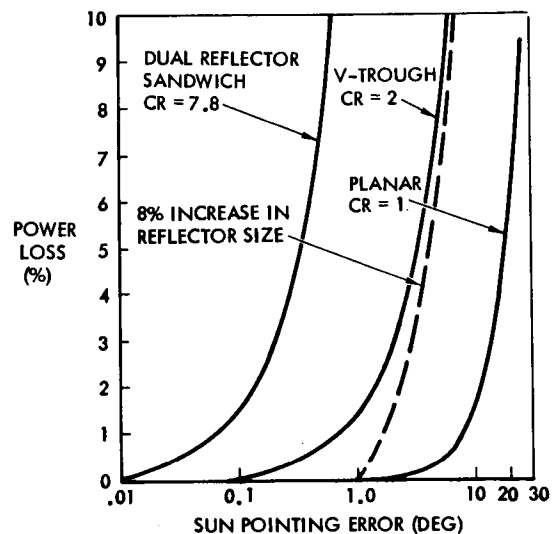
Figure 3.1-15. Concentration Ratio Impact on Solar Array Orientation Requirements

The pointing error versus power loss is summarized in the table of Figure 3.1-16. The overall power loss (directly proportional to the effective solar array area) can be obtained by superimposing the (1) average effective loss of the eight primary reflectors, and (2) effective loss of the secondary. The calculation shows a 7.1% power loss by using ±0.5 degree misorientation for both primary and secondary reflectors. The Rockwell solid-state dual sandwich concept has oversized (about 50%) each eight primary reflectors facets in order to compensate for the comatic aberration effect from its parabolic shape.

The reference klystron concept (CR = 2) attitude control holds the configuration to ±0.1 degree. The solar array is sized at summer solstice for maximum sun inclination angle in the north-south direction. During other seasons of the year, this allowance could be utilized to reduce pointing requirements, i.e., up to about ±2 degrees.

POWER LOSS VS POINTING ERROR

OPTICS BEAM TRACE
OF REFLECTOR #6 OR #8

GEOMETRIC CR = 7.8 EFF. CR = 5.37	POWER LOSS (%)		
POINTING ERROR (DEGREE)	$\pm0.1^0$	$\pm0.5^0$	$\pm1^0$
MIRROR #1 OR #3	1.1%	5.52%	11%
MIRROR #2	1.06%	5.34%	10.7%
MIRROR #4 OR #5	1.56%	7.8%	15.6%
MIRROR #7	1.54%	7.6%	15.4%
SECONDARY MIRROR	0.13	0.6%	1.3%
TOTAL (AVG.)	1.4%	7.1%	14.4%
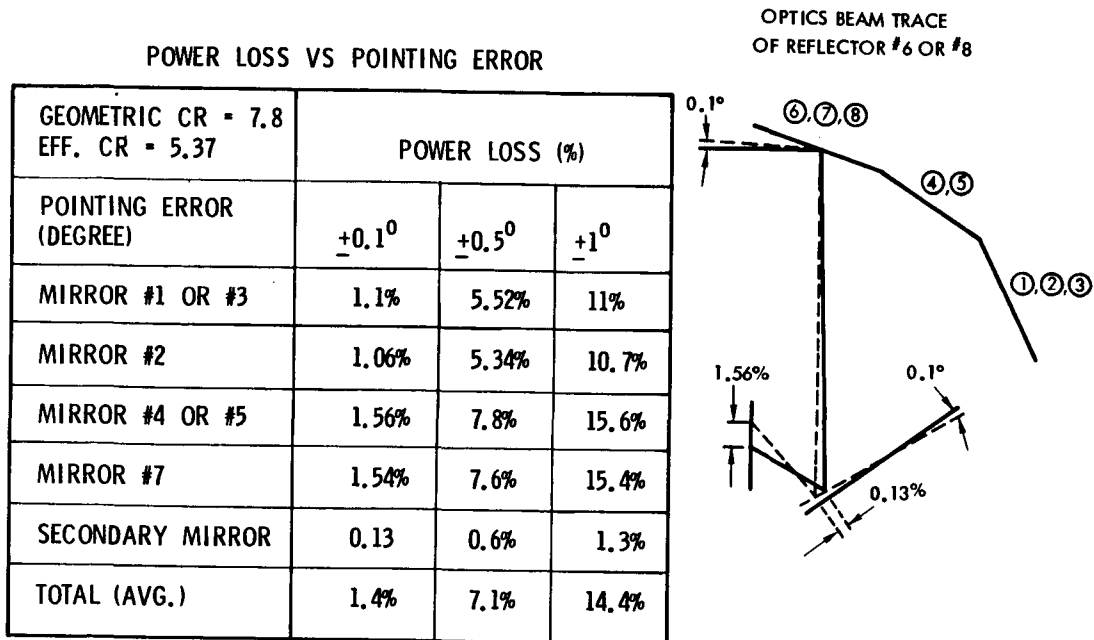
Figure 3.1-16. Pointing Error Sensitivity

3.2 POWER DISTRIBUTION

Additional analyses and evaluation of the power distribution were made on candidate SPS concepts to minimize mass and determine specific mass of power distribution. The dc converter system trades for the solid-state concept were described in Section 2.3.2. The detailed results of the analysis of dc converter technology assessments and power distribution masses are presented below.

3.2.1 DC CONVERTER TECHNOLOGY ASSESSMENT

As part of an overall system conceptual design study, Rockwell International Corporation subcontracted with Westinghouse to study the power distribution subsystem (PDS) with major emphasis on power conditioning of the Satellite Power System (SPS). The results of this study are presented below (see Reference 5).

The power conditioning portion of the vehicle functions to provide a power conditioning interface between the dc power collected by the solar cells and the transmitter loads which ultimately generate the microwave energy transmitted to the earth. Because the power level is formidable, the system must be divided into modular sections in some fashion. One of the objectives of this study is to establish the direction in which the module size should move to best meet system goals.

Because the entire space vehicle must be constructed from parts launched into earth orbit, size and weight per kilowatt of output are important figures of merit. In general, PDS optimizations can be made using these criteria

3-17

because they are intimately related to system economics. One of the goals of this study is to determine if the initial Rockwell estimate of 0.197 kg/kW for high-voltage converters is reasonable (Reference 6). Efficiency of the power conditioning equipment is also an important parameter. Because component cooling in space is costly, efficiency impacts system economics directly. A second goal of this study is to see if the initial efficiency estimate of 96% for the dc converters is reasonable.

Results were derived based on an assumption of using 1990 technology. Present technology was examined to see how well it could be utilized to meet system goals. Component technology was projected to the 1990 time frame, and an estimate of the improvement in system performance made. Necessary improvements in technology which must occur if desired system goals are to be met are also listed and discussed.

In addition to considerations of normalized weight and efficiency, the goals of the study include consideration of specific volume (m^3/kW) and dc switch gear requirements. However, because of funding constraints, very little was done in either of these areas.

In this study, the major emphasis was placed on power electronic circuit concepts for very high power using extrapolations from industrial and utility equipment. When estimating normalized weights for the systems, some allowance was made for the additional weight of structure needed for space-qualified apparatus, but the estimates were only rudimentary. Therefore, subsequent studies should further refine the weight of structure needed to mount and support the circuit components found to be required in this study.

The subject of component cooling suitable for space hardware was addressed only briefly in this work, owing to a lack of experience among the Westinghouse investigators regarding this technology. In general, the emphasis was placed on determining component weight with an additional approximate factor applied for structure and cooling. This subject needs further in-depth study by people skilled in the use of this technology.

System Configurations Evaluated

Three different SPS power distribution system concepts were studied. The basic parameters of two klystron system concepts and one solid-state system concept are listed in Table 3.2-1.

Klystron Power Distribution Concept

Solar array segments are connected in a series/parallel arrangement to form a single dc bus at a voltage of 40 kV. The power distribution system conditions and converts power drawn from the 40-kV bus to make available power for the loads at 8, 16, 24, 32, and 40 kV. Two system configurations were studied to implement this concept.

Baseline Klystron System

As shown in Table 3.2-1, output power in this concept is drawn in equal amounts at all five voltage levels.

Table 3.2-1. System Configurations Evaluated

- Klystron System

System	Input Power 40 kV	Output Power Distribution				
		8 kV	16 kV	24 kV	32 kV	40 kV
Baseline	100%	20%	20%	20%	20%	20%
Alternate	100%	5%	5%	5%	5%	80%

- Solid State

System	Input Power 20 kV	Output Power Distribution 200 V
Baseline	100%	100%

Alternate Klystron System

As shown in Table 3.2-1, 80 percent of the power in this concept is utilized at an output voltage of 40 kV, while the remaining 20 percent is divided equally between the 8-, 16-, 24-, and 32-kV levels.

Solid-State Power Distribution Concept

For the realization of this concept, the series/parallel array connection yields a bus voltage of 20 kV. Output power is utilized over a range of 30 to 500 V, although a given system will use a single, fixed output voltage. In order to simplify the analysis, a baseline solid-state system with an output voltage of 200 V was assumed. Systems in this range with output voltages other than 200 V will be considered as extrapolations of the 200-V system.

Source Characteristics

For the purposes of this study, very little is known about the characteristics of the source except that it is derived from an extensive series/parallel connection of solar photovoltaic cells. From the nature of the solar cell I-V characteristics, it can be inferred that the source is short-circuit current limited at about 120% of rated load current. This means that if all of the power transmitted (9.23 GW was used for this study) on the satellite is distributed via a single 40-kV bus, its rated current must be 230,000 A, and its short-circuit current capability approximately 276,000 A. Although no data are available, it can be assumed that the source contains considerable inductance because of the long distance over which most of the power produced by the solar cells must be carried to get to the loads.

Load Characteristics

For the klystron system concept, klystron tube transmitters will be the principal loads. Although they are more complex, the klystron loads at the various voltage levels will be considered to be resistive for the purposes of this study. The details of the interactions between the PDS and the klystron loads should be investigated in future studies. Similar considerations apply to the loads for the solid-state system concept.

General Considerations

In approaching the design of power conditioning equipment for any high power application, a number of basic considerations influence the concepts regardless of the specific application. Most of these considerations arise directly from the inevitable necessities of both series and parallel connection of semiconductor switching devices to achieve the voltage and current capabilities needed in the equipment, but some arise because of certain fundamental properties of passive components, particularly inductors and transformers.

Switching Device Considerations

Direct parallel connection of semiconductor switches present many difficulties. Apart from the obvious problems attending the steady-state current sharing in such a situation, current distribution at switching can be a major problem. Thyristors are particularly prone to problems at turn on, and transistors at turn off. Most problems can be avoided if converters, rather than switches, are parallel-connected. In the case of dc-to-dc converters of any genre, parallel connection immediately creates the possibility of polyphase operation to reduce filter requirements—an added benefit. In effect, a harmonic neutralized dc-to-dc converter reduces the filter capacitance required by N^2, where N is the number of phases (converters) combined, and reduces the inductance subject to dc magnetization by the same factor. The inductance removed is substituted, in interphase reactors, by components with symmetrical flux swings which can make full use of magnetic material capabilities. In dc-to-ac inverters, the first step is invariably to use three-phase units as basic building blocks, effectively parallel-connecting three devices and saving ~22% in transformer magnetic material. Operation of phase-staggered three-phase converters for harmonic neutralization yields benefits in the interfacing filters, both dc and ac, of the same order as those obtained in the dc-to-dc converters.

Series connection of thyristors and diodes is routinely accomplished, in several application areas, to voltage levels of several tens to a few hundred kV. Transistors have not been so treated, having failed to penetrate high power application areas to date. Despite the relative ease with which series strings are made, consideration should be given to series connection of converters rather than devices when the option is available. For dc-to-dc converters, it almost never is, since it demands either isolated supplies, isolated loads, or both. For dc-to-ac converters, the option almost always exists since transformer coupling affords the necessary isolation. Whether it is excercised or not, depends on the designer's perception as to "optimum" power level for an individual converter.

3-20

Passive Component Considerations

The question of "optimum" power level, for any converter, is a difficult one since it introduces many non-device related parameters. The most significant in the majority of cases are those pertaining to magnetic components, inductors, and transformers. Such components show pronounced economies of scale, since from a fundamental viewpoint

Power rating	α	ℓ^4
Volume, weight, and cost	α	ℓ^3
	α	$(\text{Rating})^{0.75}$
Permitted losses	α	ℓ^2
	α	$(\text{Rating})^{0.5}$

where ℓ is a linear dimension of the component. These relationships are not inherently dependent on operating frequency, but secondary considerations make for a dependence. The size, weight, and cost of a given component do not indefinitely continue to decrease with increasing operating frequency, but reach minima at a frequency which decreases with increasing component rating.

Module Size Considerations

It is generally true that for the conversion of X watts, the optimum converter size is X watts so far as passive components are concerned—no matter whether X = 1 or X = 10^{10}. However, for X > 10^9, practical considerations forbid such an approach—such large components are not yet manufacturable. Below this, practical considerations may still cause a designer to use some number of lower power modules. In part, the switch considerations first discussed will influence the decision; both parallel and series connection of devices result in extra cost and weight over the straightforward use of individual devices, producing an apparent tradeoff. It is not, however, a real tradeoff in most instances since passive component benefits generally far outweigh device penalties.

Thus, in high power applications, the passive component considerations drive the designer to use the highest possible module power consistent with other application constraints. These may include individual piece weight and volume restrictions (which are basically the reason that 10-GVA transformers have not as yet been made), system partial availability requirements, the fractionation of sources and loads, assembly and test problems in existing facilities, and so on.

Given this premise, the conversion of 10 GW, for either klystron or solid-state microwave generators, should be accomplished with as few converters as feasible within the practical constraints of the application and the switching devices used. Such a system will not operate at internal conversion frequencies of several tens of kHz, or even at several kHz, contrary to present practice where power levels are six orders of magnitude (and more) lower. However, it will be far lower in total weight and cost, have far higher an efficiency, and be far more reliable than any attempt to use 10^6 converters each of 1-kW rating.

Klystron System Analysis

Two basic configurations were considered for the PDS with klystron loads. These are shown in the block diagrams of Figures 3.2-1 and 3.2-2.

Total Power 288 MW
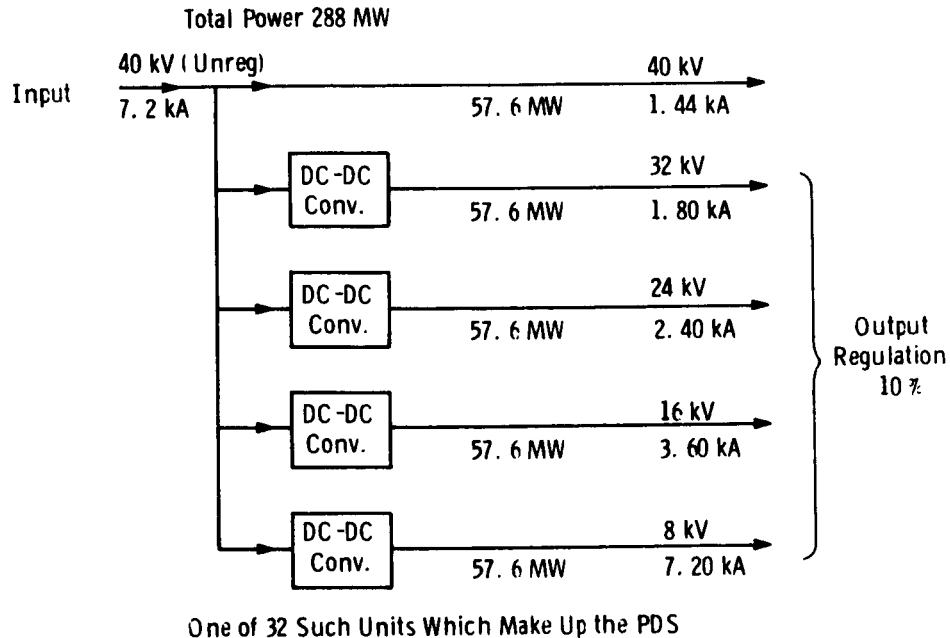
Figure 3.2-1. Klystron Baseline System

Total Power 288 MW
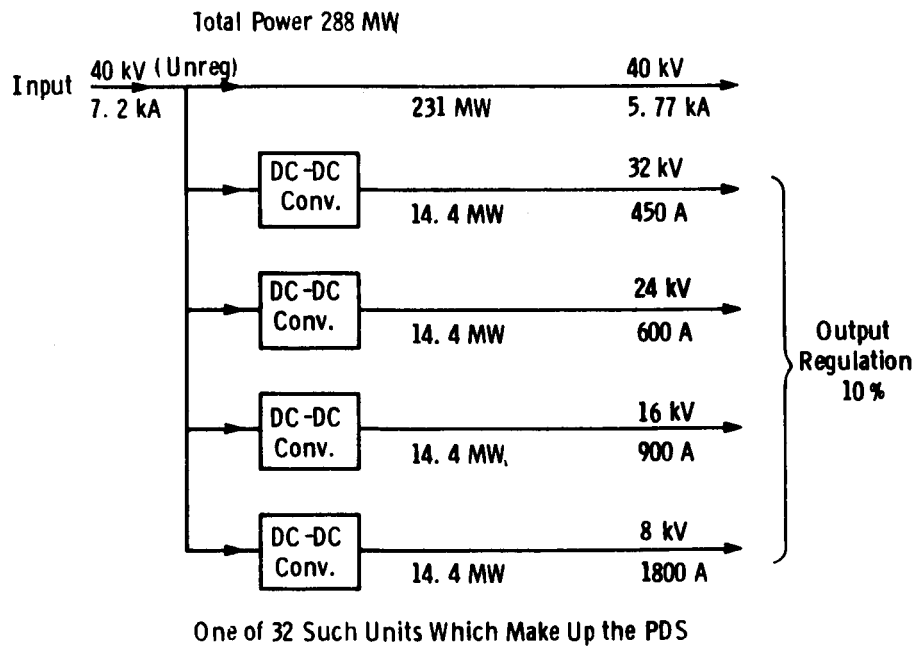
Figure 3.2-2. Klystron Alternate System

In the overall system configuration, the total input power of 9.23 GW is subdivided into 32 identical power conditioning modules of the type shown in the figures. Each of these is connected to the 40-kV dc input bus, and each serves dedicated klystron loads. The two system concepts differ only in the partitioning of power at the various levels of output voltage. Because of the power drawn at the 40-kV level is not conditioned, some saving in overall system weight appears to be possible using the system where a larger percentage of the output power is consumed at the 40-kV level.

The purposes of this study are to estimate normalized power converter weight and to estimate overall power converter efficiency. Because the power converters used in either of the two systems will differ little in design, a single power converter analysis and technology projection will be made which applies equally well to the converters of either system on a normalized basis. The differences in overall PDS normalized weight can then be handled by consideration of the partitioning of the conditioned, as opposed to unconditioned, power.

Design Using State-Of-The-Art Technology

In this section, a design will be described using state-of-the-art (SOA) technology. The dc-to-dc converters designed will be of the type used in the system configurations shown in Figures 3.2-1 and 3.2-2, but they will not be of the correct power level. Instead of designing converters rated at the power levels called for in the figures, designs will be made which best exploit the performance of SOA devices and components. The designs are for converters operating at an input voltage of 40 kV and at output voltages of 8, 16, 24, and 32 kV. The results of the design calculations will show appropriate module power ratings for converters operating at these levels using SOA technology.

The converter switching device weight estimates will be based on recent experience with arrays of series-connected thyristor switching devices constructed to operate at utility transmission voltages in industrial and utility applications.

The dc-to-dc converter circuit assumed for this design is shown in Figure 3.2-3. It does not utilize coupled output reactors or multiphase operation.
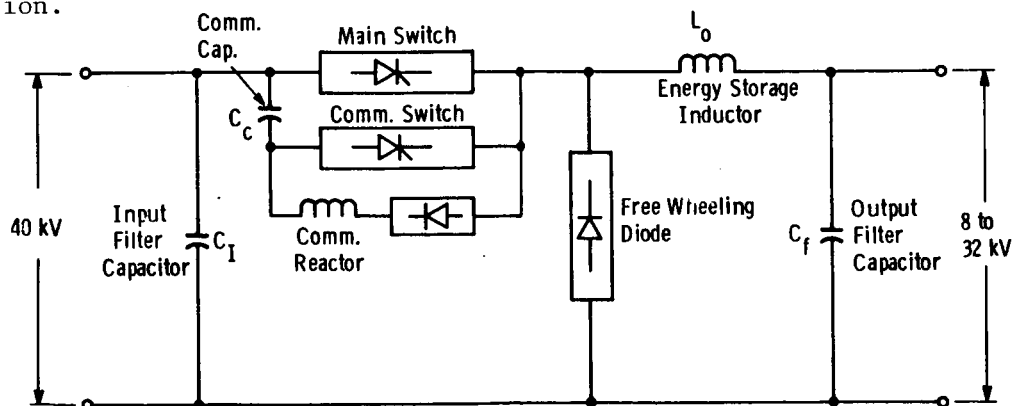
Figure 3.2-3. Basic DC-to-DC Buck Converter Circuit

Switches and Diodes

An assembly of 96 thyristors on a frame with insulators, heat sinks, plumbing, snubbers, and gate drive weighs 523.6 kg. Allowing for lower voltage capability of fast switching devices, 2×48 devices in series would comfortably make a switch for 40 kV dc-to-dc or dc-to-ac converter (active switch and commutating switch). A second frame (similar) is needed for diodes, freewheel, and commutating. Control for such an arrangement is estimated at 113.6 kg (250 lb). Total weight for a buck dc-to-dc converter switch assembly is then 637.3 kg (1402 lb).

Allowing a fast switch device drop of 2 V at 1000 A (typical of current production) and a device average loss of 800 W with liquid cooling, the average current allowed is

I_{av}	Duty Cycle	I_{peak}
300 amps	0.2	1500 A
400 amps	0.4	1000 A
450 amps	0.6	750 A
500 amps	0.8	625 A

giving powers in single converter branches of

12 MW @ 8 kV out
16 MW @ 16 kV out
18 MW @ 24 kV out
20 MW @ 32 kV out

when fed from a 40-kV source. Switch and control specific weights at the various output voltages are, then, 0.0530, 0.0398, 0.0353, and 0.0318 kg/kW; and the average if the same power is processed at all four voltages is 0.0399 kg/kW.

The remainder of the circuitry includes commutating capacitors, commutating inductors, filter inductors, and filter capacitors. With 40 µs devices (typical of present large fast switch production), the maximum operating frequency will be about 1500 Hz.

Commutating Capacitor

Simple commutating circuit design gives

$$C V_s = \hat{I} t_q$$

For V_s = 40 kV and $\hat{I}$ from the table, t_q 40×10⁻⁶ gives for the commutating capacitor

$$C_{c.2} = \frac{1500 \times 40}{40,000} = 1.5 \ \mu F$$

$$C_{c.4} = 1 \ \mu F$$

$$C_{c.6} = 0.75 \ \mu F$$

$$C_{c.8} = 0.625 \ \mu F$$

all at, say, 50-kV rating. Energy storage requirements are $(1/2 \ CV^2)$ 1875, 1250, 937.5, and 781.25 joules. From a GE commutating capacitor catalog data, paper oil capacitors at 2000 V have a volume and weight of $\simeq 4 \ in^3$/joule and ~0.28 lb/joule. At 50 kV, it will be somewhat bigger and heavier, inevitably—say by a factor of 1.5—giving estimated specific commutating capacitor weights of 0.030, 0.015, 0.010, and 0.008 kg/kW; average 0.016 kg/kW.

Commutating Reactor

For the commutating reactor to reverse the capacitors in 80 μs, say, so that minimum on and off times are comparable, gives

$$\pi = \omega \times 80 \times 10^{-6}$$

$$\omega = 1/\sqrt{LC} = 10^6 \ \pi/80$$

$$LC = 80^2/10^{12}\pi^2$$

giving $L_{c.2}$ = 430 μH (.163 Ω @ 60 Hz)

$L_{c.4}$ = 650 μH (.244 Ω @ 60 Hz)

$L_{c.6}$ = 865 μH (.326 Ω @ 60 Hz)

$L_{c.8}$ = 1040 μH (.39 Ω @ 60 Hz)

Peak inductor currents are $V_S/\sqrt{L/C}$, V_S = 40 kV, or

$$\hat{I}_{.2} = 2360 \ A$$

$$\hat{I}_{.4} = 1570 \ A$$

$$\hat{I}_{.6} = 1180 \ A$$

$$\hat{I}_{.8} = 980 \ A$$

Because of loss considerations, designs would use non-metallic or hollow (air) cores, like current-limiting reactors and without much easement for duty cycle. From a Westinghouse catalog, 15 kV class reactors are as follows:

$$0.165 \ \Omega \ @ \ 2000 \ A \qquad 1700\#, \ 76,600 \ in^3$$
$$0.255 \ \Omega \ @ \ 1600 \ A \qquad 1600\#, \ 72,650 \ in^3$$
$$0.45 \ \ \Omega \ @ \ 1200 \ A \qquad 1300\#, \ 64,800 \ in^3$$
$$0.45 \ \ \Omega \ @ \ 1000 \ A \qquad 1200\#, \ 52,500 \ in^3$$

giving estimated commutating reactor weights of 0.0644, 0.0455, 0.0328, and 0.0273 kg/kW, average 0.0425 kg/kW.

Filter Reactor

For the filter reactor design, assume a ripple current peak to peak of 20% of the output level, which is the peak switch current. The volt seconds are $(V_s - V_{out}) \ Dt$, where D is duty and t is cycle time. Because $V_{out} = DV_s$, the volt-seconds are $V_s t \ (D-D^2)$. Assuming 1500 Hz operation, $V_s t = 40,000/1500 = 400/15 = 80/3$.

The reactor volt-seconds are then 4.27, 6.4, 6.4 and 4.27 for D=0.2, 0.4, 0.6, 0.8 with I=1500, 1000, 750, and 625 A. Peak-to-peak ripples are then 300, 200, 150, and 125 A, giving inductances of

$$L_{0.2} = \frac{4.27}{300} \ H = 14.23 \ mH \quad (5.37 \ \Omega \ @ \ 60 \ Hz)$$

$$L_{0.4} = \frac{6.4}{200} \ H = 32 \ mH \quad (12.06 \ \Omega \ @ \ 60 \ Hz)$$

$$L_{0.6} = \frac{6.4}{150} \ H = 42.67 \ mH \quad (16.08 \ \Omega \ @ \ 60 \ Hz)$$

$$L_{0.8} = \frac{4.27}{125} \ H = 34.16 \ mH \quad (12.88 \ \Omega \ @ \ 60 \ Hz)$$

These are akin to shunt reactors with ratings of $2\pi 60 \ L$ ($\Omega \ @ \ 60 \ Hz) \times I^2$.

These ratings are

$$VAL_{0.2} = 5.37 \times 1500^2 = 12.08 \ MVA$$

$$VAL_{0.4} = 12.06 \times 1000^2 = 12.06 \ MVA$$

$$VAL_{0.6} = 16.08 \times 750^2 = 9.05 \ MVA$$

$$VAL_{0.8} = 12.88 \times 625^2 = 5.03 \ MVA$$

The catalog does not give sizes and weights for shunt reactors, but taking $/lb to be the same as large current-limiting reactors yields weights of about 2454.5 kg (5400 lb) for 12 MVA, 2318.2 kg (5100 lb) for 9 MVA, and 2136.4 kg (4700 lb) for 5 MVA, giving specific weights of 0.205, 0.153, 0.129, and 0.107 kg/kW, average 0.149 kg/kW.

Output Filter Capacitor

For the output filter C_f, assume that 1% ripple V is sought, i.e., 80, 160, 240, and 320 volts. Then, with 1500-Hz operation, capacitor values needed become

$$C_{f.2} = 200 \text{ } \mu F - 8 \text{ kV (10 kV rating)}$$

$$C_{f.4} = 66 \text{ } \mu F - 20 \text{ kV rating}$$

$$C_{f.6} = 33 \text{ } \mu F - 30 \text{ kV rating}$$

$$C_{f.8} = 21 \text{ } \mu F - 40 \text{ kV rating}$$

Weights estimated from the GE paper oil dc filter capacitor catalog are 840, 1100, 1400, and 1570 pounds for specific weights of 0.0318, 0.0313, 0.0354, and 0.0357 kg/kW, average 0.0336 kg/kW.

Input Filter Capacitor

For the input filter C_I, the amp-sec are $(\hat{I} - I_{av}) \text{ } Dt$

$$= \hat{I}_t \text{ } (D-D^2)$$

$$AS_{.2} = 0.16$$

$$AS_{.4} = 0.16$$

$$AS_{.6} = 0.12$$

$$AS_{.8} = 0.0667$$

Allowing 5% ΔV, with $C\Delta V = I_t$ (amp-sec) yields input filter C's of 80, 80, 53.5, and 33.3 μF at 50 kV with weights of 8960, 8960, 6000, and 3740 pounds for specific weights of 0.339, 0.255, 0.152, and 0.085 kg/kV, average 0.208 kg/kW.

Converters Weight Summary

Relying on array inductance so that input filter inductance is not required, state-of-the-art simple thyristor buck converter average weights are:

Switching devices	0.0399 kg/kW
Commutating capacitors	0.016
Commutating capacitors	0.043
Output filter inductors	0.149
Output filter capacitors	0.034
Input filter capacitors	0.208
Total	0.490 kg/kW

with power ratings of 12 MW at 8-kV output
                          16 MW at 16-kV output
                          18 MW at 24-kV output
                          20 MW at 32-kV output

from 40-kV input with simple converters. Polyphase can reduce weights of all
passive filter components, and possibly those of commutating components, by
adopting distributed commutation. The overall weight is likely to be ~30%
more than component total when supporting hardware (e.g., capacitor racks) is
included.

Summary of Design Results

The converter design results are summarized in Table 3.2-2, broken down
by output voltage level. The table includes estimated values for all design
parameters as well as converter module rating by output voltage level.

Table 3.2-2. Summary of Klystron Concept
SOA DC-to-DC Converter Design

Voltage	Switch I_{ar}	Switch I_p	Comm. Capacitor	Comm. Reactor	Comm. Inductor	Storage Inductor	Output Filter	Input Filter	Module Power
8 kV	300 A	1500 A	1.5 µF	430 µH	2360 A	14.23 mH	200 µF	80 µF	12 MW
16	400	1000	1.0	650	1570	32.0	66	80	16
24	450	750	0.75	865	1180	42.7	33	53	18
32	500	625	0.625	1040	980	34.2	21	33	20

A similar tabulation of estimated normalized converter weight is pre-
sented in Table 3.2-3. The line designated "average" contains data from a
converter operating at an output voltage which is an average of those shown.
By adding 30% of the weight of the components for structure, the estimated
result is 0.637 kg/kW.

Table 3.2-3. Summary of Klystron System Concept SOA DC-to-DC
Converter Normalized Weights

Voltage	Switch & Control	Comm. Capacitor	Comm. Reactor	Energy St. Inductor	Output Filter Cap.	Input Filter Cap.	
8 kV	.0530 kg/kW	.030 kg/kW	.0644 kg/kW	.205 kg/kW	.0318 kg/kW	.339 kg/kW	
16	.0398	.015	.0455	.153	.0313	.255	
24	.0353	.010	.0328	.129	.0354	.152	
32	.0318	.008	.0273	.107	.0357	.085	
Average	.0399	.016	.0425	.149	.0336	.208	= .490 kg/kW
					Supporting Structure		= .147 kg/kW
					TOTAL		= .637 kg/kW

Design Assuming 1990 Technology

Ratings. and Basic Philosophy of Converter

Examination of the power ratings of Figure 3.2-1 indicates some interesting points:

1. The required voltage levels are all multiples of 8 kV.

2. For a given PDS concept, each voltage level has the same power rating.

3. There are five levels between 8 kV and 40 kV.

From the above, a suitable control strategy for the individual dc-dc converters can be postulated; i.e., each converter will operate on a basic 5-interval time base. The number of intervals that each converter switch will be ON in the 5-interval sequence is thus directly proportional to the voltage level of its output. The required gating sequence for the individual stages is thus as sketched in Figure 3.2-4.
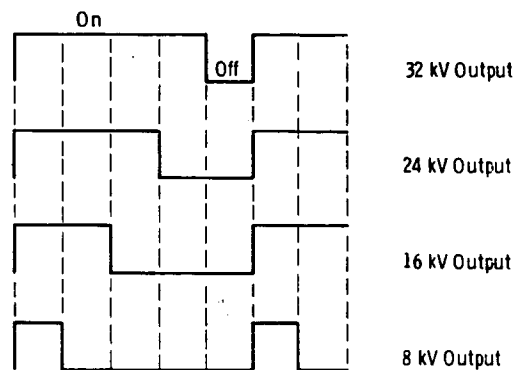
Figure 3.2-4. Basic Switching Strategy
for Multiple Levels

It is possible to consider handling the entire 57.6 MW required at each voltage level with a single channel. However, if each voltage level is broken up into five parallel channels, the individual channels can be time-multiplexed to provide considerably enhanced smoothing of the output current at each voltage level. The sequence is sketched in Figure 3.2-5, considering the 8-kV voltage level as an example. In addition, the input current to the converters will be a virtually constant 1440 A, which is sequentially "passed around" the five paralleled converters for one period of every five (Figure 3.2-6). The interleaving of the reactor currents is illustrated in Figure 3.2-7, i.e., each reactor provides a constant current of 1440 A to the load plus an ac ripple component, which depends on the choice of reactor and operating frequency. The factor of 5 reduction in the overall ripple amplitude is clearly demonstrated.
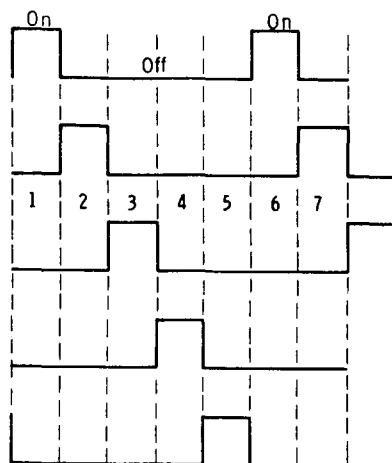
Figure 3.2-5. Five Parallel Channels with
Multiplexed Switching Sequences
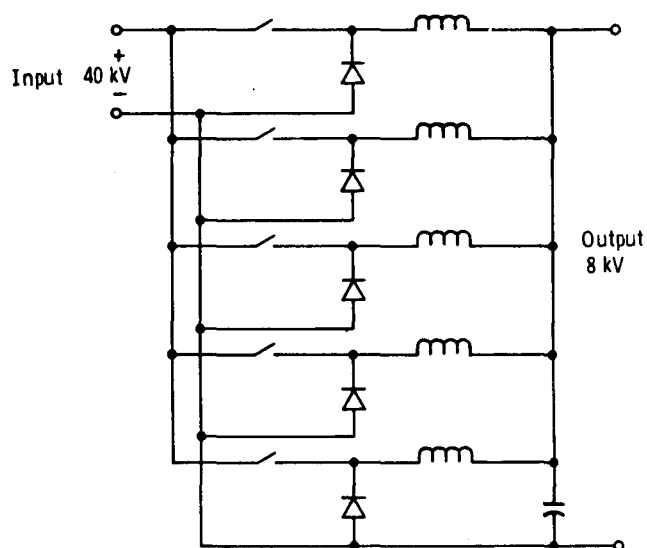
Figure 3.2-6. Parallel Connection of Five Converters
to make up One Voltage Level Converter
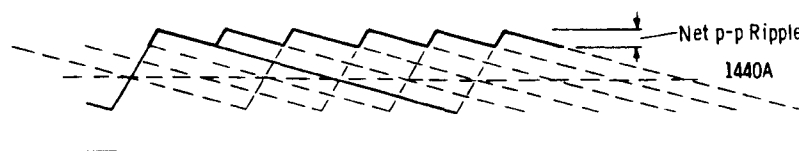
Figure 3.2-7. Interleaving of Output Currents into Five Converters

Choice of Operating Frequency and Switch

It is assumed, that in a few years time (given present devices and progress) it will be possible to develop a transistor or MOSFET which is capable of operation at 2 kV and rated at 500 A, i.e., comparable with present-day thyristors for voltage but with somewhat reduced current capability. It is also assumed that the device is capable of switching on in approximately 2 μs and off in 3 μs. With a 5:1 duty cycle, it appears that a reasonable minimum pulse width which can be considered will be around 20 μs, i.e., 10:1 ratio between turn-on and pulse width. This gives a maximum switching frequency of 10 kHz, i.e., for the 8-kV system, 20 μs on and 80 μs off. Under these circumstances, the switching waveforms for an individual parallel branch are shown in Figure 3.2-8. The waveforms are simplified and assume (for the capacitor voltage and current) a stand-alone condition for the branch.

Gating Waveforms

$$\frac{\tau_{on}}{\tau} \times 40. \, 10^3 = \frac{20}{100} \times 40. \, 10^3 = 8 \text{ kV}$$

Reactor Current

$$\delta_I = \frac{E_I - E_o}{L} \cdot \tau_{on}$$

Capacitor Current

$$\delta_{I_2} = \delta_{I_1}$$

Capacitor Voltage

$$\delta_{V_C} = \frac{\delta Q}{C} = \frac{\frac{\delta_{I_2}}{2} \times \frac{1}{2} \times \frac{\tau}{2}}{C} = \frac{\delta_{I_2} \tau}{8C} = \frac{\delta_{I_2}}{8fC}$$

Thyristor Current

Diode Current
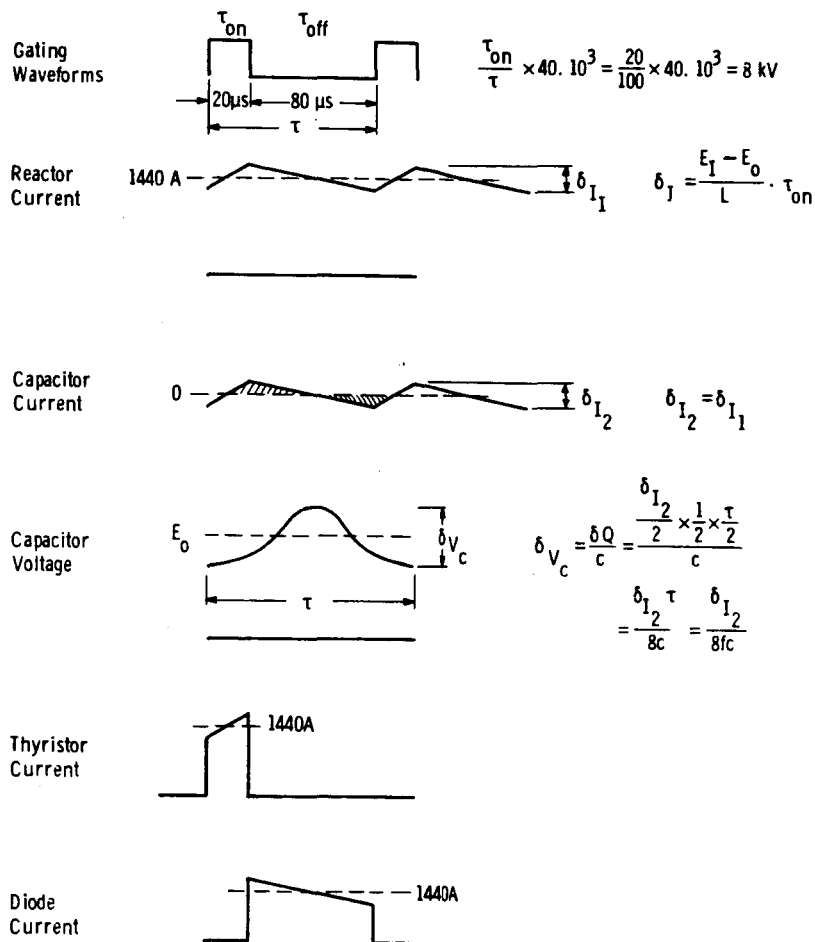
Figure 3.2-8. Typical Waveforms and Criteria (Simplified) for Conventional Stepdown DC-to-DC Converter

Choice of Inductor

The choice of inductor is fixed by operating frequency and allowed ripple. If a maximum channel ripple current of 5% is assumed, this gives approximately 72 A peak, ~144 A peak-peak of ripple current, i.e., $\delta I_1 = 144$ A. Substitution into the expression in Figure 3.2-8 and solving for L gives a required inductance of 4 mH.

Actual Output Ripple Level

The actual ripple level will depend on the mark to space ratio and will be maximum for the 8-kV level. However, the interleaving will reduce the ripple level from a maximum of 144 A p-p from one branch to approximately 28.8 A p-p with all five branches interleaved. Since the required regulation is ±10% of the combined branches and the input voltage is stabilized to within 6%, it may be possible to operate on a fixed pulse width, thus optimizing ripple. In practice, small perturbations away from the 4:1 space-mark may increase the ripple somewhat.

Choice of Capacitor

Although not specified, it is assumed that the output dc ripple voltage is to be maintained to within one percent. The relatively small ripple current already indicates a small capacitor requirement. This is confirmed by substituting into the expression in Figure 3.2-8, bearing in mind that the ripple frequency is now 50 kHz. The required capacitance is thus only 0.75 μF, though, in practice, this would probably be increased to 1 μF or more.

Physical Considerations

<u>*Simple Inductor*</u>

The current rating of the required inductor is not significant. At this energy level, the mechanical stresses involved, the dc level, and the operating frequency all militate against the use of any kind of magnetic core. Under the circumstances, it is proposed to use an "air" cored winding.

For maximum inductance with a given length of conductor, the so-called "Brooks" coil provides the optimum dimensions. The required ratios are shown in Figure 3.2-9. If we assume some form of hollow conductor, with a cooling medium circulating inside the coil and transferring heat to some external heat radiator, the choice becomes one of a suitable conductor. Obviously, reduction in conductor size, while improving the weight also puts up the losses, decreasing the efficiency. For the sake of this review we will assume a square section copper tube of one inch side and 1/8-inch wall thickness. A simple calculation

Figure 3.2-9.

Brooks Coil
Scaling

3-32

immediately reveals that the required coil dimensions are C = 9 in., and we
will have 81 turns, i.e., the coil form is 9 in. by 9 in. and it has an inside
diameter of 18 in. This requires 572 feet of copper tube and, more to the
point, will weigh 755 pounds. However, the resistance will be approximately
0.0135 Ω and the I^2R loss will only be approximately 28 kW, i.e., less than
0.25% of the branch throughput.

Capacitor

For the required capacitance, at 8 kV, it will probably be easiest to go
with an established paper-oil capacitor. The ripple current level is insignif-
icant. The energy storage is only about 32 joules and, with a typical energy/
volume ratio of 1 J/in.^{3} will require around 32 in.^{3} of volume. Since no
voltage reversal or pulse operation is required, a basic capacitor construc-
tion can be used. An oil-soaked sandwich of mylar paper and foil of about
50 in.^{3} in volume weighs about 2.5 lb, so we are considering a total capacitor
weight of something around 2 to 3 lb, including the container—i.e., negligible.
While electrolytic capacitors are traditionally used for filter applications,
their voltage ratings are relatively low (less than 1000 V). Their better
energy storage (4 J/in.^{3}) would be canceled out by the need to series several
devices.

Switch

It appears reasonable to assume that a transistor or MOSFET switch capa-
ble of 2 kV and 500 A will be physically something of the same order of size
and weight as an equivalent thyristor, i.e., around 2 inches in diameter and
1 inch high. To operate at 40 kV, around 48 devices and three chains in
parallel will be needed—i.e., 144 transistors corresponding to about 1728 lb
in weight, assuming 12 lb per device including heat sinks, voltage-sharing
components, and suppressors. Assuming approximately 2-V saturation voltage,
the total switch voltage is about 96 V. This will produce an instantaneous
loss in the chain of around 138 kW. Corresponding to an average loss for
this, the parallel branch switch at 8 kV output of 138/5 = 27.6 kW.

Cooling techniques are not yet defined. Again, it is assumed liquid
cooling is required and a weight estimate of double the device weight seems
reasonable.

Diode

The diode used at this point in the basic converter circuit must be a
fast-recovery device since, until it recovers, it presents a short circuit
to the switch. In general, present fast-recovery rectifiers are limited to
something less than 1 kV. For the purpose of this exercise, we postulate
that a 2-kV, 500-A device will be generally available. Assuming 0.7 V drop
per device, 48 devices in series and three parallel chains, this corresponds
to an instantaneous loss of 48.4 kW at 1440 A and an average loss of about
3.8 kW (again assuming the 8-kV operation level). A device and heat sink
weight of around 10 lb seems reasonable, giving a total assembly weight
(less cooling) of 1440 lb).

Coupled Reactor Circuit

The use of the coupled converter circuit of Figure 3.2-10 provides, on paper, considerable weight and volume savings as far as the reactor is concerned, i.e., replacing five separate bulky air-cored reactors with a single "iron" cored device (albeit, it has to have five limbs) and one small inductor. Since all windings are now coupled on the common five-limbed core, individual leg reset is obtained by the sequential operation of the other four channels. This provides, theoretically, no net dc in the core and thus maximum ac saving on the core. Since the stepdown ratio is 40/8 = 5:1, and there are five channels, there is an optimum condition with no net ac ripple at the combined terminal of the five-leg reactor; i.e., when operating normally, the circuit is as shown in Figure 3.2-10. The input terminal is at E, and the output terminal is at E/5 (assumed). Thus, if Switch 1 is closed, 4/5 E appears across the associated winding and, assuming a balanced magnetic circuit, each of the other windings "sees" one quarter of the flux generated by winding 1 and, hence, generates one quarter of 4/5 E, i.e., E/5. The EMF's are balanced, $I_i/5$ (average) flows in each winding, either via the switch or via the diodes as circulating current and the summing point stays at E/5.
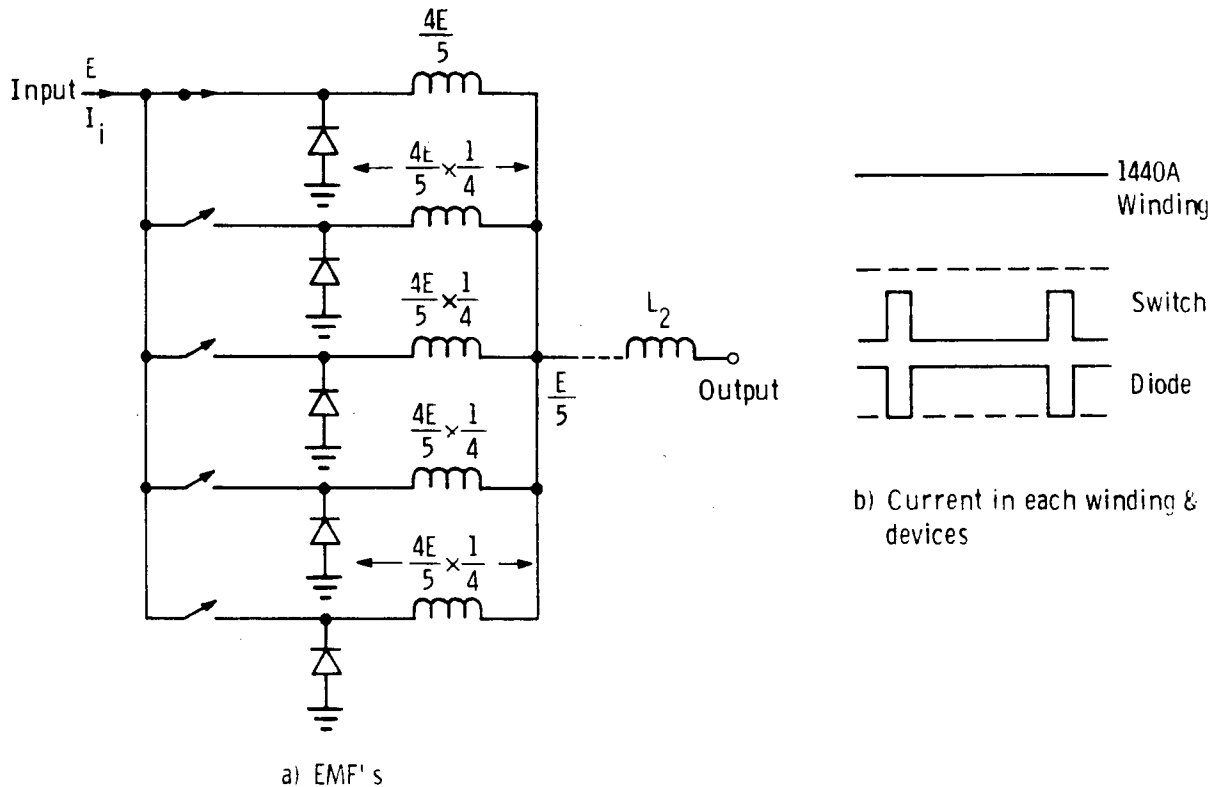
Figure 3.2-10. Ripple Cancellation with Coupled Reactors

A preliminary summary (individual reactors) is shown in Figure 3.2-11. Table 3.2-4 presents the weight and watt breakdown of individual reactors.

22175 lb

40 kV ──┬──── [938 kW] ──── 32 kV
        │   57.6 MW
        │
        │   22175 lb
        │
        ├──── [651 kW] ──── 24 kV
        │   57.6 MW
        │
        │   22175 lb
        │
        ├──── [562 kW] ──── 16 kV
        │   57.6 MW
        │
        │   22175 lb
        │
        └──── [472 kW] ──── 8 kV
                              57.6 MW
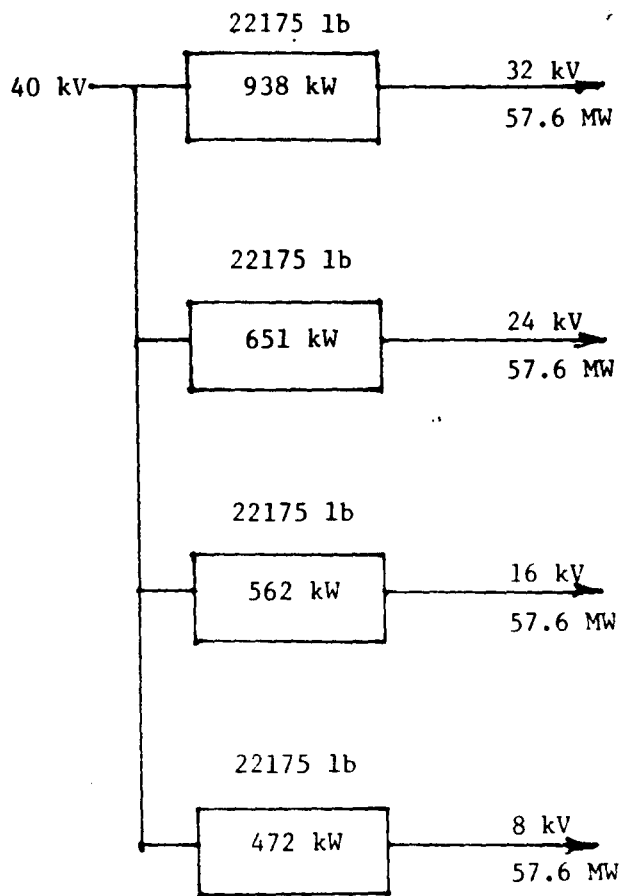
Total losses = 2.423 MW

Total weight = 88700 lb

$$\text{Eff.} = \frac{4 \times 57.6}{4 \times 57.6 + 2.423} \times \frac{100}{1} = 98.9$$

$$\text{Weight} = \frac{88700}{2.2} \text{ kg} = 40318 \text{ kg}$$

Power = 4 x 57.6 MW = 230,400 kW

$$\text{kg/kW} = \frac{40318}{230,400} = 0.175 \text{ kg/kW}$$

Figure 3.2-11. Preliminary Summary—Individual Reactors

Table 3.2-4. Weight and Watt Breakdown
(Individual Reactors)

| Channel | Watts Loss (kW) | | | | | |
| | Reactor | | Switch | | Diode | |
Channel	Per Branch	Per Channel	Per Branch	Per Channel	Per Branch	Per Channel
8 kV	28	140	27.6	138	38.7	194
16 kV	28	140	55.2	276	29.2	146
24 kV	28	140	82.8	414	19.4	97
32 kV	28	140	110.	550	9.68	48.4

Weights (lb) - Individual Reactors

| | Reactor | | 12#/Device Switch | | 10#/Device Diode | |
	Per Branch	Per Channel	Per Branch	Per Channel	Per Branch	Per Channel
Devices	755	3775	1728	8640	1440	7200
Gating & Voltage Sharing Hardware	200	1000	150	750	162	810
TOTAL		4775		9390		8010

Weight Savings by Using Coupled Reactor

The five air cored reactors of a single voltage level converter scheme (five paralleled channels) can be replaced with one five-limb interphase reactor and a small series reactor.

Preliminary calculations that indicate ten turns per coil on a 90-cm^2 core area will be adequate. The windings will be liquid-cooled as before. Copper weight is 150 lb and core weight approximately 640 lb, or 790 lb total. The small reactor will be approximately 1/25 of the size of some of the original air cored reactors (1/5 of the ripple amplitude at five times the frequency) so, to a first approximation, will be around $755/25 \simeq 30$ lb in weight. Total weight savings is thus around

$$5 \times 755 - (790 + 30) = 2955 \text{ lb}$$

However, as a note of caution, with this scheme all the five converters must operate to avoid core saturation. The five separate channels can be run independently, giving some increased reliability at reduced total power output.

Converter Efficiency

In the .circuit realizations of the klystron load systems using both SOA and 1990 technology, the power is conditioned only once. That is, it passes through a semiconductor device only once as it is regulated to the desired output level. For such systems, overall efficiencies in excess of 99% are quite possible. This value of efficiency deals only with the power conditioning equipment, and does not include busbar or conductor losses encountered in transmitting the power to the power conditioner.

Solid-State System Analysis

The power conditioning concept to be used for the solid-state system is shown in block diagram form in Figure 3.2-12. In contrast to the klystron system, the dc bus is at a potential of 20 kV. In a fashion similar to that used for the klystron concept, the total power generated (9.23 GW) is divided among 32 like power conditioners each with a rating of 288 MW. The load voltage at the output of the power conditioner can be anywhere in the range of from 30 to 500 V, but for a given system design is fixed within the range. The ratio of input to output voltage for this range of output voltages varies from 40:1 to 667:1.

Total Power-9. 23 GW

One of 32 at 288 MW Each

20 kV	667:1	30 to 500 V
288 MW	40:1	9. 6 to 0. 576 MA
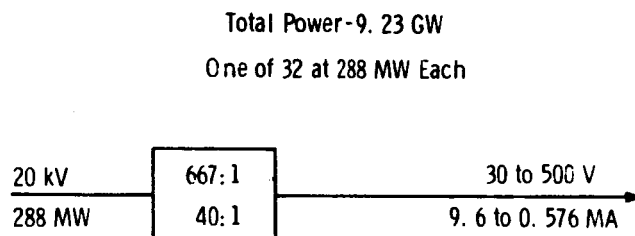
Figure 3.2-12. Solid-State System Concept

If the size of the converter is decreased by a factor of 10, the weight per kilowatt will approximately double. In addition, if the prime dc power level is raised from 20 kV to 40 kV, the weight per kilowatt will increase also.

Choice of DC-to-DC Converter Circuit

Performance requirements for the solid-state version of the PDS are sufficiently different from those of the klystron system that the entire system concept must be reviewed. In the solid-state system, the ratio of input to output voltage is sufficiently large that consideration of use of a buck converter is not feasible because of the poor utilization of the main power switching device. Therefore, circuits of the type shown in Figure 3.2-3 can be ruled out. The most likely candidate then appears to be a circuit which includes an output transformer with a secondary rectifier.

With this circuit configuration, the use of one converter with a single transformer to match input and output voltage levels would not be feasible because of the large ratios required—667:1 to 40:1. The best system

configuration, then, appears to be where a number of converters are connected
in series across the 20-kV bus. The output voltage of each converter would
then be at the desired load voltage, and the outputs of a number of converters
could then be paralleled for higher current capability. When this configura-
tion is used, the turns ratio of the output transformer used can be reduced to
a reasonable level.

Design Using SOA Technology

The state-of-the-art solid-state concept design is a combination of two
other designs described elsewhere in this report. Therefore, instead of pre-
senting the entire design here, which would be repetitious, only the results
will be discussed.

The overall system design is similar to that for the solid-state concept
using 1990 technology, described below, but using converters with thyristors
for switches instead of transistors. The converter circuit approach is shown
in Figure 3.2-13. The commutation circuits shown in the figure are similar
in function to those used for the state-of-the-art klystron system described
earlier. The results of this design are summarized in Table 3.2-5.

To Transformer Primary
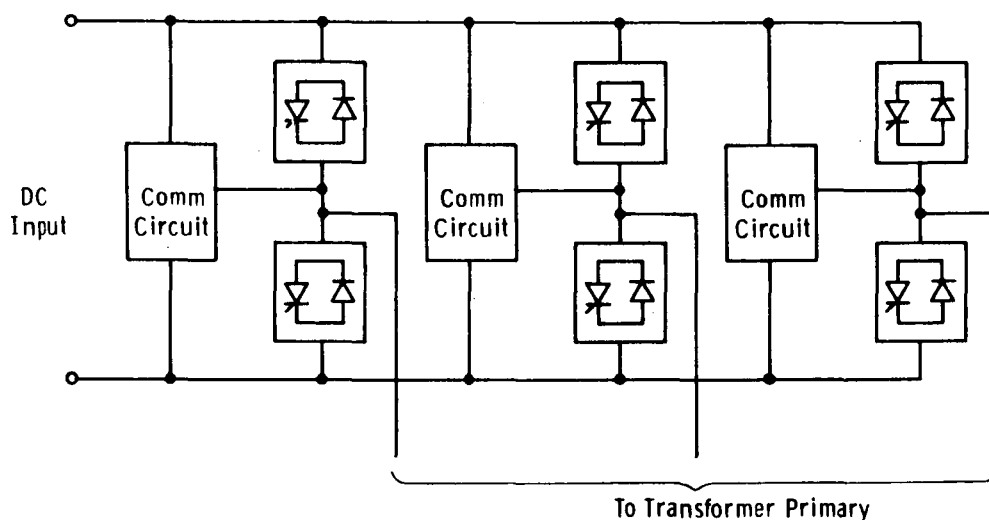
Figure 3.2-13. Block Diagram of SOA Solid-State System

Table 3.2-5. Solid-State System Concept

Switches	0.21 kg/kW
Transformer	0.16
Interphase reactor	0.06
Commutating circuit	0.09
Total	0.47 kg/kW

Design Assuming 1990 Technology

For the 1990 technology projection, assume that bipolar or field effect transistors will be available with voltage blocking of 2000 V, a power dissipation capability of 800 W, and a voltage drop of 2 V at 100 A. The basic circuit to be used with these devices is shown in Figure 3.2-14.

DC Input

To Transformer Primary
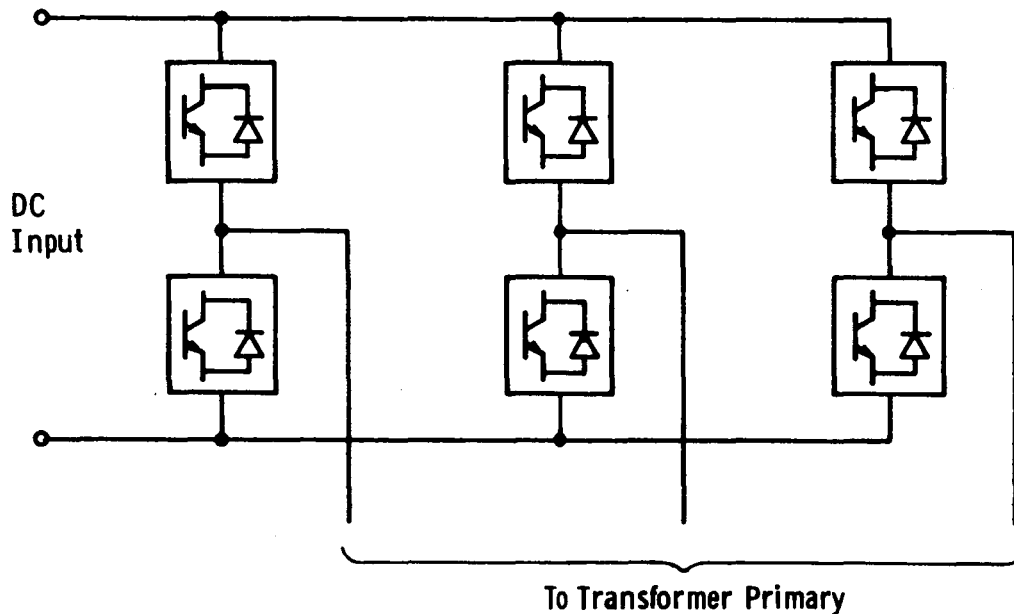
Figure 3.2-14. Basic Transistor Three-Phase Circuit
for Solid-State System

Main Switch

Using devices with these characteristics, the average current per three-phase bridge would be ~1140 A. The power output in a three-phase 20-kV bridge path, ~22.8 MW. A total of six switches is needed each 20 kV rated with 24 series devices, 144 devices in all, weighing 1728 lb + 500 lb for control (estimate) yielding 0.044 kg/kW.

Inverse Diodes

Inverse diodes will add a like amount of weight if a voltage sourced converter is used, and the output rectifier will add the same again for 0.132 kg/kW total switch weight in compound converter.

To go from 20 kV to 200 V, assume that we divide the 24 series devices in each switch among 12 converters, each having two devices per switch. Converter transformer rating is a little less than 2 MW, and the voltage is ~1.8 kV, giving 9:1 transformers, which is not unreasonable. Using 6 series converters gives 18:1 transformers at ~4 MW each, as shown in Figure 3.2-15.

3333 V/Conv, 4 MW/Conv
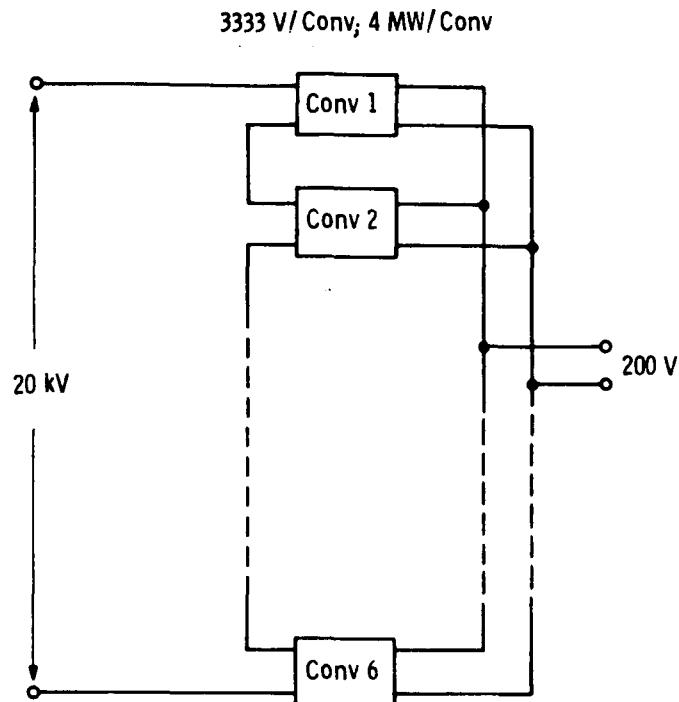
Figure 3.2-15. Series Connection of Converters

Output Transformer

A 60-Hz 3.75-MVA transformer (three-phase oil) weighs 19,300 lb split
as follows: core and coils, 7700 lb; tank, etc., 4290 lb; and oil, 5310 lb—
with core run at 17 kG. Core loss is then ~1.3 W/lb (hypersil curves); but
4-inch-thick material has same loss at 5.6 kG @ 400 Hz, 2.4 kG @ 1 kHz, giv-
ing core and coil reduction factors of 0.455 (400 Hz), 0.425 (1000 Hz). These
data are shown in Table 3.2-6 together with extrapolated data for 2-inch-thick
material curves which do not go below 5 kHz, 1.3 W/lb @ 1300 G. Extrapolating
from these curves, 2350 G @ 2.5 kHz, 4240 G @ 1.25 kHz, core and coil reduc-
tion factors are: 1.25 kHz, 0.192; 2.5 kHz, 0.174; and 5.0 kHz, 0.157—as
shown in Table 3.2-7.

Table 3.2-6. B_M for Core Loss (1.3 W/lb)

	12 Mil	Hypersil Core Lamination Thck.				
		4 Mil			2 Mil	
Frequency (Hz)		400	1000	1250	2500	5000
B_M (kG)	17	5.6	2.4	4.24	2.35	1.30

Table 3.2-7. Core and Coil Reduction Factors
(at a core loss of 1.3 W/lb)

| | 12 Mil | Hypersil Core Lamination | | | | |
		4 Mil		2 Mil		
Frequency (Hz)	60	400	1000	1250	2500	5000
Reduction Factor	1.0	.455	.425	.192	.174	.157

These are optimistic projections because of cooling and insulation considerations. With a primary current of 1140 A, running conductor at 1000 A/in^2 gives a diameter as 1.2 inches. The spacing for 20 kV (not less than 95 kV BIL) probably has to be ~1/6 of this, or 0.2 inch, so that core/coil reduction factor cannot be less than 0.143 under any circumstances, regardless of frequency.

Arbitrarily, pick 1.25 kHz and assume 0.25 reduction factor (30% higher than the 0.192 factor for core and coil alone). Then, core and coil weigh 1925 lb. Assume coolant circulates in the conductors, eliminating the tank and oil. Assume that this doubles the weight to 3850 lb, yielding a core and coil reduction factor of 0.5. Specific weight is 0.461 kg/kW.

Now, consider paralleling devices. A parallel combination of 2 gives ~8 MVA transformer; 3, ~12 MVA; and so on. Core and coil weight of 60-Hz transformers are as follows (from higher voltage units): 3750 kVa, 11,700 lb; 7500 kVA, 18,000 lb; and 10,000 kVa, 21,200 lb.

The 0.75 power law says multiplier is 1.68 every time rating doubles, so that for two-parallel devices the transformer weight might be ~0.274 kg/kW; for four-parallel it could be 0.163 kg/kW.

Input and Output Filters

Polyphasing (phase shifting three-phase bridges to get 24- or 48-pulse system), as shown in Figures 3.2-16 and 3.2-17, will essentially eliminate the need for input and output filters.

Interphase Reactors

Interphase reactors are needed and will add (on basis of rating estimate and 7500-Hz operation) ≈0.168/0.1/0.06 kg/kW for 1/2/3 parallel devices.

Summary of Results

Weights are estimated as

Parallel devices	1	2	3
Switch weight	0.132	0.132	0.132
Transformers	0.461	0.274	0.163
Interphase	0.168	0.100	0.060
Total (kg/kW)	0.761	0.506	0.355
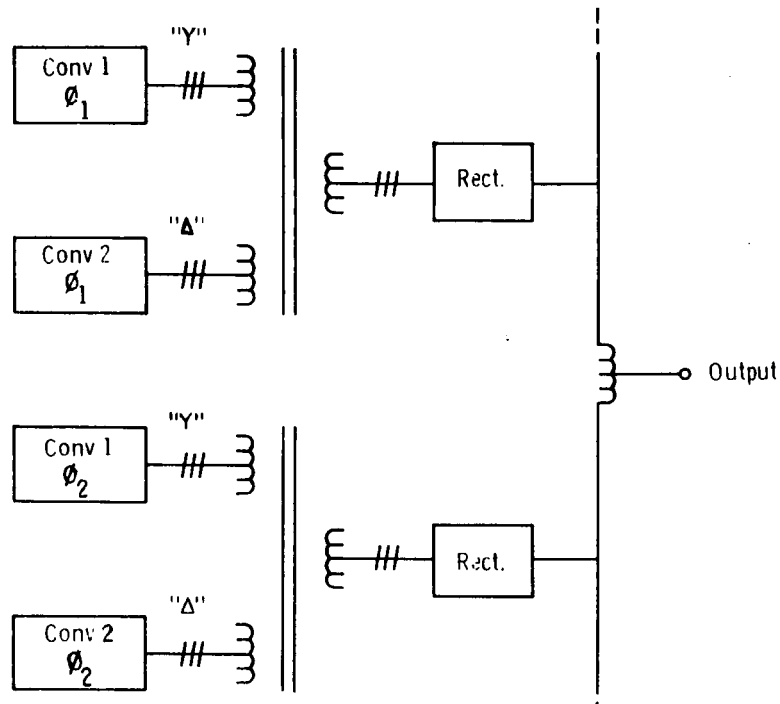
Figure 3.2-16. Paralleled Converter
Output Connection
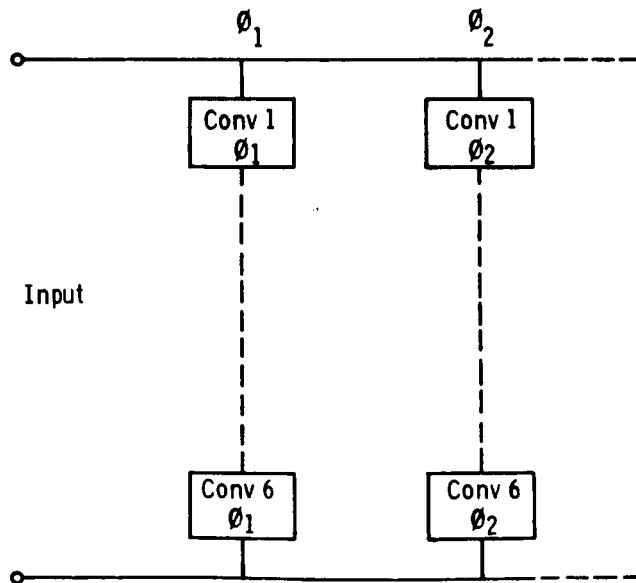
Figure 3.2-17. Paralleled Converter Input Connection
(Showing Phase Staggering)

Variations in Output Voltage about 200 V

The output voltage can be chosen to lie anywhere within the range of 30 to 500 V. The data generated in this section were for an output voltage of 200 V. The principal effect that a variation in output voltage may have will be on the size and number of output transformers. The number of main switching devices will not be affected because the dc bus voltage of 20 kV must be blocked in any case. The different output voltages can be accommodated by either adjusting the turns ratio of the output transformers or by increasing or decreasing the number of converters connected in series across the 20-kV source.

In general, the larger the kVA rating of the transformer, the lower the normalized weight. This relationship works to advantage for higher output voltages. At the low end of the output voltage range, where a larger number of smaller transformers may be needed, it may be possible to parallel more devices to increase primary current and maintain the kVA rating per transformer. Efficiency will be adversely affected as output voltage is decreased because of increase I^2R and rectifier losses due to the increased current.

Converter Efficiency

In the circuit realizations of the systems used for the solid-state load concept, all of the power is conditioned twice (i.e., it is changed from dc to ac, or ac to dc, twice), goes through a transformer, and is rectified at a relatively low voltage to yield a low output voltage. As a result, the expected efficiency of the solid-state system concept will increase slightly between the present time and 1990, but it is not expected to exceed 96% even in 1990.

Technology Improvements

The most critical technology improvements needed to meet the SPS weight goal are improved solid-state switching devices and diodes. As shown in Table 3.2-8, improvements in magnetic material properties and in capacitors are desirable and will help to ensure meeting the goals, but are not necessary —improvements in switching devices and diodes are.

Table 3.2-8. 1990 Technology Improvements

| | Improvements | |
	Desirable	Necessary
Semiconductor switching devices		✓
Semiconductor diodes		✓
Magnetic materials	✓	
Capacitors	✓	

By the year 1990, device technology must have advanced to the point where bipolar or field effect transistors are available which block 2 kV and have a forward drop of 2 V at 1000 A, and are capable of dissipating 800 W.

Fast-recovery diodes will also be needed which have low stored charge and are capable of blocking a high voltage (on the order of 2 kV).

Conclusions and Recommendations

The major conclusions of this study are:

- The specific weight goal of 0.197 kg/kW for 1990 technology appears to be reasonable.

- The 1990 efficiency goal of 96% appears to be reasonable.

- Improvements in transistor or MOSFET device technology, current, and switching time will be needed to meet the 1990 goals.

- Improvements in magnetic material properties and capacitor materials will improve system performance, but are not a precondition to meeting the 1990 goals.

- The klystron system should have lower normalized weight and higher efficiency than the solid-state system.

It appears that the 1990 goals for normalized weight per kVA of output and efficiency can be met if semiconductor device technology improves in what is considered to be a reasonable manner. Improvements in magnetic material properties as well as in capacitors will further ensure that the goals can be met. The klystron system concept holds promise of lower weight per kVA of output and higher efficiency than the solid-state system.

It is recommended that the design of klystron dc converter system be pursued in much greater depth to obtain more accurate estimates of performance.

3.2.2 POWER DISTRIBUTION MASS ANALYSIS

Additional analyses and evaluation on the selected SPS concepts are presented below.

Sandwich Concept

In previous analyses of the sandwich concept, no mass was calculated for the power distribution for routing the required power to the RF elements. These elements require two voltage levels: 10 volts, and -4 volts. The spacing between the dipoles are set at 7.81 cm. Based on this spacing, the total number within a 25-m^2 subarray would be 4096 devices. Four types of solar cells were considered, each having different voltage and current levels. The voltage and current levels are specified in Table 3.2-9.

To obtain the requirements of +10 V, eight cells of the 1.254-volt type were connected in series (8×1.254 V = 10.032); and for the -4 V, four cells were connected in series (4×1.254 = 5.016 V). Only one segment per 10-m×10-m (four subarrays) module was allocated for the negative voltage because of the

Table 3.2-9. Cell Characteristics

CELL MATERIAL	CELL OPTION	VOLTAGE/200°C		CURRENT (amp/cm²)	DIMENSION (cm)
		EOL	BOL		
GaAlAs/GaInAs DUAL JCT.	1	1.25	1.32	0.0248	3.33×2.5
GaAlAs/GaAs DUAL JCT.	2	1.82	1.92	0.0171	4.44×2.5
GaAs SINGLE JUNCTION	3	0.547	0.575	0.0387	0.399×2.41
GaAs SINGLE JUNCTION	4	0.547	0.575	0.0387	0.05×1.03

very low power requirements. A voltage drop of 0.032 V was allowed for the
+10-V power distribution wiring to the RF dipoles. For the 1.82-V cells, six
cells in series had to be connected to obtain the required +10 V (6×1.82+10.92).
In this case, a greater voltage drop was applied (0.92 V). To obtain the -4 V
three cells were connected in series (1.82×3 = 5.46 V).

The interconnection of cells for Option 1 is presented in Figure 3.2-18.
The power distribution weight to the RF dipoles for the 1.254-V configuration
was found to be 0.25 kg/m² and for the 1.82-V configuration, 0.275 kg/m². The
PDS efficiency of the 1.254-V configuration is 99.7% whereas, for the 1.82-V
configuration it would be 99.6%. The loss of cell area in a 10×10-m subarray
is approximately 0.01% due to the -4 V requirements. The weight of the PDS
was adjusted for a temperature of 200°C.

Figure 3.2-18. Solid-State Sandwich Concept,
Power Distribution System to RF Devices

Cell Options 3 and 4 represent the recommended approach and are tailored
dimensionally to match voltage and power requirements of a single dipole.
Eighteen cells are connected in series to provide the +10 V directly to one
dipole as shown in Figure 3.2-19. Cell Option 4 (0.05×1.03 cm) is installed
along the edge of a 7.81×7.81-cm section so that seven cells in series pro-
vide the -4 V. This approach reduces power distribution mass and essentially
makes the power distribution an integral part of the sandwich construction.

CELL CONFIGURATION PER DIPOLE
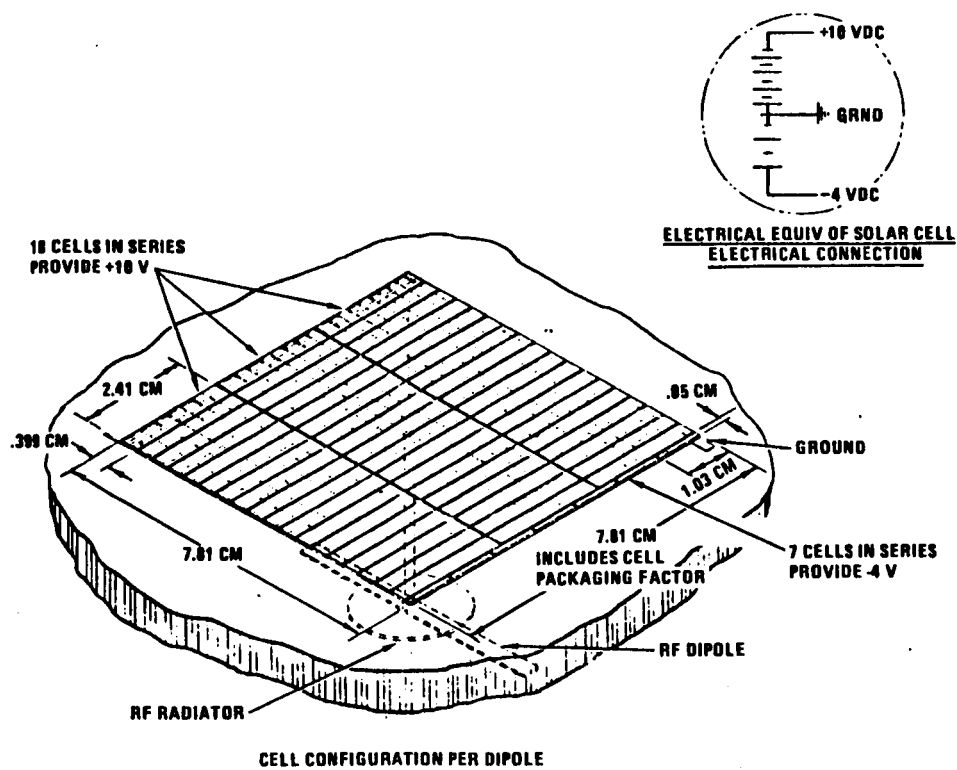
Figure 3.2-19. Satellite Sandwich Solar Cell Configuration
(Preliminary)

Solid-State End-Mounted Antenna Concept

The solid-state end-mounted concept was reconfigured from previous study
into two half-systems, each with one antenna. The following were considered:
(1) obtain the power distribution system (PDS) mass based on a 9650-m-length
configuration, (2) calculate PDS mass and specific mass when summing bus has
been eliminated to determine mass savings, and (3) determine mass of PDS for
various low-voltage transmission levels with no dc conversion.

Power Distribution Mass Analysis

The solid-state end-mounted configuration consists of transmitting 43.7 kV
from the solar array through the secondary feeders, the main feeders, summing
bus, slip rings, and risers to the dc-dc converters on the antenna array. The

dc-dc conversion is accomplished in two steps, 20÷1 and 10÷1, from 40 kV to 200 V. Ten dc-dc converters (20÷1) are mounted on both edges of the antenna and ten dc-dc converters on each subarray (10 m × 10 m). Each converter supplies 37.5 parallel strings of 20 amplifiers per string. A schematic of solid-state end-mounted system that was analyzed is presented in Figure 3.2-20, and the subarray hookup in Figure 3.2-21. A summary of the calculated mass is presented in Table 3.2-10. The antenna PDS mass was adjusted for a temperature of 125°C. The total mass of the PDS was found to be 5.13×10^6 kg. This translates to a specific PDS mass of 1.97 kg/kW_{UT}, compared to the reference concept of 1.52 kg/kW_{UT} (approximately 29.8% heavier)[1].

Power Distribution with Summing Bus Elimination

Because of the heavier mass for the end-mounted solid-state PDS, it was decided to investigate optimization techniques which could reduce the PDS mass. One such technique investigated was to remove the summing bus and use a direct interface between the main feeders and tie bars through switch gears to the slip rings. Another technique considered was to employ a smaller-diameter slip ring. Both techniques were analyzed and the overall PDS mass for this technique was found to be 5.05^6 kg. This translates to a 1.934 kg/kW_{UT} at the utility interface.

Reference Klystron Concept

The klystron concept has been updated and optimized to produce the minimum specific mass of the PDS. In previous analyses, summing buses were considered to which all of the main feeders were tied. Tie-bars were then used from the summing buses to the slip rings. In the present configuration, the summing buses on the nonrotating portion of the SPS have been eliminated (see Figure 3.2-22). Tie-bars are now interfaced at one end to the main feeders through switch gears; on the other end, they are tied directly to the slip rings. In the analysis, three different dc converter specific densities were used to show how the overall PDS will vary as a result of the dc converter specific density. The results are summarized in Table 3.2-11. When comparing the updated specific mass of the PDS of 1.172 kg/kW_{UT} (using the 0.197 kg/kW for dc converters) with the previously obtained value of 1.515 kg/kW_{UT}, we find that the updated configuration is 22.67% lighter. Additional analyses were made to determine whether elimination of dc converters is possible. A dedicated voltage system was evaluated for determining the specific mass of the PDS. A detailed breakdown of the masses are presented in Table 3.2-12. The results show that total PDS specific mass at the utility interface is 1.236 kg/kW_{UT}. When comparing the result with previous value of 1.515 kg/kW_{UT}, the dedicated system is 18.44% lighter.

In the dedicated voltage configuration, the slip rings were reconfigured for a total of 30 slip rings (15 plus and 15 minus). The characteristics of the slip rings are presented in Figure 3.2-23. There would be six (3 plus and 3 minus) slip rings for any given dedicated voltage level. On the rotating side, the pickoff voltages would be accomplished through brushes mounted in "shoes." The characteristics, as well as the brush layout per shoe assembly is also presented in Figure 3.2-23. The total mass of the slip rings would be 0.01644×10^6 kg; the total mass of the shoe assemblies would be 0.0255×10^6 kg.

---

[1] *At the end of the first quarter (October 10, 1979)*

Figure 3.2-20. Solid-State End-Mounted System
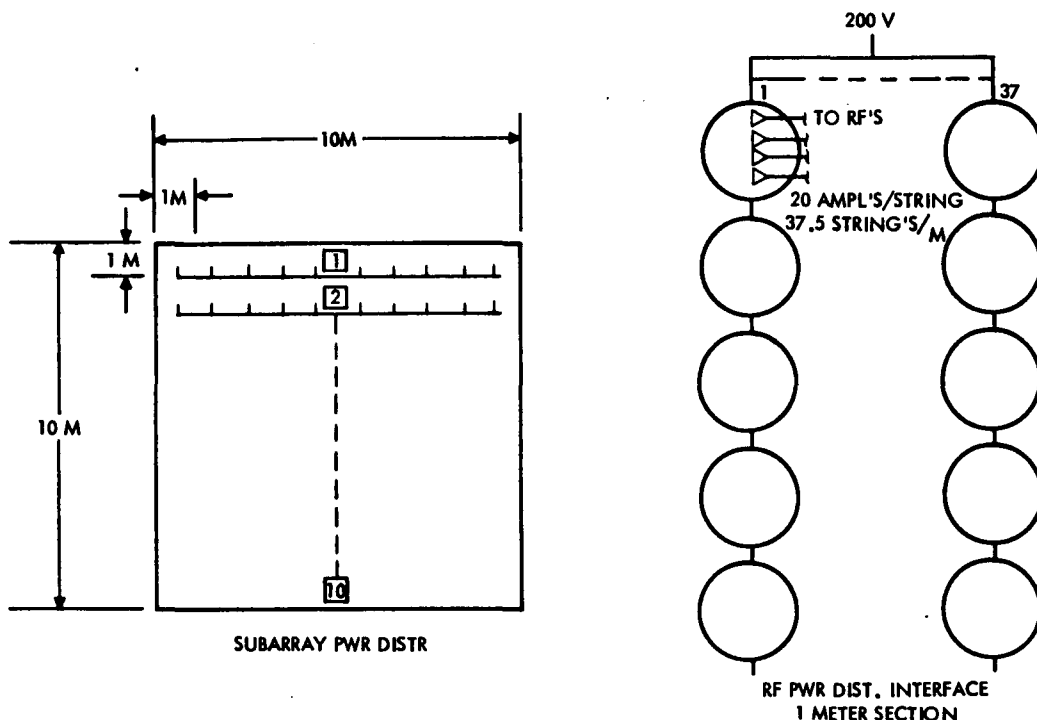
Figure 3.2-21.   Solid-State End-Mounted System (Power Distribution)

Table 3.2-10.   Calculated Mass Summary

SOLAR BLANKET WIRING	0.09395
MAIN FEEDER	0.31085
SECONDARY FEEDER	0.04694
TIE BARS	0.02395
SUMMING BUS	0.04694
INSULATION (KAPTON)	0.01045
SWITCH GEAR	0.03606
ROTARY JOINT	0.0430
INSTALLATION	0.05691
SUB—NONROTATING	0.66905
ROTARY JOINT	0.0170
RISER	0.19971
INTERCONNECT BAR	0.04383
SUMMING BUS	0.12784
DC-DC CONVERSION (@ 0.5 kg/kW)	2.64350
SWITCH GEAR	0.0396
POWER DIST. BETWEEN CONV.	0.06573
POWER DIST. OF SUBARRY	0.14429
POWER DIST. OF RF DIPOLES	0.72772
INSULATION	0.05491
INSTALLATION	0.39922
SUB—ROTATING	4.46335
TOTAL PDS	5.1324
kg/kW$_{UT}$	1.966
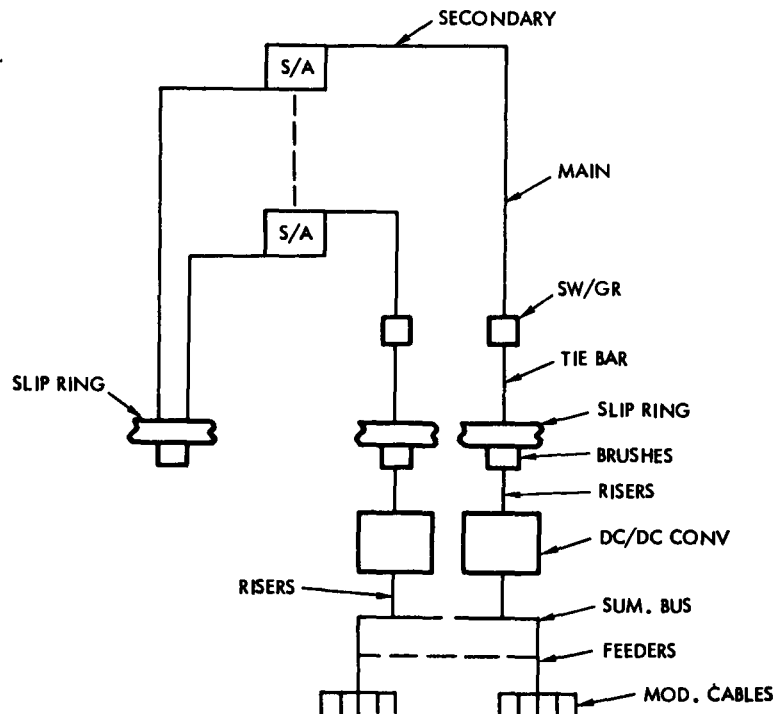
Figure 3.2-22. Updated Klystron Reference Power Distribution

Table 3.2-11. Updated Klystron Reference Concept Mass

	DC CONV., 0.197 kg/kW (MASS 10^6 kg)	DC CONV. @ 0.5 kg/kW	DC CONV. @ 1.46 kg/kW
MAIN FEEDER	2.020	2.020	2.020
SECONDARY FEEDERS	0.048	0.048	0.048
TIE BARS	0.043	0.043	0.043
INSULATION	0.032	0.032	0.032
SWITCH GEARS	0.304	0.304	0.304
REG. & CONVERTERS	0.009	0.009	0.009
ROTARY JOINT	0.043	0.043	0.043
AC THRUSTER CABLING	0.0053	0.0053	0.0053
STANDBY POWER	0.006	0.006	0.006
SUPPORT STRUCTURE	0.251	0.251	0.251
SUB—NONROTATING	2.7613	2.7613	2.7613
ROTARY JOINT	0.017	0.017	0.017
RISERS	0.02705	0.02705	0.02705
SUMMING BUS	0.32573	0.32573	0.32573
ANTENNA FEEDERS	0.31049	0.31049	0.31049
ANTENNA MOD. CABLING	0.1250	0.1250	0.1250
SWITCH GEARS	0.3430	0.3430	0.3430
DC CONVERTERS	1.480	3.7564	10.5178
INSULATION	0.0118	0.0118	0.0118
STANDBY POWER	0.250	0.250	0.250
SUPPORT STRUCTURE	0.289	0.5166	1.1928
SUB—ROTATING	3.179	5.6830	13.1206
TOTAL PDS	5.9403	8.4443	15.8819
kg/kW$_{UT}$	1.1717	1.666	3.133

Table 3.2-12. Dedicated Voltage
Klystron Concept

	MASS (10^6 kg)
MAIN FEEDER	3.75345
SECONDARY FEEDERS	0.08451
TIE BARS	0.13588
INSULATION	0.06160
SWITCH GEARS	0.19778
ROTARY JOINT	0.01644
AC THRUSTERS	0.00530
STANDBY POWER	0.00600
REG. & CONVERTERS	0.00900
SUPPORT STRUCTURE	0.426996
SUB—NONROTATING	4.696956
ROTARY JOINT	0.02550
RISERS	0.02705
SUM BUS	0.32573
ANTENNA FEEDERS	0.31049
ANTENNA MOD. CABLING	0.12500
SWITCH GEAR	0.34300
INSULATION	0.01220
STANDBY POWER	0.25000
SUPPORT STRUCTURE	0.14190
SUB—ROTATING	1.56797
TOTAL PDS	6.264926
KG/KW$_{UT}$	1.236
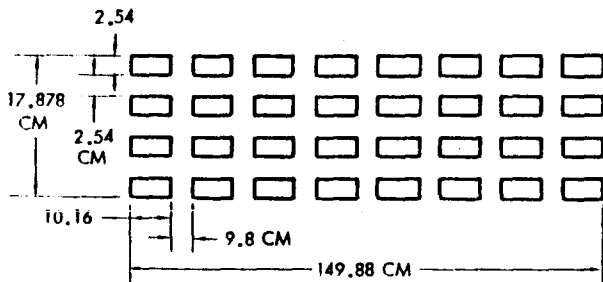
CHARACTERISTICS

SLIP RING

CORE	ALUMINUM
CLADDING	COIN-SILVER
CORE-SIZE (CM^2)	104.9 (CROSS SECTION)
DIAMETER (METER)	6.
LENGTH (METER)	18.85

SHOE BRUSH

MATERIAL	75% M_o S_2 + 25% M_o+ T_a
SHOE SIZE (CM)	20.32 W 25 H 152L
CURRENT (A/CM^2) (MAX)	7.75
CONTACT AREA (CM^2)	825.92
QUANTITY (BRUSHES PER SHOE)	32

ID	VOLTAGE (KU)	CURRENT AMPS	NO. OF RINGS	NO. OF SHOE ASSEMBLY/RING
A	41.02	19077	3	3
B1	24.61	11353	3	3
B2	16.41	17030	3	2
C1	32.81	8515	3	6
C2	8.60	34058	3	2

Figure 3.2-23. Slip Ring Shoe Assembly Layout

The study indicates that a dedicated voltage configuration may result in a mass savings; however, additional complexity results. More analysis is required to determine voltage levels requiring regulation and mass penalties associated with added control complexities and redundancy requirements.

3.3 STRUCTURE

The Exhibit C study (Reference 7) identified two basic antenna structures: compression frame/tension web, and space frame. During Exhibit C it was concluded that the space frame antenna structure would be the reference klystron design, since the depth of existing data provided a higher degree of feasibility assurance. For the initial solid-state distributed concept, it appears that the compression frame/tension web may have major advantages over the space frame in regard to thermal and modular installation. Detailed structural analysis was conducted to develop a preferred antenna structural design and determine feasibility for a solity-state concept that has the solid-state amplifiers structurally integral with the solar cells (sandwich concept). In this concept the microwave surface is directed toward the earth with the solar cells mounted on the back face and illuminated by a system of primary and secondary reflector surfaces as shown in Figure 3.3-1. An orthogonal array of cables, tension stabilized by a peripheral compression-carrying frame, provides a primary structural support system with no encroachment on either surface. Of concern is the primary structural characteristics of this structure and assessment of its feasibility for this application.

JACK
3 PLACES

VARIES

VARIES

SUPPORT
3 PLACES

TRI-BEAM

• ARRAY OF BEAMS SPAN TO
PRETENSIONED CABLES TO
SUPPORT SOLID STATE
PANELS

PERIMETER
CABLES

GRAPHITE CABLES [30-M SPACING]
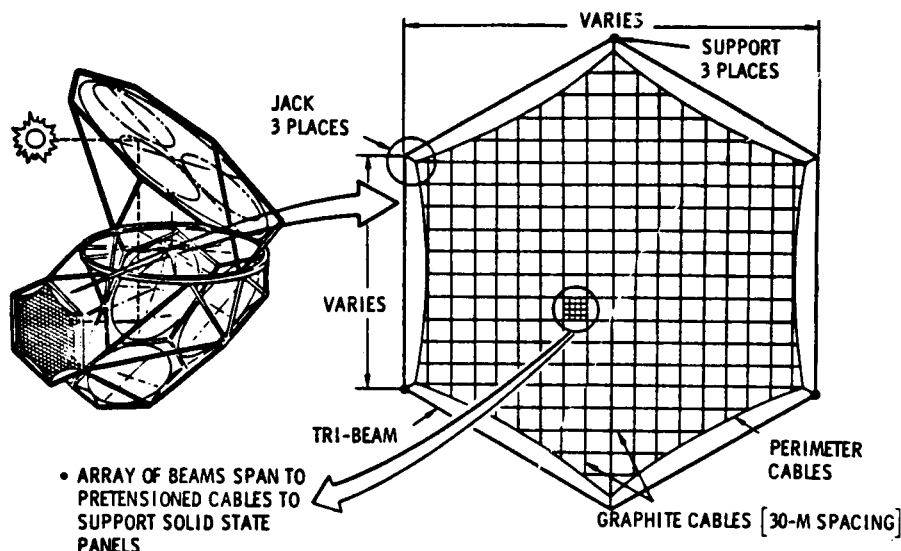
Figure 3.3-1. Microwave Antenna Structure Concept

The preliminary design structural analyses discussed here have uncovered no structural strength, stability, or stiffness issues that preclude use of the frame for this application. The frame's basic construction characteristics, structure mass, passive figure control capability, and minimum modal frequency are defined herein:

3.3.1 CONFIGURATION

The analysis was performed on the structure shown in Figure 3.3-1. The hexagonal frame is supported at three corners (120 degrees apart) by a statically determinate support system to preclude surface distortion by the supports. Contour adjustment jacks are provided at the unsupported corners of the hexagon for initial contour adjustment. Active control adjustment can be a backup alternative, but is not expected to be necessary.

The orthogonal array of tension-stabilized cables is the support for an egg-crate array of secondary structure that supports the individual solid-state sandwich panels. Tension in the cables is achieved by an appropriate system of tension devices at the extremities of the orthogonal and perimeter cables shown.

3.3.2 CONSTRUCTION

The frame, to be constructed in geosynchronous orbit, is that of a tri-beam (Figure 3.3-2), built up from the individual machine-made beam elements shown and connected by a pretensioned X-bracing system. Other constructions such as a pentahedral truss utilizing union joints, are applicable but were not studied. The machine-made beam element contains a closed-cap section fabricated of the same graphite composite material as that used in the cap of the General Dynamics design (Reference 8). The tension cables are graphite composite pultruded rods like that developed by McDonnell Douglas (Reference 9). The tri-beam bay length is the same as the width. Study of weight and construction variations with different tri-beam bay lengths was beyond the study scope.
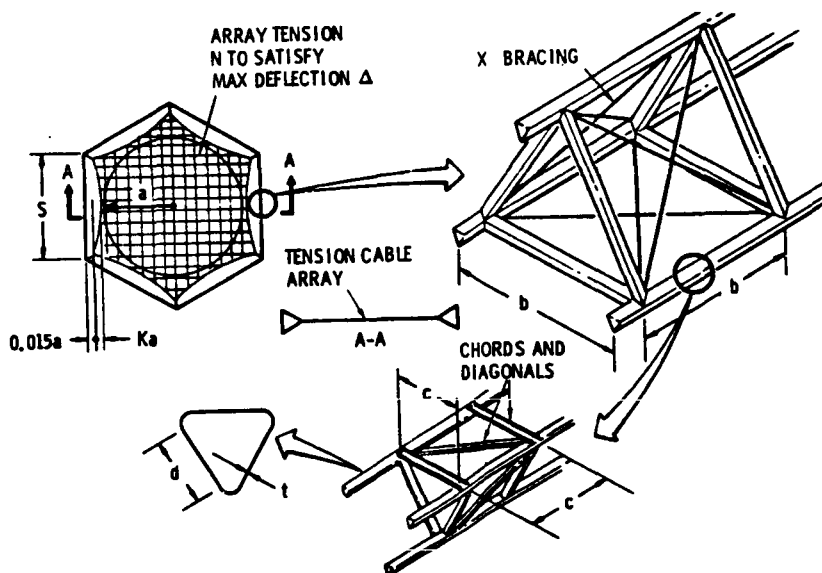
Figure 3.3-2. Tri-Beam Construction

3.3.3 REQUIREMENTS

The operational scenario shown in Figure 3.3-3 illustrates the sources of the major structural requirements:

1. Sustain the worst combination of "pretension closed-force system loads" in conjunction with

   • Structural temperature variation of 110°C (230°F) across the machine-made beam individual cap

   • Structural temperature differential of 85°C (185°F) between the orthogonal array of cables and average of machine-made beam caps

- Structural temperature differential of 55°C (131°F) between tri-beam X-bracing and average of machine-made beam caps

2. Peak out-of-plane deflection of 12 to 48 cm (0.39 to 1.57 ft) during the worst combination of

   - Reflected solar pressure 32.5×10^{-6} N/m^2 (0.67×10^{-6} lb/ft^2); gravity gradient load $- 30.0 \times 10^{-6}$ N/m^2; microwave pressure $- 2.5 \times 10^{-6}$ N/m^2 (0.051×10^{-6} lb/ft^2)

   - Thermal gradients 24°C (175°F) peak differential between average temperature of machine-made beams, 16°C (61°F) peak differential between X-bracing cables.

3. Minimum modal frequency to be compatible with overall configuration minimum of 0.0016 Hz

4. All materials to be compatible with temperatures of -170 to 200°C (-274 to 392°F)

- CONCENTRATED SOLAR PRESSURE-CONSTANT

- DIRECT SOLAR PRESSURE VARIES FROM 0 TO 360°

- GRAVITY GRADIENT TORQUE - 5.7° INCLINATION TO EARTH

- GRAVITY GRADIENT NORMAL LOAD (2000 M OFF-SET TO CENTER OF MASS) - CONSTANT

ANTENNA SHADED BY REFLECTOR

DEC 21

ANTENNA SHADED BY REFLECTOR

JUNE 21
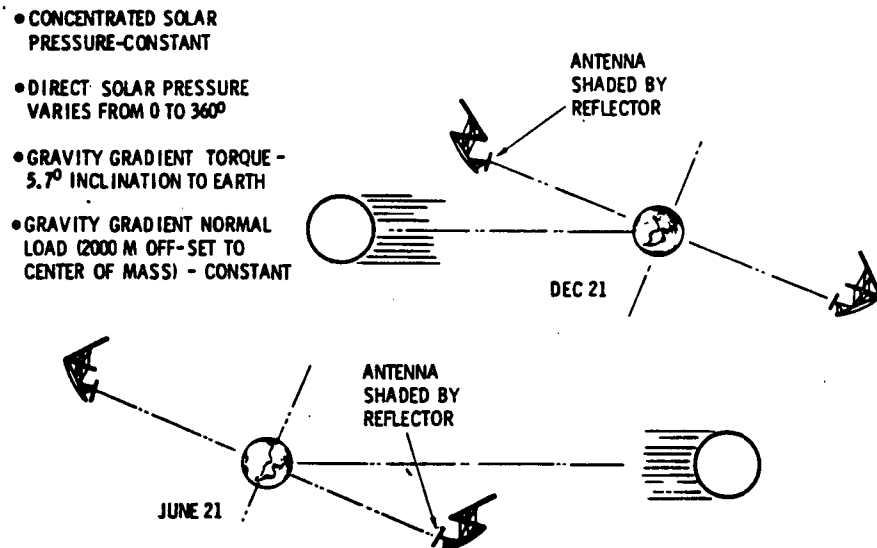
Figure 3.3-3. Microwave Antenna Operational Scenario

During operation, the concentrated solar pressure (CR=5) is of constant intensity while the direct solar radiation angle varies from 0 to 360°. This is most significant to the initial contour adjustment and results in the thermal requirements stated above. Also, of great significance is the gravity gradient loading resulting from the 2000-meter offset between the antenna and total configuration center of mass. For the configuration shown, the concentrated solar pressure and gravity gradient loading act in the same sense. An antenna located at the configuration center of mass will sustain essentially half the loading of this design.

Despite exposure to these deterring sources, the antenna surface devia-
tion from flatness must be compatible with the specific electronic efficiency
requirements. The range of these requirements is 12 to 48 cm. Also, the
integrated structure/control system must maintain the earth pointing accuracy
of the antenna to within 0.05 degree. For that requirement, classical control
techniques require the first modal frequency of this configuration (Figure 3.3-1)
to be above 0.0016 Hz.

3.3.4 STRUCTURAL ANALYSIS METHODOLOGY

The general methodology of the structural analysis performed to describe
the hexagonal frame's basic structural characteristics of mass and figure con-
trol quality is described in Figure 3.3-4. The basic closed-force system com-
pression and tension loads (Figure 3.3-5) were derived parametrically in terms
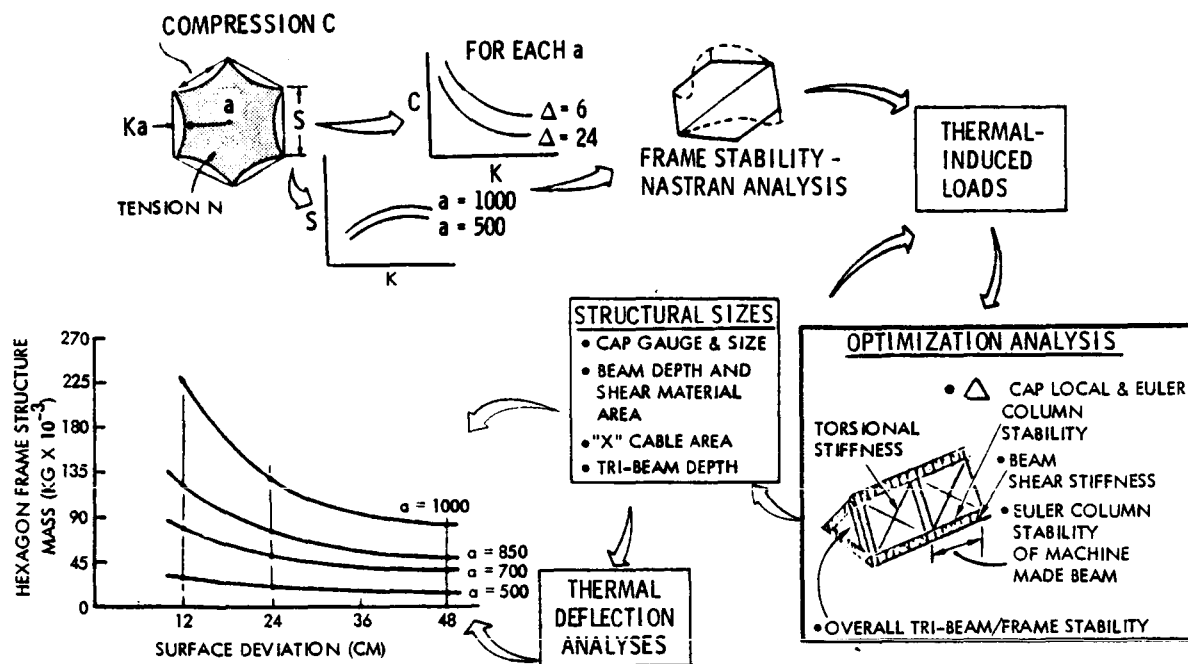
Figure 3.3-4. Structural Analysis Methodology

of the peak surface deflection Δ, antenna aperture radius a, and perimeter
cable depth Ka. The interplay between increased cable depth and frame perimeter
length with reduced compression load is shown in Figure 3.3-6. The frame com-
pression stability criteria were obtained by conducting a NASTRAN stability analysis
(Figure 3.3-7). For the first interaction thermal loads were estimated to be
negligible and confirmed in the subsequent analysis of the established designs.
Through an optimization analysis that addressed the pertinent compression load
stability requirements (Figures 3.3-7 and 3.3-8), the significant frame struc-
tural sizes and mass were determined in terms of the antenna aperture radius, a,
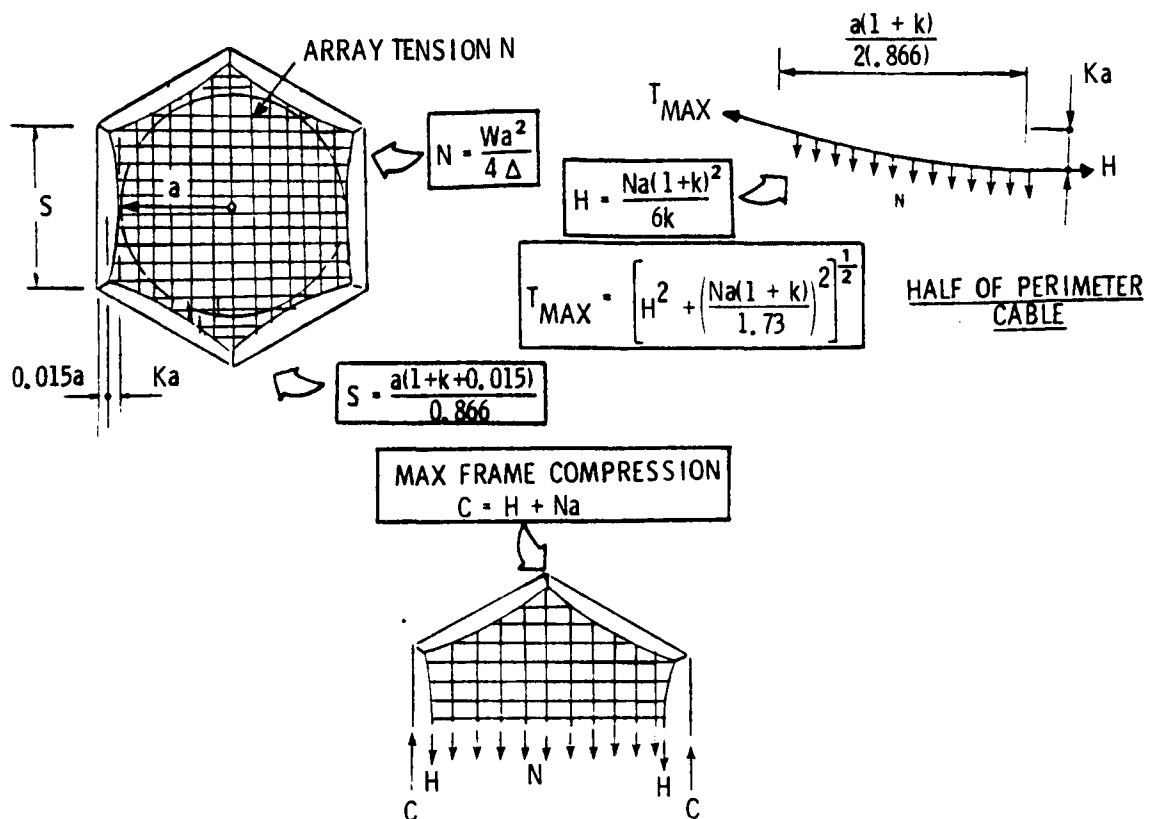
Figure 3.3-5. Basic Frame Free Body/Equations

$$N = \frac{Wa^2}{4\Delta}$$

$$H = \frac{Na(1+k)^2}{6k}$$

$$T_{MAX} = \left[H^2 + \left(\frac{Na(1+k)}{1.73} \right)^2 \right]^{\frac{1}{2}}$$

$$S = \frac{a(1+k+0.015)}{0.866}$$

MAX FRAME COMPRESSION
$$C = H + Na$$
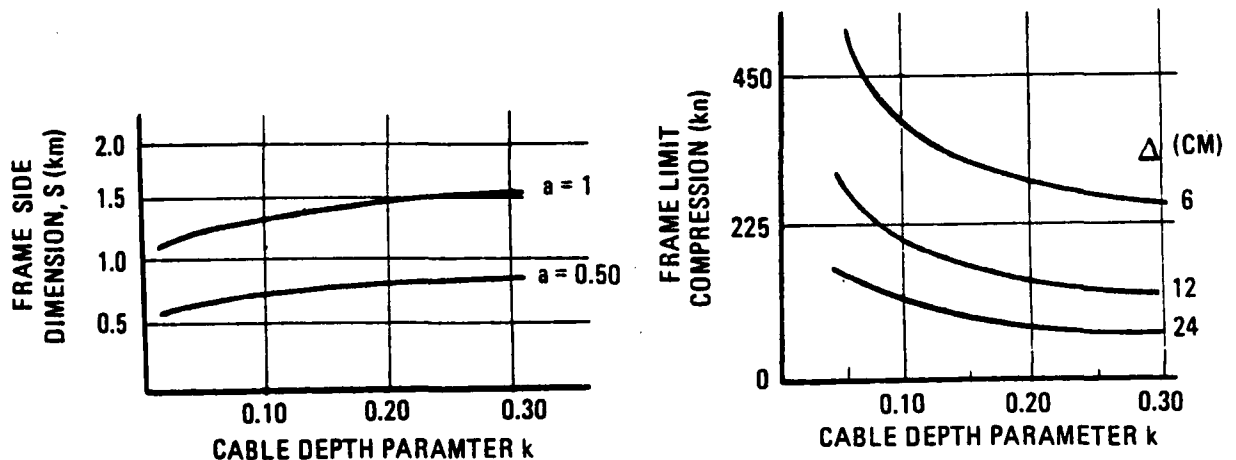
Figure 3.3-6. Compression Load/Frame Size Variation With Cable Depth

and the deflection restriction Δ (Figure 3.3-9). At this stage, the additional surface deflection due to thermal distortions was determined with appropriate adjustment of the final data (Figure 3.3-10). In all the foregoing analyses the applied loading used was 60.0×10^{-6} N/m^2 (1.25×10^{-6} lb/ft^2).

$\varnothing = 0.233$

MODEL
WITH
CABLES

$\varnothing = 0.233$

$$P = \frac{\pi^2 EI}{\ell^2}$$

— — LOAD DIRECTION
MAINTAINED

$\varnothing = 0.077$

$$P = \frac{\pi^2 EI}{4\ell^2}$$

MODEL WITHOUT
CABLES

$\varnothing = 0.077$

A

CABLE PRETENSION
INDUCED COMPRESSION

A

LOAD PASSES THROUGH SUPPORT

NASTRAN MODEL
WITH CABLES

A-A

$$P = \frac{\pi^2 EI}{\ell^2}$$
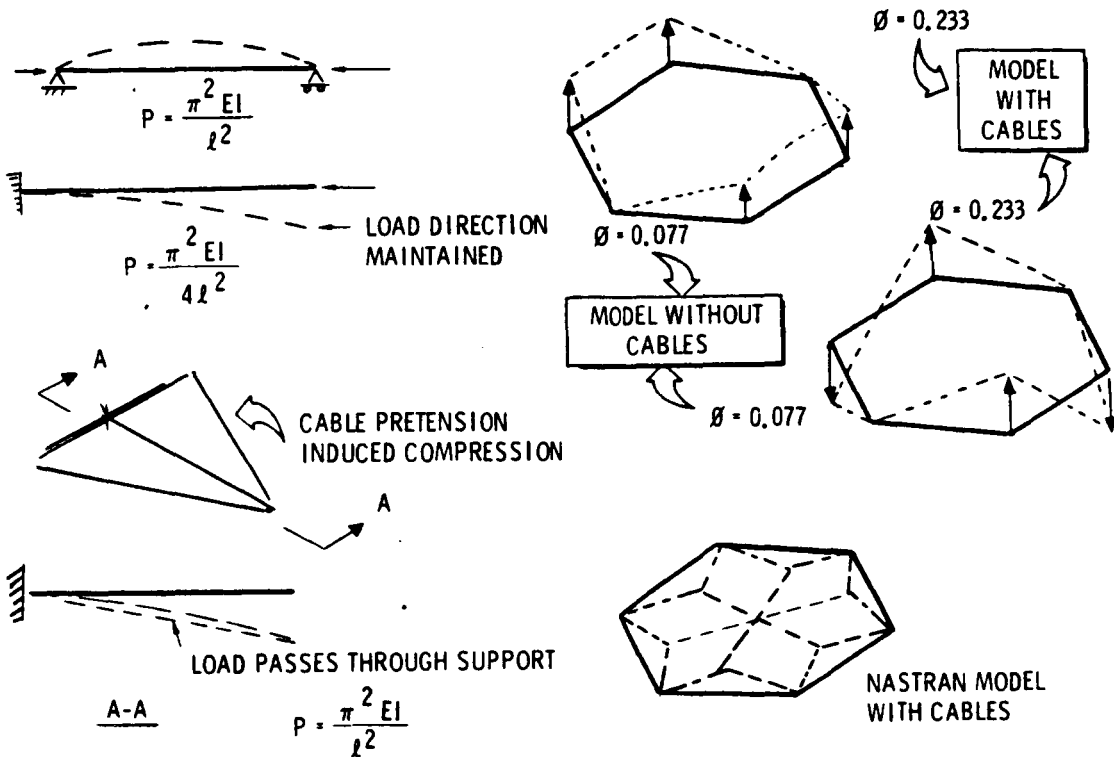
Figure 3.3-7. Hexagon Frame Stability Considerations

LOCAL BUCKLING

$$\sigma_{cc} = \frac{4\pi^2 \sqrt{E_L E_T}}{12(1-\mu^2)} \left(\frac{t}{d}\right)^2$$

MODIFIED JOHNSON

$$\sigma_{cr} = \sigma_{cc} \left[1 - \frac{\sigma_{cc}}{4\sigma_e} \right]$$

ELASTIC
BEHAVIOR

WHERE

$$\sigma_e = \frac{\pi^2 E_L \rho^2}{c^2}$$

$$\sigma_{cr} = 0.95 \frac{\pi^2 E_L \rho^2}{b^2}$$

WHERE 0.95 REPRESENTS SHEAR
REDUCTION FACTOR

STABILITY ANALYSIS PERFORMED WITH NASTRAN

* 3 SUPPORTS

* CAPABILITY DEPENDENT ON TORSIONAL AND FLEXURAL STIFFNESS
  OF TRI-BEAM

* SHEAR STIFFNESS NEGLIGIBLE AFFECTS

d

C

C

SUPPORTS
(3)
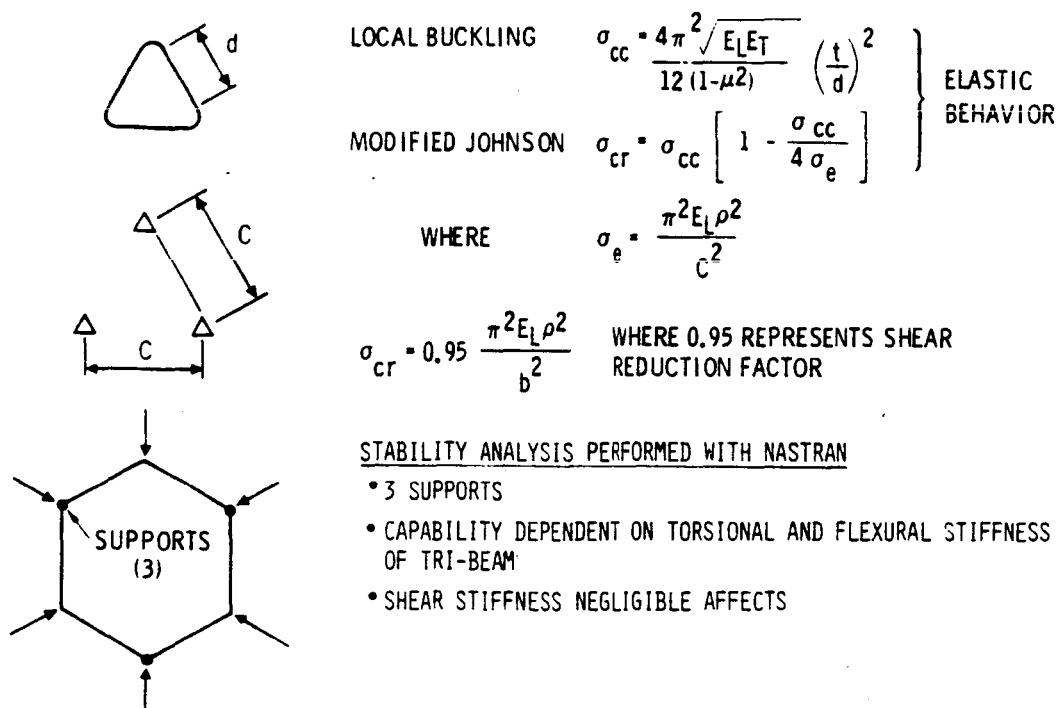
Figure 3.3-8. Hexagonal Frame Compression Stability Criteria
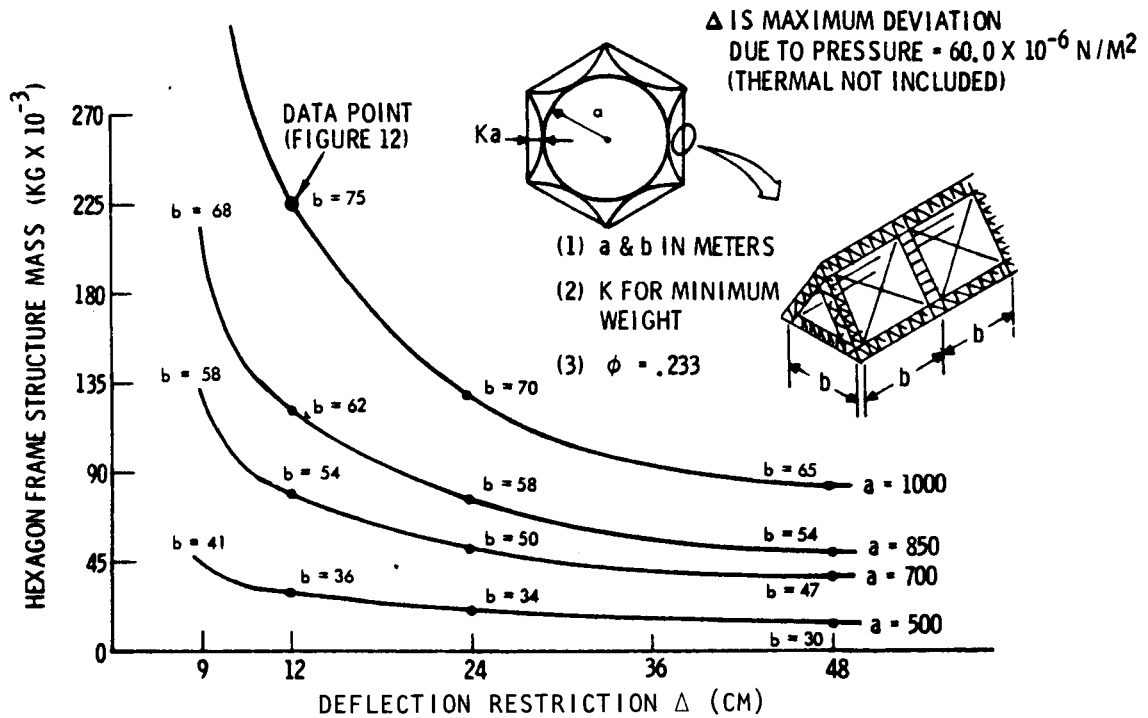
Figure 3.3-9. Preliminary Hexagonal Frame Mass Variation
With Surface Deflection Restriction
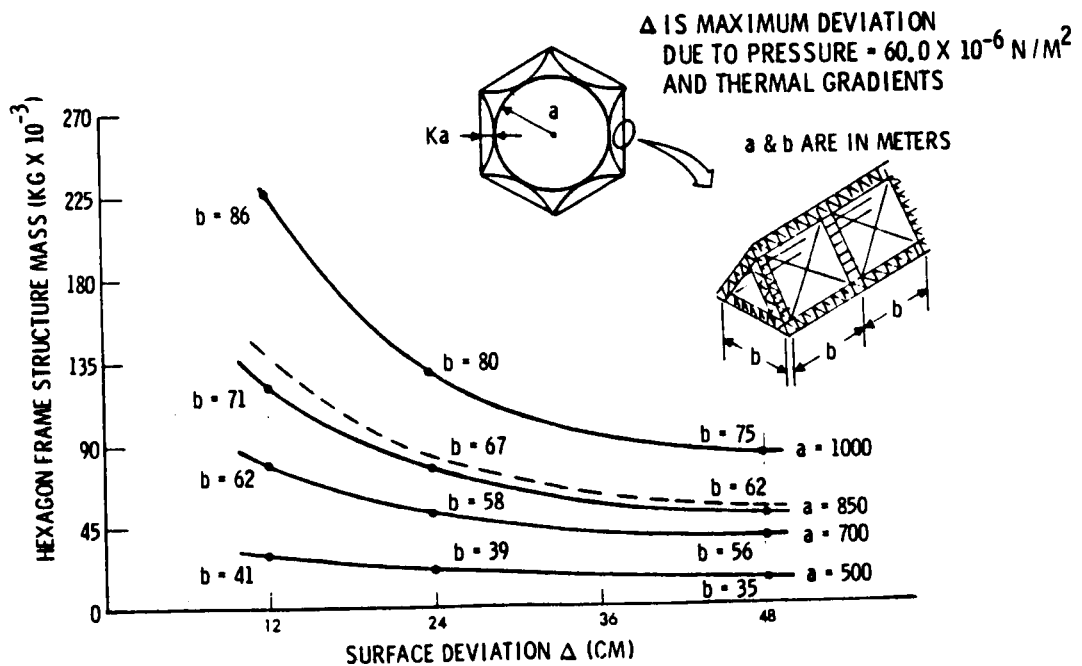
Figure 3.3-10. Hexagonal Frame Mass Variation With Surface Deviation

3.3.5 ANALYSIS

A safety factor of 1.5, applied to the calculated limit loads, was used throughout the analysis. The equation to determine the membrane tension (Figure 3.3-5), $N = wa^2/4\Delta$ (Reference 10) is exact for a circular membrane supported at its perimeter and a sufficiently accurate approximation for this application.* The equations for H, T_{max}, and C are exact and directly determined from the free bodies shown. It is apparent from a review of Figure 3.3-6 that not only does this closed-force system provide compression loads that are high by large space structure standards, but these loads are quite sensitive to the depth of the cable in the range of Ka = 0.05 to 0.15.

The machine-made triangular beam concept (Figure 3.3-2) containing a closed cap, was the basis of the optimization analysis. The closed cap was used rather than an open section in view of its structural efficiency. While it is recognized that the machine-made triangular beams under development by Grumman and General Dynamics employ open caps to permit convenient backup for the welding of the cross members, a design with a composite closed cap is being studied by Grumman for MSFC.

The stability criteria for the cap are shown in Figure 3.3-8 with σ_{cr} determined from the Johnson parabola equation. The local buckling equation shown was applied to test data stated in Reference 8 and was within 10 percent. The machine-made beam stability criteria also are shown. In the interest of a conservative approach, which is appropriate at this point in the design, the machine-made beam is treated as a pin-ended column though significant fixity is achievable. The use of the coefficient of 0.95 accounts for the loss of capability due to the beam cross and diagonal members deformation and is the criterion to which those members are sized.

The compression capability of the frame is conveniently defined by the column formula $P_F = \phi\pi^2 EI/S^2$, where ϕ is determined from NASTRAN stability analysis. During the course of these analyses (Figure 3.3-7), it was recognized that the use of externally applied radial compression loads (rather than the closed-force system loads associated with cable pretension) to predict frame stability was grossly conservative. This is demonstrated by the respective values of $\phi = 0.077$ compared to 0.233 for GJ/EI = 0.265 (see later discussion). This phenomenon is evident from examination of the examples shown at the left of Figure 3.3-7. The coefficient ϕ is reduced to 0.25 for the cantilever beam due to the load remaining parallel through deflection and hence providing a moment at the base. The same cantilever beam loaded in compression by the tension cables that are constrained to pass through the fixed support can produce no moment. NASTRAN analysis indicated a coefficient of 1.0, as anticipated.

The buckling coefficient ϕ of the hexagonal frame depends on the torsional stiffness. Figure 3.3-11 illustrates the variation of this coefficient as a function of the ratio of torsional to bending stiffness. For low GJ/EI ratios, ϕ is quite low because torsional flexibility predominates. As the parameter GJ/EI is increased to values >1.0, the coefficient ϕ varies asymptotically since the bending stiffness is constant. The variation of frame mass and depth

---

*Confirmed by analysis with NASTRAN model shown in Figure 3.3-19.

are shown in Figure 3.3-11 for two of the many cases investigated. The trend
was always the same: minimum frame mass was compatible with low values of
GJ/EI. This is not surprising since a design having equal cap and X bracing
mass, and the same elastic modulus, has a GJ/EI ratio of approximately 0.33.
It is pertinent to note that lesser frame mass is compatible with increased
tri-beam depth, which implies numerous weight/construction cost issues. Within
the context of the analysis goals, the design value selected was GJ/EI = 0.265,
and ϕ = 0.233 as the best compromise (near-minimum weight with reduced tri-beam
depth). The construction advantages of fewer bays of bracing are appreciated,
however.
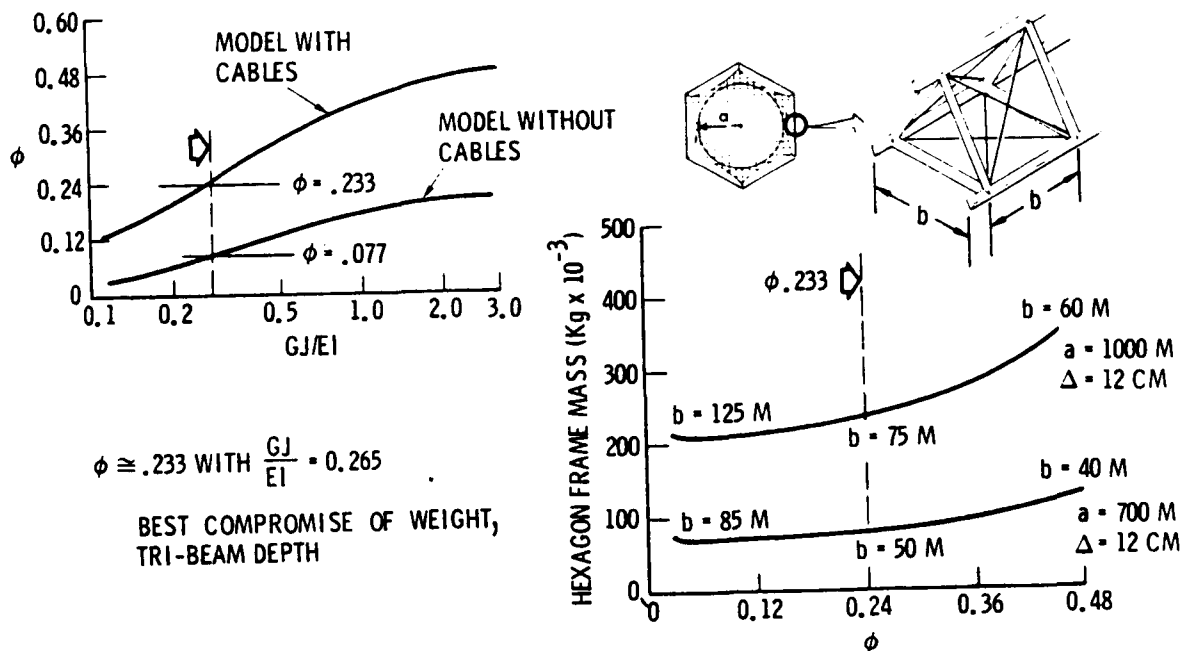
Figure 3.3-11. Frame Design Implications - GJ/EI Variation

Figure 3.3-9, therefore, parametrically presents the required frame mass
and depth for antenna aperture radii of 500 to 1000 m (1640 to 3280 ft) for
the surface deviation restrictions shown due to the distributed loading of
60.0×10^{-6} N/m^2 (1.25×10^{-6} lb/ft^2). The data are based on the cable depth
parameter k = 0.20 which resulted in the minimum weight of each design. At
this point thermal deflections have not been included. The importance of not
imposing unwarranted deflection restrictions at the lower deflection regimes
is apparent.

An illustration of the weight breakdown and significant stress levels for
the data point of Figure 3.3-9 are shown in Figure 3.3-12. It is important to
note that the weight estimate is based on use of the same machine-made beams
throughout. Undoubtedly the cross member can be lighter and fabricated by a
separate beam machine. The intent here is to be conservative, in this case
approximately 25 percent. It is also worth noting that the limit compression
is 91 MPa (13,700 psi), the peak limit cable tension is 275 MPa (40,000 psi).
While the long-term creep data for these graphite composite materials, which

NINE
9.5 MM DIA
CABLES

SEVEN
9.5 MM DIA
CABLES

a = 1000 M

1421 M

4.75 MM DIA
CABLE

75.1 M   75.1 M

AREA = 0.55 CM²
(INCL COATING)

1.92 M

1.92 M

38 MM   1.5 MM

R = 17 MM

71.6 MM

STRUCTURAL WEIGHTS

CAP (INCL THERMAL COATING)	=	1.83 KG/M
CHORDS AND DIAGONALS	=	.67
		2.50
TOTAL MACHINE-MADE BEAM		2.75 (INCL 10% DETAILS)
6 MACHINE-MADE BEAMS	=	16.5
"X" BRACING		8.0 (INCL ATTACHMTS)
		24.5
FRAME WEIGHT 6 X 24.5 X 1421 X 1.1	=	230,000 KG
WT OF TENSION CABLE ARRAY	=	19,000
TOTAL WEIGHT	=	249,000 KG

STRESS VERIFICATION -

• LOADS

$$N = \frac{Wa^2}{4\Delta} = 125 \text{ N/M (LIMIT)}$$

30 x 30 M CABLE TENSION = 3.75 KN
LIMIT STRESS FOR 4.75MM DIA CABLE = 207 MPa

$$H = \frac{Na(1+k)^2}{6k} = 150 \text{ KN (LIMIT)}$$

$$C = H + Na = 275 \text{ KN (LIMIT)} \qquad C_{ULT} = 1.5 \times C = 413 \text{ KN}$$

$$T_{max} = \left[(150)^2 + (86.7)^2\right]^{1/2} = 173 \text{ KN (LIMIT)} \qquad \text{LIMIT STRESS FOR}$$

• COMPRESSION STABILITY
9.5 MM CABLES = 275 MPa

$$\text{Cap } \sigma_e = \frac{\pi^2 E_1 \rho^2}{c^2} = \frac{\pi^2 \times 13.8 \times 10^4 \times (.0224)^2}{(1.92)^2} = 185 \text{ MPa}$$

$$\sigma_{cc} = \frac{4\pi^2 \sqrt{E_L E_T}\left(\frac{1}{d}\right)^2}{12(1-\nu^2)} = \frac{4\pi^2 \sqrt{13.8 \times .85} \times 10^4 \times \left[\frac{1.5^2}{38^2}\right]}{12(.95)} = 185 \text{ MPa}$$

$$\text{COMBINED } \sigma_{all} \text{ (JOHNSON PARABOLA)} = 185\left[1 - \frac{185}{4 \times 185}\right] = \underline{139 \text{ MPa}}$$

$$\text{APPLIED ULTIMATE STRESS} = \frac{413}{9 \times .337} = \underline{136 \text{ MPa}}$$

$$\text{MACHINE-MADE BEAM COLUMN } \sigma_{all} = \frac{.95\pi^2 \times 13.8 \times 10^4 \times (0.78)^2}{(75.1)^2} = \underline{140 \text{ MPa}}$$

$$\text{TRI-BEAM } \sigma_{all} = .95 \cdot \frac{233\pi^2 \times 13.8 \times 10^4 \times (30.7)^2}{(1421)^2} = \underline{140 \text{ MPa}}$$

Figure 3.3-12. Hexagonal Frame Illustrative Data
(Design for Δ = 12 cm)

are subjected to thermal cycling and space environment effects, are not available, stresses that are 15 to 25 percent of yield appear reasonable.

The thermal-structure considerations are classified into internal load and deflection-producing categories (Figure 3.3-13). The bending deflections shown result from gradients between the average temperature in each machine-made beam, with the average temperature being determined from the temperature of all three caps in each beam. Gradients across the closed cap of each beam produce stress, not deflection. The nature of the gradients between the X-bracing cables that produce deflections are equivalent to the strains resulting from transverse shear or torsion, with torsion being much more significant.

LOADS

CHANGES DUE TO CABLE AND TRI-BEAM TEMPERATURE DIFFERENTIAL

TRI-BEAM

CHANGES DUE TO X BRACING AND MACHINE MADE BEAM TEMPERATURE DIFFERENTIAL

THERMAL GRADIENTS ACROSS BEAM CAP

GRADIENT ACROSS MACHINE MADE BEAM

DEFLECTIONS

TRI-BEAM

GRADIENT ACROSS TRIBEAM

GRADIENT BETWEEN X BRACING CABLES
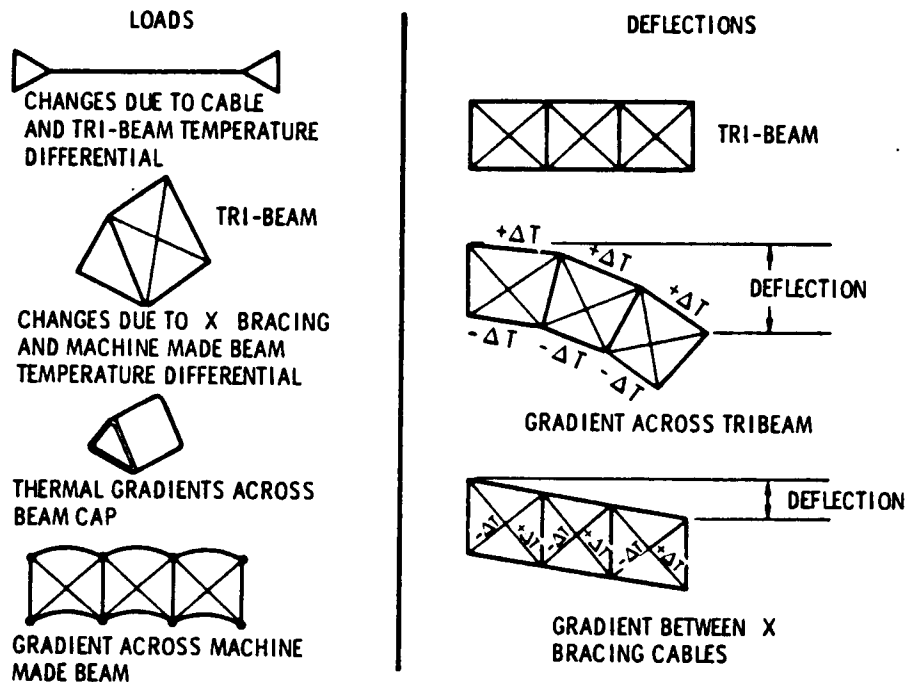
Figure 3.3-13. Thermal Structural Considerations

The most severe thermal-induced loads result from gradients between either the X-bracing or orthogonal cable array with the machine-made beam caps and occurs during an eclipse. Figure 3.3-14 illustrates the temperature history of the X-bracing cables and beam caps during an eclipse, for two cap thicknesses and two cable diameters that represent the range of designs. The peak difference in temperature between the appropriate design combinations is less than 55 C (100 F). The primary significance of the data is the suggestion that the gradients can be minimized by using more than one cable in a tension cable system. For a design with a cap of 1.8-mm gauge, the use of four 6.35-mm diameter cables rather than one 12.7-mm cable would result in a smaller gradient and could be wound on a smaller storage drum.

The magnitude of the thermal loads are addressed in Figure 3.3-15. While the cap locked in stress represents an operational condition, the remaining data pertain to an eclipse condition. The gradients across the cap induce
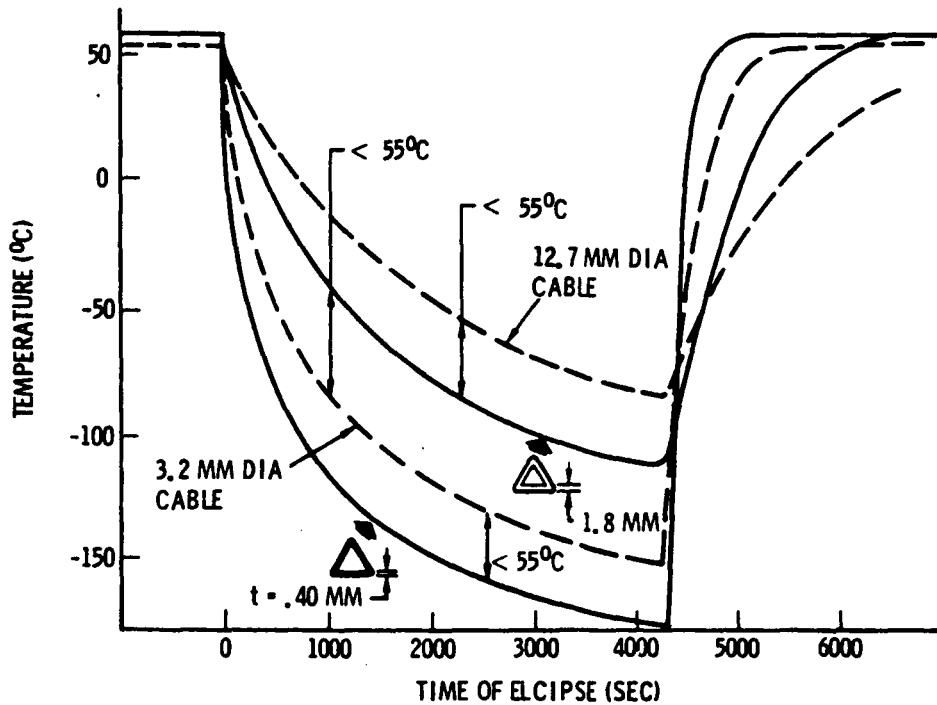
Figure 3.3-14. Structural Element Temperatures During Eclipse

TENSION CABLE ARRAY
AND TRIBEAM DIFFERENTIAL
TEMPERATURES

$\Delta T = 85°C$

THERMAL FORCE $= \alpha \Delta T E A_C$

WHERE A_C IS AREA OF CABLE
$P_T = P_I + \alpha \Delta T E A_C$
WHERE P_I IS THE INITIAL TENSION

FOR $A_C = \dfrac{P_I}{f}$ AND f IS CONSTANT (STRESS)

$P_T = P_I + \alpha \Delta T E \dfrac{P_I}{f}$

$\dfrac{P_T}{P_I} = 1 + \dfrac{\alpha \Delta T E}{f}$

$P_T / P_I = 1 + \dfrac{(.36) \times 10^{-6} (85) (13.8 \times 10^4)}{206} = 1.02$

LOCKED IN
STRESSES $= \alpha \Delta T E$

$= 0.36 \times 10^{-6} (55) (13.8 \times 10^4)$

$= 2.8 MPa$

$\dfrac{C_{MAX}}{C_A}$

$C_A = 34$ KN
$C_A = 68$ KN
$C_A = 137$ KN

← RANGE OF T MIN

ΔT BETWEEN X CABLES AND
BEAM ELEMENTS $= \pm 55°C$

T_{MIN} (N)

Figure 3.3-15. Thermal Loads

limit stresses of 2.8 MPa (400 psi) which is approximately 3 percent of the
applied limit compression stress. The data at the right address the increase
in tri-beam cap loads due to the pretension remaining in the X-bracing with
full-frame compression. The highest pretension loads will be imposed if the
pretension is totally performed prior to tensioning of the orthogonal cable
array. In this case the magnitude of pretension must be sufficient so that
subsequent to full pretension of the orthogonal cable array, and application
of the applied uniform loading, and a 55°C relative increase in the X-bracing
cables, the X-bracing cables remain in tension. Maintenance of tension in all
the X-bracing cables is required to assure accurate predictability of the frame
structural behavior. With that approach, initial cable pretension can be as
high as 67 KN (15,000 pounds) which would provide the design requirement on
the bracing attachments to the joints and cross members. However, a computer-
controlled staged pretension approach with X-bracing pretension leading the
orthogonal array could reduce the initial loading to 1 KN (225 pounds) and is
much more preferable to the structural design. The end result as far as the
load in the caps is concerned is the same and is shown at the right. This
includes the increase in cable load due to the X-bracing being 55°C cooler
than the beam caps. In all cases the thermal loads were small enough to be
negligible to this study.

The significant frame corner deflection Δ_H induced by the variation of
direct solar radiation is shown in Figure 3.3-16. The surface and frame
deflections due to thermal gradients from the reflected sunlight and distributed
loading of 60.0×10^{-6} N/m are invariant. The maximum deflection occurs at Point
H for the separate condition of gradient across the tri-beam and gradients
between the X-bracing elements shown by solid and dashed lines. The worst
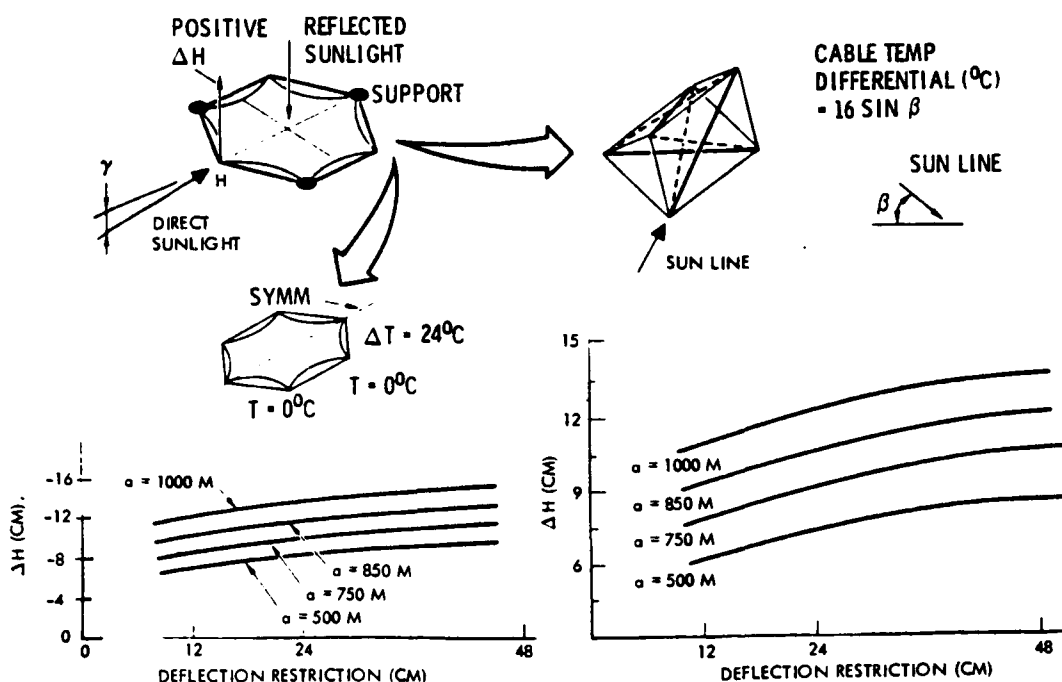
Figure 3.3-16. Thermal Deflections – Cable Temperature Differentials

gradient across the tri-beam is shown for a sun angle just above 0 and up to 30 degrees with the upper machine-made beam shadowed by the solid-state sandwich array. An opposite deflection will occur for the sun angle just below 0. The magnitude of gradients account for the continual presence of the reflected (CR=5) sunlight. The case shown for the gradients between the X-bracing cables, for a sun angle of 45°, is an upper-bound case and conservative. In both cases the thermal deflections were determined by the virtual work method applicable to trusses, in which the deflection is equal to the sum of all the $\alpha(\Delta T)u\ell$ terms in all the members. Magnification of this deflection due to secondary bending and torsion from the axial compression loading was estimated to be in accordance with the relation

$$\frac{3(\tan u - u)}{u^3} \quad \text{where} \quad u = \frac{\pi}{2} \sqrt{P/P_{cr}} \quad \text{(Reference 11)}.$$

The calculated data of Figure 3.3-16 indicate the frame corner deflections due to gradients across the tri-beam are opposite to that of the X-bracing. Since the case used for the X-bracing is an upper bound, the worst case occurs with gradient across the tri-beam due to direct sunlight at slightly above 0. While it is appreciated that the entire pretensioned orthogonal cable array will resist the deflections described, the magnitude of any reduction is not known and hence is ignored.

The issue of possible magnification of the thermal deflections due to solar induced vibrations is addressed in Figure 3.3-17. The minimum frequency of the antenna is generally in the regime of 0.0014 to 0.003 Hz (Figure 3.3-18). Sufficient frequency separation exists to preclude any magnification of thermal deflection, even without damping.
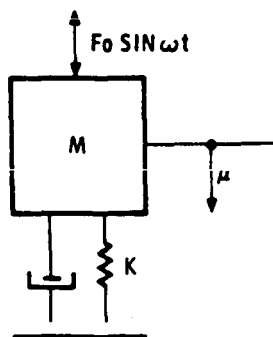
$$\frac{\mu_{max}}{F_0/K} = \frac{1}{\left\{ \left[1 - (\omega/\omega_n)^2 \right]^2 + (2r\omega/\omega_n)^2 \right\}^{1/2}}$$

WHERE $\omega_n = 2\pi f = 2\pi (.002) = .01256$ RAD/SEC

$\omega = \frac{2\pi}{24 \times 3600} = .0000727$ RAD/SEC

$\frac{\omega}{\omega_n} = .00578$

FOR ZERO DAMPING $\quad \frac{\mu_{max}}{F_0/K} = 1.00003$

DAMPING NOT REQUIRED

Figure 3.3-17. Solar Pressure-Forced Vibration Implication

1ST MODE
- FREQ 0.0028 Hz

DESIGN TO
RESTRICTION
OF Δ = 12 CMS
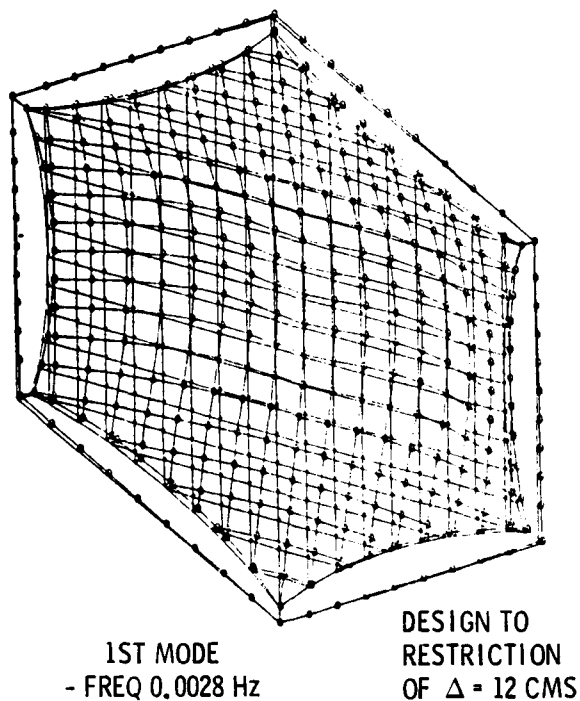
Figure 3.3-18.   Hexagonal Frame Minimum Modal Frequency*

The implication on total surface deviation of the direct sun-induced deflections was studied using the McNeal Schwendler version of NASTRAN with the model shown in Figure 3.3-19. This version of NASTRAN accounts for the change

• CBAR ELEMENTS USED
  FOR BENDING MEMBERS
• CROD ELEMENTS FOR
  TENSION CABLES
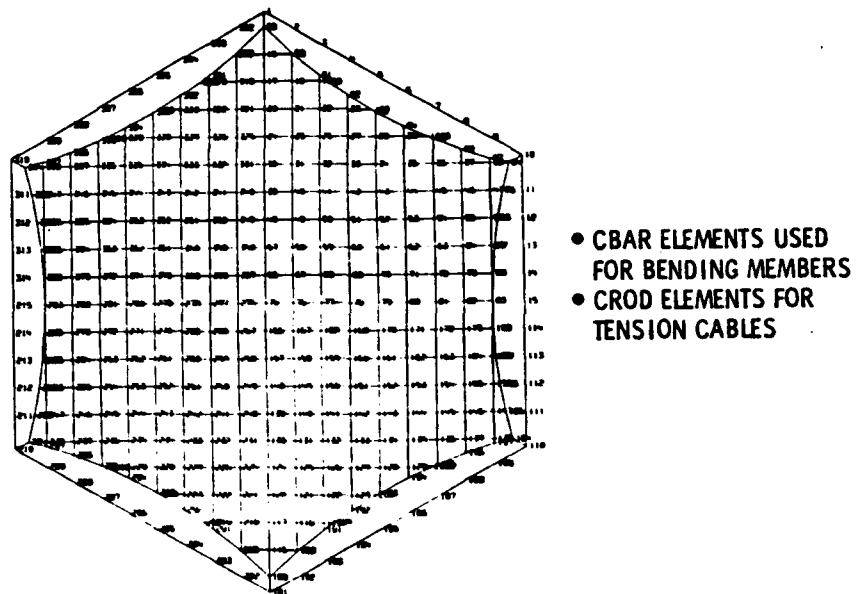
Figure 3.3-19.   NASTRAN Model of Antenna Structure

*The slight shape deviation shown results from a state of non-uniform tension throughout the array. The present NASTRAN analysis technique does not provide explicit establishment of uniform tension. This variation is, however, not significant to results.

in load compatible with deflection and hence provides exact analysis results
for structures containing tension stabilized cables. Table 3.3-1 presents the
maximum surface deviation obtained by superimposing the maximum corner deflec-
tion shown on the basic pressure load deflected shape, which is invariant.
The appropriate lesser deflections at the other two corners were also included.
It is evident that deflection of the corner opposite to that of the solar
pressure/gravity gradient loads produces the maximum deviation, and introduces
the advantage of a bias in the initial jack setting. A bias of 5 cm for the
design shown in Figure 3.3-20 together with the thermal deflections results in an
additional 2.5 cm (6.3 in.) or deviation above that of the basic uniform loading,
or an increase of 20 percent. Incorporation of this effect would shift the mass
curves to the right as suggested by the dotted line of Figure 3.3-10. However,

Table 3.3-1. Maximum Surface Deviation
Dimensions in cm (in.)

Deflection at Corner	Maximum Deflection of Array	Minimum Deflection of Array	Maximum Deviation
9.1 (23.1)	-14.8 (37.6)	2.1 (-5.3)	16.9 (42.9)
0	-15.1 (38.4)	-2.6 (6.6)	12.5 (31.7)
-9.9 (25.1)	-15.5 (39.4)	-2.1 (5.3)	13.4 (34.0)
Note: Sign convention is per Figure 3.3-16.			
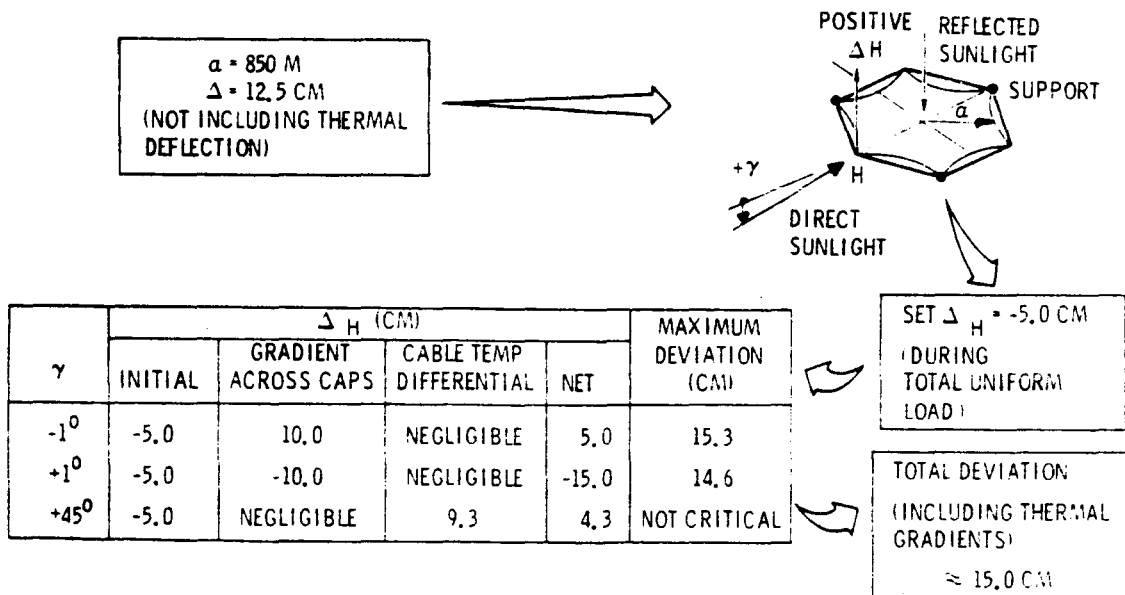
Figure 3.3-20. Example Thermal Deflection Effect on Deviation

in view of the design conservatism previously discussed, the curves shown in Figure 3.3-9 were maintained in Figure 3.3-10 and are quite accurate for the purposes of this study. The only modification made was the increase of tri-beam depth by 15 percent to limit the secondary deflection magnification. The machine-made beam element now has a fixity factor of 1.15 which is still conservative.

The data of Figure 3.3-10 can be used for estimation of the mass and depth characteristics of frames subject to other loadings. For example, a frame subject to half the total uniform loading will have the same depth and mass for essentially half the surface deviation. The method is limited to designs with surface deviation no less than 9 cm.

Finally of concern to the construction operation is the modal frequency of the frame during construction. Figure 3.3-21 illustrates the minimum modal frequency of the hexagonal frame in its weakest configuration, which is just prior to frame closure. Here too, the minimum frequency is well above the frequency of geosynchronous orbit gravity gradient disturbances, which is 0.000023 Hz, and with it adequate frequency separation.

OVERVIEW OF FRAME
CONSTRUCTION PRIOR TO
COMPLETION OF LAST BAY

1ST FREQUENCY = 0.0041 Hz
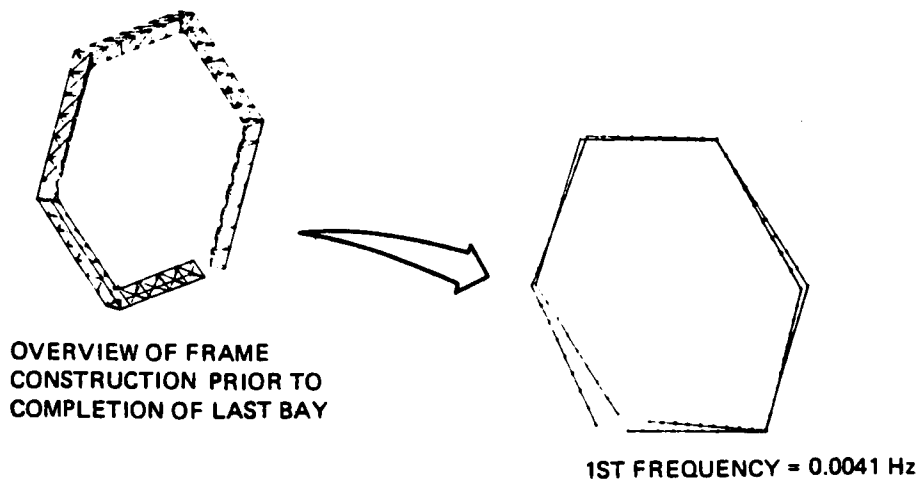
Figure 3.3-21. Construction Phase Minimum Modal Frequency

Configuration Analyses

Subsequent to completion of the foregoing described hexagonal frame analysis, a structural analysis review was performed upon the SPS solid state configuration shown in Figure 3.3-22.

The review resulted in the following:

- The estimated tri-beam structural characteristics, for system weights analysis are tabulated in Table 3.3-2. These characteristics were determined to sustain the frame compression loads incurred with develop-ment of the in plane tension loads necessary to limit the primary and secondary reflector surface deviations from flatness to no more than 1 meter.

3-68

"X" BRACING
CABLE AREA

CHORDS AND
DIAGONALS
AREAS

F

F

E

A

D

C

C

B

A & C

REFER TO TABLE 3.3-2 FOR
DESCRIPTION OF ELEMENTS
A THROUGH F
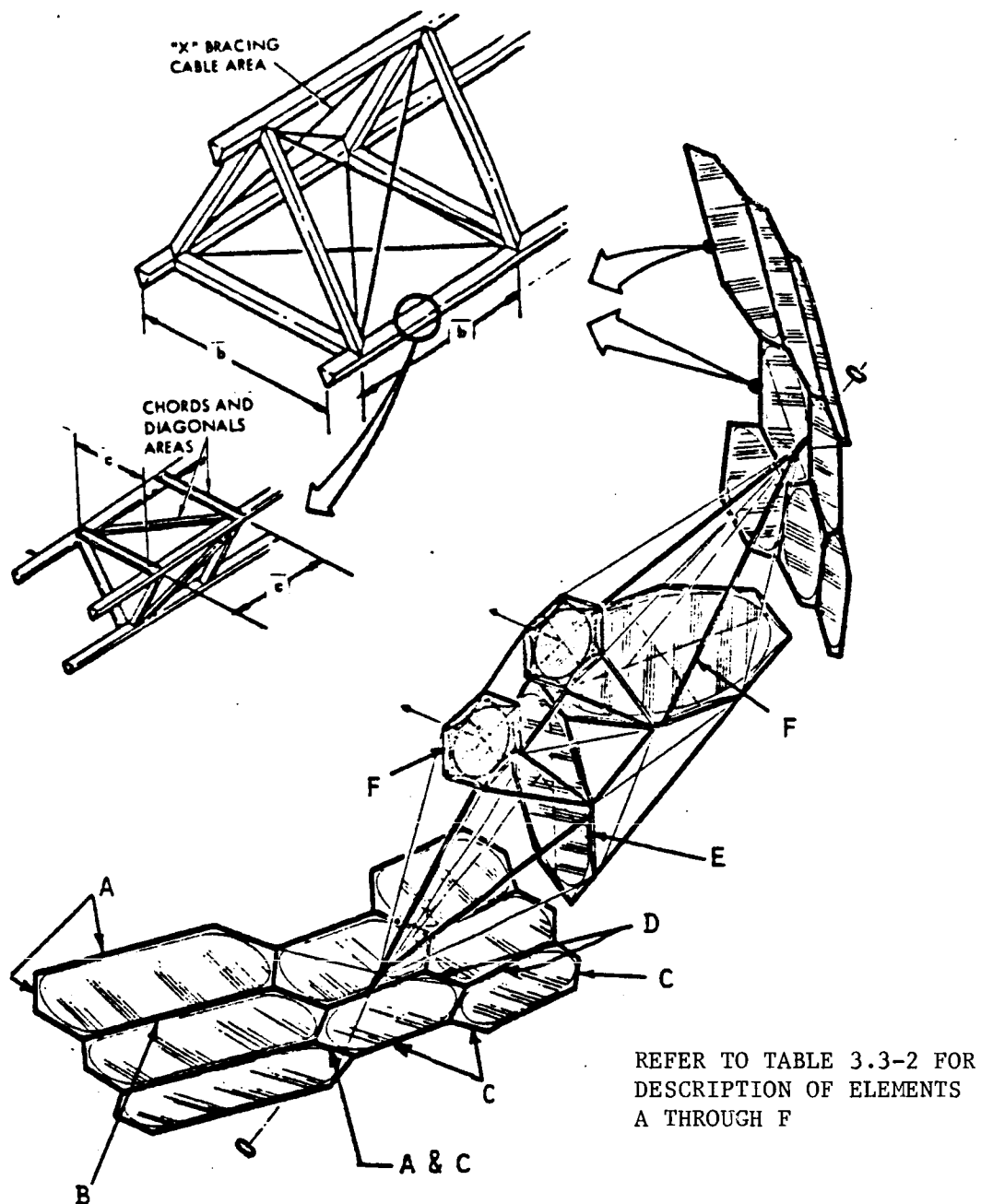
Figure 3.3 -22.   Solar Power Satellite - Sandwich Configuration -
Dual Solar Reflectors

Table 3.3-2. Frame Structural Characteristics
(Refer to Figure 3.3-10)

Element	Type	b (m)	a (m)	Unit Mass (kg/m)	Cross-Section Area (cm²)	Minimum Inertia, I (m⁴)
A		122	2.0	12.5	13.9	3.45
B		122	2.0	25.0	27.8	6.90
C		97	1.6	8.3	8.0	1.26
D		97	1.6	16.6	16.0	2.52
E		140	2.3	15.8	18.5	6.0
F		67	2.3	10.4	11.0	0.82

NOTE: $GI/EI = 0.265$ for all designs.

. The modal analyses results are shown in Figure 3.3-23. The first and
second minimum modal frequencies shown are 0.00196 and 0.002065 Hz.
The modal data were obtained from the modal defined by the CRT plot
shown which contains the structural characteristics shown in Table 3.3-2.
The microwave antenna structure characteristics used were determined
from the hexagonal frame data contained herein.

Discussion of the modal analysis results, described above, with controls
personnel, indicated there is adequate frequency separation to satisfy mainte-
nance of the required pointing accuracy and stability.

The analysis to satisfy the frame compression loads used the NASTRAN model
described by the CRT plots of Figures 3.3-24, 3.3-25, and 3.3-26. In each case
the frame analysis was based on each frame acting as an entity in itself and
independent of the other frames, which is considered to be accurate.

The compression loads were based upon achieving isotropic tension in the
membranes. The dimensions of the frame shown in Figures 3.3-24, 3.3-25, and
3.3-26 are such that the frames sustain axial compression without bending due

MODE 13 FREQ. 0.001966

MODE 14 FREQ. 0.002065
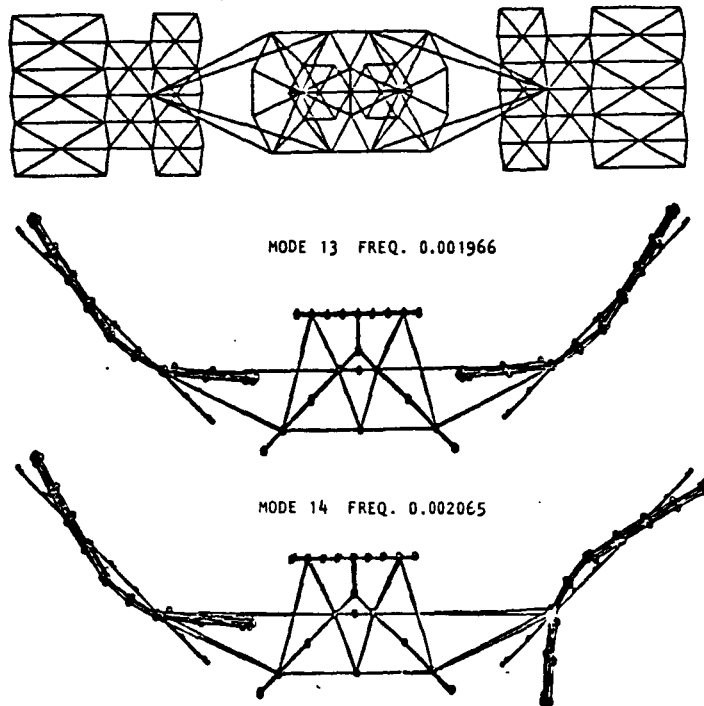
Figure 3.3-23. CRT of SPS Modal Model — First Two (Non-Rigid)
Body/Modal Shapes
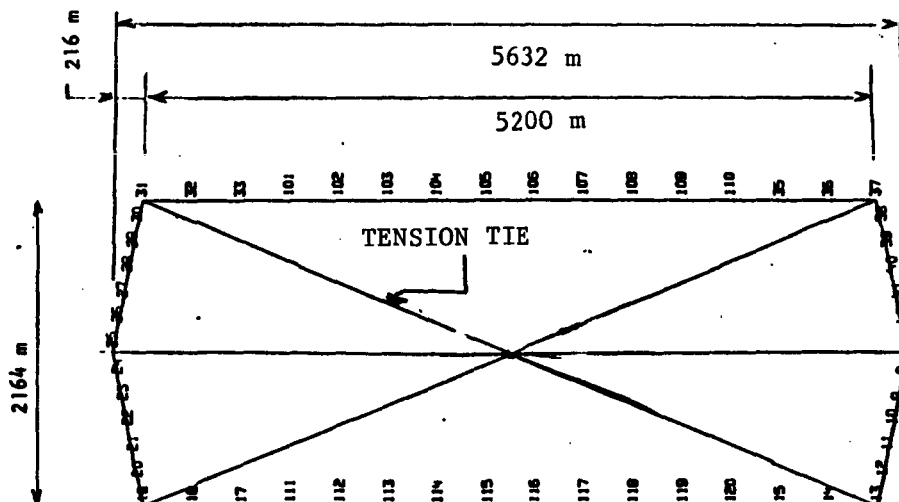
Figure 3.3-24. Primary Reflector Surface Compression Frame 1
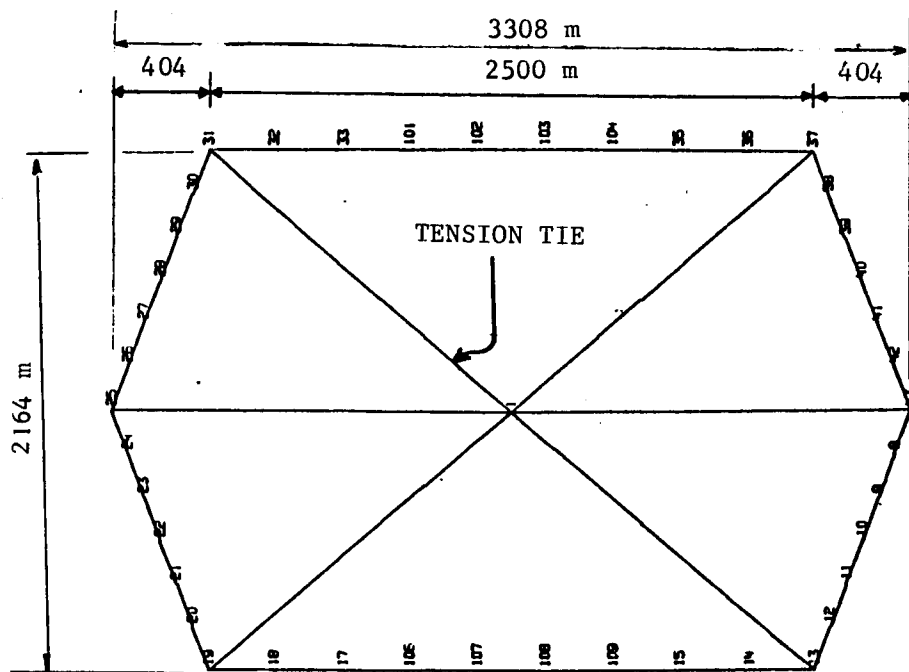
Figure 3.3-25. Primary Reflector Surface Compression Frame II
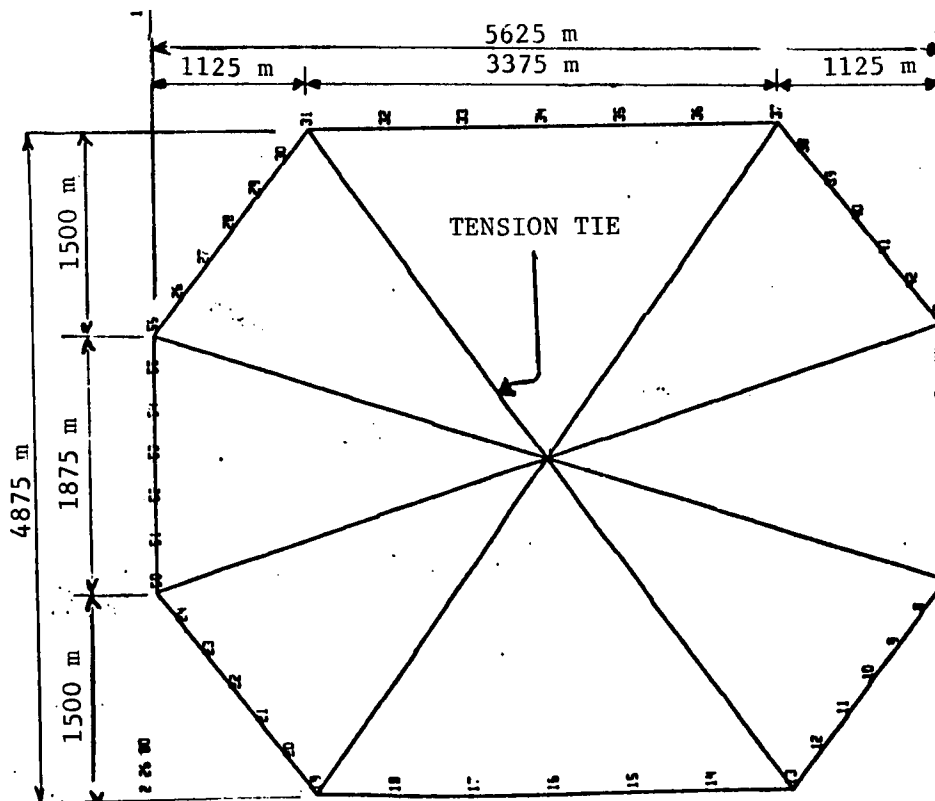
Figure 3.3-26. Secondary Reflector Surface Compression Frame III

to the loads delivered by perimeter cables attached to the corners of the frames. Finally, it is pertinent to note that during the analysis a determination was made of the equivalent buckling coefficients for each frame for different tri-beam GJ/EI stiffness ratios. These values are shown in Table 3.3-3. Based on the detailed trade study of the hexagonal frame, the selected designs utilized the buckling coefficients for a GJ/EI = .265.

Table 3.3-3. Frame Buckling Coefficient, η*
(Variation with Ratio of GI/EI)

Frame	Reference Figure	GI/EI = 0.053	GI/EI = 0.265	GI/EI = 0.53
I	3.3-24	0.193	0.873	0.984
II	3.3-25	0.072	0.31	0.52
III	3.3-26	0.097	0.286	0.365
$*\eta = \dfrac{P_1 \ell^2}{\pi^2 EI}$				

An alternative structural system to support the reflector surfaces are shown in Figure 3.3-25. The frame is comprised of radial compression members identified in the figure as 1-31, 1-25, 1-19, 1-13, 1-43, and 1-37. Future study of the solid state configuration shown in Figure 3.3-22, if required, will consider this option. While this configuration may be more efficient for the basic compression loading it has essentially the same overall modal frequency characteristics.

3.3.6 SUMMARY

In summary, the analyses conducted demonstrate the structural capability of the hexagonal frame/tension cable array to maintain the required surface flatness regimes. Active control is not required. While construction implications have not been analyzed, no construction problem is foreseen that would preclude achievement of the parametric design data shown. The data are directly dependent on successful development of a long-term, space suitable, low coefficient of expansion (0.36×10^{-6} m/m/°C) graphite composite machine-made beam. Achievement of the closed cap design is essential to the frame masses shown. The increased mass of an open cap design remains to be determined and may not be prohibitive. It is also appropriate to note that the analysis used the highest operational uniform loading foreseeable. Loads, during construction must, and can be compatible with the design, with appropriate on-orbit construction techniques and associated costs.

Also, the overall configuration minimum modal frequency was above 0.0016 Hz, providing significant frequency separation and use of classical control techniques.

3.4 THERMAL CONTROL

Thermal control supports all SPS satellite subsystems. Temperature is a significant parameter affecting all subsystems, material selections, and mass. Heat rejection is a particularly critical issue in the antenna design with use of solid-state elements, i.e., low-junction temperature allowables restricting baseplate temperatures to $\leq 125°C$. Thermal analysis was conducted to evaluate both the sandwich and end-mounted solid-state concepts and the magnetron concept. The objective of this analysis was to evaluate the design concepts, identify problems, and suggest design solutions. The approach was necessarily simplified. All thermal models were limited to six nodes or less and solutions were carried out with a programmable calculator. Therefore, temperature and power-level predictions are approximate. However, the models do reflect the major features of the three designs and are believed to be a good guide to trends and general levels. More detailed analysis will be required at a later date for design verification.

3.4.1 SANDWICH CONFIGURATION

This configuration is characterized by dipoles distributed over the back surface of the solar panel itself. Each dipole is supplied by a small solid-state amplifier. The antenna ground plane is separated from the solar panel by a honeycomb sandwich. The significant features from a thermal point of view are shown in Figure 3.4-1.
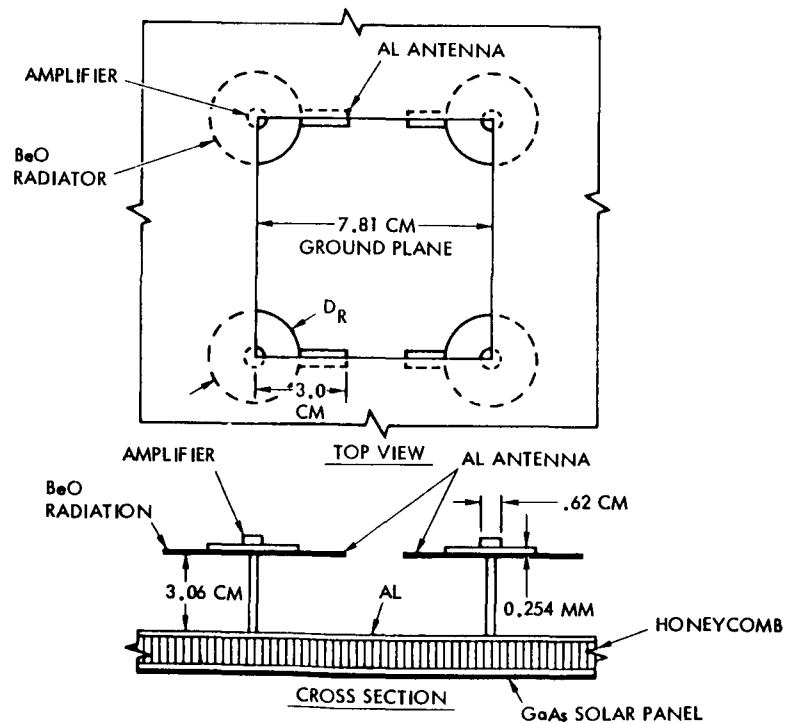
Figure 3.4-1. Sandwich Configuration

The solar panel is exposed to concentrated sunlight with an intensity of 5-6 suns. The solar cell temperature is limited to 200°C. On the opposite (antenna) side of the antenna, amplifier and ground plane are exposed to direct sunlight (one sun, worst case). In addition, there is power dissipation in the amplifier and heat leaking through the honeycomb from the solar cells. Amplifier baseplate temperature is limited to 125°C.

Early calculations showed that it would be very difficult to achieve the temperature limitations imposed on the solar cells and amplifier at CR = 6 or higher. A number of design features were varied parametrically in order to approach this goal. Selective thermo-optical properties were assumed on surfaces exposed to direct sun. A circular disk radiator made of BeO (Berlox) was used to carry away heat from the amplifier. Berlox has a high thermal conductivity, but is dielectric and does not impair the functioning of the dipole radiator.

A final set of performance calculations were carried out for the optimized design. Solar cell and amplifier temperatures were assigned their limiting values. The calculation then determined the value of the solar concentration ratio which could be used, and the radiator diameter required. These parameters determine the array power output.

The thermal model employed is shown in Figure 3.4-2. It contains four nodes and three heat sources. Heat transfer is primarily by radiation, but conduction through the honeycomb sandwich is also considered. Lateral temperature gradients in the radiator were taken into account by means of a radiator efficiency. Radiation exchange factors were estimated. Table 3.4-1 summarizes the assumptions employed.
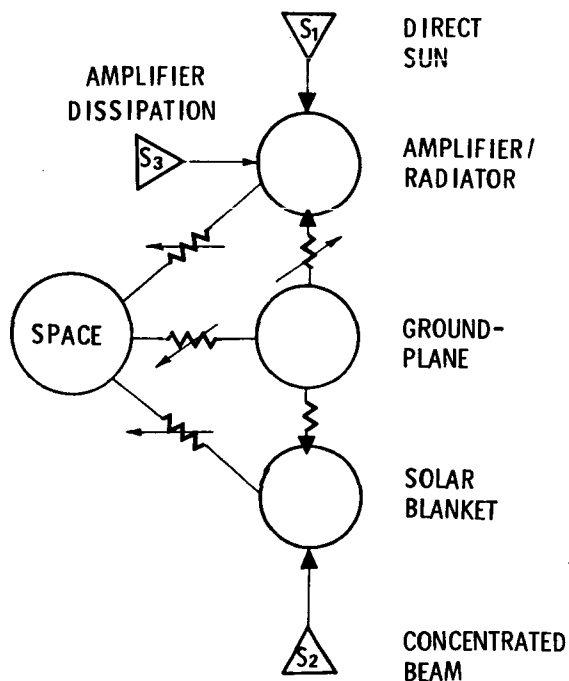
Figure 3.4-2. Thermal Model for Sandwich Configuration

Table 3.4-1.   Assumptions used for
Sandwich Antenna Thermal Model

SOLAR CONSTANT, 1385 W/m² (WINTER SOLSTICE)		
SOLAR PANEL CHARACTERISTICS	GaAs	MULTI-BANDGAP
SOLAR, α	0.56	0.60
EMISSIVITY, ϵ	0.84	0.84
EFFICIENCY (200°C)	0.151	0.2506
ARRAY FACTOR	0.94	0.94
PACKING FACTOR	0.95	0.95
DEGRADATION (EOL)	0.96	0.96
CELL OPERATING TEMPERATURE	200°C	200°C

HONEYCOMB STRUCTURE

   6.35-mm HEXCELLS WITH 50-μm WALLS
   INNER SURFACES BLACKENED (ϵ = 0.9)

GROUNDPLANE SURFACE

   SELECTIVE (α/ϵ = 0.2/0.8)
   VIEW FACTOR TO SPACE $\approx$ FRACTION UNBLOCKED BY RADIATOR

BERLOX RADIATOR

   SELECTIVE (α/ϵ = 0.2/0.8)
   OPERATING TEMPERATURE (INNER RADIUS), 125°C

Final calculations were made for two cases—one for single-junction GaAs and the other for a multi-bandgap (MBG) solar cell. Node temperatures and steady-state power flows per amplifier are listed in Tables 3.4-2 and 3.4-3. The results show that, with a 4-1/2 cm radiator, the GaAs array can operate at about CR = 5-1/2. The MBG array can go to about CR = 5-3/4 by increasing the radiator diameter to 6 cm. The amplifier power for the MBG array is almost twice that for the GaAs array because of the greater cell conversion efficiency.

Table 3.4-2.   Node Temperatures and Energy Flow for
Sandwich Configuration (GaAs Cells)

	ENERGY FLOW (WATTS/AMPLIFIER)	
ENERGY BALANCE ON SOLAR BLANKET	BOL	EOL
CONCENTRATED INCIDENT BEAM	46.55 (CR = 5.51)	45.96 (CR = 5.44)
SUNLIGHT ABSORBED	26.07	25.74
NET POWER TO AMPLIFIER	6.28 (η_E = 0.135)	5.95 (η_E = 0.129)
RADIATED FROM CELL SURFACES	14.54 (T_C = 200°C)	14.54 (T_C = 200°C)
RADIATED/CONDUCTED FROM GROUND-PLANE	5.25 (T_G = 150°C)	5.25 (T_G = 150°C)
ENERGY BALANCE ON AMPLIFIER/RADIATOR		
HEAT DISSIPATED BY AMPLIFIER	1.26 (η_A = 0.8)	1.19 (η_A = 0.8)
DIRECT SUNLIGHT ABSORBED	0.45 (D_R = 4.59 cm)	0.43 (D_R = 4.46 cm)
RADIATION FROM GROUNDPLANE	0.13	0.12
RADIATION TO SPACE	1.84 (T_R = 125°C, η_R = 0.98)	1.74 (T_R = 125°C, η_R = 0.98)

Table 3.4-3. Node Temperatures and Energy Flow for
Sandwich Configuration (MBG Cells)

ENERGY BALANCE ON SOLAR BLANKET	ENERGY FLOW (WATTS/AMPLIFIER)	
	BOL	EOL
CONCENTRATED INCIDENT BEAM	49.17 (CR = 5.82)	48.06 (CR = 5.69)
SUNLIGHT ABSORBED	29.50	28.83
NET POWER TO AMPLIFIER	11.01 (η_E = 0.224)	10.34 (η_E = 0.215
RADIATED FROM CELL SURFACES	14.54 (T_C = 200°C)	14.54 (T_C = 200°C
RADIATED/CONDUCTED TO GROUNDPLANE	3.95 (T_G = 163°C)	3.95 (T_G = 163°C)
ENERGY BALANCE ON AMPLIFIER/ RADIATOR		
HEAT DISSIPATED BY AMPLIFIER	2.20 (η_A = 0.8)	2.04 (η_A = 0.8)
DIRECT SUNLIGHT ABSORBED	0.86 (D_R = 6.28 cm)	0.81 (D_R = 6.09 cm)
RADIATION FROM GROUNDPLANE	0.39	0.37
RADIATION FROM SPACE	3.45 (T_R = 125°C, η_R = 0.98)	3.25 (T_R = 125°C, η_R = 0.98)

3.4.2 END-MOUNTED CONCEPT

This configuration decouples the solar array from the antenna, and the analysis involves antennas and amplifiers only (no solar panels). In this case, the amplifiers are solid state and similar to the ones used in the sandwich configuration. They are clustered in groups of nine or less at the end of dipole antenna supports (Figure 3.4-3). The amplifiers are bonded thermally to an aluminum close-out dish which acts as both fin and conductor. The close-out is attached around its perimeter to a doubled groundplane. The groundplane is separated from a bottom sheet by a honeycomb structure.
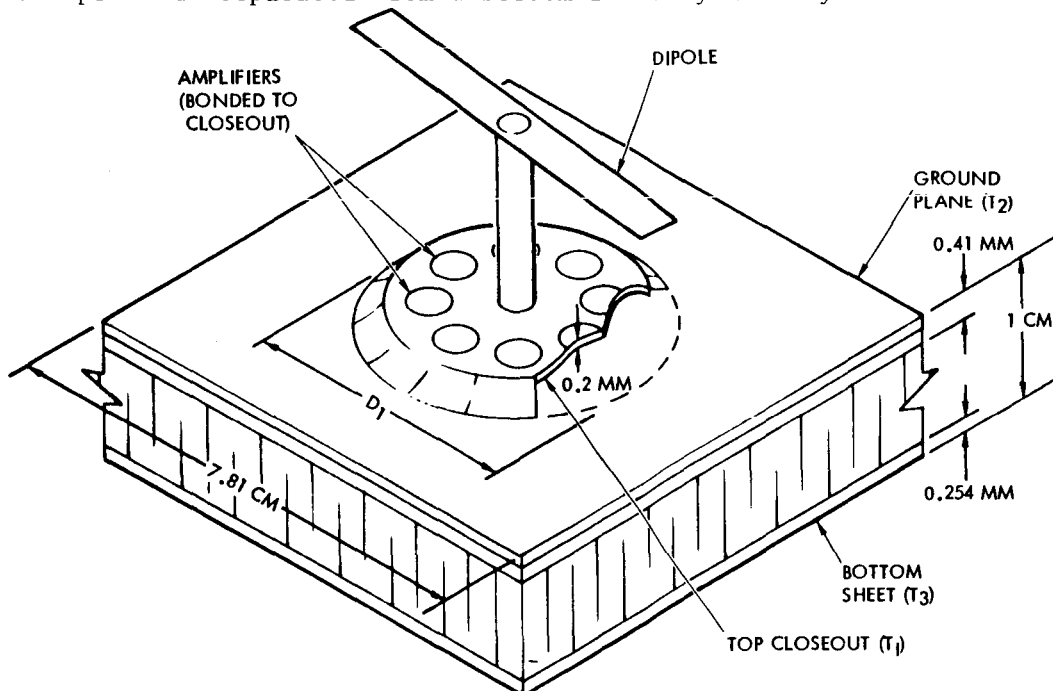
Figure 3.4-3. End-Mounted Concept

The thermal model employed is illustrated in Figure 3.4-4. Amplifier
base temperature was held to the maximum allowable temperature of 125°C.
Maximum amplifier dissipated power was calculated for two close-out sizes and
two direct sun exposures—from the top (amplifier) side and from the bottom.
Corresponding microwave power per unit area was calculated from component effi-
ciencies and the module size (7.81 cm by 7.81 cm). Table 3.4-4 lists the
assumptions employed in the thermal calculations. Maximum microwave output
permitted under the 125°C amplifier temperature limitation is given in
Table 3.4-5 for the cases considered.
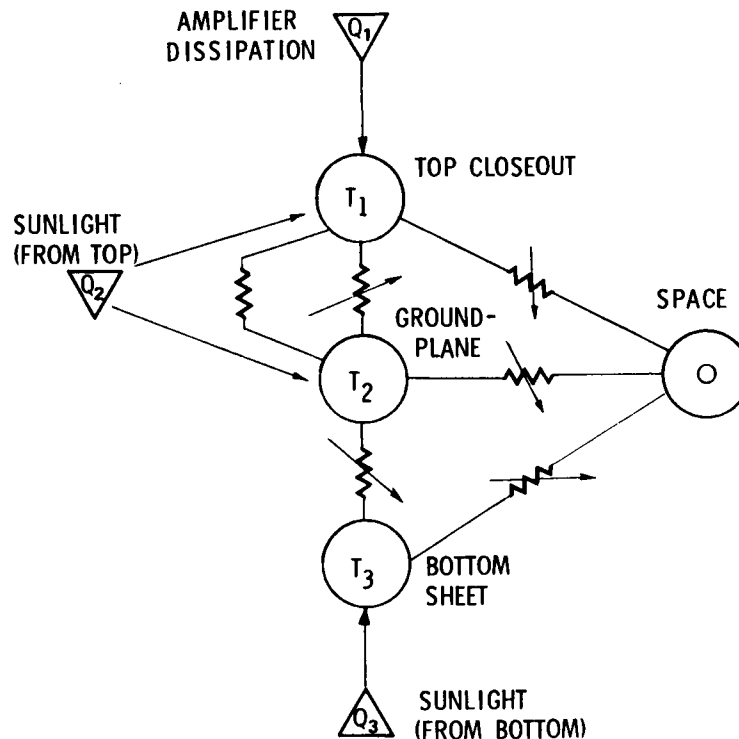
Figure 3.4-4. Thermal Model for End-Mounted Configuration

Table 3.4-4. Assumptions for Analysis of
End-Mounted Configuration

Component Efficiencies:	
Amplifier	0.80
Driver	0.99
Antenna	0.96
Fin (Close-out Disk)	0.75
Thermo-Optical Properties: (α/ϵ)	
Outer (Sun-Exposed) Surfaces	0.2/0.8
Inner Surfaces	0.9/0.9
Honeycomb Conductance (W/K)	
3 cm Diameter	0.27
4 cm Diameter	0.35

Table 3.4-5. Maximum Microwave Output for
End-Mounted Configuration

SUN ($1385\ W/M^2$)	CLOSEOUT Diam D_1 (CM)	TEMPERATURES (C) Amplifier	Groundplane	Bottom	MICROWAVE Power (W/M^2)
TOP	3.0	125	104	33	3867
	4.0	125	109	37	4175
BOTTOM	3.0	125	102	58	4332
	4.0	125	108	62	4685

3.4.3 MAGNETRON CONCEPT

This configuration involves antennas and power amplifiers only—no solar panels are involved. The thermally significant features are illustrated in Figure 3.4-5.
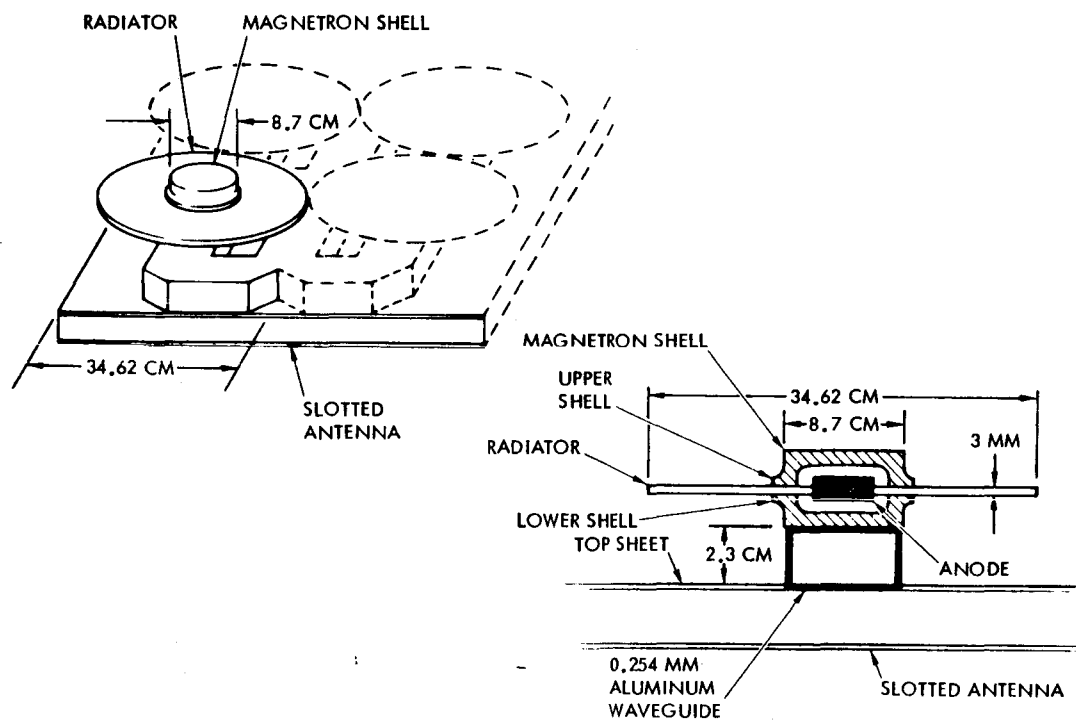
Figure 3.4-5. Magnetron Concept

The magnetron anode is surrounded by a top and bottom shell and is assumed to exchange heat with both by radiation only. (No interior details of the magnetron are available.) The anode is assumed to be the site of all thermal dissipation. It is surrounded by an annular disk of pyrolytic graphite which extends beyond the shells so as to act as a radiating fin. This fin exchanges radiation with space and with the top sheet covering the slotted antenna.

The lower shell of the magnetron rests on an aluminum waveguide mounted on the top sheet. Heat is exchanged between the lower shell and top sheet by conduction and radiation. The thermal model is shown in Figure 3.4-6.
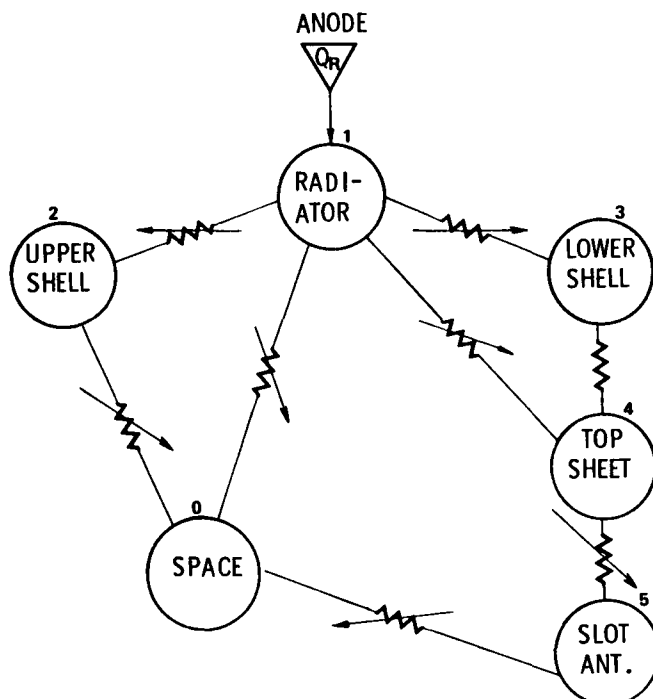
Figure 3.4-6. Thermal Model for Magnetron Configuration

The diameter of the graphite fin is rather large (35 cm) and its effectiveness is critically dependent on thickness and thermal conductivity. The 3-mm thickness shown is a compromise between mechanical strength and system weight. A thermal conductivity of 250 W/MK at 300°C was taken from Reference 12. Raytheon (Reference 13), who proposed the magnetron approach, has assumed a tapered fin (3 mm at the root and 0.5 mm at the outer edge. They have also used thermal conductivity about three times as high.

Further assumptions used in the present analysis were:

1. Direct solar heating was ignored (but is not negligible).

2. The top sheet has a 90% reflectivity, and promotes heat loss to space by reflecting emission from the lower fin surface.

3. Inner surfaces of top sheet and slotted antenna are blackened (ε= 0.9) for better radiation transfer.

4. View factors were estimated based on percent of blackage.

5. Radial temperature gradients in fin and top sheet approximated by fin efficiencies.

Parametric calculations of node temperatures were carried out for two values of magnetron input power at two efficiencies. The results are shown in Table 3.4-6. Despite detailed differences in the two analyses, the results agree fairly well with those presented by Raytheon (Reference 13). A comparison between Reference 13 predictions and those described here are shown in Figure 3.4-7.

Table 3.4-6. Node Temperature Predictions for
Magnetron Configuration

RF Input Power Per Magnetron	Magnetron Efficiency	Dissipation Q_R	Radiator (Center)	Temperatures (C)			
				Upper Shell	Lower Shell	Top Sheet	Antenna
3000 W	.85	529.4 W	350	265	346	70	12
	.90	333.3 W	282	206	229	32	-2
4000 W	.85	705.9 W	397	305	393	95	33
	.90	444.4 W	324	242	320	55	0
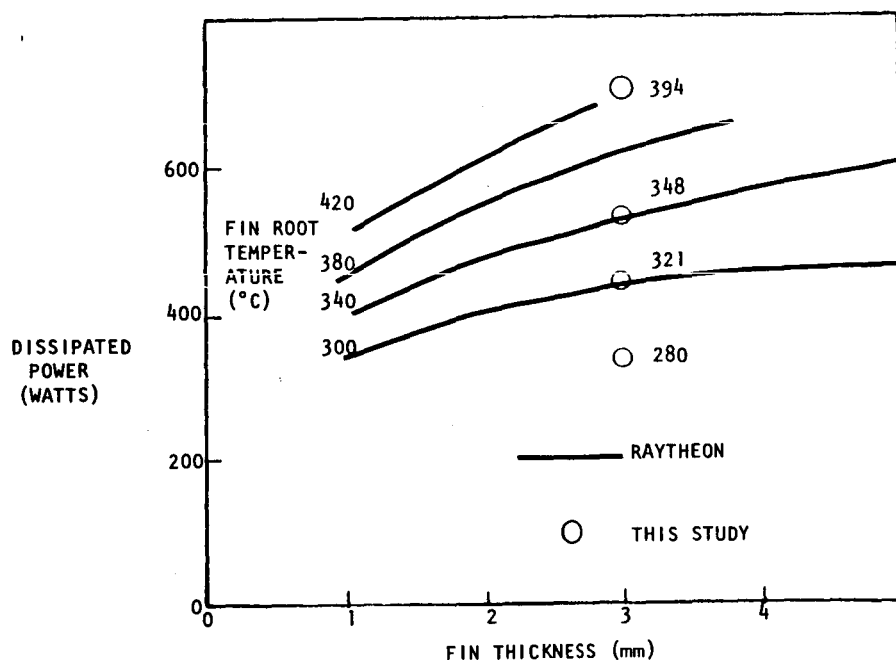
Figure 3.4-7. Predicted Node Temperature Comparisons
for Magnetron Configuration

3-81

3.5 ATTITUDE CONTROL AND STATIONKEEPING

Attitude control requirements are configuration dependent. As an entity, the vehicle control subsystem is only a small portion of the total vehicle mass, representing approximately two percent of the in-orbit mass. However, it has a disporportionate effect on the overall system performance and operation. It is the only subsystem that may require large quantities of material (propellants) resupplied on a regular basis after IOC. Pointing accuracy and shape of high-tolerance surfaces (reflector, microwave antenna) affect the efficiency of solar collection and microwave transmission. The most important configuration trades must recognize this effect and optimize the system accordingly. These trades are performed between the vehicle control subsystem and other subsystems and the satellite configuration. The following describes the control analysis performed on the SPS sandwich configuration. This analysis was conducted to evaluate the magnitude of the control problems related to the configurations.

The configuration initially studied is the same concept presented in Section 3.3 (Figure 3.3-1) used for the structural analysis. For this spacecraft geometry, substantial gravity-gradient and solar-pressure torques result. Also, large solar-pressure forces act on the system due to the large surfaces of the primary reflector and secondary mirror system. Thus, for this configuration, these torques and solar-pressure forces have a large impact on the attitude control and stationkeeping (ACSS) design.

The analysis also included the concept of free-flying various parts of the spacecraft relative to each other. The objective was to determine the impact these concepts may have in terms of propellant consumption and thruster requirements. It must be pointed out that this portion of the study is based on simplified models. The realization is immediate that the control and navigation problems for free flying are complex.

The coordinate system chosen is a local vertical frame with the X and Z axes the in-plane coordinates and the remaining Y-axis normal to the orbit plane. The coordinate system is presented in Figure 3.5-1. The X-axis is positive in the direction of the velocity vector; Z is positive, pointing toward the earth; and Y positive to complete the triad. The flight attitude of the spacecraft is Y-POP.

3.5.1 PROPELLANT REQUIREMENTS

The RCS propellant requirements are dominated by two factors. The most dominant factor is the stationkeeping propellant requirements to correct the inertial solar pressure force acting on the primary reflector. The other is the gravity-gradient torque about the X-axis. These contribute approximately 83% to the propellant requirements for the system.

The large gravity-gradient torque along the X-axis (M_{GGX}) results from the asymmetry of the spacecraft in the y-z plane. Referring to Figure 3.5-2, the asymmetry results from the large offset between the primary reflector mass and overall c.m., and the offset between sandwich mass and overall c.m. These
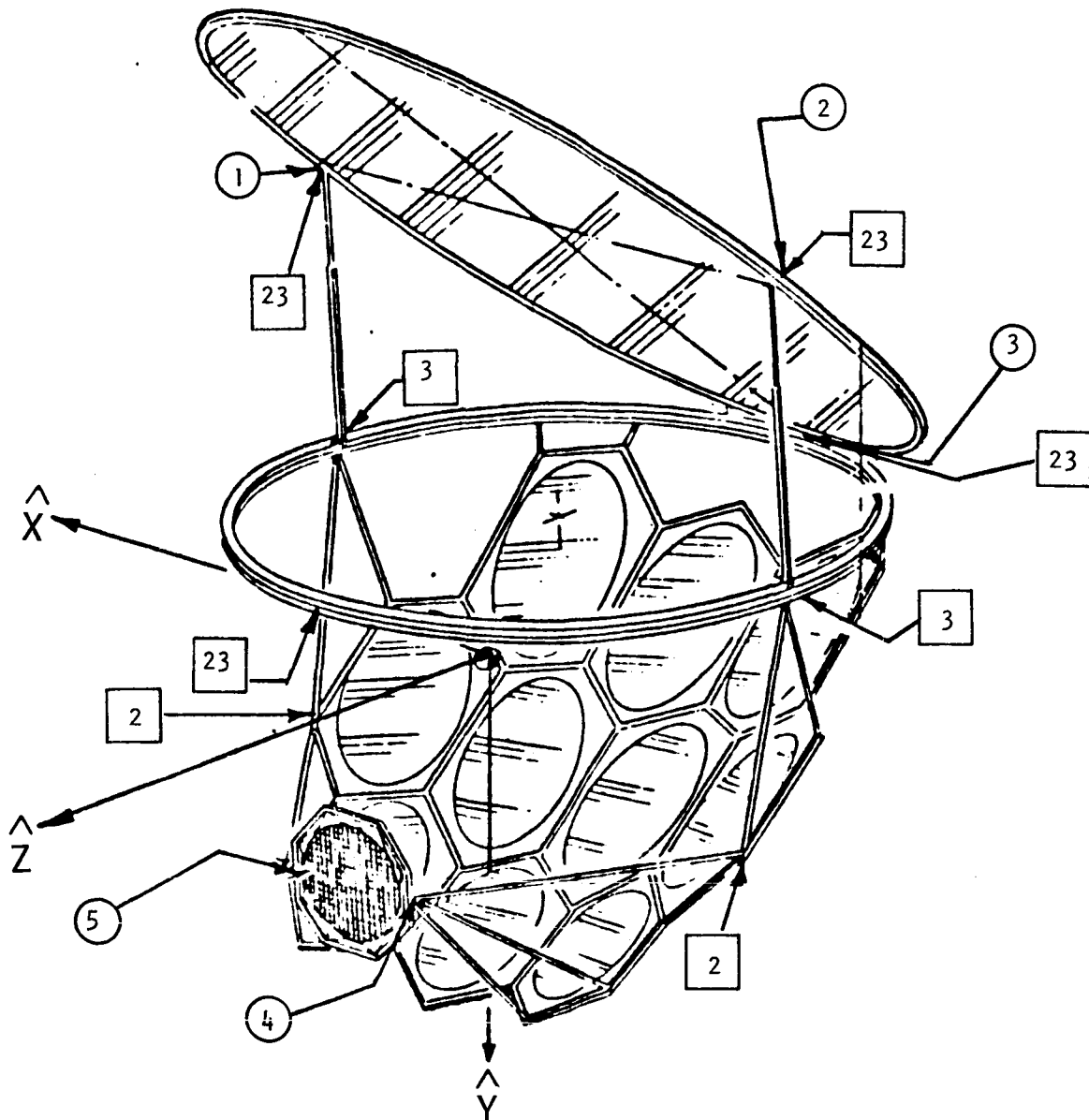
ATTITUDE DETERMINATION SYSTEM

5 LOCATIONS ◯

- CCD SUN SENSOR (1/SYSTEM)

- CCD STAR SENSOR (2/SYST.)

- ELECTROSTATIC OR LASER
  GYROS (3/SYSTEM)

- DEDICATED MINIPROCESSOR

THRUSTERS—102

8 LOCATIONS ☐

- 46 THRUSTERS MOUNTED
  ON PRIMARY REFLECTOR
  ARE GIMBALED ±11.75°

- 4 THRUSTERS MOUNTED ON
  SECONDARY MIRROR ARE
  DIFFERENTIALLY GIMBALED
  39°

Figure 3.5-1.   ACSS Equipment Location

$$\left| M_{GGX} \right| > 100 \left[\left| M_{GGY} \right| \text{ OR } \left| M_{GGZ} \right| \right]$$

$$M_{PR} = 1.5 \times 10^6 \text{ kg}$$

$$M_{SAND} = 4.4 \times 10^6 \text{ kg}$$
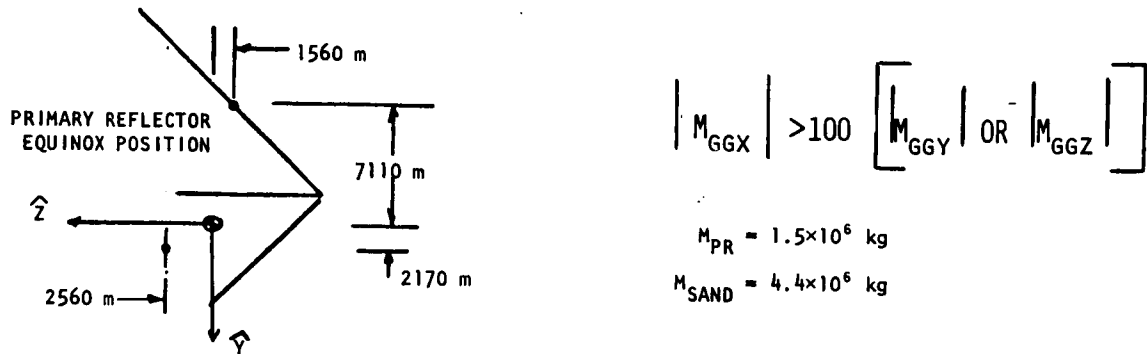
Figure 3.5-2. Gravity-Gradient Torque

two properties are additive and give rise to a secular gravity-gradient torque, the magnitude of which is better than 100 times the magnitude of the gravity-gradient torques along the Y or Z axes. Further, the value of M_{GGX} is essentially constant for all pointing errors of ≤ 0.5 degree. (The design point is 0.05 degree.) The propellant penalty attributed to M_{GGX} is 33% of the total. There is a significant RCS propellant penalty for attitude control of this geometry.

Three solar pressure forces act on the spacecraft. However, only the solar radial force (inertial) gives rise to a secular orbit perturbation. Referring to Figure 3.5-3, the other two forces designated as FSP1 and FSP2 give rise to cyclical perturbations. The FSP1 force is directed radially in the negative Z-direction and FSP2 acts normal to the orbit plane in the negative Y-direction.

PERTURBATIONS	ΔV (M/SEC/YR)	
	INTEGRATED CONCEPT 1	BASELINE COPLANAR
• SOLAR PRESSURE SOLAR RADIAL	974	285.2 (E-W)
• EARTH TRIAXIALITY (E-W)	1.83	
• SOLAR-LUNAR (N-S)	53.3	53.3
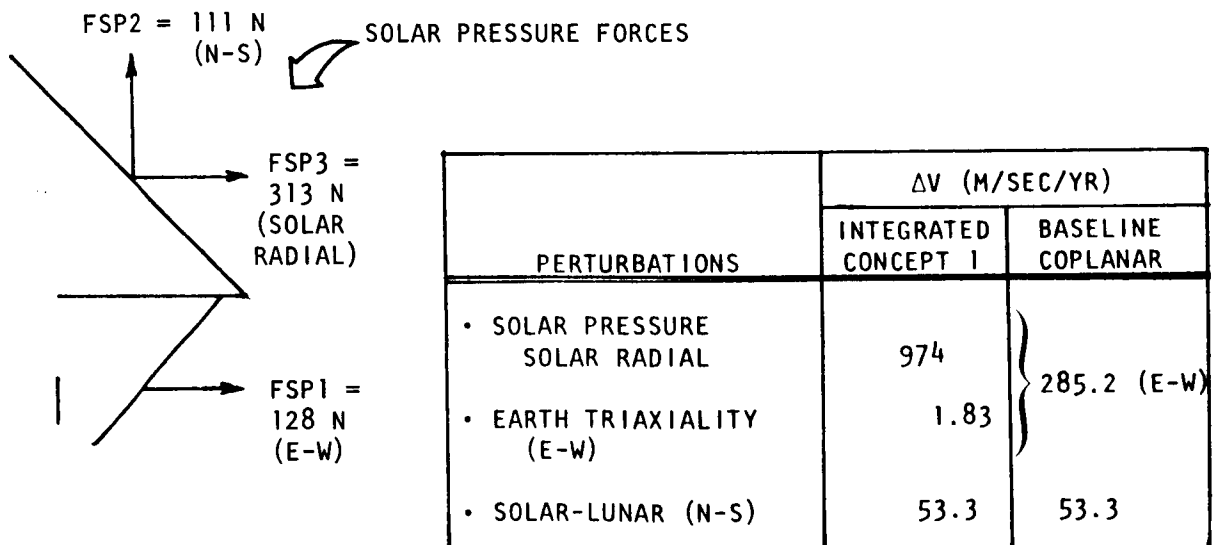
Figure 3.5-3. Stationkeeping ΔV Requirements
—Sandwich Concept

3-84

The solar radial force results in a ΔV requirement of 3.4 times the ΔV requirement of the coplanar design. This stationkeeping correction results in a propellant penalty of 50% the total propellant mass.

Table 3.5-1 presents RCS propellant requirements. The results are summarized in terms of stationkeeping and attitude control propellant requirements. From the table, the propellant requirements are equally divided between stationkeeping and attitude control. Also, as indicated in the table, this configuration requires a propellant mass of 48.5% of spacecraft mass over 30 years; this compares to only 8% required for the reference klystron coplanar design.

Table 3.5-1. RCS Propellant Requirements

FUNCTION	PROPELLANT MASS	
	KG/YR×10⁴	% S/C MASS OVER 30 YR
STATIONKEEPING		
• SOLAR-LUNAR	0.42	1.24
• SOLAR RADIAL	7.74	22.92
SUBTOTAL	8.16	24.16
ATTITUDE CONTROL		
• GRAVITY-GRADIENT TORQUE		
X-AXIS	5.46	16.17
Y & Z AXES	0.05	0.15
• SOLAR PRESSURE TORQUE X-AXIS	2.70	8.00
SUBTOTAL	8.21	24.32
TOTAL	16.37	48.48

NOTE: CONSTANT SOLAR PRESSURE CORRECTION POLICY—
ANNUAL PROPELLANT REQUIREMENT = 19.54×10⁴ KG

Another stationkeeping policy was considered in which a constant correction is applied to all the solar pressure forces. This constant correction policy resulted in a propellant requirement of 58% of spacecraft mass over 30 years. The policy of allowing cyclical perturbations results in a propellant reduction of 9.5%.

3.5.2 THRUSTER REQUIREMENTS

The SPS sandwich concept (Figure 3.5-1) shows the location and number of thrusters. The thrusters are mounted at eight locations. The RCS operates an average of 66 thrusters. A total of 102 thrusters is included to provide the necessary redundancy. Figure 3.5-4 shows further details of the thruster system, indicating some of the thruster characteristics and thrusting directions. The thrusters mounted on the primary reflector are gimbaled ±11.75° to provide a constant correction force to counter the solar radial force as the sun travels ±23.5° from the equinox position. The thrusters mounted on the seconary mirror system are differentially gimbaled 39° to control the gravity-gradient torques about the Y and Z axes. The remaining thrusters mounted on

the ring are to control the M_{GGX} disturbance, solar-lunar perturbation, and the solar pressure torques resulting from FSP1 and FSP2 (refer to Figure 3.5-3). Approximately 55% more thrusters are required for the sandwich configuration than for the coplanar system. Locations and types of sensors for the attitude reference determination system were shown in Figure 3.5-1.

GIMBALED
THRUSTERS

11.75°
11.75°

30

13

4

13

2

15

2

DIFFERENTIALLY
GIMBALED 39°

THRUSTER CHARACTERISTICS

* THRUST: 13 N
* SPECIFIC IMPULSE: 13,000 SEC
* MASS: 120 KG
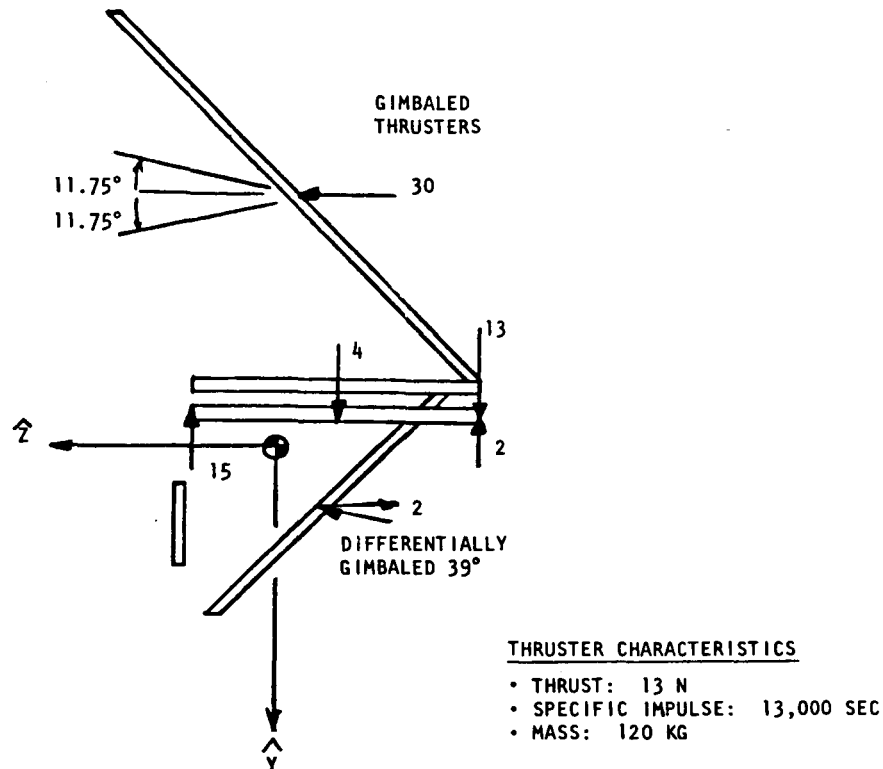
Figure 3.5-4. RCS Thruster Requirements

3.5.3 ACSS MASS SUMMARY AND POWER

The mass properties for the ACSS are summarized in Table 3.5-2. The summary includes the mass of the individual elements and propellant mass. The system average operating power which is proportional to the propellant mass is 65 megawatts.

Table 3.5-2. ACSS Mass Summary

ITEM	MASS $(\times 10^3)$ kg
ATTITUDE DETERMINATION SYSTEM	0.23
THRUSTERS—INCLUDING SUPPORT STRUCTURE 102 @ 120 kg/THRUSTER	12.24
TANKS, LINES, AND REFRIGERATION	28.91
POWER PROCESSING EQUIPMENT	TBD
ARGON PROPELLANT (ANNUAL REQUIREMENT)	163.38
TOTAL (DRY)	41.38
TOTAL (WITH PROPELLANT)	204.76

3.5.4 FREE-FLYING CONCEPTS

Referring to Figure 3.5-5, two systems were considered for the free-flying concept. The first configuration is a two-body system in which the primary reflector is separated from the lower body consisting of the secondary mirror and sandwich with associated structure. The second concept is a three-body option in which the primary reflector, secondary mirror, and sandwich were considered as separate bodies. The objective of the analysis was limited to determining propellant and thruster requirements. It must be emphasized that the analysis was based on simplified models and approximations. More work is required to obtain definitive results for the free-flying concepts.

- THRUSTERS: 68
- PROPELLANT: 15.4×10^4 KG/YR

20

TWO-BODY

14

4

4

2

2

GIMBALED THRUSTERS
2.3° GIMBAL RANGE

7

THREE-BODY

**THRUSTER CONFIGURATION
OF PRIMARY REFLECTOR
SAME AS TWO-BODY**

8

6

2

2

8

6

GIMBALED
THRUSTERS

GIMBAL ANGLE
49°

INTEGRATED CONCEPT NO. 1
THRUSTERS: 66 (NO SPARES)
PROPELLANT: 16.4×10^4 KG/YR
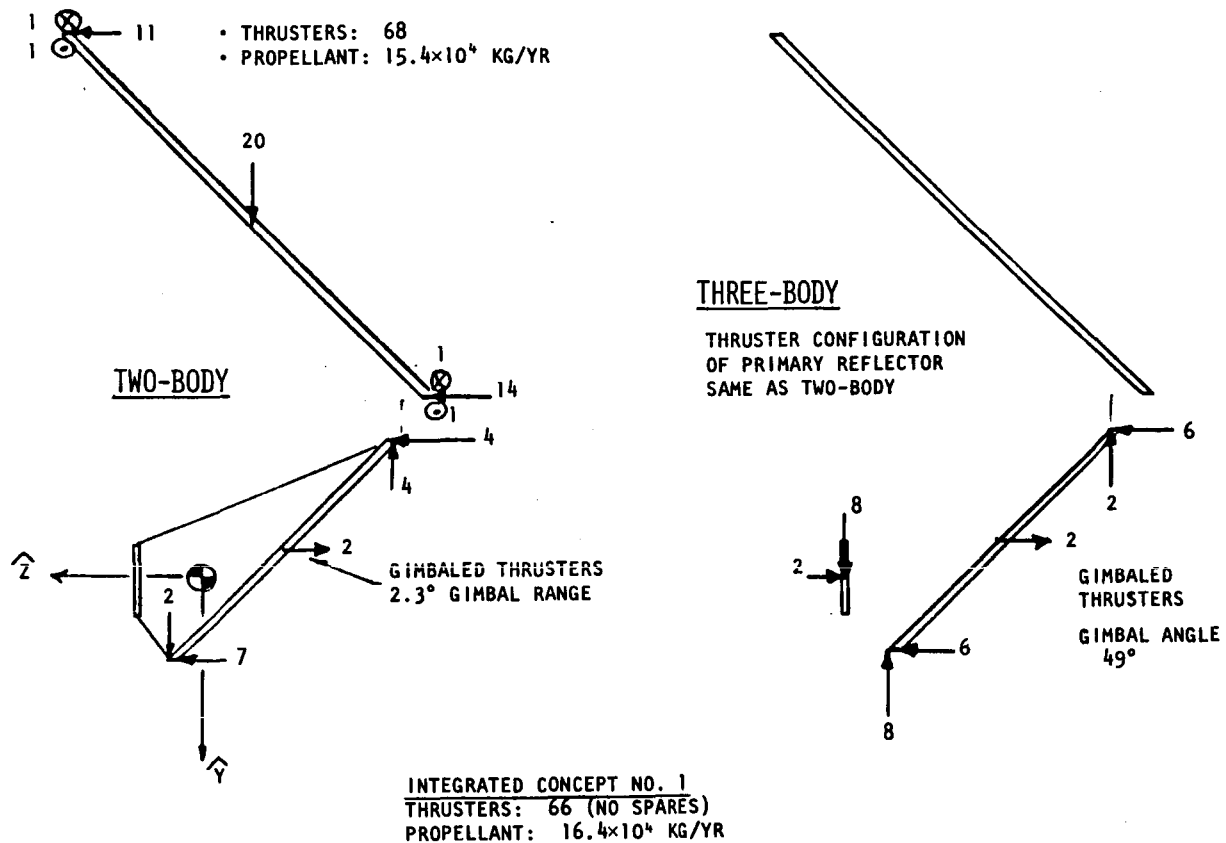
Figure 3.5-5.   Free-Flying Concepts

The results summarized in Figure 3.5-5 show that the two-body concept is competitive in terms of propellant and thruster requirements with the concept of Figure 3.5-1. However, the free-flying modes present very significant navigation and control problems. Some of the issues involved are: (1) the orbits are not Keplerian, (2) orbit determination—navigation and tracking, (3) six-degree-of-freedom control for each body, (4) individual control systems for each body, and (5) relative motion determination and control for each body.

3.5.5 IMPACT OF SOLAR PRESSURE AND SPACECRAFT SYMMETRY

For all SPS configurations the stationkeeping of the solar pressure force
is one of the dominant drivers affecting propellant consumption. The solar
pressure force is directly proportional to the effective or capture area,

$$F_S + P_S A \text{ where } A \triangleq \sum_i (\text{surface geometry, orientation reflectivity})_i,$$

and thus the propellant mass is proportional to the area independent of space-
craft mass. The clamshell-type SPS has a large area-to-mass ratio which drives
up the percent of spacecraft mass over the 30-year number. The effective areas
of the coplanar and clamshell are essentially the same, but the area-to-mass
ratio is 1.89 for the coplanar and 7.81 for the Clamshell-6 which directly
reflects in the 6.3 and 26% of spacecraft mass requirements shown in Table 3.5-3.

$$Note: \quad MP = \frac{(P_S \; t_{sec/yr})}{g \; I_{sp}} A$$

Thus, for a clamshell-type SPS the expected minimum achievable propellant mass
is in the range of approximately 22 to 27% with stationkeeping as a requirement.

Table 3.5-3. Impact of Solar Pressure

CONFIGURATION	AREA, m² ×10⁶	PROPELLANT KG/YR×10⁴	S/C MASS, kg ×10⁶	% S/C MASS OVER 30 YR
COPLANAR	69	7.67	36.6	6.3
SANDWICH	64	7.12	8.19	26

The impact of spacecraft geometry on the propellant requirements were
evaluated for the two configurations shown in Figure 3.5-6. The clamshell SPS
has large gravity-gradient and solar-pressure torques about the X-axis. These
torques result from spacecraft asymmetry in the Y-Z plane. The clamshell con-
figuration has a propellant penalty of 14.7% of spacecraft mass over 30 years.
The value assumes control torques result from thrusters mounted on the primary
mirror (details are discussed in the following section). The penalty doubles
to 29.6% if control torques result from thrusters mounted on secondary mirror
structure (free-pivoted primary mirror). However, the dual spacecraft, because
of its symmetry, has a substantial reduction in gravity-gradient torque about
the X-axis and much smaller solar-pressure torques. Assuming maximum moment
arm, the propellant mass for attitude control is reduced to 0.1%. Substantial
propellant savings are realized with the dual SPS vehicle.

3.5.6 RCS REQUIREMENTS

The RCS requirements for the clamshell and dual spacecraft are presented
in Table 3.5-4. Three approaches of thruster arrangements were considered for
the clamshell and only one for the dual because the disturbance torques were
small.

In the first approach, the primary mirror is considered to be free-pivoted
and the control torques result from thrusters located on the secondary mirror

CLAMSHELL CONFIGURATION
CONTROL ACCURACY ±0.05°

DUAL SPACECRAFT
CONTROL ACCURACY
±0.05°

COORDINATES
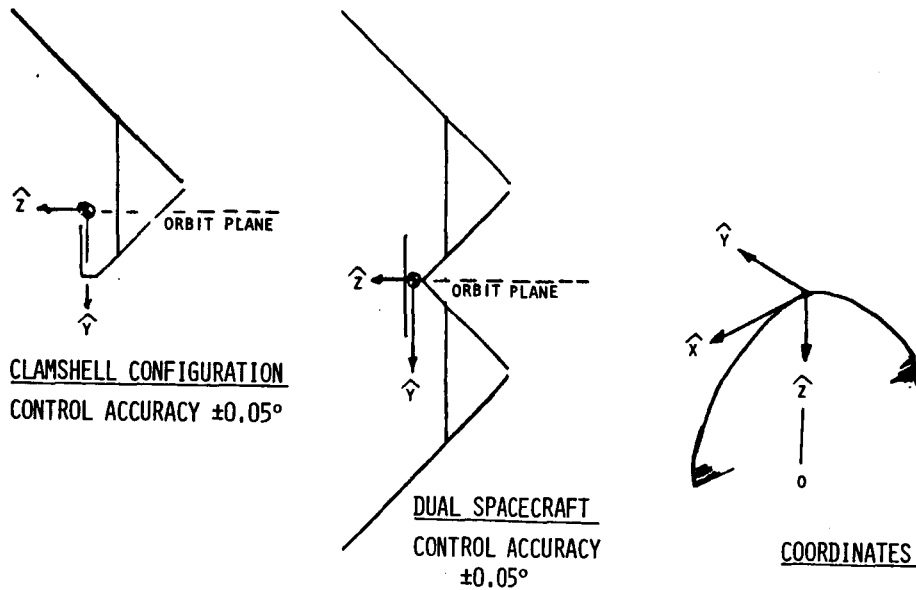
Figure 3.5-6. Satellite Concepts

Table 3.5-4. RCS Requirements

	PROPELLANT KG/YR × 10⁴	% S/C MASS OVER 30 YR	THRUSTERS REQUIRED*
CLAMSHELL SPACECRAFT FREE PIVOTED PRIMARY MIRROR 1. M_X ATTITUDE CONTROL THRUSTERS MOUNTED ON SECONDARY MIRROR SERVO MOTORS CONTROL PRIMARY MIRROR WITH RESPECT TO MAIN BODY	15.5	56.9	73
2. M_X ATTITUDE CONTROL THRUSTERS MOUNTED ON PRIMARY MIRROR, RADIALLY FIXED	11.5	41.1	63
3. M_X ATTITUDE CONTROL THRUSTERS MOUNTED ON PRIMARY MIRROR, INERTIALLY FIXED	13.5	48.5	111
DUAL SPACECRAFT	15.0	27.5	90

*SPARES NOT INCLUDED

structure. The second and third options have servo motors to control the primary mirror relative to the main body, and the thrusters to control large disturbance torque along the X-axis (M_X) are located on the primary mirror. In the latter two approaches, longer moment arms are available, which results in propellant savings. The difference between the two options is that in the second M_X control, thrusters are radially fixed; and in the third, the thrusters

are inertially fixed. Inertially fixed thrusters are stationary with respect to the primary mirror, and radially fixed thrusters rotate once per orbit relative to the mirror to maintain a thrust direction along the radial Z-axis. The locations of the stationkeeping thrusters remain the same for the three clamshell thruster configurations.

For the clamshell spacecraft, the highest propellant penalty of 56.9% over the lifetime of the spacecraft resulted from the first approach, and the highest number of thrusters which total 111 (not including spares) resulted from the third arrangement. The second approach results in the lowest propellant and thruster requirements. A propellant penalty of 41.1% of spacecraft mass over 30 years was achieved, and an average of 63 thrusters are required to operate. Reductions of propellant mass of 15.8% and 7.5% were obtained relative to configurations one and three, respectively. Thus, the preferred approach is the second option.

The dual spacecraft has a propellant penalty of 27.5% of spacecraft mass over 30 years, which approaches the minimum achievable value. The RCS operates on an average of 90 thrusters. A reduction in propellant penalty of 13.6% is realized compared to the second approach, single configuration clamshell. However, relative to this option, there is an increase of 46% in thruster requirements. If the propellant savings offset the cost of additional thrusters, the dual vehicle is an attractive concept.

The thruster systems for the preferred option of the clamshell and the dual are shown in Figures 3.5-7 and 3.5-8, respectively. For the clamshell, the thrusters are mounted at four locations; and at eight locations for the dual. Each figure shows the details of the thruster configurations which include the thrusting directions and the total number of thrusters. The totals include the number of thrusters the RCS operates, on the average, to provide control, and the number of spares required to provide the necessary redundancy.

Referring to Figures 3.5-7 and 3.5-8, the thrusters are located on the centerline at the tips of the primary mirror and at the opposite ends of the minor axis of the secondary mirror. The thrusters on the primary mirror are gimbaled ±11.75° to compensate for the mirror motion as the sun travels ±23.5° from the equinox position. The function of these thrusters is to provide (1) stationkeeping for the solar pressure which results from direct sunlight and reflected sunlight off the secondary mirror and solar-lunar perturbation, and (2) attitude control for the disturbance torque along the X-axis. Attitude control for the clamshell requires 16 thrusters, and only two for the dual. The thrusters mounted on the secondary mirror provide the stationkeeping of the solar-pressure force resulting from direct sunlight on the mirror, and control torques to correct the gravity-gradient disturbance torques about the Y and Z axes. The radial thrusters, differentially gimbaled, provide the control along these axes.
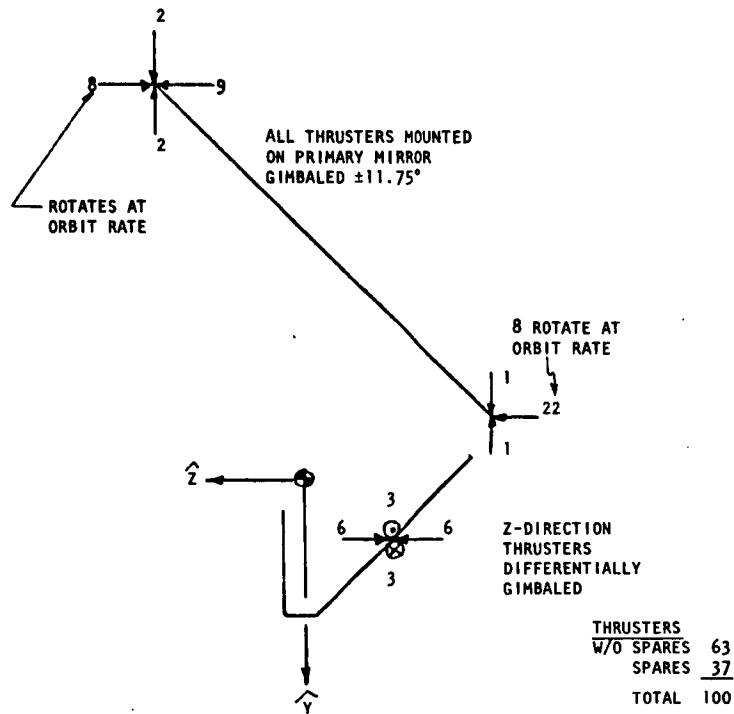
Figure 3.5-7.   Thruster Configuration—Clamshell
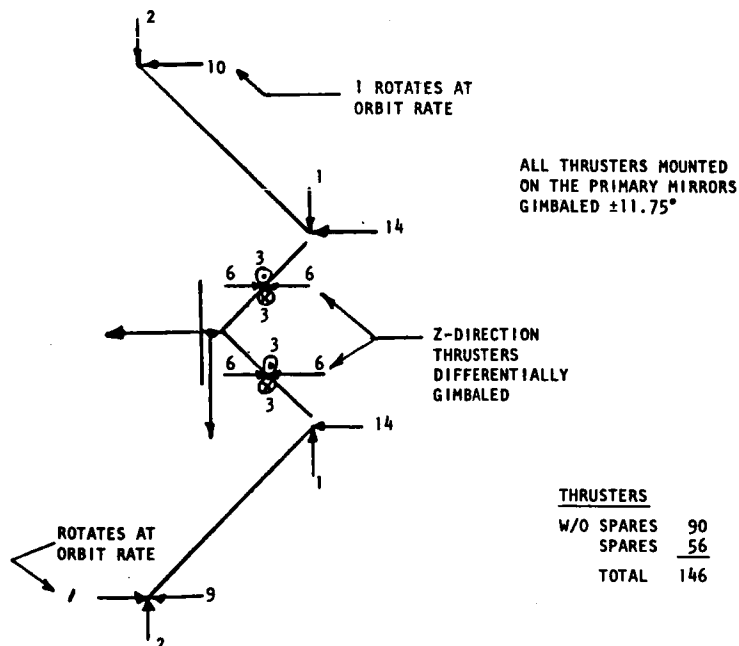
Figure 3.5-8.   Thruster Configuration—Dual Spacecraft

3.5.7 ACSS MASS SUMMARY AND POWER REQUIREMENTS

The mass properties and power requirements for the ACSS are summarized for the clamshell and dual spacecraft in Table 3.5-5. The summary includes the mass of the individual elements and propellant mass. The average power requirement which is proportional to propellant consumption is 45.46 megawatts for the clamshell, and 59.34 megawatts for the dual spacecraft.

Table 3.5-5. Mass Summary and Power Requirements

	CLAMSHELL	DUAL SPACECRAFT
MASS SUMMARY	kg×10³	kg×10³
ATTITUDE DETERMINATION SYSTEM	0.23	0.23
THRUSTERS—INCLUDING SUPPORT STRUCTURE $\frac{100}{146}$ @ 120 kg	12.00	17.52
TANKS, LINES, AND REFRIGERATION	20.24	25.45
POWER PROCESSING EQUIPMENT	-	-
ARGON PROPELLANT (ANNUAL REQMT)	114.66	149.88
TOTAL (DRY)	32.46	43.20
TOTAL (W/PROPELLANT)	147.12	193.03
POWER REQUIREMENTS	MW	MW
	45.46	59.34

3.5.8 CONCLUSIONS

The analysis shows that the propellant requirements for the clamshell are large and are substantially reduced for the dual. The propellant penalty for the clamshell is 56.9% of spacecraft mass over 30 years if the primary mirror is treated as a free-pivoted structure. If servo motors control the primary mirror relative to the main body, the preferred approach consisting of radially fixed thrusters results in a propellant mass of 41.1% over the lifetime of the spacecraft. A reduction of 17.8% is realized with the preferred approach. The RCS for the preferred configuration operates an average of 63 thrusters for stationkeeping and attitude control. A total of 100 thrusters (37 spares) is included to provide the required redundancy. The propellant penalty for the dual is 27.5% of spacecraft mass over 30 years. A substantial reduction of at least 13.6% is realized relative to the single clamshell. Propellant requirements for attitude control are small. The total number of thrusters required for the RCS is 146, and 56 of them are spares to provide the redundancy. An average of 90 thrusters operate to deliver the control forces and torques. In terms of ACSS requirements, the dual is an attractive SPS concept.

The results obtained to date are based on simplified dynamic models. If the clamshell-type SPS is to be competitive, a refinement in the dynamic models is required to obtain definitive results. With the clamshell-type SPS, there is relative motion between the two bodies which gives rise to time-varying inertia properties and time-varying gravity-gradient and solar-pressure

torques. The position of the mass center varies annually. These effects must be included in a rigorous analysis. A valuable analysis and design tool to accurately assess the magnitude of ACSS requirements is a digital computer simulation that includes the complex dynamics and control models. A development of a digital simulation program is recommended for the SPS ACSS analysis and design.

3.6 MICROWAVE POWER TRANSMISSION

This section covers the space segment of the microwave power transmission system, i.e., the antenna and transmitter subsystems, including associated phase control, beam pointing and signal distribution. A key tradeoff in prior MPTS trade studies has been selection of the basic microwave power amplifier. Major areas of investigation undertaken in this study included examining in greater detail the implication of developing a satellite concept predicated upon use of solid-state microwave power amplification devices without constraining the concept to be directly interchangeable with the klystron. Two fundamentally different SPS approaches were studied: (1) a system using the baseline SPS, i.e., a large satellite with low concentration ratio, high-voltage dc distribution, and two end-mounted solid-state active antennas[1] with approximately the same transmitted power level as the baseline system; and (2) a sandwich system using an arrangement of mirrors to concentrate solar energy with the intensity of up to six suns on the rear of the sandwich (where solar cells are located), and an active array at the other side of the sandwich with simple, direct feed-through from the solar cells to the microwave amplifiers.

An overall comparison of SPS concepts is illustrated in a comparison of installation cost versus energy cost at the utility interface (Figure 3.6-1). Klystron (or, generally speaking, tube) concepts are more fully developed and have less of a spread in installation cost. Solid-state concepts are less defined, and reach over a larger installation cost regime, but offer more potential improvement as the state of the art is developed. Fundamentally, they require lower operating and maintenance costs (because of the inherently high lifetime of the space segment) and should, therefore, ultimately result in a lesser total energy cost, even though the installation cost may be higher —at least initially.

In addition to the solid-state amplifiers, a study was done to design a magnetron-powered antenna and transmission concept which could be compared to the existing klystron reference concept. Technological advancements have made the magnetron an attractive candidate for SPS. Total system comparisons and configurations are described elsewhere in this report (see Sections 1.1.1, 1.1.2, 1.4, 2.3.1, and 2.3.2). This section describes the microwave power transmission analyses and tradeoff studies that were conducted in support of the final selected concept definitions.

---

[1]The definition of "active antennas" as used here implies power amplification immediately at the radiating elements, i.e., power combining in space.
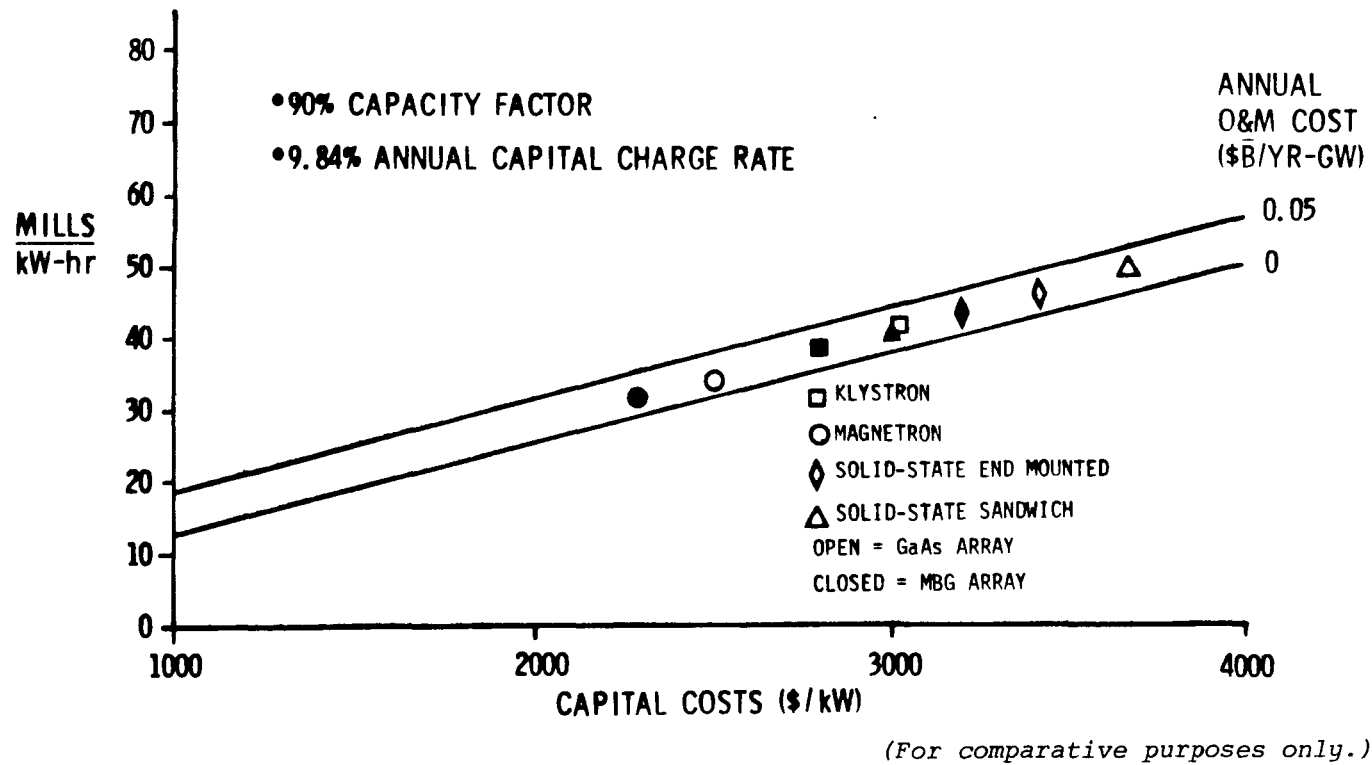
Figure 3.6-1. Simplified Utility Interface Power Cost Relationship

3.6.1 SPS TRANSMITTING ANTENNA ANALYSIS

This analysis is presented in order to provide a consistent basis for designing and comparing different SPS microwave power distribution systems. It takes account of constraints on radiated RF power density that are imposed, both at the transmitting antenna by thermal considerations, and at the rectenna by ionospheric effects.

The actual transmitting array, often referred to as the spacetenna, in all cases is modeled as a circular aperture in which the amplitude and phase distributions are functions only of radius and are independent of azimuthal angle, i.e., circular symmetry is assumed.

Power Density Distribution in the Aperture

In accordance with the above the distribution of electric field in the aperture is described by an illumination function f(r), where r is radius in the aperture normalized to unity at the edge. The power density at any point in the aperture, whose diameter is $D_T = 2a$, is

$$\frac{dP}{dA} = \eta_H S_T |f(r)|^2$$

where the elemental area dA is given by

$$dA = 2\pi a^2 r dr$$

and S_T represents the input power density at the array center, r = 0. Ohmic loss in the array is assumed to be small and is accounted for by the efficiency factor η_H.

The total power transmitted through the aperture is then given by

$$P_T = \eta_H \int dP = 2\pi a^2 \eta_H S_T \int_0^1 |f(r)|^2 r dr$$

$$P_T = \eta_H KAS_T \quad W/m^2 \tag{3.6-1}$$

where $A = \pi a^2$ is the area of the aperture and K is a parameter which will be called the aperture power coefficient, given by

$$K = 2 \int_0^1 |f(r)|^2 r dr . \tag{3.6-2}$$

It is clear from Equation (3.6-1) that the product KS_T is just the average power density over the aperture as a whole. It is noteworthy that the illumination function f(r) may be complex without influencing K. It is only the amplitude distribution that affects K and not the phase distribution.

Power Density at the Rectenna

It is now assumed that the transmitting antenna is boresighted on a rectenna at range R and that far-field conditions prevail. The latter assumption implies one of the following two conditions: Either

$$R > \frac{2D_T^2}{\lambda}$$

or else the transmitting antenna is given a phase distribution such that it is focused on the rectenna at range R. This simply means that f(r) is complex and the array radiates a convergent spherical wave, rather than a plane wave.

The flux at the rectenna then becomes

$$S_R = \frac{GP_T}{4\pi R^2} \quad W/m^2$$

where G is the gain of the transmitting antenna and is given by

$$G = \eta_A \frac{4\pi A}{\lambda^2} = \eta_A k^2 a^2 = \eta_A \left(\frac{\pi D_T}{\lambda}\right)^2 . \tag{3.6-3}$$

Combining these equations yields

$$S_R = \eta_A P_T \frac{\pi}{4} \left(\frac{D_T}{\lambda R}\right)^2$$

and, on introducing Equation (3.6-1),

$$\frac{S_R}{S_T} = \eta_A \eta_H K \left(\frac{\pi}{4\lambda R}\right)^2 D_T^4 .$$

From these relations the following two design equations immediately follow:

$$D_T = \sqrt{\frac{4\lambda R}{\pi}} \left(\frac{S_R}{\eta_A \eta_H K S_T}\right)^{\frac{1}{4}} \tag{3.6-4}$$

$$P_T = \lambda R \sqrt{\frac{\eta_H}{\eta_A}} K S_R S_T . \tag{3.6-5}$$

The aperture efficiency, η_A, depends upon the illumination function and can be calculated from the relation

$$\eta_A = 2 \frac{\left|\int_0^1 f(r) r \, dr\right|^2}{\int_0^1 |f(r)|^2 r \, dr} . \tag{3.6-6}$$

Unlike K, the efficiency η_A is highly dependent on the phase distribution over the aperture whenever $f(r)$ happens to be a complex function.

Power Incident on Rectenna

At range R the power pattern of the transmitting antenna produces circular contours of constant power density on a plane perpendicular to the boresight direction. The contours are circular because the radiating aperture is circular and has a circularly symmetric field distribution, $f(r)$. Let the projection of the rectenna on this plane correspond to one of those circular contours with diameter D_R. The rectenna itself will have an elliptical shape with minor diameter equal to D_R and major diameter greater than D_R, depending on latitude of the rectenna site.

As shown by Figure 3.6-2, the diameter D_R is given by

$$D_R = 2R\theta_N \tag{3.6-7}$$

where $2\theta_N$ is the full angular beamwidth at the $-N$ dB pattern level. This angle depends upon the size of the transmitting aperture and its illumination function, thus

$$2\theta_N = B \frac{\lambda}{D_T} \tag{3.6-8}$$

where B is the beamwidth constant in radians at the $-N$ dB level, and depends only on $f(r)$. Combining the two equations gives

$$D_R = \frac{B\lambda R}{D_T} , \tag{3.6-9}$$

and this relation sizes the rectenna.

The actual power incident upon the rectenna is a fraction of the total radiated power,

$$P_R = \eta_B P_T \tag{3.6-10}$$

where η_B is the beam efficiency of the transmitting antenna at the $-N$ dB power level.

The determination of the parameters η_B and B is not so simple as was the case for η_A and K. The reason for this is that η_B and B depend on the shape of the radiated power pattern of the transmitting antenna. This pattern, in turn, depends upon $f(r)$ in a complicated way, to be discussed in the next section.
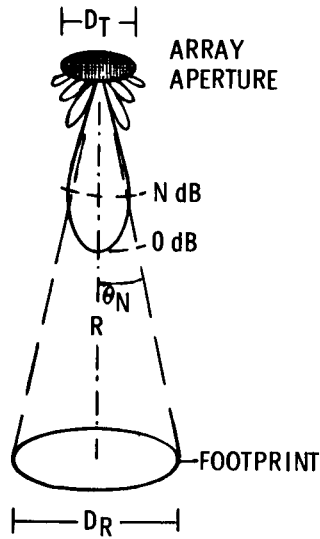
Figure 3.6-2. Footprint of Transmitting Antenna

Space Antenna Radiation Pattern Analysis

For analysis of circular aperture radiation patterns it is convenient to use the reduced variable u which is related to the polar angle θ, measured from the boresight direction, by

$$u = ka\sin\theta = \frac{\pi D_T}{\lambda} \sin\theta, \quad \left(k = \frac{2\pi}{\lambda}\right) . \tag{3.6-11}$$

The distant electric field is then described by g(u) where

$$g(u) = 2\int_0^1 f(r) \, J_0(ur) \, r\,dr \tag{3.6-12}$$

in which the Bessel function $J_0(ur)$ arises as a result of the assumed circular symmetry in f(r). The multiplier 2 ensures that g(u) is normalized to unity in the boresight direction (θ=0, hence u=0). The normalized power pattern is then

$$P(\theta) = |g(u)|^2 .$$

Once the aperture illumination function f(r) is given, be it real or complex, the pattern function g(u) is determined. The beamwidth constant, B, then comes from a solution to the equation.

$$20 \log_{10}|g(u)| = -N .$$

If this solution is u_N then Equation (3.6-11) shows that the angle θ_N at the -N dB level is given by

$$\theta_N = \sin^{-1} \frac{\lambda u}{\pi D_T} \quad .$$

Because $D_T >> \lambda$ the small sine approximation is valid and the use of Equation (3.6-8) immediately gives

$$B = \frac{2u_N}{\pi} \quad . \tag{3.6-13}$$

Calculation of beam efficiency, η_B, is more difficult. This parameter is defined to be the fraction of the power radiated between $\theta=0$ and θ_N in the main beam to the total power radiated in all directions, including side lobes. Analytically,

$$\eta_B = \frac{\displaystyle\int_0^{\theta_N} P(\theta) \sin\theta \, d\theta}{\displaystyle\int_0^{\pi} P(\theta) \sin\theta \, d\theta} \quad .$$

The directive gain, G, of the antenna is known to be given by

$$G = \frac{2}{\displaystyle\int_0^{\pi} P(\theta) \sin\theta \, d\theta}$$

so that beam efficiency becomes

$$\eta_B = \frac{G}{2} \int_0^{\theta_N} P(\theta) \sin\theta \, d\theta \quad . \tag{3.6-14}$$

In general Equation (3.6-14) must be evaluated by machine computation. However, for very large antennas ($D_T >> \lambda$) it is possible to obtain an accurate approximation which enables the integration to be carried out in closed form in certain interesting cases. To do this, the change of variable suggested by Equation (3.6-11) is made and Equation (3.6-3) is used for G, giving

$$\eta_B = \tfrac{1}{2}\eta_A \int_0^{u_N} |g(u)|^2 u \, du \quad . \tag{3.6-15}$$

With this expression it is possible to derive closed form expressions for beam efficiency in at least two important cases, namely uniform illumination, and the special kind of aperture distribution described by Hansen.

Properties of Radiation Patterns for Different Illumination Functions

Truncated Gaussian Distribution

In this case the function $f(r)$ has the general complex form

$$f(r) = e^{-(\alpha+j\beta)\, r^2} \tag{3.6-16}$$

and it includes uniform illumination as a special case when $\alpha=\beta=0$. With $\beta=0$ the value of α sets the edge truncation level for the usual Gaussian case. The value of β determines the magnitude of any quadratic phase distribution that might exist in the aperture. The general case, when neither α nor β is zero, has been treated by Love (Reference 14). He finds the following expressions for aperture efficiency and power coefficient:

$$\eta_A = \frac{2\alpha}{\alpha^2+\beta^2} \cdot \frac{\cosh\alpha - \cos\beta}{\sinh\alpha} \tag{3.6-17}$$

$$K = \frac{1-e^{-2\alpha}}{2\alpha} \cdot \tag{3.6-18}$$

For the usual Gaussian case, in which the phase is uniform and $\beta=0$, Equation (3.6-17) becomes

$$\eta_A = \frac{\tanh\alpha/2}{\alpha/2} \cdot \tag{3.6-17a}$$

Another interesting case is that of uniform illumination ($\alpha=0$) with quadratic phase error, for which Equation (3.6-17) reduces to

$$\eta_A = \left(\frac{\sin\beta/2}{\beta/2}\right)^2 \tag{3.6-17b}$$

Equation (3.6-12) can only be evaluated by machine computation in the general case. Consequently, the parameters B and η_B must be similarly evaluated. An exception occurs for the case of a uniform phase and amplitude distribution, for which

$$g(u) = \frac{2J_1(u)}{u} = \Lambda_1(u) \cdot \tag{3.6-19}$$

Thus, $g(u)$ can easily be plotted by referring to tables of the Bessel functions. There, the value of u_N at the $-N$ dB pattern level can readily be determined, and the parameter B found at once from Equation (3.6-13). Equation (3.6-15) is integrable in closed form and, since $\eta_A=1$, it gives

$$\eta_B = 1 - J_0^2(u_N) - J_1^2(u_N) \cdot \tag{3.6-20}$$

Hansen's One-Parameter Distribution

This distribution provides an optimum compromise between narrow beamwidth, low sidelobes and beam efficiency. Like all high efficiency illuminations it has a pedestal, i.e., it is truncated at some specified level at the aperture edge. It has the virtues of needing only one parameter and of possessing, simple, analytical expressions for nearly all quantities of interest. The following results are taken from the paper by Hansen (Reference 15).

The distribution itself is given by

$$f(r) = \frac{I_0\left(h\sqrt{1-r^2}\right)}{I_0(h)} \qquad (3.6-21)$$

in which I_0 is the modified Bessel function of order zero, $I_0(x) = J_0(jx)$. The single parameter h sets the pedestal level. The function $f(r)$ varies smoothly and monotonically with r, much as does the Gaussian form given by Equation (3.6-16) when $\beta=0$. Aperture efficiency and power coefficient turn out to be simply expressed as

$$\eta_A = \frac{4I_1^2(h)}{h\left[I_0^2(h) - I_1^2(h)\right]} \qquad (3.6-22)$$

$$K = 1 - \frac{I_1^2(h)}{I_0^2(h)} \qquad (3.6-23)$$

in which I_1 is the modified Bessel function of order one, $I_1(x) = -jJ_1(jx)$.

The far field pattern function is expressed by the two forms

$$g(u) = \frac{h}{I_1(h)} \frac{I_1\left(\sqrt{h^2-u^2}\right)}{\sqrt{h^2-u^2}} , \quad 0<u<h$$

$$g(u) = \frac{h}{I_1(h)} \frac{J_1\left(\sqrt{u^2-h^2}\right)}{\sqrt{u^2-h^2}} , \quad u>h$$

$$(3.6-24)$$

The first sidelobe for this pattern occurs at a level determined by h and given by

$$SLL = -17.57 - 20\log_{10} \frac{2I_1(h)}{h} \text{ dB} . \qquad (3.6-25)$$

The value of u_N corresponding to the $-N$ dB level of the main beam can be found by interpolation using tables for the modified Bessel functions I_0 and I_1.

Although not derived by Hansen in his paper it is also possible to use Equation (3.6-15) to obtain an expression for beam efficiency. This formula is

$$\eta_B = 1 - \frac{J_0^2\left(\sqrt{u^2-h^2}\right) + J_1^2\left(\sqrt{u^2-h^2}\right)}{I_0^2(h) - I_1^2(h)} \ . \tag{3.6-26}$$

Evaluation of Parameters for Comparison of Uniform, Gaussian and Hansen Cases

Smoothly tapered distributions over the very large aperture of the SPS array are difficult to achieve. Consequently, it has been the practice to approximate some desired distribution by a series of steps, in each of which the power density remains constant. The further desire to use identical power tubes and to adopt a standard sub-array size leads to certain quantized steps and fixes the level of the last step. Both the klystron reference system and a magnetron system have used a truncation level of -9.54 dB, i.e., the power level in the last step is 1/9 of the central level. It is therefore instructive to compare the properties of the smooth Gaussian and Hansen distributions for this condition and to place them alongside those for the uniform distribution. The phase distribution in all cases is assumed constant. The values of B and η_B shown in Table 3.6-1 have been evaluated at the -13.62 dB level of the main beam, where far field power density is 1/23 of the peak.

Table 3.6-1. Comparison of Radiation Characteristics
for Different Array Illuminations ($\beta=0$)

PARAMETER OR CHARACTERISTIC	UNIFORM (0 dB) $\alpha = 0$	GAUSSIAN (-9.54 dB) $\alpha = 1.099$	HANSEN (-9.54 dB) $h = 2.378$
APERTURE EFFICIENCY, η_A	1.000	0.910	0.914
POWER COEFFICIENT, K	1.000	0.405	0.436
BEAMWIDTH CONSTANT[1], B	1.94	2.19	2.20
BEAM EFFICIENCY[1], η_B	0.821	0.945	0.937
FIRST SIDELOBE LEVEL, dB	-17.6	-23.9	-23.2
[1]EVALUATED AT THE -13.62 dB LEVEL			

Although the uniform distribution creates an undesirably high sidelobe level it proves to be a useful case, in terms of maximizing the power delivered to the rectenna, in the event the array flux, S_T, is constrained to low values. This occurs, for example, in the sandwich concept in which the array is powered by solid state amplifiers and is integrated with the solar photovoltaic array. In this case the problem of dissipating waste heat appears to limit the RF flux density to about 1000 W/m^2 at the array center.

When the solar array is separate from the antenna, and the latter is solid-state powered, greater heat dissipation is possible and S_T may be increased to about 5500 W/m^2. Finally, in the klystron concept, S_T can be as high as 21,000 W/m^2. Table 3.6-2 provides a comparison between the three aperture

Table 3.6-2. Performance Comparison Summary
(R = 37,500 km, Rectenna at 40° Latitude)

S_T (W/m²)	APERTURE DISTRIBUTION	D_T (km)	P_T (GW)	D_R (km)	P_R (GW)
1,000	UNIFORM	1.67	2.20	5.33	1.81
	GAUSSIAN	2.15	1.47	4.68	1.39
	HANSEN	2.11	1.52	4.79	1.42
5,500	UNIFORM	1.09	5.16	8.15	4.24
	GAUSSIAN	1.40	3.44	7.17	3.25
	HANSEN	1.38	3.57	7.34	3.34
21,000	UNIFORM	0.78	10.1	11.4	8.28
	GAUSSIAN	1.00	6.73	10.0	6.36
	HANSEN	0.98	6.97	10.3	6.53

distributions for these three different flux densities. In all cases, the density at the rectenna, S_R, is held constant at 23 mW/cm².

In preparing Table 3.6-2 the appropriate parameters have been taken from Table 3.6-1 for substitution into equations (3.6-4, -5, -9 and -10) to determine spacetenna and rectenna diameters, total radiated power, P_T, and power incident on the rectenna, P_R. The table serves only for comparative purposes since many important links in the SPS power chain have not been taken into consideration. For simplicity, ohmic loss has been ignored ($\eta_H = 1$) in all cases. The calculations have been performed for range R = 37,500 km, corresponding to a rectenna at 40° latitude, with λ = .1224 m.

Two points concerning the comparative figures given in Table 3.6-2 are worthy of note. First, the uniform distribution is greatly superior in terms of maximizing the delivered power but its high sidelobe level mitigates against this choice for all except the case S_T = 1000 W/m², i.e., the sandwich concept. The second point is that the Hansen distribution delivers about 2.5 percent more power than does the Gaussian, with a 2% smaller spacetenna and a 2.5% larger rectenna. The two have very nearly the same sidelobe levels.

Figure 3.6-3 shows the two -9.54 dB distributions; the Hansen case in solid line and the Gaussian in dashed line. Figure 3.6-4 shows the far-field power pattern $|g(u)|^2$ for the Hansen case out to the first sidelobe. The corresponding Gaussian pattern is virtually indistinguishable from this.

Use of Quadratic Phase with Uniform Amplitude Distribution

From the foregoing it is apparent that the thermal limitation of S_T to 1000 W/m² for the sandwich concept results in a low level of delivered power, 1.8 GW at most. If the spacetenna could be made larger in diameter then more power could be transmitted. In the normal course of events this would result in increased spacetenna gain and the ionospheric limit, S_R = 23 mW/cm², would be exceeded.
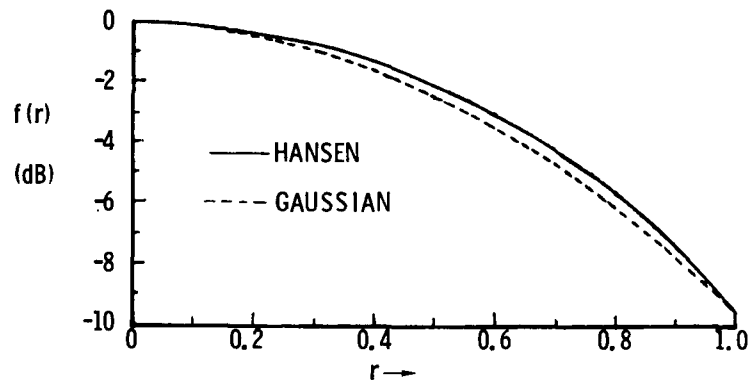
Figure 3.6-3. Truncated Aperture Distribution, -9.54 dB
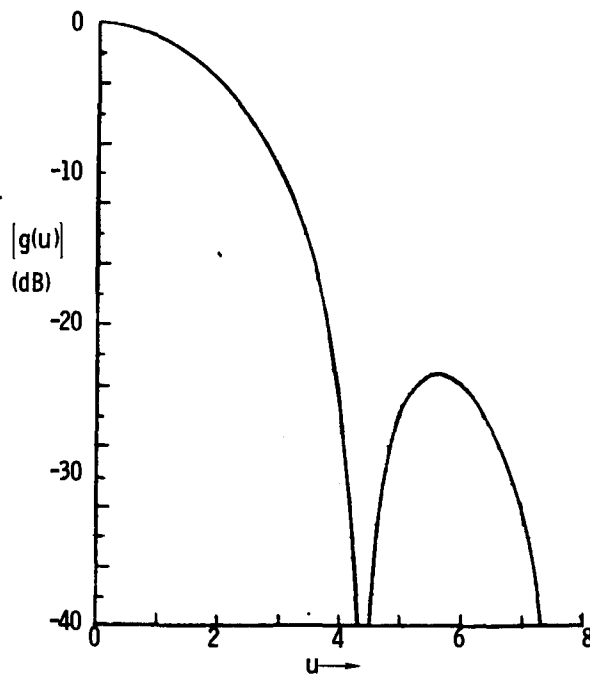
Figure 3.6-4. Far-Field Radiation Pattern for Hansen
Distribution

If, however, a quadratic phase distribution is used over the array aperture, its diameter can be made larger without increasing the gain and without affecting the aperture power coefficient. In this case more power can be delivered without violating the constraints on S_T and S_R. Equations (3.6-4, -5, -9, and -10) are still valid for determining power levels and antenna diameters, but new values for the parameters η_A, B and η_B are needed.

With a uniform amplitude and quadratic phase distribution η_A is given by Equation (3.6-17b) while K is unity, regardless of the value of the phase angle β. Computer evaluation of Equations (3.6-12) and (3.6-15) is necessary in order to obtain the far-field pattern, g(u), and the parameters B and ηB.

It turns out that when β exceeds about $3\pi/2$ radians the far field pattern no longer has its peak in the boresight direction, i.e., at u=0. Instead, the pattern maximum is shifted to some location u^1 which can be determined from an inspection of the computed patterns. This requires a slight modification to the definition of aperture efficiency, such that

$$\eta_A^1 = \eta_A \left| \frac{g(u^1)}{g(o)} \right|^2 \qquad (3.6\text{-}27)$$

in which η_A is calculated from Equation (3.6-17b).

The necessary calculations and computations have been performed for β in the range 0 to 1.75π radians and the results are summarized in Table 3.6-3.

Table 3.6-3. System Performance with Quadratic Phase
($S_T = 1000$ W/m^2, $S_R = 23$ mW/cm^2)

β RADIANS	η_A OR η'_A	B	η_B	D_T (km)	P_T (GW)	D_R (km)	P_R (GW)
0	1.000	1.94	0.821	1.67	2.20	5.33	1.81
0.25 π	0.950	1.98	0.795	1.70	2.26	5.35	1.80
0.5 π	0.811	2.15	0.717	1.76	2.44	5.58	1.75
0.75 π	0.615	3.57	0.814	1.89	2.81	8.67	2.28
1.0 π	0.405	3.98	0.779	2.10	3.46	8.59	2.69
1.25 π	0.221	5.65	0.852	2.44	4.66	10.6	3.98
1.5 π	0.0901	7.67	0.900	3.06	7.33	11.5	6.66
1.75 π	0.0691	8.05	0.884	3.27	8.37	11.3	7.40

Figure 3.6-5 shows the far field pattern of the spacetenna for the case $\beta = 1.75\pi$ radians. It displays the bifurcated main beam and the lack of pattern nulls which are typical of defocusing due to large quadratic phase error.
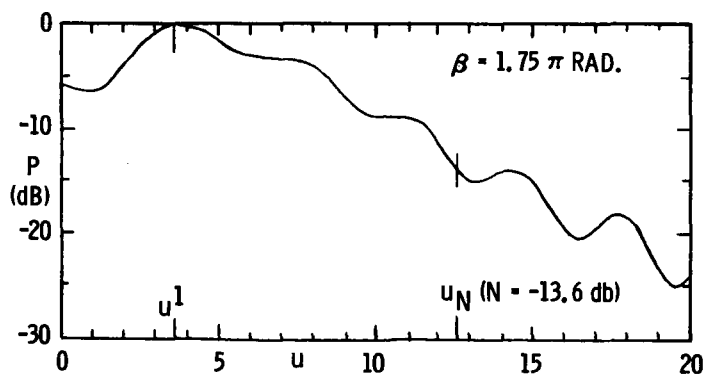
Figure 3.6-5. Pattern of Spacetenna with Uniform Amplitude and Quadratic Phase Distribution

3.6.2 GaAs MESFET DEVICE MODELING AND 2.45-GHz CLASS C AND CLASS E POWER CONVERTER SIMULATION

This section summarizes the work done by the University of Waterloo Research Institute in the MESFET power converter study (Reference 16). The goal is the determination of power conversion efficiencies and power gains at 2.45 GHz for various GaAs MESFET designs using the UNIPOLE and WATAND computer programs.

Method Used for the SPS MESFET Study

The technique is similar to that used for the bipolar transistor SPS study conducted during Exhibit C (References 17, 18, and 19). First, a fast numerical analysis is performed on a MESFET with given fabrication data (Figure 3.6-6). The UNIPOLE program (References 20 and 21) is used for this purpose. Secondly, CAD model parameters are generated for one or more model types (Figure 3.6-7). This model is then imbedded in a circuit (Figure 3.6-8), described and analyzed by the WATAND program—an efficient interactive program for nonlinear dynamic analyses. The WATAND program is used to determine the steady-state solutions and, hence, to calculate power conversion efficiency, power gain, and power output for the 2.45-GHz converter. The WATAND analysis is carried out for various drive and bias conditions corresponding to Class C or Class E operation. The results are examined and new input data to the UNIPOLE program is selected and the process repeated.
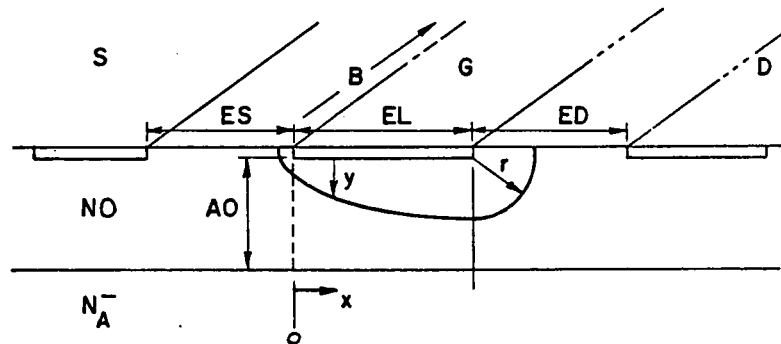
Figure 3.6-6.   FET Structure Analyzed in UNIPOLE with
Definitions of Significant Input Variables

MESFET Analysis

The guiding idea in developing the UNIPOLE numerical program was to provide a tool for the design engineer interested in either studying the initial behavior of a given MESFET or JFET structure, or in studying its terminal characteristics as a function of device parameters and, finally, in observing overall circuit response of the device by coupling the UNIPOLE program to the WATAND program (Reference 17) already developed for circuit analysis and design.
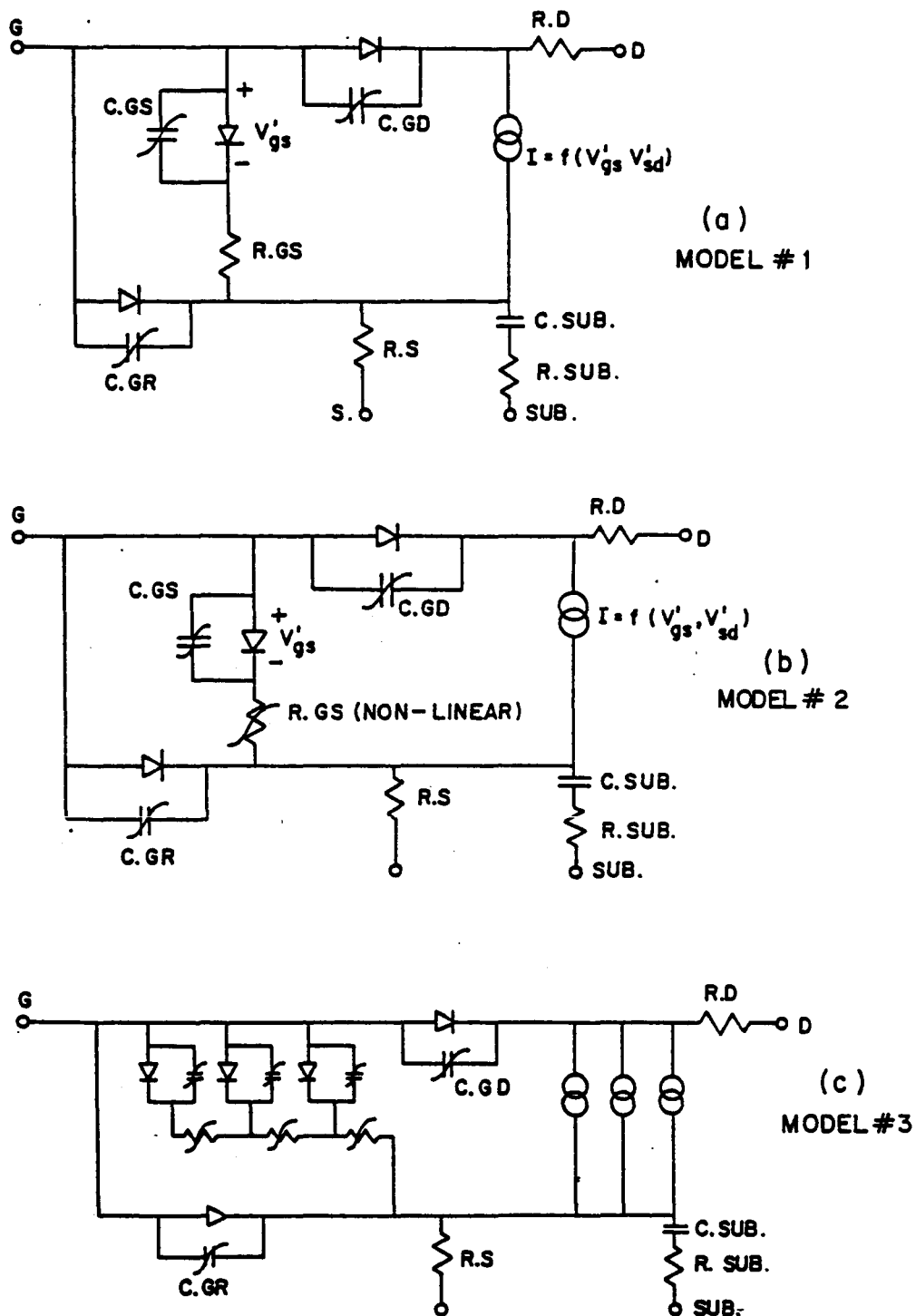
Figure 3.6-7.   Three CAD Models used in WATAND
(using FET Parameters generated from UNIPOLE)

(a)
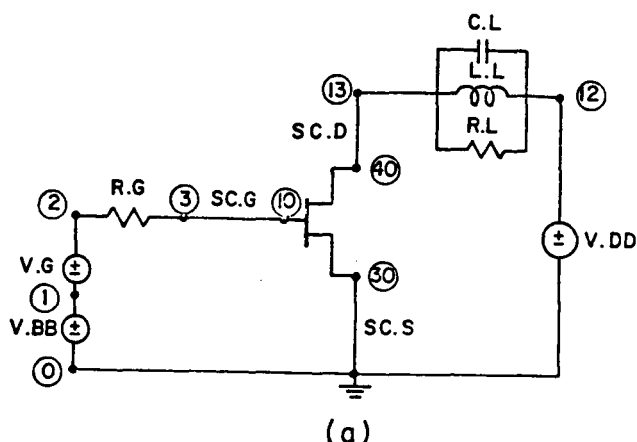
Figure 3.6-8.   Class C Amplifier Circuit
used in MESFET SPS Study

UNIPOLE Program

A basic requirement of the UNIPOLE program was that it must be economical in terms of execution time and core requirements and, at the same time, provide terminal characteristics with a degree of precision compatible with the accuracy with which the original fabrication data is known.

An approach similar to that developed for the bipolar transistor (References 16, 18, and 19) (the BIPOLE program) is used. The MESFET is divided into space charge regions and quasi-neutral regions, with the abrupt space charge layer boundary approximation. Referring to the diagram of Figure 3.6-6, the fields in the two regions are assumed to be mutually perpendicular. Furthermore it is assumed d^2V_x/dx^2 in the quasi-neutral channel is much less than d^2V_y/dy^2 in the space charge layer.

However, the mobility of the carriers in the channel is allowed to vary with the electric field E_x and the carrier concentration in the channel is allowed to deviate from the doping level; i.e., charge accumulation and depletion effects can, and do, exist in this model (as predicted in the exact analysis of Kennedy and O'Brian (Reference 22).

Generation of CAD Models

It was decided to use an approach similar to that used in the bipolar transistor SPS power converter study (Reference 17). For this purpose a non-linear dynamic analytic model of the MESFET was developed. The basic idea is that of the classical Ebers-Moll model, i.e., superposition of static non-linear elements (current sources and resistances dependent on one or two variables) and dynamic elements representing stored charge (nonlinear capacitance elements).

The models used were shown in Figure 3.6-7. The current generator is described as a function of V_{gs} and V_{sd} optionally by either:

$$I_{dsp} = I_{dd}(V_{sd}/V_{pd})/[1 + A_1(V_{sd}/V_{pd})^\alpha]^{1/\alpha} \qquad (3.6-28)$$

$$I_{dsp} = [I_{dd}(V_{sd}/V_{pd}) + A_2(V_{sd}/V_{pd})^\alpha]/[1 + A_3(V_{sd}/V_{pd})^\alpha] \qquad (3.6-29)$$

$$I_{ds} = I_{dsp}[1 - A_4(V'_{gs}/V_{gp}) - (1 - A_4)(V_{gs}/V'_{gp})^{3/2}] \qquad (3.6-30)$$

where $V'_{sd} = V_{sd}$ if $V_{sd} \geq 0$ and $V'_{gs} = V_{gs}$ if $V_{gs} \geq 0$.

Otherwise $V'_{sd} = 0$ and $V'_{gs} = 0$.

The parameters for these equations are computed in UNIPOLE: (1) gives an improved fit between the "ohmic" and "saturation" regions - this is important for accurate efficiency calculations; and (2) gives the double valued characteristics.

These are empirical fits to the UNIPOLE I_{sd} - V_{sd} - V_{gs} characteristics and the parameters V_{pd}, V_{gp}, A_1, A_2, A_3, A_4 and I_{dd} are computed within the UNIPOLE program: V_{gp} is the conventional gate pinch off voltage required to reduce the current I_{ds} to zero; V_{pd} is the nominal computed value of drain-source voltage required to reach maximum I_{ds} for $V_{gs} = 0$. The breakdown voltage V_{br} is computed in UNIPOLE using a simple empirical formula which takes only channel doping into account. Three values are printed (see sample output in Figure 3.6-9). VBRP is the classical "material" breakdown voltage; VBR is an empirically estimated value taking account of the field distribution between gate and drain; VDOM is an empirical estimation of domain limited breakdown using the results taken from (Reference 23).

The capacitive elements, C_{gs} and C_{gd} are modeled as depletion layer capacitances:

$$C_{gs} = C_{gso}/(1 - V_{gs}/V_{bi})^{\gamma_1} \qquad (3.6-31)$$

$$C_{gs} = C_{gdo}/(1 - V_{gd}/V_{bi})^{\gamma_2} \qquad (3.6-32)$$

C_{gs} has the possibility of saturating at the pinch off voltage. The parameters in the voltage capacitance laws (γ, V_{bi} and the zero bias values) are computed in the UNIPOLE program. Although not intended to be significant in the present study, both capacitive elements have associated junction static current sources; the model will therefore take into account the effect of forward bias (V_{gs} or V_{gd}).

The source resistance is computed directly in UNIPOLE from the geometry and doping level. The channel resistance is also computed in UNIPOLE.

Devices Studied

In order to determine fabrication data likely to yield good power conversion efficiency combined with high power gain at 2.45 GHz, it was necessary to

```
UNI: SP45

FILE NAME: SP45
NOV. 27, 1979      17:31:01       **** UNIPOLE - JFET/MESFET PROGRAM: VERSION 15 NOV. 1979

DEVICE DATA:          B       EL      ED      AO       NO  IMPUR
   GAAS   N CHANNEL  0.40E-01 0.30E-03 0.30E-03 0.15E-03 0.60E+16  0

PARAMETERS       VGP       VBR      VBRP     VCRI     VPHI      EMUO      TOL   KV  FD
           0.105E+02 0.462E+02 0.130E+03 0.600E+01 0.601E+00 0.662E+04 0.100E-01  2  40.
              VDOM = 0.121E+03

VG      = 0.0
WSCL(0) = 0.349E-04
RGT     = 0.204E+02


          ISD       VSD      R-DC    WSCL(L)    EX(L)      CGS
        0.109E-02 0.222E-01 0.204E+02 0.349E-04 0.370E+02 0.335E-12
        0.305E-01 0.658E+00 0.216E+02 0.443E-04 0.126E+04 0.296E-12
        0.444E-01 0.103E+01 0.231E+02 0.492E-04 0.216E+04 0.279E-12
        0.557E-01 0.144E+01 0.258E+02 0.547E-04 0.343E+04 0.263E-12
KNEE 50 %
        0.613E-01 0.179E+01 0.292E+02 0.601E-04 0.656E+04 0.252E-12
        0.628E-01 0.192E+01 0.306E+02 0.613E-04 0.694E+04 0.249E-12
        0.635E-01 0.206E+01 0.325E+02 0.640E-04 0.123E+05 0.247E-12
KNEE 90 %
        0.638E-01 0.215E+01 0.337E+02 0.648E-04 0.246E+05 0.246E-12
KNEE 92 %


FCIV = 0.492E+11 FCVV = 0.473E+11 FTAU = 0.871E+10 FMAXO = 0.216E+11
CAPACITANCE CDG  =  0.123E-12


VG      = 0.524E+01
WSCL(0) = 0.109E-03
RGT     = 0.571E+02


          ISD       VSD      R-DC    WSCL(L)    EX(L)      CGS
        0.388E-03 0.151E-01 0.388E+02 0.109E-03 0.370E+02 0.107E-12
        0.159E-01 0.727E+00 0.458E+02 0.113E-03 0.192E+04 0.105E-12
        0.191E-01 0.989E+00 0.517E+02 0.116E-03 0.307E+04 0.104E-12
KNEE 50 %
        0.208E-01 0.120E+01 0.577E+02 0.117E-03 0.469E+04 0.104E-12
        0.216E-01 0.146E+01 0.675E+02 0.121E-03 0.109E+05 0.103E-12
        0.220E-01 0.154E+01 0.702E+02 0.120E-03 0.112E+05 0.103E-12
        0.221E-01 0.158E+01 0.716E+02 0.121E-03 0.260E+05 0.103E-12
KNEE 83 %


FCIV = 0.499E+11 FCVV = 0.475E+11 FTAU = 0.843E+10 FMAXO = 0.219E+11
CAPACITANCE CDG  =  0.515E-13



   VA      IMAX      GM      WMAX     WMAX2     REFO      RS       RD
0.158E+01 0.638E-01-0.796E-02 0.354E+00 0.271E+00 0.940E+01 0.262E+01 0.102E+02

EXECUTION TIME = 7.28 SEC.
```

Figure 3.6-9. SP45 UNIPOLE Output

develop some simple analytic relations between fabrication data (channel doping level and geometry) on the one hand, and circuit performance on the other hand. The basic relations are summarized in Figure 3.6-10.

Condition for maximum transconductance

$$q \, \mu_n \, N_D \, a^2/L \; \simeq 2 \, \epsilon \; V_{th} \simeq 2 \times 10^{-5} \; F/s \tag{1}$$

Maximum power output

$$W_{max} \; \simeq I_{DSS} \; V_{br}/8 \tag{2}$$

$$\simeq 0.25 \times 10^5 \; Z \; watts \tag{3}$$

Condition for high power conversion efficiency

$$V_{br}/V_{ko} >> 1$$

$$V_{br}/V_{ko} \simeq [\epsilon \, E_{br}^2 / (2 \, q \, E_c)] \, (1/L \, N_D) \tag{4}$$

Cut off frequency

$$f_c \simeq V_{th} / \pi L \tag{5}$$

q = electronic charge = 1.6×10^{-19} c μ = carrier mobility

ϵ = $\epsilon_r \epsilon_0$ – permittivity $\simeq 10^{-12}$ F/cm N_D = channel doping

V_{th} = saturated drift velocity (1 to 2×10^7 cm/9) a = channel thickness

E_{br} = breakdown value of field (2×10^5 V/cm L = channel length (S → D)

E_c = critical field = V_{th} / μ Z = channel width

I_{DSS} = maximum drain current, V_{gs} = 0

V_{br} = source-drain breakdown voltage

V_{ko} = knee voltage on $I_{sd} = V_{sd}$ curve

for V_{gs} = 0

f_c = cut-off frequency

Figure 3.6-10. Analytic Relations used to
Select Input Data for the UNIPOLE Program

Determination of (Input) Fabrication Data for UNIPOLE

The first equation is the condition for maximum transconductance. It indicates that optimum structure is shorter than one for which Shockley's theory applies, but longer than one for which limit velocity conditions may be approximated throughout the ("open") channel [see Reference (24), eq. 8.66].

The second and third equations relate to power output and assume a source to drain breakdown voltage significantly greater than the knee voltage V_{ko} at which the $I_{sd} - V_{sd}$ characteristic passes from the ohmic to the saturated region for $V_{gs} = 0$. Figure 3.6-10 , eq. (3) implies a thick channel depth (large a) and of course a large channel in the 'Z' direction. Note that this

automatically implies as long a channel (large 'L') in the source-drain direc-
tion as possible since, for a given channel metallization sheet resistance,
the ratio Z/L will remain approximately constant.

For Class C high power-conversion efficiency the ratio V_{br}/V_{ko} must be as
large as possible. Hence the importance of eq. (4) of Figure 3.6-10. This
is analogous to saying that the saturation voltage, $V_{ce\ sat.}$, of a bipolar
transistor must be small compared to its breakdown voltage for efficient Class
C operation, eq. (2). The implication is that the FET structure used must
have small channel length L and low doping N_D.

Finally, the cut off frequency f_c is given by eq. (5) of Figure 3.6-10.
This is directly related to the high frequency power gain, G_p, and indicates
a maximum allowable value of L for a given frequency. Since the actual Class
C power gain is a complicated function of the static and dynamic non-linearit-
ies, no attempt has been made to calculate this analytically. This is, in fact,
where WATAND becomes essential.

UNIPOLE Output

Five MESFET structures (out of more than 20 studied with UNIPOLE in the
course of this work) are summarized in Table 3.6-4. Sample UNIPOLE output
data for one of them was given in Figure 3.6-9. This is a 3 μm gate (EL)
structure with a channel doped (NO) 6×10^{15} cm^{-3} to a depth (AA) of 1.5 μm.
The gate pinch off voltage (VGP) is 10.5 volts, and the knee voltage is 1.8 V
(where the initial slope of the $I_{sd} - V_{sd}$ characteristics has decreased by a
factor of 2). The knee voltage corresponding to a 10-times decrease in slope
is 2.15 V. The empirically calculated breakdown voltage (VBR) is 46 V. The
UNIPOLE output gives tabulated values of V_{sd} (VSD) C_{gs} (CGS) as functions of
I_{sd} (ISD) for two values of V_{gs} (VG), 0 and VGP/2. The drain-gate capacitance
(CDG) is computed near the 90% knee voltage for each case. The cut-off
frequencies FCIV, FCVV, are obtained from a small signal analysis of the dis-
tributed R-C line for the last tabulated dc conditions. FTAU is the cut-off
frequency computed from the channel transit time. FMAXO is the maximum
oscillation frequency. The powers WMAX and WMAX2 are maximum theoretical
powers obtainable for the given value of VBR. WMAX omits the effect of pinch-
off voltage (V_{gp}), WMAX2 includes it.

Table 3.6-4 contains a summary of the UNIPOLE output for 4 MESFETs. SP01
is a standard 1 μm reference device. The SP41, SP45 and SP46 each have 3 μm
gates and are considered "good" designs for 2.45 GHz power conversion. The
SP47 with a 6 μm gate is included as an extreme case for comparison purpose.
The important parameters for power conversion efficiency is V_{br}/V_k. Power
gain is related to $f_{max\ osc}$ and power output is related to the "ideal" class
A output W_{max}. The SP41 device has very low channel doping (2×10^{15} cm^{-3}) and
should give high conversion efficiency. Its power output is however, consider-
ably less than the SP45 or SP46.

No precise information about Class C performance can be obtained from the
UNIPOLE output so at this point, we proceed to describe the WATAND results
obtained on these devices using the UNIPOLE generated CAD model.

Table 3.6-4. Summary of UNIPOLE Data
for 5 GaAs FET Structures

	Variable	Units	SP01	SP41	SP45	SP46	SP47
INPUT DATA	B	μm	100	400	400	400	800
	L	μm	1.0	3.0	3.0	3.0	6.0
	L_d	μm	2.0	3.0	3.0	3.0	6.0
	Ao	μm	0.35	1.5	1.5	1.5	1.5
	No	cm^{-3}	5×10^{16}	2×10^{15}	6×10^{15}	1×10^{16}	6×10^{15}
DATA	V_{brm}	Volt	27	297	130	89	130
	V_{br}	Volt	17	71	46	37	46
	V_{dom}	Volt	42	209	121	94	121
	V_{gp}	Volt	4.4	3.1	10.5	18.0	10.5
	V_k	Volt	1.1	1.5	2.2	2.4	3.5
	V_{br}/V_k	-	15.4	47.3	21.0	15.4	13.1
OUTPUT	f_t	GHz	26	7.4	8.7	9.1	4.0
	$f_{max\ osc}$	GHz	77	14	21	25	12
	W_{max}	Watt	.056	0.11	0.35	0.53	0.59
	$W_{max\ 2}$	Watt	.040	0.11	0.27	0.27	0.45

It is important, in a study of this type, to estimate the precision with which the electrical performance of the MESFET is predicted from the fabrication data. The UNIPOLE-WATAND system has been tested with an existing MESFET on a 10-GHz Class A amplifier. A sample comparison of measured and computed results is given in Table 3.6-5 (Reference 20 and 21). We conclude that the power gain is predictable to better than 3 dB accuracy if parasitic elements are known and included. One of the principal sources of additional loss is the gate resistance due to metalization. For the purpose of this study, it is assumed that this can be reduced to a small enough value by using sufficiently thick gate metalization. Note that we have kept the B/L ratio constant at 133 so this resistance can easily be calculated for a given metalization thickness (approximately 3 Ω for a 0.7 μm Aℓ metalization).

The computed values of I_{dss} and g_m have been compared to measured values of many Si and GaAs devices and the difference is invariably less than 10% [i.e., comparable to the accuracy with which fabrication data (N_0, a) is known].

The pinch off voltage V_{gp} and knee voltage V_k are also computed to better than 10% accuracy as verified by comparison with measured data.

3-113

Table 3.6-5. Sample Comparison of Measured and Computed Results

10 GHz results	P_{out}(mW)	G_p(dB)
Measured values	12.0	9.5
Computed (no parasitics) tuned	15.7	14.5
Computed (with parasitics) tuned	11.9	12.4
Computed (no parasitics) untuned	-	14.4
Computed (with parasitics) untuned	-	12.5

MESFET data:

Gate length:	0.8 μm
Total gate width:	150 μm
Channel depth:	0.4 μm
Channel doping:	6×10^{16} cm^{-3}

The one parameter which cannot yet be predicted accurately with the UNIPOLE program for GaAs is the breakdown voltage. The value VBR referred to in the above is typically about 1/3 of the material breakdown voltage, and is in all cases less than the estimated domain limited voltage VDOM. Since we have no useful measured data on breakdown in GaAs MESFET, and since only two dimensional time dependent solutions (Reference 25) can yield detailed information we have used the VBR value in the WATAND computations. Results have been computed for Si type behaviors, where $|V_{sdbr}| = |V_{gsbr}| - |V_{gs}|$ and also for the behavior observed in many GaAs devices where V_{sdbr} = constant.

In terms of the results, it should be noted that a factor of 2 increase in V_{sdbr} would reduce the V_{sdbr}/V_k conversion efficiency loss by a factor of 2. For the SP45 device (Table 3.6-4) this would represent an increase in efficiency of about 2.4%. For the SP46, the corresponding increase would be about 3.3%. It is highly likely that losses due to parasitics [e.g., see (Reference 17)] will be greater than these values so in terms of the results obtained, the difficulty in computing maximum source drain voltage accurately is not felt to be a serious limitation.

WATAND Analysis

Initially the dc characteristics are displayed (Figures 3.6-11 and 3.6-12). Two different model descriptions were used, one giving "flat" characteristics beyond saturation (silicon type), the other giving double valued $I_{ds} - V_{ds}$ characteristics. Because the Class C dynamic locus is below the Class A load line [Figure 3.6-13(b)], the large-signal power conversion and gains are not significantly affected by choice of model type.

Figure 3.6-11.   SP41 dc I_{ds}-V_{ds} Characteristics

DT   V1.06-07 25-NOV-79 10:21:26   FILE 45286L1
1T SP45 NOV 15 MODEL LINEAR 1-SECTION
1T SP45   TRANSISTOR MODEL   NOV. 16, 1979   09:06:37

(a) PEAKED

(b) FLAT
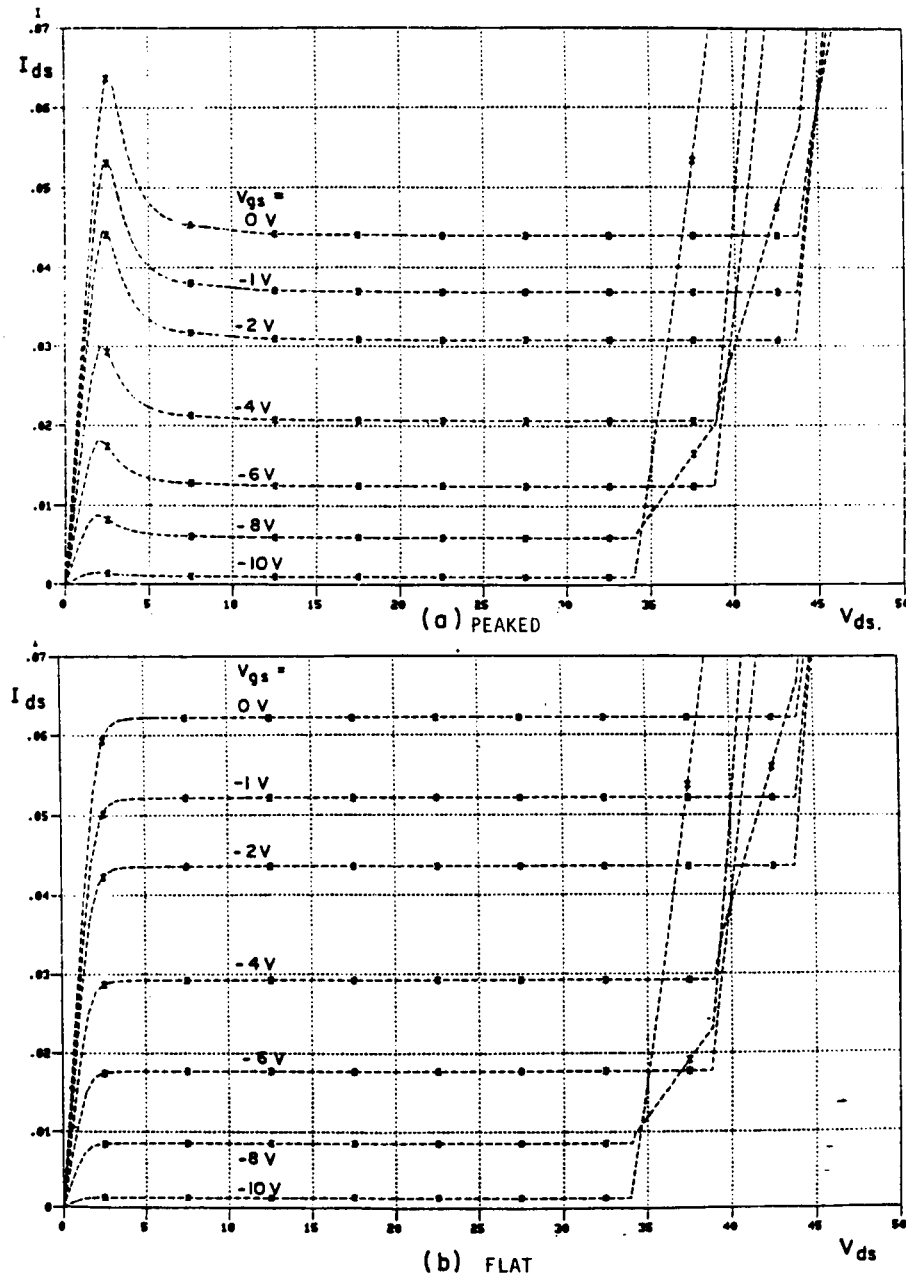
Figure 3.6-12.   SP45 dc I_{ds}-V_{ds} Characteristics
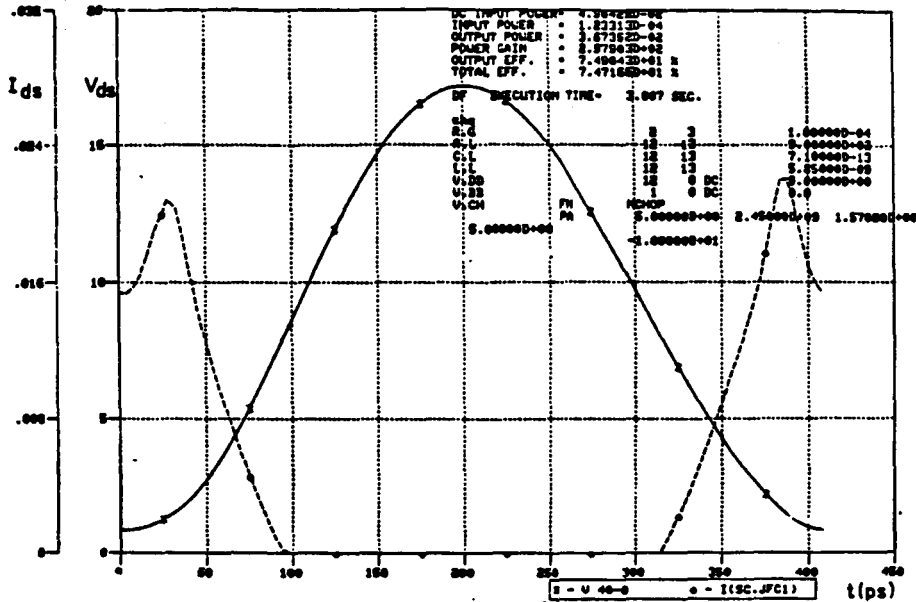
(a) STEADY STATE WAVEFORMS OF I_{ds} AND V_{ds}
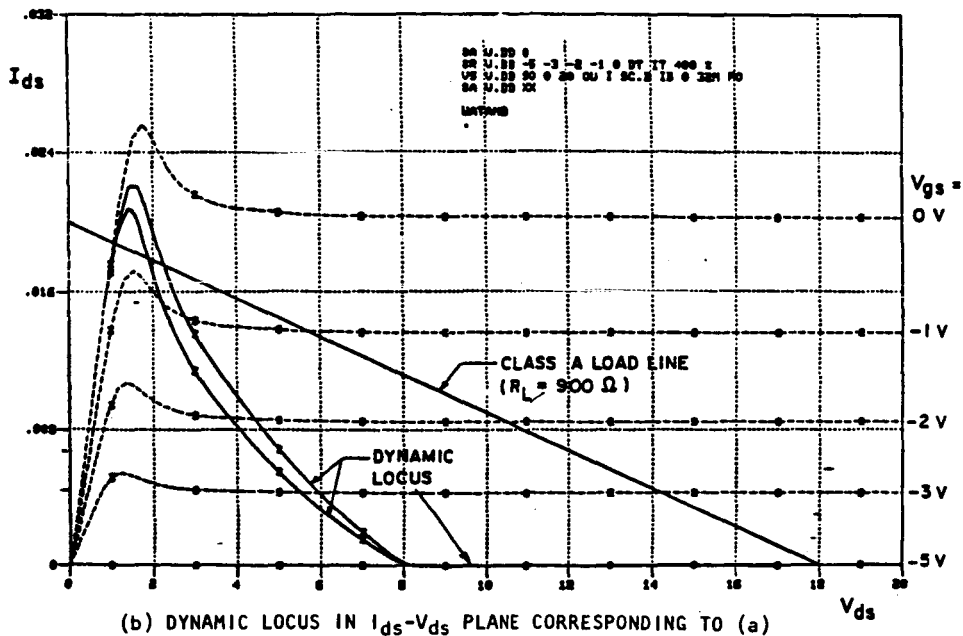
(b) DYNAMIC LOCUS IN I_{ds}-V_{ds} PLANE CORRESPONDING TO (a)

Figure 3.6-13. Steady State Waveforms and Dynamic Loci

From the dc characteristics, suitable values for R.L, C.L and L.L (Figure 3.6-8) are chosen. The circuit is set up with bias conditions for Class C operation and R.L and C.L are adjusted manually until the efficiency and power gain are approximately optimum. Many iterations are required to achieve this condition and both the interactive facility and steady state analysis are essential in this part of the study. Typical steady state waveforms, and the associated dynamic I_{ds} - V_{ds} loci are shown in Figure 3.6-13.

WATAND Comparison of Five-Section Nonlinear Model with One-Section Linear Model

WATAND runs for the device SP45 were made for the linear one-section model and for the nonlinear five-section model (see Figure 3.6-7). First the I_{ds} - V_{ds} characteristics were run for the two models and the two sets of characteristics were found to be identical.

Following this, the Class B (180° conduction angle) steady states were obtained for the two models. The results are summarized in Table 3.6-6 and repeated here.

	Linear 1-Section	Nonlinear 5-Section
DC input power	314 mW	327 mW
Input power	4.6 mW	3.1 mW
Output power	249 mW	247 mW
Power gain	54.0	79.4
Output efficiency	79.2%	75.5%
Total efficiency	78.1%	74.8%

Table 3.6-6. Comparing the 1-Section and the 5-Section Models

	SP45 LINEAR R.GS 1-SECTION	SP45 NONLINEAR R.GS 5-SECTION
CONDUCTION ANGLE	180°	180°
n_0%	79.2	75.5
n_T%	78.1	74.8
P_0(mW)	249	247
G_p	54	79.4
P_0/WMAX	0.7	0.7

It was noticed that for the multi-section model the channel current was not completely switched off during the transistor 'off' time. This was because in this model [Figure 3.6-7(c)], once the first of the nonlinear resistors along the distributed line has reached open circuit at the gate pinch voltage V_{gp}, the remaining line voltages cannot quite reach V_{gp}, with the result that channel current sources controlled by these voltages do not quite reach zero. This effect is of course not present in one section models. Because of this, the efficiencies for the nonlinear 5-section models are rather lower than those for the linear 1-section model. Slight discrepancies between the various powers are to be expected, since the linear 1-section model is only an approximation to the more accurate nonlinear 5-section model. It was felt that the results were close enough to allow us to proceed using the linear 1-section model only. This is advantageous because using multiple sections implies much greater computing times.

Matching Study

In our WATAND runs we usually assume an ideal voltage source as driving the gate. Such an ideal source is capable of supplying infinite power. In practice a source with finite available power must be used, and in a linear sinusoidal steady state situation the source requiring minimum available power would be that which is conjugately matched to the input impedance of the FET seen at the gate. In this case, the maximum power available from the source will in fact be supplied to the FET. If the input impedance to the FET at the particular sinusoidal frequency of operation is $Z_G = R_G - jX_G$ ohms, then the matched source impedance is $Z_S = R_G + jX_G$ ohms, and if the amplitude of the open circuited sinusoidal voltage source is $|V_S|$, then the power into the FET, which is the maximum available power, is

$$P_{max} = \frac{1}{2} \left| \frac{V_S}{2} \right|^2 / R_G = |V_X|^2 / 8R_G \quad .$$

When operating with this matched impedance generator, the voltage at the gate will be the voltage across Z_G, and will be a sinusoid whose phasor is

$$\frac{V_X Z_G}{Z_S + Z_G} = \frac{V_S(R_G - jX_G)}{2R_G}$$

Thus if when operating in our usual unmatched mode we require a sinusoidal voltage source with phasor V_a, in the matched case we will require a voltage source of approximately V_S where

$$\left| \frac{V_S(R_G - jX_G)}{2R_G} \right| = |V_a| \quad .$$

The result with this V_S should then be approximately a phase-shifted version of the result with V_a; in particular the output power P_O should be approximately the same. Note that the above "approximations" would be "equalities" if we were dealing with a linear system. The purpose of carrying out the conjugate

matched runs is to determine the effect of replacing the input current path
(which was a short circuit) by a finite impedance.

The power gain in the usual unmatched case is defined by

$$
G_P \bigg|_{\text{unmatched}} = \frac{P_o}{P_{\text{in}}} \bigg|_{\text{unmatched}} = \frac{P_o}{\frac{1}{2} |V_a|^2 \text{Re}(V_G)} = \frac{2P_o (R_G^2 + X_G^2)}{R_G |V_a|^2}
$$

The power gain in the matched case is

$$
G_P \bigg|_{\text{matched}} = \frac{P_o}{P_{\text{available}}} \bigg|_{\text{matched}} = \frac{P_o}{P_{\text{in}}} \bigg|_{\text{matched}} = \frac{8R_G P_o}{|V_S|^2}
$$

Using the relation between V_S and V_a we get

$$
G_P \bigg|_{\text{matched}} = \frac{8R_G P_o}{4R_G^2 |V_a|^2 / (R_G^2 + X_G^2)} = \frac{2P_o (R_G^2 + X_G^2)}{R_G |V_a|^2} = G_P \bigg|_{\text{unmatched}}
$$

It was felt necessary to confirm the calculations for at least one of our
operating points. However, it must be remembered that because the MESFET is
modeled as a nonlinear circuit element the above equality between matched and
unmatched power gains can only be approximate. If the input (gate) voltage
is sinusoidal, the current is non-sinusoidal and vice-versa.

Results

We chose (arbitrarily) to use the SP45 device operating in Class B (180°
conduction angle) as our test situation. The test was in fact carried out
before finalizing the actual model parameters, using a model designated as
model 4. In the linear one-section case, the main differences between this
and our final model were that in model 4, R.GS11 (and so also the input losses)
were lower than in the final version (4.5 Ω instead of 18.8 Ω); also the drain
resistor R.D1, and the substrate capacitor and resistor C.SUB1 and R.SUB1,
were absent.

We started our computations with the unmatched Class B situation. The
harmonic content of the input waveforms and some calculations show that in
this situation the large signal input impedance at 2.45 GHz is $Z_G = (15.9 -
j363)$. The reactive part of this impedance corresponds with a capacitance of
0.178 pf which in the matched source impedance becomes an inductance of $L_S =
23.598$ nH. These impedances have a Q of 23. The required matching source
amplitude $|V_S|$ is calculated to be 0.965 V.

A matched circuit with the required source amplitude and impedance was
simulated, and attempts made to obtain a steady state. Because of the high
Q of the input impedance (Q = 23) the gate voltage waveform is highly sensitive

It was noticed that for the multi-section model the channel current was not completely switched off during the transistor 'off' time. This was because in this model [Figure 3.6-7(c)], once the first of the nonlinear resistors along the distributed line has reached open circuit at the gate pinch voltage V_{gp}, the remaining line voltages cannot quite reach V_{gp}, with the result that channel current sources controlled by these voltages do not quite reach zero. This effect is of course not present in one section models. Because of this, the efficiencies for the nonlinear 5-section models are rather lower than those for the linear 1-section model. Slight discrepancies between the various powers are to be expected, since the linear 1-section model is only an approximation to the more accurate nonlinear 5-section model. It was felt that the results were close enough to allow us to proceed using the linear 1-section model only. This is advantageous because using multiple sections implies much greater computing times.

Matching Study

In our WATAND runs we usually assume an ideal voltage source as driving the gate. Such an ideal source is capable of supplying infinite power. In practice a source with finite available power must be used, and in a linear sinusoidal steady state situation the source requiring minimum available power would be that which is conjugately matched to the input impedance of the FET seen at the gate. In this case, the maximum power available from the source will in fact be supplied to the FET. If the input impedance to the FET at the particular sinusoidal frequency of operation is $Z_G = R_G - jX_G$ ohms, then the matched source impedance is $Z_S = R_G + jX_G$ ohms, and if the amplitude of the open circuited sinusoidal voltage source is $|V_S|$, then the power into the FET, which is the maximum available power, is

$$P_{max} = \frac{1}{2} \left| \frac{V_S}{2} \right|^2 / R_G = |V_X|^2 / 8R_G \ .$$

When operating with this matched impedance generator, the voltage at the gate will be the voltage across Z_G, and will be a sinusoid whose phasor is

$$\frac{V_X Z_G}{Z_S + Z_G} = \frac{V_S (R_G - jX_G)}{2R_G}$$

Thus if when operating in our usual unmatched mode we require a sinusoidal voltage source with phasor V_a, in the matched case we will require a voltage source of approximately V_S where

$$\left| \frac{V_S (R_G - jX_G)}{2R_G} \right| = |V_a| \ .$$

The result with this V_S should then be approximately a phase-shifted version of the result with V_a; in particular the output power P_O should be approximately the same. Note that the above "approximations" would be "equalities" if we were dealing with a linear system. The purpose of carrying out the conjugate

matched runs is to determine the effect of replacing the input current path (which was a short circuit) by a finite impedance.

The power gain in the usual unmatched case is defined by

$$
G_P \bigg|_{unmatched} = \frac{P_o}{P_{in}}\bigg|_{unmatched} = \frac{P_o}{\frac{1}{2}|V_a|^2 \, Re(V_G)} = \frac{2P_o(R_G^2 + X_G^2)}{R_G \, |V_a|^2}
$$

The power gain in the matched case is

$$
G_P \bigg|_{matched} = \frac{P_o}{P_{available}}\bigg|_{matched} = \frac{P_o}{P_{in}}\bigg|_{matched} = \frac{8R_G \, P_o}{|V_S|^2}
$$

Using the relation between V_S and V_a we get

$$
G_P \bigg|_{matched} = \frac{8R_G \, P_o}{4R_G^2 \, |V_a|^2/(R_G^2 + X_G^2)} = \frac{2P_o(R_G^2 + X_G^2)}{R_G \, |V_a|^2} = G_P \bigg|_{unmatched}
$$

It was felt necessary to confirm the calculations for at least one of our operating points. However, it must be remembered that because the MESFET is modeled as a nonlinear circuit element the above equality between matched and unmatched power gains can only be approximate. If the input (gate) voltage is sinusoidal, the current is non-sinusoidal and vice-versa.

Results

We chose (arbitrarily) to use the SP45 device operating in Class B (180° conduction angle) as our test situation. The test was in fact carried out before finalizing the actual model parameters, using a model designated as model 4. In the linear one-section case, the main differences between this and our final model were that in model 4, R.GS11 (and so also the input losses) were lower than in the final version (4.5 Ω instead of 18.8 Ω); also the drain resistor R.D1, and the substrate capacitor and resistor C.SUB1 and R.SUB1, were absent.

We started our computations with the unmatched Class B situation. The harmonic content of the input waveforms and some calculations show that in this situation the large signal input impedance at 2.45 GHz is $Z_G = (15.9 - j363)$. The reactive part of this impedance corresponds with a capacitance of 0.178 pf which in the matched source impedance becomes an inductance of $L_S = 23.598$ nH. These impedances have a Q of 23. The required matching source amplitude $|V_S|$ is calculated to be 0.965 V.

A matched circuit with the required source amplitude and impedance was simulated, and attempts made to obtain a steady state. Because of the high Q of the input impedance (Q = 23) the gate voltage waveform is highly sensitive

to small variations, and it was found difficult to proceed directly to the steady state. It was found necessary to gradually increase the amplitude of the source voltage starting from $|V_S| = 0.1$ V. In order to produce output waveforms which approximated those of the unmatched case, it was found necessary to increase $|V_S|$ to 1.3 V (instead of the calculated 0.97 V).

The output waveform was shifted somewhat and the conduction angle increased to about 210° (from 180°). The results, shown in Table 3.6-7, indicate however that although the circuit operation is perturbed, "reasonable" efficiencies and power gains are attainable. Since a conjugate matched input would probably not be used in practice, this point was not pursued.

Table 3.6-7. Comparison Between the Unmatched and Approximately Matched Performances for SP45

SP45: LINEAR R.GS, 1-SECTION		
	UNMATCHED	APPROXIMATELY MATCHED
CONDUCTION ANGLE	180°	210°
$|V_S|$ (V)	11	1.3
$n_o\%$	79	68
$n_T\%$	77	67
P_o (mW)	266	259
G_p	36	43*
$Z_G(\Omega)$	(159-j363)	(132-j395)

*__Note:__ Power gain in the approximately matched case is

calculated from

$$G_p = \frac{2P_o|(R_G+R_s) + j(X_G+X_s)|^2}{R_G|V_s|^2}$$

Final WATAND Results on Five Different MESFET Designs

Having finalized the modeling technique to be used, the six MESFETS, designated SP01, SP41, SP45, SP46 and SP47, were studied using WATAND. As mentioned earlier, each model is capable of being modeled with two types of $I_{sd} - V_{sd}$ characteristics; the "real" characteristics, which include the effect of the double-valued velocity field relation and the "flat" character-istics, which do not include this effect.

We attempted to use the former "real" models throughout the work now being reported. We succeeded in all devices except for SP41, for which we had to use the flat model. The probable reason for this is the "narrowness" of bump in the characteristics; see Figure 3.6-13(b).

For each device model, having first obtained the static (dc) $I_{ds} - V_{ds}$ characteristics, we obtained three steady state output waveforms for three conduction angles: 180° (Class B), 120° and 80°. For each such steady state the powers, power gains and efficiencies were calculated.

Throughout this report our circuit is driven by a gate-source voltage named V.G defined by

$$V.G = Max\{\alpha_5; (\alpha_1 \sin(2\pi \alpha_2 t + \alpha_3) - \alpha_4)\} ,$$

where $\alpha_1, \ldots, \alpha_5$ are five variable parameters. This waveform is just a dc bias (α_4) imposed on an ac signal, with possibility of clipping at α_5. By varying α_1, α_4 and α_5 we are able to obtain the various driving waveforms we require. Note that in this application we usually require V.G to have zero as its maximum value, requiring $\alpha_1 = \alpha_4$; we also wish for this to occur at time $t = 0$, requiring $\alpha_3 = \pi/2$.

For tuned Class B operation, with V_{ds} swinging between breakdown voltage V_{br} and the knee voltage V_{ko}, the value of the load resistance should be approximately $(V_{br} - V_{ko})/I_{DSS}$ giving $R_L \approx 600 \ \Omega$ for SP01 $R_L \approx 6$ kΩ for SP41, and $R_L \approx 700 \ \Omega$ for SP45. The values of C.L and L.L are chosen to resonate at the drive frequency, and to yield a Q of approximately 10.

Resulting steady state waveforms of V_{ds} and I_{ds} for SP01 in Class B together with powers, power gains and efficiencies are shown in Figure 3.6-13. Note that I_{ds} is the actual channel current in the device (the current flowing in the short-circuit SC.JFC1 in Figure 3.6-14(a). Because the drain current includes the high frequency capacitor currents it is easier to monitor the device behavior by using this channel current.

If P_{dc} denotes input dc power, if P_{in} denotes input (fundamental) micro-wave power, and if P_{out} denotes output (fundamental) microwave power, then we define:

Power gain $(G_p) \triangleq P_{out}/P_{in}$ \qquad (absolute)

Output efficiency $(\eta_o) \triangleq (P_{out}/P_{dc}) \times 100\%$

Total efficiency $(\eta_T) \triangleq P_{out}/(P_{dc} + P_{in}) \times 100\%$

i.e., $\dfrac{1}{\eta_T} = \dfrac{1}{\eta_o} + \dfrac{1}{100 \ G_p}$

Although an argument could be made that by appropriate use of harmonic filters these powers should be the complete waveform powers (rather than the fundamental powers), it was felt that it would be better to be on the safe side and use fundamental power only in our calculations.
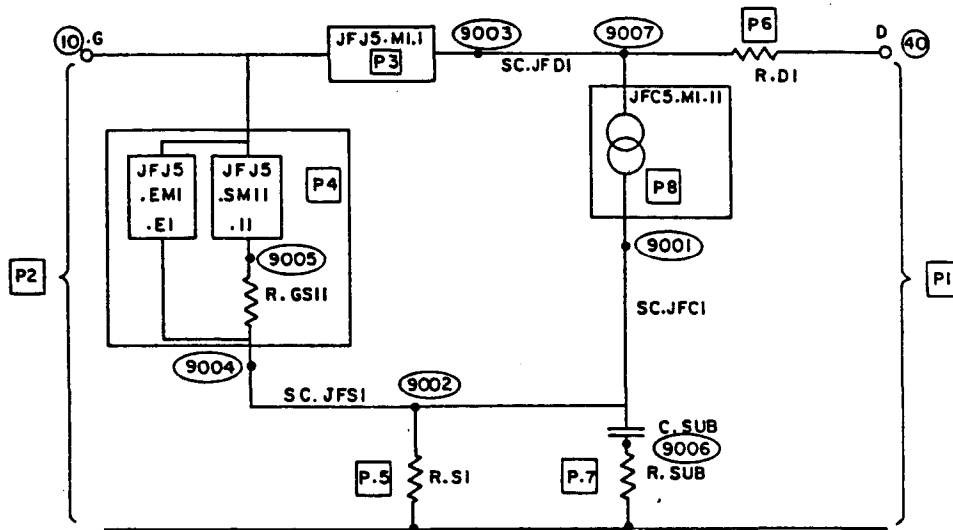
(a) The one-section model showing the
definitions of P1 to P8.

	SP41: 1-SECTION LINEAR R.GS			SP45: 1-SECTION LINEAR R.GS		
Conduction Angle	80°	120°	180°	80°	120°	180°
P_o(mW)	41.6	62.0	87.4	96.4	157	249
P_1(mW)	5.6	5.1	20	-5.4	19.6	64.4
P_2(mW)	10.2	5.9	1.4	74.0	12.3	4.6
P_T(mW)	15.8	11.0	21.4	68.6	31.9	69.0
P_3/P_T(%)	0	0	0	0	0	0
P_4/P_T(%)	60.0	2.3	3.4	74.7	25.9	3.7
P_5/P_T(%)	11.1	5.5	1.6	13.1	6.7	2.7
P_6/P_T(%)	11.1	14.1	9.5	3.5	10.5	_8.5
P_7/P_T(%)	0	0	0	0	0	_ 0
P_8/P_T(%)	17.7	57.6	85.5	8.7	56.9	85.1

(b) The internal distribution of P1 to
P8 for SP41 and SP45.

Figure 3.6-14. Sources of Power Losses

In our earlier investigations involving bipolar transistors (Reference 17) it was found advantageous to drive the transistor in the Class B or C configuration slightly into saturation. The equivalent operating condition for the MESFET is to swing the V_{ds} waveform to operate from below the knee voltage V_{ko} for part of its cycle. We accomplish this by slightly increasing R_L and V_{DD}.

In order to obtain greater efficiency of operation we continued to drive the devices from slightly below the knee voltages and we moved from Class B to Class C operation by decreasing the conduction angle by changing the input drive. Thus if the gate pinch voltage is V_{gp}, and if $V.G = \alpha[\sin(2\pi\,ft + \pi/2) - 1]$, then the conduction angle θ is given by

$$\theta = 2\cos^{-1}(1 - \frac{V_{gp}}{\alpha})\quad.$$

With a reduced conduction angle it is necessary to increase R.L in order to swing V_{DS} from just below the knee voltage V_{ko} to the breakdown voltage V_{br}. Since the output power is approximately $W_{max} = (V_{br} - V_{ko})/8R_L$ (Reference 26), we thus increase our efficiency at the expense of decreased output power.

Figures 3.6-14, 3.6-15, and Tables 3.6-8 and 3.6-9 present the main results of this study. They indicate that the SP41 device can give 85% power added efficiency with a power gain of 10 dB and a power output of 67 mW, or 81% efficiency with a power gain of 18 dB and a power output of 90 mW. The SP45 device has a peak efficiency of 83% for a gain of 11 dB and a power output of 152 mW or 78% for a gain of 17 dB and 245 mW. Both the devices (Table 3.6-4) have 3 micron × 400 micron gates and the breakdown voltage V_{sdbr} is assumed constant. Figure 3.6-14 and Table 3.6-9 tabulate the various sources of power loss within the MESFET for the five devices.
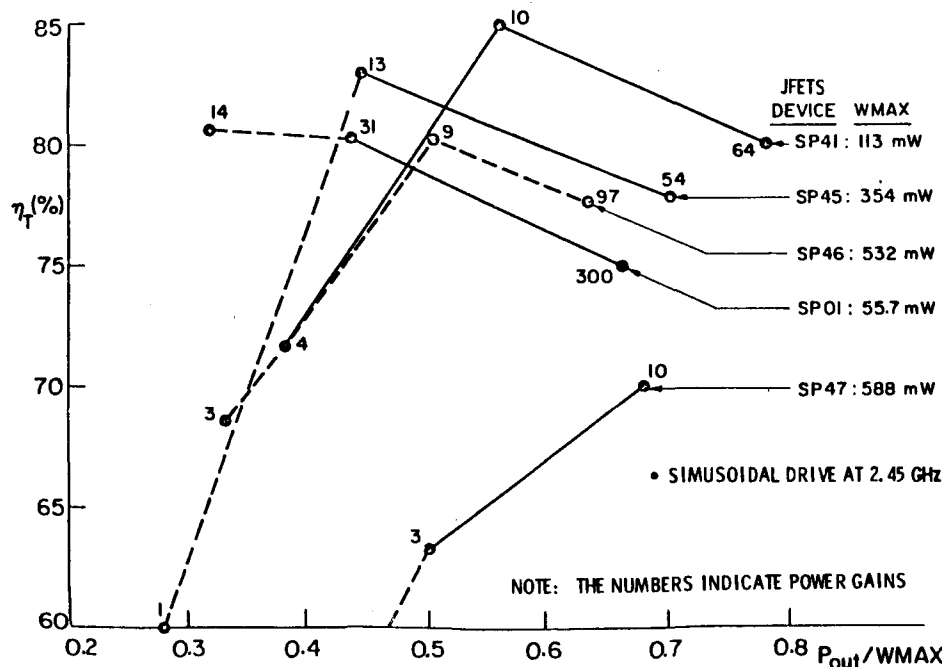
Figure 3.6-15. Total Efficiency (η_T%) versus Output Power/Wmax)

Table 3.6-8. Details of Performance of
SP41 and SP45

	SP41: 1-SECTION LINEAR R.GS			SP45: 1-SECTION LINEAR R.GS		
$V_{br}(V)$	71			46		
$I_{ds\ max}$ (mA)	12			63		
Wmax (mW)	113			354		
Conduction Angle	80^0	120^0	180^0	80^0	120^0	180^0
$\eta_0\%$	87.6	92.0	81.2	105	88.5	79.2
$\eta_T\%$	72.2	84.6	80.0	58.7	82.8	78.1
$P_0(mW)$	41.6	62.0	87.4	96.4	157	249
G_p	4.1	10.5	64.3	1.3	12.8	54
P_0/W_{max}	.37	.55	.77	.27	.44	.7
Q	25	31	23	28	19	12

It must be pointed out that all of the above dynamic (steady-state) results were obtained under the assumption that the source-drain breakdown voltage V_{sdbr} remains constant. To achieve this, and for numerical convenience, we set V_{br} to V_{br} = 1kV, and then ensured by visual inspection that the value of $|V_{sd}|$ did not exceed the assumed constant value of $|V_{sdbr}| = |V_{gsbr}|$. If instead the source-drain breakdown voltage V_{sdbr} is modeled by the 'silicon' formula:

$$|V_{sdbr}| = |V_{gsbr}| - |V_{gs}|$$

Then the worst case situation for each device would be as shown in the following table. Note that a zero in the last row of this table indicates that the

	SP01			SP41			SP45			SP46			SP47		
	80°	120°	180°	80°	120°	180°	80°	120°	180°	80°	120°	180°	80°	120°	180°
$\|V_{gsbr}\|$	17	17	17	71	71	71	66	66	66	37	37	37	46	46	46
$Max\|V_{gs}\|$	40	20	10	30	15	7.4	84	45	22	128	74	37	84	42	21
$Max\|V_{sd}\|$	0	0	7	41	55	63	0	21	44	0	0-	0	0	4	25

Table 3.6-9. Performance Tabulation of Devices

	SP01:	LIN: WMax = 55.7 mW	1-SECT:	SP41:	LIN: WMax = 113 mW	1-SECT:	SP45	LIN: WMax = 354 mW	1-SECT:	SP45 NON LIN 5 SECT.	SP46	LIN: WMax = 532 mW	1-SECT:	SP47	LIN: WMax = 588 mW	1-SECT:
	80°	120°	180°	80°	120°	180°	80°	120°	180°	180°	80°	120°	180°	80°	120°	180°
Ref.#	772	771	770	523	521	520	452	451	450		613	612	610	802	801	800
η_o %	86.5	83.0	74.9	87.6	92.0	81.2	105	88.5	79.2	75.5	88.8	88.4	77.7	114	83.3	75.6
η_T %	81.5	80.9	74.7	72.2	84.6	80.0	58.7	82.8	78.1	74.8	68.6	80.6	77.1	35.6	63.3	70.1
P_o (mW)	17.5	24.1	36.7	41.6	62.0	87.4	96.4	157	249	247	182	267	334	245	296	402
G_p	14.1	31.0	298	4.1	10.5	64.3	1.3	12.8	54	79.4	3	9	97	.5	2.64	9.6
P_o/W_{max}	.31	.43	.66	.37	.55	.77	.27	.44	.7	.7	.34	.5	.63	.42	.5	.68
Q	9.7	9.9	8.8	25	31	23	28	19	12	-	11.8	20	17	9	8.5	11.4
P_1 (mW)	2.6	4.8	12.2	5.6	5.1	20	-5.4	19.6	64.4		21.8	34.0	95.6	-31.7	57.4	129.0
P_2 (mW)	1.3	.8	0.1	10.2	5.9	1.4	74.0	12.3	4.6		61.8	29.2	3.5	473.4	112.2	41.9
P_T (mW)	3.9	5.6	12.3	15.8	11.0	21.4	68.6	31.9	69.0		83.6	63.3	99.1	441.8	169.6	170.9
(P_3/P_T)%	0	0	0	0	0	0	0	0	0		0	0	0	0	0	0
(P_4/P_T)%	17.1	3.2	.4	60.0	2.3	3.4	74.7	25.9	3.7		61.0	23.0	4.9	82.1	59.8	19.2
(P_5/P_T)%	13.3	6.8	4.6	11.1	5.5	1.6	13.1	6.7	2.7		11.2	6.7	3.2	7.3	5.9	2.8
(P_6/P_T)%	15.0	14.7	13.6	11.1	14.1	9.5	3.5	10.5	8.5		6.1	10.5	9.6	1.6	7.1	10.2
(P_7/P_T)%	0	0	0	0	0	0	0	0	0		0	0	0	0	0	0
(P_8/P_T)%	54.6	75.4	81.3	17.7	57.6	85.5	8.7	56.9	85.1		21.6	59.8	82.3	9.0	27.2	67.7

NOTE: FOR KEY TO POWER NUMBERS [SEE FIGURE 3.6-15(a)].

corresponding conduction angle for that device cannot be achieved using the 'silicon' breakdown formula. Non-zero values indicate the possibility of attaining the corresponding conduction angle, but only with this maximum voltage of $|V_{sd}|$ (to be compared with a maximum of $|V_{gsbr}|$ assumed in our calculations). This reduced value of $|V_{sd\ max}|$ implies of course very different values for load resistor R_L and very different steady state dynamic behavior. We have not felt it worthwhile to investigate this.

Figure 3.6-16 and Table 3.6-10 give results for the case where the input drive is clipped, so that the input waveform only goes down to the gate pinch-off voltage. This improves the performance considerably, but it should be noted that power loss in the clipping circuit is not examined here. Figure 3.6-16 also shows the effect of using the "silicon" breakdown formula:

$$|V_{gsbr}| = |V_{gsbr}| - |V_{sg}| \quad ,$$

for both the clipped and unclipped drive. Note that in the latter case only the Class B (180° conduction angle) operation can be obtained.
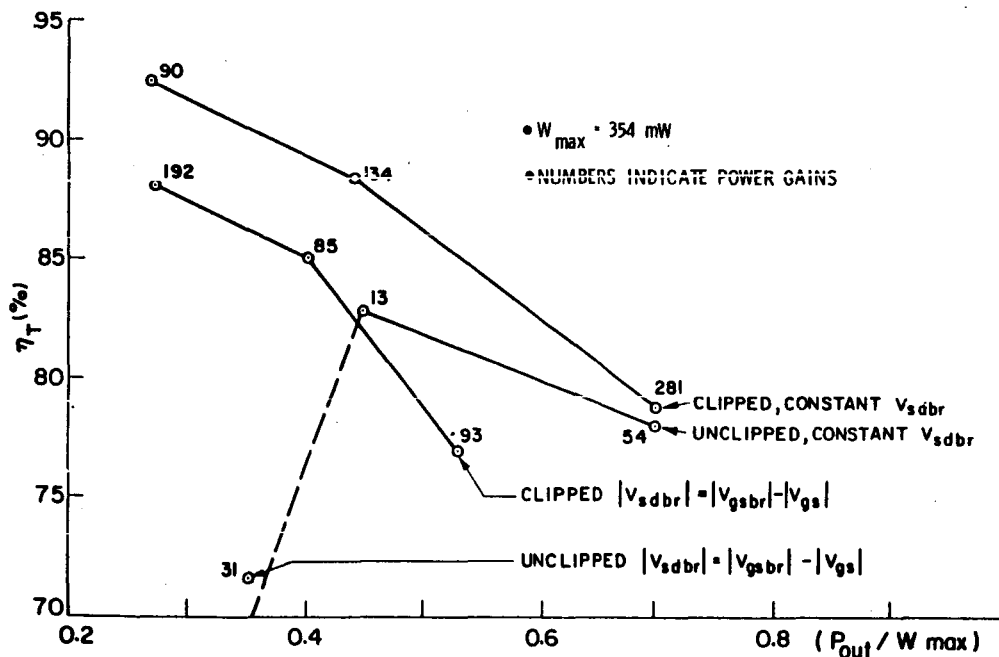
Figure 3.6-16. SP45: Total Efficiency ($\eta_T\%$)
versus Output Power/Wmax

Class E Operation

The theory of Class E operation is discussed in (Reference 17). The Class E circuit investigated is shown in Figure 3.6-17.

Table 3.6-10. Comparison of Performance Between
Unclipped Drive and Clipped Drive for SP45

	SP45: 1-SECTION MODEL LINEAR R.GS					
	Unclipped Drive			Clipped Drive		
Conduction Angle	80°	120°	180°	80°	120°	180°
$\eta_o\%$	105	88.5	79.2	93.1	88.2	78.9
$\eta_T\%$	58.7	82.8	78.1	92.1	87.6	78.7
P_o(mW)	96.4	157	249	94.1	157	250
G_p	1.3	12.8	54	89.6	134	281
P_o/W_{max}	0.27	0.44	0.7	0.27	0.44	0.7
P_1(mW)	-5.4	19.6	64.4	6.4	19.7	63
P_2(mW)	74	12.3	4.6	8.4	6.1	5.9
P_T(mW)	68.6	31.9	69.0	14.9	25.8	68.9
P_3/P_T(%)	0	0	0	0	0	0
P_4/P_T(%)	74.7	25.9	3.7	31.6	10.5	2.5
P_5/P_T(%)	13.1	6.7	2.7	9.3	4.7	2.5
P_6/P_T(%)	3.5	10.5	8.5	11.7	11.4	7.8
P_7/P_T(%)	0	0	0	0	0	0
P_8/P_T(%)	8.7	56.9	85.1	46.7	73.4	87.6

Note: W_{max} = 354 mW.

Using the ideal design formulae for this Class E circuit for device
SP45 yields the following design parameters:

Q	Power	η	V.DD	R.L	L.2	C.2	C.1
10	308mW	100%	14.2V	3,543Ω	2,302nH	2D-3pF	3.6D-3pF

It is obvious that such small capacitance values cannot be accommodated with
the (comparatively) low frequency device SP45.

3-128
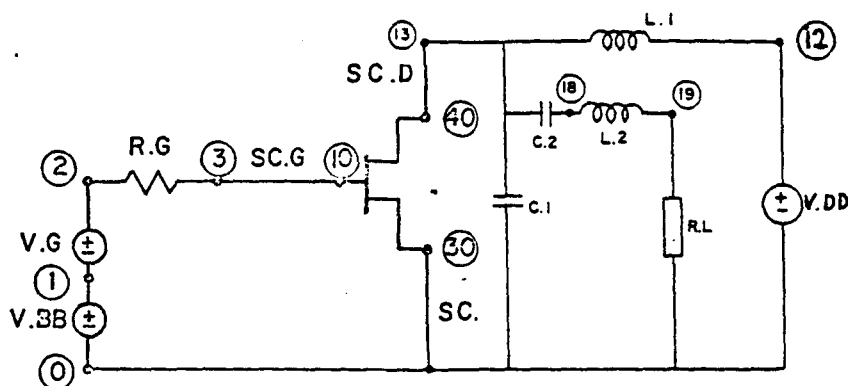
Figure 3.6-17. Class E Amplifier Circuit
Used in MESFET SPS Study

For the (comparatively) high frequency device SP01 however, the design becomes just feasible. In Table 3.6-11 we show the design values and the actual values used with results for this device. In these results, the gate voltage drive used was a clipped Class B drive. We also show results for Class C (120°) unclipped and clipped drive. We see that using the Class E configuration with the clipped Class B drive provides very little advantage compared with the clipped Class C configuration at the same output power.

We have concluded that there is very little point in pursuing any further the investigation of the Class E configuration.

Conclusions

The modeling technique developed for this study has been evaluated both by reference to available experimental data and by considering two different models. The results are estimated to be correct to within about 5% for power conversion efficiencies and about 3 dB for power gain. It is important to note that in the power converter designs no parasitic elements have been included. It was found that the negative resistance region of the GaAs characteristic did not significantly affect the results obtained with the CAD model. More accurate calculation of this region with the UNIPOLE program was therefore felt to be unnecessary at this stage.

In terms of the WATAND simulation, it was concluded that [as in the bipolar transistor study (Reference 17)] Class E does not offer any significant advantage over Class C. In fact, for the 3-μm devices finally selected for 2.45 GHz Class C operation, correct Class E performance was not even possible due to the output capacitance.

We have shown that conventional (X-band) GaAs MESFETs are not best suited for the 2.45 GHz power converter. Conversion efficiency is improved by choosing different geometry. The final design uses 3-micron gates, but if this were reduced to 2 microns the power gain could be increased somewhat. The 3-micron value was chosen as the upper limit and has the advantage of yielding higher output power per unit cell. Since paralleling of MESFETs is a problem which has not yet been satisfactorily solved, it seemed to us that a high

Table 3.6-11. Design and Performance Data Comparison

	Class E Design	Class E Obtained (Using Clipped Class B Drive)	Class C 120° (Unclipped Drive)	Class C 120° (Clipped Drive)
Q	10	12	10	10
P_o (mW)	38	22	24	24
G_p	∞	-63	31	300
η (%)	100	84	81	83
V.DD (V)	5.4	6.5	9	9
R .L(Ω)	500	400	1,400	1,400
L.2(nH)	300	300	-	-
C.2(pF)	.02	.0165	-	-
C.1(pF)	.02	.04	-	-
P_1(mW)	0	4.1	4.8	4.9
P_2(mW)	0	-0.2	.8	.3
P_T(mW)	0	3.9	5.6	5.2
P_3/P_T(%)	-	0	0	0
P_4/P_T(%)	-	.9	3.2	1.1
P_5/P_T(%)	-	6.8	6.8	6.1
P_6/P_T(%)	-	22.7	14.7	16.2
P_7/P_T(%)	-	0	0	0
P_8/P_T(%)	-	69.6	75.4	76.5

NOTE: FOR KEY TO POWER NUMBER SEE FIGURE 3.6-15(a).

power per cell was desirable. Without knowing the extent to which cells can be paralleled without degradation in performance due to increased parasitics, it is not obvious that the GaAs FET power converter is better than the GaAs bipolar version studied in (Reference 17). For 2-micron gates (and 2-micron emitter stripes) the efficiencies obtainable are comparable, but the power output obtainable from bipolar complete multi-stripe structures is, at today's state of the art, much greater than that of the MESFET.

3.6.3 PHASE CONJUGATING IN AN ACTIVE RETRODIRECTIVE ARRAY

The following describes the problem of phase conjugation in an active retrodirective array. The effects of steady-state ionosphere on uplink and downlink signals are analyzed. The phase ambiguity problem is introduced and a potential solution provided that employs a 3-tone pilot beam. An estimate of integrated electron density along radio links of interest is obtained by making appropriate phase measurements on the three received tones. Using this information, a phase conjugator is mechanized such that ionosphere related discrepancies are automatically compensated. This represents a significant extension of the capabilities of existing conjugators. Much statistical analysis related to ionospheric turbulence remains to be done.

The retrodirective antenna array works on the so-called phase-conjugation principle whereby an incident wavefront is processed in such a manner that when it is retransmitted (possibly at a much higher power level), it returns whence it came as a coherent wavefront. An important feature of this mechanism of retrodirectivity is that one does not require prior knowledge of either the source's location or character of the incident wavefront; e.g., equiphase surfaces need not be planes. In the context of the Solar Power Satellite, the incident wavefront is created by a pilot source on the ground and the antenna array (where phase processing occurs) is situated in a geosynchronous orbit. The downcoming signal (power beam) is intercepted by a rectifying antenna (and not a phased array) of appropriate dimensions on the ground.

The main object of this discussion is to establish preliminary requirements on the signal structure of the uplink pilot beam so that phase conjugation can be correctly performed and retrodirectivity achieved. As will be seen shortly, the problem gets complicated by the presence of the dispersive ionosphere and its spatial and temporal characteristics. Before proceeding with the main task mentioned above, it is worthwhile to discuss briefly the principle of phase conjugation.

Phase Conjugation (References 27 and 28)

A retrodirective or self-phasing antenna array senses the phase information incident across the aperture and uses this information in proper manner to transmit back to the source a coherent signal. The signal radiated by the self-phasing antenna may or may not be coherent across the aperture but it is coherent when it arrives back at the source. In principle, the self-phasing antenna can operate regardless of the shape of the wavefront incident on the aperture.

Consider the situation shown in Figure 3.6-18. To operate as a self-phasing antenna, the aperture is divided into many subarrays. The question of subarray size is not considered in this report. It is assumed that phase processing occurs at each subarray.

Let the signal at the pilot source be given by

$$S(t) = A \cos (\omega_o t + \theta_o) \tag{3.6-33}$$
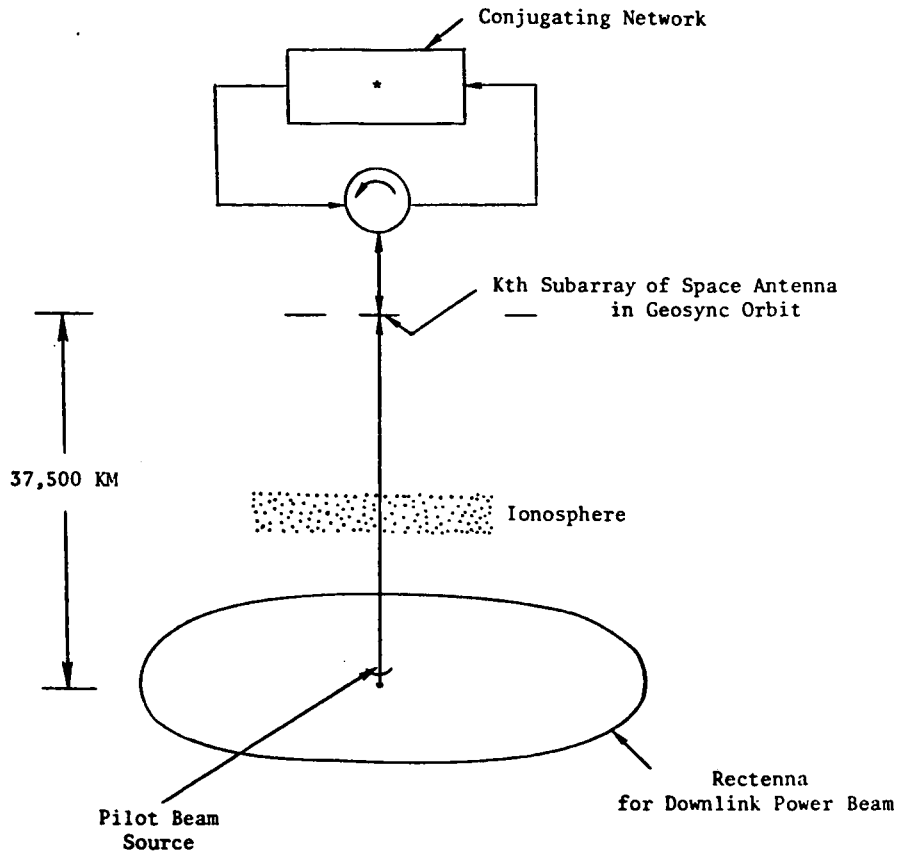
Figure 3.6-18. Sketch of Antenna—Rectenna Relationships

where A is the amplitude, ω_0 is the angular frequency and ϕ_0 is the phase.
The signal received at the Kth subarray is of the form

$$S_K(t) = A_K \cos [\omega_o (t-T_K) + \theta_o] \qquad (3.6-34)$$

where

$$T_K = \frac{r_K}{C} \qquad (3.6-35)$$

In Equation (3.6-34), T_K is the propagation time involved and ionospheric
effects are ignored for the present. The received signal is passed through a
conjugating network that reverses the sign of the phase. A circulator is
shown in Figure 3.6-18 which separates the uplink and downlink signals. Thus,
the conjugate signal radiated by the Kth subarray is given by

$$S_K^*(t) = A_K' \cos [\omega_o (t+T_K) - \theta_o] \qquad (3.6-36)$$

where, in general, $A_K' \gg A_K$. Under the assumption that the propagation medium
is reciprocal, the signal that arrives back at the source can be written as

3-132

$$S'(t) = A' \cos (\omega_o t - \theta_o) \qquad (3.6\text{-}37)$$

where A' is the received amplitude. The argument of the returned signal in Equation (3.6-37) is the same as that originally radiated by the source [see Equation (3.6-33)] except for the fact that the sign of θ_o has been reversed. The important thing to note in Equation (3.6-37) is that the signal radiated by the subarray is independent of the transit time T_K when it arrives back at the source. Thus the signals from the different subarrays have the same phase no matter what the individual transit times might be. The resultant signal is therefore the coherent addition of the various subarray signals. The fact that the signal of θ_o has been reversed is of no consequence since it happens at every subarray and has no effect on phase coherence. Indeed, one could introduce a constant phase shift ψ_o at all the subarrays without affecting phase coherence at all. The principle of phase conjugation discussed above is depicted in Figure 3.6-19. At the heart of this operation lies a separate reference source whose phase (and, of course, frequency) needs to be distributed over the entire aperture within close tolerance. This is the problem of phase control and distribution and is discussed elsewhere (Reference 28). For the present, it is assumed that the pair $\{\omega_r, \phi_r\}$ are available at all subarrays where conjugation is being performed. While the principle of conjugation is clear from Figure 3.6-19, as far as SPS is concerned, there are some operational constraints. In particular, the uplink and downlink frequencies cannot be the same. Any processing of the uplink signal is rendered impossible because of the high-energy downlink beam. An obvious way of avoiding this problem is to perturb the reference frequency ω_r by $\delta\omega$; i.e., set

$$\omega_r = 2 \omega_o + \delta\omega \qquad (3.6\text{-}38)$$

and under this condition, the radiated wave from the Kth subarray is given by

$$
\begin{aligned}
S_K^*(t) &= A_K' \cos \left[(\omega_o + \delta\omega)\, t + \omega_o \frac{r_K}{C} + \phi_r \right] \\[2mm]
&= A_K' \cos \left[(\omega_o + \delta\omega)\, t + (\omega_o + \delta\omega) \frac{r_K}{C} + \phi_r - \frac{\delta\omega\, r_K}{C} \right] \\[2mm]
&= A_K' \cos \left[(\omega_o + \delta\omega) (t + \frac{r_K}{C}) + (\phi_r - \frac{\delta\omega\, r_K}{C}) \right] \\[2mm]
&= A_K' \cos \left[(\omega_o + \delta\omega) (t + \frac{r_K}{C}) + \beta_K \right] \qquad (3.6\text{-}39)
\end{aligned}
$$

where

$$\beta_K = (\phi_r - \frac{\delta\omega\, r_K}{C}) \qquad (3.6\text{-}40)$$

$$\psi_{REF} = \omega_r t + \phi_r$$
$$= 2\omega_0 t + \phi_r$$

$$\psi_K = \omega_0 (t - \frac{r_K}{c})$$

$$\psi_K^* = \omega_0 (t + \frac{r_K}{c}) + \phi_r$$

NOTE: ϕ_r IS SAME FOR EVERY SUBARRAY. UPLINK AND DOWNLINK AT SAME FREQUENCY.
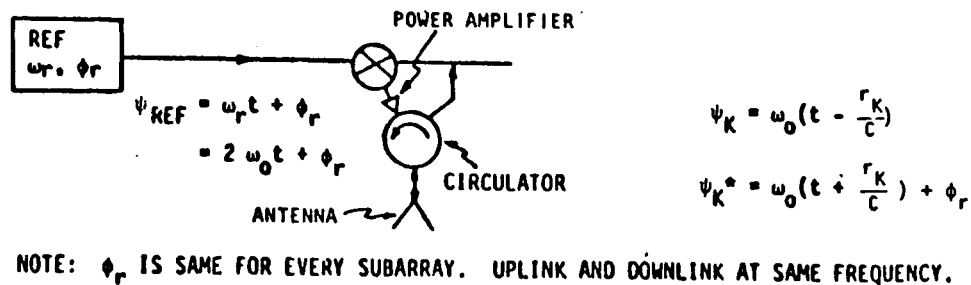
Figure 3.6-19. Principle of Phase Conjugation

From Equation (3.6-39) it is clear that signals from the different subarrays do not add coherently at the source because of the β_Ks. In general, the down-link beam points in some undesired direction and this is called "beam squint." In Figure 3.6-20, a different mechanization is given which achieves the task of phase conjugation with different uplink and downlink frequencies and no beam squint (Reference 28). Instead of the circulator, a diplexer is used to channel the uplink and downlink frequencies.

$$\psi_K = \omega_0 (t - \frac{r_K}{c})$$

$$\psi_K^* = \left(\frac{n}{n-2}\right)\left(2\psi_0 - \psi_K\right)$$

$$= \left(\frac{n}{n-2}\right) \omega_0 \left(t + \frac{1}{c} (r_K - 2 r_0)\right)$$

$$= \omega' \left(t + \frac{1}{c} (r_K - 2 r_0)\right)$$

ψ_0 = REFERENCE PHASE
$$= \omega_0 (t - \frac{r_0}{c})$$

COMMENT: THE SIGNAL FROM ONE PARTICULAR ARRAY ELEMENT CAN BE USED AS THE REFERENCE. NO EXTERNAL SOURCE IS NECESSARY.
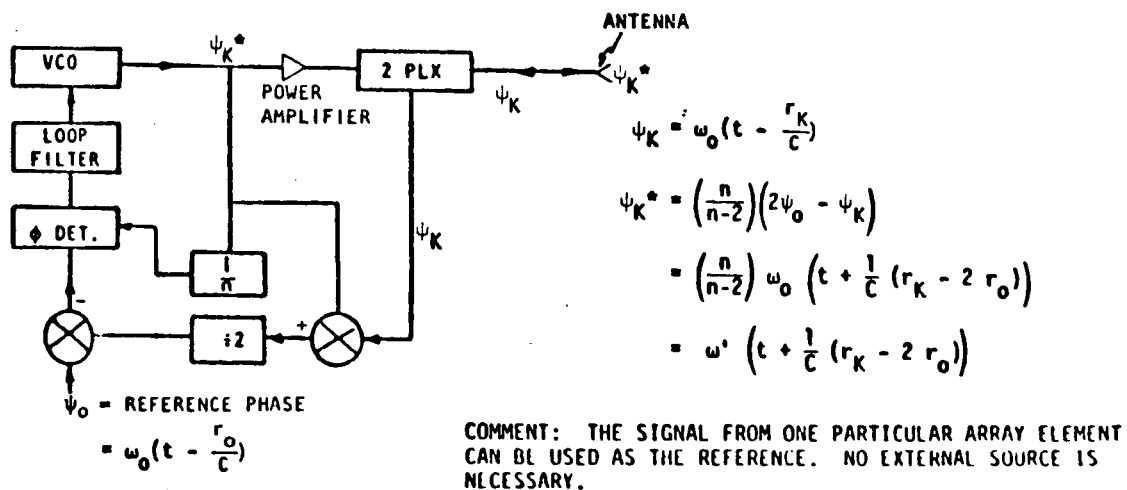
Figure 3.6-20. Beam Mechanization Concept

During the course of the work reported here, it was discovered that the conjugator in Figure 3.6-20 has two distinct modes of operation. The equations accompanying Figure 3.6-20 describe the (original) mode of operation as in (Reference 28). In this write-up, the other mode is used.

From what has been said above, it appears that the phase conjugation problem associated with the retrodirective array has been, largely speaking, solved. However, the preceding discussion on conjugation has completely avoided ionospheric propagation effects and in a real-life SPS situation, this is hardly acceptable. In the next section, the effects of ionospheric dispersion, inhomogeneity and time instability on the single-tone pilot beam system are examined.

3-134

Ionospheric Effects On Single-Tone Pilot Beam

It was stated earlier that an important feature of the retrodirective array is that the downcoming beam is phase coherent when it arrives at the source. This statement is rigorously correct only if the propagation medium is reciprocal, spatially homogeneous and temporally stable. In case of the ionosphere, one or more of the above conditions are violated. Under certain conditions, beam pointing error can occur and phase coherence at the source can be lost.

Assume the uplink and downlink frequencies are given by f_u and f_D, respectively ($f_u \neq f_D$). The (path-dependent) phase shift at f_u on one particular radio link can be written as (Reference 29 and 30)

$$\phi(f_u) = \frac{2\Pi f_u L}{C} - \frac{b}{2\Pi f_u C} \int_0^L N \, d\ell \qquad (3.6\text{-}41)$$

where

$$b = \frac{e^2}{2 \, \epsilon_o \, m}; \quad e = \text{electron charge}, \quad m = \text{electron mass}, \quad \epsilon_o = \text{free-space permittivity}$$

$$= 1.6 \times 10^3 \text{ mks}$$

L is the physical path length involved and $\int_0^L N \, d\ell$ is the integrated electron density along the path under consideration ($\approx 10^{17} - 10^{19}$). Note the second quantity on the right hand side of Equation (3.6-41) accounts for ionospheric effects on a CW tone. On using appropriate constants one can write

$$\phi(f_u) = \frac{2\Pi f_u L}{C} - 40.5 \times \frac{2\Pi}{f_u C} \int_0^L N \, d\ell$$

$$= \frac{2\Pi f_u L}{C} - \frac{K_u}{f_u} \qquad (3.6\text{-}42)$$

Since one is interested in knowing the phase shift at f_D, a reasonable estimate of the phase can be obtained by multiplying $\phi(f_u)$ by f_D/f_u (this estimate becomes increasingly accurate as $f_u \rightarrow f_D$). Thus,

$$\tilde{\phi}(f_D) = f_D/f_u \times \phi(f_u)$$

$$= \frac{2\Pi f_D L}{C} - \frac{K_u}{f_u^2} \cdot f_D \qquad (3.6\text{-}43)$$

On conjugating this phase, one obtains

3-135

$$\tilde{\phi}*(f_D) = - \frac{2\Pi \, f_D \, L}{C} + K_u \, \frac{f_D}{f_u^2} \tag{3.6-44}$$

The downlink signal at the transmitting end can be written as

$$S_{down}^T (t) = \cos \left[\omega_D t + 2\Pi \, f_D \, \frac{L}{C} - K_u \, \frac{f_D}{f_u^2} \right] \tag{3.6-45}$$

The downlink signal at the receiving end is given by

$$S_{down}^R (t) = \cos \left[\omega_D t + 2\Pi \, f_D \, (\frac{L}{C} - \frac{L}{C}) - K_u \, \frac{f_D}{f_u^2} + \frac{K_D}{f_D} \right]$$

$$= \cos \left[\omega_D t - (K_u \, \frac{f_D}{f_u^2} - \frac{K_D}{f_D}) \right] \tag{3.6-46}$$

For a temporally stable ionosphere, one can set $K_u = K_D$ in Equation 3.6-46)
and obtain

$$S_{down}^R (t) = \cos \left[\omega_D t - K_u \, (\frac{f_D}{f_u^2} - \frac{1}{f_D}) \right] \tag{3.6-47}$$

If, in addition, the propagation medium is assumed non-dispersive, then the
second term on the right hand side of Equation (3.6-47) involving K_u could be
equated to zero. In the present situation, this kind of assumption is highly
unrealistic. Note in Equation (3.6-47), K_u applies to a particular radio path
and will, in general, be different on different paths because of ionospheric
inhomogeneity. A consequence of this fact is that the phase coherence (at
source) property of the downlink signal mentioned earlier does no longer hold
good. Furthermore, if a coherent phase perturbation occurs due to some
ionospheric large-scale features (such as a wedge), then even a beam pointing
error is possible. The magnitude of these effects need to be evaluated for
worst-case ionospheric conditions. The two tone pilot beam system which aims
at alleviating some of the ionospheric problems mentioned above is discussed
next.

Two-Tone Pilot Beam System

This is the so-called baseline concept and rests on the fact that if two
tones (symmetrically situated around the downlink frequency) are used on the
uplink transmission, then under appropriate conditions an average of the
phases of the uplink tones can be taken to be a good estimate of the phase
at the downlink frequency. The idea here is that the phase errors caused by
a stationary ionosphere can be largely eliminated by this approach. Let f_1
and f_2 be the two tones constituting the pilot beam and symmetrically located
around the downlink frequency f_D as shown in Figure 3.6-21. The choice of
Δf is based on conflicting requirements and is not discussed here.
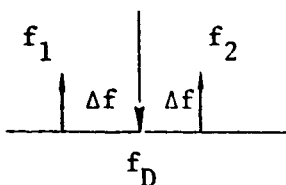
Figure 3.6-21. Sample Relationship Diagram

Using the notation as before, for a given link one can write

$$\phi_1 = \phi(f_1)$$

$$= 2\Pi f_1 \frac{L}{C} - \frac{40.5}{f} \times \frac{2\Pi}{C} \int_0^L N \, d\ell \tag{3.6-48}$$

and

$$\phi_2 = 2\Pi f_2 \frac{L}{C} - \frac{40.5}{f} \times \frac{2\Pi}{C} \int_0^L N \, d\ell \tag{3.6-49}$$

On taking the average of ϕ_1 and ϕ_2 one obtains

$$\bar{\phi} = \frac{\phi_1 + \phi_2}{2}$$

$$= 2\Pi \frac{L}{C} \left(\frac{f_1 + f_2}{2}\right) - \frac{40.5}{2} \times \frac{2\Pi}{C} \int N \, d\ell \left(\frac{1}{f_1} + \frac{1}{f_2}\right)$$

$$= 2\Pi \frac{L}{C} f_D \quad \frac{40.5}{2} \cdots \frac{2\Pi}{C} \int N \, d\ell \left(\frac{f_1 + f_2}{f_1 \, f_2}\right)$$

$$= 2\Pi \frac{L}{C} f_D - \frac{40.5}{2} \times \frac{2\Pi}{C} \int N \, d\ell \cdot \frac{2 \, f_D}{f_D{}^2 - \Delta^2 f} \tag{3.6-50}$$

If $\left|\frac{\Delta f}{f_D}\right| \ll 1$, then the above expression for $\bar{\phi}$ simplifies as below

$$\bar{\phi} \doteq 2\Pi \frac{L}{C} f_D - \frac{40.5}{f_D} \times \frac{2\Pi}{C} \int_0^L N \, d\ell$$

$$= \phi(f_D) \tag{3.6-51}$$

Note $\bar{\phi}$ is a desirable quantity as far as correct retrodirective array operation is concerned. Assuming that there are no serious errors involved in obtaining $\bar{\phi}$, all one needs to do is to conjugate this quantity and use it as the phase of the downlink signal leaving the space antenna. However, the

arithmetic averaging indicated in Equation (3.6-50) can, under certain conditions, provide **wrong** answers for $\bar{\phi}$ [called ambiguities in (Reference 30)] and this is the topic for the next section.

Computation of $\bar{\phi}$ and Phase Ambiguity

As shown in the preceding section, if $\bar{\phi}$ could be computed without errors or ambiguities, then it closely approximates $\phi(f_D)$ and one could get rid of systematic phase errors (biases) introduced in the power beam due to ionospheric dispersion and inhomogeneity (see *Ionospheric Effects on Single-Tone Pilot Beam* section).

In this section, it is shown that computation of $\bar{\phi}$ involves incoherent phase processing; e.g., frequency division and, in certain cases, this can cause trouble. Let the received phases corresponding to the two tones of the pilot beam (of a given subarray of the space antenna) be given by

$$\psi_1(t) = \omega_1 t - \phi_1$$

$$= \omega_1 \left(t - \frac{L}{C} \right) + \frac{40.5 \times 2}{f_1 C} \int_0^L N \, d\ell \qquad (3.6-52)$$

and

$$\psi_2(t) = \omega_2 t - \phi_2$$

$$= \omega_2 \left(t - \frac{L}{C} \right) + \frac{40.5 \times 2}{f_2 C} \int_0^L N \, d\ell \qquad (3.6-53)$$

where ϕ_1 and ϕ_2 are given by Equations (3.6-48) and (3.6-49), respectively. Define

$$\bar{\psi}(t) = \frac{\psi_1(t) + \psi_2(t)}{2}$$

$$= \omega_D t - \bar{\phi} \qquad (3.6-54)$$

where $\bar{\phi}$ is given by Equation (3.6-51). Note $\bar{\phi}$ is only path dependent. In order to obtain $\bar{\psi}(t)$, the kind of signal processing shown in Figure 3.6-22 seems logical.
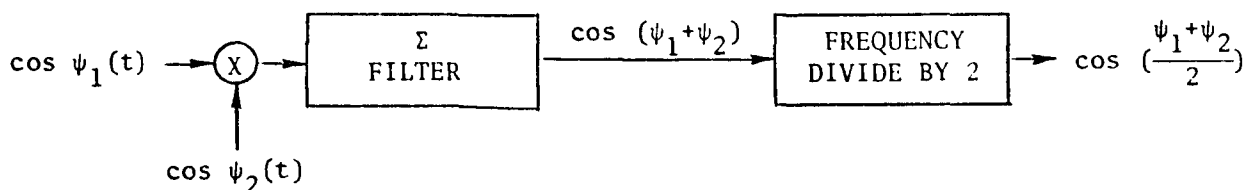
Figure 3.6-22. Signal Processing Diagram

Let the phases corresponding to the two pilot frequencies f_1 and f_2 be as shown in Figure 3.6-23.
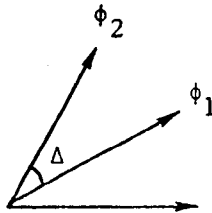
Figure 3.6-23. Phase Relationship Diagram

Let

$$\phi_2 - \phi_1 = K \, (2\Pi) + \Delta \tag{3.6-55}$$

where

$$|\Delta| < 2\Pi \text{ and } K = 0, 1, 2, 3, \ldots \ldots$$

From Equation (3.6-55), one writes

$$\overline{\phi} = \frac{\phi_1 + \phi_2}{2}$$

$$= \phi_1 + K\Pi + \frac{\Delta}{2} \tag{3.6-56}$$

In performing the operations shown in Figure 3.6-22, the $K\Pi$ term in Equation (3.6-56) could get lost. For K even, no damage is done when this happens. For K odd, a Π error occurs and one would conjugate the wrong phase. The important point then is to keep track of $K\Pi$ during averaging at every subarray or avoid averaging altogether. One approach is to use a system of synchronous dividers which is fairly complicated. Another approach is due to Boeing where a 2-tone pilot beam is used but phase processing is done at an intermediate frequency and frequency division is avoided (Reference 31). This method seems to ignore possible phase variations across the aperture due to a steady-state ionosphere. Raytheon solves the ambiguity problem by using a 3-tone method (Reference 30). The technique utilizes two pulse-modulated tones and a CW tone. By measuring the differential group delay between two pulsed signals, the ionospheric electron content $\int N \, d\ell$ on desired radio links is computed and this information is used to find the correct phases for the downlink signals. In this note, a method based on three CW tones is used (Reference 32).

Solution of the Phase Ambiguity Problem

Before proceeding with the main task of solving the phase ambiguity problem, it is worthwhile to examine Equation (3.6-55) in some detail and find out whether ϕ_1 and ϕ_2 could indeed differ by integral multiples of 2Π when typical SPS parameters are used. For the present problem, it is sufficient to show that ionospheric effects alone can give rise to phase differences

which are multiples of 2Π. A measure of this effect is obtained by multiplying ϕ_1 [Equation (3.6-46)] by f_2/f_1 and subtracting ϕ_2 [Equation (3.6-47)]. Thus

$$\Delta\phi = \frac{f_2}{f_1} \phi_1 - \phi_2$$

$$= 2\Pi \times \left\{\frac{40.5}{C} \times \int_0^L N \, d\ell \times \left[\frac{1}{f_2} - \frac{f_2}{f_1^2}\right]\right\} \qquad (3.6-57)$$

Let

$$f_D = 2.45 \times 10^9 \qquad (3.6-58a)$$

and

$$\begin{cases} f_1 = f_D - \Delta f \qquad (3.6-58b) \\ f_2 = f_D + \Delta f \qquad (3.6-58c) \end{cases}$$

then, the number of 2Π phase changes obtained for different values of $N \, d\ell$ and Δf is shown in Table 3.6-12.

Table 3.6-12. Number of Ambiguities
(η) versus Δf

Δf MHz	f_1 GHz	f_2 GHz	10^{19} el/m^2 η	10^{18} el/m^2 η	$\int N \, d\ell$
100	2.350	2.550	92	9.2	← Baseline
50	2.400	2.500	45	4.5	
10	2.440	2.460	8.9	0.89	
5	2.445	2.455	4.4	0.44	
1	2.449	2.451	0.9	0.09	

It is clear from Table 3.6-12 that in order to avoid ionospheric ambiguity for the strongest concentration under consideration, Δf should not exceed 1 MHz. Other operational constraints render such a choice unacceptable.

In what follows, a 3-tone approach due to Burns and Fremouw (Reference 38) is used to resolve the ambiguity problem. It is based on a direct measurement of $\int N \, d\ell$ along the paths of interest and then using this information to estimate the path related phase shift at the downlink frequency f_D.

Consider a frequency-amplitude pattern as shown in Figure 3.6-24 where the three uplink tones f_1, f_2 and f_3 are coherent at ground. Indeed, the three tones can be generated by a low-deviation phase-modulated transmitter.

Thus, using equations similar to Equation (3.6-46) for three frequencies f_1, f_2 and f_3, one can write

$$\delta\phi_A = \phi_2 - \phi_1$$

$$= \frac{2\Pi}{C}\left\{(f_2 - f_1)\ L - 40.5 \times \int N\ d\ell \times (\frac{1}{f_2} - \frac{1}{f_1})\right\} \qquad (3.6-59)$$

and

$$\delta\phi_B = \phi_1 - \phi_3$$

$$= \frac{2\Pi}{C}\left\{(f_1 - f_3)\ L - 40.5 \times \int N\ d\ell \times (\frac{1}{f_1} - \frac{1}{f_3})\right\} \qquad (3.6-60)$$

The second difference of phase shift is given by

$$\delta_2\phi = \delta\phi_A - \delta\phi_B$$

$$= \frac{2\Pi}{C} \times 40.5 \times \int N\ d\ell \times \left[\frac{2}{f_1} - \frac{1}{f_3} - \frac{1}{f_2}\right] \qquad (3.6-61)$$
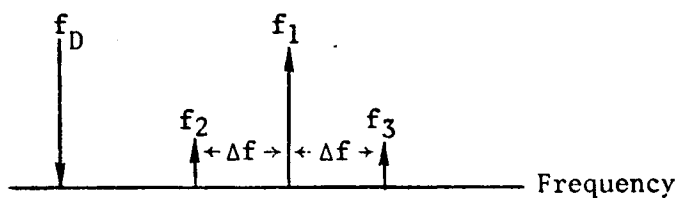
Figure 3.6-24. Frequency-Amplitude Pattern

For suitably chosen Δf, one obtains

$$\delta_2\phi \doteq \frac{2\Pi}{C} \times 40.5 \times \int N\ d\ell \times \frac{2\ \Delta f^2}{f_1{}^3} \qquad (3.6-62)$$

Suppose one needs to avoid a 360° ambiguity in $\delta_2\phi$ for values of $\int N\ d\ell$ less than 10^{19}. From Equation (3.6-62), one easily finds

$$\Delta f^2 \doteq -\delta_2\phi \times f_1{}^3 / (\frac{2\Pi}{C} \times 40.5 \times 2 \times \int N\ d\ell) \qquad (3.6-63)$$

Let

$$f\ = 2.45 + 0.153125 \text{ (this choice will be justified later)}$$

$$= 2.603125 \text{ GHz} \qquad (3.6-64)$$

Then

$$\Delta f^2 \doteq (2\Pi) \times (2.6 \times 10^9)^3 \times C/(2\Pi \times 81 \times 10^{19})$$

$$= \frac{(2.6 \times 10^9)^3 \times 3 \times 10^8}{81 \times 10^{19}}$$

$$= \frac{17.6 \times 3 \times 10^{35}}{81 \times 10^{19}}$$

$$= 0.651 \times 10^{16}$$

or

$$\Delta f \doteq 80.6 \text{ MHz} \qquad\qquad (3.6\text{-}65)$$

Thus, with $\Delta f \leq 80.6$ MHz and assuming that $\delta_2\phi$ can be measured, then $\int N \, d\ell$ can be calculated rather easily from Equation (3.6-62). An implementation that measures $\delta_2\phi$ with relative ease is shown in Figure 3.6-25.
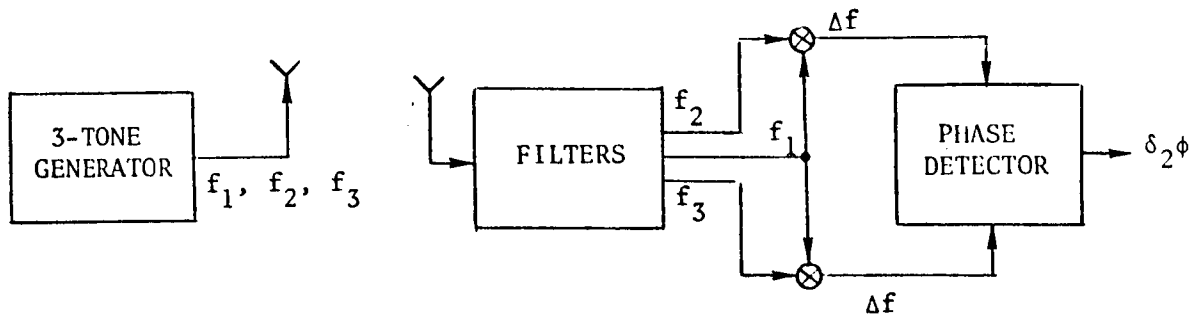
Figure 3.6-25. Measurement of $\delta_2\phi$

Reordering Equation (3.6-62), one easily obtains

$$\hat{N} = \text{computed value of } \int N \, d\ell$$

$$= \frac{f_1^3}{2 \, \Delta f^2} \times \frac{C}{2\Pi} \times \frac{1}{40.5} \times (-\delta_2\phi)_{\text{measured}}$$

$$= \alpha \cdot (-\delta_2\phi)_{\text{measured}} \qquad\qquad (3.6\text{-}66)$$

For $f_1 = 2.603$ GHz and $\Delta f = 80.0$ MHz, one can compute

$$\alpha = 1.6 \times 10^{18} \qquad\qquad (3.6\text{-}67)$$

Based on S/N ratio considerations, the accuracy of the $\hat{N}$ computation in Equation (3.6-66) is determined by the accuracy of $\delta_2\phi$ measurement and is given by

$$\sigma_{\hat{N}} = \alpha \cdot \sigma_{\delta_2\phi} \qquad\qquad (3.6\text{-}68)$$

Once an estimate of $\hat{N}$ for a given link is found, one needs to perform several steps of signal processing starting with the phase at f_1 and finishing with the conjugated phase at f_D. These steps are outlined below.

STEP 1

From $\phi(f_1)$ [as in Equation 3.6-48)] subtract estimated ionosphere contribution

$$\phi'(f_1) = \phi(f_1) + \frac{40.5}{f_1} \times \frac{2\Pi}{C} \times \hat{N}$$

$$= \omega_1 \frac{L}{C} - \frac{40.5}{f_1} \times \frac{2\Pi}{C} (\textstyle\int N \, d\ell - \hat{N}) \qquad (3.6\text{-}69)$$

STEP 2

Perform frequency transformation on $\phi'(f_1)$

$$\phi'(f_D) = \phi'(f_1) \times \frac{f_D}{f_1}$$

$$= \omega_D \frac{L}{C} - \frac{f_D}{f_1^2} \times 40.5 \times \frac{2\Pi}{C} \times (\textstyle\int N \, d\ell - \hat{N}) \qquad (3.6\text{-}70)$$

STEP 3

Conjugate $\phi'(f_D)$

$$\overset{*}{\phi}{}'(f_D) = - \phi'(f_D) \qquad (3.6\text{-}71)$$

STEP 4

Add ionosphere contribution to $\overset{*}{\phi}{}'(f_D)$

$$\overset{*}{\phi}(f_D) = \overset{*}{\phi}{}'(f_D) + \frac{40.5}{f_D} \times \frac{2\Pi}{C} \times \hat{N}$$

$$= - \phi'(f_D) + \frac{40.5}{f_D} \times \frac{2\Pi}{C} \times \hat{N}$$

$$= - \omega_D \frac{L}{C} + \frac{40.5}{C} \times \frac{2\Pi}{f_D} \, [\frac{f_D^2}{f_1^2} (\textstyle\int N \, d\ell - \hat{N}) + \hat{N})] \qquad (3.6\text{-}72)$$

STEP 5

Use $\overset{*}{\phi}(f_D)$ as the subarray transmit phase

All the signal processing indicated above that yields conjugated phase as the end product can be accomplished by suitably modifying the conjugator shown

in Figure 3.6-20. The new conjugator which takes into account steady-state ionospheric effects is shown in Figure 3.6-26.
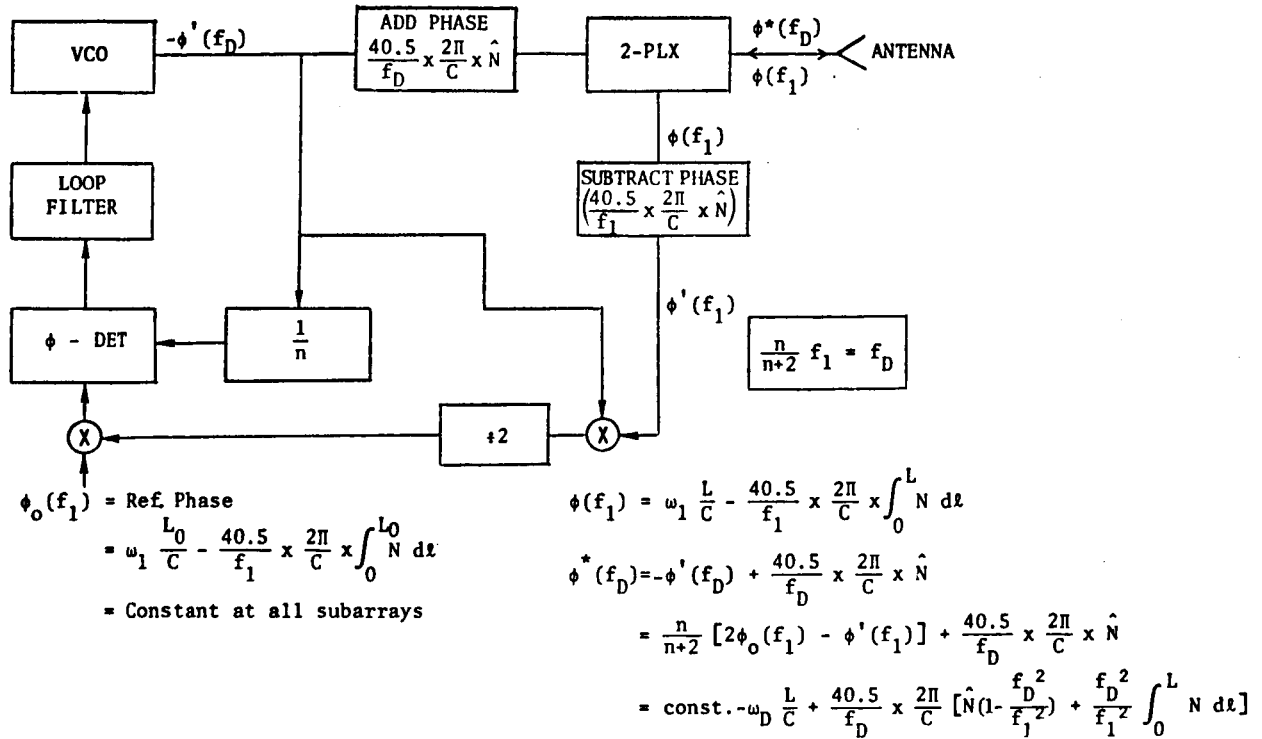
Figure 3.6-26. Modified Conjugator

Note that except for a constant term, the output $\phi*(f_D)$ of the conjugator is identical to Equation (3.6-72). For the present configuration, the uplink and downlink frequencies are related by the equation

$$\frac{n}{n+2} \cdot f_1 = f_D$$

or

$$f_1 = \frac{n+2}{n} f_D \qquad\qquad (3.6\text{-}73)$$

For f_D = 2.45 GHz and n = 32, one obtains

$$f_1 = 2.603125 \text{ GHz [see Equation 3.6-64)]}$$

Performance Analysis of the 3-Tone System

In this section, a performance analysis of the 3-tone ambiguity resolution system is provided based on S/N ratio considerations. The analysis applies to a steady-state (or slowly-varying) ionosphere. Basically, the problem is that even though $\int N \, d\ell$ is constant on a given link, an estimation of this quantity (i.e., $\hat{N}$) involves $\delta_2\phi$ measurement in a thermal noise environment. Therefore,

the rms accuracy of $\hat{N}$ is a function of available S/N ratio at the receiver under consideration. Any deviations of $\hat{N}$ show up as phase jitter on the sub-array transmitted phase $\phi*(f_D)$. Since the phase jitters at different subarrays can be considered independent, these contribute to the (downlink) beam spread-ing and loss of efficiency. Clearly, one needs to bound the amount of tolerable phase jitter at any subarray.

In order to proceed with the analysis, it is convenient to recall the measurement set up in Figure 3.6-25. The filtering operations are shown in little more detail in Figure 3.6-27.
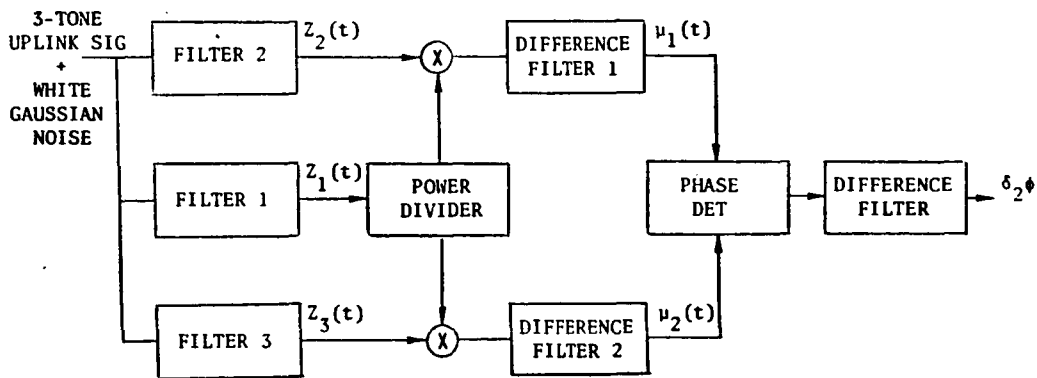
Figure 3.6-27. Filter Operations Diagram

The three CW tones and additive White Gaussian Noise $\eta(t)$ are filtered by ideal bandpass filters of (narrow) bandwidth B. The bandwidth B is, essentially, determined by the stability of the pilot beam transmitter and doppler effects. The passbands of the filters are non-overlapping. The three filter outputs are given by

$$Z_1(t) = A_1 \cos(\omega_1 t - \phi_1) + \eta_1(t)$$

$$= V_1(t) \cos[\omega_1 t - \theta_1(t)] \qquad (3.6-74)$$

$$Z(t) = A_2 \cos(\omega_2 t = \phi_2) + \eta_2(t)$$

$$= V_2(t) \cos[\omega_2 t - \phi_2(t)] \qquad (3.6-75)$$

and

$$Z(t) = A_3 \cos(\omega_3 t - \phi_3) + \eta_3(t)$$

$$= V_3(t) \cos[\omega_3 t - \phi_3(t)] \qquad (3.6-76)$$

where η_1, η_2 and η_3 are zero-mean, Gaussian noise variables such that

$$E \eta_1^2 = E \eta_2^2 = E \eta_3^2 = \sigma^2$$

$$= N_o B \qquad (3.6-77)$$

and Equations (3.6-74), (3.6-75) and (3.6-76) are typical representations of the sinewave signal plus narrowband noise situation. Furthermore, ϕ_1, ϕ_2 and ϕ_3 are the phases associated with the three tones (includes ionospheric effects). Note: for any t, one has

$$E\ \theta_K(t) = \phi_K; \quad K = 1, 2, 3 \tag{3.6-78}$$

Letting

$$\psi_K(t) = \theta_K(t) - \phi_K; \quad K = 1, 2, 3 \tag{3.6-79}$$

the probability density function of $\psi_K(t)$ is given by the expression (Reference 33)

$$\tag{3.6-80}$$

$$P(\psi_K) = \frac{e^{-(S/N)_K}}{2\Pi} + \sqrt{\left(\frac{S}{N}\right)_K}\ \cos\ \psi_K\ \frac{e^{-\sin^2\psi_K(S/N)_K}}{2\sqrt{\Pi}}\ \left(1 + 2\ \mathrm{erf}\ [\sqrt{2(S/N)_K}\ )\cos\ \psi_K]\right)$$

where

$$\left(\frac{S}{N}\right)_K = \frac{A_K{}^2}{2\sigma^2} \tag{3.6-81}$$

and

$$\mathrm{erf}\ x = \frac{1}{\sqrt{2\Pi}} \int_0^x e^{-y^2/2}\ dy \tag{3.6-82}$$

Now, the outputs of the two difference filters are given by the following expressions

$$\mu_1(t) = \frac{V_1(t)\ V_2(t)}{2\ \sqrt{2}}\ \cos\ [(\omega_1 - \omega_2)t - \phi_1(t) + \phi_2(t)] \tag{3.6-83}$$

and

$$\mu_2(t) = \frac{V_1(t)\ V_3(t)}{2\ \sqrt{2}}\ \cos\ [(\omega_1 - \omega_3)t - \theta_1(t) + \theta_3(t)] \tag{3.6-84}$$

Assuming that the phase detector responds only to the phase difference between the input signals and remembering the fact that $\omega_1 - \omega_2 = \omega_3 - \omega_1$, one easily obtains

$$\delta_2\phi(t) = \theta_2(t) + \theta_3(t) - 2\ \theta_1(t) \tag{3.6-85}$$

3-146

Since the filters are operating on white Gaussian noise and have disjoint passbands, the random variables θ_1, θ_2 and θ_3 are independent (Reference 34) (this conclusion is based on a representation of the white noise process in terms of a countable orthonormal set of basis functions; e.g.,

$$\eta(t) = \sum_K [x_k(t) \cos \omega_K t + y_K(t) \sin \omega_K t] \tag{3.6-86}$$

and one can write

$$\text{Var } \delta_2\phi = \text{Var } \theta_2 + \text{Var } \theta_3 + 4 \text{ Var } \theta_1 \tag{3.6-87}$$

In order to compute the variances on the right hand side of Equation (3.6-85), one needs to use the Equations (3.6-78), (3.6-79), and (3.6-80). In the present situation, main interest lies in the high (S/N) ratio case and an appropriate expression for Equation (3.6-85) is the following (also examine Figure 3.6-28 for high SNR).

$$\text{Var } \delta_2\phi \simeq \frac{1}{2} \left(\frac{\sigma^2}{(A_2{}^2/2} + \frac{\sigma^2}{(A_3{}^2/2)} + \frac{4 \sigma^2}{(A_1{}^2/2)} \right)$$

$$= \frac{\sigma^2}{A_2{}^2} + \frac{\sigma^2}{A_3{}^2} + \frac{4 \sigma^2}{A_1{}^2} \tag{3.6-88}$$
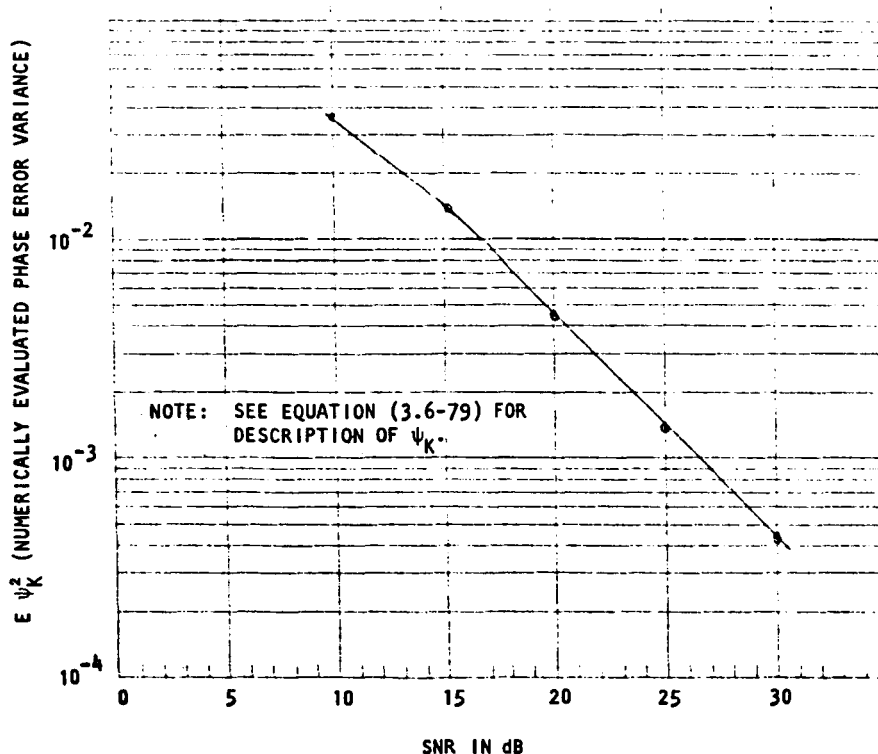
Figure 3.6-28. Phase Error Variances

Assume that the total pilot transmitter power P_T is split between the carrier and two (equal) sidebands in the ratio α, $(1 - \alpha)/2$ and $(1 - \alpha)/2$ where $\alpha < 1$. If P_R is the total pilot signal power received at the subarray under consideration, then

$$P = A_1^2/2$$

$$= \alpha \, P_R \tag{3.6-89a}$$

and

$$P_\ell = \frac{A_\ell^2}{2}; \quad \ell = 2, \, 3$$

$$= \frac{(1 - \alpha)}{2} \, P_R \tag{3.6-89b}$$

For a given transmitted power P_T (and received power P_R) it is possible to choose α such that Var $\delta_2\phi$ in Equation (3.6-88) is a minimum. On using Equation (3.6-89) in Equation (3.6-88), one obtains

$$\text{Var } \delta_2\phi = \frac{\sigma^2}{(1-\alpha) \, P_R} + \frac{\sigma^2}{(1-\alpha) \, P_R} + \frac{4 \, \sigma^2}{2\alpha \, P_R} \tag{3.6-90}$$

On differentiating Equation (3.6-90) with respect to α and equating to zero, one finds

$$\frac{2}{(1-\alpha)^2} - \frac{2}{\alpha^2} = 0$$

or

$$\alpha^2 - (1 - 2\alpha + \alpha^2) = 0$$

or

$$\alpha = 0.5 \tag{3.6-91}$$

With the optimum choice of $\alpha = 0.5$, the variance expression in Equation (3.6-90) reduces to

$$(\text{Var } \delta_2\phi)_{opt} = \frac{8 \, \sigma^2}{P_R} \tag{3.6-92}$$

In order to make some sense out of all these deviations, one needs to go back to Equation (3.6-72). On taking differentials, one obtains

$$\Delta\phi^*(f_D) \simeq \frac{40.5}{f_D} \times \frac{2\Pi}{C} (1 - f_D^2/f_1^2) \, \Delta\hat{N} \tag{3.6-93}$$

On using $f_D = 2.45$ GHz and $f_1 = 2.603$ GHz, the above equation simplifies to

$$\Delta\phi*(f_D) \simeq 3.95 \times 10^{-17} \Delta\hat{N} \tag{3.6-94}$$

so that

$$\Delta\hat{N} = 2.53 \times 10^{16} \times \Delta\phi*(f_D) \tag{3.6-95}$$

Suppose one requires an rms accuracy of $10°$ (= .174 rad) on $\phi*(f_D)$. Then, the required accuracy on $\hat{N}$ is given by

$$\sigma_{\hat{N}} = 2.53 \times 10^{16} \times .174$$

$$= 4.41 \times 10^{15} \tag{3.6-96}$$

On going back to Equation (3.6-68), one finds

$$\sigma_{\delta_2\phi} = \sigma_{\hat{N}}/\alpha, \quad \alpha = 1.6 \times 10^{18}$$

$$= 2.76 \times 10^{-3} \tag{3.6-97}$$

Squaring the quantity on the right hand side of Equation (3.6-97) and on using Equation (3.6-92), one obtains a value of P_R/σ^2. Thus,

$$P_R/\sigma^2 = \frac{8}{\text{var } (\delta_2\phi)_{opt}}$$

$$- \frac{8}{7.62 \times 10^{-6}}$$

$$= 1.05 \times 10^6; \text{ i.e., } 60 \text{ dB} \tag{3.6-98}$$

The above computation shows that the (S/N) requirements are fairly stringent if the object is to keep the ionosphere related (phase) conjugation errors small. The variation of rms accuracy on $\phi*(f_D)$ with P_R/σ^2 at the subarray receiver is shown in Figure 3.6-29.

Areas For Further Investigation

The following areas have been identified for further investigation:

• Statistical analysis related to ionospheric turbulence.

• The problem of ionosphere heating due to the downlink power beam and its effect on overall system operation.

• Performance analysis of the Raytheon solution for ambiguity resolution.

• Implication of changing divider ratio n in Chernoff conjugator.
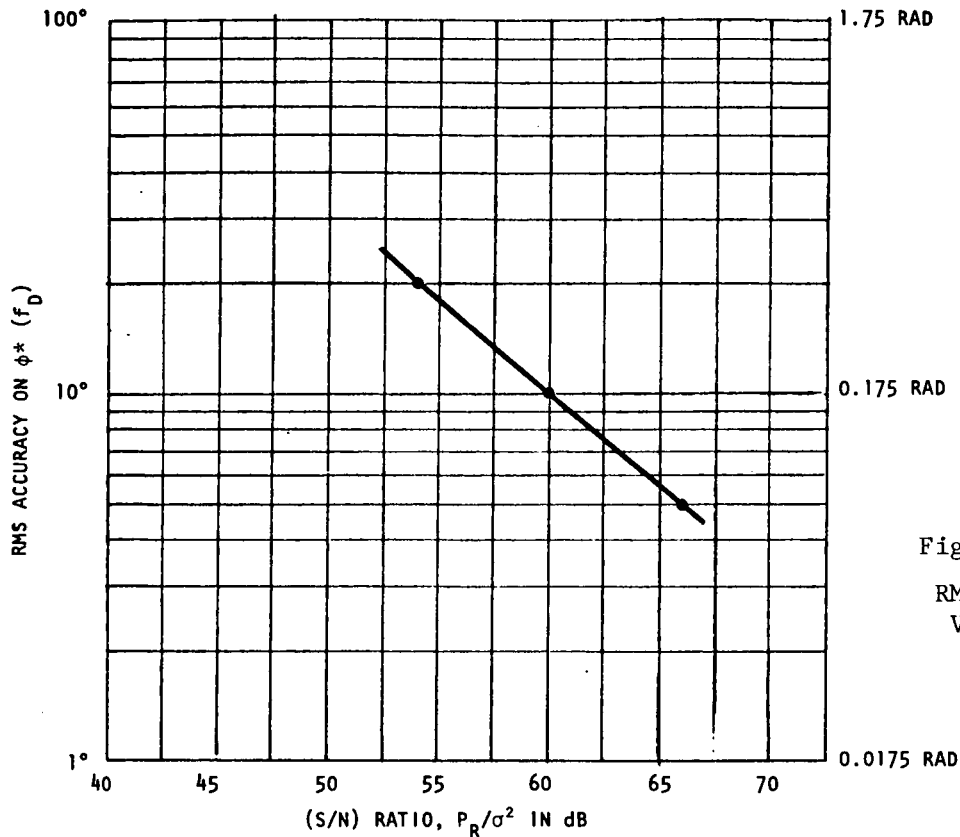
Figure 3.6-29.

RMS Accuracy Variations

- Possibility of spatial and temporal filtering to reduce ionospheric effects.

- Effects of changing the frequencies of pilot tones and their spacing.

- Practical implementation of Figure 3.6-26. How to introduce the ionosphere related phase compensation?

- Waveform definition and coding considerations in a multi-satellite environment.

A telephone conversation was initiated to find out whether Dr. Chernoff and his colleagues at JPL were aware of the existence of a second mode of operation of the conjugator described in Figure 3.6-20. He said that he was unaware of this fact and over a period of about three years of conjugator work no one seemed to recognize this dual-mode problem. All the hardware they built, performed in accordance with their equations and so there was no problem. He agreed, however, that the second mode was perfectly legitimate but did not appear in their conjugator because of the limited tuning range of the VCO that they used. As the conversation proceeded, he pointed out two important limitations of the present conjugator as far as direct S-band operation is concerned. One is the problem of divider ambiguity that was not mentioned in Reference 28. This necessitates conjugation at IF followed by frequency multiplication before transmission. The second problem is related to the switching speeds of currently available digital devices and 2.5 GHz is too high. These remarks of Dr. Chernoff have direct bearing and suitable modifications have to be made.

3.6.4 SOLID-STATE MICROWAVE POWER TRANSMISSION SYSTEM

As a part of the overall space segment description of the microwave power
transmission system, the following items are discussed: associated phase con-
trol, beam pointing, signal distribution, and power amplifier elements. The
solid-state arrays (both end-mounted and sandwich concepts) are subdivided into
square subarrays of 5 m by 5 m each. This subarray size is sufficiently small
to keep the gain (efficiency) loss due to main beam wander within the subarray
pattern to less than 2% maximum. This implies an antenna attitude control
accuracy of ±6 minutes of arc, or a total swing of 12 minutes of arc, or 0.2°.
The attitude control of the satellite holds the configuration to ±3 arc minutes
or 0.05° error. If more linear deviations have to be allowed, the subarray size
might have to be reduced. However, the number of control circuits goes up
directly with the number of subarrays. As an example, going from a 10-m to a
5-m subarray increased the number of subarrays by four, i.e., from ~7000 to
28,000 for the end-mounted arrays, and minimally from ~15,000 to 60,000 for the
sandwich arrays. It is desirable, therefore, to keep the subarray size as
large as possible. The current baseline is 5×5 m, and all amplifiers within
that area are controlled together, i.e., they are fed in phase. A view from
the bottom of the solid-state array is illustrated in Figure 3.6-30. Power
dipoles are seen radiating downward in the "power beam" and a high-gain (in
this case, a yagi) pilot antenna receives a pilot beam coming from the ground.
The received pilot beam signal is then processed to direct the power beam. An
alternate pilot antenna is shown in the square insert symbolizing (not to scale)
a subarray—an array of dipoles. The pilot antennas are always orthogonally
polarized to the power dipoles to avoid interference from the power signal to
the pilot signal.
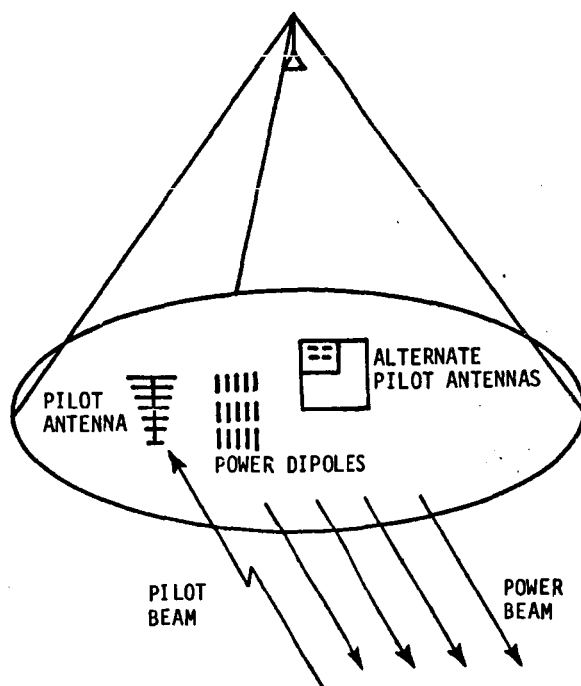
Figure 3.6-30. Spacetenna Total View (Bottom)

The pilot signal received by the antenna is amplified, filtered, and then processed in a phase conjugation circuit, which gets a phase reference signal from the rear of the array (see Figure 3.6-31). A reference signal transmitter is located somewhere near the center of the array, and sufficiently above to allow reception with a high-gain reference signal receiver antenna. An approximate range of reference transmitter heights is indicated also in Figure 3.6-31. One would like to mount the transmitter as low as possible, but gain variations at the receiving point are also of some concern. All circuits should be identical, to minimize fabrication costs. Again, the reference signal receiver antennas are normally polarized to the power dipoles, to avoid interference. A common feature in all solid-state approaches is an element spacing of 7.81 cm, which results in 16,384 elements per 10-m subarray, and 4096 per 5-m subarray.
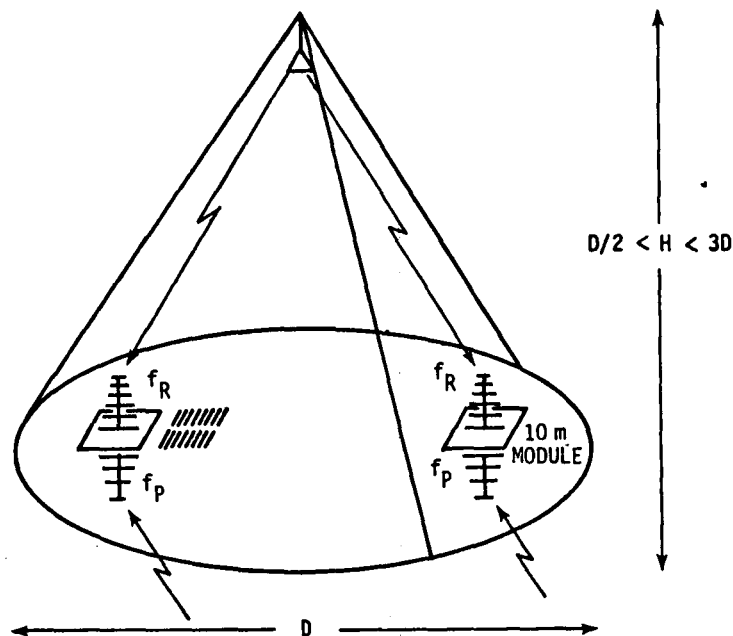
Figure 3.6-31. Spacetenna Total View (Top)

Phase Control System

While several systems characteristics are generic for a solid-state approach, one selected feature of the beam control system will henceforth be common to all Rockwell systems, and that is the way in which the reference phase signal is distributed over the spacetenna aperture.

Reference Phase Distribution

Figure 3.6-31 illustrated this method in a very general way, giving a perspective view of the top of a circular aperture. (An actual aperture will have steps in the boundary.) Two important features are illustrated: (1) the phase reference's signal originates from a single transmit location at the rear of the aperture, and (2) phase reference and pilot antennas are orthogonally polarized with respect to the power dipoles; this is necessary in order to avoid feedback loops. Also shown in Figure 3.6-30 is an alternate pilot

antenna layout using a broadside array of dipoles instead of an endfire (e.g.,
"cigar") array. Both configurations are not only possible but practical, and
shall be considered in more detail in future studies. The reference pickup
antenna can utilize an array as well.

The broadside array of antenna dipoles needs only be placed over approxi-
mately a 0.31×0.31-m portion within a 10-m×10-m subarray. (A logical place
for this portion will be shown later.) No constraints exist for such an array
for the reference phase pickup, except for the sandwich, when it has to be
integrated with or placed over the solar cells. For the end-mounted approach,
locations have to be found where the dc distribution system causes no interfer-
ence, but this should pose no problem. Details are given in Figure 3.6-32 to
explain how the phase reference signal is distributed.

SELF-CONTAINED
TRANSMITTER WITH
OWN SOLAR PANEL

SHAPED BEAM
ILLUMINATOR

$\theta_1 \leq 90$ DEGREES

f_{RO}

f_{R1} f_{R2}

$f_R = f_{R1}, f_{R2}$

(f_{RO})

$\Delta f_R \sim 100$ MHz

$\Delta \phi \approx 5$ DEGREES
(6-BIT QUANTIZATION)

~EQUAL AMPLITUDE,
~CONSTANT PHASE ILLUMINATION

$\Delta \ell \approx 6$ cm
$= 0.5 \lambda_q$
$\approx 180° @ f_0$

f_R PICK-UP ANTENNAS (~130,000)
(ONE PER 5-METER SUBARRAY)
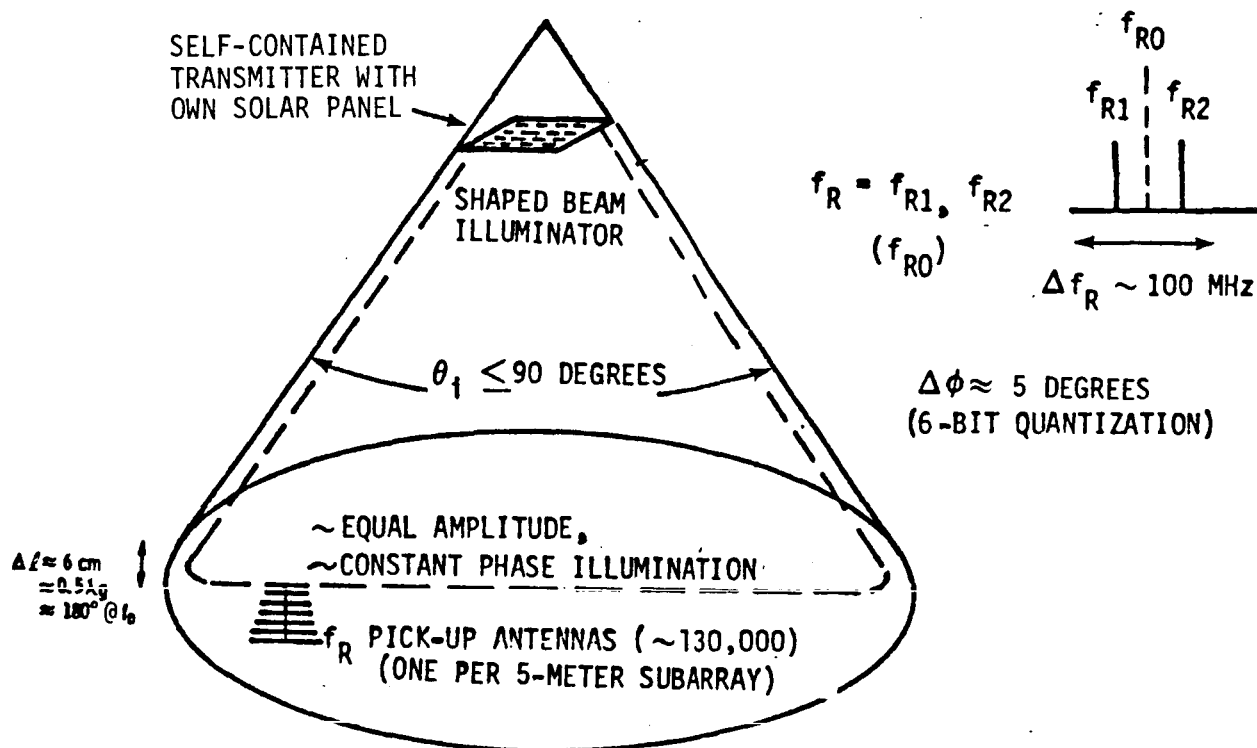
Note: Pick-up antenna orthogonally polarized with respect to power beam;
       total isolation $I_T \geq 40 + 60$ dB ≥ 100 dB

       Cross Pol.   Front-to-back ratio (can be made >100 dB)

Figure 3.6-32. Phase Reference Signal Distribution System

From the shaped-beam illuminator, antenna or RF signal is distributed over
a cone with maximally 90° beamwidth. The illuminator may be a corrugated,
phase-corrected horn or a synthetic-beam array using multiple weighted gener-
ating beams. The latter approach has the advantage of very tight control over
the amplitude function, so that all reference pickup antennas see the same
signal strength, and of very high reliability because a large number of dis-
tributed transmitters is used, with built-in redundancy, so that only the
local oscillators and drive amplifiers need to be made redundant. Current

plans call for a structural integrity of the array aperture to within ±20 cm
flatness. However, larger variations could be taken out modulo 2π, since
bandwidth is of no concern for the reference phase signal. The phase at each
subarray pickup point is normalized with respect to a perfectly flat uniform
aperture by means of a servo loop, shown in Figure 3.6-33. For each subarray
center location, a phase delay differential ("reference standard") is computed,
which occurs for the two generating frequencies, f_{R1} and f_{R2}, if the receiving
antenna is located on a perfect plane. These delays can be calculated and
tuned in the lab to fractions of a degree. The output of the phase bridge
then drives a phase shifter until the path delay differential equals that of
the reference standard. Whether or not the center frequency, f_{R0}, has to be
transmitted in addition to the two coherent tones, f_{R1} and f_{R2}, depends on L.O.
stability. Since this circuit is used at every subarray, the subarray center
points are electrically normalized to show $\phi = \phi_0$ constant across the entire
array. This provides the conjugation circuit with the required reference phase.
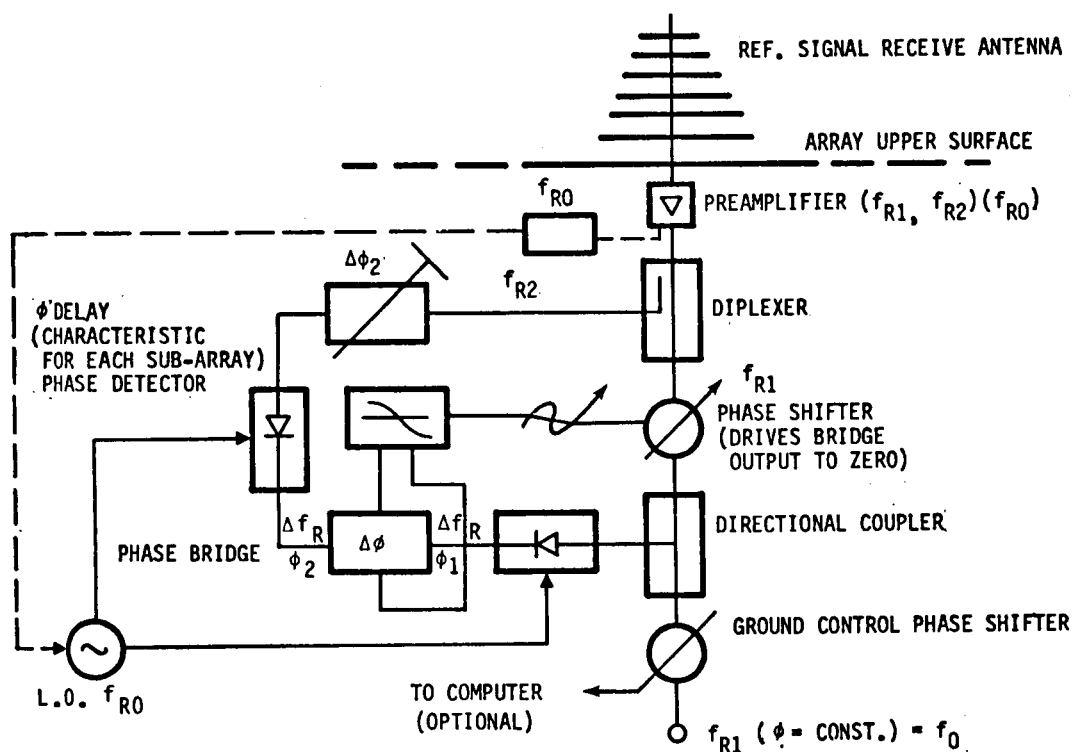
Figure 3.6-33. Reference Signal Control Loop

Retrodirective Beam Control

A simple retrodirective circuit is shown in Figure 3.6-34. Here, a pilot
frequency ω steers a beam at $\omega - \Delta\omega$ into a direction given by

$$\Delta\theta = \frac{-\Delta\omega}{\omega} \tan\theta_1.$$

3-154

The beam offset is small, but requires that the pilot transmitter antennas are located somewhere to the side of the rectenna. This may have advantages in addition to yielding a very simple on-board circuit. However, pilot beam disturbances may result in on-board compensation of the power beam phase which is not warranted, because the same conditions do not exist for the power beam, since different paths are involved.
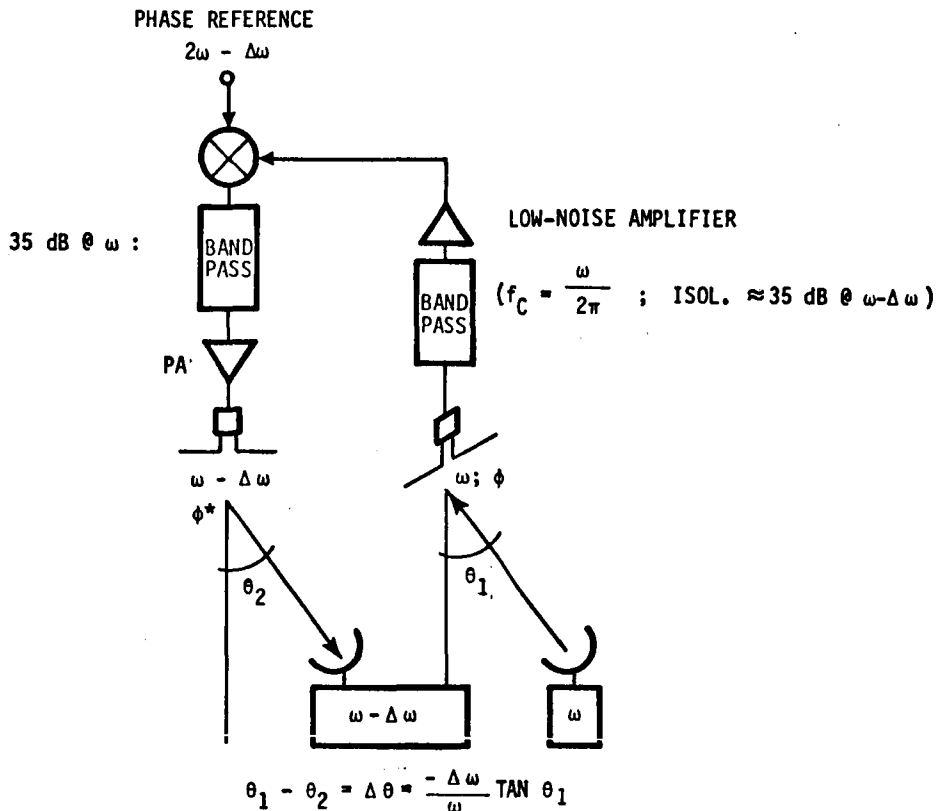
Figure 3.6-34. Simple Single-Tone Conjugator

A retrodirective control circuit which compensates for pilot-generated beam shifts (without ionospheric effects) is shown in Figure 3.6-35. This is a modified Chernoff circuit with additional isolation added by (1) separating the pilot and power frequency paths, (2) using orthogonally polarized radiating elements, and (3) providing the remaining isolation in separate bandpass filters. The total required filter isolation is 70 dB, according to pilot system calculations presented in Table 3.6-13.

Pilot System

This pilot system is predicated on 100-dBw pilot power on the ground. The proposed implementation of this pilot system consists of a circular array (one or more rings) of low- to medium-gain elements placed at the periphery of the rectenna, on top of utility poles if necessary, to avoid interference

SIMPLIFIED CONJUGATOR FOR DEMONSTRATION
(AFTER CHERNOFF)
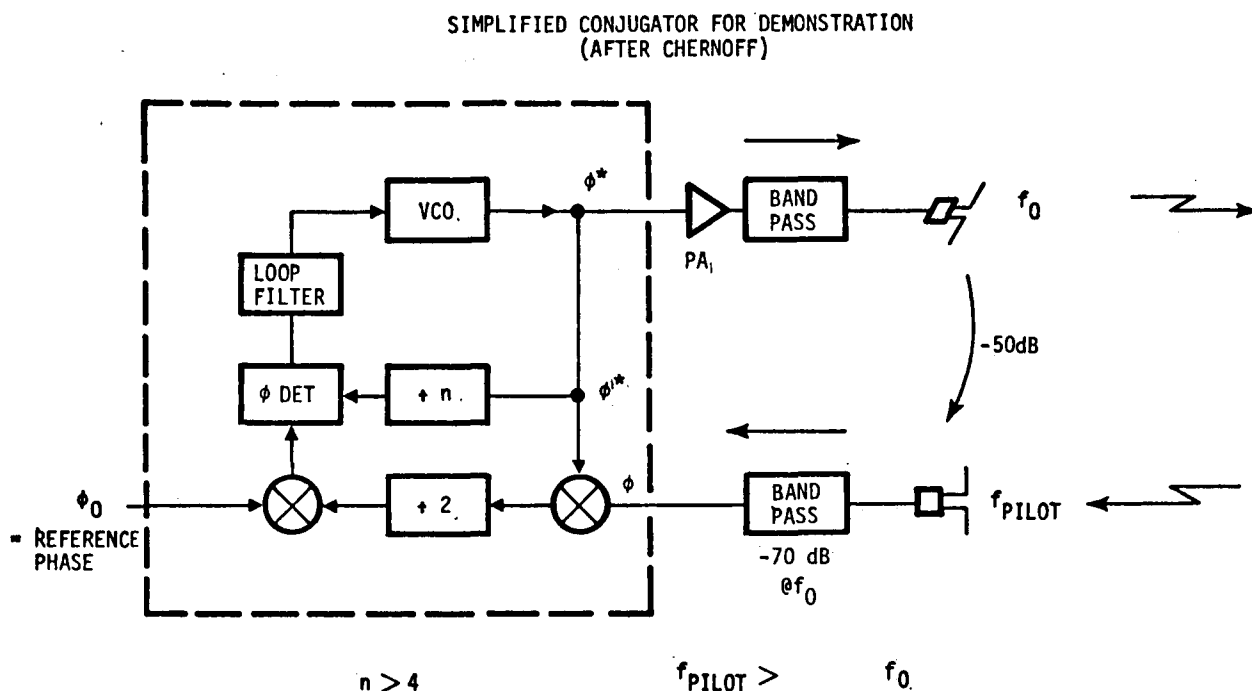
Figure 3.6-35. Single Pilot Circuit Diagram

Table 3.6-13. Pilot System Link Budget

PILOT SYSTEM	BUDGET	COMMENT
GOUND SIGNAL ERP	100 dBw	
SPACE LOSS	-192 dB	
POWER AT SPACETENNA	-92 dBw	
PILOT ANTENNA RECEIVE GAIN	18 dB	-74 dBw
ISOLATION TO POWER DIPOLE	20 dB	INCLUDES DIPOLE GAIN
POWER DIPOLE OUTPUT	-10 dBw	
CROSS-POLARIZ. ATTENUATION	30 dB	
PILOT-TO-POWER SIGNAL RATIO	-34 dB	
NOTCH FILTER ATTENUATION (RELATIVE TO TWO PILOT SIGNALS SYMMETRICAL TO CARRIER)	+80 dB	
NET PILOT SIGNAL-TO-POWER SIGNAL RATIO	+36 dB	
PILOT-TO-THERMAL NOISE RATIO (ASSUMING 3 dB NOISE FIGURE & 3 dB NOTCH FILTER LOSS)	∿37 dB	THERMAL NOISE ≈ -117 dBw for 500-MHz PILOT WIDTH

from the power collection and transmission system. The characteristics of this pilot transmit system are summarized as follows:

- Circular array of low-gain elements at 3.14-m ($\approx$25 λ) spacing; elements fed in phase

- 10,000 pilot array elements of 10-dB gain each

- Minimum 50-dB array gain

- 10-W solid-state transmitter at each element

- Phase distribution using fiber optics

- Beam steered to satellite location by time-delay compensation at each element

- Total ERP—100 dBw

The pilot array layout is compared with a dish in Figure 3.6-36. The system provides vastly improved reliability over a single-dish, concentrated amplifier pilot system, and also has such a wide beamwidth when the beam enters the ionosphere that certain ionospheric effects will be mitigated as discussed below. The on-board system uses the reference phase distribution (previously described), one of the conjugators (previously described), and a pilot receiver antenna of sufficient gain and isolation. Either high-gain endfire pilot antennas can be used, or broadside arrays of low-gain elements.

NO BEAM SYMMETRY   BEAM SYMMETRY
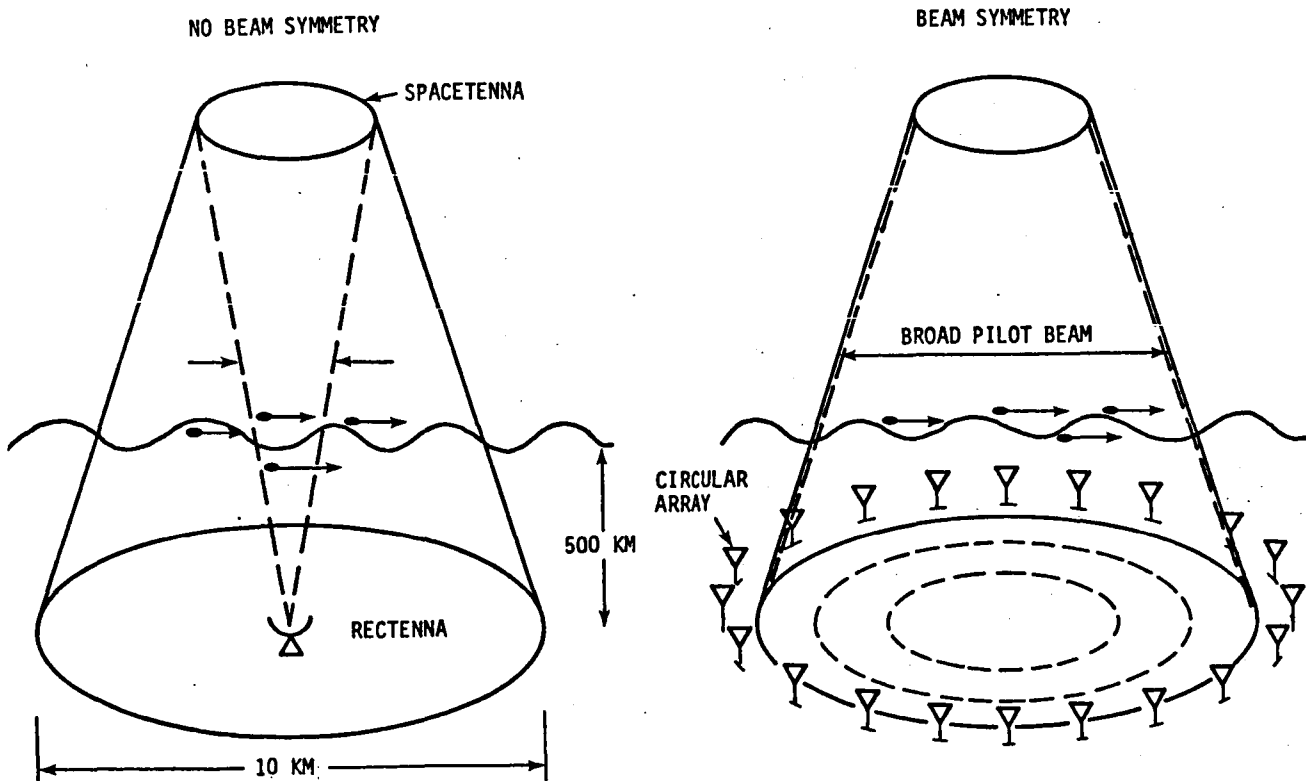
Figure 3.6-36. Pilot Beam Ground System Layout

Two solutions are possible for the broadside array—either the elements are interlaced with the power dipoles, which is possible because of the orthogonal polarization, but might still result in unacceptably high coupling to the power dipoles; or, alternatively, the 0.31×0.31-m portion is reserved for the pilot elements only, containing 16 dipoles. In the latter case, the required isolation is quite easy to achieve, but the 5-m×5-m subarray of power dipoles suffers a loss of

$$\frac{(16)^2}{4096} \approx 6.3\%$$

of transmitted energy. This is so because both the power and the gain associated with the transmit dipoles are lost. (If the lost power is redistributed to the remaining dipoles, so that only a gain loss occurs, the energy transmission loss is reduced to 0.39%, a more tolerable percentage. The power output per device has to be increased by ~6%, which is hardly noticeable.)

It must be noted that neither the exact design of the ground pilot array, nor that of the on-board pilot receive antenna, is available at this point. The final on-board system for the end-mounted concept will probably be a yagi (for simplicity), and the final sandwich pilot antenna will be an array, because installation of an endfire system in orbit may be difficult. Similarly, the layout of the ground array depends on special considerations, such as the nature and extent of fast-moving ionospheric disturbances. Nevertheless, whatever the final design may turn out to be, it should be bounded by the techniques outlined above, and no insurmountable difficulties exist in the development and construction of the ultimate configuration. Until this configuration has crystallized out, however, a lot more peripheral studies and investigations have to be conducted, or brought to a point of completion (such as the currently on-going ionospheric experiments), which allow fairly precise extrapolation of the available data so that the SPS pilot system design can be definitized.

Ground-Based Amplitude Sensors

A potential backup system for detecting and compensating slow (cycle time greater than 0.25 second) beam wander is shown in Figure 3.6-37. Three rings of sensors monitor the beam level close to the first null inside the rectenna capture area (one sensor ring) and outside the rectenna (two sensor rings). Alternately, several sensor rings (fairly wide spacings can be tolerated) are placed inside to monitor the slope of the beam. In either case, beam shift information is derived from any unbalance in the sensor outputs, and can be used to set on-board phase shifters (see reference phase servo loop), so as to drive the beam back into the center of the rectenna. This system will work even in the absence of a pilot, provided an on-board L.O. will be used. An alternate phase compensation system is summarized below.

- Three rings of amplitude sensors, one combined with pilot ring subarray

- Beam amplitude asymmetry recomputed into equivalent phase front (linear + quadratic) and spacetenna

- Phase bias shifters in pilot reference signal path (alternatively, in conjugated signal path) will be reset to compensate for slow beam wander

- System cycle time ≈one round trip delay, or ~0.25 sec

- Catastrophic shifts (can also be due to jamming, false pilots, lack of pilot) will be defined as level increases above 1 mW/cm^2 (or 5 mW/cm^2) and will trigger a complete shutdown until cause is determined.

THREE LINES OF
AMPLITUDE SENSORS
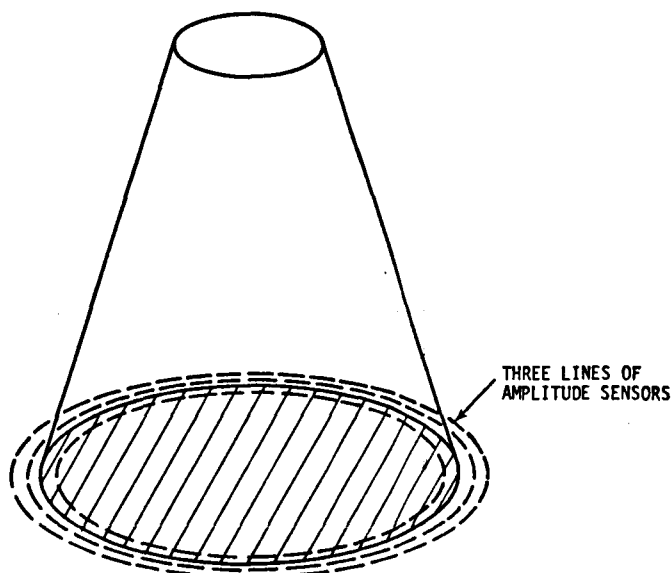
Figure 3.6-37.   Alternate Phase Compensation System

On-Board Monopulse Angle-Sensing Systems

Several sensing systems can be used instead of retrodirectivity—for example—an on board phase monopulse, using ~24-m portion of total array with on-board computation and phase shifters at distribution inputs; on-board amplitude monopulse; and on-board conical scan, averaging pilot direction over a number of scans.   (Note: This may be a good solution to eliminate short-term beam jitter.)

The monopulse system was previously recommended by Rockwell for the klystron "reference system."   It can be implemented either alone, or as part of multiple redundancy system to avoid catastrophic failure and subsequent shutdown.   Much more comparative analysis is required to determine relative merits, weights, cost, etc.

Alternate Aperture Correction System

Instead of or in addition to the RF phase reference system, laser surface sensors can be used.   A preliminary overview is given by the following:

- Dual 8-micron lasers scanning total array structure surface once a second to detect structural deformations and/or variations in reference signal transmitter location; calculation of required phase compensation (modulo 2 π)

• Neon/helium laser with wideband modulator; performing same
function as above

• Mirrors at each subarray center to enhance laser signal
return, and provide precise time reference for scanning
raster

• Other optical approaches: "staring system"

RF Signal Distribution System

Table 3.6-14 gives a summary of the current baseline distribution system
for the conjugated RF signal. This system is probably the same for both solid-
state concepts (end-mounted and sandwich), with only few alternatives remaining.
The reason is the excessive weight and loss of a continuous stripline feed sys-
tem, and the limited applicability of other distribution techniques, such as
space feeding. See Figures 3.6-38 through 3.6-41 for stripline calculations
(Reference 35).

Table 3.6-14. Basic Solid-State Reference
Distribution Concept (Subminiature Coax)

5-m by 5-m SUBARRAY, CONJUGATED, + GROUND CONTROL

ALL ELEMENTS WITHIN 5×5 SUBARRAY ARE IN PHASE

TRANSPORTATION MODULE SIZE: 5 m × 5 m

FIRST LEVEL RF SIGNAL DISTRIBUTION (FROM CONJUGATION NETWORK)
INTERCONNECTED IN SPACE CENTER OF 5-m BY 5-m MODULE

FIRST-LEVEL DISTRIBUTION (NON-ISOLATED) = "REAR" LAYER

SECOND, THIRD, AND FOURTH LEVELS = SECOND LAYER

FIFTH AND SIXTH LEVEL (ISOLATED) HYBRID DIVIDERS = THIRD LAYER

GROUND PLANE BETWEEN THIRD LAYER AND AMPLIFIERS/DIPOLES

ALL RF DISTRIBUTION LINES USE HIGH-TEMP. SUB-MIN. COAX

DC DISTRIBUTION IN BACK OF REAR RF DISTRIBUTION LAYER

ALL LEVELS CAN BE COMBINED IN A SINGLE LAYER OF ≈50-MIL
THICKNESS, IF THERMAL TRANSFER REQUIRES THIS

The principal (baseline) subarray layout for both solid-state concepts is
shown in Figure 3.6-42. The pilot submodule size (as discussed above) need
only be approximately 0.3×0.3 m, if an endfire element is not used. Also, the
pilot submodule array could be split into four dipoles each and located sym-
metrically around the subarray centerpoint. Interconnections can be made
together with all the other interconnections in space. (This mode will be
selected if compensation of the pilot array phase center shift poses any
problems.)

From the output of the conjugation box, a first-level distribution takes
place as shown in Figure 3.6-43. This assures equal phase distribution of the
signal down to the amplifiers.

The second, third, and fourth levels of distribution are illustrated in
Figures 3.6-44, and the fifth and sixth level in Figure 3.6-45. A summary of
all the system parameters is given in Table 3.6-15. The total element number
in each 5-m×5-m subarray is 4096, and there are this many isolated output
ports in the sixth distribution level.

3-160
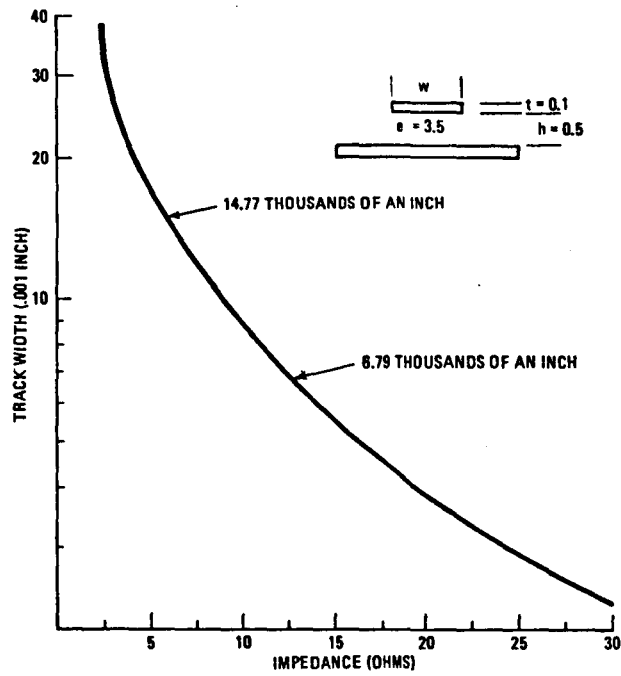
Figure 3.6-38. Microstrip (Kapton)—Line Width Vs. Impedance
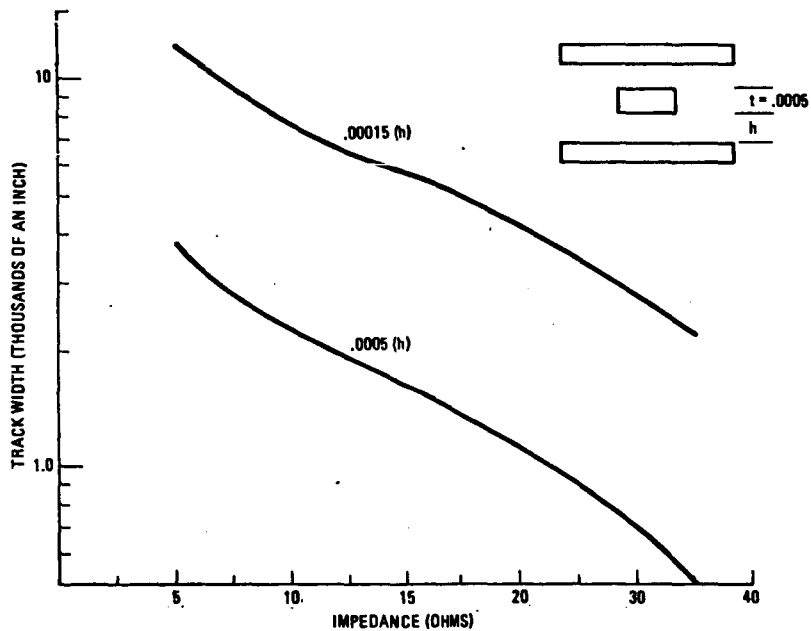
Figure 3.6-39. Line Width Vs. Z_O and h (Kapton)
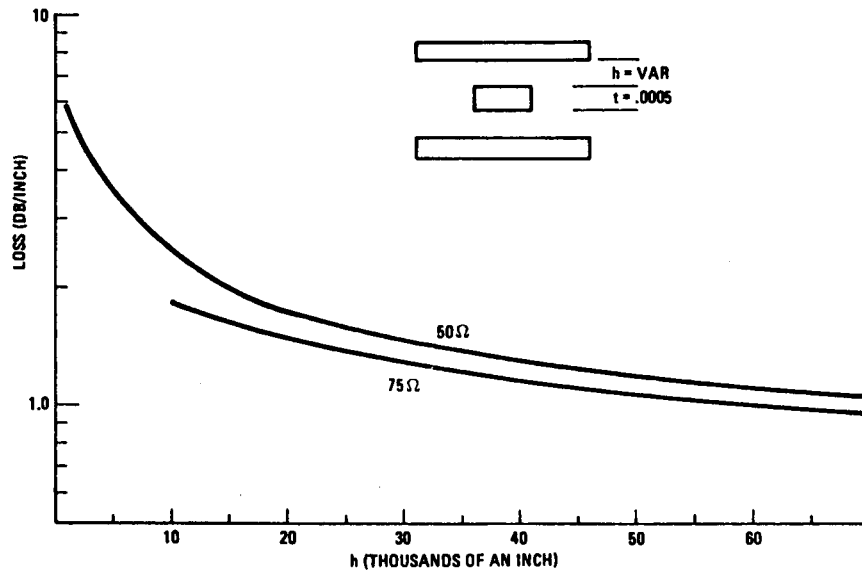
Figure 3.6-40.   Loss Vs. h and Z_0
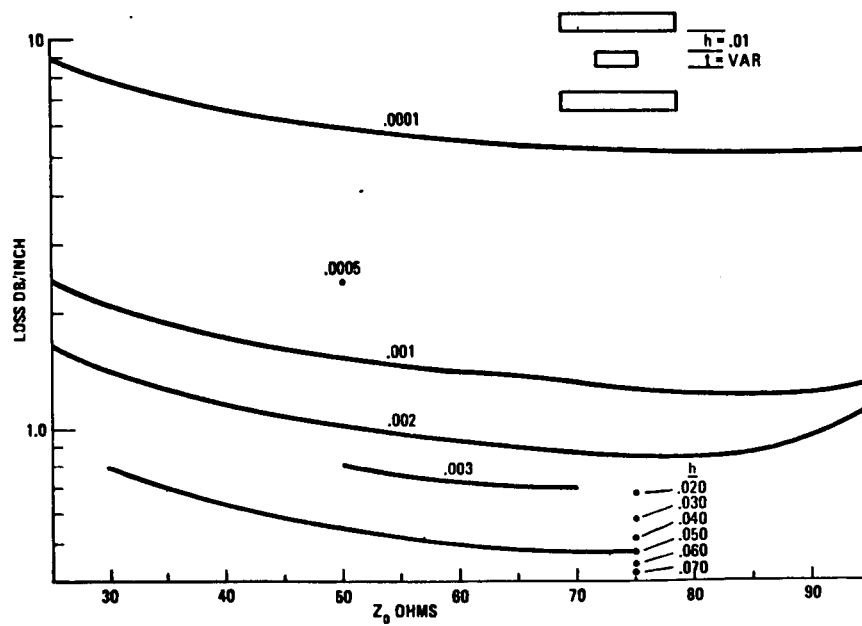
Figure 3.6-41.   Loss Vs. Z_0 and "t" (Conductor Thickness)
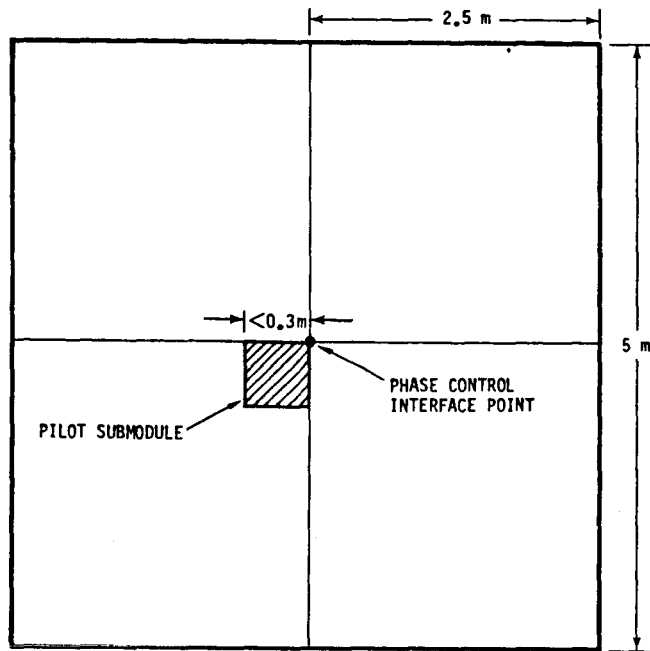
Figure 3.6-42. Subarray Layout
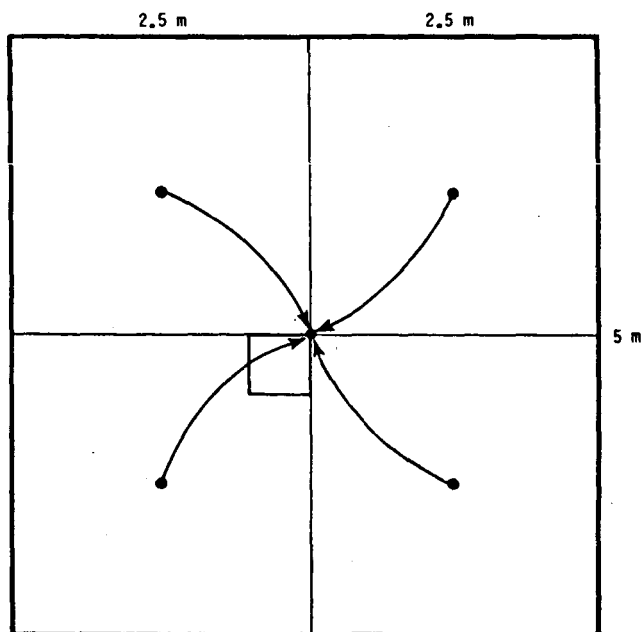
Figure 3.6-43. First-Level Subarray Signal Distribution
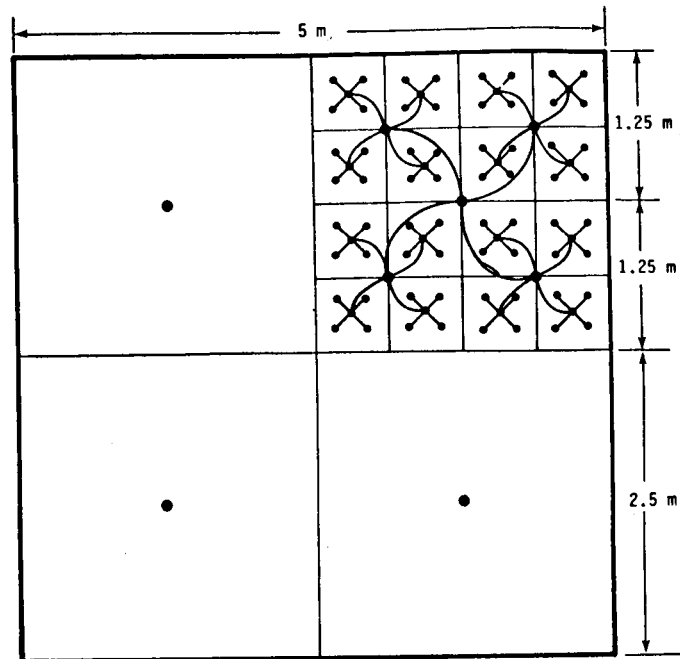
Figure 3.6-44. Second-, Third-, and Fourth-Level
Signal Distribution
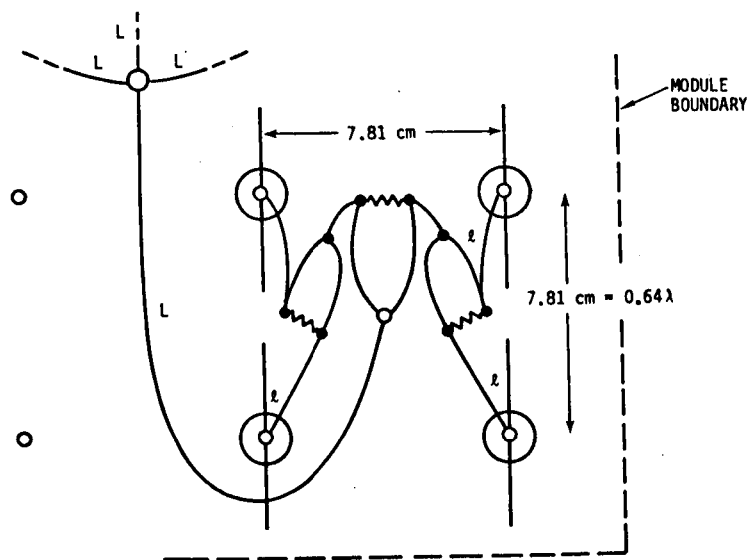
Figure 3.6-45. Hybrid (Isolated) Divider Detail
for Fifth and Sixth Levels

Table 3.6-15. Conjugated Signal Distribution
System Parameters

LEVEL	1	2	3	4	5	6
SPLITTING LOSS (dB)	6	12	18	24	30	36
ELEMENT NUMBER	4	16	64	256	1024	4096
AMPLIFIER GAIN (dB)	43	-	-	-	-	-
CABLE LENGTH* (m)	3.54	1.77	0.885	0.44	0.22	0.11
SUM OF LENGTHS	14.14	28.28	56.57	113.14	228.27	452.55

*FROM CENTER TO NEXT DISTRIBUTION POINT

The salient features of the signal distribution system (assuming the use of subminiature coax) are:

- Typically two layers of circuits, including dc distribution

- One amplifier at input with ~20-W output for ~1-mW signal at element amplifier input

- Total distribution length of ~0.45 km per subarray

- If same weight as UT 141 subminiature coax system mass $\approx 1.3 \times 10^6$ kg and ~0.6×10^6 kg for UM-47

- Last two junctions are isolated, to protect amplifiers and avoid amplitude and phase errors due to impedance match

The weight of 1.3-million kilograms can be reduced substantially, if smaller diameter coaxial solid-jacket cable can be used. The present limitation is set by the temperature capability—200 degrees Celsius for UT-141 with 141 mils outer diameter and approximately 50 kg/km. The next smaller size cable will weigh only about one third of the above weight. However, Teflon-insulated UT-47 will only withstand 100 degrees Celsius. Irradiated polylefin is one solution (UM-47) and more studies are being conducted in this area. Of course, manufacturability is of importance also and will indeed determine, at least to some extent, the ultimate sandwich design. When using one layer of coax, pressed together behind the groundplane, very little thermal resistance should be presented to the heat being radiated rearward with the groundplane in the end-mounted concept, and toward the groundplane(from the solar cells) in the sandwich concept.

Element/Power Module

End-Mounted Concept

Because of the higher power levels involved (≈ 40 W per dipole in the center of the array), all the cooling will have to be provided by the ground-plane. Also, there is no need for a rear view, because the solar panels are

independent. The critical thermal issue then is how good the thermal transfer is between the amplifier package and the ground plane. Figure 3.6-46 shows a second version of the same element layout already presented in Figure 2.3-18, the only difference being that the amplifier chips are split up into two hous- ings, one on each side of a dipole radiator. The two outputs can be made to be 180° out of phase, so that no balun is required for the dipole. The internal layout will depend on the position within the array—up to 9 in the center of the array, with 4.5 W per chip, and either 9 or fewer chips per amplifier housing.
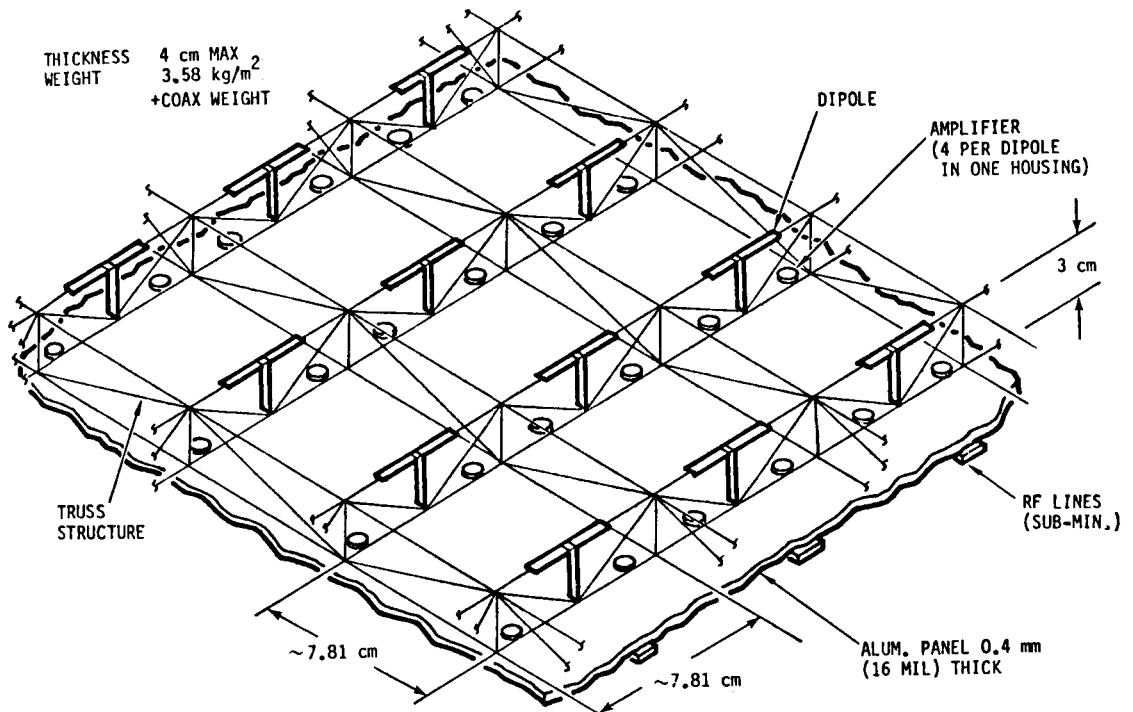
Figure 3.6-46. End-Mounted Antenna with Dipoles over Groundplane

Sandwich Concept

Figure 3.6-47 is the element/amplifier layout for the sandwich concept. The amplifiers are elevated to the level of the dipoles above the groundplane, so that the rear-view heat from the solar cells can be radiated into space from the groundplane, whereas the heat from the amplifiers is radiated from the berlox discs. Feed details and disc layout are shown in Figures 3.6-48 and 3.6-49; Table 3.6-16 summarizes the design details of the antenna in the GaAs sandwich concept. Preliminary analyses show that one probably has to back off from a CR_E = 6 sandwich because equilibrium temperatures exceed both the solar cell and the amplifier long-term capabilities. This thermal anal- ysis is presented elsewhere in the report and shall not be repeated here. For a CR_E = 5.2, for instance, preliminary indications are that the solar cell temperatures will stabilize at 206 degrees Celsius, with a groundplane temper- ature of 127 degrees Celsius, and a disc (amplifier case) temperature of 114 degrees Celsius. These are numbers we may be able to live with. Higher effective solar conversion efficiencies and more sophisticated spectral

THICKNESS ~ 4 CM

USE .05 x .05: IN
BAR (SILICA FIBERS)
FOR ALL MEMBERS

GROUND PLANE
(0.4 MM)

3 CM

~ 1 CM

PILOT
PICK-UP
ELEMENT

SOLAR CELLS

RF & DC Lines

~7.81 CM

~7.81 CM

NOTE: BAR JOINING TO BE
ULTRASONIC BY MACHINE THAT
AUTOMATICALLY FABRICATES TRUSSES
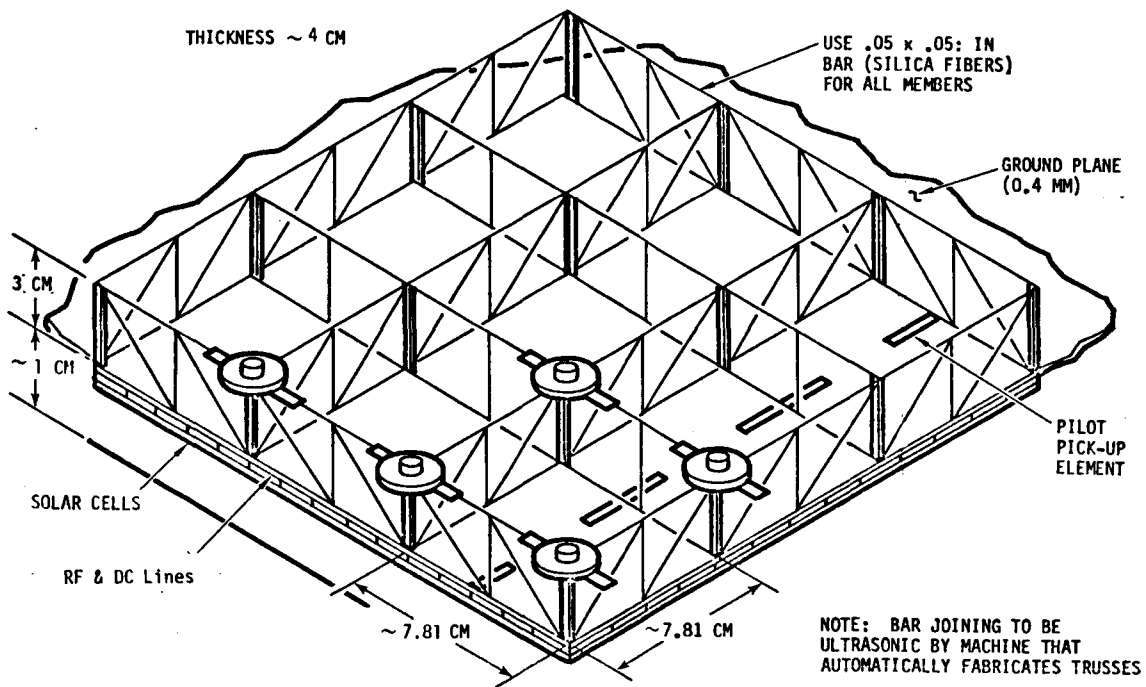
Figure 3.6-47. Sandwich Antenna with Dipoles over Groundplane

BERYLLIUM OXIDE DISC HEAT RADIATOR

DIPOLE ARM

AMPLIFIER

STRIPLINE + COAX
FEED STRUCTURE
(RF & DC)

FEED LINES

PRINTED
CIRCUIT
GND PLANE
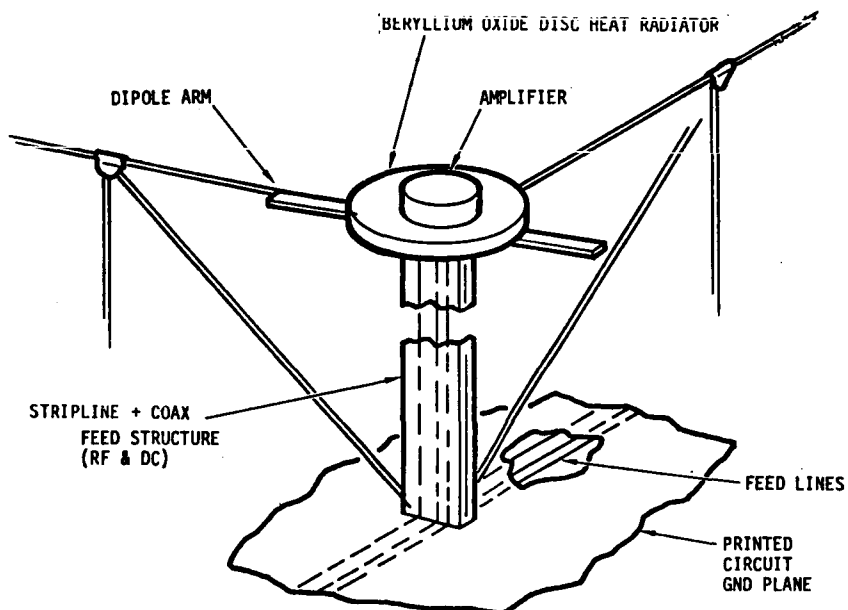
Figure 3.6-48. Dipole and Stripline/Coaxial Feed Detail
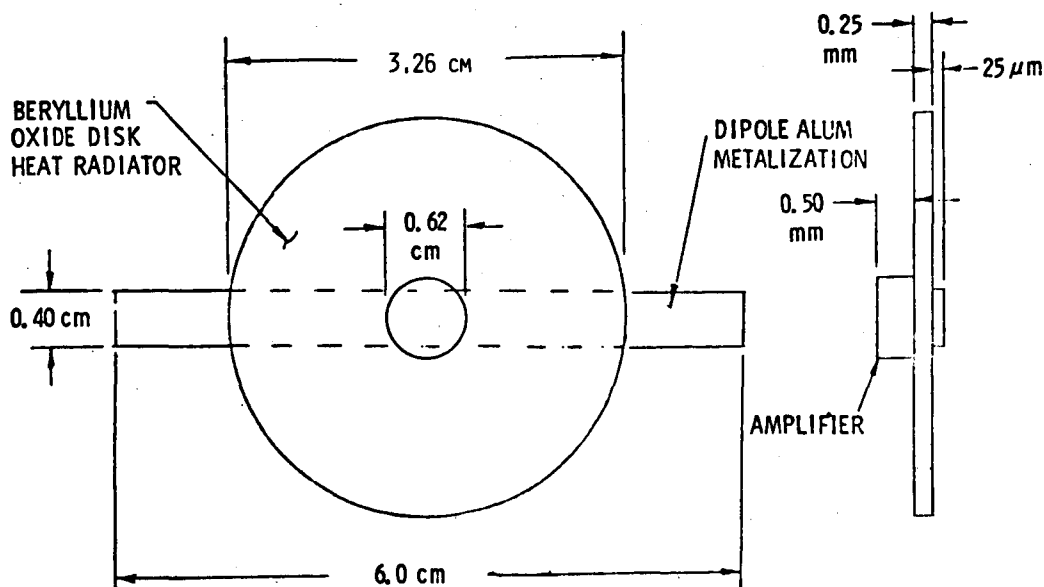
Figure 3.6-49. Dipole and Heat Radiator Detail

Table 3.6-16. Antenna Detail for
GaAs Sandwich Concept

TYPE—DIPOLE WITH DIPOLE-MOUNTED AMPLIFIERS	
ELEMENT SPACING (cm)	7.81
NUMBER OF ELEMENTS/m^2	164
OUTPUT POWER/DEVICE (W)	4.95
HEAT DISSIPATED/DEVICE (W)	1.24
GROUND PLANE TO DIPOLE LENGTH (cm)	3.05
BERLOX DISC DIAMETER (cm)	3.26
BERLOX DISC AREA (cm^2)	8.4
BERLOX DISC THICKNESS (cm)	0.0254
BERLOX DISC VOLUME (cm^3)	0.213
DISC/ANTENNA AREA RATIO	0.138

filtering techniques may increase the usable CR_E back up to 6, but much more work is required in the areas of both solar cell and power amplifier lifetime versus temperature. For $CR_E = 5.2$, the power output per amplifier would be reduced to a little over 4 watts.

Mass and Cost Estimates

Figure 3.6-50 shows a general cost history breakdown versus elapsed time for low-complexity hybrid circuits and for monolithics. Original predictions and final experiences are compared. The hybrid circuit cost trend has a tendancy to flatten out after a while, and even increase again, because of rework problems. In the case of monolithic circuits, however, the opposite has been found to be true; original predictions tend to be pessimistic. This makes a

very strong case for going toward monolithic amplifiers early in the SPS development program to assure minimum production costs.
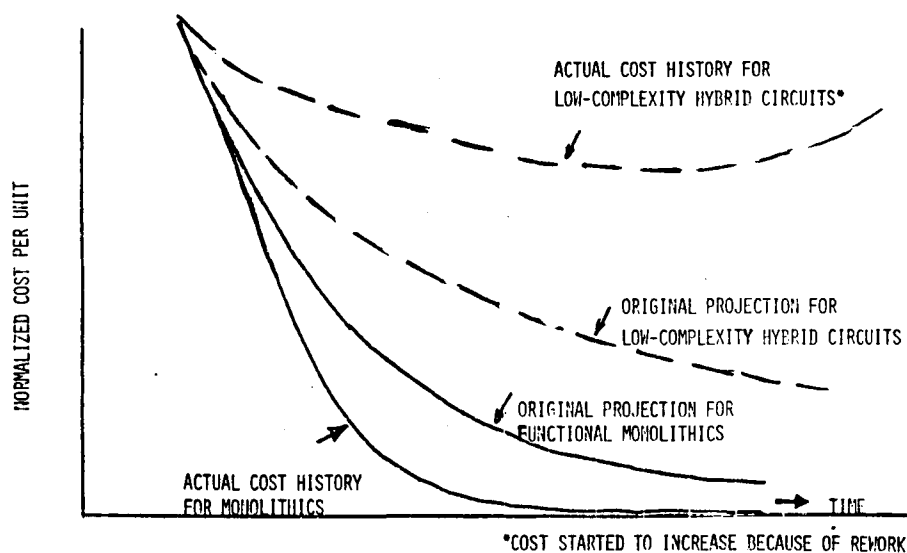
Figure 3.6-50. Solid-State Cost Trends
—Hybrids Vs. Monolithics

The ultimate component cost (the critical component is the power amplifier) is probably given by the material cost required to produce a certain average power. Because of the large amounts involved, the cost per unit weight will approach the asymptotic value (in 1979) of 50 cents per gram. The following "optimistic" cost projections are based on this number (Figure 3.6-51).
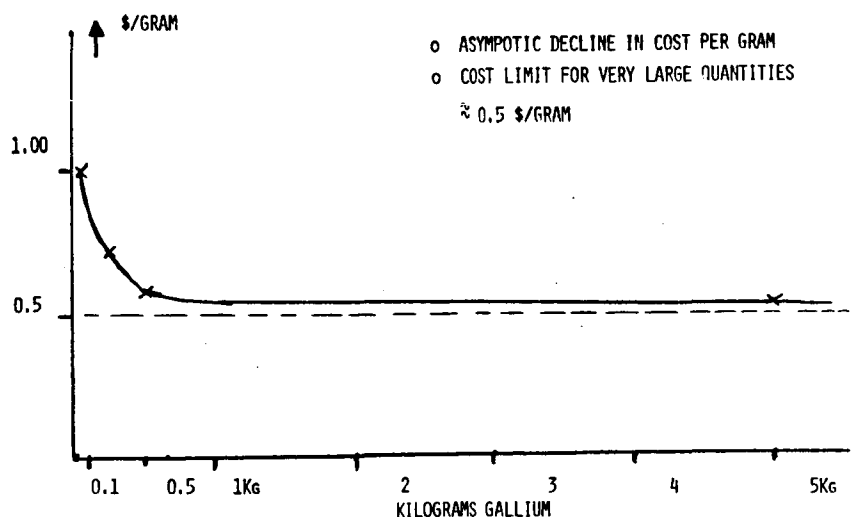
Figure 3.6-51. End-Mounted Solid-State System Cost Data Base
for Power Amplifier

End-Mounted System

Not counting dc distribution and primary structure, a preliminary mass breakdown for the study baseline end-mounted concept is shown in Table 3.6-17, normalized to kilograms per square meter of array surface. Total mass and volume are given in Table 3.6-18. The cost of the array is estimated in Table 3.6-18 and 3.6-19 for the fundamental assumption that the cost of the amplifiers is the driving factor, i.e., cost of phase control and distribution circuitry is relatively small.

Table 3.6-17. MPTS End-Mounted System
Mass Breakdown

	kg/m²
STRUCTURE	∿0.5
DIPOLES	0.32
AMPLIFIER MODULES	∿1.3*
GROUND PLANE	0.2
RF DISTRIBUTION	0.3
RF CONTROL	0.05
CONTINGENCY	0.03
TOTAL	∿2.7

*AVERAGE OVER ARRAY

Table 3.6-18. MPTS End-Mounted System
Mass and Volume Summary

ARRAY DIAMETER	1.35 km
ARRAY AREA	1.43 km² = 1.43×10⁶ m²
ARRAY DEPTH	∿4 cm
ARRAY VOLUME	1.43×10⁶ × 4×10⁻² = 5.73×10⁴ m³
TWO ANTENNAS TOTAL VOLUME	1.145×10⁵ m³
MASS	2.7 kg/m² = 3.86×10⁶ km
TOTAL MASS (EXCLUDING SOLAR CELLS AND DC DISTRIBUTION)	7.72×10⁶ kg

Table 3.6-19. MPTS End-Mounted System Cost Estimates

```
ARRAY DIAMETER (km)                 1.35
NUMBER OF SUBARRAYS                 ~14,000
NUMBER OF ELEMENTS                  ~2.3×10⁸
NUMBER OF AMPLIFIERS                2.3×10⁸
POWER PER AMPLIFIER CHIP (W)        36 (MAX., CENTER OF ARRAY)
TOTAL POWER TRANSMITTED (GW)        3.833
MAXIMUM POWER DENSITY (kW/m²)       5.9 (CENTER OF ARRAY)

NUMBER OF INTEGRATED DEVICES
PER CHIP OF 9 W EACH                4 (MAX., CENTER OF ARRAY)

DEVICESPER CHIP OF 6 W EACH         6 (CENTER OF ARRAY)

DEVICES PER CHIP OF 4.5 W EACH      9 (MAX., CENTER OF ARRAY)

NUMBER OF 4.5 W DEVICES             8.5·10"

COST (@ $0.5/DEVICE)                ≈$4.25×10⁸ (OPTIMISTIC)

COST (@ $5/DEVICE                   ≈$4.25×10⁹ (PESSIMISTIC)


NUMBER OF CONJUGATING MODULES       14,000
COST OF CONJUGATING MODULES
    @ $1000/MODULE                  $1.4×10⁷
DISTRIBUTION SYST. LENGTH (km)      25,000
COST OF DISTRIBUTION
    @ $10/LB                        $3.7×10⁶
COST OF ARRAY @ $0.1/ELEMENT        $2.3×10⁷
```

TOTAL COST (INCLUDING 0.34 10 CONTINGENCY)	OPTIMISTIC	PESSIMISTIC
TOTAL COST	5×10⁸	5×10⁹
×2	$10⁹	$10¹⁰
POWER AT UT: 5.22 GW		
5.22×10⁶ kW		
DOLLARS PER KILOWATT	$190	$1900

The cost philosophy that was used is listed below:

• Cost of power amplifier devices predominates, same as with
  the sandwich concept.

• Optimistic system cost (based on approximately $0.1/W) is
  $190/kW$_{UI}$

• It is not likely that this cost is achievable, because limits
  of automation of production are reached sooner than with the
  sandwich concept: amplifier housings have to be mounted on
  groundplane and connected to dipoles; RF feed; dc distribution

• Estimate of true systems cost will be extremely difficult to
  achieve because of hybrid character of radiating assembly.

Sandwich System

A mass normalized breakdown for the study baseline sandwich concept, including solar cells and dc distribution (but excluding primary structure) is presented in Table 3.6-20. The structure mentioned here is the one holding the transportation modules in place within the overall satellite; dc distribution and solar cells are an integral part and have, therefore, been included.

Table 3.6-21 presents a mass and volume summary for the sandwich concept; both optimistic and pessimistic cost estimates are given in Table 3.6-22.

Critical Technology Issues

Table 3.6-23 points out the important technology assessment issues. The are grouped into three major areas—analyses, development, and experiments. The table depicts only a cursory assessment of these issues. Detailed issue trees and associated research and technology plans (Form 243) have been included in Volume VI (Cost and Programmatics).

Table 3.6-20. MPTS Sandwich Concept Mass Breakdown

	kg/m^2
STRUCTURE	0.5
AMPLIFIER MODULES, DIPOLES, AND HEAT SINKS	0.65
GROUND PLANE	0.1
RF DISTRIBUTION	0.27
RF CONTROL	0.05
SOLAR CELLS	0.252
DC DISTRIBUTION	0.05
CONTINGENCY	0.028
TOTAL	∿1.9

Table 3.6-21. MPTS Sandwich Antenna Concept (GaAs) Mass and Volume Summary

DIAMETER	1.77 km
AREA	2.46 km^2
DEPTH OF SANDWICH	∿4 cm (ALLOWING APPROX. 1 cm FOR DC SYSTEM)
VOLUME	$2.46 \times 10^6 \times 4 \times 10^{-2}$ m^3 = 9.84×10^4 m^3
MASS (INCL. STRUCTURE, SOLAR CELLS, POWER DISTRIBUTION)	1.9 kg/m → 4.674×10^6 kg

Table 3.6-22. MPTS Sandwich System Cost Estimates

ARRAY DIAMETER:	1.77K	
NUMBER OF SUBARRAYS:	25,000	
NUMBER OF ELEMENTS:	∿4×10^8	
POWER/MONOLITHIC AMPLIFER:	∿5 W	
AMPLIFIER COST @ $0.5:	$2×10^8	
PHASE CONTROL COST @ $1000/SUBARRAY:	$2.5×10^7	
RF DISTRIB. COST @ $10/LB:	$1.5×10^7	
ARRAY COST @ $0./ELEMENT:	$4×10^7	
CONTINGENCY:	$2×10^7	
TOTAL (OPTIMISTIC)	$3×10^8	3×10^9 (PESSIMISTIC)
POWER AT U.I.	1.26 GW	
$/KW	238	2380

Table 3.6-23. SPS MPTS Technology Assessment

DESCRIPTION	TYPE OF EFFORT

IONOSPHERIC IRREGULARITIES AND ASSOCIATED DESIGN ASPECTS
 	
• EXACT QUANTIFICATION OF STEADY-STATE DELAY/PHASE SHIFT
• STATISTICAL ANALYSES OF IONOSPHERIC TURBULENCE
• DEVICE INVESTIGATIONS (E.G., DIVIDER RATIOS IN CHERNOFF CONJUGATORS,
    PRACTICAL IMPLEMENTATIONS OF THREE-TONE CIRCUITS)
• PILOT WAVEFORM DEFINITION IN MULTI-SATELLITE ENVIRONMENT
 	
• STUDY OF IONOSPHERIC HEATING AND POTENTIAL SYSTEMS
    LIMITATIONS
• STUDY OF DIFFERENT PILOT FREQUENCIES
• STUDY OF SPATIAL AND TEMPORAL FILTERING
• EVALUATION OF LARGE PILOT APERTURE
	ANALYSES

INTERFERENCE CAUSES AND SUPPRESSION TECHNIQUES
 	
• HARMONICS
  - AMPLIFIER DESIGN
  - RADIATING ELEMENT DESIGN—FILTERING, LOSSES
  - FILTERING IN FEED CIRCUIT (ACTIVE FILTERS)
  - FREQUENCY ALLOCATIONS FOR HARMONICS
  - INCREASE IN FUNDAMENTAL FREQUENCY
 	
• SIDEBANDS
  - SELECT COLD CATHODE TUBES
  - SELECT SOLID-STATE AMPLIFIERS
  - USE NARROW-BAND PHASE CONTROL LOOPS
	ANALYSES

PHASE REFERENCE TRANSMITTER • TOTAL SYSTEM DESIGN—PATTERN, POWER, MOUNTING & INSTALLATION • ULTRA-STABLE SOURCE DEVELOPMENT • SHIELD-BEAM ACTIVE ARRAY DESIGN AND DEVELOPMENT • INTEGRAL SOLAR CELL POWER SUPPLY DESIGN • REDUNDANCY DESIGN • RELIABILITY • MAINTAINABILITY	DEVELOPMENT
PHASE REFERENCE CIRCUITS • COMPLETE DUAL-TONE REFERENCE MODULE CIRCUIT DESIGN • PHASE BRIDGE AND PHASE SHIFTER • SYNCHRONOUS DETECTOR WITH ONE-DEGREE ACCURACY • MONOLITHIC MODULE DESIGN	DEVELOPMENT
CONJUGATING CIRCUITS AND DISTRIBUTION • CHERNOFF CIRCUITS • SIMPLE BEAM-SQUINTING CIRCUITS • THREE-TONE CIRCUITS • SELECTION OF OPTIMUM CIRCUITS FOR OVERALL PERFORMANCE (INCLUDING INPUTS FROM IONOSPHERIC STUDIES) • MONOLITHIC DESIGN • SIGNAL DISTRIB. SYST. DESIGN (SANDWICH/HARNESS LAYOUT)	DEVELOPMENT
SOLID-STATE AMPLIFIERS • 80% EFFICIENCY GaAs FET's • HIGH-EFFICIENCY, HIGH TEMP. SILICON DEVICES • SINGLE-CHIP 50-WATT AMPLIFIERS • 50-DECIBEL GAIN MONOLITHICS • COMPLETE AMPLIFIER & PHASE SHIFTER MODULES	DEVELOPMENT
RADIATOR DESIGNS • NARROW-BAND DIPOLES FOR POWER TRANSMISSION • ENDFIRE ELEMENTS FOR REF. SIGNAL PICKUP & PILOT TONE PICKUP • BROADSIDE ARRAYS FOR REF. SIGNAL & PILOT PICKUP • MICROSTRIP DESIGNS AS ALTERNATE SOLUTIONS	DEVELOPMENT
PILOT TRANSMITTER SYSTEM • PHASED ARRAY DESIGN • PHASE REFERENCE SYSTEM DESIGN • AMPLIFIER DESIGN • CENTRAL GENERATOR DESIGN	DEVELOPMENT

PHASE-LOCK LOOP TESTS
 	
• LAB TESTS OF REPEATABILITY (UNIT TO UNIT) AND LONG-TERM STABILITY
    OF KLYSTRON AND MAGNETRON PHASE-LOCK LOOPS
• LAB TESTS OF ENVIRONMENTAL EFFECTS ON ABOVE PERFORMANCE PARAMETERS
 	
• LAB TESTS OF REPEATABILITY (UNIT TO UNIT) & LONG-TERM
    STABILITY OF REF. PHASE NORMALIZATION CIRCUIT
• LAB TESTS OF ENVIR. EFFECTS ON ABOVE PERF. PARAMETERS
	EXPERIMENTS

IONOSPHERIC TESTS
 	
• UPSIDE-DOWN LARGE ARRAY TESTS (CONJUGATED ONE-KILOMETER LINEAR
    ARRAY WITH PILOT ON SATELLITE)
• SMALL-APERTURE GROUND-BASED PILOT WITH TWO-SATELLITE
    INTERFEROMETER MEASUREMENT SYSTEM
 	
• LARGE-APERTURE GROUND-BASED PILOT SYSTEM WITH
    TWO-SATELLITE INTERFEROMETER
• THREE-PILOT-TONE SYSTEM TEST (ABILITY TO MEASURE
    IONOSPHERIC DELAY)
	EXPERIMENTS

3.6.5 MAGNETRON-POWERED SPS ANTENNA STUDY

Cross-field tubes have long been considered potential candidates for use as dc to RF conversion devices in the SPS system. Indeed, early studies, circa 1969, pre-supposed the use of the amplitron tube (Reference 36), chiefly because of its high conversion efficiency. However, perhaps because of its low gain (5 to 10 dB) and reputation for having a noisy output spectrum, the amplitron lost out to the linear beam klystron, despite the latter's lower efficiency. Very detailed system studies have since resulted in a well-defined microwave power transmission system referred to as the "klystron reference concept."

In 1978, Brown (Reference 37) made two discoveries that catapulted the crossed-field device back into contention for SPS use. He found that noise in the output spectrum of a conventional microwave oven magnetron was dramatically reduced when the tube was operated with no cathode heater power, its emission temperature being maintained only by back bombardment of electrons in the tube. The other finding was that, under these circumstances, the low cathode temperature could be expected to lead to a cathode lifetime of many tens of years.

It has been the objective of this study to design a magnetron-powered SPS antenna and transmission system which could be compared with the existing klystron reference concept on a mass and cost basis. Such a magnetron design concept is presented and described herein. Because of the limited time available for this study, the magnetron system design has not yet achieved the level of detail that has evolved over the years for the klystron reference. Nevertheless, the magnetron design concept is sufficiently well-founded that a valid comparison may be made with its klystron counterpart.

This systems study has relied heavily upon the results of the Raytheon Company's magnetron tube assessment study and frequent references will be made to Raytheon progress reports, numbers 1 through 6, under this MSFC sponsored program (Reference 38). Credit for the technological advances which have made the magnetron an attractive candidate for SPS dc to RF conversion purposes must go to W. C. Brown and other Raytheon investigators who have carried out that development effort.

Injection Locked Magnetron Amplifier

The conventional magnetron is a single port device which normally functions as a free-running oscillator at a frequency determined by anode voltage, magnetic field and RF load reflection coefficent. Because all power converter devices used in the SPS antenna array must operate at exactly the same frequency with precisely controlled output phases, a free-running oscillator cannot be used as such. What is needed, of course, is a two-port amplifying device to which a master control signal can be applied so that all the devices may be slaved to a single reference. There are two principal ways in which a one-port device may be converted to a two-port. In the case of the magnetron, both of these techniques make use of the fact that the magnetron cannot distinguish between an applied input signal and a reflection of its own output from a load impedance. A good qualitative explanation of these methods, one using two magnetrons and a magic-T, the other a single tube with a three-port circulator, is to be

found in Reference 37. This explanation, however, does not address certain quantitative questions which must be answered before a choice can be made so that a system design may proceed. For this reason, a quantitative analysis of the two techniques has been carried out and is presented herein.

Pair of Magnetrons with 3 dB Hybrid

This technique, using two similar magnetrons and a symmetrical 3 dB hybrid combiner, is shown in Figure 3.6-52. A low level input signal, lying within the magnetrons' locking frequency range, is applied to port 1 of the hybrid. This signal splits equally between ports 2 and 3, locking the two oscillators. The combined output of the magnetrons then appears at port 4 with no output at port 1 under ideal conditions. In order to investigate behavior under non-ideal conditions a scattering matrix analysis has been performed.
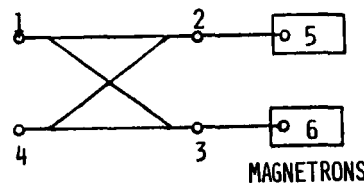
Figure 3.6-52. Pair of Magnetrons
With Hybrid Combiner

Ports 2 and 3 of the hybrid are connected by short lengths of lossless line to the magnetron ports 5 and 6, respectively. It can be shown that (Reference 38)

$$S_{14} \, e^{-j\theta_{14}} = S_{12} \sqrt{1 - S_{12}^2} \; e^{-j\left(2\theta_{12} + \frac{\pi}{2}\right)} \left[S_{55} \; e^{-j\left(2\theta_{25} + \theta_{55}\right)} \right.$$

$$\left. + \, S_{66} \; e^{-j\left(2\theta_{36} + \theta_{66}\right)} \right]$$

$$S_{11} \, e^{-j\theta_{11}} = S_{12}^2 \, e^{-j \, 2\theta_{12}} \, S_{55} \; e^{-j\left(2\theta_{25} + \theta_{55}\right)}$$

$$- \left(1 - S_{12}^2\right) \, e^{-j \, 2\theta_{12}} \, S_{66} \; e^{-j\left(2\theta_{36} + \theta_{66}\right)}$$

where subscripts 55 and 66 describe the scattering parameters of the two magnetrons. If the short transmission lines from ports 2 and 3 to magnetron input ports 5 and 6 are equal in length, then $\theta_{25} = \theta_{26}$ and both are constant at fixed frequency. The electrical length θ_{12} of the hybrid is also constant so these constant phase shifts may be ignored. The above expressions then simplify to

$$S_{14} \, e^{-j\theta_{14}} = -j \, S_{12} \sqrt{1 - S_{12}^2} \left[S_{55} \, e^{-j\theta_{55}} + S_{66} \, e^{-j\theta_{66}} \right] \quad (3.6\text{-}99)$$

$$S_{11} \, e^{-j\theta_{11}} = S_{12}^2 \, S_{55} \, e^{-j\theta_{55}} - \left(1 - S_{12}^2 \right) S_{66} \, e^{-j\theta_{66}} \,. \quad (3.6\text{-}100)$$

Equation (3.6-99) gives the transmission coefficient from input port 1 to output port 4, while Equation (3.6-100) gives the reflection coefficient at port 1. Power, of course, is proportional to $|S|^2$.

As a check, suppose the hybrid is ideally balanced, so that $S_{12} = 1/\sqrt{2}$, and the magnetrons are identical with $S_{55} = S_{66} = S$ and $\theta_{55} = \theta_{66} = \theta$. Then these equations show that

$$S_{14} \, e^{-j\theta_{14}} = S \, e^{-j\left(\theta + \frac{\pi}{2}\right)} \,, \quad \text{hence} \quad S_{14} = S \,, \quad \theta_{14} = \theta + \frac{\pi}{2} \,,$$

$$S_{11} \, e^{-j\theta_{11}} = 0.$$

Thus, under ideal conditions there is no reflected signal at the input and the magnetron signals combine totally at the output, port 4.

The effect of unbalance in the hybrid can be estimated by assuming that

$$S_{12} = \frac{1}{\sqrt{2}} + \Delta \,, \quad \text{whence} \quad \sqrt{1 - S_{12}^2} \simeq \frac{1}{\sqrt{2}} - \Delta$$

providing Δ is small. It is then found that

$$S_{14} \, e^{-j\theta_{14}} \simeq \left(1 - 2\Delta^2\right) S \, e^{-j\left(\theta + \frac{\pi}{2}\right)}$$

$$S_{11} \, e^{-j\theta_{11}} \simeq 2 \, \Delta \, S \, e^{-j\theta} \,.$$

It is clear that the transmission coefficient is quite insensitive to unbalance in the hybrid but the "reflection coefficient" at the input is directly proportional to the difference in coupled signal levels. For example, if the coupling factor S_{12} for the hybrid is -3.2 dB then $\Delta = .0153$. The change in S_{14} is less than .05% (i.e., a change in power level of -.004 dB), but S_{11} increases from zero to a level that is 30.3 dB below S_{14}.

It is assumed now that the hybrid is ideal, but that the two magnetrons are unbalanced both in phase and amplitude. Equations (3.6-99) and (3.6-100) now become

$$S_{14} e^{-j\left(\theta_{14} - \frac{\pi}{2}\right)} = \frac{1}{2} \left[S_{55} e^{-j\theta_{55}} + S_{66} e^{-j\theta_{66}} \right] \qquad (3.6\text{-}101)$$

$$S_{11} e^{-j\theta_{11}} = \frac{1}{2} \left[S_{55} e^{-j\theta_{55}} - S_{66} e^{-j\theta_{66}} \right] . \qquad (3.6\text{-}102)$$

For small unbalances it is permissible to write

$$S_{55} = S (1 + \epsilon) \quad , \quad \theta_{55} = \theta + \delta$$

$$S_{66} = S (1 - \epsilon) \quad , \quad \theta_{66} = \theta - \delta .$$

Denoting the bracketed expressions in Equations (3.6-101) and 3.6-102) by $F_{\pm} e^{j\theta_{\pm}}$ it is found that

$$F_{+} e^{-j\theta_{+}} = 2 S e^{-j\theta} \left(\cos \delta - j \epsilon \sin \delta \right)$$

$$F_{-} e^{-j\theta_{-}} = 2 S e^{-j\theta} \left(\epsilon \cos \delta - j \sin \delta \right) .$$

Then, from Equations (3.6-101) and (3.6-102) it is seen that

$$\left. \begin{array}{l} S_{14} = S \sqrt{\cos^2 \delta + \epsilon^2 \sin^2 \delta} \\ \\ \theta_{14} = \theta + \arctan \left(\epsilon \tan \delta \right) + \frac{\pi}{2} \end{array} \right\} \qquad (3.6\text{-}103)$$

$$\left. \begin{array}{l} S_{11} = S \sqrt{\sin^2 \delta + \epsilon^2 \cos^2 \delta} \\ \\ \theta_{11} = \theta + \arctan \left(\frac{\tan \delta}{\epsilon} \right) \end{array} \right\} \qquad (3.6\text{-}104)$$

Equation (3.6-103) shows that the transmission coefficient is once again extremely insensitive to imbalance. Thus if ϵ and δ are small then

$$S_{14} \simeq S \left(1 - \frac{\delta^2}{2} \right) \quad \text{while} \quad \theta_{14} \simeq \theta + \epsilon \delta + \frac{\pi}{2}$$

and in each case the effect of the unbalance terms, δ^2 and $\epsilon \delta$, is of second order. This is a fortunate circumstance for SPS for it means that insertion phase and gain differences in magnetron pairs will not cause serious phase and amplitude errors in the spacetenna array.

On the other hand, Equation (3.6-104) shows that reflected power at the input to the hybrid does depend upon magnetron imbalance. The following example serves to illustrate the two cases. Suppose that $\epsilon = 0.1$, which represents nearly 2 dB difference between magnetron output levels, while $\delta = 0.1$ radians, corresponding to a difference of $11.5°$ in their output phases. The output at port 4 changes by only .04 dB in level and 0.6 degrees in phase. At the input port, however, $S_{11} = .14\ S$. If the magnetrons have a nominal gain of 20 dB then $S = 10$ and the "reflection coefficient" is 1.4. This simply means that the reflected power level at port 1 is about twice that of the injected signal. In this case it might be necessary to incorporate an isolator ahead of port 1 in order to eliminate reaction by the strong reflected signal on the injection signal source. The assumed unbalance conditions used in this example, however, are so unduly severe that the reflected signal will, in practice, be considerably less than that calculated above. This is shown in Figure 3.6-53 by contours of constant loss and phase shift as functions of magnetron unbalance.

Ohmic loss occurs only in the waveguide walls and since a short-slot side-wall hybrid in WR340 waveguide is only about 7 inches long this loss is very small.
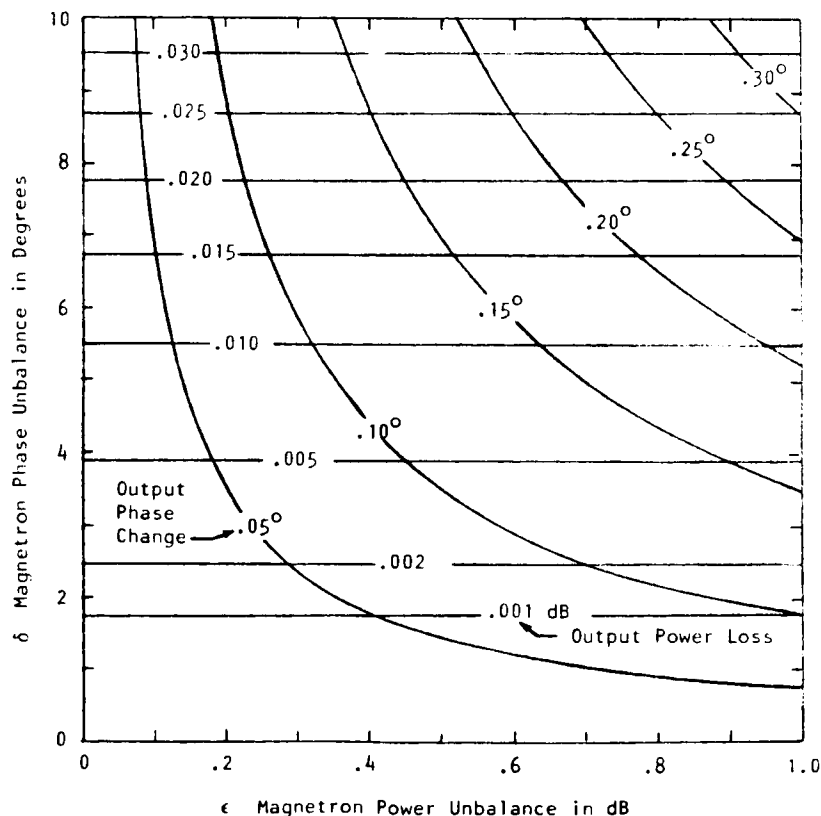
Figure 3.6-53. Contours of Constant Output Power Loss and Phase Shift versus Magnetron Unbalance

Single Magnetron with Circulator

In this method a single magnetron and 3-port circulator are used as shown in Figure 3.6-54.
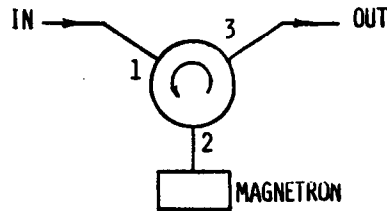
Figure 3.6-54. Single Magnetron with Circulator

A low level locking signal, injected at port 1, circulates to port 2 and serves to lock the magnetron whose output then circulates to exit port 3. Under ideal matched conditions a good circulator will have an isolation of 35 dB or more. What this means is that magnetron output power which anti-circulates from port 2 to 1 will be 35 dB below that at port 3. Thus, if the nominal gain of the magnetron is 20 dB, then the anti-circulating signal going back out of arm 1 will be 15 dB below the injected locking signal and will, therefore, not react adversely on the locking source.

Mismatches are certain to exist, however, and those at arms 2 and 3 are of particular interest. A reflection at arm 3 may easily cause a severe reaction on the injection signal source. Similarly, a mismatch at arm 2 will return a signal to the magnetron which will combine vectorially with the injected signal and may cause loss of lock. Some of these problems can be alleviated by using three circulators to construct a five-port device, as is often done with tunnel diode amplifiers. For SPS application the added complexity and increased loss are very undesirable and this case will not be considered further.

For the moment it is assumed that the circulator is ideal and lossless. E_{in} denotes the actual locking signal that enters the magnetron. Then the output of the tube is given by

$$E_{out} = E_{in} \, S \, e^{-j\theta} \tag{3.6-105}$$

where S and θ have the same meanings as before. A portion of this output is reflected at circulator port 2 where the magnitude of the reflection coefficient is assumed to be ρ. This reflected signal, which is returned to the magnetron, is given by

$$E_{refl} = \rho \, E_{out} \, e^{-j\phi} \tag{3.6-106}$$

where ϕ is an angle that includes the phase of the reflection coefficient and the two-way electrical path from magnetron to port 2 and back again. The signal described by Equation (3.6-105) adds to the control signal injected at arm 1 to form the total input signal E_{in}. If the injected control signal at circulator port 1 is denoted by E_{cont} then

$$E_{in} = E_{cont} + E_{refl} = E_{cont} + \rho\, E_{out}\, e^{-j\phi}$$

and with substitution from (3.6-105) it is found that

$$\frac{E_{out}}{E_{cont}} = \frac{S\, e^{-j\theta}}{1 - \rho\, S\, e^{-j(\theta + \phi)}} \quad . \tag{3.6-107}$$

The above complex ratio defines the effective gain and insertion phase of the magnetron. It is noted that if $\rho S = 1$ the gain can become very large or even infinite for certain ranges of the angle $\theta + \phi$. This condition implies instability, with the possibility of free running oscillations and therefore loss of lock. Unless the product ρS is small it is clear that the magnetron gain and insertion phase will be affected by changes in the reflection coefficient at arm 2. Thus, if it is required that $\rho S \leq 0.1$ then for $S = 10$ (i.e., nominal gain of 20 dB) ρ must be less than .01, corresponding to a VSWR of less than 1.02. This indicates the likely need for a matching network between magnetron and circulator.

It was noted earlier that a signal that anti-circulates from port 2 to port 1 will generally be very small compared to the injected signal. However, this may not be true of the reflected signal caused by load mismatch at arm 3. The magnitude of this signal will be $\rho_L E_{out}$ or, ideally, $\rho_L S E_{cont}$. This signal may adversely react on the injection source unless $\rho_L S \ll 1$ so that once again rather stringent matching conditions must apply, this time to the load impedance.

On top of the difficulties discussed above is the problem created by ohmic loss between ports 2 and 3 in the circulator. It is unlikely that this loss can be held below .06 to .07 dB, i.e., about 1.4 to 1.6%, and this directly affects overall dc to RF conversion efficiency. For a 3 port junction circulator in WR340 waveguide the ferrite material would be in the form of a puck about 3 cm in diameter and 1 cm high. Essentially all the loss occurs in this ferrite puck and it is in excess of 50 watts for a 3500 watt magnetron. This may necessitate auxiliary cooling devices in order to limit temperature rise in the ferrite, which is already operating in an environment at 300°C.

Finally, it appears that a circulator designed to operate at that relatively high temperature might perform very poorly, or not at all, at room temperature. This could necessitate use of a heater at start-up in order to raise the initially cold ferrite temperature to the point where non-reciprocal circulation begins.

Basic Power Module and Subarray Design

As a result of the preceding analysis of injection locking techniques the
two-magnetron technique with 3 dB hybrid combiner has been selected. There are
numerous types of 3 dB hybrid in waveguide, coaxial and strip transmission line
forms. For SPS purposes a waveguide form is preferred because of its compati-
bility with a slotted waveguide radiator. The two basic waveguide forms are
the magic-Tee, which requires internal matching ports and irises, and the short-
slot coupler which needs no tuning devices and has a very compact form. There
are two variants of this latter hybrid device, one called a top-wall coupler,
the other a side-wall coupler. It is the sidewall coupler which has been chosen
for this application since it is structurally the most compatible with a slotted
waveguide planar array.

The basic building blocks for constructing the very large space antenna are
power modules comprising a slotted waveguide planar array excited by one or more
pairs of magnetrons whose outputs are combined in a 3 dB short-slot, side-wall
coupler and fed to a short length of waveguide feed line. The planar array
could consist of the conventional arrangement of side-by-side slotted waveguides.
Alternatively it may be a Resonant Cavity Radiator (RCR) as described in previous
Rockwell reports, and also at the January 1980 Microwave Workshop at JSC (Ref-
erence 40). The RCR has been chosen as the basic radiating element because of its
lesser mass and lower ohmic loss, both of which result from the elimination of
internal common waveguide walls.

Nine different power module configurations, having different dimensions
and/or numbers of magnetrons, have been designed in such a way that standard
subarrays, all square and having identical dimensions, can be formed from the
power modules of any one of the nine different types. As a result, the complete
spacetenna can be built from these standard size subarrays and since there are
nine types of subarrays, differing only in numbers of magnetron tubes, it is
possible to create a nine-step approximation to any desired power distribution
across the array aperture. It is emphasized that all magnetrons, wherever used
in the array, are identical and have the same power output levels. The change
in power density across the array is created by the varying numbers of tubes
associated with each of the nine types of subarrays.

The use of power modules with varying dimensions to create standard size
subarrays, along with the need for RCR dimensions to be integral multiples of
$\lambda g/2$, are factors which constrain power module dimensions and geometry, as will
become apparent. The two orthogonal dimensions of an RCR will be in the ratio
of two integers if the slot spacing is s = $\lambda g/2$ in both those directions. This
condition uniquely determines s, as is now shown. Imagine a planar array
of side-by-side slotted waveguides. In each individual guide the slots must be
spaced $\lambda g/2$ apart, where guide wavelength and cut-off wavelength are related by

$$\frac{1}{\lambda_g^2} + \frac{1}{\lambda_c^2} = \frac{1}{\lambda^2} \quad ,$$

and λ_c = 2a where a is the broad dimension of the guide. In the orthogonal
direction the slot spacing will be a+δ where δ is the thickness of adjacent
guide walls. The RCR is a special case of this arrangement in which the

3-181

internal guide walls are eliminated so that $\delta = 0$. In this case the two
orthogonal spacings will be the same if s = a = $\lambda_g/2$. Along with the above
equations this leads to the unique solution

$$s = \frac{\lambda_g}{2} = \frac{\lambda_c}{2} = a = \frac{\lambda}{\sqrt{2}} \quad .$$

At 2450 MHz this gives a = s = 8.65 cm, which happens to be almost exactly the
width of standard WR340 waveguide. All RCR's will have lateral dimensions
which are integral multiples of 8.65 cm. The only restriction on the height,
b, of the cavity radiator is that it be less than $\lambda/2$ (6.1 cm). It could well
be taken to be 4.32 cm (1.7 in), which is the height of WR340 waveguide.
However, in the interest of saving mass b has been chosen to be 2.0 cm.

High Power Density Module, Type 1

Highest RF power density occurs at the array center, consequently the
power module for this region will require the greatest number of magnetron
tubes per unit area. A design for this module, which will be termed a type 1
power module, is shown in Figure 3.6-55. Its aluminum RCR has 8×8 = 64 slots
and dimensions of 8×8.65 cm = 69.2 cm square. A symmetrical arrangement of
two pairs of magnetrons is used which maximizes the surface area of the
pyrolytic graphite heat radiating discs which are attached to each magnetron.
These discs are made as large in diameter as possible, so that adjacent discs
touch one another, in order to dissipate as much waste heat as possible from
each tube. A thermal analysis, to be discussed in the next section, has shown
that each magnetron may then operate at a 3.5 kW RF output level, if its dc to
RF conversion efficiency is 90%. The area of this RCR's radiating surface is
$(0.692)^2 = 0.479$ m^2 so that with 4, 3.5 kW tubes the radiated RF power density
is theoretically 29.2 kW/m^2.
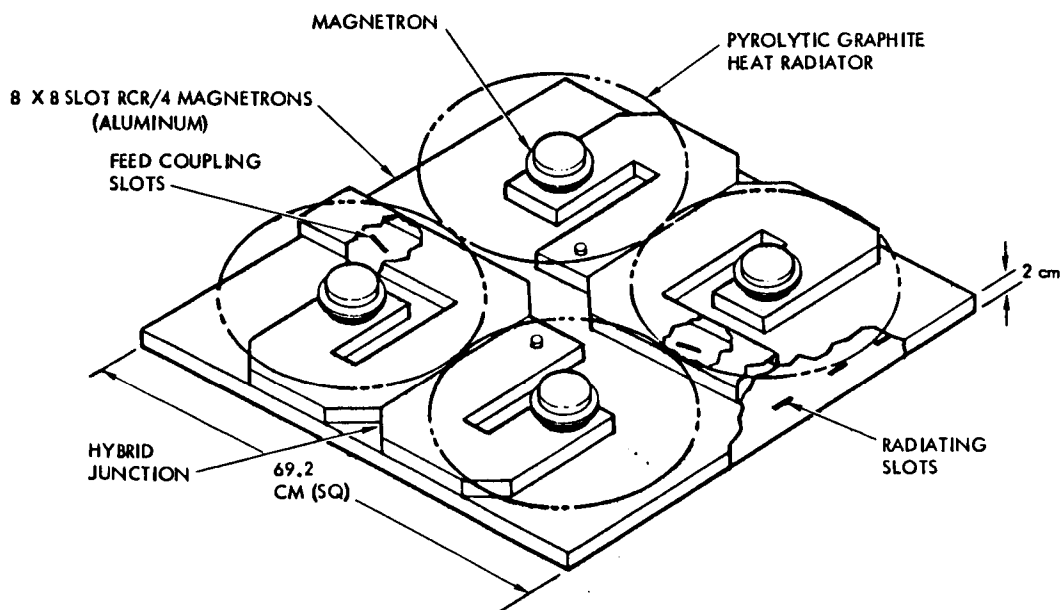
Figure 3.6-55. High Power Density Power Module for Array Center

The two short slot hybrid couplers and feed waveguides are also constructed of aluminum whose internal dimensions are a = 8.65 cm, b = 2.0 cm. Aluminum wall thickness is 0.25 mm (.010 in) for the RCR, hybrid couplers and feed guides. Figure 3.6-56 is a schematic sectional view through the power module which indicates the locations of the radiating slots in the lower face of the RCR and the coupling slots in the upper face of the RCR which forms a common wall with the feed waveguides. The radiating slots are displaced, longitudinal, shunt elements in which slot displacements are staggered alternately across the center lines in order to obtain successive phase shifts of π radians from slot to slot. Coupled with the π radians shift due to the $\lambda g/2$ spacing, this means that all slots are in phase and the RCR radiates a broadside beam. The feed, or coupling slots, are inclined series elements in the broad wall of the feed waveguide. The total of six coupling slots, located as shown, are sufficient to ensure that only the desired $TE_{8,8,0}$ cavity mode is excited within the RCR.

The magnetron tubes, to be described later, are coupled into the hybrid waveguide arms by means of coaxial probes. The reference (excitation) signals to the hybrid input arms are also probe coupled through small coaxial connectors.

Lower Density Power Modules, Types 2 to 9

If the size of the 8×8 slot RCR shown in Figure 3.6-56 is increased to 8×12 slots and the same 4-magnetron excitation arrangement is used, the power module dimensions now become 69.2×103.8×2.0 cm. The separation between magnetron pairs will increase due to the increase from 69.2 to 103.8 cm in the one dimension. This type 2 module has an area of 0.718 m^2 and a theoretical power density of 19.5 kW/m^2.
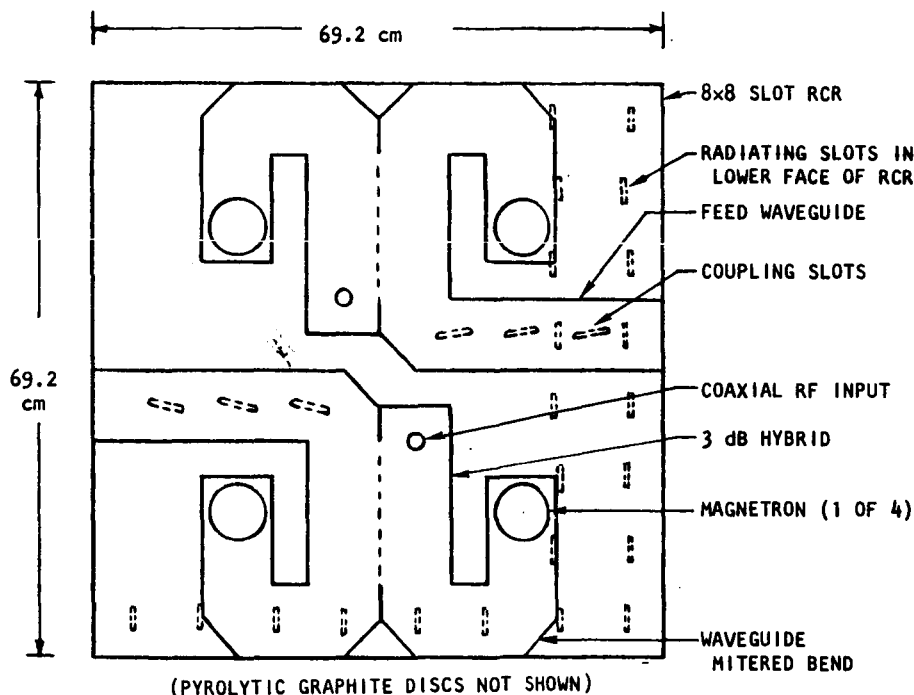
Figure 3.6-56. Sectional View of Type 1 High
Power Density Module

A type 3 module is shown in Figure 3.6-57. In this case the 8×8 slot RCR is the same as that for the type 1 module, but only one pair of magnetrons is used for excitation, leading to a theoretical power density of one-half that of type 1, i.e., 14.6 kW/m^2. The feed waveguide now extends fully across the width of the RCR and has seven inclined coupling slots. The output of the hybrid combiner is fed to the feed waveguide by means of an H-plane T-junction.

(PYROLYTIC GRAPHITE DISCS NOT SHOWN)
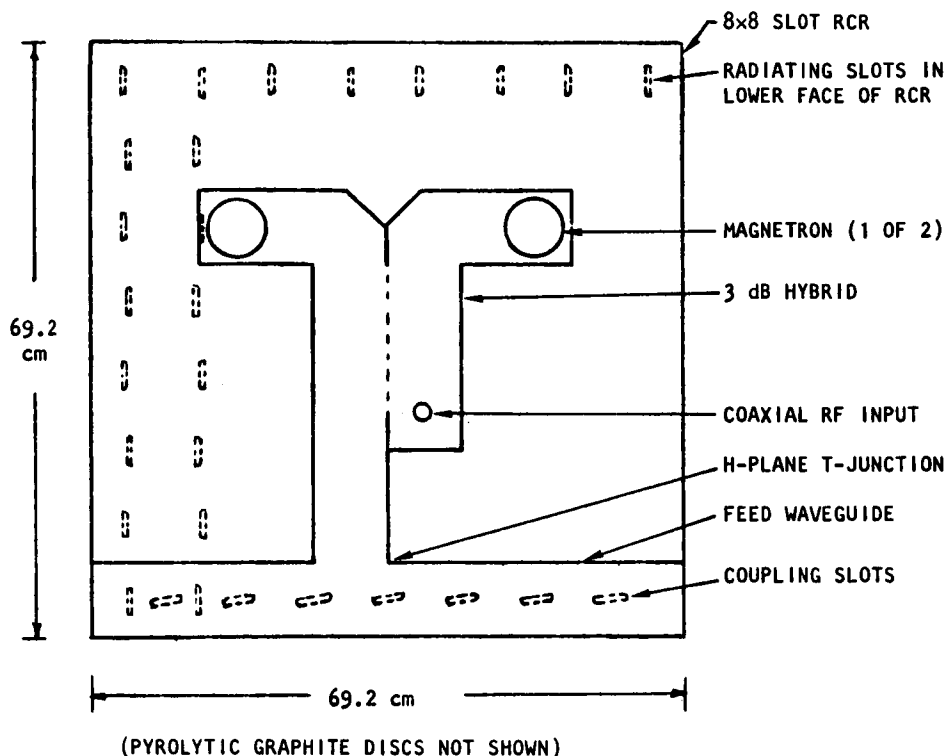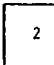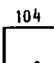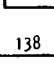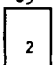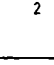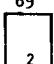
Figure 3.6-57. Type 3, Lower Power Density Module

Type 4 to type 9 power modules all have a feed arrangement similar to that of type 3 and utilize only a single pair of magnetrons. The RCR dimensions, however, become progressively larger and therefore RF power density becomes progressively lower in going from type 4 to type 9.

Subarray Design

Corresponding to the nine different power modules there are nine standard subarrays, also designated types 1 to 9. These standard subarrays are all square, with identical dimensions, and differ only in numbers of tubes and therefore in power density levels. The way in which these subarrays are constructed from the various power modules is indicated in Table 3.6-24. The first column shows module dimensions (to nearest cm) and number of tubes. The second and third columns give the module type number and slot configuration. Column 4 indicates the number and arrangement of modules used to form a subarray of a given type. Column 5 lists the total number of magnetron tubes in the subarray. Since all subarrays have the same area, the number of tubes is proportional to the RF power density, and this relative level, in dB, is shown in the last column of the table.

Table 3.6-24. Nine Basic Power Module/Panel Configurations

MODULE CONFIGURATION, DIMENSIONS IN cm AND NO. OF TUBES	MODULE OR SUBARRAY TYPE NO.	NO. OF SLOTS PER MODULE	NO. OF MODULES PER SUBARRAY	NO. OF TUBES PER SUBARRAY	RELATIVE RF POWER DENSITY IN dB	MODULE CONFIGURATION, DIMENSIONS IN cm AND NO. OF TUBES	MODULE OR SUBARRAY TYPE NO.	NO. OF SLOTS PER MODULE	NO. OF MODULES PER SUBARRAY	NO. OF TUBES PER SUBARRAY	RELATIVE RF POWER DENSITY IN dB
69 / 4 / 69	1	8×8	6×6	144	0	104 / 2 / 104	6	12×12	4×4	32	-6.53
69 / 4 / 104	2	8×12	6×4	96	-1.76	104 / 2 / 138	7	12×16	4×3	24	-7.78
69 / 2 / 69	3	8×8	6×6	72	-3.01	138 / 2 / 138	8	16×16	3×3	18	-9.03
69 / 2 / 104	4	8×12	6×4	48	-4.77	104 / 2 / 208	9	12×24	2×4	16	-9.54
69 / 2 / 138	5	8×16	6×3	36	-6.02						

Every subarray has 48×48 = 2304 slots and, if its component power modules were tightly packed, would have dimensions of 48×8.65 = 415.2 cm per side (neglecting RCR wall thicknesses). Some kind of mounting frame, however, is required in order to assemble and hold together the various RCR's which make up a sub-array. The frame members will therefore force some separation between modules, so that overall subarray dimensions must be increased. For this reason a standard subarray size of 4.2 m² has been adopted. For the type 1 subarray the effective power density is then slightly reduced and, when rounded-off, becomes 28 kW/m². The gaps between adjacent power modules will vary from nearly 1 cm in a type 1 subarray to a maximum of about 2.5 cm in a type 9 subarray. This is not enough to cause a serious grating lobe problem.

Two examples of subarray formation are shown in Figure 3.6-58. The one at the left uses 16 modules of type 6 to form a complete type 6 subarray. The one at the right utilizes 8 type 9 modules arranged to fit into a standard sub-array of type 9. At the center of each subarray a solid state amplifier is located which feeds the master phase reference signal through a corporate distribution network of coaxial cables (shown in dashed line) to the solid-state driver power amplifiers associated with each of the power modules.

Solid-state driver amplifiers, about which more will be said in the section on magnetron tube description, will be located in the gaps between adjacent RCR's and these spaces will also be utilized for location of pilot tone receiving antennas and amplifiers.
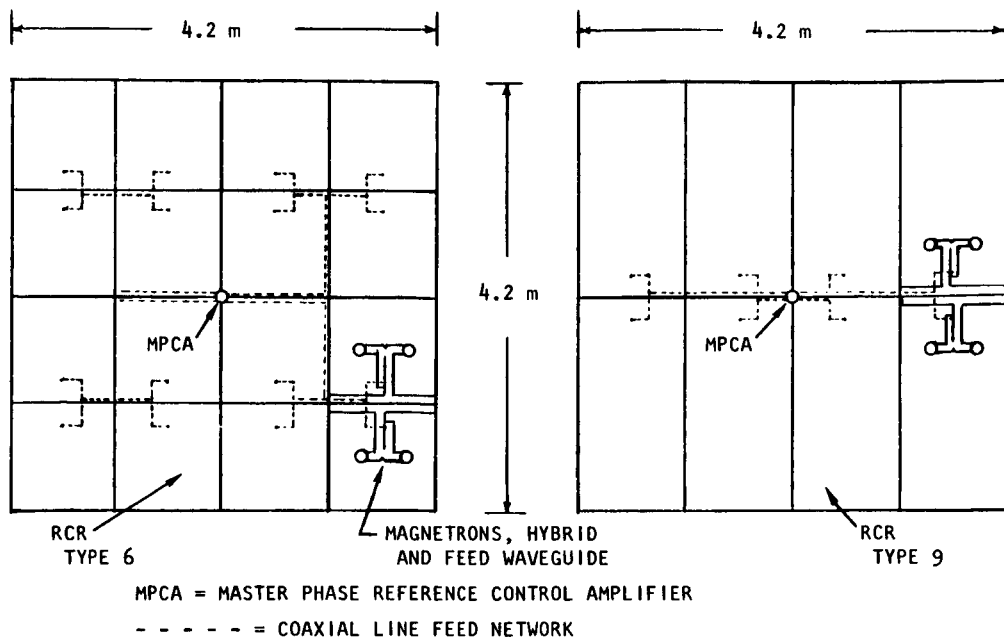
Figure 3.6-58. Two Examples of Subarray Formation
(Type 6 at Left, Type 9 at Right)

Nine-Step, -9.54 dB Aperture Distribution

In section 3.6.1 a comparison between Gaussian and Hansen aperture
distributions, both truncated at -9.54 dB, revealed a slight superiority for
the latter in terms of ability to radiate more total power. For this reason
a 9-step approximation to the Hansen distribution has been chosen and is shown
in Figure 3.6-59. The power densities at each level are, of course, those
given in the last column of Table 3.6-24. The normalized radii at which the
step changes occur are indicated on the figure. They have been chosen in such
a way as to make the aperture power coefficient K (section 3.6.1) the same for
the stepped approximation as for the smooth Hansen curve, namely 0.436.
Radiation pattern characteristics and microwave system performance resulting
from this choice will be discussed in a later section.

Ohmic Loss

The theoretical ohmic loss for the dominant mode in aluminum waveguide
of dimensions a, b at 2450 MHz is

$$\alpha = \frac{3.7 \times 10^{-4}}{b} \left[1 + \frac{2b}{a} \left(\frac{\lambda}{\lambda c} \right)^2 \right] \frac{\lambda g}{\lambda} \quad \text{dB/unit length}.$$

With a = 8.65 cm, b = 2.0 cm, the loss in the feed waveguide will be
$\alpha = 3.2 \ 10^{-4}$ dB per cm.
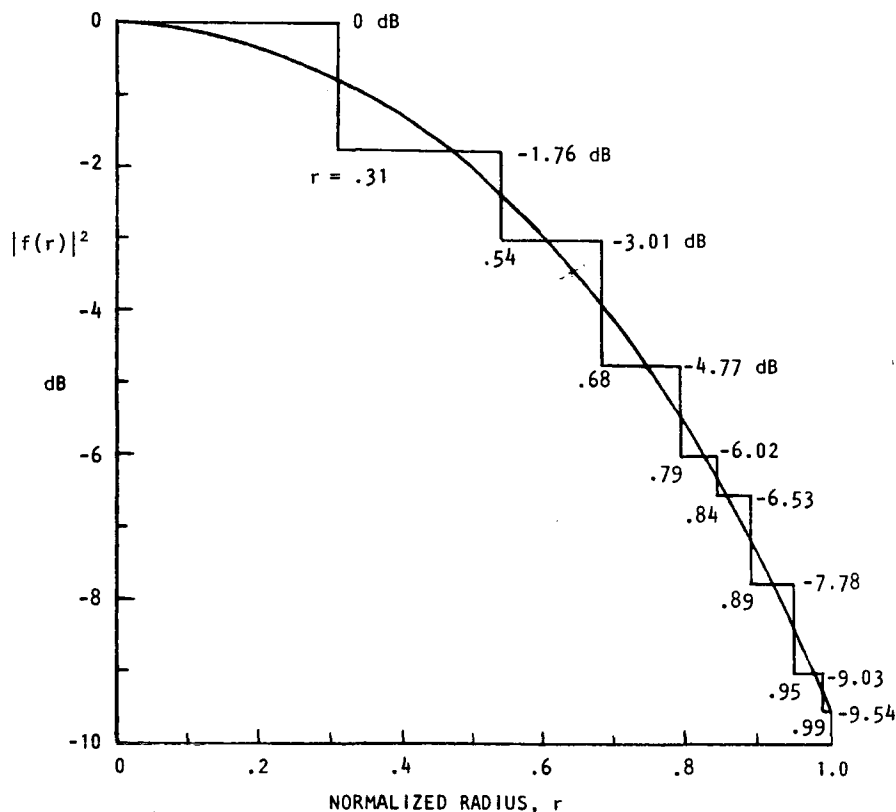
Figure 3.6-59. Nine-Step Approximation to Hansen
Aperture Distribution Truncated at -9.54 dB

In the RCR the loss will be smaller because inner waveguide walls are eliminated; it turns out that this simply has the effect of making the second term within the square brackets above essentially negligible. As a result, loss in the RCR's is only about 2.6×10^{-4} dB/cm in the direction perpendicular to the feed waveguide.

For type 1 power modules the RCR length is 69.2 cm, hence loss within the RCR is only 0.018 dB. The total length of waveguide in the feed and hybrid network is also about 70 cm, so that feeder loss amounts to 0.022 dB. Thus the total theoretical loss in a type 1 power module is .040 dB or about 0.9%. The losses are higher in other power modules, reaching .095 dB in the type 9 module. Using equations (3.6-1) and (3.6-2) to obtain an integrated value for ohmic loss over the whole array gives η_H = 0.988 $\simeq$ 0.99.

Thermal Analysis of Tube Heat Dissipation

The problem of getting rid of waste heat generated by the magnetron tubes is most severe for type 1 power modules. The operating power level of the tubes, and ultimately the total amount of RF power radiated by the spacetenna, are governed by the amount of heat which can be dissipated while maintaining a safe operating temperature at the magnetron anodes.

Discussions with Raytheon investigators, and a study of their report
No. 4 (Reference 38) have established 300°C as the upper limit for magnetron
anode block temperature. The temperature at the vane tips will be considerably
higher than the 300°C at the anode block, and vapor pressure in the interaction
region may become excessively high if this temperature is exceeded. Although
the samarium-cobalt permanent magnets have a Curie temperature considerably
above 300°C the likelihood of metallurgical changes and increased mobility of
lattice defects becomes a factor above this temperature. Finally, the thermal
conductivity of pyrolytic graphite, selected as the heat radiating material,
begins to decrease at temperatures above 300°C.

No doubt copper discs could dissipate waste tube heat, but the weight
penalty would be excessive. Aluminum is another possibility and a brief trade
study of the use of this material is given later. For the present, pyrolytic
graphite (PG) has been chosen for the radiating discs, following the recommend-
ation of the Raytheon investigators. In the directions of its A-B axes this
material has a thermal conductivity greater than that of aluminum and about
equal to that of copper, yet its density is only 2.2 g/cm^3 compared to 8.9 g/
cm^3 for copper and 2.8 for aluminum.

The model used for thermal analysis is shown in Figure 3.6-60. The thick-
ness of the pyrographite disc has been taken to be constant and equal to 3 mm.
For type 1 modules, adjacent discs are assumed to be touching, which limits
disc diameter to 34.6 cm. Assumptions underlying use of the model shown
schematically in the figure are the following:
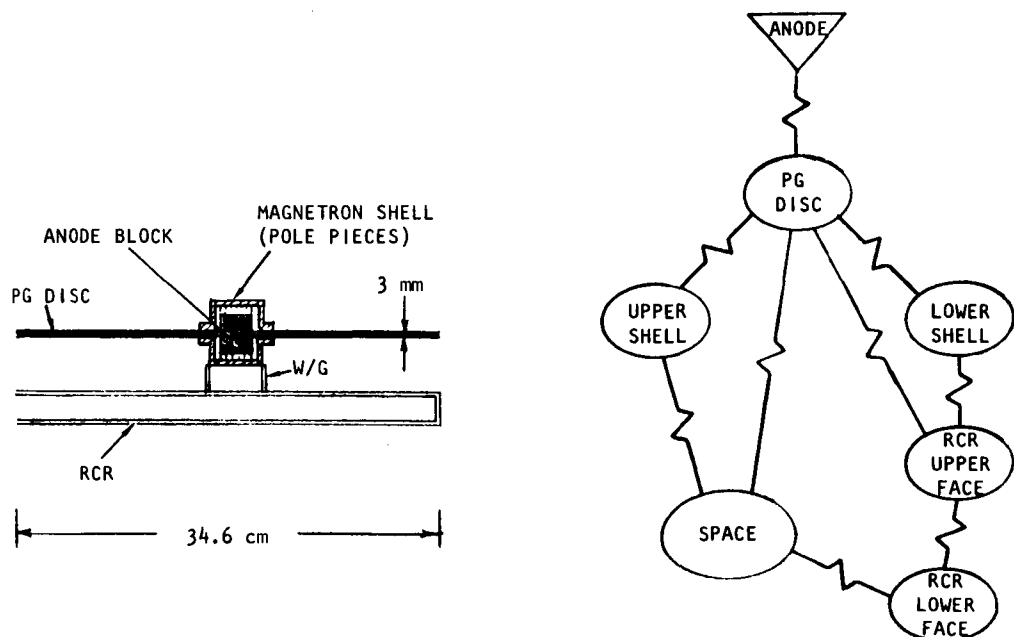
Figure 3.6-60. Model for Thermal Analysis of
Magnetron Tube Heat Dissipation

• Direct solar heating ignored

• Magnetron heat concentrated at anode and transferred by
  conduction to PG disc

• PG disc radiates to space and to upper face of RCR

• Other heat paths as shown

• Upper RCR surface is reflective with ρ = 0.9

• Inner and lower RCR surfaces treated to give α = ϵ = 0.9.

The results of the analysis are given in Table 3.6-25, in which tempera-
ture at various locations are shown for four different values of waste heat
dissipation.

Table 3.6-25. Results of Thermal Analysis

WASTE HEAT DISSIPATED (WATTS)	TEMPERATURE (°C) AND LOCATION				
	ANODE BLOCK	UPPER SHELL	LOWER SHELL	UPPER FACE RCR	LOWER FACE RCR
333	282	206	279	32	-2
444	324	242	320	55	0
529	350	265	346	70	12
706	397	305	393	95	33

After plotting these results for purposes of interpolation it is found
that a temperature of 300°C at the anode block corresponds to a waste heat
dissipation level of 390 watts. Under these same conditions the upper face
of the RCR is at 44°C while the lower face is at about -1°C.

In order to establish magnetron operating level, a tube conversion effi-
ciency of 0.90 is projected. To justify this projection it is noted that the
highest measured efficiency to date for a magnetron of the type required is
0.85 (Reference 41). The improvement needed to reach the level 0.90 is 6% and
is felt to be realistic by Raytheon investigators. By way of contrast, the
klystron reference concept assumes that tube efficiency, using depressed
collector techniques, can be increased to 0.85, which is 14% above the best
reported efficiency to date, namely 0.744.

It follows at once that a tube having 90% efficiency and dissipating
390 watts of heat will have an RF output level of 3.5 kW.

The weight of pyrographite in the disc of Figure 3.6-60 is 616 grams. It
is clear that this could be halved if the disc thickness were tapered from 3 mm
at the center to a sharp edge at the rim. Of course this would entail a reduc-
tion in heat radiating efficiency but certainly not in proportion to the reduc-
tion in mass. At the time that this modification was incorporated into the
thermal model it was learned from Raytheon report No. 4 (Reference 38) that
the thermal conductivity of pyrolytic graphite is significantly increased by
heat treatment at 2900°C for two hours. The new value of conductivity is
about 795 watts m^{-1}K^{-1} at 300°C, compared to 380 watts m^{-1}K^{1} for copper. The
net result is that the cooling efficiency of the tapered disc is not reduced

at all if heat-treated PG is used. Thus, the mass of the PG disc is reduced
to 310 grams.

It was noted above that a temperature difference of 45°C exists between
the top and bottom faces of the RCR. This can cause the RCR to warp so that
its faces become curved surfaces. The departure from planarity is approximately
given by

$$\pm \frac{\alpha \ell^2 \Delta T}{16b}$$

where ℓ and b are the RCR dimensions (69.2 and 2.0 cm), α is the coefficient
of linear expansion (2.4×10^{-5} per °C for aluminum) and $\Delta T = 45$°C. This turns
out to be ±0.16 cm or ±4.7° in electrical phase angle. This small perturbation
can be eliminated altogether by predistorting the RCR.

Magnetron Tube Description and Performance Characteristics

This section is a brief summary of pertinent magnetron tube character-
istics that are described in considerably greater detail in the Raytheon
reports of **Reference 38.**

Physically the tube will be very much like the modified oven magnetron*
shown in Figure 3.6-61 and mounted on a section of WR340 waveguide. Overall
dimensions are expected to be about 8 cm in diameter by about 7 cm high,
exclusive of pyrolytic graphite heat radiator. In the photograph of Figure
3.6-61 the heater leads are at the top, and the steel pole pieces, or shells,
enclose the magnetron anode, the samarium-cobalt magnets and a buck-boost coil
whose leads are brought out at the right. The tube has a coaxial output ter-
minating in a probe coupler inside the waveguide. In the SPS version of the
tube a pyrographite disc will replace the water-cooled copper tubing shown in
the photograph. The heater/cathode is simply a helical coil of thoriated
tungsten wire.

Anode Voltage and Current

The operating anode voltage and current for a 3.5 kW tube can be obtained
from the curves in figure 10 of the Raytheon report No. 4 of **Reference 38.**
First, however, it is noted that microwave circuit losses amount to 4% while
another 1% loss occurs due to electron back bombardment which maintains
cathode temperature after the heater power is turned off. Thus, to obtain
an overall efficiency of 90% requires an electronic efficiency of 94.7%. The
curves show that this requires an anode potential of almost 20 kilovolts with
a current of nearly 0.2 amperes.

Alternatively, the anode voltage may be obtained from the equation

$$\eta_e = \frac{V - V_o}{V_o}$$

where $V_o = 1038.3$ volts and η_e is the electronic efficiency, .947. This gives
$V = 19,600$ volts. The magnetic field, B, required to be supplied by the
samarium-cobalt magnets can be found from the equation

---

*Photograph supplied by W. C. Brown, Raytheon Co.
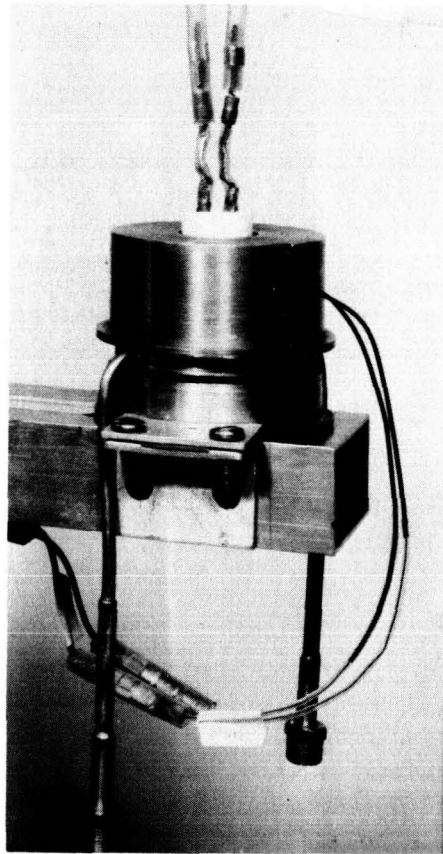
Figure 3.6-61. Typical Magnetron Mounted
on WR340 Waveguide

$$V = V_O \left(\frac{2B}{B_O} - 1 \right)$$

where B_O = 354.7 Gauss. It is found that B = 3524 Gauss.

Feedback Control of Output

Stability and control of the amplitude and phase of the magnetron's output is essential in the SPS application. Raytheon investigators have devised a technique in which a buck-boost coil is used to produce small variations around the mean or static level of magnetic field produced by the samarium-cobalt magnets in the tube itself. With an amplitude sensing device in the tube's output (e.g., directional coupler or loosely coupled probe, plus detector) and suitable feedback amplifiers and circuitry the output power level of the tube can be controlled over a considerable range (e.g., 3 to 4 dB) with little change in tube efficiency. The feedback control may also be applied to hold the output level constant to within tenths of a dB in the face of wide variations (15%) in applied anode voltage. Raytheon reports No's. 3, 4 and 5 of Reference 38 describe these techniques and how they may also be applied to match the magnetron power tube V-I characteristics to those of the solar photovoltaic array in order to optimize performance under varying solar flux conditions. In effect, this means that the magnetrons can always be operated optimally at close to maximum efficiency from an unregulated power supply. Thus the need for complex dc power conditioning is obviated; the magnetrons can run directly off the solar array busses.

Use of feedback to control the **magnetron's output phase has also been** convincingly demonstrated in the course of the above noted Raytheon work. For example, a normal output phase variation of 110° due to a change of 15% in applied anode voltage is reduced to about 2° by the application of feedback. In these demonstrations the output is sampled and compared to a fixed phase reference. In this way a dc error voltage is derived and is used to drive a motor-driven mechanical phase shifter in the magnetron input circuit. Clearly, this technique is somewhat cumbersome and undesirable in the SPS but there are at least two ways in which the motor-driven mechanical phase shifter may be eliminated. For example a varactor diode type of phase shifter could be used, preferably operating at low power level ahead of the magnetron's driver amplifier. Another technique has been suggested by Brown, report No. 5 in reference **38.** It is based upon the observation that the magnetron's free-running frequency is largely determined by its "cavity" dimensions. A change in these dimensions, or introduction of a tuning post, will cause a change in frequency. When operating as an injection locked amplifier the magnetron frequency cannot change in response to a change in "cavity" dimensions or introduction of a tuning device. What happens, instead, is that the magnetron's output phase undergoes a change in response to the "stimulus".

Brown's concept, then, is to utilize a tuning mechanism, which could be built into the tube itself, and whose very small movements are controlled by a small electromagnetic driving coil similar to the voice coil in a loudspeaker. The error signal from the phase sensing network would then be amplified and used to drive a restoring current through the driving coil. A clever design might even utilize the existing magnetic field provided by the samarium-cobalt magnets. This excellent phase-shifting technique turns out to have an additional benefit. Since the tuning mechanism acts in such a way as to cause the tube's free-running frequency to track the driving signal's frequency, the injection locking range is considerably increased. This appears to have important implications for gain and excitation requirements, as discussed in the next section.

It is noteworthy that little power is required by the buck-boost coil in controlling tube output. In one extreme test such a coil was used to maintain high efficiency magnetron amplification over a range of 2:1 in anode voltage. The necessary coil current varied from -2.0 to +2.0 amperes and power consumed by the coil from 0 to 30 watts. Such a drastic change in anode voltage is unlikely ever to occur in SPS operation and it appears that no more than 5 watts of coil power would be sufficient for control purposes.

A "demand-control" concept conceived by Raytheon investigators (report No. 3 of Reference **38)** may prove to be operationally valuable to the overall SPS system. It would make use of the amplitude feedback control circuitry to vary the total amount of power delivered to the grid in such a way as to match the utility's demand for power. It is proposed that this be done by telemetering a command signal from the rectenna site to the spacetenna which will alter the control reference voltage in the feedback circuits. This will have the effect of adjusting the coupling between magnetron tubes and the photovoltaic array in order to change the operating power level in accordance with demand.

Gain and Drive Power Requirements

In the injection locked mode the range of locked operation decreases as
the level of the input signal is decreased. An example of this is to be found
in figures 2, 3 and 4 of Raytheon report No. 5, reference 38. These figures
display V-I curves for a single tube under three different input drive levels,
50, 10 and 2.5 watts. For an essentially constant output power level of 1000
watts the locked ranges of anode voltage at 2450 MHz for the three conditions
are respectively 3400 to 4850 volts, 4400 to 4900 volts and 4650 to 4900 volts.
Thus the range of anode voltage for locked operation as a function of tube
gain may be summarized as:

Tube gain dB	Anode voltage range
13	1.43:1
20	1.11:1
26	1.05:1

A change in anode voltage implies a reciprocal change in anode current
and, owing to the "pushing" characteristic of the magnetron tube, is accompanied
by a change in the tube's free-running oscillation frequency. If this frequency
departs too much from the excitation frequency of 2450 MHz the magnetron falls
out of lock. It was noted in the previous section that the feedback controlled,
electromagnetically driven tuning device proposed by Brown, acts to make the
tube's free running frequency track the excitation frequency. Therefore, devel-
opment of this tuning concept will extend the range of anode voltage over which
locking occurs, permitting use of a low level drive signal and high gain opera-
tion of the tube over an appreciable locking range.

For this reason it appears reasonable to assume that operation at a gain
of 26 dB is feasible and, with the feedback tuning technique, will yield a
reasonably large range of anode voltage (e.g., 1.2:1) over which locking is
assured. The input power required to injection lock a 3.5 kW tube at a gain
level of 26 dB is 8.8 watts, which is within the predicted capability of solid-
state amplifiers in the near future. It is proposed that these driver amplifiers
be located in the narrow spaces between the power modules that form a subarray.
Temperatures in these regions are predicted to be modest, not exceeding about
45°C.

Startup, Heater Shutdown and Lifetime

A startup procedure which makes use of the feedback amplitude control
circuit has been devised and demonstrated experimentally by the Raytheon team
(Report No. 4 of Reference 38). The procedure is as follows:

Step 1. DC anode voltage is applied to the tube but no heater power
is present and the cathode is non-emitting.

Step 2. A reference control voltage is applied to the amplitude feed-
back circuit that results in a relatively high current in the
buck-boost coil. The resulting magnetic field, superimposed
on the static field provided by the permanent magnets, results
in a total magnetic field of a magnitude such that the tube
cannot oscillate at the applied anode voltage even when the
heater power is turned on and cathode emission occurs.

Step 3. Heater power is turned on, the cathode heats up and in about
5 seconds the normal emission level is reached.

Step 4. After 5 seconds of cathode warm-up the heater power is removed
entirely. At the same time the reference control voltage
applied to the feedback circuit is changed to its operating
level. At this point the magnetic field in the tube assumes
its proper operating value and the tube begins to function in
the locked mode.

During the 5 second cathode warm-up period a relatively high heater input
is needed, estimated to be about 65 watts for a 3.5 kW tube. When heater power
is removed and the magnetic field is changing to its correct value there is a
build-up of oscillation in the tube. This transient condition lasts only for
a few milliseconds before the tube settles into stable, controlled amplifica-
tion.

The fact that external heater power is not required after the 5-second
start-up period does not imply cold cathode operation of the tube. Parenthet-
ically, it should be noted that heater and cathode are one and the same—a
simple helical coil of carburized thoriated tungsten wire. The cathode surface
is maintained at the required high electron-emitting temperature by backbombard-
ment, in which some electrons, after acceleration by the field in the tube,
actually return to the cathode where their kinetic energy is converted to heat.
It is well established that the lifetime of such a cathode (operating in a
high vacuum, of course) is a very sensitive function of its operating temper-
ature. For example, a ten-fold increase in life occurs if this temperature
is reduced from 2000 K to 1900 K. The backbombardment heating in a magnetron
tube appears to be governed by a built-in regulatory mechanism which acts to
hold cathode temperature to the lowest value that is sufficient to supply the
necessary anode current. Thus the longest possible lifetime is assured.

Raytheon investigations (Reference 41) indicate that an SPS magnetron tube
could utilize a 50% carburized thoriated tungsten filament winding with wire
diameter of 1 mm (0.040 in.) operating at a temperature that is possibly as low
as 1900 K. Based on current life test data projections, a lifetime of from
30 to 50 years is anticipated.

Output Spectrum of Magnetron

Measurements of the noise power spectrum of any tube operating at high
output power levels are difficult. In the case of the magnetron operating
without external heater power the carrier to noise level is extremely high
and, even with notch filter suppression of the carrier power by at least 49 dB

3-194

in a 20 MHz band, measurements can be limited by the dynamic range of the
spectrum analyzer. Observations by Raytheon investigators on a number of
different tubes (Report No. 5 of Reference 38) show considerable variability
among the devices. Certain tubes have shown a carrier to noise level of at
least 188 dB per Hertz at frequencies outside of a 60 MHz band centered on
the 2450 MHz carrier. Refinements to the measurement technique may indicate
even better performance on the part of selected tubes.

Little information on harmonic content in the output of high-power magne-
trons is available. Some recent measurements (Reference 41) on two tubes show
the following levels of harmonic content, relative to the fundamental.

Harmonic	Level in dB	
	Tube A	Tube B
1	−71	−69
2	−97	< −85
3	−86	−93
4	−62	−64

Overall System Description and Performance Summary

The complete spacetenna is constructed from the nine different subarrays
described above. Type 1 arrays are used in the central region out to normalized
radius r = 0.31, then type 2 arrays to radius r = 0.54, and so on, as indicated
in Figure 3.6-59. Each subarray is a complete entity that includes a solid-
state driver amplifier (~9 watts output) for each of its magnetrons, and a
corporate feed network of RG141 or equivalent semi-rigid coaxial cables with
appropriate power splitters. This corporate feed network branches from a
master phase reference control amplifier (MPCA) as shown in Figure 3.6-58.
Assuming that the solid state drivers have a gain of 25 dB, then input power
per driver is about 30 mW. In a type 1 subarray there are 144 such drivers
with a total input power requirement of 4.3 watts. Allowing for losses in the
coaxial transmission lines of the feed network, an output level of 10 watts
from the MPCA will suffice for the type 1 subarray. Because 144 is not an
integral power of 2, simple binary division cannot be used in the corporate
feed network. However, a combination of binary and ternary dividers will do
the job; for example 4 binary levels plus 2 ternary levels. This is also true
of type 2, 3, 4, 5, 7 and 8 subarrays except that the numbers of binary and
ternary levels will change. The type 6 and type 9 subarrays require only
binary dividers.

When the subarrays are put together to form a complete spacetenna, each
will have to be provided with a source of high voltage (20 kV dc) power for the
magnetron anodes, plus low-voltage power (presumably 10 V dc) for the feedback
circuitry, buck-boost coils, solid state driver amplifiers, and master phase
reference control amplifier (MPCA), as well as for heater power for the short,
5-second, startup period. In addition a 2450 MHz phase reference signal must
be supplied to each subarray whose phase is controlled by suitable phase
conjugation circuitry associated with a pilot tone antenna and receiver that
are also a part of the subarray. No further description of this retrodirective

control system will be given here; it is simply assumed that it is essentially identical to the system used with the klystron reference concept, with minor modifications as needed to suit the magnetron system.

In the klystron reference concept the subarray size is approximately 10×10 m^2, whereas it is only 4.2×4.2 m^2 for the magnetron system. It is therefore proposed that retrodirective phase control be applied to groups of $2 \times 2 = 4$ subarrays in the magnetron system. This will result in an effective subarray size of 8.4×8.4 m^2, which is closer, for comparative purposes, to that of the klystron system.

Spacetenna Performance Characteristics

The design parameters and pertinent pattern characteristics of the spacetenna are given in Table 3.6-26.

Table 3.6-26. Spacetenna Characteristics

CHARACTERISTIC OR PARAMETER	VALUE
APERTURE FIELD	
AMPLITUDE DISTRIBUTION	9-STEP APPROX. TO -9.54 dB HANSEN
PHASE DISTRIBUTION	IDEAL UNIFORM
POWER COEFFICIENT	K = .436
APERTURE EFFICIENCY	η_A = .914
OHMIC EFFICIENCY	η_H = .99
FAR-FIELD PATTERN	
HPBW	1.138 λ/D RADIANS
BEAMWIDTH CONSTANT AT -13.6 dB	B = 2.20
BEAM EFFICIENCY AT -13.6 dB	η_B = .937
FULL WIDTH AT -23.6 dB	2.60 λ/D
FIRST SIDELOBE LEVEL	-23.2 dB

The performance of this antenna when the central power density is limited to $S_T = 28$ kW/m^2 and received power density to $S_R = 230$ W/m^2 can now be readily determined from equations (3.6-4, 3.6-5, 3.6-9, and 3.6-10), using the parameter values given in Table 3.6-26. The results are given below on the assumption that the rectenna is located at latitude 40°, so that the range is $R = 37,500$ km.

- Spacetenna diameter $D_T = 918$ m
- Total RF radiated power $P_T = 8.00$ GW
- Rectenna minor diameter $D_R = 11.0$ km
- Power incident on rectenna $P_R = 7.50$ GW
- Safety fence minor diameter $D_F = 13.0$ km

To see how much power is actually delivered to the utility grid interface under actual conditions, the efficiency chain figures derived for the klystron reference concept will be applied. This requires the following allowances for additional losses:

Random phase errors over spacetenna	.945
Magnetron tube outages	.980
Atmospheric losses	.980
Rectenna conversion efficiency	.880
Switch gear and busses (dc)	.987
DC/AC conversion at rectenna	.960
Switch gear and busses (ac)	.988
Overall efficiency	.7476

Using 7.50 GW for the power incident on the rectenna under ideal conditions and multiplying by .7476 gives 5.61 GW of ac power delivered to the utility grid.

Mass Estimate for Spacetenna

A careful estimate of the masses of all components comprising the space-tenna as described above has been made. Not included in this estimate are the masses of the 20 kV dc busses required for magnetron power, the 10 V dc busses for solid-state circuitry, the pilot tone antennas and receivers and the master phase reference distribution system.

From Report No. 3 of Reference 38, the following estimate of magnetron tube mass has been made:

Magnetic circuit	266 g
Copper anode and vanes	81
Ceramic insulators	30
Output RF line	30
Buck-boost coil	76
Heater/cathode	6
Tuner and drive coil	50
Miscellaneous	57
Total mass	590 g

Each pyrolytic graphite heat radiator has an overall diameter of 34.6 cm and tapers from 0.3 cm thickness at the central hole to 0.05 cm at the edge. With density of 2.2 g/cm^3 the mass is found to be 310 g per disc. Thus, a single magnetron tube, complete with its heat radiator, will have a mass of 900 g or 0.90 kg.

The masses of each type of RCR and waveguide feeder have been calculated using previously noted dimensions and assuming they are fabricated of 0.25 mm (.010 in) thick aluminum. Then, the masses of RCR, tubes and heat radiators were combined to find the total mass for each of the nine kinds of power modules.

Standard subarray masses were next computed using the appropriate number and masses of **modules.** To this was added an allowance to account for the mass of the aluminum frame in which power modules are assembled and mounted. Finally, for each subarray type an estimate was made for the total masses of coaxial feed lines (assumed to be RG-141), solid-state drivers and feedback circuitry, etc. The resulting mass breakdown and totals for the nine different kinds of subarrays are summarized in Table 3.6-27.

Table 3.6-27. Mass Breakdown for Subarrays

| ITEM | MASS IN kg SUBARRAY TYPE | | | | | | | | | TOTAL |
	1	2	3	4	5	6	7	8	9	
MAGNETRON TUBES	85.0	56.6	42.5	28.3	21.2	18.9	14.2	10.6	9.4	286.7
PG HEAT RADIATORS	44.6	29.8	22.3	14.9	11.2	9.9	7.4	5.6	5.0	150.7
RCR, W/G AND FRAME	34.4	31.7	32.5	30.4	29.5	29.8	28.8	28.4	27.8	273.3
COAX LINE AND SOLID-STATE ELECTRONICS	2.2	1.7	1.4	1.1	0.9	0.9	0.8	0.7	0.7	10.4
TOTAL	166.2	119.8	98.7	74.7	62.8	59.5	51.2	45.3	42.9	721.1

The number of a given type of subarray in the full spacetenna is obtained by dividing the area of one subarray (17.64 m^2) into the area of the appropriate zone (i.e., power density step) in the antenna. The areas of the various zones are calculated using the fractional radii indicated in Figure 3.6-59 along with a full diameter of 918 km.

Table 3.6-28 then shows the numbers of each kind of subarray, the total masses of all component sections (tubes, PG discs, RCR's, etc.) and finally the mass of the full spacetenna, namely

3.32×10^6 kg.

The total number of magnetron tubes is 2.35×10^6 and the mass of PG is 729 metric tons.

Table 3.6-28. Mass Breakdown for Spacetenna

| ITEM | | SUBARRAY TYPE | | | | | | | | | TOTALS |
		1	2	3	4	5	6	7	8	9	
NO. OF SUBARRAYS		3606	7335	6409	6067	3058	3246	4142	2912	747	37522
TOTAL MASSES IN kg × 10^3	TUBES	305.9	415.2	272.3	171.9	65.0	61.2	58.6	30.9	7.0	1388.0
	PYRO. GRAPHITE	160.7	218.1	143.1	90.3	34.1	32.1	30.8	16.2	3.7	729.1
	RCR'S & W/G	123.8	232.4	208.3	184.5	90.3	96.6	119.2	82.6	20.6	1158.3
	COAX AND SS ELECTRONICS	7.9	12.5	9.0	6.7	2.8	2.9	3.3	2.0	0.5	47.6
GRAND TOTALS IN kg×10^3		598.3	878.2	632.7	453.4	192.2	192.8	211.9	131.7	31.8	3323.0

Trade Study of Aluminum Heat Radiating Discs

It is of interest to estimate the effect on mass and cost of the space-tenna system if aluminum is used instead of pyrolytic graphite for the heat radiating discs. At 300°C the thermal conductivities of heat treated pyrolytic graphite and aluminum are 795 and 265 watts $m^{-1}K^{-1}$ respectively. Thus PG is the better heat conductor by a factor of 3.0.

Referring to the model of Figure 3.6-60, used for thermal analysis, it is clear that the rate of heat removal from the anode block will be substantially unchanged if an aluminum disc is used instead of graphite, provided that the aluminum disc is three times as thick, in order to make up for its lower heat conductivity. In this case the tube operating level will remain at 3.5 kW and anode temperature at 300°C, just as before. Since the height of the anode cylinder is about 1.0 cm it can accommodate the increased disc thickness. The only concern is that the magnetic pole pieces are forced further apart, thereby increasing the reluctance of the magnetic path. This might necessitate redesign of the magnetic circuit.

The density of aluminum is 2.77 g/cm^3 versus 2.2 g/cm^3 for pyrolytic graphite. Thus the mass of aluminum will be $3.0\times2.77/2.2 = 3.78$ times the mass of graphite. From Table 3.6-28 the total mass of PG is 0.729×10^6 kg, hence the mass of aluminum required will be 2.76×10^6 kg.

Raytheon's estimate of the cost of pyrolytic graphite in report No. 3 of reference 38, works out to $193 per kg or about $60 per disc. Taking transportation costs to be $60 per kg, the total cost for pyrolitic graphite is

$$\$(193+60)\times0.729\times10^6 = \$184 \text{ M} .$$

Taking the cost of the aluminum discs to be $2 per kg the total costs if aluminum radiators are used become

$$\$(2+60)\times2.76\times10^6 = \$171 \text{ M}.$$

Thus, in spite of a very large weight penalty the use of aluminum appears to have a slight cost benefit. Due to the great uncertainty attached to the graphite material cost estimates, this benefit may disappear altogether, or it may become very substantial.

3.7 LASER BEAM INVESTIGATIONS

The following section presents the results of a study to determine the meteorological effect on laser beam propagation as well as a short investigation considering advanced laser concepts. The included text consists of an edited version of the complete report by R. E. Beverly III, consulting physicist, Columbus, Ohio. The complete report is being published under separate cover (Reference 42).

3.7.1 METEOROLOGICAL EFFECTS ON LASER BEAM PROPAGATION

Introduction

Lasers are presently being evaluated as an alternate power beaming technique to microwaves for space-to-earth power transmission. Although a preliminary study (Reference 43) indicates that laser power transmission has the advantages of negligible environmental damage and small land requirements associated with the receptor sites; meteorological conditions influence the transmission efficiency to a much greater extent than with microwaves. With proper selection of laser wavelength, clear-air propagation can be very efficient; however, haze, fog, clouds, and rain can severely attenuate the beam.

This study investigates potential mitigation techniques which may minimize this effect by a judicious choice of laser operating parameters. Using these techniques, the availability of power at selected sites is determined using statistical meteorological data for each site. When technically feasible, siting criteria and laser parameters are defined such that the power availability is comparable to the microwave SPS concept or to conventional electric power plants.

Propagation Characteristics under Various Meteorological Conditions

Physical Mechanisms

The attenuation of laser radiation passing through the earth's atmosphere is termed *linear attenuation* if the processes responsible are independent of the beam intensity. In general, molecular scattering, molecular absorption, aerosol scattering, and aerosol absorption contribute to linear attenuation. To calculate the transmittance of any single laser line in propagating from outside the earth's atmosphere to a terrestrial receptor site, the attenuation coefficient due to each of the above processes must be known at a sufficient number of points along the beam path. This implies the necessity for local atmospheric data as well as basic physical parameters related to absorption and scattering.

If the attenuation depends on the beam intensity, however, the propagation is termed *nonlinear*. The most commonly encountered nonlinear mechanism in connection with high-energy laser propagation is thermal blooming (Reference 44). Thermal blooming is characterized by self-induced spreading, distortion, and bending of the laser beam as a result of molecular and aerosol absorption within the beam path. Absorption leads to heating of the air

causing density and, hence, refractive index gradients which act as a distributed lens. Another nonlinear mechanism is aerosol droplet vaporization. With sufficiently large laser power densities, hole boring through various types of meteorological formations may be affected with a concomitant increase in transmission efficiency.

Mitigation Techniques

A number of high transparency spectral "windows" are present for which laser radiation will propagate from space to earth with only minimal attenuation due to molecular absorption and scattering. The transmission efficiency may be improved during adverse meteorological conditions by (1) selection of wavelength region which minimizes the effects of aerosol absorption and scattering, (2) increasing the elevation of receptor sites, (3) using a vertical propagation path (zenith angle $\theta = 0°$) rather than line-of-sight propagation from a satellite in geosynchronous equatorial orbit ($\theta \approx 50°$), and (4) by hole boring, i.e., vaporization of the aerosol droplets within the beam path.

Wavelength Selection

Preliminary information (References 45, 46, and 47) indicates that operation in the spectral region around 11 μm may reduce and partially mitigate the loss in transmission efficiency caused by light fog and light cloud cover. This phenomenon occurs for two reasons: (1) the real part of the complex refractive index of water has a minimum at about 12 μm, and (2) the aerosol size distribution of certain fogs and clouds decreases more steeply than (particle radius)$^{-2}$ above 7-10 μm radius, thus reducing the scattering and absorption coefficients. Numerical investigations conducted (Reference 45) assumed that all droplets were homogeneous and composed of pure water; furthermore, their data were reported as relative coefficients and ice-crystal clouds were not investigated. All of these restrictions are removed in this study.

The clear-air transmission efficiency (considering molecular absorption only) is, unfortunately, undesirably low everywhere in the 11-μm window, except for high-elevation receptor sites. Alternately, we have identified an extremely high-transmission region around 2 μm in which molecular absorption coefficient of water based droplets. The attenuation due to various types of meteorological aerosols and molecular absorption is extensively investigated in both spectral regions.

Receptor Elevation

The selection of receptor sites at high elevation can reduce the deleterious effects of haze and can mitigate the problems caused at lower elevations (river valleys, coastal regions, etc.) by many types of advection and radiation fogs. In addition, if water vapor is an important molecular absorber for a specific laser line, high elevation receptor sites can "get above" a large fraciton of the humid air in the lower troposphere and result in improved transmission efficiency. However, we must recognize that constraining receptor siting to high elevations may jeopardize the viability of the laser-SPS concept as an alternate energy source.

Zenith Angle

The space-to-earth transmission efficiency for all linear attenuation mechanisms and a propagation zenith angle θ scales as $\exp(-\sec\theta)$. If molecular absorption is strong, for example, operation at a propagation zenith angle of 0° rather than 50° results in a significant improvement in the transmission efficiency. If the laser wavelength is properly optimized, however, vertical propagation does not afford a significant improvement in the power availability (all meteorological conditions considered) and cannot be justified in terms of the increased cost and complexity of the required space hardware. This effect is discussed further in connection with the power availability model.

Hole Boring

Hole boring through monodisperse and polydisperse aerosols has been addressed for both continuous-wave (cw) and pulsed lasers. Numerous theoretical studies and experimental measurements using artificial and natural aerosols have been conducted over a wide range of parameters. Steady-state evaporation, which is the simplest model and which is applicable to small-diameter particles irradiated at lower intensities, assumes that the energy liberated in the droplet is proportional to its volume and the temperature rise in the droplet is uniform (References 48, 49, 50, 51, 52, 53, and 54). Hence, the absorption coefficient is proportional to water content and is independent of the details of the particle-size distribution. Inclusion of diffusion, heat conduction, and Stefan flow in the evaporation model was investigated (References 55, 56, and 57). Introduction of fresh aerosol into the beam path by wind convection was included in the steady-state model (References 58, 59, 60, 61, and 62), including the effects of diffusional blurring. All of the aforementioned effects (diffusion, heat conducting, Stefan flow, and wind) were included in the work of Reference 63. The effects of nonuniform internal temperature profiles were considered in References 64 and 65. Solution of the evaporation equations self-consistently with absorption and scattering coefficients which explicitly depend on the droplet radius was performed (References 66, 67, 68, and 69). At higher intensities, such as obtained with pulse lasers, droplet explosion can occur (References 56, 69, and 70). This process is considerably more efficient than simple evaporation and can reduce the energy requirement necessary to clear a given volume.

Using hole-boring models applicable to the range of laser-beam parameters of interest for power transmission, we have estimated the power densities necessary to affect aerosol clearing under various meteorological conditions. Laser hole boring through certain types of hazes, fogs, and clouds may be possible consistent with safety and environmental concerns. In particular, all but the thickest cirriform clouds and all stratiform clouds with the exception of nimostratus can be penetrated without the need for weapon-quality beams. For lasers operating in the 11-μm window, cw power densities of 100 to 200 W/cm^2 are required. Because of the small aerosol absorption coefficient in the 2-μm window, hole boring at these wavelengths using a cw beam alone will be ineffective. A train of short-duration pulses superimposed on the "main" cw beam will, however, affect penetration under these circumstances. More detailed calculations are given in the section describing the power availability model.

Several other physical mechanisms must be considered in conjunction with hole boring. Intensity fluctuations can be induced by temperature and water-vapor gradients within the beam path (References 71 and 72), and gross refractive bending of the beam can be enhanced under certain conditions by droplet vaporization (References 73, 74, 75, 76, 77, and 78). For laser-power transmission, intensity fluctuations which do not result in significant beam spreading should be of no concern. We have examined the regime in which refractive bending occurs and found that severe distortion should be negligible for the power densities and beam diameters under consideration here. Another phenomenon which has been recently considered is droplet recondensation in a laser-vaporized path. Overheating of the particles produces local supersaturation, resulting in the production of a large number of fine particles which may attenuate the beam and limit its penetration (References 79, 80, and 81). This effect is pronounced at higher radiation intensities, for larger particles, and at lower temperatures. Again, for conditions anticipated here, this effect should not occur.

Propagation Calculations—Aerosols

Models

Aerosol scattering, absorption, and extinction coefficients and differential scattering cross-sections were calculated for haze, advection and radiation fogs, various types of clouds, and rain and snow distributions at various precipitation rates. These calculations require detailed properties of the various aerosols, such as composition, size distribution, particle concentration, and complex index of refraction as a function of wavelength. Index of refraction data is given in Table 3.7-1. For the calculations involving haze, absorption and scattering coefficients for the various aerosol models were taken directly from Reference 82. For most types of fogs and precipitation, it is a good approximation to assume that the particles consist of pure water with the appropriate index of refraction data from Table 3.7-1. For clouds, which consist of nuclei surrounded by condensed water, this assumption may not be valid. Several different compositions are modeled in the present study.

In the Mie scattering regime, scattering, absorption, and extinction coefficients and differential scattering cross-sections are calculated using the code HSPHR developed in Reference 83. The code is restricted to spherical particles but does have provisions for heterogeneous compositions in which a spherical nucleus of radius a_0 and complex index of refraction n_0 is surrounded by a second material having a concentric radius a and complex index of refraction n. The code was modified by the author to allow modeling of dispersive particle distributions. Graphical plotting capabilities were also added. Theoretical treatments of the Mie problem are well documented in the literature and will not be repeated here. The method adopted here is the classical numerical treatment given in Reference 84, and the interested reader is referred to this reference for further details.

For large particles, such that $2\pi a/\lambda \gg 1$, a geometrical optics model may be used. Although the Mie program will work for large particles, it is unnecessary and wasteful of computer time since the time required per problem is

3-203

Table 3.7-1. Complex Refractive Indices (n=n'-ik) for
Characteristic Components of Aerosol Particles*

Wavelength (μm)	Water soluble fraction		Water insoluble fraction		Sea salt		Soot		Water	
0.2000	1.530	0.070	1.530	0.070	1.450	0.000			1.396	0.000
0.2500	1.530	0.030	1.530	0.030	1.450	0.000			1.362	0.000
0.3000	1.530	0.008	1.530	0.008	1.450	0.000			1.349	0.000
0.3371	1.530	0.005	1.530	0.008	1.450	0.000			1.345	0.000
0.4880	1.530	0.005	1.530	0.008	1.450	0.000	1.560	0.490	1.335	0.000
0.5145	1.530	0.005	1.530	0.008	1.450	0.000	1.560	0.490	1.334	0.000
0.5500	1.530	0.005	1.530	0.008	1.450	0.000	1.570	0.500	1.333	0.000
0.6328	1.530	0.006	1.530	0.008	1.450	0.000	1.570	0.480	1.332	0.000
0.6943	1.530	0.007	1.530	0.008	1.450	0.000	1.570	0.480	1.331	0.000
0.7000	1.530	0.007	1.530	0.008	1.450	0.000	1.570	0.480	1.331	0.000
0.8000	1.524	0.010	1.524	0.008	1.450	0.000	1.570	0.480	1.329	0.000
0.8600	1.520	0.012	1.520	0.008	1.450	0.000	1.580	0.490	1.329	0.000
0.9100	1.520	0.013	1.520	0.008	1.450	0.000	1.590	0.510	1.328	0.000
1.0600	1.520	0.017	1.520	0.008	1.450	0.000	1.610	0.540	1.326	0.000
1.1300	1.519	0.018	1.502	0.008	1.450	0.000	1.620	0.540	1.325	0.000
1.5360	1.510	0.023	1.400	0.008	1.450	0.000	1.660	0.570	1.318	0.000
1.7000	1.478	0.018	1.351	0.008	1.450	0.000	1.680	0.580	1.315	0.000
2.0000	1.420	0.008	1.260	0.008	1.450	0.000	1.720	0.600	1.306	0.001
2.1600	1.420	0.009	1.234	0.008	1.450	0.000	1.740	0.610	1.298	0.000
2.4000	1.420	0.011	1.196	0.009	1.450	0.000	1.770	0.620	1.279	0.001
2.5000	1.420	0.012	1.180	0.009	1.425	0.007	1.780	0.620	1.261	0.002
2.6000	1.410	0.034	1.180	0.011	1.414	0.009	1.790	0.610	1.242	0.003
2.7000	1.400	0.055	1.160	0.013	1.410	0.012	1.790	0.610	1.188	0.019
2.8000	1.407	0.044	1.173	0.013	1.418	0.014	1.800	0.610	1.142	0.115
2.9500	1.417	0.027	1.163	0.012	1.527	0.006	1.810	0.610	1.292	0.298
3.0000	1.420	0.022	1.160	0.012	1.607	0.005	1.820	0.600	1.371	0.272
3.1500	1.428	0.011	1.205	0.011	1.520	0.003	1.820	0.590	1.483	0.135
3.2000	1.430	0.008	1.220	0.010	1.509	0.002	1.820	0.590	1.478	0.092
3.3923	1.430	0.007	1.260	0.013	1.489	0.002	1.830	0.570	1.422	0.021
3.5000	1.450	0.005	1.280	0.011	1.485	0.002	1.830	0.570	1.400	0.009
3.7500	1.452	0.004	1.270	0.011	1.476	0.001	1.840	0.590	1.369	0.004
3.8000	1.453	0.004	1.268	0.011	1.474	0.001	1.840	0.590	1.364	0.003
4.0000	1.455	0.005	1.260	0.012	1.476	0.002	1.850	0.600	1.351	0.005
4.5000	1.460	0.013	1.260	0.014	1.486	0.004	1.850	0.580	1.332	0.013
4.7300	1.455	0.014	1.251	0.016	1.478	0.003	1.850	0.580	1.330	0.016
5.0000	1.450	0.016	1.240	0.018	1.465	0.003	1.850	0.570	1.325	0.012
5.3000	1.444	0.017	1.228	0.020	1.449	0.003	1.870	0.540	1.312	0.010
5.5000	1.440	0.018	1.220	0.021	1.439	0.003	1.900	0.530	1.298	0.012
5.9000	1.416	0.022	1.164	0.034	1.423	0.011	1.950	0.500	1.248	0.062
6.0000	1.410	0.023	1.150	0.037	1.429	0.015	1.960	0.490	1.265	0.107
6.2000	1.430	0.027	1.142	0.039	1.574	0.022	1.980	0.510	1.363	0.088
6.5000	1.460	0.033	1.130	0.042	1.479	0.005	2.000	0.540	1.339	0.039
7.0000	1.417	0.059	1.323	0.051	1.449	0.006	2.040	0.510	1.317	0.032
7.2000	1.400	0.070	1.400	0.055	1.439	0.008	2.060	0.520	1.312	0.032
7.9000	1.200	0.065	1.150	0.040	1.404	0.018	2.090	0.560	1.294	0.034
8.2000	1.010	0.100	1.130	0.074	1.413	0.022	2.120	0.630	1.286	0.035
8.5000	1.300	0.215	1.300	0.090	1.461	0.027	2.160	0.730	1.278	0.037
8.7000	2.400	0.290	1.400	0.100	1.566	0.029	2.190	0.820	1.272	0.038
9.0000	2.560	0.370	1.700	0.140	1.667	0.028	2.220	0.980	1.262	0.040
9.2000	2.200	0.420	1.720	0.150	1.627	0.026	2.230	1.070	1.255	0.042
9.5000	1.950	0.160	1.730	0.162	1.584	0.022	2.250	1.150	1.243	0.044
10.0000	1.820	0.030	1.750	0.162	1.534	0.016	2.300	1.290	1.218	0.051
10.5910	1.760	0.070	1.620	0.120	1.510	0.014			1.179	0.072
10.7000	1.749	0.065	1.620	0.116	1.506	0.014			1.172	0.078
11.0000	1.720	0.050	1.620	0.105	1.494	0.014			1.153	0.097
12.0000	1.670	0.053	1.545	0.103	1.466	0.015			1.111	0.199
12.4900	1.646	0.054	1.508	0.101	1.428	0.017			1.123	0.258
13.0000	1.620	0.055	1.470	0.100	1.412	0.019			1.146	0.305
14.8000	1.400	0.100	1.570	0.100	1.434	0.030			1.258	0.396
15.0000	1.420	0.200	1.570	0.100	1.440	0.032			1.270	0.402
17.2000	2.080	0.240	1.630	0.100	1.668	0.064			1.386	0.429
18.5000	1.850	0.170	1.648	0.120	1.737	0.113			1.443	0.421
19.5000	2.030	0.203	1.669	0.187	1.750	0.138			1.476	0.404
20.0000	2.120	0.220	1.680	0.220	1.747	0.149			1.480	0.393
25.0000	1.880	0.280	1.970	0.248	1.738	0.214			1.531	0.356
27.9000	1.840	0.290	1.890	0.320	1.744	0.251			1.549	0.339
30.0000	1.820	0.300	1.800	0.420	1.745	0.279			1.551	0.328
32.0000	1.860	0.340	1.840	0.452	1.741	0.383			1.546	0.324
35.0000	1.920	0.400	1.900	0.500	1.735	0.553			1.525	0.336
40.0000	1.860	0.500	2.100	0.600	1.707	0.000			1.519	0.385

(REFERENCE 50)

proportional to $2\pi a/\lambda$. Hence, for most types of rain we can use the geometrical optics model as outlined below.

The visibility or, more precisely, meteorological range as used in this study is defined by Koschmieder's relation

$$R_m = \frac{1}{\beta_{sc}} \ln \frac{1}{0.02} = \frac{3.912}{\beta_{sc}} \qquad (3.7-1)$$

where β_{sc} is the aerosol scattering coefficient at 0.55 μm, chosen because the peak sensitivity of the human eye occurs at this wavelength. The use of β_{sc} instead of β_{ex} (extinction coefficient) implies that the absorption coefficient (β_a) is small enough to neglect at visual wavelengths, a good assumption except for polluted air. From the foregoing relation, it is evident that the transmittance for a path length equal to R_m is 0.02. Table 3.7-2 gives values of the meteorological range and scattering coefficient for the indicated meteorological conditions.

Table 3.7-2. Meteorological Range
and Scattering Coefficient*

Code no.	Weather condition	Meteorological range, R_m		Scattering coefficient, β_{sc} (km^{-1})
		metric	English	
0	Dense fog	< 50 m	< 50 yd	> 78.2
1	Thick fog	50 m	50 yd	78.2
		200 m	219 yd	19.6
2	Moderate fog	200 m	219 yd	19.6
		500 m	547 yd	7.82
3	Light fog	500 m	547 yd	7.82
		1000 m	1095 yd	3.91
4	Thin fog	1 km	1095 yd	3.91
		2 km	1.1 nmi	1.96
5	Haze	2 km	1.1 nmi	1.96
		4 km	2.2 nmi	0.954
6	Light haze	4 km	2.2 nmi	0.954
		10 km	5.4 nmi	0.391
7	Clear	10 km	5.4 nmi	0.391
		20 km	11 nmi	0.196
8	Very clear	20 km	11 nmi	0.196
		50 km	27 nmi	0.078
9	Exceptionally clear	> 50 km	> 27 nmi	0.078
—	Pure air	277 km	149 nmi	0.0141 (β_{sc})

*Reference 85

Haze

The atmospheric transmission efficiency for hazy conditions was calculated using representative aerosol models selected from the work of Reference 82. The vertical distribution of the aerosol extinction coefficient at 0.55 μm for the different models is shown in Figure 3.7-1. Between 2 and 30 km, where a distinction is made on a seasonal basis, the spring-summer conditions are indicated by a solid line and fall-winter conditions by a dashed line. A computer code was written to calculate transmission efficiency for space-to-earth
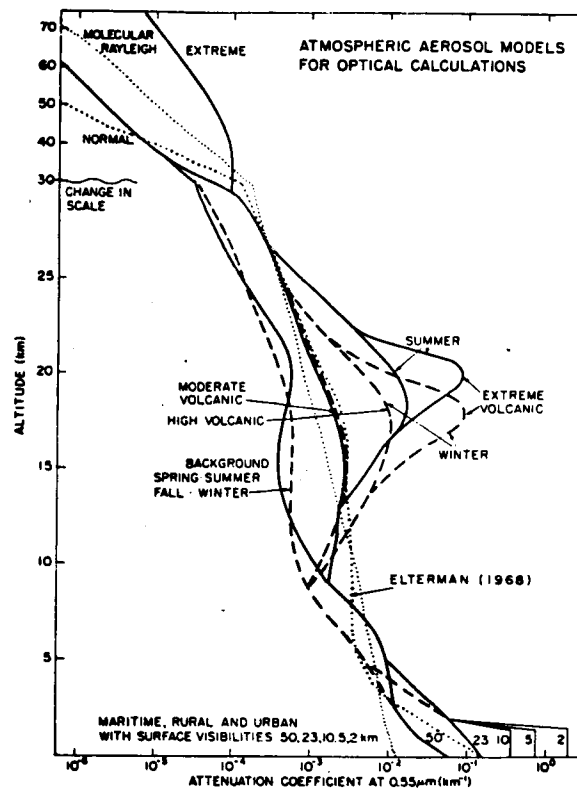
Figure 3.7-1. The Vertical Distribution
of the Aerosol Extinction *

propagation to an elevation h given the wavelength λ, zenith angle θ, and surface visibility R_m. For clear conditions ($R_m = 23$ km) as shown in Figure 3.7-2. The solid curves denote $\theta = 0°$ and the dashed curves are for $\theta = 50°$. The actual aerosol models employed for each atmospheric layer are given in the figure inserts. These curves show little fine structure as would be expected, since molecular absorption has been neglected. We can conclude that selection of a laser wavelength shorter than about 2 μm is undesirable for propagation through haze. Furthermore, Rayleigh (molecular) scattering becomes significant at shorter wavelengths, scaling as λ^{-4}, and visible lasers would suffer attenuation due to this mechanism as well as because of haze aerosol extinction.

The transmission efficiency as a function of altitude for propagation at a zenith angle of 50° under clear and hazy conditions is shown in Figure 3.7-3. Clearly, receptor siting at elevations $h \geq 1$ km is desirable to partially mitigate the effects of haze.

Fog

It has been recently shown (Reference 86 and 87) that a linear relationship, independent of the form of the size distribution, exists between infrared extinction and liquid water content of fogs under many conditions. The relation is given by
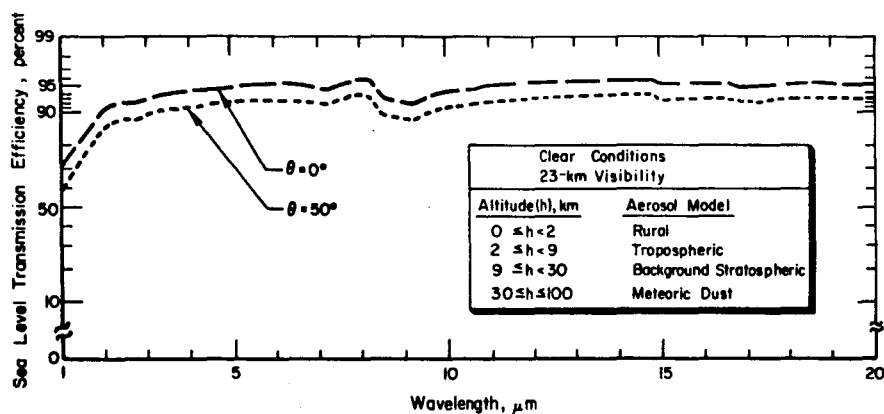
Figure 3.7-2. Transmission Efficiency for Space-to-Earth
Propagation to Sea Level Under Clear Atmospheric Conditions
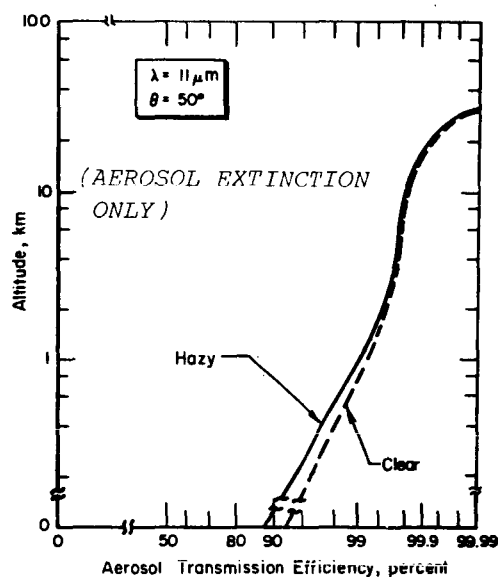
Figure 3.7-3. Space-to-Earth Transmission Efficiency
as a Function of Altitude

$$\beta_{ex} = \frac{3\pi c}{2\rho\lambda}\, W, \tag{3.7-2}$$

where W is the liquid water content, ρ is the density of water, and c is the
slope of a straight line that approximates the Mie extinction efficiency
curve $Q_{ex}(\chi,\lambda)$ by

$$Q_{ex}(\chi,\lambda) \simeq c(\lambda)\chi \tag{3.7-3}$$

where $\chi = 2\pi a/\lambda$ is the size parameter. The approximately linear relation
between Q_{ex} and χ holds below some cutoff value χ_m, and as long as a signific-
ant fraction of the particle distribution curve has $\chi \leq \chi_m$, then relation (3.7-2)

3-207

is a good approximation. Now χ_m is largest for λ = 10-11 μm and, thus, many fog distributions obey relation (3.7-2) using c ≃ 0.3 with good accuracy. The largest χ_m corresponds to a_m = 14 μm; either above or below λ = 10-11 μm, χ_m and, hence, a_m are smaller, placing greater restrictions on the fog distributions for which relation (3.7-2) is applicable. In a similar manner, the absorption coefficient β_a can be related to liquid water content, although the numerical values of c and χ_m are different.

Rather than using Equation (3.7-2) in the present study, we have taken the Mie calculations of (Reference 87) for four liquid water contents and replotted the extinction and absorption data as functions of wavelength. The fog measurements judged to be reliable were chosen to represent a wide range of conditions ranging from maritime and continental advection fogs (References 88, 89 and 90) to inland radiation fogs (Reference 90, 91, 92 and 93). The result of one of these calculations is shown in Figure 3.7-4.
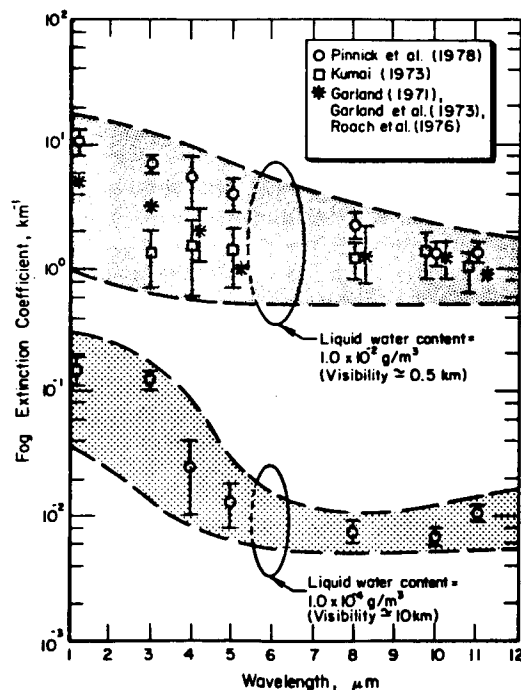
Figure 3.7-4. Calculated Extinction Coefficients
for Code 2 and Code 6 Fogs

This figure shows that laser operation at a wavelength around 11 μm may be effective in partially mitigating the effects of light fog as has been confirmed experimentally (References 94 and 95). The minimum scatter in these data around 11 μm is in conformance with the fact that χ_m is largest in this vicinity and the explicit details of the size distributions have less influence on β_{ex}. As the water content increases, accompanied by a decrease is visibility, the minimum in β_{ex} near 11 μm disappears and the extinction coefficient is nearly flat with wavelength.

In addition, fog banks are not homogeneous and may display considerable vertical structure. The trend toward increasing concentration of larger droplets with increasing altitude, found in Reference 93, for inland radiation fogs near Grafenwöhr, West Germany is in agreement with measurements of advection fogs over San Francisco in Reference 96. Other continental fogs, notably those of Reference 97 for fogs in the Chemung River Valley in New York, show directly contradictory behavior. Clearly, average fog bank properties must be adopted for the present study.

Clouds

Because many of the candidate receptor sites are subject to extended periods of cloudiness, these meteorological formations may be responsible for the greatest decrease in power availability. The wide variety of cloud types taken with the difficulties inherent in determining statistical information related to cloud thickness and receptor obscuration frequency, make any calculation of transmission efficiency and power availability subject to a large error. Guidelines for this evaluation are developed in the section describing the power availability model; for the present purpose, however, we wich to examine the effects of the choice of wavelength on the absorption and scattering coefficients.

Using size distribution data given by the references in Table 3.7-1 as input to the Mie scattering code NSPHR, β_a, β_{sc}, and β_{ex}, and the forward and backward angular scattering coefficients, k_f and k_b, were calculated for a variety of the middle- and low-level cloud types. Two particle compositions were modeled: (1) homogeneous particle polydispersions of pure water, and (2) heterogeneous particle polydispersions consisting of nuclei of fixed radius a_0 surrounded concentrically by liquid water. Hence, the thickness of the liquid water shell varies according to the particle size distribution while the diameter of the nuclei remain constant. Nuclei models used in the heterogeneous aerosol calculations were taken from Reference 98 and their parameters are given in Table 3.7-3. There are many different processes which generate the aerosol particles comprising cloud nuclei. Each generating process, called a "mode," produces particles of a certain chemical composition within a limited size range. Continental air masses are seldom characterized by a single mode; but, because of mixing, different air masses have different proportions of the various modes.

Comparisons were made between homogeneous (water mode) and heterogeneous particle models for two cloud types—cumulus and cumulonimbus—which are representative of cloud distributions having only small particles (a < 20 μm) and those having a significant fraction of larger particles with a > 20 μm. The wavelength dependencies of the absorption and extinction coefficients for a typical mode are shown in Figure 3.7-5, respectively. The presence of nuclei strongly influences the behavior at shorter wavelengths, whereas negligible differences exist between calculated coefficients at wavelengths longer than about 5 μm. The extinction coefficient as a function of wavelength for $\lambda \lesssim 9$ μm is relatively constant for homogeneous (water mode) particle calculations. For particle distributions with small-diameter nuclei, however, the extinction coefficient decreases with decreasing wavelength for $\lambda < 5$ μm. When the nuclei diameter increases, as with the coarse particle mode, the extinction

Table 3.7-3. Nuclei Models Used in Heterogeneous
Aerosol Calculations

Aerosol description	Type*	Nuclei radius (a_0), μm	Mass fractions Water soluble	Mass fractions Water insoluble
Nuclei mode	1	0.015	0.8	0.2
Accumulation mode				
Rural, average	2	0.05	0.7	0.3
Normal, mode average	3	0.1	0.8	0.2
Coarse particle mode				
Normal, mode average	5	2.0	0.4	0.6

*According to the classification proposed in Reference 98.

WATER MODE
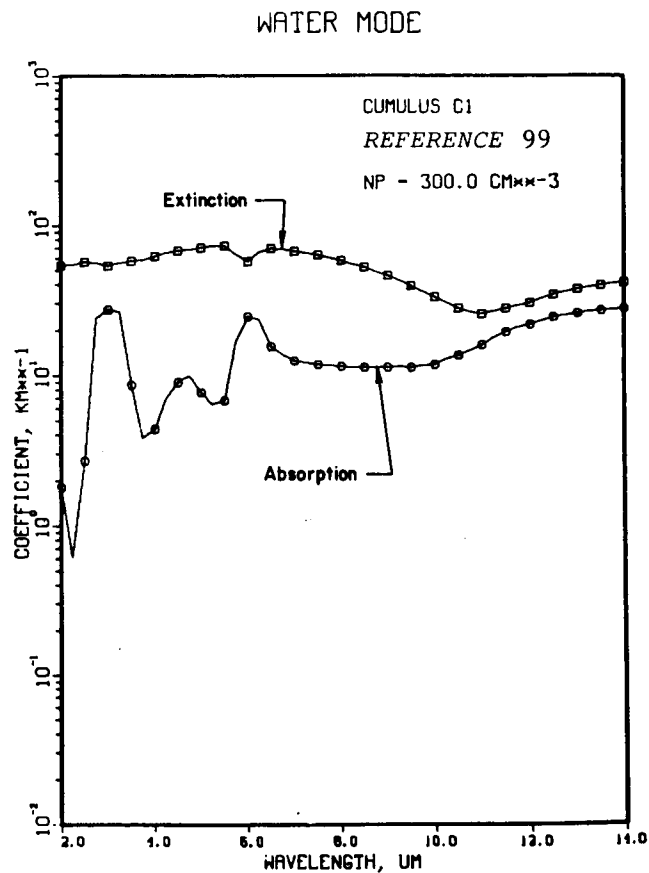
Figure 3.7-5. Wavelength Dependencies of Absorption and
Extinction Coefficiencies for a Typical Mode

coefficients at these shorter wavelengths increase in magnitude. We note that observational measurements do not show a decrease in β_{ex} with decreasing wavelength as predicted by the accumulation mode, which may result from certain experimental anomalies or, more likely, from the assumption in the present models, i.e., use of constant-diameter nuclei.

Because of the uncertainties inherent in the heterogeneous particle models (especially at shorter wavelengths), we have performed calculations for all remaining low- and medium-level clouds using the water mode. The assumption that cloud particles are homogeneous and composed entirely of pure water is perfectly acceptable in the middle- and far-infrared spectral regions and is subject to error only for UV, visible, and near-infrared wavelengths.

Particle size distributions taken from Reference 100, respresentative of many of the cloud types modeled here, are shown in Figure 3.7-6. All distributions were divided into as many as 20 bins for numerical input to the code, and the wavelength interval from 2 μm to 14 μm was spanned in 0.25-μm increments. Calculational results for a typical cloud type is shown in Figure 3.7-7. Water mode calculations were checked for numerical accuracy by using the particle distributions of Reference 101, and comparing our results (Figure 3.7-7) with published results (Figure 3.7-8). The agreement is excellent.
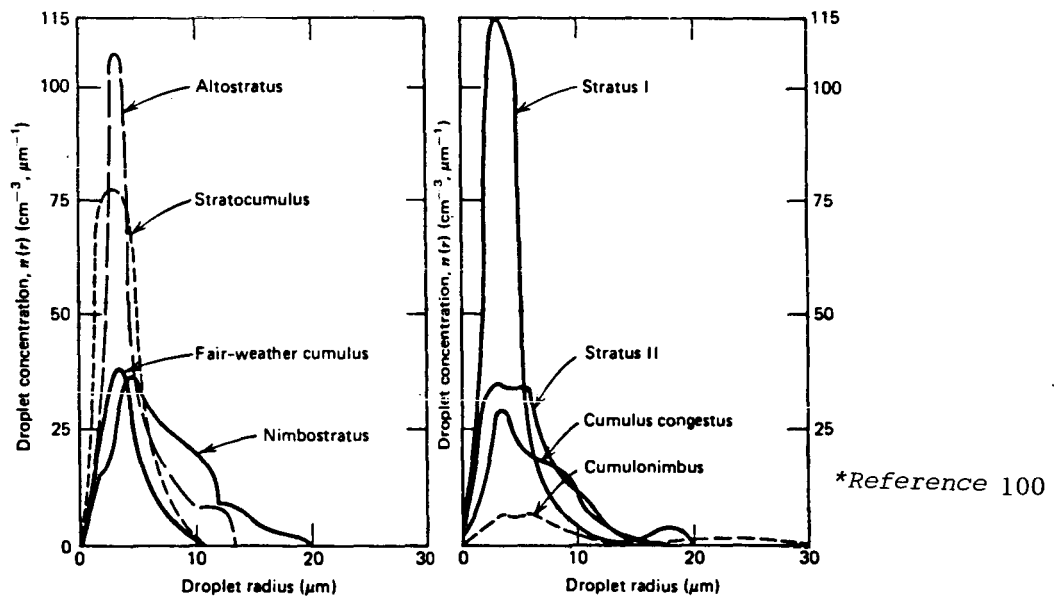
*Reference 100

Figure 3.7-6. Representative Particle Size Distributions
for Various Cloud Types *

As noted (Reference 45), a significant reduction in β_{ex} occurs around 11 μm for clouds in which the large-particle distribution decays more rapidly than a^{-2}. This effect is particularly noticeable in calculations for altostratus, stratocumulus, and stratus clouds (Figure 3.7-7). Clouds characterized by a greater proportion of larger particles, e.g., nimbostratus and cumulonimbus show little improvement in β_{ex} at 11 μm. Alternately, operation at a laser wavelength near 2.25 μm may offer improved transmission through

WATER MODE
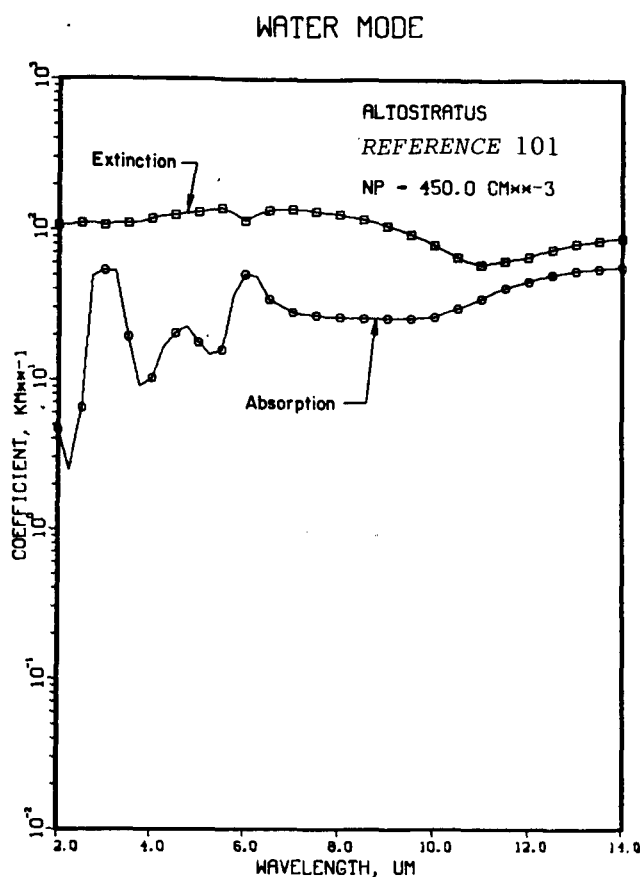
Figure 3.7-7. Altostratus Extinction and
Absorption Coefficients

thin clouds because of the minimum in β_a. Operation at even shorter wavelengths
is undesirable because of the increased attenuation due to haze and molecular
scattering. Tabulated absorption and extinction coefficients for the two
spectral windows of interest are given in Table 3.7-4.

All of the thicker cloud types (especially cumuliform types) are highly
attenuating and are impenetrable unless hole boring at very high intensities
is employed. Those cloud types which are characteristically thinner, such as
middle and stratiform types, can be partially transparent.

Calculation of the transmission efficiency through such formations should
use forward-scattering corrections since Mie scattering from cloud particles
is predominately in a forward direction. While this correction may result in
a change in the transmission efficiency of perhaps 20%, this effect is unimport-
ant compared with statistical uncertainties inherent in the power availability
model. Because the cloud transmission models described later bound the range
of expected behavior by estimating average cloud transmissivities as a function
of total sky cover, such detailed propagation calculations are unwarranted.

(Reference 101)
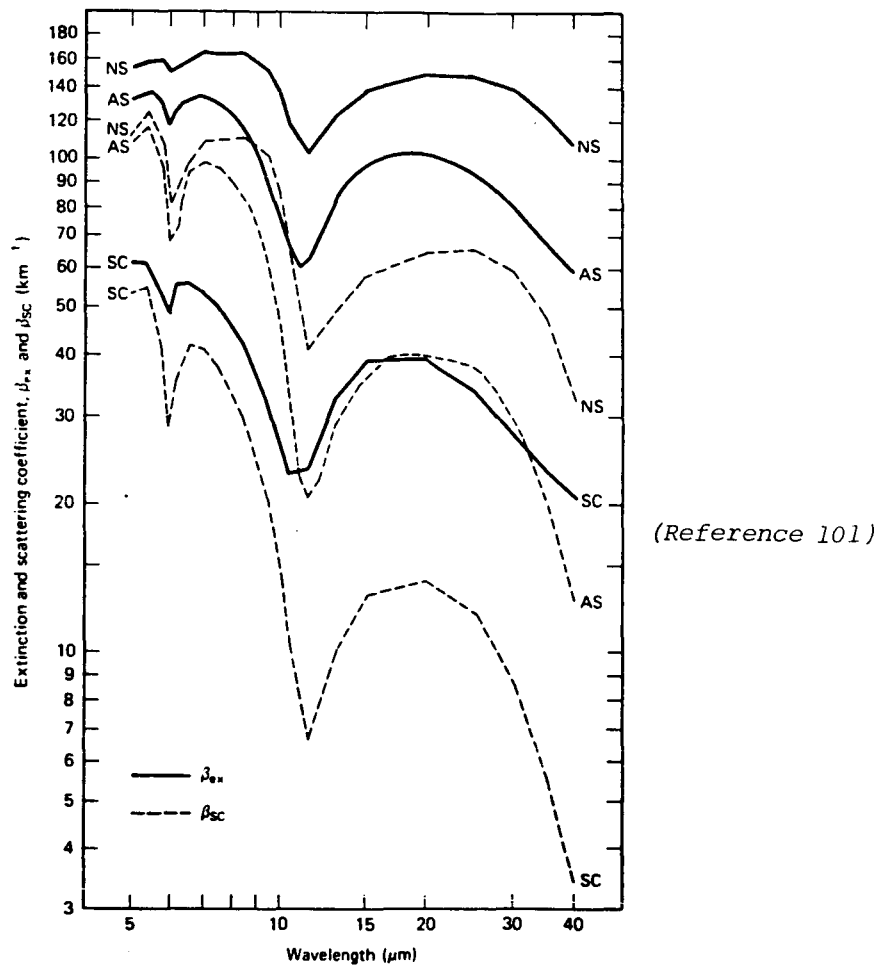
Figure 3.7-8. Calculated Extinction and Scattering
Coefficients for Various Cloud Types

Table 3.7-4. Calculated Absorption and Extinction
Coefficients for Middle- and Low-Level Clouds

Cloud type	$\lambda = 2.25$ μm		$\lambda = 11.0$ μm	
	β_a, km^{-1}	β_{ex}, km^{-1}	β_a, km^{-1}	β_{ex}, km^{-1}
As	2.47×10^0	1.07×10^2	3.49×10^1	5.97×10^1
Ac	8.59×10^{-1}	2.91×10^1	1.13×10^1	2.12×10^1
Sc	$(0.89\text{-}1.80) \times 10^0$	$(5.11\text{-}6.20) \times 10^1$	$(1.38\text{-}2.33) \times 10^1$	$(2.19\text{-}4.30) \times 10^1$
St	$(1.38\text{-}2.26) \times 10^0$	$(7.03\text{-}7.70) \times 10^1$	$(2.01\text{-}2.84) \times 10^1$	$(3.32\text{-}5.24) \times 10^1$
Ns	$(5.28\text{-}5.63) \times 10^0$	$(1.52\text{-}1.57) \times 10^2$	$(6.12\text{-}6.46) \times 10^1$	$(1.18\text{-}1.26) \times 10^2$
Cu humulis	$(0.63\text{-}3.21) \times 10^0$	$(0.55\text{-}1.07) \times 10^2$	$(1.62\text{-}4.50) \times 10^1$	$(2.51\text{-}7.67) \times 10^1$
Cu congestus	2.16×10^0	7.15×10^1	2.71×10^1	5.06×10^1
Cb	$(2.54\text{-}5.03) \times 10^0$	$(6.67\text{-}8.17) \times 10^1$	$(2.89\text{-}4.02) \times 10^1$	$(5.77\text{-}8.19) \times 10^1$

Ice Clouds

Ice clouds forming at high altitudes contain predominantly non-spherical crystals and, hence, the Mie scattering code HSPHR is unsuitable for calculating extinction and absorption coefficients. For example, cirriform clouds are composed mainly of hexagonal-column crystals several hundred micrometers long at a concentration of 0.1 to 1 cm^{-3}. Several authors have measured the transmissivity of various cloud types at different wavelengths. Few however, have simultaneously measured the cloud thickness so that β_{ex} can be estimated.

For those instances where the cloud thickness is known, the transmissivity at 11 μm was plotted as a function of cloud thickness for various cirriform clouds (Figure 3.7-9). The upper curve is a least-squares fit to the measurements of Reference 102 for cirrus clouds. Cirrus-cloud measurements of other references are in close agreement with this curve. Denser cirriform clouds, such as cirrostratus, are more opaque to infrared radiation even though their average thickness is generally less than for cirrus clouds. Unlike many water-based cloud types occurring at lower altitudes, dense cirriform clouds may attenuate more strongly at 11 μm than at shorter wavelengths (References 103, 104 and 105), although this effect amounts to a difference in transmissivity of perhaps 20% at most.
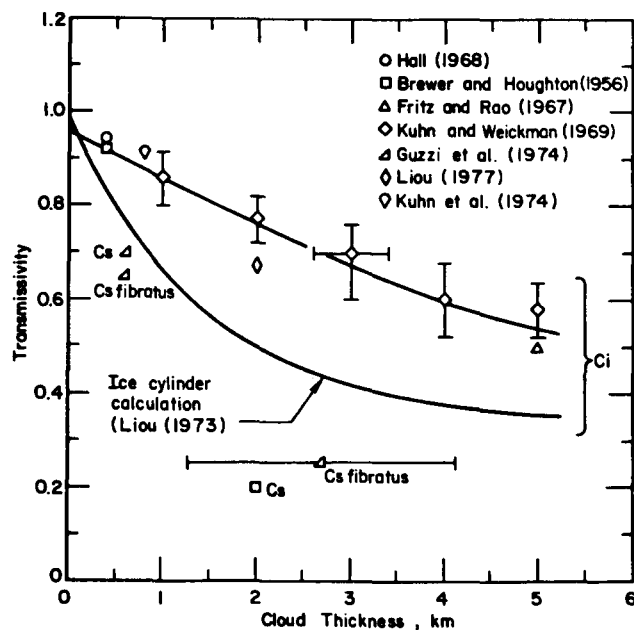
Figure 3.7-9. Measured and Calculated Transmissivities
of Cirriform Clouds for λ ≃ 11 μm

Rain

For large, homogeneous, and spherical droplets such as rain, light absorption and extinction can be approximated by geometrical optics. A computer code (RAIN) was written to evaluate the geometrical optics model assuming that rain

is composed entirely of pure water with index of refraction data given in
Table 3.7-1. The presence of condensation nuclei may be neglected because of
the small size and mass of the nuclei compared with the raindrop as a whole.

Calculational results for a wavelength of 11 μm are shown in Figure 3.7-10.
Because of the large particle diameters in the rain distributions, Q_{ex} and Q_a
rapidly converges to values of 2 and 1, respectively, as we integrate from a_1
to a_2. For R > 0.1 mm/hr, therefore, the present results are effectively in-
dependent of wavelength for wavelengths in the infrared, and depend only upon
the explicit details of the particle distribution. Observational measurements,
however, show distinct differences between the total attenuation coefficient
for different wavelengths, partly due to differences in molecular absorption.
We notice that the corrected extinction curve obtained is in good agreement
with theoretical predictions using the continuous rainfall particle distribu-
tion. Reference 106 found values of $\tilde{\beta}/R$ in the range $2.3-2.8 \times 10^{-2}$ km^{-1}mm^{-1}
for R < 50 mm/hr, in good agreement with our theoretical predictions without
any correction.
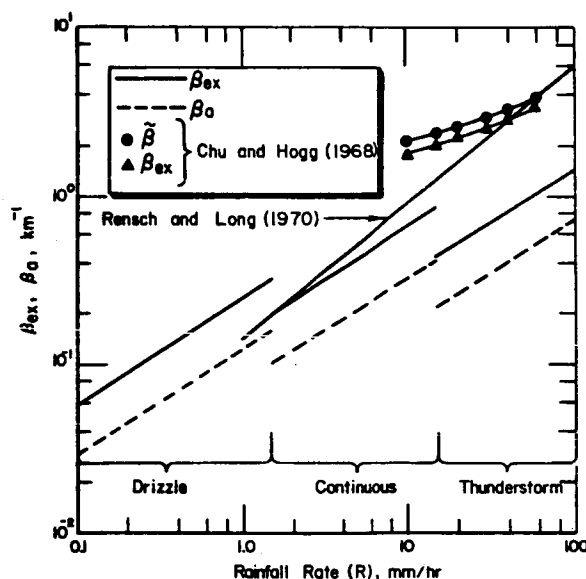
Figure 3.7-10. Calculated and Measured Extinction
and Absorption Coefficients for Rain

Snow

Little theoretical or observational data of laser propagation in snow
exists. Observational measurements taken (Reference 106, 107 and 108) show
severe attenuation for moderate precipitation rates, and preliminary measure-
ments indicate that the attenuation at 10.6 μm is significantly greater than
at 0.63 μm and 3.5 μm.

As with their measurement of the attenuation of rain at several wavelengths,
the researchers found more severe attenuation at 10.6 μm than at the shorter
wavelengths and, in general, the attenuation and forward scattering properties
of snow appear to be between those of rain and dense fog. At present, there

is no satisfactory theoretical method for calculating the scattering properties
of snowflake crystals, although Monte Carlo techniques have been applied with
some degree of success (Reference 108).

Propagation Calculations—Molecular Absorption

Calculational Models

Molecular absorption is calculated for a given laser wavelength λ by the
computer Code LASER (Reference 109). Absorption line parameters for atmospheric
molecular species are taken from the AFGL line-parameter compilation (Reference
110). The average molecular absorption coefficient for each of 32 atmospheric
layers was calculated for the following atmospheric models: U.S. Standard,
Tropical, Midlatitude Summer, Midlatitude Winter, Subarctic Summer, and Sub-
arctic Winter. In addition, several of the aerosol models of Reference 82
were considered, and the code also calculates aerosol absorption and scatter-
ing coefficients for each atmospheric layer. The results consider molecular
absorption only to permit better understanding of the roles of the various
attenuation mechanisms. Molecular (Rayleigh) scattering is important only at
$\lambda \lesssim 1$ µm.

Transmission Efficiencies

The transmission efficiency for space-to-earth propagation was calculated
for a number of laser lines in the 2-µm, 9-µm, and 11-µm spectral regions.
The 1-µm and 11-µm regions were chosen because they may afford an improvement
in transmission through various meteorological aerosols. The 9-µm region was
chosen because the laser lines of certain isotopic species of CO_2 may offer
higher transmission efficiencies than their naturally occurring counterpart,
$^{12}C^{16}O_2$; $^{12}C^{16}O_2$ is uniformly distributed in the atmosphere and its strong
absorption lines should be avoided by selection of alternate laser wavelengths.
All calculations are for propagation to receptor site elevations of 0.0, 0.5,
and 3.0 km for a zenith angle of 50°.

The spectral region from 2.100 µm to 2.315 µm offers an excellent high-
transparency window with relatively few strong absorption features. Calculated
transmission efficiencies of three sample lines, as given in Table 3.7-5,
exceed 99.9% for all site elevations and are insensitive to seasonal variations.
Since the individual windows between absorption features are wide (in many
cases > 10 cm^{-1}), there is hope that a scalable, high-power laser operating at
a wavelength in one of these windows can be developed.

The transmission efficiency of several midrotational P- and R-branch
laser lines of the isotopic-species $^{12}C^{18}O_2$ laser operating on the $10°0 \rightarrow 02°0$
band are given in Table 3.7-6. Operation of a CO_2 laser in this mode results
in a significant improvement in the transmission efficiency compared with
operation on "standard" lines of the $00°1 \rightarrow 10°0$ band of $^{12}C^{16}O_2$; seasonal
variations, however, are pronounced and the highest annual transmission
efficiency to typical receptor sites (h = 0.5 km) is only 87.7% for the
9.124-µm line.

Table 3.7-5. Transmission Efficiencies of Selected Laser Lines
(2.100-2.315-μm Window Region)

Transition	ν, cm^{-1}	λ, μm	Transmission efficiency to elevation h					
			Midlatitude Summer			Midlatitude Winter		
			0.0 km	0.5 km	3.0 km	0.0 km	0.5 km	3.0 km
--	4444.444	2.250	0.99947	0.99950	0.99964	0.99949	0.99952	0.99965
--	4484.000	2.230	0.99945	0.99948	0.99963	0.99947	0.99950	0.99964
--	4666.000	2.143	0.99901	0.99912	0.99949	0.99922	0.99928	0.99952

Table 3.7-6. Transmission Efficiencies of Selected Laser Lines
(11-μm Window Region)

Transition	ν, cm^{-1}	λ, μm	Transmission efficiency to elevation h					
			Midlatitude Summer			Midlatitude Winter		
			0.0 km	0.5 km	3.0 km	0.0 km	0.5 km	3.0 km
--	875.000	11.429	0.553	0.653	0.960	0.921	0.939	0.991
$^{13}C^{16}O_2$ $P_I(24)$*	893.372	11.194	0.571	0.665	0.952	0.918	0.935	0.985
$^{13}C^{16}O_2$ $P_I(16)$	900.369	11.107	0.572	0.664	0.943	0.912	0.929	0.978
$^{13}C^{16}O_2$ $P_I(12)$	903.750	11.065	0.581	0.673	0.948	0.915	0.932	0.979
N_2O $P_I(30)$	912.359	10.961	0.600	0.691	0.964	0.930	0.946	0.992
N_2O $P_I(26)$	916.065	10.916	0.607	0.697	0.965	0.933	0.948	0.992
$^{12}C^{16}O_2$ $P_I(20)$	944.195	10.591	0.192	0.232	0.412	0.439	0.463	0.570
$^{13}C^{16}O_2$ $P_{II}(26)$	994.986	10.050	0.472	0.526	0.681	0.660	0.669	0.697

*Subscript denotes vibrational-rotational band: $I = 00°1 \rightarrow 10°0$; $II = 00°1 \rightarrow 02°0$.

Windows which were at least 1.0 cm^{-1} wide with edges at least 1.0 cm^{-1} from a major absorption line were selected for detailed calculations. If a known (high-power) laser line exists within a window, this wavelength was used in the LASER-code calculation; for those windows for which no laser line could be identified, the central wavelength was used. The transmission efficiencies for all windows identified in this manner are given in Table 3.7-6. For comparison, calculations are also shown for the "standard" 10.6-μm CO_2 laser line, which is totally unsuitable for space-to-earth power beaming. Most of the absorption occurs in the lower troposphere and seasonal variations in the transmission efficiency are again pronounced. The highest annual transmission efficiency to typical receptor sites is 82.3% for the 10.916-μm line. High-elevation operation (h = 3.0 km) increases this value to 96.3%. Indeed, power transmission in the 9-μm and 11-μm regions is probably limited to high-elevation sites. The examination of the 10-μm to 12-μm spectral region was exhaustive and it is believed that no high-transparency window was overlooked.

Receptor Siting Criteria

Laser receptor siting criteria are far less restrictive than their micro-
wave rectenna counterparts, due primarily to the smaller land area requirement.
Estimates (Reference 43) predict a necessary land area of only a few square
kilometers, roughly two orders of magnitude smaller than necessary for the
microwave rectenna. In addition, siting criteria are less restrictive in terms
of topological acceptability, permitting siting in closer proximity to load
centers and/or existing power transmission lines. Many of the exclusion areas
for receptor siting as listed in Table 3.7-7 are identical to those involved
in microwave-rectenna siting. Because of the proposed power density for laser
transmission (~ 1-$100\,W/cm^2$), however, it is unlikely that any site will be
subject to multiple land use.

Table 3.7-7. Receptor Siting Exclusion Areas

Absolute exclusion areas:

    Military and DOE reservations
    National and state parks
    National wildlife preserves
    Indian reservations
    Lakes and navigable waterways
    Off-shore locations
    Marshlands
    Metropolitan areas
    Metropolitan and county airports, including approach corridors
    Interstate highways
    Preferentially flooded lands
    Wild and scenic rivers

Probable exclusion areas:

    High-quality agricultural land
    Coastal regions, river valleys, and other locations subject
       to persistent fog
    Topographically unacceptable land

Area of unknown impact:

    Migratory pathways of birds

Because the purpose of this research was to bound cogent power-availability
parameters for the various regions of the United States and to develop mitiga-
tion techniques and siting criteria which will diminish the deleterious effects
of inclimate weather, detailed land tract evaluations were not performed.
Furthermore, siting criteria based on projected electrical power demand are
beyond the scope of this study, and no attempt was made to identify planned
transmission line additions or to project future expansion of any grid.

Since detailed statistical meteorological data are required by the power
availability model, the sites selected are identified by their associated
weather station. If the actual site tract is in close proximity to the weather
station, the assumption of identical statistics is usually good for most

midlatitude climates. For our purposes, sites were chosen which were within 100 miles of an existing extra-high-voltage (EHV) transmission line, consistent with the exclusion areas listed in Table 3.6-7. No closely spaced sites were chosen and attempts were made to distribute the sites throughout the contiguous United States. Because the layout of the EHV grid is strongly correlated with existing load-demand centers, the number of sites selected was not evenly proportioned by geographical region. Difficulties in obtaining the necessary statistical meteorological data also precluded selection of the "best" sites for certain geographical regions. However, the number of sites selected (22) is statistically significant enough so that patterns of expected performance for the different regions can be gleaned, especially considering the climatic similarity of many sites within the same region.

Power Availability

Introduction and Sources of Statistical Climatic Data

Introduction

Calculation of the power availability at any given site requires statistical climatic data in much greater detail than is routinely accumulated by the U.S. Weather Service for any of their stations. For instance, an extensive model will require information not only concerning sky cover but regarding cloud type, thickness, and frequency of occurrence, which is not available for civilian stations. In this section, sources of such data are reviewed and their applicability in formulating a power-availability model for space-to-earth laser power transmission is discussed.

Considerable work has been performed in developing empirical global cloud-cover models and representative theoretical statistical distributions. This work was motivated principally by earth-viewing space missions, such as NASA's Skylab program. Although a substantial amount of data was accumulated during the course of these studies, the various statistical distributions are unsuitable for modeling space-to-earth power availability for the following reasons. First, the models are representative of large areas and assume homogeneous cloud cover distributions within each region. The earth's surface is divided into 29 regions of different areas, which is too coarse for present purposes. Furthermore, such models give the probability of a specific type of cloud cover within a 55.6-km diameter circle, which can be quite different from the cloud-cover probability within the small area typified by a laser beam. Second, only 5 sky cover categories were employed rather than the customary 11 categories (0 to 10-tenths sky cover). This lack of detail would hamper our ability to estimate transmission efficiencies through clouds on the basis of their types and thicknesses as statistical functions of cloud cover.

A large number of models exist which relate laser attenuation at a specific wavelength to the meteorological visibility. These models are suitable only for horizontal or near-horizontal laser propagation where the beam is attenuated by haze, fog, or precipitation. Such models are completely useless for space-to-earth propagation where the most frequently encountered obscurring media are clouds.

A three-dimensional nephanalysis program was developed at the Air Force
Global Weather Center (AFGWC) to process the tremendous quantity of satellite-
sensed cloud data and conventionally-sensed meteorological parameters into a
three-dimensional cloud model of the atmosphere. The horizontal resolution
is defined by a grid array projected onto a polar stereographic map; at 60°
latitude, the distance between grid points is 40 km. The vertical resolution
is defined by 15 atmospheric layers ranging from ground level to 55,000 ft
(16.8 km) above mean sea level. Data available at each point include cloud
amounts, types, maximum tops and minimum bases, the total cloud cover, and
the current weather. Civilian satellites used for such observations include
the Synchronous Meteorological Satellite (SMS)/Geostationary Operational
Environmental Satellite (GEOS) series and the Improved TIROS (ITOS) polar-
orbiting series. These satellites use scanning radiometers with one channel
each of visible and IR data. It is not known whether a statistical data base
exists which incorporates these variables into an analyzed format and which
could be referenced to particular receptor locations.

The most useful climatic data for present purposes are the frequencies
of total sky cover (0 to 10-tenths), which are observational data gathered
at almost all military air bases. The power availability model developed
here considers laser transmission udner two conditions, i.e., when a cloud-
free line-of-sight (CFLOS) exists between the satellite transmitter and the
receptor site and when clouds obscure the beam. The probability of a CFLOS
is a function of the observed frequencies of sky cover and the propagation
zenith angle. Statistical data needed to estimate this probability were
obtained from the work of Lund at the Air Force Geophysics Laboratory. The
transmission efficiency through cloud cover was calculated using three schemes.
The first cloud-cover transmission model gives the worst-case behavior and is
believed to establish a lower bound on the calculated power availability by
assuming zero transmission through all cloud types except for thin cirriform,
middle, and stratiform types. The second model is the best estimate which,
admittedly, represents a large amount of subjective judgment. The third and
most optimistic model assumes considerable transmission through certain cloud
types by virtue of substantial hole boring. These models are believed to
accurately bound the expected performance of space-to-earth laser energy
transmission. The statistical distribution of cloud types is estimated using
Lund's data for midlatitude sites and is a function of total sky cover.

Cloud Transmission Model 1

The first cloud transmission model is the most conservative and is
utilized to establish a lower bound on the calculated power availability. It
is assumed that only thin cirriform, middle, and stratiform clouds are par-
tially transmissive when they are observed at total sky covers less than or
equal to 6 tenths. Furthermore, we are implicitly assuming that the thickness
of these cloud forms increases in a manner directly proportional to sky cover
so that the cloud-form transmission efficiency decreases with increasing sky
cover. Numerically, Model 1 specified (1) zero transmission efficiency for
cumuliform or mixed-form clouds, (2) zero transmission efficiency for all cloud
forms observed at total sky covers greater than 6-tenths, (3) the cirriform
transmission efficiency decreases from 90% to 30% as the total sky cover
increases from 0 to 6-tenths, in correlation with the lower range of observations

in Figure 3.7-9, and (4) the transmission efficiency of middle and stratiform
clouds decreases from 40% to 10% and 60% to 20%, respectively, in the same sky
cover range. Also, to account for statistical variations in the persistence
probabilities, E_j values (function of total sky cover and persistence time)
used in Model 1 were reduced by 8%, consistent with the observational results
of Reference 111 and the conservative nature of this model.

Cloud Transmission Model 2

The second model represents the best estimate for cloud transmission under
conditions not involving hole boring. The model is based largely on subjective
judgments and some comments and observations on the sensitivity of the power
availability model to the estimated cloud-form transmission efficiencies will
be presented in a later section. Specifically, Model 2 assumes (1) zero trans-
mission efficiency through cumuliform clouds, (2) the cirriform transmission
efficiency decreases from 90% to 35% as the total sky cover increases from 0
to 10-tenths, in correlation with the Kuhn-Weickmann curve in Figure 3.7-9,
(3) the transmission efficiency of middle and stratiform clouds decreases from
40% to 10% and 60% to 20%, respectively, over the same sky cover limits, and
(4) the transmission efficiency for mixed cloud forms decreases from 30% to 9%
as the total sky cover increases from 0 to 10-tenths. Therefore, compared
with the first model, Model 2 allows partial transmission during certain over-
cast conditions and through mixed cloud forms if they are observed during
periods of lesser sky cover. Cumuliform clouds are again assumed to be com-
pletely opaque.

Cloud Transmission Model 3

To complete the power-availability model, a third cloud transmission model
is proposed which assumes substantial penetration of certain cloud types by
hole boring. From an environmental and safety standpoint, the maximum CW
laser intensity is probably limited to 100-200 W/cm . For 11-μm operation,
therefore, all fogs, cirriform clouds with $\mu \leq 0.005$ g/cm^2, middle clouds with
$\mu \leq 0.02$ g/cm^2, and stratiform clouds with $\mu < 0.03$ g/cm^2 can be bored at these
intensities. All cumuliform cloud types and nimbostratus clouds are impenetrable
except with weapon-quality ($I \geq 1$ kW/cm^2) beams. Although the environmental
consequences of laser-power transmission at these intensities are probably
negligible, the transmission air-zone associated with each receptor must be
restricted to all aircraft due to potential ocular hazards posed by the
randomly-pointing and highly-reflective aluminum aircraft skins.

For 2-μm operation, however, substantially higher CW intensities are
necessary to affect hole boring because the aerosol absorption coefficient
(β_a) is much smaller at 2 μm than at 11 μm. A potentially viable and attrac-
tive solution is to combine CW laser-power transmission with pulsed laser hole
boring. At $I \sim 10^5$ W/cm^2, the internal heat generation in an aerosol droplet
is so violent that shock waves form which explosively shatter the droplet.
Thus, a train of intense, short-duration pulses can be superimposed on the
main CW beam allowing a reduction in average power density. A repetitively
pulsed laser producing ~ 100 pulses/sec with a pulsewidth ~ 1 μsec and an
energy density ~ 0.1 J/cm^2 gives an average power density ~ 10 W/cm^2. Now
if the CW power-transmission component is reduced to $I \sim 1$-10 W/cm^2, the

ocular hazards from quasi-specular reflection are greatly reduced and the transmission air zone would no longer be restricted to aircraft. Note that the pulse train can be turned off for clear periods and that the relative power densities of the beam components can be adjusted according to prevailing meteorological conditions to maintain a constant total average power density at the receptor. More theoretical and experimental research is needed to demonstrate the feasibility of this technique since the laser parameters suggested here are only rough estimates.

Numerically, the third cloud transmission model assumes (1) zero transmission efficiency for cumuliform clouds, (2) the transmission efficiency for cirriform and middle clouds decreases from 95% to 80% as the total sky cover increases from 0 to 10-tenths, i.e., 5% to 20% of the transmitted power is lost to aerosol vaporization, (3) the transmission efficiency for stratiform clouds decreases from 90% to 60% over the same sky-cover range, and (4) for mixed cloud forms, the transmission efficiency decreases from 80% to 30% as the total sky cover increases from 0 to 8-tenths; overcast conditions (9-10 tenths sky cover) with mixed-form clouds are impenetrable. Also, to account for statistical variations in the persistence probabilities, E_j values used in model 3 were increased by 9%, consistent with the observational results of Reference 111 and the optimistic nature of the model.

The weighted cloud transmissivity for a given sky cover is calculated by multiplying the probability of occurrence of a cloud form if a cloud is present by the respective transmission efficiency and summing over all cloud-form categories. A partial listing using this procedure is shown in Figure 3.7-8, where the occurrence probabilities of the various cloud forms as a function of sky cover were inferred from data of Reference 112. These data are observational results for Columbia, Missouri, although it was suggested that they can be generalized to other continental midlatitude sites without substantial error. Occurrence probabilities for each site should be used but, as discussed previously, such statistical data are not routinely available. Histograms of the weighted cloud transmissivity τ_j as a function of total sky cover j for the three models are shown in Figure 3.7-11.

Statistical Results and Analysis

Statistical calculations of the seasonal and annual power availabilities, transmission frequencies, and persistence frequencies were performed for each of the sites designated in Table 3.7-9. The results clearly demonstrate the marked influence meteorological conditions have on laser propagation. Indeed, operational procedures and siting criteria must be much different for power transmission employing laser radiation rather than microwaves. This analysis leads to a reformulation of these requirements so that laser power transmission can achieve power-availability levels at the commercial grid equivalent to those for the microwave-SPS concept and conventional electric-power plants. This performance is believed to be feasible within constraints imposed by safety and environmental considerations.

A comparison of the annual power availability for the various U.S. regions is shown in Figure 3.7-12. The low end of the range corresponds to average results for Model 1, while the high end corresponds to the improved conditions

Table 3.7-8. Calculation of Weighted Cloud
Transmissivities (Partial)

| Sky cover, tenths | Cloud-form | | | | | Weighted cloud transmissivity, τ | | |
| | Category | Probability of occurrence if cloud is present* | Transmission efficiency for model: | | | Model | | |
			1	2	3	1	2	3
0	Cirriform	0.31	0.90	0.90	0.95			
	Middle	0.14	0.40	0.40	0.95			
	Cumuliform	0.40	0.00	0.00	0.00	0.40	0.41	0.56
	Stratiform	0.10	0.60	0.60	0.90			
	Mixed	0.05	0.00	0.30	0.80			
1	Cirriform	0.47	0.60	0.80	0.95			
	Middle	0.09	0.40	0.40	0.95			
	Cumuliform	0.28	0.00	0.00	0.00	0.37	0.49	0.67
	Stratiform	0.09	0.60	0.60	0.90			
	Mixed	0.07	0.00	0.30	0.80			
2	Cirriform	0.37	0.50	0.70	0.95			
	Middle	0.06	0.20	0.40	0.95			
	Cumuliform	0.30	0.00	0.00	0.00	0.21	0.38	0.63
	Stratiform	0.04	0.40	0.60	0.90			
	Mixed	0.23	0.00	0.30	0.80			
3	Cirriform	0.38	0.45	0.60	0.90			
	Middle	0.06	0.20	0.40	0.90			
	Cumuliform	0.30	0.00	0.00	0.00	0.22	0.36	0.57
	Stratiform	0.10	0.40	0.60	0.80			
	Mixed	0.16	0.00	0.30	0.60			
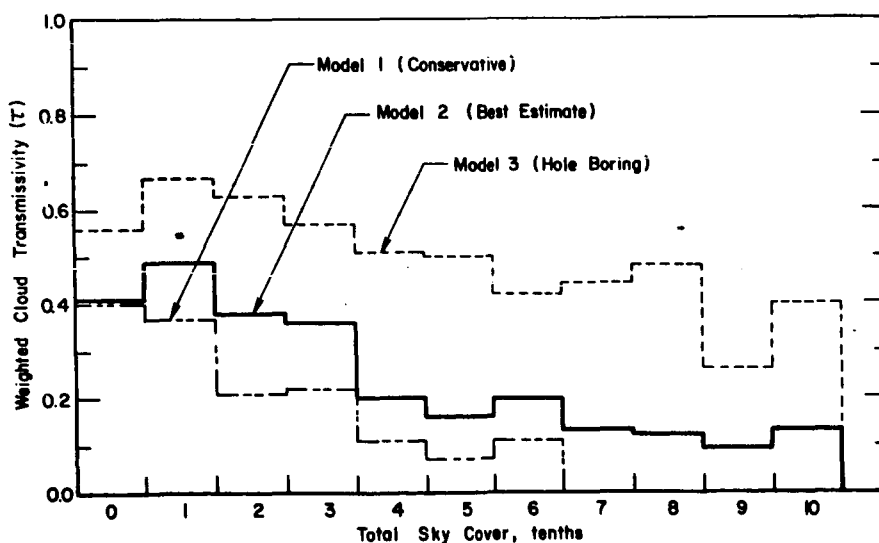
Figure 3.7-11. Cloud Transmissivity Models

affected by hole boring (Model 3). Average results for Model 2 usually fall close to the low end of the range and are only slightly better than for Model 1. Seasonal variations for all models are highly region-dependent, as would be expected intuitively, and are often pronounced. Hole boring affords an improvement in the annual power availability of from 9% to 33% compared with Model 2; significantly larger improvements are not possible without utilizing weapon-quality beams. Seasonal improvements can exceed 50%.

Table 3.7-9. Receptor Sites and Associated Sources
of Statistical Climatological Data

Geographical region	Site number	Weather station
Southeast	SE-1	Huntsville, Alabama
	SE-2	MacDill AFB (Tampa), Florida
	SE-3	Dobbins AFB (Marietta), Georgia
	SE-4	Columbus AFB, Mississippi
	SE-5	Fort Bragg (Fayetteville), North Carolina
South Central	SC-1	Little Rock AFB, Arkansas
	SC-2	Barksdale AFB (Shreveport), Louisiana
	SC-3	Kirtland AFB (Albuquerque), New Mexico
	SC-4	Sheppard AFB (Wichita Falls), Texas
	SC-5	Connally AFB (Waco), Texas
Southwest	SW-1	Luke AFB (Phoenix), Arizona
	SW-2	McClellan AFB (Sacramento), California
	SW-3	Nellis AFB (Las Vegas), Nevada
Atlantic	AT-1	Griffis AFB (Rome), New York
	AT-2	Quantico, Virginia
New England	NE-1	Pease AFB (Portsmouth), New Hampshire
Midwest	MW-1	Chanute AFB (Rantoul), Illinois
	MW-2	Wright-Patterson AFB (Dayton), Ohio
Central	CN-1	Whiteman AFB, Missouri
North Central	NC-1	Ellsworth AFB (Rapid City), South Dakota
	NC-2	Hill AFB (Ogden), Utah
Northwest	NW-1	Fort Lewis (Gray), Washington
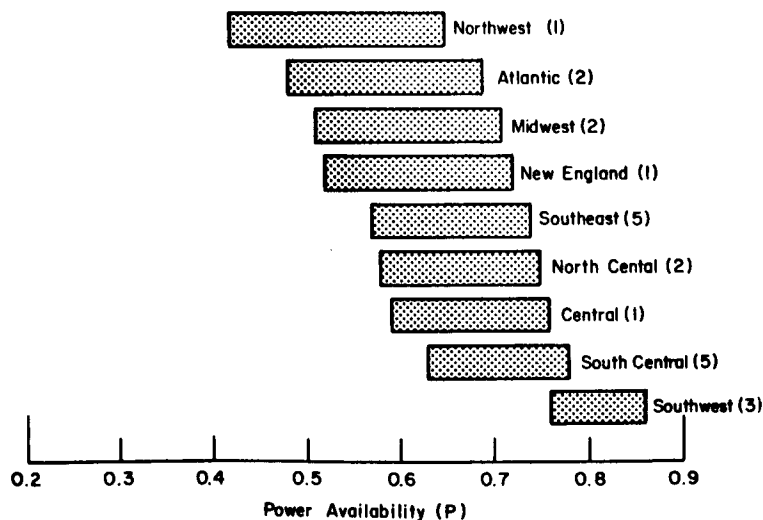
(   ) = NUMBER OF SITES ANALYZED IN THE REGION

Figure 3.7-12. Annual Power Availability for Various
U.S. Regions

Differences in the prevailing meteorological conditions within the regions are more readily apparent when transmission frequencies are compared, as in Figure 3.7-13. The poor performance of sites in the northwest, Atlantic, midwest, and New England regions is particularly noticeable. Only sites in the southwest region offer a power availability in excess of 80% and a frequency for acceptable transmission efficiency (T $\geq$ 0.80) are suitable for commercial interest. To remedy this situation, it is obvious that the laser-SPS concept must rely upon multiple receptor sites for each transmitted beam and furthermore, rapid-switching capability is essential.

Northwest (1)
Atlantic (2)
Midwest (2)
New England (1)
Southeast (5)
North Central (2)
Central (1)
South Central (5)
Southwest (3)

0.2 0.3 0.4 0.5 0.6 0.7 0.8 0.9
Frequency for T $\geq$ 0.8
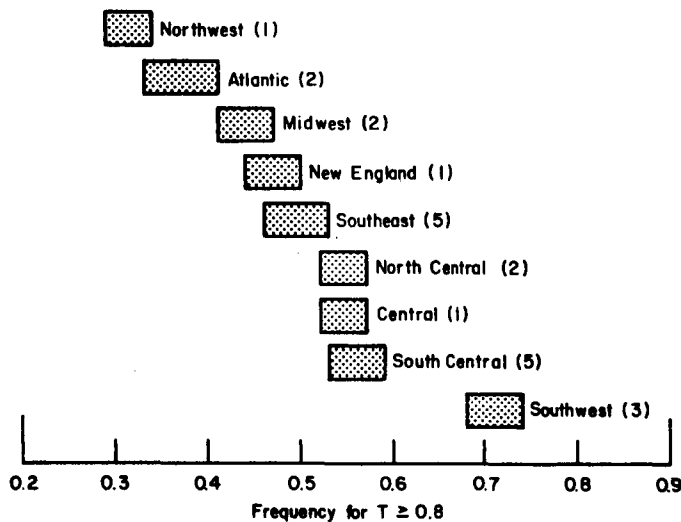
Figure 3.7-13. Annual Frequency for Transmission
Efficiency for $\geq$80% for Various U.S. Regions

Conclusions and Recommendations

This study has examined potential mitigation techniques which can minimize the deleterious effects of inclimate weather on space-to-earth power transmission using lasers. The investigation has considered the choice of laser wavelength, propagation zenith angle, receptor-site elevation, and the potential of laser hole boring. An extensive series of propagation calculations have been performed to estimate the attenuation due to molecular absorption and aerosol absorption and scattering. All commonly encountered meteorological conditions have been modeled, including haze, fog, clouds, rain and snow, and compared with observational data when available.

Using these mitigation techniques as guidelines, preliminary receptor siting criteria were defined and 22 candidate sites in the contiguous U.S. were selected for detailed study. A power availability model has been developed which uses statistical meteorological data for each site to calculate the annual and seasonal power availability (average transmission efficiency assuming constant power beaming) and the frequency for which the transmission efficiency exceeds a given value for a specified persistence time. The results of this work enable us to redefine siting criteria and laser parameters such that the power availability is comparable to the microwave-SPS concept or to conventional electric-power plants.

Specific conclusions of this research are as follows:

• At high elevations, atmospheric transmission windows in the wavelength region around 11 µm provide the best combined propagation efficiency considering both molecular absorption and aerosol extinction. At low elevations, laser operation at a wavelength near 2.25 µm is preferable.

• If the laser wavelength is properly optimized, operating at a propagation zenith angle of 0° instead of 50° does not afford a significant improvement in the power availability and cannot be justified in terms of the increased cost and complexity of the required space hardware.

• High-elevation receptor sites are desirable although not essential to the laser-SPS concept because of the reduction in attenuation due to haze and molecular absorption.

• Laser hole boring at $\lambda \simeq 11$ µm through certain types of haze, fogs, and clouds may be possible consistent with safety and environmental concerns and without the need for weapon-quality laser beams; in particular, all but the thickest cirriform and middle clouds and all stratiform clouds with the exception of nimbostratus can be penetrated with power densities of 100–200 W/cm^2. All other cloud types will require substantially higher ower densities for penetration, which is unacceptable given the present safety margins.

• At $\lambda \simeq 2$ µm, hole boring is only feasible using combined repetitively-pulsed/CW operation; this mode of operation may be preferable, however, since the average power density can be reduced to allow unrestricted transmission air-zone access.

• Power availabilities in excess of 80% are unattainable in most geographical regions of the United States if only a single receptor site is available for each transmitted laser beam (the exception is the southwestern United States).

• If an 80% frequency for the transmission efficiency to equal or exceed 80% is defined as the minimum requirement for commercial viability of the laser-SPS concept, then three receptor sites separated by a centroid radius of from 200 to 300 miles must be available for each transmitted laser beam for most regions of the United States; for the southwest region, however, only two sites separated by as little as 200 miles will be sufficient.

• The average persistence time, during which the prevailing meteorological conditions allow a high transmission efficiency, is considerably shorter than 8 hours at many sites, so that any viable laser-SPS concept must be capable of frequent beam switching between sites with a minimum of downtime.

• Under the aforementioned circumstances, thermodynamic laser-energy conversion schemes may be unsuitable because of the long start-up times required by rotating turbomachinery.

Therefore, the laser-SPS concept must be based on the availability of multiple sites for each transmitted beam, accompanied by frequent beam-switching between sites. Obviously, this operational scenario is considerably different from that envisioned for the microwave-SPS concept, and the economic and engineering viability of the multiple-site concept must be further evaluated. Superficially, it seems that the smaller land area required for each laser-receptor site will outweigh the additional cost of three times the number of sites and their associated hardware when compared with the microwave-SPS concept. An evaluation of the effects of frequent beam switching will require an analysis of the dynamic response of the electric-power grid. Additional recommendations of needed research include:

- Examination of potential short-wavelength transmission windows for aerosols

- Further theoretical and experimental research on combined repetitively pulsed/CW laser hole boring.

- Development of efficient laser-energy conversion schemes not based on thermal cycles

- Development of a joint power-availability model for multiple sites including more sophisticated statistical cloud-cover models and the statistical effects of frontal passage over multiple-site clusters.

3.7.2 ADVANCED LASER CONCEPTS

Introduction

Although laser power transmission has the advantages of negligible environmental damage and small land requirements associated with the receptor sites (Reference 113), meteorological conditions influence the transmission efficiency to a much greater extent than with microwaves, and no viable and substantiated laser concept exists which can compete with the microwave concept in terms of overall efficiency and specific mass (mass per unit of radiated power). The specific mass is of crucial importance because of the large cost of space transportation to high earth orbit. The influence of meteorological conditions on laser beam propagation is investigated in detail in Reference 114; the present study is concerned with a limited examination of advanced laser systems for the Satellite Power System (SPS).

Laser SPS systems can be classified according to the method of solar power conversion and the type of laser. Specifically, the following combinations appear possible and have been investigated to various extents.

Solar-Power Conversion	Laser Type
Photovoltaic	Electric-Discharge Laser
Photovoltaic	Chemical
Photovoltaic	Free-Electron Laser
Thermal	Electric-Discharge Laser
Thermal	Chemical
Thermal	Free-Electron Laser
Thermal	Gas-Dynamic Laser
Thermal	Optically Pumped Laser
Quantum	Optically Pumped Laser
Quantum	Free-Electron Laser

The conversion efficiency of solar cells is $\leq 20\%$, and huge collector areas, often with solar concentrators, are required to achieve the desired power output. Thermal conversion is limited by the thermodynamic efficiency of the respective cycle. The high temperatures and exotic working fluids required for high-efficiency operation may pose problems with system reliability. Furthermore, large-area space radiators are necessary to dispose of waste heat, thus adding to the satellite specific mass.

Quantum conversion relies upon excitation of discrete states in atomic or molecular systems via the solar flux. The conversion efficiency depends upon the fraction and wavelength interval of the solar spectrum which affect excitation and the portion of the excited-state energy which is consumed in the lasing process. Solar concentration undoubtedly will be needed; to limit undue heating, the concentrators can be optically coated to pass that portion of the solar spectrum which is unusable and to reflect the useful portion into the lasing medium.

A detailed investigation of all of the laser systems listed above is not possible in conjunction with this limited study. Comparisons of some of the various possibilities were performed (Reference 115), although the work was far from exhaustive. Several candidate lasing schemes were examined, employing quantum conversion of the solar flux and optical pumping, i.e., "direct" solar pumped lasers. In particular, investigation was made of optically pumped lasers employing electronic-vibrational energy transfer to triatomic molecules, atomic transitions in alkali metals, and atomic transitions in vapor-complex rare-earth-lanthanide ions.

Photoexcited E-V Transfer Lasers

Electronic-vibrational (E-V) transfer lasers operate by near-resonant energy transfer from an electronically excited atom (donor) to the lasing molecule (acceptor). The laser transition occurs between vibrational-rotational levels in the acceptor molecule. Two electronically excited atomic species which can be readily produced by optical pumping have been investigated and shown to achieve lasing in a number of molecular systems (References 116 and 117), namely, $I(5^2P_{\frac{1}{2}})$ and $Br(4^2P_{\frac{1}{2}})$. $I(5^2P_{\frac{1}{2}})$ and $Br(4^2P_{\frac{1}{2}})$ are optically metastable, spin-orbit excited states with energies 7603 cm^{-1} and 3685 cm^{-1} above ground state. For solar photoexcitation, photodissociation of bromide compounds is preferred because a better spectral match exists between absorption features and the solar spectrum. Approximately 24% of the solar spectrum is useful in producing excited Br atoms, whereas only about 1% of the solar spectrum can produce excited I atoms since the photodissociation continuum lies in the soft-ultraviolet spectral region. Furthermore, if Br_2 is used as the photolytic source of excited Br atoms, then self-rejuvination of the working gases will occur via recombination of ground-state Br atoms. Unfortunately, I_2 cannot be used as a photolytic source of excited I atoms since this molecule itself is the strongest quenching agent known. Other iodide compounds can be used, e.g., the perfluoroalkyl iodides, but the kinetics are more complicated and secondary byproducts quickly accumulate during the lasing process (Reference 118). Complex chemical processing of the lasing gas mixture is required to rejuvenate the original iodide compound (Reference 119).

To attain maximum laser efficiency, E-V energy transfer should be specific
to the vibrational mode of the upper laser level. Energy transfer to competing
modes should be avoided by selection of an appropriate acceptor molecule. The
energy levels of several acceptor molecules made to lase in a $Br(4^2P_{\frac{1}{2}})$ E-V
transfer laser are shown in Figure 3.7-14, and Table 3.7-10 lists observed
transitions. Energy transfer to N_2O, for example, involves levels (140) and
(101) resulting in several kinetic paths for energy flow. Lasing on transi-
tions in the 001→100 band has been observed, but complete energy channeling
into the upper-level vibrational mode is impossible. For space-to-earth laser
propagation, multiline laser operation characteristic of the heteronuclear
diatomic molecules is undesirable because of beam focusing and pointing diffi-
culties and transmission inefficiencies. If atmospheric transmission effici-
ency is also considered, only two of the molecular species listed in Table 3.7-10
remain as potentially viable candidates for a direct solar-pumped E-V transfer
laser, namely, HCN (001→010) with $\lambda \simeq 11$ μm. Because kinetic data are readily
available for the CO_2 system, this laser was chosen for detailed modeling.

(Reference 116)
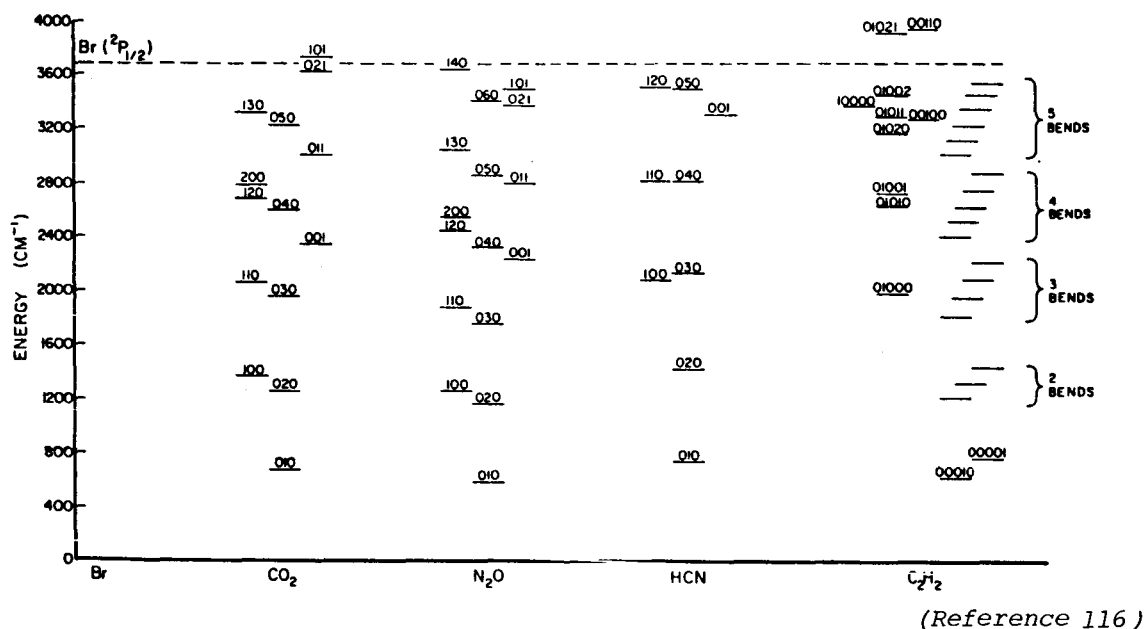
Figure 3.7-14. Molecular Energy Levels and $Br(4^2P_{\frac{1}{2}})$
Excited State-Energy

The lasing scheme is shown energetically in Figure 3.7-15. Optical pump-
ing produces bromine atoms in both the excited $4^2P_{\frac{1}{2}}$ and ground $4^2P_{3/2}$ states.
Collisions of excited Br atoms with CO_2 molecules in the ground state produce
vibrational excitation of the (101) level which relaxes almost immediately
into the (001) level via rapid intramode vibrational-vibrational (VV) processes.
Stimulated emission (lasing) occurs between the asymmetric stretch (001) level
and the symmetric stretch (100) level. Rapid intermode VV relaxation occurs
between the (100) and (020) levels and, finally, the bending mode relaxes to
the ground (000) state via vibrational-translational (VT) collisions. Because
of the close proximity of the (010) level of the bending mode to the ground
state, it is important that a buffer gas (e.g., He) be provided to affect

Table 3.7-10. E-V Laser Transitions Pumped by $Br(4\,^2P_{1/2})$

Molecule	Transition	Approximate wavelength, μm	Reference
CO_2	101→100	4.3	116,120,121,
	001→020	9.6	122,127
	001→100	10.6	
	101→011	14.1	
C_2H_2	00100→01000 (?)	7-8	116
HBr (DBr)*	v=1→0 (v=1→0)	3.9-4.2 (5.4-5.7)	122
HCl (DCl)	v=1→0 (v=1→0)	3.5-3.8 (4.8-5.1)	122,123
N_2O	001→100	10.9	116,124
HF (DF)	v=1→0 (v=1→0)	2.6-3.1 (3.5-4.0)	125
HCN	001→010 001→100	3.85 8.48	116,126
H_2O	020→010	7.1-7.7	124,126
NO	v=2→1	5.5	124

*Deuterated analogs are shown even though lasing with these molecules
has not been attempted.

Energy, cm^{-1}

4000

(101)
(021)   Br(^{2}P$_{1/2}$)   Photon Pumping

E-V Energy
Transfer

(011)   VV Relaxation

3000

VT or ET
Relaxation

(001)

2000

Stimulated
Emission

(100)
(020)

1000

(010)

0   (000)

Br(4^{2}P$_{3/2}$)   Br$_2$

CO$_2$
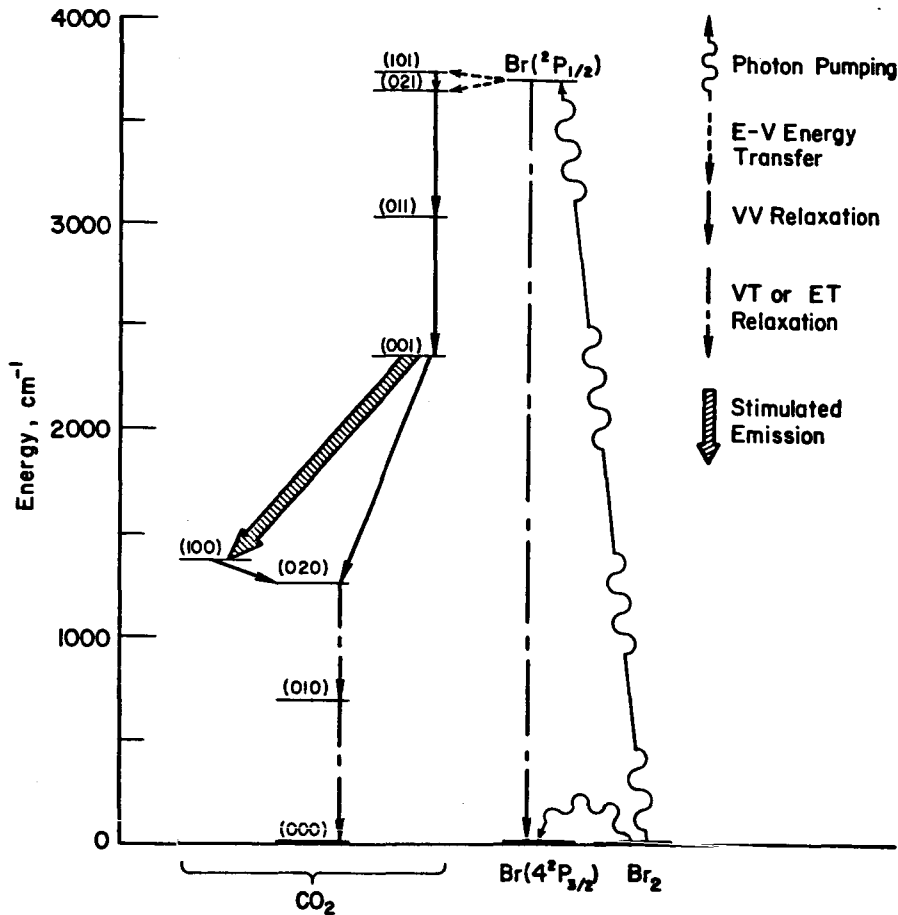
Figure 3.7-15. Br*-^{13}C^{16}O$_2$ Solar-Pumped E-V Transfer Laser

collisional depopulation. Furthermore, the gas-kinetic temperature T cannot exceed approximately 400°K, otherwise significant thermal population of the (010) level will occur with subsequent "bottle-necking" of the laser inversion. Ground-state Br atoms recombine to form molecular bromine and the photoexcitation process can then be repeated.

Even with large solar concentration ratios, the stored power density in the E-V lasing mode is several orders of magnitude smaller than obtained with electrical (gas-discharge) excitation, as shown in Figure 3.7-16. The extractable power density is less than Q_ℓ because of optical losses and limitations on depopulation of the lower laser level imposed by VV equilibrium to the bending mode and subsequent VT relaxation. The thermal power density due to nonproductive photoabsorption processes, Q_{th}, is 45 times greater than Q_ℓ if wavelength-selective solar concentrators are employed and 130 times greater if the full solar spectrum is used. Since this is only one source of thermal power, waste-heat management is a critical issue with this type of laser.
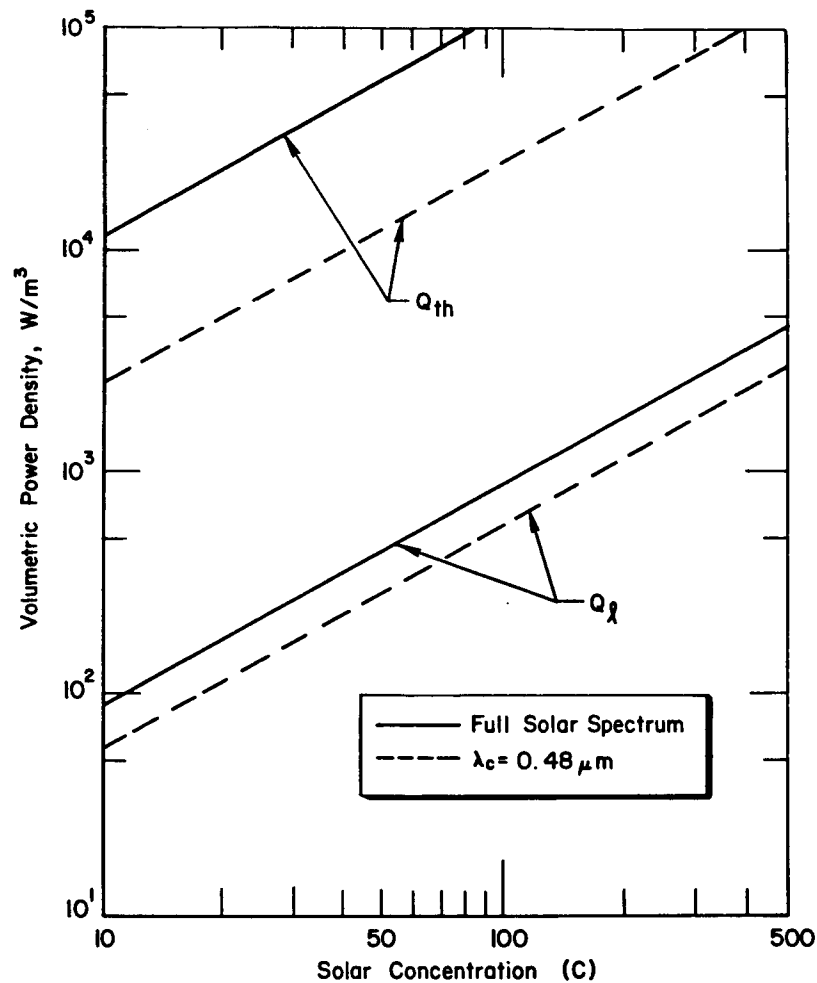
Figure 3.7-16. Stored Power Densities

For a 100-MW laser based on this concept, we estimate that the necessary solar collection area will exceed that required by the 5-GW baseline photoelectric/microwave concept. The shortcomings of this lasing scheme are easily isolated by examination of photon economics and energetics. Under best conditions, only 34% of the absorbed solar photons produce excitation of the upper laser level. One absorbed solar photon of average energy 2.6 eV produces one 0.457-eV Br* atom which liberates "1/2" (f = 0.50) laser photon having an energy of only 0.112 eV, representing a loss of almost all of the original photon's energy to heat. To improve this situation, the upper-level energy of the lasing molecule should be in close proximity to the Br* energy (3685 cm^{-1}), the Br* deactivation rate coefficient (k_1) should be large, accompanied by efficient branching to the E-V transfer reaction (f≈1), and the lower-level lasing energy should be as close to the ground state as possible. In this connection, the 001→010 transition in HCN may be a better choice than $^{13}C^{16}O_2$. As shown in Figure 3.7-17, the probability of Br* quenching per collision within an HCN molecule is better than with many other hydrides and the branching fraction is large (f≈0.9). The HCN laser, like the $^{13}C^{16}O_2$ laser, cannot operate at high temperatures so waste heat disposal is still a major problem.
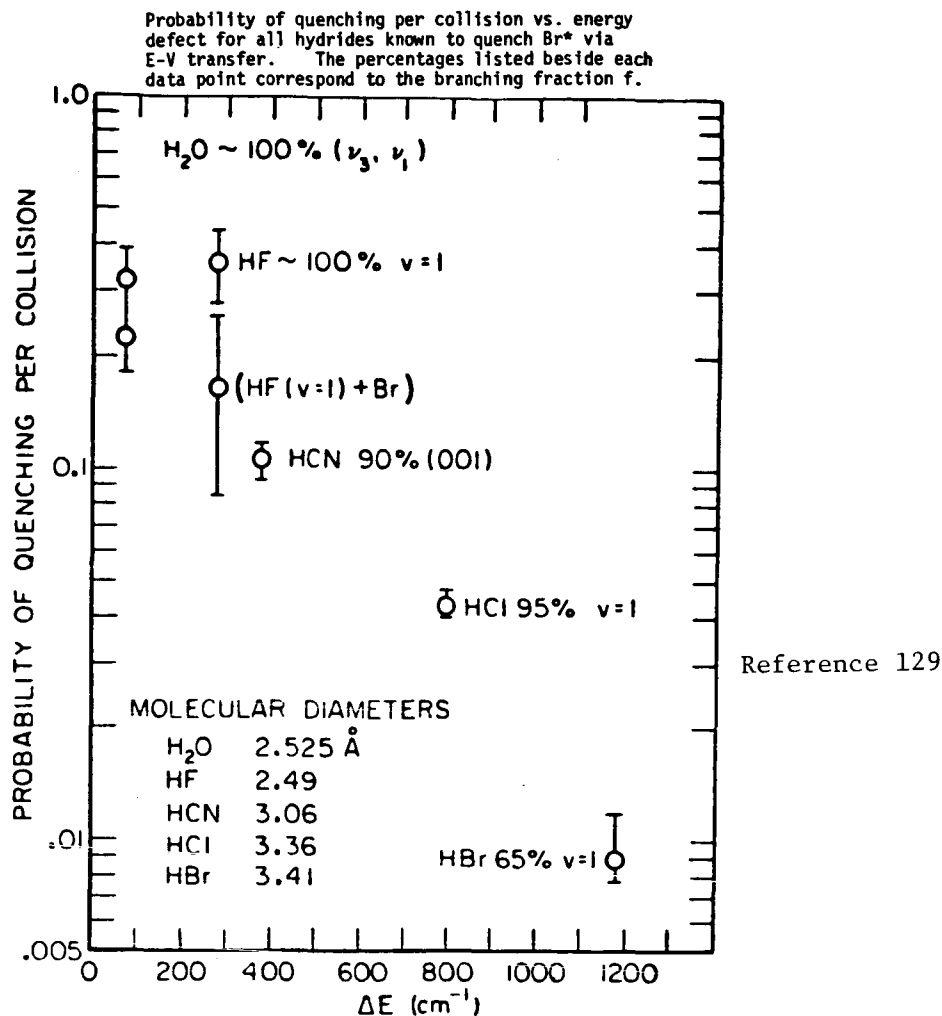
Figure 3.7-17. Probability of Quenching per Collision Vs. Energy Defect

Optically Pumped Alkali-Metal Atomic-Transition Lasers

Golger et al. (Reference 130) recently proposed a scheme for direct solar pumping of an atomic-transition alkali-metal laser. Their calculations estimate that an extractable laser power of ≈ 7 kW is obtainable from a $0.4 \times 0.1 \times 25$ m^3 volume using a solar concentration ratio of 20 and a gas mixture consisting of cesium vapor and xenon gas. Operations at a temperature of 650°K gives a cesium dimer (Cs_2) concentration $\sim 10^{15}$ cm^3. Absorption of part of the incident solar flux produces excited cesium molecules (CS_2^*) in the $A^1\Sigma_u^+$ state:

$$Cs_2(X^1\Sigma_g^+) + h\nu_{pump}(445-523 \text{ nm}) \rightarrow Cs_2^*(A^1\Sigma_u^+)$$
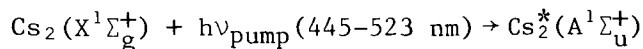
Collision induced dissociation then produces one Cs atom in the upper laser level ($7^2S_{1/2}$) and one Cs atom in the ground state ($6^2S_{1/2}$):

$$Cs_2^* + Xe \rightarrow Cs(7^2S_{1/2}) + Cs(6^2S_{1/2}) + Xe$$
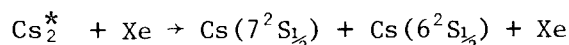
Stimulated emission is then possible between the 7S and 6P states:

$$Cs(7^2S_{1/2}) \rightarrow Cs(6^2P_{1/2}) + h\nu_{laser}(1358.9 \text{ nm})$$

$$\rightarrow Cs(6^2P_{3/2}) + h\nu_{laser}(1469.5 \text{ nm})$$
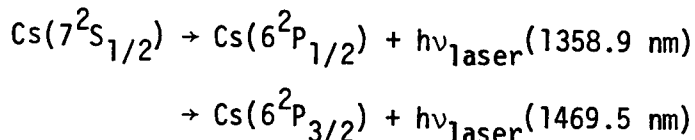
The lower lasing level $[Cs(6^2P_{1/2,3/2})]$ cannot be depopulated radiatively because these are the resonant states and optical emission will not escape the medium efficiently. Instead, operation at high buffer gas pressure promotes formation of the rare-gas excimer CsRg:

$$Cs(6^2P_{1/2,3/2}) + Xe \rightarrow CsXe^{*(1,2)}$$

$$[\tau \sim 1 \text{ } \mu\text{sec removal rate at } P_{Xe} = 30 \text{ atm}]$$

Radiative de-excitation is followed immediately by dissociation of the repulsive ground state; this optical emission is not absorbed by the medium:

$$CsXe^{*(1,2)} \rightarrow CsXe + h\nu_{1,2} \rightarrow Cs + Xe$$

The atmospheric transmission efficiencies of both wavelengths emitted by this laser, however, are very poor. Analogous kinetic schemes for the other alkali-metal atoms were examined to determine if more favorable transitions exist, as listed in Table 3.7-11. Operation with Li, Na, or K will be difficult because of the te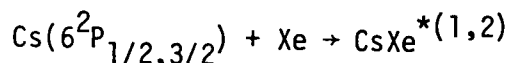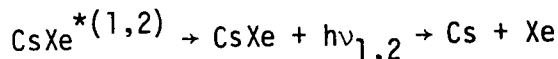mperatures required to maintain the necessary vapor pressures and because excitation of the X→A transition requires ultraviolet light. The Rb line at 1.3237 μm may yield a viable alternative. Detailed kinetic modeling will be necessary to establish the operating parameters of this system, and atmospheric propagation calculations are needed to quantitize the transmission efficiency.

Rare-Earth Vapor-Complex Lasers

Lasing on various electronic states in rare-earth, actinide, and transition metal ions held in an insulating crystal host is well known and highly documented. More recently, the trivalent rare-earth lanthanides have been investigated (References 131-135). In an effort to develop flowing gas lasers having superior performance compared with their solid-state counterparts. In particular, high average-power operation is possible if waste heat can be removed in a flow cycle, and the stringent system constraints dictated by nonlinear optical properties of the solid-state host can be relaxed.

Gaseous trivalent rare earths (RE^{3+}) which have been investigated include two component transition metal-trihalide molecular complexes (e.g., $RECl_3 \cdot (AlCl_3)_x$) that are generated thermochemically (References 131-134) and $RE(thd)_3$ chelates (Reference 135). The former complexes require an operating temperature of 800°K to achieve an RE^{3+} concentration of about 5×10^{17} ions/cm3; by contrast, the RE(thd)

Table 3.7-11. Alkali-Metal Atomic Transitions Pumped by
Photodissociation of Alkali Dimer States

Atom	Transition	ν, cm^{-1}	λ, μm	Transmission Efficiency*
Li	$3^2S_{1/2} \rightarrow 2^2P_{1/2}$	12302.5	0.8128	excellent
	$\rightarrow 2^2P_{3/2}$	12302.1	0.8129	excellent
Na	$4^2S_{1/2} \rightarrow 3^2P_{1/2}$	8783.7	1.1385	very poor
	$\rightarrow 3^2P_{3/2}$	8766.5	1.1407	poor
K	$5^2S_{1/2} \rightarrow 4^2P_{1/2}$	8041.6	1.2435	excellent
	$\rightarrow 4^2P_{3/2}$	7983.9	1.2525	fair
Rb	$6^2S_{1/2} \rightarrow 5^2P_{1/2}$	7554.6	1.3237	fair
	$\rightarrow 5^2P_{3/2}$	7317.0	1.3667	very poor
Cs	$7^2S_{1/2} \rightarrow 6^2P_{1/2}$	7358.9	1.3589	very poor
	$\rightarrow 6^2P_{3/2}$	6805.0	1.4695	very poor

*Estimated based on the HITRAN spectral curves given in R. A. McClatchey
and J. E. A. Selby, "Atmospheric attenuation of laser radiation from
0.76 to 31.25 µm," AFCRL-TR-74-0003 (1974); excellent -- >95%,
fair -- 50-90%, poor -- <10%, very poor -- ≈0% (attenuation due to
molecular absorption only).

chelates (2,2,6,6-tetramethyl-3,5-heptanedione) have a significantly higher
vapor pressure and permit a low operating temperature, i.e., 10 torr at about
230°C. Furthermore, the RE(thd)$_3$ chelates are thermally stable and optically
resilient so that prolonged operation appears feasible (Reference 135). To
date, only neodymium (Nd^{3+}) and terbium (Tb^{3+}) complexes lasing at 1.06 µm and
0.545 µm, respectively have been studied. Collisional deactivation rates and
radiative lifetimes are suitable for pulsed operation with possible laser-
fusion applications.

CW operation of other rare-earth vapor complexes may be possible using
other lasing ions having transition wavelengths more suited to efficient
atmospheric propagation. Numerous possibilities exist, as illustrated by the
transitions shown in Figures 3.7-18 and 3.7-19. In particular, the
Dy^{2+}($^5I_7 \rightarrow ^5I_8$) transition at 2.06 µm, and the Er^{3+}($^4I_{13/2} \rightarrow ^4I_{15/2}$) transition
at 1.62 µm are interesting possibilities. It remains to be determined if
their radiative lifetimes are sufficiently long and their collisional deacti-
vation rates are sufficiently small to permit cw operation. All of these ions
have strong absorption structure in the visible and near infrared so that
pumping via concentrated solar radiation may be possible. The kinetics of
each lasing compound must be examined in detail to determine if direct solar
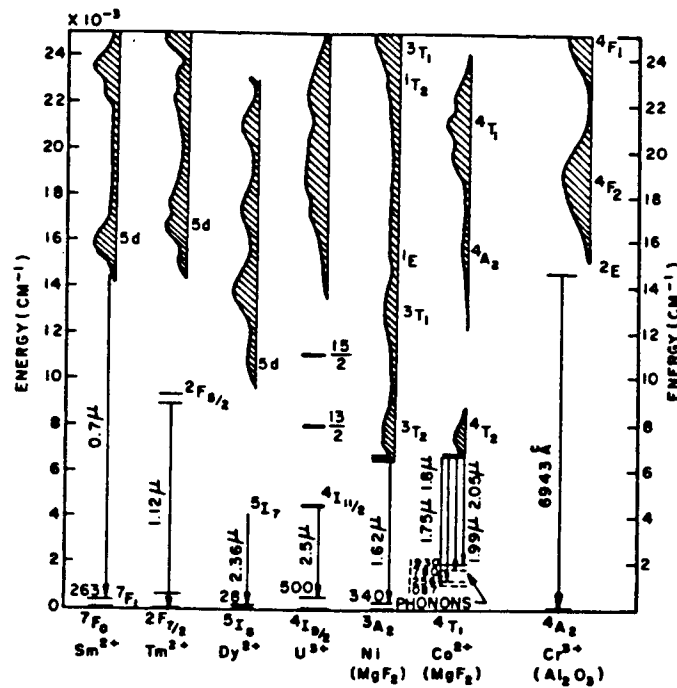pumped laser operation is feasible.

Figure 3.7-18. Energy Levels and Laser Transitions of Divalent
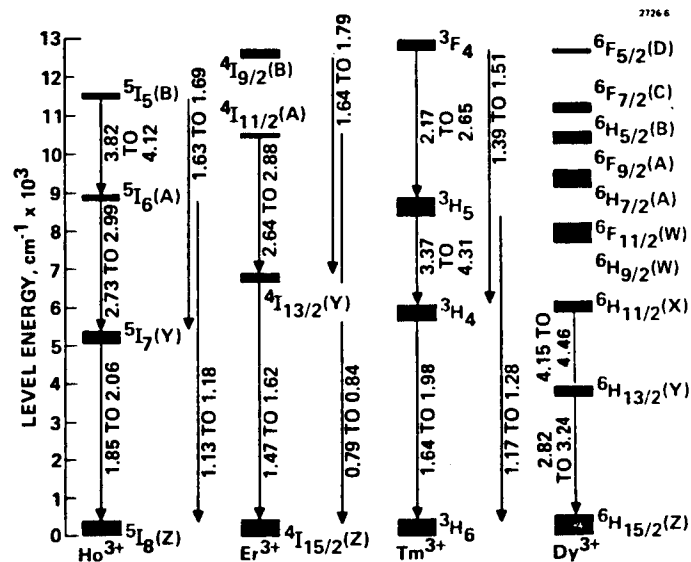Rare-Earth, Actinide, and Transition Metal Ions

Figure 3.7-19. Energy Levels and Laser Transitions of Trivalent
Rare-Earth Ions

3-236

Conclusions and Recommendations

Photoexcited E-V transfer lasers, optically pumped alkali-metal atomic-transition lasers, and rare-earth vapor-complex lasers have been discussed as potential candidates for direct solar excitation and application to the SPS concept. The $Br*-^{13}C^{16}O_2$ E-V transfer laser, which was kinetically modeled in some detail, is not a viable concept because of its small lasing mode power density and large thermal-energy generation rate. The $Br*$-HCN laser is a better candidate, although the problems associated with waste-heat management may be insurmountable. In particular, E-V lasers using molecules such as CO_2 and HCN must operate at low temperature ($<400°K$), requiring waste-heat radiators with large areas. The optically pumped atomic-transition Rb laser and various (Dy^{2+}, Ho^{3+}, Er^{3+}) rare-earth vapor-complex lasers were also identified as potential SPS candidates, although detailed modeling was not performed. Kinetic data for various radiative and collisional processes are unknown for many of the excited states of interest and further experimental research is warranted. Sufficient information exists, however, to determine if direct solar pumping is feasible and if the laser operating parameters are appropriate for the SPS.

A number of additional laser candidates exist which were not considered in this study. Because the viability of the overall laser-SPS concept hinges on finding a suitable advanced laser system capable of achieving a satellite specific mass $\lesssim 5$ kg/kW (Reference 113), further research is needed to adequately model both the Rb atomic-transition laser and the rare-earth vapor-complex lasers as well as all other potentially viable laser schemes involving direct pumping.

3.8 REFERENCES

1. *Development of High Efficiency Stacked Multi-Bandgap Solar Cells (SMBSC)*, Contract F33615-78-C2036; 24-month program initiated August 1, 1978.

2. Jackson, E.D., *Transaction of the Conference on the Use of Solar Energy*, Tucson Arizona, 1955, p. 111, also U.S. Patent No. 2,949,498, issued August 16, 1960.

3. Shockley, W. and H. Dueisser, J. Appl. Phys. 32, 1961, p. 510.

4. Iles, Peter; Applied Solar Energy Corp., personal communication, 31 July 1979.

5. *Satellite Power System (SPS) Power Distribution Study, Final Report to Rockwell International Corporation*, Advanced Energy Systems Division of Westinghouse Electric Corporation, Pittsburgh, Pa., M9L8GDS-897407D (March 1980).

6. *Satellite Power Systems (SPS) Concept Definition Study*; Rockwell International; Final Report (Exhibit C) Vol. II, pp. 2-25 through 2-27 (March 1979).

7. *Satellite Power Systems (SPS) Concept Definition Study, System Engineering,* Part 1, Vol. II, Rockwell International, SSD 79-0010-2-1 (March 1979).

8. *Space Construction Fabrication Experiment Definition Study, Final Report,* Vol. II, CASD-ASP77-017 (May 1978).

9. *Development of a Composite Geodetic Structure for Space Construction, Phase I,* Final Briefing, Contract NAS9-15678, McDonnell Douglas Corp., September 1977.

10. Gatewood, B.F., *Thermal Stresses,* McGraw Hill, Inc. (1957).

11. Timoshenko, S., *Theory of Elastic Stability,* McGraw Hill, Inc.

12. Smith, William H. and Leeds, Donald H., *Pyrolytic Graphite,* in Modern Materials, V. 7, Academic Press, N.Y., 1970.

13. Brown, William C., *Satellite Power System (SPS) Magnetron Tube Assessment Study*—Monthly Report No. 4, Raytheon Report PT-5575 (NAS8-33157), dated 25 February 1980.

14. Love, A.W., *Quadratic Phase Error Loss in Circular Apertures,* Electronics Lett., Vol. 15, No. 10, pp. 276-277, 10 May 1979.

15. Hansen, R.C., *A One-Parameter Circular Aperture Distribution with Narrow Beamwidth and Low Sidelobes,* IEEE Trans. Antenna Propagation, Vol. AP-24, pp. 477-480, July 1976.

16. Subcontract to Rockwell International, Agreement for Services, No. M9L 8GDS-897405D (completed January 1980).

17. Roulston, D.J., Hajj, I.N., and P.R. Bryant, *Design and Evaluation of High Efficiency Si and GaAs Bipolar Transistors and of their Performance in Class C and Class E Circuits used for Microwave Transmission in the Satellite Power System.* Prepared for Rockwell International, Dec. 1978.

18. Hajj, I.N., Roulston, D.J., and P.R. Bryant, *Generation of Transient Response of Nonlinear Bipolar Transistor Circuits from Device Fabrication Data.* IEEE Jnl. Solid-State Circuits, SC-12, pp. 29-38 (Feb. 1977).

19. Roulston, D.J., Chamberlain, S.G., and J. Sehgal, *Simplified Computer-Aided Analysis of Double Diffused Transistor including Two-Dimensional High-Level Effects,* IEEE Trans. Electron Devices, ED-19, pp. 809-820 (June 1972).

20. Roulston, D.J., Chamberlain, S.G., Bryant, P.R., Hajj, I.N., and P. Dufond, *Computer-Aided Analysis of Nonlinear JFET Amplifiers from Device Fabrication Data,* IEEE Jnl. Solid-State Circuits, SC-13, pp. 266-268 (April 1978).

21. Dufond, P., and H. Derewenko, *Characterization of Power Microwave FET,* 6th European Microwave Conference, Rome, Italy; Paper 554.1 (Sept. 1976).

22. Kennedy, D.P. and R.R. O'Brien, *Computer-Aided Two-Dimensional Analysis
of the Junction Field Effect Transistor*, IBM Jnl., Res. Development, <u>14</u>,
pp. 95-116 (1971).

23. Kohn, E., *Power Handling Capability of GaAs MESFETs*, Electronics Letters,
<u>14</u>, No. 24, pp. 786-788 (November 1978).

24. Roulston, D.J., *Junction Field Effect Transistor*, Chapter 8.3, in
<u>Microwave Integrated Circuits</u>; Ed. Gupta and Singh, Wiley Eastern (1974).

25. Yamaguchi, K., Asai, S., and H. Kodera, *Two Dimensional Numerical Analysis
of Stability Criteria of GaAs FETS*, IEEE Trans. Electron Devices, ED-23,
pp. 1283-1290 (December 1976).

26. Dilorenzo, J.V. and W.R. Wisseman, *GaAs Power MESFETs: Design, Fabrication,
and Performance*, IEEE Trans. MTT, MTT-27, pp. 367-378 (May 1979).

27. Skolnik, M.I. and D.D. King, *Self-Phasing Array Antennas*, IEEE Trans. on
Antennas and Propagation, pp. 142-149 (March 1964).

28. Chernoff, R.C., *Large Active Retrodirective Array for Space Application*,
IEEE Trans. on Antennas and Propagation, pp. 489-496 (July 1979).

29. Lawrence, R.S., Little, C.G. and H.J. Chivers, *A Survey of Ionospheric
Effects upon Earth-Space Radio Propagation*, Proc. IEEE, pp. 4-27
(January 1964).

30. Raytheon Report No. ER79-4032, *Solar Power Satellite (SPS) Pilot Beam
and Communication Link Subsystem Investigation Study—Phase 1*, Contract
NAS8-33157 (January 31, 1979).

31. Boeing Report No. D180-24635-1, *Microwave Power Transmission System*
(1978).

32. Burns, A.A. and E.J. Fremouw, *A Real-Time Correction Technique for
Transionospheric Ranging Error*, IEEE Trans. on Antennas and Propagation,
pp. 785-790 (November 1970).

33. Papoulis, A., *Probability, Random Variables and Stochastic Processes*,
McGraw-Hill, New York, p. 501 (1965).

34. Van Trees, H.L., *Detection, Estimation and Modulation Theory*,
Wiley, New York, p. 197 (1968).

35. Wheeler, Harold A., *Transmission Line Properties of a Stripline between Parallel Planes*, IEEE Transactions on Microwave Theory and Techniques, Vol. MIT-26, No. 11 (November 1978).

36. Brown, W.C., *High Power Generators of the Cross-Field Type*, Jnl. Microwave Power, Vol. 5, pp. 245-259 (Dec. 1970).

37. Briefing document by Raytheon, *Cross-Field Directional Amplifier for Use in the Solar Power Satellite*; to NASA/JSC and NASA/MSFC (Sept. 1978).

38. Brown, W.C., *SPS Magnetron Tube Assessment Study*, NAS8-3327, Progress Reports No. 1 through 6 (Nov. 1979—April 1980).

39. Mohr, R.J., *Some Design Aspects of Components Utilizing Symmetric 3-dB Hybrids*, Microwave Jnl., June 1962.

40. Schroeder, K.G., Carlisle, R.L. and C.Y. Tomita, *The Resonant Cavity Radiator (RCR)*, in paper summaries of the Workshop on Microwave Power Transmission and Reception, NASA/JSC (Jan. 15-18, 1980).

41. Brown, W.C., *Progress Report on the Adapting of the Cross-Field Directional Amplifier to the Requirements of the SPS*, presented at the Workshop on Microwave Power Transmission and Reception, NASA/JSC (Jan. 15-18, 1980).

42. Beverly, R.E. III, *SPS Laser Impact Studies*, Tech. Memo, Rockwell International, SSD 80-   ; performed under subcontracts M9M 8BNB-896662D (1979) and MOL 8GNS-897409D (1980).

43. Beverly, R. E. III, *Laser-SPS Systems Analysis and Environmental Impact Assessment*, submitted to Space Solar Power Review (1980).

44. Gebhardt, F.G., *High Power Laser Propagation*, Appl. Opt. 15, 1479 (1976).

45. Ruppersberg, G.H., et al., *Calculations About the Transmittance Window of Clouds and Fog at about 10.5 μm Wavelength*, Atmos. Environ. 9, 723 (1975).

46. Orlov, A.P. et al., *Aircraft Studies of Vertical Infrared Extinction Profiles in the 10-12 μm Window*, Izv. Acad. Sci. USSR Atmos. Oceanic Phys. 12, 433 (1976).

47. Tomasi, C. and Tampieri, F., *Size Distribution Models of Small Water Droplets in Mist and their Volume Extinction Coefficients at Visible and Infrared Wavelengths*, Atmos. Environ. 10, 1005 (1976).

48. Bukatyi, V.I. and Pogodaev, V.A., *Evaporation of a Water Drop by IR Radiation*, Sov. Phys. J., No. 1, 119 (1970).

49. Glicker, S.L., *Propagation of a 10.6-μ Laser through a Cloud including Droplet Vaporization*, Appl. Opt. 10, 644 (1971).

50. Lamb, G.L. Jr. and Kinney, R.B., *Evaporation of Mist by an Intense Light Beam*, J. Appl. Phys. 40, 416 (1969).

51. Mullaney, G.J. et al., *Fog Dissipation using a CO$_2$ Laser*, Appl. Phys. Lett. 13, 145 (1968).

52. Kuzikovskii, A.V. and Khmelevitsov, S.S., *Kinetics of the Evaporation of an Aqueous Aerosol in an Optical Radiation Field*, Izv. Acad. Sci. USSR Atmos. Oceanic Phys. 4, 206 (1968).

53. Shifrin, K.S. and Zolotova, Zh.K., *Kinetics of the Evaporation of Drops in a Radiation Field*, Izv. Acad. Sci. USSR Atmos. Oceanic Phys. 2, 800 (1966).

54. Sutton, G.W., *Fog Dispersal by High-Power Lasers*, AIAA J. 8, 1907 (1970).

55. Kuzikovskii, A.V., *Dynamics of a Spherical Particle in an Intense Optical Field*, Sov. Phys. J., No. 5, 615 (1970).

56. Kuzikovskii, A.V. et al., *Evaporation of a Drop of Water under the Influence of a Pulse of Light*, Sov. J. Engr. Phys. 20, 12 (1971).

57. Zuev, V.E. et al., *Effect of Heating Water Droplets by Optical Radiation*, Sov. Phys. Dokl. 17, 765 (1973).

58. Belyayev, V.P. et al., *Observational Studies of the Clearing of Fog by Laser Radiation at λ = 10.6 μm*, Izv. Acad. Sci. USSR Atmos. Oceanic Phys. 11, 678 (1975).

59. Harney, R.C., *Hole-Boring in Clouds by High Intensity Laser Beams: Theory*, Appl. Opt. 16, 2974 (1977).

60. Sukhorukov, A.P. and Shumilov, E.N., *Brightening of a Polydisperse Fog*, Sov. Phys. Tech. Phys. 18, 650 (1973).

61. Sukhorukov, A.P. et al., *Dynamics of Clearing Clouds with a Laser Beam*, JETP Lett. 14, 161 (1971).

62. Volkovitskii, O.A., *Experimental Studies of the Effect of CO$_2$-Laser Emission upon the Cloud Droplet Medium (in Russian)*, Meteor. Hydrol. (USSR) 9, 9 (1977).

63. Gordin, M.P. and Strelkov, G.M., *The Passage of Laser Radiation through a Fine-Droplet Water Aerosol*, Radio Eng. Electron. Phys. (USSR) 20, 1 (1975a).

64. Caledonia, G.E. and Wray, K.L., *Aerosol Propagation Effects*, Physical Sciences, Inc., Final Report on Contract N00014-74-C-0254 (1974).

65. Semenov, L.P. and Svirkunov, P.N., *Evaporation of a Drop in the Presence of a Considerable Internal Heat Release (in Russian)*, Tr. Inst. Eksp. Meteorol., No. 23, 91 (1971).

66. Bedair, S.M. and Aly, S.S., *Fog Dissipation using 10.6 μm Radiation*, Infrared Phys. 15, 233 (1975).

67. Bukatyi, V.I. et al., *Thermal Effects of Intense Light Beams on Droplet Aerosols*, Sov. Phys. Dokl. 19, 425 (1975).

68. Romanov, G.S. and Pustovalov, V.K., *Transillumination of a Water Droplet Containing Cloudy Atmosphere with an Intensive Monochromatic Radiation*, J. Appl. Spectrosc. 19, 1072 (1973).

69. Sutton, G.W., *Fog Hole Boring with Pulsed High-Energy Lasers: An Exact Solution including Scattering and Absorption*, Appl. Opt. 17, 3424 (1978).

70. Friedmann, D. et al., *Nonlinear Transmission of Fog for Laser Light*, J. Appl. Phys. 50, 5998 (1979).

71. Almayev, R. Kh. et al., *The Temperature and Water Content in the Cloud Clearance Zone*, Izv. Acad. Sci. USSR Atmos. Oceanic Phys. 14, 208 (1978).

72. Volkovitskii, O.V. et al., *Turbidizing Effect of CO_2 Laser Radiation on Crystalline Clouds*, Izv. Acad. Sci. USSR Atmos. Oceanic Phys. 11, 543 (1975).

73. Akhmanov, S.A. et al., *Thermal Self-Actions of Laser Beams*, IEEE J. Quant. Electron. QE-4, 568 (1968).

74. Bukatyi, V.I. et al., *Thermal Defocusing of the Optical Radiation Traveling in an Absorbing Disperse Medium*, Sov. J. Quant. Electron. 3, 37 (1973).

75. Kolosov, V.V. and Kuzikovskii, A.V., *Focusing and Defocusing of Light in an Aerosol exploded by a Laser Beam*, Sov. Phys. Tech. Phys. 24, 56 (1979).

76. Nerushev, A.F. and Semenov, L.P., *Propagation of a Light Beam in an Evaporating Liquid-Drop Medium in the Presence of Wind Refraction*, Sov. J. Quant. Electron. 6, 665 (1976).

77. Svirkunov, P.N., *Possibility of Self-Focusing in the Evaporation of a Cloud Medium by CO_2 Laser Radiation*, Sov. J. Quant. Electron. 8, 509 (1978).

78. Vorob'yev, V.V. and Shemetov, V.V., *Forced Convection in the Atmosphere due to Absorption of Luminous Radiation*, Izv. Acad. Sci. USSR Atmos. Oceanic Phys. 11, 186 (1975).

79. Gordin, M.P. and Strelkov, G.M., *Supercondensation Effect in Diffusion Evaporation of a Water Aerosol in Radiation Field*, Sov. J. Quant. Electron. 5, 315 (1975b).

80. Kuzikovskii, A.V. and Khmelevitsov, S.S., *Influence of Overcondensation on the Evaporation of a Water Aerosol in a Radiation Field*, Izv. Acad. Sci. USSR Atmos. Oceanic Phys. 11, 219 (1975).

81. Volkovitskii, O.A. et al., *Optical 'Dimming' of Cloud Medium due to Interaction with CO_2 Laser Radiation*, Sov. J. Quant. Electron. 6, 215 (1976).

82. Shettle, E.P. and Fenn, R.W., *Models of Atmospheric Aerosols and their Optical Properties*, AGARD Conf. Proc. 183, Optical Propagation in the Atmosphere. Available from NTIS, Springfield, VA.

83. Ruck, G.T., personal communication (1980).

84. van de Hulst, H., *Light Scattering by Small Particles*, John Wiley and Sons, N.Y. (1964).

85. McCartney, E.J., *Optics of the Atmosphere, Scattering by Molecules and Particles*, John Wiley and Sons, N.Y. (1976).

86. Chýlek, P., *Extinction and Liquid Water Content of Fogs and Clouds*, J. Atmos. Sci. 35, 296 (1978).

87. Pinnick, R.G. et al., *Verification of a Linear Relation between Air Extinction, Absorption and Liquid Water Content of Fogs*, J. Atmos. Sci. 36, 1577-1586 (see also U.S. Army Atmospheric Sciences Laboratory Report No. ASL-TR-0037); 1979.

88. Kumai, M., *Arctic Fog Droplet Size Distribution and its Effect on Light Attenuation*, J. Atmos. Sci. 30, 635 (1973).

89. Kunkel, B.A., *Fog Drop-Size Distributions measured with a Laser Hologram Camera*, J. Appl. Meteor. 10, 482 (1971).

90. Garland, J.A., *Some Fog Droplet Size Distributions obtained by an Impaction Method*, Quart. J. R. Met. Soc. 97, 483 (1971).

91. Garland, J.A. et al., *A Study of the Contribution of Pollution to Visibility in a Radiation Fog*, Atmos. Environ. 7, 1079 (1973).

92. Roach, W.T. et al., *The Physics of Radiation Fog: I—A Field Study*, Quart. J. R. Met. Soc. 102, 313 (1976).

93. Pinnick, R.G. et al., *Vertical Structure in Atmospheric Fog and Haze and its Effects on Visible and Infrared Extinction*, J. Atmos. Sci. 35, 2020-2032 (see also U.S. Army Atmospheric Sciences Laboratory Report No. ASL-TR-0010); 1978.

94. Chu, T.S. and Hogg, D.C., *Effects of Precipitation on Propagation at 0.63, 3.5, and 10.6 microns*, Bell Sys. Tech. J. 47, 723 (1968).

95. Rensch, D.B. and Long, R.K., *Comparative Studies of Extinction and Backscattering by Aerosols, Fog, and Rain at 10.6 and 0.63 microns*, Appl. Opt. 9, 1563 (1970).

96. Goodmann, J., *The Microstructure of California Coastal Fog and Stratus*, J. Appl. Meteor. 16, 1056 (1977).

97. Pilié, R.J. et al., *The Life Cycle of Valley Fog, Part II; Fog Microphysics*, J. Appl. Meteor. 14, 364 (1975).

98. Nilsson, B., *Meteorological Influence on Aerosol Extinction in the 0.2-40-μm Wavelength Range*, Appl. Opt. <u>18</u>, 3457 (1979).

99. Deirmendjian, D., *Electromagnetic Scattering on Spherical Polydispersions*, American Elsevier, N.Y.

100. Carrier, L.E. et al., *The Backscattering and Extinction of Visible and Infrared Radiation by Selected Major Cloud Models*, Appl. Opt. <u>6</u>, 1209 (1967).

101. Yamamoto, G. et al., *Table of Scattering Function of Infrared Radiation for Water Clouds*, NOAA Report No. COM-71-50312 (1971).

102. Kuhn, P.M. and Weickmann, H.K., *High Altitude Radiometric Measurements of Cirrus*, J. Appl. Meteor. <u>8</u>, 147 (1969).

103. Guzzi, R. et al., *Sun Spectra through Optically Thin Clouds*, J. Atmos. Sci. <u>31</u>, 251 (1974).

104. Georgiyevskii, Yu. S. and Shukurov, A. Kh., *Certain Results of Measurements of the Transmission of Thin Clouds in the Visible and Infrared*, Izv. Acad. Sci. USSR Atmos. Oceanic Phys. <u>10</u>, 53 (1974).

105. Hall, F.F. Jr., *The Effect of Cirrus Clouds on 8-13 μm Infrared Sky Radiance*, Appl. Opt. <u>7</u>, 891; *Physical Model of Cirrus 8-13 μm Infrared Radiance*, Appl. Opt. <u>7</u>, 2264 (1968).

106. Wilson, R.W. and A.A. Penzias, *Effect of Precipitation on Transmission through the Atmosphere at 10 microns*, Nature <u>211</u>, 1081 (1966).

107. Sokolov, A.V., *Attenuation of Visible and Infrared Radiation in Rain and Snow*, Radio Eng. Electron. Phys. (USSR) <u>15</u>, 2175 (1970).

108. Nakajima, S. et al., *Propagation of the Laser Light in Snowfall*, Electron. Commun. Japan <u>56B</u>, 79 (1973).

109. McClatchey, R.A. and D'Agati, A.P., *Atmospheric Transmission of Laser Radiation: Computer Code LASER*, Air Force Geophysics Laboratory Report No. AFGL-TR-78-0029 (1978).

110. McClatchey, R.A. et al., *AFCRL Atmospheric Line Parameters Compilation*, Air Force Geophysics Laboratory Report No. AFCRL-TR-73-0096 [The latest version of the computer tape (October 1978) was used in these calculations] (1973).

111. Lund, I.A., *Persistance and Recurrence Probabilities of Cloud-Free and Cloudy Lines of Sight through the Atmosphere*, J. Appl. Meteor. <u>12</u>, 1222 (1973b).

112. Lund, I.A. and Shanklin, M.D., *Universal Methods for Estimating Probabilities of Cloud-Free Lines of Sight through the Atmosphere*, J. Appl. Meteor. <u>12</u>, 28 (1973).

113. Beverly, R.E. III, *SPS-Laser Environmental Impact Study*, Final Technical Report to Rockwell International Corporation, on Contract M9M 8BNB-896662D (1979); submitted to Space Solar Power Review.

114. Beverly, R.E. III, *Meteorological Effects on Laser Beam Propagation*, Final Technical Report to Rockwell International on Contract MOL-8GNS-897409D (1980).

115. Taussig, R. et al., *Design Investigation of Solar Powered Lasers for Space Applications*, Mathematical Sciences Northwest Final Technical Report to NASA Lewis Research Center on NAS3-21134 (1979).

116. Petersen, A.B., Wittig, C. and S.R. Leone, *Infrared Molecular Lasers pumped by Electronic-Vibrational Energy Transfer from Br ($4^2P_{1/2}$): CO_2, N_2O, HCN, and C_2H_2*, Appl. Phys. Lett. **27**, 305 (1975).

117. Grimley, A.J. and P.L. Houston, *Electronic to Vibrational Energy Transfer from I($5^2P_{1/2}$). I. HCl, HBr, and NO; II. H_2O, HDO, and D_2O; III. H_2, HD, and D_2*, J. Chem. Phys. **68**, 3366 (1978); **69**, 2339 (1978); **70**, 4724 (1979).

118. Beverly, R.E. III, *Pressure-Broadened Iodine-Laser-Amplifier Kinetics and a Comparison of Diluent Effectiveness*, Opt. Commun., **15**, 204 (1975).

119. Fisk, G.A., *The Effects of Chemical Kinetics and Starting Material Regeneration on the Efficiency of the Iodine Laser Amplifier*, Sandia Laboratories Report No. SAND77-0880 (1977).

120. Petersen, A.B., Wittig, C. and S.R. Leone, *Electronic-to-Vibrational Pumped CO_2 Laser Operating at 4.3, 10.6, and 14.1 μm*, J. Appl. Phys. **47**, 1051 (1976).

121. Petersen, A.B. and C. Wittig, *Line-Tunable CO_2 Laser Operating in the Region 2280-2360 cm-1 Pumped by Energy Transfer from Br($4^2P_{1/2}$)* J. Appl. Phys. **48**, 3665 (1977).

122. Hariri, A. and C. Wittig, *Electronic to Vibrational Engery Transfer from Br($4^2P_{1/2}$) to CO_2, COS, and CS_2*, J. Chem. Phys. **67**, 4454 (1977).

123. Reisler, H. and C. Wittig, *Temperature Dependence of Electronic to Vibrational Energy Transfer from Br($4^2P_{1/2}$) to $^{12}CO_2$ and $^{13}CO_2$*, J. Chem. Phys. **69**, 3729 (1978).

124. Leone, S.R. and F.J. Wodarczyk, *Laser-Excited Electronic-to-Vibrational Energy Transfer from Br($4^2P_{1/2}$) to HCl and HBr*, J. Chem. Phys. **60**, 314 (1974).

125. Reisler, H. and C. Wittig, *Temperature Dependence of the Quenching of Br($4^2P_{1/2}$) by CO_2 and HCl with Accompanying Vibrational Excitation*, J. Chem. Phys. **68**, 3308 (1978).

126. Petersen, A.B., Braverman, L.E. and C. Wittig, *H_2O, NO, and N_2O Infrared Lasers pumped Directly and Indirectly by Electronic-Vibrational Energy Transfer*, J. Appl. Phys. **48**, 230 (1977).

127. Wodarczyk, F.J. and P.B. Sackett, *Electronic-to-Vibrational Energy Transfer from $Br(4^2P_{1/2})$ to HF*, Chem. Phys. <u>12</u>, 65 (1976).

128. Hariri, A., Petersen, A.B. and C. Wittig, *Electronic-Vibrational Energy Transfer from $Br(4^2P_{1/2})$ to HCN, and Deactivation of HCN(001)*, J. Chem. Phys. <u>65</u>, 1872 (1976).

129. Hariri, A. and C. Wittig, *Electronic to Vibrational Energy Transfer from $Br(4^2P_{1/2})$ to H_2O*, J. Chem. Phys. <u>68</u>, 2109 (1978).

130. Golger, A.L., Gudzenko, L.I. and S.I. Yakovlenko, *Direct Conversion of Solar Energy into Laser Radiation,* Sov. J. Quant. Electron. <u>8</u>, 1118 (1978).

131. Jacobs, R.R., Krupke, W.F., Hessler, J. P. and W.T. Carnall, *Deactivation of the $Nd^{3+}(4F_{3/2})$ Level in Neodymium Chloride-Aluminum Chloride Vapor Complexes*, Opt. Commun. <u>21</u>, 395 (1977).

132. Jacobs, R.R. and W.F. Krupke, *Trivalent Rare Earth Molecular Vapor Laser Systems*, in <u>Electronic Transition Lasers II</u>; L. E. Wilson, S. N. Suchard, and J. I. Steinfeld, eds. (MIT Press, Cambridge, MA, 1977), pp. 246.

133. Jacobs, R.R. and W.F. Krupke, *Optical Gain at 1.06 μm in the Neodymium Chloride-Aluminum Chloride Vapor Complex*, Appl. Phys. Lett. <u>32</u>, 31 (1978).

134. Jacobs, R.R. and W.F. Krupke, *Kinetics and Fusion Laser Potential for the Terbium Chloride-Aluminum Chloride Vapor Complex*, Appl. Phys. Lett. <u>35</u>, 126 (1979).

135. Jacobs, R.R. and W.F. Krupke, *Excited-State Kinetics for $Nd(thd)_3$ and $Tb(thd)_3$ Chelate Vapor and Prospects for Fusion Laser Media*, Appl. Phys. Lett. <u>34</u>, 497 (1979).